Université de Paris 6, Pierre & Marie Curie
UFR 924 : Applications de la Physique

Mémoire

présenté en vue du diplôme

d'Habilitation à Diriger des Recherches

spécialité : *Astrophysique*

par

Gary Allan MAMON

Statistique des interactions dans l'Univers : des molécules aux galaxies

Soutenu le 3 juillet 2000 à l'Institut d'Astrophysique de Paris
devant le jury composé de :

Patrick BOISSÉ	Professeur, Université de Paris 6	Rapporteur
Guy MATHEZ	Directeur de Recherches, Observatoire Midi-Pyrénées	Rapporteur
Joseph SILK	Professor, University of Oxford	Rapporteur
Françoise COMBES	Astronome, Observatoire de Paris	Examinateur
Daniel GERBAL	Directeur de Recherches, Institut d'Astrophysique	Examinateur
Eduard SALVADOR-SOLÉ	Professor, Universitat de Barcelona	Examinateur
Simon D. M. WHITE	Professor, Max Planck Institut für Astrophysik	Examinateur

Table des matières

Table des figures

Remerciements

Je voudrais profiter de ce mémoire pour remercier un grand nombre de personnes qui m'ont aidé à poursuivre mes recherches.

Je remercie d'abord Daniel Gerbal et Chantal Balkowski qui m'ont accueilli en France et œuvré pour mon recrutement, et Lucienne Gouguenheim pour m'avoir fortement soutenu pour mon recrutement comme astronome-adjoint en 1990. Merci encore à Alain Omont et Michel Dennefeld qui m'ont invité à l'IAP.

Puis je voudrais remercier Al Glassgold pour m'avoir enseigné la belle physico-chimie des enveloppes circumstellaires, Alain Blanchard qui m'a presque tout appris en cosmologie et Mark Henriksen, qui m'a introduit à l'astronomie en rayons X. Merci à Daniel Gerbal et à Florence Durret pour l'apport de critiques constructives sur mes travaux. Merci aussi à Jim Bartlett, Matthew Colless, Gus Evrard, Bernard Fort, Bruno Guiderdoni, Mark Henriksen, Cedric Lacey, Ofer Lahav, Trevor Ponman, Boud Roukema, Will Saunders, Joe Silk, François Simien, Ed Turner, Patrick Valageas, David Valls-Gabaud, Simon White et probablement encore beaucoup d'autres pour des nombreuses discussions fructueuses. J'ai eu beaucoup de plaisir à diriger les thèses de doctorat de Sergio Dos Santos et Barbara Lanzoni, qui m'ont chacun beaucoup appris, et qui, j'espère, continueront à m'apprendre des choses.

Merci à Nicolas Epchtein, Alain Omont et Guy Simon pour leur confiance dans mes travaux sur DENIS et Brian Boyle pour m'avoir associé au groupe de travail du 6dF. D'ailleurs, je remercie Brigitte Rocca-Volmerange pour m'avoir poussé à considérer le télescope UKST pour les suivis spectroscopiques de DENIS et 2MASS.

Je voudrais encore remercier Catherine Grenet, Jean-François Sygnet et Georges Debève pour la maintenance de l'excellent service informatique de l'IAP et Jean Borsenberger et Lionel Provost pour le centre de traitements parisien des données DENIS. Je voudrais particulièrement remercier Jean pour l'excellent travail qu'il a fourni en amont sur les images DENIS, ainsi que Emmanuel Bertin pour son aide avec son excellent logiciel SExtractor.

J'ai eu la chance de trouver un comité d'habilitation à l'UFR 924 de l'Université Paris 6 (Pierre et Marie Curie), d'une grande flexibilité et gentillesse, et je tiens donc à remercier ses deux membres, Georges Alquié et Hubert Cachet. Et un merci à Julien Devriendt qui a eu la bonne idée de laisser ses macros LaTeX disponibles en lecture, car j'ai pu ainsi les adapter à l'écriture de ce mémoire.

J'ai eu aussi beaucoup de chance d'avoir trouvé un jury de très grande qualité et je remercie donc Patrick Boissé, Françoise Combes, Daniel Gerbal, Guy Mathez, Eduard Salvador-Solé, Joe Silk et Simon White, pour avoir tous accepté, sans hésiter, d'en faire partie. J'en profite pour m'excuser d'avance pour toute souffrance liée à la lecture de ce manuscrit et pour leur remercier d'avance pour toutes les questions intéressantes qu'ils me poseront. Je leur remercie aussi des commentaires sur le fond et les erreurs typographiques ou de français.

Et puis, il me faut remercier le staff de la NASA ADS pour avoir conçu une base de données bibliographique si utile pour les astronomes, le staff de Los Alamos National Laboratories pour le très utile serveur de pré-prints, et Richard Stallman pour tous ses logiciels GNU, en particulier `emacs`.

Je voudrais exprimer ma très grande affection pour ma mère Enna et ma sœur Delia, pour leur soutien constant.

Je termine par un énorme merci et un grand message d'amour à mon épouse Gabrielle, qui a enduré, avec une très grande patience, bien des soirées et week-ends sans mari, et j'en profite pour immortaliser nos enfants adorés, Ariane, Daphné et Eliott, et je leur dis ce mot, adapté de Nietzsche :

L'être humain doit se surpasser !

Résumé

Je présente ici les travaux que j'ai effectués depuis 1985, l'année de mon doctorat. Ces travaux se subdivisent en cinq principales branches :

1) La chimie et le transfert de rayonnement dans les environnements circumstellaires (étoiles AGB, carbonées, et étoiles jeunes), avec la prédiction de la distribution radiale des abondances des atomes, ions, molécules, et certains ions moléculaires.

2) La formation et l'évolution des galaxies : sur-refroidissement, taux de coalescences et de collisions rapides (en fonction de la masse des galaxies, la richesse de leur environnement — groupes ou amas — et leur position dans ces structures), en vue de déterminer l'origine de la séquence de Hubble.

3) Les contraintes (dynamiques, cosmologiques et par observations de rayons X du plasma intergalactique) sur la nature des groupes compacts de galaxies. Ainsi, environ le quart des groupes compacts ont des dispersions de vitesses trop faibles pour être très denses en 3D et pourraient être causés par alignements fortuits de galaxies le long de la ligne de visée. Mais le taux de formation des groupes compacts semble suffisamment grand pour expliquer la plupart de ces systèmes comme bien denses en 3D.

4) L'Univers local en proche-IR, domaine spectral qui apporte une vision non-biaisée de la distribution de masse de l'Univers : relevé en imagerie DENIS de l'hémisphère austral (de plus grande fiabilité et complétude que les relevés optiques, et apportant une contrainte forte contre l'hypothèse d'un Univers fractal) et suivis spectroscopiques du 6dF, avec le but d'estimer précisément les champs de vitesse et de densité de matière de l'Univers local.

5) La densité de masse de l'Univers, mesurée par trois méthodes : la dynamique hors-équilibre des groupes de galaxies, leur fraction de baryons (mesurée par leur émission X) et l'application d'une règle, comobile avec l'expansion de l'Univers, aux structures de quasars à $z = 2$. Ces trois méthodes convergent vers $\Omega = 0.3$ et la dernière implique aussi une constante cosmologique non-nulle.

1 Introduction

1.1 Introduction générale

Le titre de cet exposé, *Statistique des interactions dans l'Univers : des molécules aux galaxies*, peut paraître présomptueux, et certes tous les aspects des interactions entre les échelles des molécules et celles des galaxies ne seront pas traitées ici. Néanmoins, il s'agira de montrer les résultats de modélisations sur 1) les *interactions chimiques* entre molécules dans les environnements circumstellaires, 2) les *interactions gravitationnelles* entre galaxies dans les groupes et amas de galaxies, et 3) la *statistique* de la distribution des galaxies à grande échelle.

On verra qu'il existe des liens entre ces trois grandes thématiques. Néanmoins, le premier thème apparaît quand même très différent des deux autres. On peut donc se demander ce qui peut pousser un astrophysicien à travailler sur des sujets apparemment si différents.

La raison est purement matérielle ! Après une thèse de doctorat poursuivie à l'Université de Princeton aux Etats-Unis sur les interactions gravitationnelles dans les groupes de galaxies, qui suivait elle-même un travail avec J. Binney (Oxford) sur la modélisation de la cinématique interne des galaxies elliptiques (Binney & Mamon 1982), des raisons personnelles m'ont contraint de chercher un travail postdoctoral sur la région de New York. J'ai eu la chance de recevoir le seul poste alors offert dans l'agglomération de la *Grande Pomme*, à l'Université de New York, où l'on faisait de l'astrophysique inter- et circumstellaire, et j'en ai donc profité pour m'initier aux vents circumstellaires. De retour en France, en 1988, je me suis remis à l'astrophysique extragalactique, mais mes collaborations sur les environnements circumstellaires avec A. Glassgold et P. Huggins (Université de New York) ont néanmoins continué, à un rythme certes décroissant.

L'approche des travaux qui vont être présentés est principalement *théorique*, mais avec une grande variété d'approches : des calculs simples sur le dos d'une enveloppe (Mamon 1992a), des calculs analytiques compliqués (Walke & Mamon 1989), des analyse de données observationnelles (Mamon 1989; Mamon et al. 1998), des calculs numériques (e.g. Glassgold et al. 1987), des simulations numériques (Mamon 1987; Lanzoni, Mamon, & Guiderdoni 2000), et des simulations d'images et de calculs sur ces images simulées (Harmon & Mamon 1993). Mais ces différentes approches théoriques sont généralement entreprises pour comparer, voire confronter à des observations, ou souvent sur des propriétés statistiques tirées d'observations.

1.2 Contexte global

L'Univers est un formidable laboratoire de physique, dans lequel se mêlent des objets de nature très différente, telles que les planètes solides comme la Terre ou fluides comme Jupiter; les étoiles avec des diverses réactions nucléaires en leur centre, et des divers phénomènes de transport dans leur photosphère et finalement des émissions radiales de particules appelées *vents*; les nuages de gaz et de poussières dans lesquels se forment ces étoiles; les

galaxies d'étoiles de morphologie visible plate comme les *galaxies spirales* et *lenticulaires* ou arrondie comme les *galaxies elliptiques*; les petits *groupes* ou grands *amas* de galaxies; les *très grandes structures* de galaxies dans l'Univers.

La compréhension de beaucoup de ces objets est liée aux autres familles d'objets. On peut raisonner en amont, en commençant par l'Univers primordial, caractérisé par un ensemble de paramètres qui peuvent être exprimés par les valeurs qu'ils atteignent dans l'Univers actuel. Ces paramètres sont le *taux actuel d'expansion* de l'Univers, H_0, le *paramètre de densité de masse*, Ω_0 (ou Ω_m où le 'm' signifie matière), qui représente la densité moyenne de l'Univers, normalisée à la *densité critique* $\rho_c^0 = 3H_0^2/(8\pi G)$ que devrait avoir l'Univers pour que son expansion continue indéfiniment, une *constante cosmologique*, Λ, qui dénote une densité en énergie sombre, $\lambda = \Omega_\Lambda = \Lambda/(3\,H_0^2)$, et un *spectre de fluctuations primordiales de densité*, $P(k)$. Les indices '0' représentent l'Univers actuel.

Après l'explosion du *Big Bang* (probablement suivi d'une époque courte d'expansion inflationnaire), l'Univers se refroidit. Environ 700 000 ans après le Big Bang, l'Univers est assez froid ($T \simeq 3000\,\mathrm{K}$) pour que les électrons des atomes d'Hydrogène (principal constituant de l'Univers) puissent se recombiner aux noyaux (protons) pour former ainsi des atomes neutres. Ce faisant, les photons, précédemment piégés par les électrons libres des atomes encore ionisés, viennent librement à nous en forme de fond cosmique micro-ondes, dit *CMB* (*Cosmic Microwave Fond Background* en anglais), dont l'émission nous parvient comme un corps noir de 2.73 K, qui trace l'époque de la *recombinaison* à laquelle l'Univers avait une température de $\simeq 3000\,\mathrm{K}$. Ces paramètres laissent des empreintes très fortes sur les *fluctuations angulaires du CMB*, qui commencent à être mesurées avec les expériences en ballon BOOMERANG, MAXIMA et bientôt ARCHEOPS, et seront mesurées avec une grande précision avec les satellites MAP et Planck Surveyor.

Depuis la recombinaison, la structuration de la matière dans l'Univers est régie par la *gravitation*. Les régions sur-denses de l'Univers attirent de préférence la matière environnante et deviennent encore plus denses, tandis que la matière quitte les régions sous-denses pour aller vers des zones plus denses. Ainsi les contrastes de densité s'accroissent, et cette croissance de contrastes de densité est régie par l'*instabilité gravitationnelle*.

Lorsque les contrastes de densité sont encore faibles, l'Univers est dit dans le *régime linéaire* car la croissance des fluctuations de densité par instabilité gravitationnelle peut être décrite de façon analytique, qui s'avère être linéaire en fonction de $(1 + z)$, dans un repère *comobile* avec l'expansion de l'Univers, lorsque l'Univers est plat sans constante cosmologique ($\Omega_0 = 1$), où z est le *décalage spectral* (*redshift* en anglais). Dans une seconde phase, dite *non-linéaire*, les fluctuations de densité sont au moins du même ordre que la densité moyenne de l'Univers. Les structures sur-denses se détachent alors de leur expansion de Hubble, pour s'effondrer, possiblement rebondir, et atteindre un équilibre dynamique dit *viriel* (car le théorème du même nom est satisfait). Les systèmes dynamiques astrophysiques en équilibre viriel vont du Système Solaire aux cœurs des amas de galaxies.

Au premier ordre, les galaxies devraient être des bons traceurs de la distribution de masse dans l'Univers. Comme la distribution de masse porte les empreintes des paramètres cosmologiques Ω_0, λ_0 et $P(k)$, on peut espérer recouvrer ces paramètres par des analyses appropriées de la distribution des galaxies, soit dans le champ, soit dans les grands amas de galaxies, soit encore dans les petits groupes de galaxies.

A noter que la masse de l'Univers est dominée par de la *matière noire* (ou sombre) non-baryonique (car toutes les estimations de Ω_0 donnent des valeurs $\gtrsim 0.2$ bien plus grandes que les estimations de la densité de matière baryonique — $\Omega_0 \lesssim 0.1$). La forte structuration de l'Univers aux échelles des petits groupes de galaxies suggère que la matière noire est principalement froide, dite *CDM* (Cold Dark Matter), avec $P(k) \sim k$ aux grandes échelles (confirmé par le satellite COBE de mesures du CMB) et $P(k) \sim k^{-3}$ aux petites échelles. Les particules de matière noire pourraient être des axions, des WIMPs ou bien des partenaires super-symétriques de particules, en particulier le Higgsino. Leur détection est difficile et leurs sections efficaces sont généralement très mal connues.

A partir du spectre $P(k)$, il est facile de trouver l'amplitude typique des fluctuations de densité à une échelle R, ou une masse M (ce qui revient au même, puisque l'Univers primordial est quasiment homogène).[1] La variance des fluctuations s'écrit :

$$\sigma^2(R) = \frac{1}{(2\pi)^3} \int_0^\infty \widetilde{W}^2(kR)\, P(k)\, d^3k \ ,$$

où $\widetilde{W}$ est la transformée de Fourier de la fenêtre de lissage, qui est une *fonction de créneau* (*top hat* en anglais) si l'on considère le cas simple d'une boule de rayon R. Pour le spectre CDM, σ est une fonction décroissante de la masse, de sorte que

$$\lim_{M=0} \sigma \to \infty \ .$$

Les fluctuations des galaxies ont un écart type de 1 à l'échelle de $8\,h^{-1}\,\mathrm{Mpc}$ (où $h = H_0/[100\,\mathrm{km\,s^{-1}\,Mpc^{-1}}]$). Mais comme on n'observe pas la distribution de la matière noire (cela viendra avec les grands sondages de vitesses particulières comme 6dF — voir Sec. 5.3, plus bas, ou par la mesure des effets de lentilles gravitationnelles faibles à grande échelle), il faut supposer un paramètre de biais des galaxies par rapport à la matière noire. Par simplicité on adopte un biais local linéaire, b, ce qui se traduit par des fluctuations d'écart-type $\sigma_8 = 1/b$ pour la matière noire à l'échelle de $8\,h^{-1}\,\mathrm{Mpc}$.

On comprend relativement bien les conditions pour qu'une structure, dit *halo de matière noire*, atteigne l'équilibre viriel à une époque donnée. Cela s'exprime par un seuil du contraste de densité moyen du halo (par rapport à la densité moyenne de l'Univers), qui croît avec z, et qui à $z = 0$ est $\Delta = 178$ pour ($\Omega_0 = 1$, $\lambda_0 = 0$) tandis que pour ($\Omega_0 = 0.3$, $\lambda_0 = 0.7$), $\Delta = 334$ (Kitayama & Suto 1996b). Ainsi, *les structures les plus denses se forment d'abord*. On appelle alors le *rayon du viriel*, le rayon d'un halo à l'intérieur duquel la densité moyenne est de Δ fois la densité moyenne de l'Univers.[2]

Etant donné que la gravitation engendre des fluctuations de densité de statistique gaussienne, la probabilité qu'un objet de taille comobile R, c'est-à-dire de masse $M = 4\pi\bar{\rho}R^3$ s'effondre *avant* l'époque z peut s'écrire

$$P(z_c > z|R) = \mathrm{erfc}\left(\frac{\delta_c(z)}{\sigma(R)\sqrt{2}}\right) \ , \qquad (1)$$

1. Pour éviter le choix d'un décalage spectral primordial de référence ($z_i = 1000$ ou $z_i = 100$, etc.), on préfère exprimer les échelles (R) et nombres d'onde (k), par extrapolation du régime linéaire au temps présent ($z = 0$) — les échelles sont alors dites *comobiles*. De même, les fluctuations de densité, leur spectre $P(k)$ et leur écart-type $\sigma(R)$ sont exprimés par extrapolation du régime linéaire à $z = 0$.

2. Δ est parfois définie comme la densité d'une structure relative à la *densité critique*.

où erfc est la fonction complémentaire d'erreur, δ_c est le seuil de densité linéaire ($\delta_c(z) \simeq 1.68\,(1+z)$ pour le cas $\Omega_0 = 1$, $\lambda_0 = 0$), c'est-à-dire que $\delta_c(z)$ est la fluctuation de densité, extrapolée dans le régime linéaire jusqu'au temps présent ($z = 0$), qui va s'effondrer à l'époque z. Comme σ est une fonction décroissante de la masse et que δ_c est une fonction croissante de z, l'équation (1) implique que *les structures peu massives s'effondrent les premières.*

La croissance des halos peut être quiescente, par accrétion de très petits halos, ou bien violente, par coalescence avec un halo de masse comparable (e.g. Salvador-Sole, Solanes, & Manrique 1998). On sait aussi caractériser la fonction de masse des halos, par un formalisme dit de *Press & Schechter* (1974), et ses extensions (Bower 1991; Bond et al. 1991; Lacey & Cole 1993; Kitayama & Suto 1996a) et améliorations récentes (Sheth, Mo, & Tormen 2000), qui donnent des très bons accords avec les résultats des simulations cosmologiques à N-corps (Jenkins et al. 2000; Sigad et al. 2000).

L'ansatz de Press & Schechter suppose que lorsque l'on passe d'un rayon R à un rayon $R+dR$, c'est-à-dire quand on augmente légèrement le rayon de lissage, on perd les structures de tailles comprises entre R et $R + dR$. Ainsi, la fraction de masse de l'Univers dans les structures de taille R est :

$$F(R) = -\frac{\partial}{\partial R}\left[P(z_c > z|R)\right] \ . \tag{2}$$

Appliquant l'équation (2) à l'équation (1), la fonction de masse des halos s'écrit alors (Press & Schechter 1974)

$$n(M) = 2\,\frac{\bar{\rho}\,F(R)}{M} = \sqrt{\frac{2}{\pi}}\,\frac{\rho(z)}{M^2}\left|\frac{d\log\sigma}{d\log M}\right|\,\nu\,\exp(-\nu^2/2)\ , \tag{3}$$

où $\nu = \delta_c(z)/\sigma[M(R)]$ et où le facteur 2 de normalisation a été ajouté pour tenir compte des halos dans les structures sous-denses de l'Univers.

D'après l'équation (3), la fonction de masse de Press & Schechter varie à peu près comme $1/M^2$ aux petites masses, avec une coupure de forme exponentielle, et une masse maximale caractéristique, M_*, au delà de laquelle peu de structures se forment, satisfaisant $\nu = 1$, c'est-à-dire $\sigma(M_*) \simeq \delta_c(z)$. La masse M_* croît avec le temps, car, comme on a vu plus haut, les halos peu massifs se forment les premiers. A $z = 0$, la masse caractéristique est $M_* \simeq 10^{14}\,M_\odot$. A noter que le formalisme de Press & Schechter tient compte de la coalescence des structures, mais sans introduire de *vitesses particulières* de ces halos par rapport à l'expansion de Hubble.

Dans cette vision d'un *Univers hiérarchique* (White & Rees 1978), les objets actuels de l'Univers sont composés de morceaux qui se sont détachés très tôt de l'expansion de Hubble. Les galaxies se forment dans ces halos de matière noire. Contrairement aux groupes et amas de galaxies, la formation des galaxies elles-mêmes est largement influencée par les processus de physique dissipative. Comme une galaxie est composée (en grande partie) d'étoiles, qui se forment dans des nuages froids de gaz moléculaire, le refroidissement du gaz primordial est un ingrédient essentiel dans la formation des galaxies (Silk 1977; Binney 1977; Rees & Ostriker 1977).

2 Chimie des environnements circumstellaires

2.1 Introduction

Alors que les *intérieurs* des étoiles sont difficilement observables du fait de leur forte opacité, les environnements circumstellaires, moins denses, sont généralement facilement observables. Ceux-ci sont composés de gaz et de poussières qui se condensent à une température d'environ 1000 K, et ce mélange s'éloigne de l'étoile de façon radiale, d'où le nom de *vents circumstellaires*. Cette perte de masse des étoiles peuvent atteindre $10^{-5}\,M_\odot$/an, soit un milliard de fois plus que la perte de masse du Soleil (qui a aussi son *vent solaire*). Les vitesses d'éjection sont de l'ordre de 10 à 20 $\mathrm{km\,s^{-1}}$ pour les étoiles évoluées, et 10 fois plus pour les étoiles jeunes. Le profil de densité de l'enveloppe circumstellaire satisfait la relation de continuité, qui en symétrie sphérique s'écrit :

$$\dot{M} = 4\pi\, r^2\, n(r)\, v(r) \ ,$$

où $\dot{M}$ est la perte de masse. Ainsi, pour une vitesse uniforme du vent, le profil de densité du gaz est $n \sim r^{-2}$.

Quelle est l'origine des vents? Autour d'étoiles évoluées, on pense que le vent provient de la pression de rayonnement sur les poussières, qui entraînent alors le gaz avec elles. Autour d'étoiles jeunes supermassives, les vents sont probablement propulsés par l'absorption dans certaines raies de résonance. Autour des étoiles en formation, il semble que les champs magnétiques jouent un grand rôle.

On observe les constituants du gaz, soit par l'*émission en ondes millimétriques* de raies moléculaires correspondant à des transitions quantiques entre deux niveaux de *rotation* différents de ces molécules, soit par l'*absorption en infrarouge* de lumière photosphérique par des transitions quantiques entre deux niveaux de *vibration* différents de ces molécules.

Il se trouve que les vents circumstellaires ont une chimie *en phase gazeuse*[3] très riche, à base de réactions chimiques traditionnelles : réactions ions-moléculaires, neutres-neutres (bien plus lents), à transfert de charge, de recombinaison radiative, etc. Les taux de réaction s'écrivent comme la moyenne de la vitesse relative multipliée par la section efficace de collision :

$$k = \langle v\, \sigma(v) \rangle \ , \tag{4}$$

où σ est la section efficace de collision et v la vitesse relative.

Mais les photons ultraviolets (UV), donc de hautes énergies, provenant soit de l'étoile centrale, soit du milieu interstellaire ambiant, ionisent les atomes et molécules (*photo-ionisation*), et parfois cassent les molécules (*photo-dissociation*). Le taux de photo-absorption, non-atténué, dans le continu pour l'espèce j s'écrit

$$G_j^0 = \sum_j \int \frac{\sigma_j(\nu)\, 4\pi I_\nu}{h\nu}\, d\nu = \frac{4\pi}{hc} \sum_j \int \sigma_j(\lambda)\, I_\lambda\, \lambda\, d\lambda \ ,$$

3. Il existe aussi une chimie de déplétion des éléments gazeux sur des grains et de réaction sur les grains.

où $\sigma_j(\nu) \equiv \sigma_j(\lambda)$ représente la section efficace de photo-absorption pour l'espèce j, $I_\nu\, d\nu = I_\lambda d\lambda$ représente l'intensité du champ de rayonnement, h est la constante de Planck et c est la vitesse de la lumière. Il arrive que les molécules absorbent des photons dans des raies, et le taux de photo-absorption non-atténué pour une raie i s'écrit

$$G_i^0 = \frac{\pi e^2}{m_e c}\, f_i\, 4\pi\, I(\lambda_i) \ , \tag{5}$$

où e et m_e représentent respectivement la charge et la masse de l'électron, tandis que λ_i et f_i représentent respectivement la longueur d'onde et la force d'oscillateur de la raie.

Le transfert de ces photons dans les vents circumstellaires est déterminant pour la chimie du vent. Malheureusement, ce transfert de rayonnement n'est pas simple. Les poussières absorbent et diffusent les photons UV, mais on a dû mal à modéliser la composante *diffusion* de l'extinction. Les molécules et atomes absorbent aussi les photons UV, en vue de leur dissociation et ionisation respectives, et chaque constituant gazeux a sa propre section efficace, qui dépend de son état d'excitation (par exemple, chez les atomes, les excités s'ionisent mieux! — car leur état est énergétiquement plus proche de l'état ionisé). Ces sections efficaces semblent être de nature plutôt continue, bien que dans certains cas (Hydrogène atomique et moléculaire, ainsi que le CO) l'absorption se fait dans des raies.

L'épaisseur optique dans le continu pour une espèce j s'écrit

$$\tau_j(\lambda,r) = \sigma_j(\lambda)\, N_j(r) \ , \tag{6}$$

où N_j est la colonne densité de l'espèce j (évaluée soit vers l'intérieur pour des photons stellaires, soit vers l'extérieur pour des photons interstellaires), tandis que $\sigma_j(\lambda)$ est sa section efficace à la longueur d'onde λ. Pour du rayonnement stellaire, l'atténuation du taux de photo-absorption est simplement

$$G_j(r) = G_j^0\, \exp[-\tau(\lambda,r)] \ , \tag{7}$$

où $\tau(\lambda,r) = \sum_j \tau_j(\lambda,r) + \tau_{\rm pous}(\lambda,r)$ est la somme des épaisseurs optiques, à la longueur d'onde λ et au rayon r, des poussières et des espèces absorbantes dans le continu. Mais pour du rayonnement interstellaire, un point de l'enveloppe circumstellaire reçoit des photons depuis toutes les directions. En moyennant sur les directions, Morris & Jura (1983) ont montré que si on ne prend en compte que l'absorption (en négligeant donc les effets de diffusion), l'atténuation se réduit à l'approximation

$$\begin{aligned} G_j(r) &\simeq G_j^0\, \gamma[\tau(\lambda,r)] \ , \\ \gamma(\tau) &= \exp\left(-1.644\, \tau^{0.86}\right) \end{aligned}$$

Pour une raie absorbante, l'atténuation est celle de l'équation (7) pour du rayonnement stellaire (on ne tient pas compte de l'auto-absorption de la raie, mais on bloque le rayonnement par les absorbants en continu, poussières comprises). Pour du rayonnement externe (interstellaire), l'atténuation s'écrit

$$G_i(r) \simeq G_i^0\, \langle \beta(\tau_r(\lambda_i,r)) \rangle\, \gamma(\tau) \ ,$$

où τ_r est l'épaisseur optique dans la raie, et $\langle\beta\rangle$ représente la probabilité moyenne d'échappement (voir Sec. 2.4, plus bas), et τ est l'épaisseur optique totale des bloquants dans le

continu (poussières comprises). Comme le vent est en expansion, il y a des effets pervers, qui font qu'un photon qui se meut dans un vent, se meut aussi dans l'espace des énergies d'absorption des constituants, à moins que l'expansion se fasse à vitesse constante. Si c'est le cas, alors les photons d'incidence radiale seront fortement absorbés par le gaz tandis que ceux en incidence tangentielle sont fortement absorbés par les poussières.

La modélisation ci-dessous concerne 3 différents types d'étoiles : 1) Les étoiles évoluées à chimie carbonée (étoiles carbonées, nébuleuses proto-planétaires), 2) Les étoiles évoluées à chimie oxygénée (géantes et supergéantes rouges), 3) Les objets stellaires jeunes (étoiles pré-T Tauri).

Il est intéressant de comparer le temps dynamique, $\tau_{\rm dyn} = r/v$ au temps chimique, $\tau_{\rm chim} = 1/(nk) \sim r^2$ (pour les vents à vitesse constante), ou au temps photo-chimique $\tau_{\rm photo} = 1/G$. A la base des vents dans les étoiles froides, les temps chimiques et photo-chimiques sont faibles, et les abondances chimiques sont celles de la photosphère. Si les temps chimiques étaient beaucoup plus courts que les temps dynamiques, alors les abondances chimiques pourraient être calculées indépendamment, à chaque rayon, en *équilibre thermodynamique local* (*ETL*). Mais cette condition n'est pas satisfaite dans les vents circumstellaires, ce qui implique que l'on doit effectuer un calcul où la chimie est couplée à la dynamique du vent.

Ainsi, on effectue un calcul *lagrangien* (qui suit le vent), en débutant à la base du vent (dans la photosphère ou chromosphère), là ou il commence à être accéléré. On suppose un mélange de constituants gazeux, déterminé par un calcul en équilibre thermique. Puis on calcule comment les abondances des composants gazeux varient avec leur distance à l'étoile centrale, en intégrant les réaction chimiques et de photo-destruction. Si on veut étudier une enveloppe circumstellaire illuminée de l'intérieur par l'étoile et à l'extérieur par le champ UV interstellaire, il faut coupler les équations du type (6) aux équations (photo-)chimiques et itérer les calculs d'abondance (en supposant, au premier ordre, des épaisseurs optiques nulles).

L'idée est alors de comparer les abondances à celles observées, principalement en émission millimétrique. Notons que ces observations se font principalement sur les radio-téléscopes à Kitt Peak (12m), Onsala (20m), l'IRAM (30m), et Nobeyama (40m) et depuis cinq ans on peut mieux mesurer la variation des abondances avec la distance à l'étoile, grâce aux interféromètres de Hat Creek et de l'IRAM. On peut aller plus loin bien sûr et faire des prédictions sur des futures détections.

2.2 Enveloppes circumstellaires carbonées

Les amateurs d'étoiles carbonées ont la chance de pouvoir observer un exemple d'étoile carbonée qui se trouve être une des sources les plus brillantes en infrarouge proche : IRC +10216. On y observe à ce jour plus de 40 molécules différentes (Glassgold & Mamon 1992; Glassgold 1996). L'excès de carbone par rapport à l'oxygène dans la photosphère entraîne une chimie à base d'hydrocarbures dans l'enveloppe circumstellaire. Les molécules dominantes sont CO, bien sûr, et aussi, C_2H_2, HCN, et SiS, qui se trouvent à la base du vent, et sont photo-dissociées par les UV du milieu interstellaire ambiant. Les résidus de

photo-dissociation peuvent être photo-dissociés à leur tour ce qui donne lieu à des *photo-chaînes de dissociation* telles que $CO \rightarrow C \rightarrow C^+$, $C_2H_2 \rightarrow C_2H \rightarrow C_2 \rightarrow C \rightarrow C^+$, et $HCN \rightarrow CN \rightarrow C \rightarrow C^+$.

Outre ces molécules abondantes, nos calculs (Glassgold et al. 1987) montrent que l'on doit s'attendre à observer quelques ions moléculaires, qui constituent d'importants diagnostics de l'ionisation des enveloppes circumstellaires. Ainsi nous avions prédit que l'ion HCO^+, atteint une abondance de quelques 10^{-10}, et cet ion a depuis été détecté à l'IRAM avec une abondance comparable (Lucas & Guélin 1990). Nous avions aussi expliqué le grand rapport entre l'abondance de HCN et celui de son isomère HNC. Au delà de HCN, on observe une séquence de *cyanopolyynes* : HC_3N, HC_5N, HC_7N, HC_9N, $HC_{11}N$, et leurs résidus de photo-dissociation. Nos derniers calculs (Cherchneff, Glassgold, & Mamon 1993) ont permis de modéliser ces observations, avec comme corollaire que le taux de rayons cosmiques semble être 10 fois inférieur à celui du milieu interstellaire ambiant, l'enveloppe étant peut-être protégée par les champs magnétiques émanant de l'étoile centrale. Finalement, l'observation de six molécules à base de silicium nous a conduits à développer la chimie silicée et nos résultats préliminaires sont en bon accord avec les observations (Glassgold & Mamon 1992; Glassgold 1996).

2.3 Enveloppes circumstellaires oxygénées

Alors que tout l'oxygène en phase gazeuse des enveloppes carbonées se trouve dans du CO, dans les enveloppes oxygénées (étoiles AGB comme αOri, proto-nébuleuses planétaires comme OH231.8+4.2, voire même nébuleuses planétaires comme NGC 7027)[4] le surplus d'oxygène donne lieu à une chimie différente, où cette fois-ci tout le carbone gazeux se trouve dans du CO et il ne se forme pas d'hydrocarbures. L'absence de phares tels que IRC +10216 a retardé la compréhension de cette chimie oxygénée, qui n'est pourtant pas moins intéressante, vu la présence de masers (OH, H_2O, SiO) dans ces enveloppes. Nous avons donc été les premiers à présenter une modélisation de la chimie des enveloppes oxygénées (Mamon, Glassgold, & Omont 1987). La principale photo-chaîne est maintenant $H_2O \rightarrow OH \rightarrow O$. Nous avons prédit la détection des ions moléculaires HCO^+ et H_3O^+, dont le premier a été par la suite détectée et la seconde nécessite des observations sub-millimétriques (difficiles) pour observer ses transitions rotationnelles.

2.4 Transfert dans les raies de CO

On a longtemps supposé que la molécule CO photo-absorbe en continu, et on s'est basé sur cette idée pour déduire des taux de perte de masse des étoiles à partir de l'extension du monoxyde de carbone (Knapp & Morris 1985). L'équipe de F. Rostas (DAMAP, Meudon) a mesuré la spectre de photo-absorption UV du CO, et en a déduit que la photo-absorption s'effectue principalement en raies (Letzelter et al. 1987).

4. La modélisation de la chimie des nébuleuses planétaires est plus difficile, le vent n'étant pas stationnaire mais détaché.

Pour la molécule CO, on considère des transitions électro-vibrationnelles ℓ,u ('lower', 'upper') et des niveaux de rotation J,J', de sorte que la force d'oscillateur de la transition $\ell J \rightarrow u J'$ s'écrit

$$f_{\ell J,uJ'} = f_i \, f_{J,J'} \ ,$$

où le premier terme à droite est la force d'oscillateur classique (qui rentre dans l'éq. [5]) tandis que le second terme représente le facteur de *Hönl-London* normalisé : avec $f_{J,J+1} = (J+1)/(2J+1)$ et $f_{J,J-1} = J/(2J+1)$. La probabilité moyenne d'échappement s'écrit

$$\begin{aligned} \langle \beta_i \rangle &\equiv \langle \beta(\tau_r) \rangle = \sum_{JJ'} P_J f_{JJ'} \beta_{\ell,J,u,J'} \\ \beta_{\ell,J,u,J'} &= \frac{1 - \exp(-3\tau_r/2)}{3\tau_r/2} \end{aligned} \tag{8}$$

où

$$\tau_r \equiv \tau_{\ell,J,u,J'} = P_J \, f_i \, f_{J,J'} \left(\frac{\pi e^2}{m_e \, c} \right) \lambda_i \left(\frac{r \, n_H(r)}{v} \right) x_j(r) \ ,$$

et où P_J représente la probabilité de se trouver dans le niveau rotationnel J :

$$P_J = (2J+1) \, \exp \left[-J(J+1) \, \frac{T_{\rm CO}}{T} \right] \ ,$$

où $T_{\rm CO} = 2.78\,{\rm K}$ est la température de rotation du CO.

Nous avons alors appliqué les résultats de Letzelter et al. (1987) aux enveloppes circumstellaires en expansion (Mamon, Glassgold, & Huggins 1988). La photo-absorption en raies implique un transfert de rayonnement différent, où *l'auto-écrantage est très efficace et intervient de façon beaucoup plus abrupte que dans le cas continu.*

De plus, nous en avons déduit un *taux de photo-dissociation du CO (non-atténué) dix fois plus grand qu'admis précédemment.* En utilisant les données pour 34 bandes de photo-absorption CO données par Letzelter et al. (1987), et en supposant que ces bandes sont subdivisées en raies de transitions entre niveaux rotationnels en équilibre thermique, nous avons donc développé un modèle précis de la photo-chaîne de CO dans les enveloppes circumstellaires et proposé une approximation simple avec une seule raie (Mamon et al. 1988).

Alors que pour les enveloppes carbonées, la chimie se fait à l'intérieur de la zone de photo-dissociation de CO, dans les enveloppes oxygénées, chimie et photo-dissociation du CO se font au même endroit, ce qui rend l'examen de cette photo-dissociation critique (Mamon, Glassgold, & Omont 1987).

2.5 Enveloppes circumstellaires autour d'étoiles jeunes

L'annonce de la détection de CO dans une enveloppe essentiellement atomique autour d'un proto-étoile (Lizano et al. 1988), nous a conduits à essayer de modéliser la formation de molécules dans les enveloppes de ces proto-étoiles. Il s'agissait de savoir si ce CO était de nature interstellaire, et accélérée par le vent circumstellaire, ce qui était alors l'idée

à la mode, ou bien si elle était formée dans le vent circumstellaire. Ici, les contraintes observationnelles sont peu nombreuses, car les enveloppes sont mille fois plus petites.

La chimie est bien différente car les enveloppes sont aussi beaucoup plus denses, donc les collisions jouent un rôle très accru. Nous avons dû tenir compte de certains niveaux d'Hydrogène et de Carbone, qui jouent un rôle important dans le transfert de rayonnement.

Nous avons montré (Glassgold, Mamon, & Huggins 1989, 1991) qu'à partir d'une photosphère entièrement atomique, et dans certaines conditions, *des molécules telles que* H_2*, CO, et OH se synthétisent à l'intérieur du vent.* Pour cela il faut que l'étoile et son vent ne soient pas trop chauds et que la perte de masse soit assez forte (ce qui correspond à une assez forte densité).

2.6 Epilogue

Etant revenu à la cosmologie, je n'ai plus contribué sur le sujet des milieux circumstellaires, mise-à-part la mise à disposition sur le Web de mon code de chimie circumstellaire,[5] qui a ainsi été utilisé par plusieurs auteurs.

Néanmoins, les études des vents circumstellaires profitent des avancées théoriques, comme les mesures ou calculs de sections efficaces de photo-absorption ou de réaction, ainsi que d'observations de qualité croissante, en particulier en résolution spatiale. Ainsi, une observation HST de IRC +10216 montre que l'enveloppe est composée de coquilles, par résultats de chocs (Mauron & Huggins 1999), ce qui implique qu'une grande partie de la chimie de l'enveloppe est à revoir !

5. Mon code CSENV se trouve sur `http://www.iap.fr/users/gam/csenv.html`.

3 Formation et évolution des galaxies

3.1 Formation de galaxies et le problème du sur-refroidissement

On a vu plus haut (Sec. 1.2) que la formation des galaxies est régie par des processus dissipatifs. La Figure 1 illustre l'intérêt de combiner l'analyse de refroidissement du gaz à la statistique des halos de matière noire donnée par le formalisme de Press & Schechter (1974).[6] Ce diagramme, tracé d'abord par Silk (1977), montre comment la condition d'avoir du gaz froid (dans les nuages moléculaires) contraint la formation de galaxies. On y incorpore (Blumenthal et al. 1984; Blanchard, Valls-Gabaud, & Mamon 1992) les tracés de fluctuations de densité extrêmes et moyennes, prédits par la fonction de masse de Press & Schechter et couplés à la relation masse-température, obtenue depuis le seuil de densité des halos, la relation dispersion de vitesses / température et le théorème du viriel :

$$\bar{\rho}(z) = \frac{3M}{4\pi R^3} = \Delta\,\Omega(z)\,\rho_c(z) = \frac{3\,\Delta\,\Omega_0 H_0^2}{8\pi\,G}\,(1+z)^3\ , \tag{9}$$

$$\mu m_p\,\sigma_v^2 = \beta_s\,k\,T\ , \tag{10}$$

$$\sigma_v^2 = \gamma\,\frac{GM}{R}\ , \tag{11}$$

où Δ est le facteur (non-linéaire) de surdensité, par rapport à la densité critique $\rho_c(z)$, $\mu\,m_p$ est la masse moyenne des particules du gaz, β_s est une constante d'ordre 1 qui mesure le rapport entre la 'température' des particules d'un halo sur la température du gaz, et $\gamma = \sigma_v^2/v_{\rm circ}^2(R)$ est un facteur de forme du halo. Donc, en combinant les équations (9), (10) et (11), on arrive à la relation masse-température :

$$kT = \frac{\gamma\,\mu\,m_p}{\beta_s}\,\left(\frac{\Omega_0\,\Delta}{2}\right)^{1/3}\,(G\,H_0)^{2/3}\,M^{2/3}\,(1+z)\ .$$

A une époque z correspond une densité critique pour l'effondrement d'un halo, $\rho(z) = \Delta(z)\,\rho_c^0 \simeq 180\,(1+z)\,\rho_c^0$ dans le cas simple de $\Omega_0 = 1$ et $\lambda_0 = 0$, où ρ_c^0 est la densité critique de l'Univers actuel. La densité du gaz est simplement $\rho_{\rm gaz} = \Omega_b/\Omega_0\,\rho$. Le refroidissement se fait à un taux $n_{\rm gaz}^2\,\Lambda(T)$, où $n_{\rm gaz}$ est la densité en nombre de gaz, tandis que $\Lambda(T)$ est la fonction de refroidissement (et dépend légèrement de l'abondance en éléments lourds, dénoté Z — à ne pas confondre avec le décalage spectral, z). Pour un plasma chaud monoatomique d'énergie interne $(3/2)n_{\rm gaz}kT$, il en résulte un temps de refroidissement qui vaut environ

$$t_{\rm froid} = \frac{\frac{3}{2}\,n_{\rm gaz}\,kT}{n_{\rm gaz}^2\,\Lambda(T)}\ . \tag{12}$$

Les deux courbes (pleines et pointillées) de la Figure 1 indiquent les conditions pour que $t_{\rm froid} = t_{\rm Univers}$ et $t_{\rm froid} = t_{\rm dyn}$, c'est-à-dire, où le refroidissement se fait soit sur un âge de l'Univers, soit sur le temps dynamique du halo. Ainsi, à $z \gtrsim 0$, à densité de gaz donné, il existe un intervalle de température pour lequel le refroidissement est rapide.

6. White & Rees (1978) ont été les premiers à relier le formalisme de Press & Schechter (1974) et celui du refroidissement du gaz.

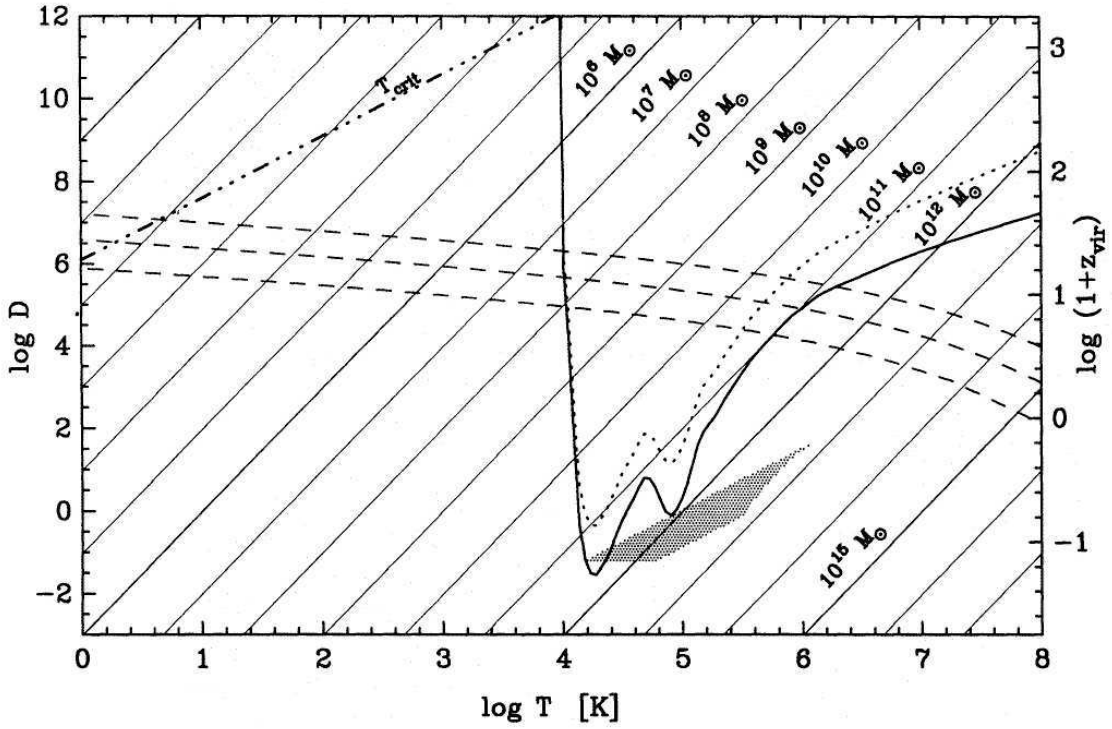

FIG. 1 – *Diagramme densité-température pour du gaz sans éléments lourds (Blanchard, Valls-Gabaud, & Mamon 1992). L'ordonnée D représente la densité locale divisée par la densité critique actuelle ($D = \rho(r,z)/\rho_c^0$). L'autre ordonnée $z_{\rm vir}$ donne l'époque de virialisation de la structure. Les* courbes pleine *et* pointillée *indiquent les condition de refroidissement $t_{\rm froid} = t_{\rm Univers}$ et $t_{\rm froid} = t_{\rm dyn}$, respectivement. Les* lignes droites obliques *représentent les masses des halos. Les* courbes hachurées *représentent, pour un z donné, la masse au dessus de laquelle se trouvent 50%, 10% et 1% des halos (de* bas *en* haut*), selon le formalisme de Press & Schechter (1974). Ce diagramme suppose $Z = 0$, $\Omega_0 = 1$, $\lambda_0 = 0$, $\Omega_b = 0.06$, $h = 0.5$ et $\sigma_8 = 0.7$.*

Ainsi, considérons une époque z, et donc la densité de gaz associée d'un halo qui se forme à l'époque z. D'abord, l'intersection avec les courbes hachurées donne les masses typiques des halos à ce décalage spectral. Les galaxies se forment dans les halos de température comprises entre $\approx 10^4$ K et $\approx 10^6$ K, c'est-à-dire dans la zone où le refroidissement est rapide. Ainsi, d'après la Figure 1, les premières galaxies se forment dans des halos de masse $2 \times 10^7\, M_\odot$ à $z \simeq 25$, les galaxies les plus massives se forment dans des halos de $10^{11}\, M_\odot$ à $z \simeq 4$, et dans l'Univers actuel, la formation de galaxies est pratiquement nulle. On remarque aussi que les galaxies naines se forment encore après l'apparition des premières galaxies géantes.

Ces chiffres ne sont peut-être pas complètement réalistes, et ce diagramme pourrait être amélioré en prenant le modèle cosmologique le plus en vue aujourd'hui, c'est-à-dire $\Omega_0 = 0.3$, $\Lambda = 0.7$ et $h = 0.7$, avec une meilleure fonction de masse (Sheth et al. 2000). D'autre part, l'apparition des éléments lourds avec les premières galaxies accroît le refroidissement et permet d'obtenir des galaxies se formant dans des halos de masse environ 10 fois plus grande (voir Fig. 3 de Blumenthal et al. 1984).

L'intérêt principal du travail de Blanchard, Valls-Gabaud, & Mamon (1992) a été le calcul de la fraction de baryons à $z = 0$ qui est sous forme froide. On trouve que, sans

réchauffage, 80% des baryons devrait être sous forme froide à $z = 0$. Mais on sait que la fraction de baryons sous forme froide est bien plus faible que 50% : les étoiles contribuent $\Omega_* \simeq 0.003$ (voir Fukugita, Hogan, & Peebles 1998 et références incluses) tandis que le gaz froid dans les galaxies fournit une densité au mieux comparable (voir Fukugita et al. 1998 et références incluses). La somme des deux est donc négligeable par rapport à la densité baryonique de l'Univers, $\Omega_b \simeq 0.02$ (Fukugita et al. 1998 et références incluses). Pour éviter ce problème de *sur-refroidissement*, on est amené à postuler *un processus de réchauffage de l'Univers* pour ralentir le refroidissement des baryons et empêcher ainsi la formation de trop d'étoiles, en particulier en augmentant *l'entropie spécifique* du gaz intergalactique pour l'empêcher de s'effondrer dans des halos de matière noire (sinon leur entropie spécifique diminuerait, voir Ponman, Cannon, & Navarro 1999). Ce réchauffage explique aussi l'absence de gaz neutre à $z \simeq 2$ (test de Gunn & Peterson 1965). Un modèle récent confirme l'importance de ce réchauffage sous forme de quasars (Valageas & Silk 1999).

3.2 Analyse semi-analytique et l'origine de la séquence de Hubble

On sait (depuis Hubble & Humason 1931) que les cœurs denses des amas riches de galaxies sont peuplés presque uniquement de galaxies elliptiques (et quelques lenticulaires — ou galaxies S0), tandis que les galaxies spirales y sont rares, et on appelle cela la *ségrégation morphologique*.

Mais on ne connaît toujours pas l'origine de la séquence de Hubble, ni de la ségrégation morphologique. Une possibilité souvent considérée serait que les galaxies elliptiques proviennent de *coalescences* (appelées aussi *fusions* ou *mergers*) de galaxies spirales. En effet, les simulations numériques à haute résolution de la collision lente de deux galaxies spirales *de masse comparable* produit invariablement une galaxie elliptique (Gerhard 1981; Barnes 1992), comme cela avait été prévu par Toomre (1977). Les *coalescences majeures* pourraient donc être le mécanisme responsable de la distinction entre galaxies spirales et lenticulaires, d'une part et galaxies elliptiques d'autre part.

Pour tester cette possibilité, j'ai encadré en 1994 le stage de DEA de Sergio Dos Santos (maintenant postdoc à Leicester, Royaume-Uni), qui a considéré le rôle des coalescences majeures de galaxies, dans le contexte d'un univers hiérarchique, avec le gaz, qui se refroidit dans des halos de matière noire, puis génère des étoiles, qui elles-mêmes donnent des supernovae qui rapportent de l'énergie au gaz qui essaie de refroidir (sinon, on aurait trop d'étoiles formées, voir Blanchard, Valls-Gabaud, & Mamon 1992). Les résultats de cette modélisation *semi-analytique* étaient prometteurs, mais Sergio est parti au service militaire après son stage de DEA, et à son retour un préprint est sorti d'Angleterre (Baugh, Cole, & Frenk 1996) faisant pratiquement exactement la même chose !

Mais il n'y a pas que les coalescences entre spirales de masse comparables qui peuvent expliquer la distinction entre galaxies à disque et elliptiques. Une autre idée attrayante est le fait que les spirales ne peuvent se former dans les amas car, étant donné que leurs disques proviennent de la dissipation d'un très grand halo de gaz, si ces halos de gaz sont dissipés par les effets de marée de l'amas, ils ne pourront s'effondrer pour former des disques de galaxies spirales (Larson, Tinsley, & Caldwell 1980; Whitmore & Gilmore 1991; Whitmore,

Gilmore, & Jones 1993). Une dernière idée est tout simplement que les galaxies elliptiques sont celles qui s'effondrent le plus rapidement (Evrard, Silk, & Szalay 1990), sans pouvoir recevoir du moment angulaire par couples de marées avec les (proto-)galaxies avoisinantes.

D'autre part, la distinction entre galaxies spirales en lenticulaires (pauvres en gaz et poussières), est expliquée de plusieurs façons : par ablation du gaz des disques lors de collisions (Spitzer & Baade 1951), par la pression de choc du gaz intergalactique (Gunn & Gott 1972), ou par évaporation par conduction du gaz intergalactique (Cowie & Songaila 1977), ou encore la consommation du gaz lors de sursauts de formation d'étoiles (Larson, Tinsley, & Caldwell 1980).

On peut être plus ambitieux et chercher à expliquer toute la séquence de Hubble. Par exemple, les accrétions de petites galaxies satellites par leurs parents, qui épaississent d'abord les disques de ces galaxies parentes (Quinn & Goodman 1986), puis après formation de barres, on prévoit le transport de matière vers les régions centrales, ce qui augmente le rapport bulbe sur disque des galaxies (Pfenniger & Norman 1990; Combes 2000). Ainsi, la séquence de Hubble pourrait s'expliquer entièrement par l'historique de ces accrétions et coalescences majeures (Schweizer 1992; Charlton, Whitmore, & Gilmore 1995). De même, les marées causées par les collisions rapides, non-suivies de coalescences, devraient faire évoluer les disques sur la séquence de Hubble, et la première modélisation de ce phénomène dans un contexte cosmologique est prometteuse (Balland, Silk, & Schaeffer 1998).

Les théoriciens (dont moi-même : Mamon 1992a) ont été assez astucieux pour "prouver" que tel ou tel processus physique est efficace, mais comment connaître *le moteur véritable de la séquence de Hubble* ? La réponse sera fournie, je l'espère, par le travail de ma doctorante Barbara Lanzoni (boursière TMR), en collaboration avec Bruno Guiderdoni (IAP). Notre démarche, dite *semi-analytique*, se fait en 3 étapes :

1. On décrit l'évolution de la matière noire d'un morceau d'Univers

2. On incorpore tous les processus physiques dans le formalisme de l'Univers hiérarchique mentionné plus haut (et amélioré de façon adéquate) et on cherche l'ensemble des paramètres satisfaisant au mieux les très nombreuses contraintes observationnelles (ségrégation morphologique, mais aussi fonction de luminosité des galaxies, évolution de ces relations avec le décalage spectral, etc.).

3. On itère avec $N-1$ processus au lieu des N processus originaux, et on cherche le processus qui, une fois retiré de la simulation, fait le modèle s'éloigner au maximum des contraintes observationnelles.

Nous avons d'abord codé et testé une méthode très rapide (dite MCM due à Rodrigues & Thomas 1996) qui permet de suivre l'évolution de la matière noire d'un morceau d'Univers dans l'approximation linéaire (c'est-à-dire sur des échelles assez grands pour que le contraste moyen de densité soit faible), et nos tests (Lanzoni, Mamon, & Guiderdoni 2000) montrent que ce code reproduit de façon excellente les fonctions de masse prédite par le formalisme de Press & Schechter (1974), ainsi que les fonctions de masse des progéniteurs d'un halo de masse donnée. Nous montrons aussi que *les halos MCM sont bien corrélés dans l'espace, et que leur fonction de corrélation reproduit bien les prédictions analytiques* (de Mo & White 1996 et Catelan et al. 1998).

Toutefois, les processus d'évolution morphologique des galaxies seront les plus efficaces dans les régions denses de l'Univers, qui terminent à $z = 0$ dans les amas riches de galaxies (où le mélange des morphologies de galaxies est la plus différente par rapport au champ), et l'approximation linéaire faite par MCM ne peut en principe bien reproduire ces régions très *non-linéaires*. L'alternative est d'entreprendre des *simulations cosmologiques* de l'évolution de matière noire de l'Univers à partir de *codes gravitationnels*. Au début de la thèse de Barbara, les codes existants étaient beaucoup trop lents pour pouvoir envisager sérieusement une telle approche, mais nous avons pu bénéficier d'un code à architecture parallèle très rapide, écrit par V. Springel (alors étudiant de S. White à Garching, maintenant postdoc à Harvard, USA), qui s'avère être 10 fois plus rapide que les codes similaires dont nous disposions à l'IAP. Nous avons obtenu 15 000 puis 25 000 heures de temps sur l'IBM SP2 (plus de 200 processeurs) du CINES (anciennement CNUSC) et nous avons entrepris une série de simulations d'amas, dans plusieurs gammes de masse, ayant chacun plus d'un million de particules.

Barbara (qui doit soutenir sa thèse vers la fin 2000) est en train d'intégrer ses simulations aux codes d'évolution semi-analytique des galaxies développé à l'IAP par Ninin (1999), Devriendt (1999) et S. Hatton.[7] Pour avoir des résultats plus réalistes, elle modifie ces immenses codes, afin de mieux suivre les orbites des galaxies, une fois qu'elles tombent dans des groupes ou amas.

3.3 Taux de coalescences et de collisions rapides de galaxies dans les groupes et amas

Dans le modèle de formation et évolution des galaxies dans un Univers hiérarchique (Sec. 3.2), la prise en compte de toutes les paires de galaxies en interaction dans un amas donné, pour le calcul des effets de collisions et de coalescences directes, revient à entreprendre une simulation à N corps *pour les galaxies*, ce qui est très coûteux en temps de calcul.

Pour plus d'efficacité, la modélisation semi-analytique va devoir incorporer des calculs analytiques des taux de coalescences directes et de collisions rapides dans les groupes et amas (Mamon 2000b).

Le taux de coalescences s'écrit de manière similaire à l'équation (4) :

$$k \equiv \frac{1}{n^2}\frac{d^2N}{dt\,dV} = \langle vs(v)\rangle = \int_0^\infty dv f(v) vs(v) \ , \tag{13}$$

où $s(v)$ est la section efficace de coalescence et $f(v)$ est la distribution Maxwellienne normalisée de vitesses relatives. Alors une galaxie subit des coalescences à un taux $nk \equiv dN/dt$.

On peut séparer les coalescences en trois catégories : 1) les *coalescences mineures* avec des objets beaucoup moins massifs, comme l'accrétion de petits satellites; 2) les *coalescences majeures* avec des objets légèrement moins massifs, qui doivent détruire la morphologie

7. Un premier code crée l'arbre de coalescences des halos, tandis que le second incorpore les baryons et crée une arbre de coalescences des galaxies.

disque de galaxies spirales en interaction et engendrer par conséquent des galaxies elliptiques; 3) les *coalescences destructrices* avec des objets plus massifs.

La Figure 2 montre les taux sans dimension de coalescences majeures, $k/(r_h^2 v_g)$, où r_h est le rayon de moitié de masse moyen des deux galaxies, tandis que v_g est leur dispersion interne de vitesses moyenne.

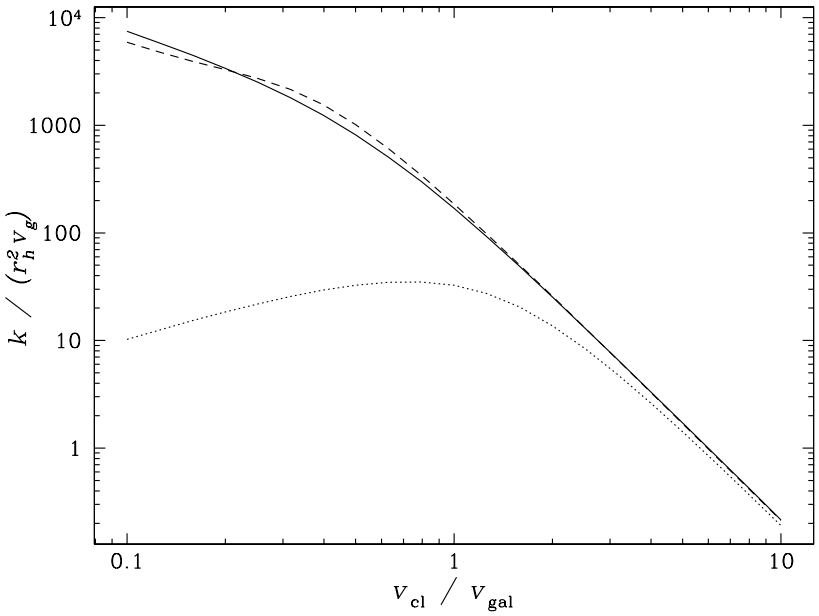

FIG. 2 – *Taux de coalescence sans dimension $k/(r_h^2 v_g)$ en fonction du rapport des dispersions de vitesses entre groupe ou amas et galaxies (Mamon 2000b). La* courbe pointillée *correspond au taux de Mamon (1992a), la* courbe hachurée *au taux de Krivitsky & Kontorovich (1997, re-normalisé verticalement, car ils ont raisonné en termes de rayons des galaxies au lieu de rayons de moitié de masse), et la* courbe pleine *aux taux déduits des simulations numériques de Makino & Hut (1997).*

On remarque d'une part une excellente concordance (à 15% près) entre les taux de coalescences majeures de Mamon (1992a) et Makino & Hut dans le régime des amas, alors que Mamon (1992a) sous-estime les taux pour les groupes, car la *focalisation gravitationnelle* lors des rencontres de galaxies n'est pas prise en compte. D'autre part, le calcul de Krivitsky & Kontorovich, une fois re-normalisé, donne un accord remarquable avec les simulations de Makino & Hut (c'est d'autant plus remarquable que la forme de la section efficace $s(v)$ adoptée par Krivitsky & Kontorovich n'était pas très réaliste).

Dans le régime des amas, le taux de coalescences majeures s'écrit simplement (Mamon 1992a)

$$k = b\,\frac{r_h^2 v_g^4}{v_{\rm cl}^3} = a\,\frac{G^2 m^2}{v_{\rm cl}^3}\ , \tag{14}$$

où $v_{\rm cl}$ est la dispersion de vitesses du groupe ou amas (cluster), avec $a \simeq 8$ (Mamon 1992a). En fait, la relation $k \sim v_{\rm cl}^{-3}$ ne dépend pas de la section efficace, tant que celle-ci diminue fortement (ou est tronquée) aux grandes vitesses relatives (Mamon 2000b). D'après la Figure 2, *les coalescences majeures sont environ 100 fois plus fréquentes dans les groupes que dans les amas riches* (par unité de densité en nombre de galaxies).

Lorsque les deux galaxies qui vont coalescer ensemble ne sont pas de même masse, l'équation (14) se généralise par la relation

$$k \sim \langle r_h \rangle^2 \langle v_g^2 \rangle^2 \ . \tag{15}$$

Ainsi, étant donné les équations (14) et (15) et $m \propto r_h^3$ (on suppose l'auto-similarité des profils de masse, et on prend la densité moyenne constante à l'intérieur du rayon du viriel), le taux de coalescences majeures d'une galaxie de masse m avec une autre galaxie de masse λm s'écrit (Mamon 2000b)

$$k(m,\lambda m) = \frac{aG^2m^2}{v_{\rm cl}^3} \left(\frac{1+\lambda^{1/3}}{2}\right)^2 \left(\frac{1+\lambda^{2/3}}{2}\right)^2 \ . \tag{16}$$

Une galaxie donnée subit des coalescences avec d'autres galaxies au taux

$$\mathcal{R} \equiv n\bar{k}(m) = \int_{\lambda_{\rm min}}^{\lambda_{\rm max}} k(m,\lambda m)\, n(\lambda m)\, d(\lambda m) \ , \tag{17}$$

où $n(m)$ est la fonction de masse des galaxies. Ainsi, $\lambda_{\rm min} \simeq 1/3$ et $\lambda_{\rm max} = 1$ pour les coalescences majeures, tandis que $\lambda_{\rm min} = 1$ and $\lambda_{\rm max} \to \infty$ pour les coalescences destructrices.

La Figure 3 montre les taux de coalescences en fonction des masses des galaxies, obtenue par l'équation (17), quand on adopte une fonction de Schechter (1976) de pente asymptotique α pour la fonction de masse.[8]

$$\phi(m) = \frac{\phi_*}{m_*} \left(\frac{m}{m_*}\right)^\alpha \exp\left(-\frac{m}{m_*}\right) \ . \tag{18}$$

Ces taux sont traduits en termes du nombre de coalescences majeures subies, extrapolé sur un temps de Hubble. Il est important de rappeler que les taux de coalescences et de collisions rapides calculés ici doivent être considérés dans le contexte d'un Univers hiérarchique. En d'autres termes, ces taux ne représentent que des photographies d'un système, qu'on ne peux extrapoler dans le temps, car les propriétés des groupes et amas évoluent vite dans l'Univers hiérarchique.

La croissance des taux à faible masse reflète la croissance des sections efficaces avec la masse, tandis que la chute des taux aux très grandes masses est due au manque de galaxies avec qui coalescer. La Figure 3 indique que les galaxies de faible masse sont mangées par des plus grosses avant de pouvoir se transformer en elliptiques par coalescences majeures.

On peut aller plus loin et prédire aussi la variation du taux de coalescences majeures avec la position dans les groupes et amas. Pour ce faire, il est crucial de prendre en compte

8. On aurait probablement dû adopter la fonction de masse de Press & Schechter (1974), car celle-ci est plus réaliste que la fonction de Schechter (1976), qui ne s'applique qu'aux *luminosités*. Toutefois, la fonction de Schechter est plus simple et on pourrait argumenter que la fonction de Press & Schechter n'est pas complètement réaliste, car elle compte toutes les structures, qu'elles aient ou non des galaxies en leur sein. De plus, la fonction de Press & Schechter ne compte pas les galaxies situées dans de plus grandes structures comme des groupes en équilibre ou des amas.

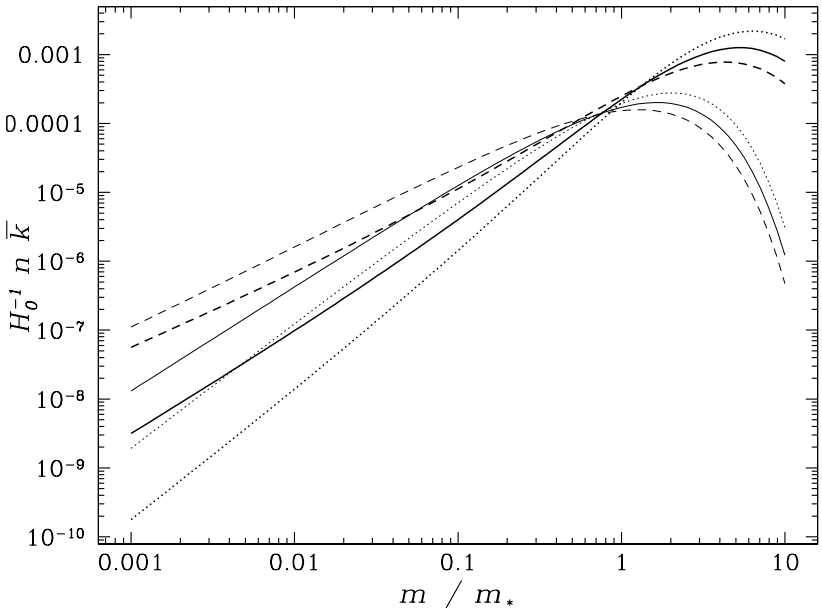

FIG. 3 – *Nombre de coalescences majeures (*courbes épaisses*) et destructrices (*courbes fines*), extrapolé pour un taux de Hubble en fonction de la masse de la galaxie, (eqs. [16] et [17], Mamon 2000b). Les* courbes pointillées, pleines *et* hachurées *sont pour des pentes asymptotiques de la fonction de masse (eq. [18]) de* $\alpha = -1.1$, -1.3 *et* -1.5, *respectivement. La normalisation suppose* $a = 12$, $v_{\rm cl} = 1000\,{\rm km\,s^{-1}}$, $n_* = 200\,n_*^{\rm champ}$, *avec* $n_*^{\rm champ} = 0.013\,h^3{\rm Mpc}^{-3}$ *(Marzke et al. 1998), et* $m_* = 0.1\,(M/L)_{\rm amas}\,\ell_* = 3\times10^{11}h^{-1}M_\odot$.

les marées du potentiel du groupe ou amas. En effet, les galaxies qui chutent sur un tel système peuvent posséder de très gros halos qui vont être sévèrement tronqués (Merritt 1984; Mamon 1992a). Plus précisément, on peut montrer par des considérations analytiques simples que, pour les orbites allongées observées dans les simulations cosmologiques d'amas (Ghigna et al. 1998), les galaxies vont être tronquées à un rayon r_t qui satisfait (Mamon 2000b)

$$\frac{r_t}{R_p}\left(\frac{V_{\rm cl}}{v_{\rm g}}\right) \simeq 1.2 - 1.5\ ,$$

où R_p est le *péricentre* de la trajectoire de la galaxie chutant dans l'amas. On s'attend ainsi à ce que les masses caractéristiques des galaxies croissent avec leur distance au centre de leur amas (nous ne prenons pas en compte ici les galaxies supergéantes cD situées au centre des amas), sauf dans les régions centrales où la relaxation à 2 corps mélangera efficacement les galaxies ayant au départ des différents R_p.

Les diagrammes dans la Figure 4 montrent la variation radiale des taux de coalescences majeures, quand on fait le calcul pour des profils de densité de masse suivant la loi caractéristique de Navarro, Frenk, & White (1995) (NFW):

$$\rho(r) = \frac{4\,\rho(a)}{(r/a)\ (r/a+1)^2}$$

et quand on adopte la non-auto-similarité de ces profils pour les objets de différentes masses (Navarro, Frenk, & White 1997). On confirme que les coalescences de galaxies sont

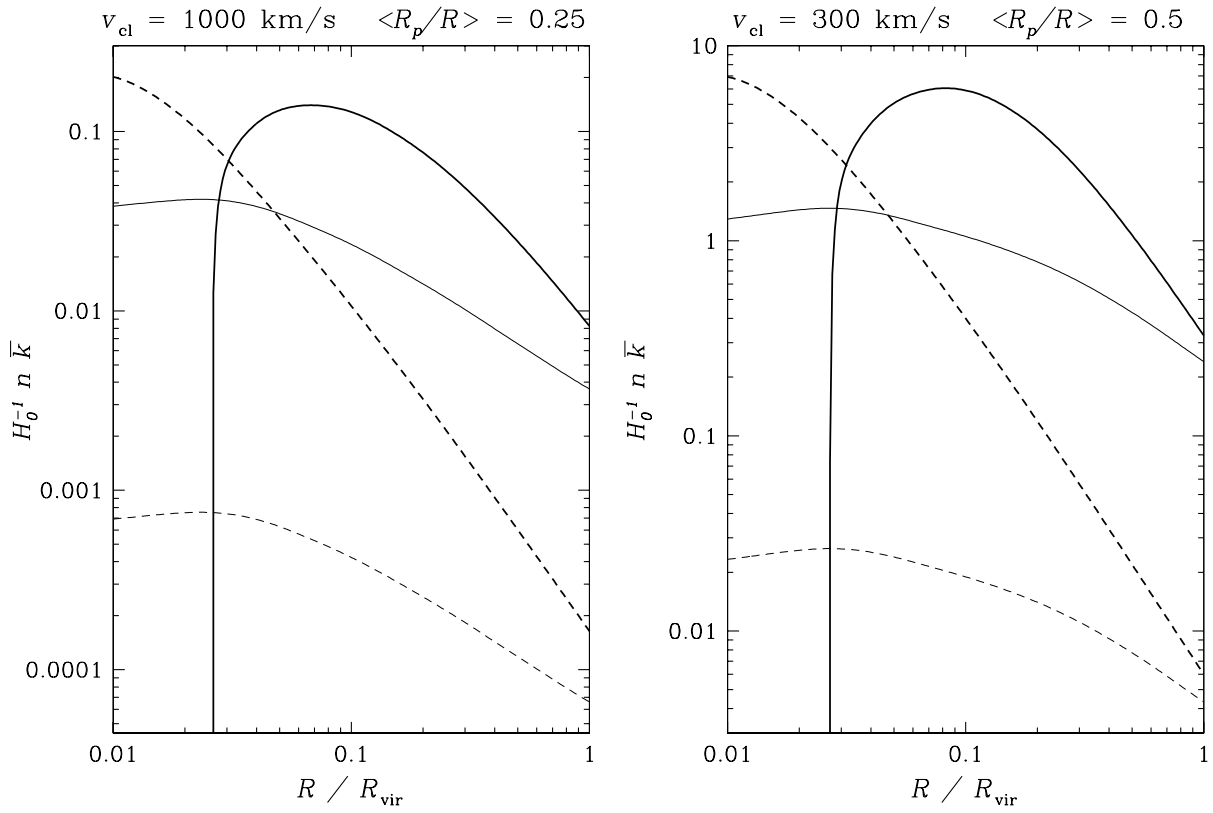

FIG. 4 – *Nombre de coalescences majeures subies par une galaxie donnée en fonction de sa position dans son groupe ou amas, extrapolé à un temps de Hubble, pour un amas (*gauche*) ou groupe (*droite*), d'après Mamon (2000b). On a pris une pente asymptotique de la fonction de masse des galaxies (eq. [18]) de* $\alpha = -1.3$. *Les* courbes épaisses, pleines *et* hachurées *représentent le nombre de coalescences pour des galaxies de masse* $m = m_*^{\rm champ} = 5 \times 10^{12} h^{-1} M_\odot$ *et* $m = 0.1\, m_*^{\rm champ} = 5 \times 10^{11} h^{-1} M_\odot$, *respectivement. Les* courbes fines, pleines *et* hachurées *sont pour des masses de galaxies de* $m = m_*(R)$ *et* $m = 0.1\, m_*(R)$, *respectivement.*

rares dans les amas[9], mais fréquents dans les groupes compacts (voir Sec. 4), surtout vers $R = R_{\rm vir}/10$ pour les galaxies massives (notez que, d'après la Fig. 3, les galaxies $m = 0.1\, m_*$ sont détruites par coalescences avant de subir des coalescences majeures avec des galaxies légèrement moins massives).

Finalement, on peut aussi calculer le taux auquel une galaxie de masse et position données dans un groupe ou amas (de dispersion de vitesses donnée) subit des *collisions rapides*, non suivies de coalescence, mais qui contribuent à modifier la morphologie de la galaxie par les marées induites par la seconde galaxie perturbatrice.

9. Cette conclusion est contraire à celle de Mamon (1992a), qui s'appuie sur une analyse similaire, mais avec des profils de densité en loi de puissance, et surtout avec la non prise en compte du fait que la fraction de masse d'un amas ou groupe à une distance donnée de son centre varie de la même manière que varie la masse caractéristique — du fait de la marée du potentiel. Ainsi, dans le passage de la densité de masse $\rho(R)$ à la densité en nombre de galaxies $n(R)$, Mamon (1992a) a surestimé $n(R)$ et donc surestimé la fréquence de coalescences majeures au petits R.

Une étoile de la galaxie test, située à une distance r de son centre, reçoit un incrément de vitesse

$$\Delta v \sim F_{\rm marée}\,\Delta t \sim \frac{GM(p)\,r}{p^3}\left(\frac{p}{V_p}\right) = C\,\frac{GM(p)\,r}{p^2\,V_p}\ , \tag{19}$$

où C est une constante sans dimension, proche de l'unité. La galaxie reçoit alors une énergie qui est γ fois son énergie de liaison :

$$\Delta E \approx \frac{1}{2}\,(\Delta v)^2 = \gamma |E| = 3\,\gamma\,v_g^2\ , \tag{20}$$

où v_g est la dispersion de vitesses de la galaxie test. Les équations (19) et (20) conduisent à un paramètre d'impact critique de

$$p_{\rm crit} = \frac{r_g}{(3\gamma)^{1/2}}\frac{v_{\rm circ,p}^2}{v_g V}\ , \tag{21}$$

où r_g est le rayon rms des étoiles de la galaxie test, et $v_{\rm circ,p}$ est la vitesse circulaire de la galaxie perturbatrice, qui dépend très peu de la distance au centre. Avec la section efficace $\pi p_{\rm crit}^2$ et l'équation (21), le taux de collisions rapides laissant des traces se détermine pour un seuil du paramètre γ :

$$k = \langle vs(v)\rangle = \frac{\pi^{1/2}}{3\gamma}\left(\frac{r_g}{v_g}\right)^2\frac{v_{\rm circ,p}^4}{v_{\rm cl}}\ , \tag{22}$$

qui est pratiquement indépendant du paramètre d'impact.

La Figure 5 montre la variation avec la position dans le groupe ou amas du taux de collisions rapides, obtenu en intégrant l'équation (22) sur les masses des galaxies perturbatrices, en remarquant que les galaxies test et perturbatrices sont toutes deux limitées par les marées de leur amas ou groupe. La Figure 5 montre que *les galaxies perturbées par collisions rapides sont très fréquentes dans les groupes*, en particulier dans leurs parties externes. Mais *les galaxies perturbées par collisions rapides sont aussi relativement fréquentes dans les régions externes des amas.*

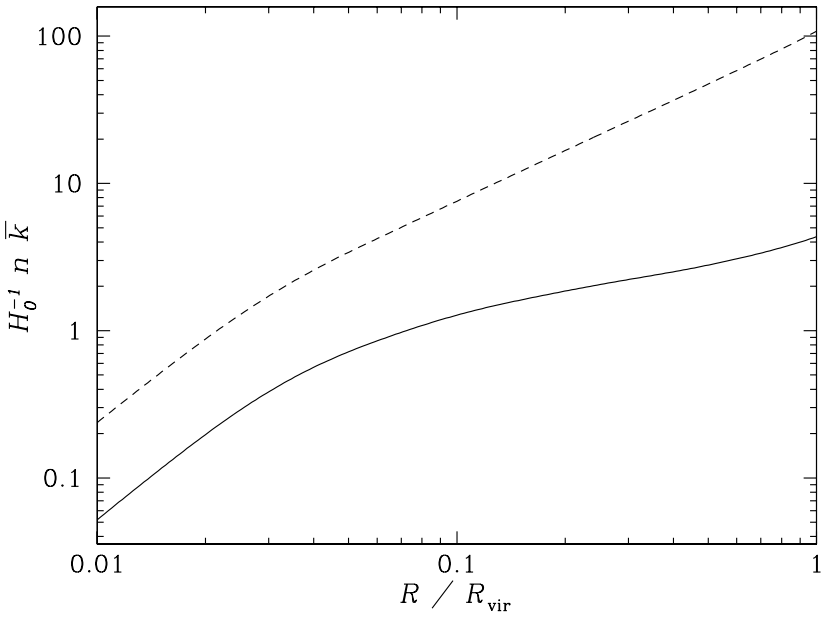

FIG. 5 – *Nombre de collisions rapides fortes ($\gamma = 1/3$) subies par une galaxie, extrapolé sur un temps de Hubble, en fonction de la distance au centre du groupe ou amas (Mamon 2000b). La* courbe pleine *correspond au cas d'un amas NFW, avec une dispersion de vitesses* $v_{\rm cl} = 1000\,{\rm km\,s^{-1}}$, *tandis que le* courbe hachurée *correspond à un groupe NFW, avec* $v_{\rm cl} = 300\,{\rm km\,s^{-1}}$. *La fonction de masse des galaxies (eq. [18]) a une pente asymptotique* $\alpha = -1.3$ *et on adopte* $m_*^{\rm champ} = 5 \times 10^{12}\,h^{-1}\,M_\odot$.

4 Groupes compacts de galaxies

4.1 Introduction

Mes travaux de thèse de doctorat sur la dynamique des groupes de galaxies se sont poursuivis jusqu'à maintenant. Grâce à la gravitation, environ la moitié des galaxies dans l'Univers se situent dans des groupements liés d'au moins quatre galaxies (dans un intervalle de typiquement trois magnitudes, c'est-à-dire un facteur de douze en luminosité). Ces groupes de galaxies sont intéressants pour au moins quatre raisons : a) Ce sont des laboratoires pour étudier la dynamique des galaxies. b) Les interactions dynamiques entre galaxies d'un groupe engendrent des sursauts de formation d'étoiles. c) Ils servent comme indicateurs de distance (en améliorant la précision sur les indicateurs de distance par un facteur $N^{1/2}$, où N est le nombre de galaxies dans le groupe). d) Ils servent à contraindre les paramètres cosmologiques.

Si les groupes paraissent si intéressants, alors pourquoi travaille t-on plus sur les grands amas de galaxies, contenant pourtant dix fois moins de galaxies ? Indubitablement, les amas de galaxies ont des apparences plus spectaculaires. De plus, on pense que les amas de galaxies souffrent moins d'effets de projection que les plus petits groupes. Aussi, même si un groupe est lié gravitationnellement, il peut ne pas être en équilibre, subissant toujours les effets de son expansion de Hubble initiale. Et comme les groupes ont un faible nombre de membres (ou *multiplicité*), le bruit statistique sur leurs propriétés globales est grand. Et finalement, le gaz chaud intergalactique des amas émet fortement en rayons X, alors que le gaz intragroupe n'est observé que depuis quelques années (avec les satellites X ROSAT et ASCA : Pildis, Bregman, & Evrard 1995; Saracco & Ciliegi 1995; Ponman et al. 1996; Mulchaey et al. 1996).

Les groupes dans les grands catalogues (Geller & Huchra 1983; Tully 1987; Maia, da Costa, & Latham 1989; Ramella, Geller, & Huchra 1989; Gourgoulhon, Chamaraux, & Fouqué 1992; Nolthenius 1993; Garcia 1993; Ramella, Pisani, & Geller 1997; Trasarti-Battistoni 1998; Ramella et al. 1999) sont sélectionnés de sorte que leur densité soit de l'ordre de 20 à 100 fois la densité de l'Univers. Ces *groupes diffus ne sont donc pas encore en équilibre viriel* (Byrd & Valtonen 1985; Giuricin et al. 1988; Diaferio et al. 1993; Mamon 1993). L'exemple le plus connu de groupe diffus est le *Groupe Local*, constitué principalement de la galaxie M31 (Andromède) et la Voie Lactée. Comme le décalage spectral de M31 est vers le *bleu*, la galaxie s'approche de nous, et donc le Groupe Local s'effondre probablement pour la première fois (sinon, il faudrait y mettre une masse bien trop grande).

Parmi les groupes de galaxies, le pour-cent des plus compacts est une catégorie à-part : en effet les *groupes compacts* apparaissent, en projection sur le ciel, au moins aussi denses (en 3D) que les cœurs des amas riches de galaxies, et donc comme les régions les plus denses (en galaxies) de l'Univers. Un échantillon de 100 groupes compacts isolés a été sélectionné (Hickson 1982) en 2D sur les planches du Palomar, et sert de référence pour les études de groupes compacts. D'après les données cinématiques de Hickson et al. (1992), la densité de masse moyenne des groupes compacts de Hickson (HCGs) est de l'ordre de 40 000 fois la densité critique de l'Univers. Par conséquent, les groupes compacts devraient constituer le

laboratoire privilégié pour étudier les interactions de galaxies et les sursauts de formation d'étoiles qui doivent en découler.

La première question que l'on doit poser est de savoir si les groupes compacts sont aussi denses en 3D qu'ils apparaissent en 2D? Si la réponse est positive, qu'apprend t-on alors sur les effets des environnements extrêmement denses sur les galaxies et leurs taux de formation d'étoiles?

Dans un article quelque peu provocateur (Mamon 1986), j'avais énuméré un grand nombre d'arguments allant contre l'idée que la majorité de groupes compacts sont aussi denses qu'ils apparaissent en projection, et favorisant l'hypothèse contraire : la plupart des groupes compacts proviendrait d'*alignements fortuits* de galaxies le long de la ligne de visée *à l'intérieur de plus grands groupes.*

Ainsi a débuté un débat entre les partisans de la forte densité 3D des groupes compacts (Sulentic 1987; Hickson & Rood 1988; Hickson 1997) et les partisans des effets de projection, c'est-à-dire moi tout seul au départ (Mamon 1986, 1987, 1992b), puis Hernquist, Katz, & Weinberg (1995), qui ont noté dans leurs simulations cosmologiques quelques cas de groupes compacts, tous causés par des alignements fortuits de galaxies le long de la ligne de visée *à l'intérieur de longs filaments cosmologiques.*

Les groupes compacts de Hickson ont été systématiquement étudiés dans tout le spectre de longueurs d'onde, afin de tirer des informations sur les anomalies morphologiques et de cinématique interne de leurs galaxies, ainsi que sur le taux de formation d'étoiles. Ces études indiquent que les galaxies des groupes compacts sont significativement plus aptes à subir des interactions dynamiques avec leurs voisins que les galaxies isolées ((Hickson 1997) et références incluses). Mais, paradoxalement, les galaxies de groupes compacts montrent significativement moins de coalescences en cours (Zepf 1993) et de formation d'étoiles (Moles et al. 1994) que les galaxies dans des échantillons de paires serrées.

Depuis quinze ans, le sujet des groupes compacts est en croissance exponentielle (le nombre de publications sur les groupes compacts de galaxies étant passé de 3 par an dans les années '80, à 15 par an depuis 1993).[10]

4.2 Effets de projection dans les groupes et amas

Parmi les arguments que j'ai avancés (Mamon 1986) en faveur de l'hypothèse de groupes compacts comme alignements fortuits de galaxies à l'intérieur de plus grands groupes, la plus directe vient de mes simulations de groupes diffus en équilibre (Mamon 1987). J'ai étudié la fréquence avec laquelle on y voyait des sous-groupes en projection satisfaisant exactement les critères que Hickson (1982) a employés pour sélectionner ses groupes compacts. J'ai ainsi montré qu'un groupe diffus avait environ 10% de chances de montrer, dans une projection donnée, un sous-groupe compact et isolé. De plus ces sous-groupes compacts ne sont généralement vus que le long d'un seul parmi trois axes orthogonaux

10. D'après l'ADS (NASA Astrophysics Data System).

de visée, suggérant que la grande majorité de ces sous-groupes proviennent d'alignements fortuits à l'intérieur des groupes diffus.

A noter que la faiblesse de cette étude provient du fait que les groupes diffus que j'ai simulés étaient un peu trop diffus pour pouvoir s'être détachés à temps de leur expansion de Hubble initiale et se trouver en équilibre aujourd'hui.

Cette grande fréquence d'alignements fortuits a été contestée par une étude (Hickson & Rood 1988) basée sur des simulations Monte-Carlo (sans dynamique) qui concluait que le groupe diffus *typique* avait une probabilité de quelques 10^{-5} de donner un alignements fortuit (soit 3000 fois moins que dans mes simulations dynamiques). Peu après, nous avons refait cette étude de manière analytique, en reproduisant les critères d'isolation et de compacité de Hickson (Walke & Mamon 1989), confirmant cette faible probabilité. Toutefois, nous montrons que la probabilité (ou fréquence) d'alignements fortuits dépend très sensiblement de la taille et de la multiplicité du groupe parent. En particulier, plus le groupe parent est grand, plus difficile il est d'aligner des galaxies pour former des groupes plus compacts qu'un seuil absolu. La fréquence d'alignements fortuits varie à peu près comme $R_{\rm parent}^{-4}$, et la fréquence *moyenne* est alors environ 10 fois plus grande que la fréquence *médiane* utilisée par Hickson & Rood. De plus, les deux modèles (Hickson & Rood et Walke & Mamon) supposent une distribution homogène dans le groupe parent, alors que la gravitation force les galaxies à se distribuer de façon très hiérarchique, en paires, etc. En corrigeant pour le nombre de paires observées dans les groupes diffus, on arrive a une fréquence encore 200 fois plus grande, réconciliant ainsi les fréquences très différentes entre simulations Monte-Carlo et simulations dynamiques.

L'autre résultat du travail de Walke & Mamon a été de prédire que les amas de galaxies (c'est-à-dire les groupes à grande multiplicité) doivent donner lieu à une plus grande fréquence d'alignements fortuits que les groupes. En effet, plus il y a de membres dans le groupe parent, plus il y a de façons de les aligner pour en faire un groupe compact et isolé. J'ai testé cette idée en faisant une recherche automatique de groupes compacts dans Virgo (l'amas le plus proche), et j'ai pu ainsi détecter (Mamon 1989) un groupe compact, que Hickson (1982) avait manqué, et qui est alors *le groupe compact le plus proche* (autour de la troisième galaxie de Virgo, Messier 60, alias NGC 4649).

Parmi les autres arguments en faveur d'alignements fortuits et contre l'idée que les groupes compacts sont denses en 3D, il faut noter que les groupes compacts ont une relation morphologie-densité (Mamon 1986) et des rapports M/L (Mamon 1992b) qui sont précisément ce à quoi on s'attend avec des alignements fortuits (la fraction de galaxies spirales est beaucoup plus forte que dans les régions d'amas à densité comparable, et les M/L sont beaucoup plus faibles que ceux des groupes diffus). D'autre part, la moyenne $\langle m_1 - m_2 \rangle$ de la différence de magnitudes entre les 2 galaxies les plus brillantes de chaque groupe compact est statistiquement compatible avec une fonction de luminosité normale (Mamon 1986) , alors que dans les groupes denses simulés, $\langle m_1 - m_2 \rangle$ est significativement plus grand (Mamon 1987), à cause des coalescences de galaxies.

Mais alors, comment expliquer les nombreux signes d'interaction dynamique et de formation d'étoiles accrue dans les galaxies des groupes compacts de Hickson, bien que moins importants que dans les galaxies des paires serrées? En regardant plus en détail les propriétés des alignements fortuits dans mes groupes diffus simulés (Mamon 1992b),

j'ai remarqué que celles-ci ne sont généralement pas constituées de quatre ou cinq galaxies sans association particulière, mais au contraire les trois-quarts des alignements fortuits contiennent au moins une paire serrée. En d'autres termes, *les groupes compacts seraient causés, pour la plupart, par des alignements fortuits de galaxies, naturellement riches en paires*, grâce à la gravitation qui attire les galaxies. Le débat sur les groupes compacts est alors de savoir si les signes modérés d'interaction et de formation d'étoiles accrues dans les galaxies des groupes compacts sont dûs à des groupes denses en 3D ou bien à des paires de galaxies alignées, le long de la ligne de visée, avec d'autres galaxies ou paires.

4.3 Emission diffuse X des groupes compacts

Il est bien connu que le milieu intergalactique dans les amas de galaxies est un plasma très chaud, à peu près en équilibre hydrostatique avec le potentiel de l'amas, et émettant fortement en rayons X, principalement par rayonnement de freinage des électrons dans le potentiel Coulombien des ions du plasma, appelé *bremsstrahlung thermique*, ainsi que par rayonnement en raies, principalement du Fer. Ces rayons X pourraient apporter la solution au débat sur la nature des groupes compacts. En effet, l'émission X est moins sujette aux effets de projection, car l'émissivité X (du gaz diffus et chaud intergalactique) varie comme la densité locale de gaz chaud *au carré*.

Durant les années '90, le satellite ROSAT a permis, pour la première fois, la détection de quelques groupes compacts en rayons X, en particulier avec son spectro-imageur PSPC. Mais d'autres n'ont pas été détectés, et la fraction de groupes compacts détectables, tenant compte des effets de sélection est sujette à débat entre les observateurs. Sergio Dos Santos (alors doctorant à l'IAP, maintenant postdoc au centre de données XMM-Newton à Leicester) et moi avons ré-analysé les images d'archives de ROSAT sur deux groupes compacts extrêmes.

Le premier groupe, HCG 16, est composé de galaxies spirales en interaction, ayant toutes des spectres Starburst, Seyfert ou LINER et avec une dispersion de vitesses très basse ($100\,\mathrm{km\,s^{-1}}$). Deux équipes différentes avaient analysé ce groupe et conclu à l'opposé sur la présence d'émission diffuse : Saracco & Ciliegi (1995) n'en ont pas trouvé, tandis que Ponman et al. (1996) ont en détecté à un niveau 30 fois supérieur à la limite supérieure de Saracco & Ciliegi ! Notre propre analyse d'image bidimensionnelle et multi-longueurs d'onde montre des fortes similarités entre les morphologies X (ROSAT/PSPC) et continu radio à 20 cm (NVSS[11]) Nous avons démontré que plus de la moitié de l'émission X découverte par Ponman et al. était due à des sources (C1A, C1B et C5) en arrière plan et à une étoile (C1C) en avant plan.[12] Donc, *l'émission diffuse en X de HCG 16 est très morcelée, et la plupart est située dans les environnements autour des galaxies du groupe*, ce qui suggère que le groupe est loin de l'état virialisé (Dos Santos & Mamon 1999). Alternativement, la morphologie morcelée du groupe pourrait signifier que le gaz primordial n'ait pu chuter dans le potentiel du groupe parce que son entropie spéficique est plus grande qu'elle ne serait au fond du potentiel (Ponman et al. 1999), et comme l'entropie ne peut diminuer cela revient à une *barrière d'entropie spécifique*.

11. NRAO VLA Sky Survey.

12. Ironiquement, Saracco & Ciliegi, Ponman et al., et nous (Dos Santos & Mamon 1999) avons analysé les *mêmes* observations.

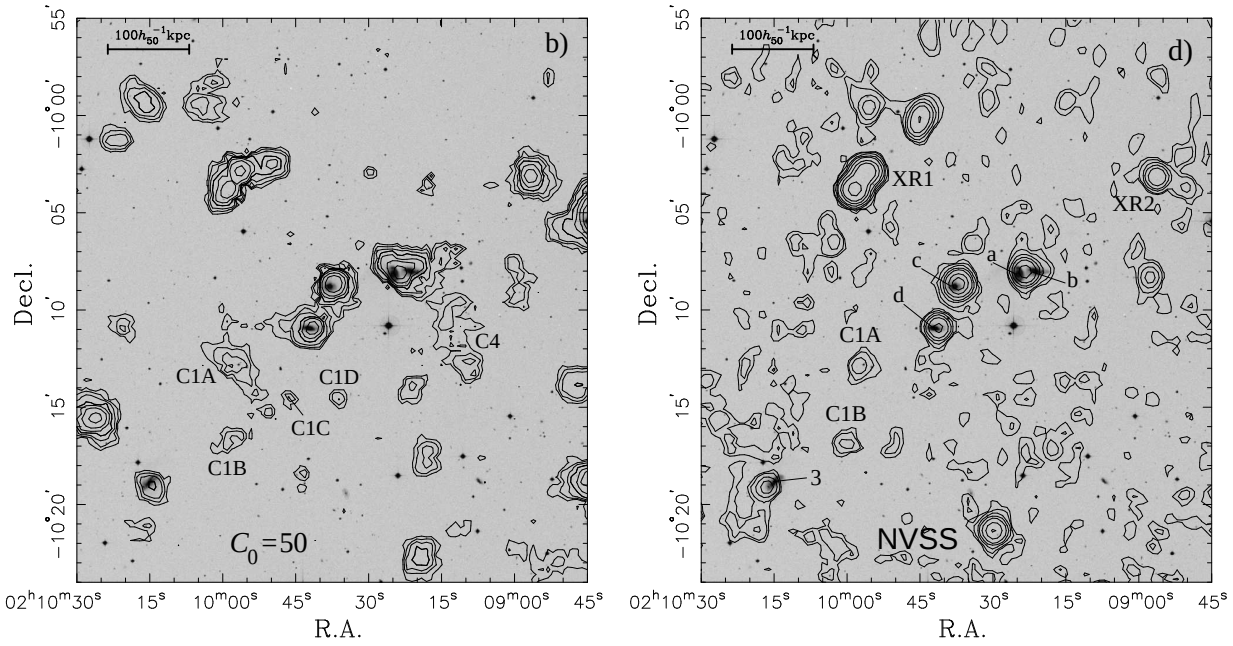

FIG. 6 – Contours *X, après lissage adaptatif (*gauche*) et continu radio à 20 cm, observé par* NVSS *(*droite*) du groupe compact HCG 16, superposés sur l'image optique (*niveaux de gris*), tiré de Dos Santos & Mamon (1999).*

Nous avons obtenu du temps sur le nouveau satellite X Américain Chandra (anciennement AXAF) pour mesurer la température et l'abondance en métaux lourds de la seule région d'émission de HCG 16 qui soit loin des galaxies (C4, qui pourrait représenter une épisode de vent galactique, ou bien un morceau de galaxie, arraché par effets de marée lors d'une collision avec une autre galaxie, ou encore des sources en arrière-plan).

D'autre part, nous sommes en train d'analyser l'émission X de ROSAT provenant du groupe chaud et très probablement virialisé HCG 62, au moyen d'une nouvelle technique que nous avons développée qui permet de cartographier la température et l'abondance en métaux d'un groupe ou amas, au moyen de cartes de dureté obtenues à partir d'images filtrées par ondelettes. Cette méthode est prometteuse pour les analyses d'amas avec Chandra ou avec l'autre nouveau satellite X, Européen, XMM-Newton.

Finalement, dans le but de rassembler un maximum de données X sur les groupes, dont les propriétés X sont très divers, S. Dos Santos et moi venons de former un consortium avec J. Vrtilek, W. Forman, C. Jones (CfA Harvard) et T. Ponman (Birmingham) sur l'analyse X des groupes compacts à partir des données Chandra et XMM-Newton.

4.4 La dispersion de vitesses minimale des systèmes de galaxies

Pour qu'un groupe ou amas de galaxies soit en équilibre dynamique, il lui faut une dispersion de vitesses minimale. L'idée est fort simple : *un système de galaxies doit avoir plus de masse que la somme des masses de ses galaxies*, c'est-à-dire

$$M_{\rm groupe}(R_{\rm vir}) \geq \sum_j m_{{\rm gal},j}(r_{{\rm vir},j}) \ ,$$

où $R_{\rm vir}$ est le rayon du viriel du groupe, tandis que $r_{{\rm vir},j}$ correspond au rayon du viriel de la galaxie j. Comme les systèmes assez denses pour se détacher de leur expansion de Hubble initiale et obéissant au théorème du viriel doivent suivre une relation $M \sim \sigma_v^3$ (vérifiée par divers auteurs à partir de simulations cosmologiques), un minimum de masse est équivalent à un minimum de dispersion de vitesses.

Comme les HCGs sont définis comme des systèmes *isolés*, on peut trouver un critère plus contraignant en considérant, à un rayon R beaucoup plus grand que la séparation typique entre galaxies du groupe, la masse contenue dans le groupe :

$$M(R) \geq \sum_j m_j(R) \ .$$

En adoptant des profils NFW, à la fois pour le groupe et pour les galaxies, et en tenant compte de la variation de la concentration des profils NFW avec la masse (Navarro et al. 1997), j'arrive à la condition

$$\sigma^2_{v,,{\rm gpe}} \geq 0.5 \sum_E \sigma^2_{v,j}(0) + 0.14 \sum_D v^2_{{\rm rot},j} \ , \tag{23}$$

où les sommes sont sur les galaxies elliptiques (E) et à disque (D), et où $\sigma_{v,j}$ est la dispersion de vitesses de la galaxie elliptique j, tandis que $v_{{\rm rot},j}$ est la vitesse de rotation maximale de la galaxie disque j.

Il faut noter que si un groupe est dans sa phase d'effondrement maximal, sa dispersion de vitesses sera encore plus grande que lorsqu'elle aura atteint son équilibre viriel. En revanche, un groupe qui coalesce globalement aura une dispersion de vitesses faible (qui devient nulle lorsque la coalescence est achevée). Cela semble être le cas pour un groupe compact découvert par Weinberger, Temporin, & Kerber (1999), mais de tels cas sont très rares.

Malheureusement, l'équation (23) nécessite la connaissance de la cinématique interne des galaxies des groupes compacts, et l'information n'est connue que pour quelques galaxies dans quelques groupes. Mais on peut employer les relation d'échelle reliant la cinématique interne aux luminosités connues des galaxies :

- La relation Faber & Jackson (1976) pour les galaxies elliptiques et bulbes des lenticulaires, renormalisée par de Vaucouleurs & Olson (1982)

  $$M_B - 5 \log h = -A - 9 \ (\log \sigma_v - 2.3) \ ,$$

  où M_B est la magnitude absolue, avec $A = 19.4$ pour les elliptiques et $A = 19.6$ pour les S0.

- La relation Tully & Fisher (1977) pour les galaxies à disque, calibrée avec les distances aux galaxies, déterminées avec des étoiles Céphéïdes par Sakai et al. (2000)

  $$M_B = -7.85 \ (\log W^c_{20} - 2.5) - 19.7 \ ,$$

  où M_B est la magnitude absolue totale extrapolée de la galaxie, après correction pour l'extinction interne et de notre Galaxie, tandis que W^c_{20} est la largeur de la raie d'Hydrogène neutre à 21 cm, mesurée à 20% du maximum et corrigée de l'inclinaison et du décalage spectral.

On obtient alors, avec $h = 0.7$ (e.g. Sakai et al. 2000), une dispersion de vitesses minimale pour le groupe qui satisfait

$$\begin{aligned}\left(\frac{\sigma_{v,\mathrm{gpe}}}{100\,\mathrm{km\,s^{-1}}}\right)^2 &\geq 2.1\sum_E \mathrm{dex}[-(M_B+20)/4.5] \\ &+ 1.9\sum_L \mathrm{dex}[-(M_B+20)/4.5] \\ &+ 0.4\sum_S \mathrm{dex}[-(M_B+20)/3.9]\ ,\end{aligned}$$

où les sommes sont sur les galaxies elliptiques, lenticulaires et spirales, respectivement.

Hélas, les groupes compacts de Hickson ont trop peu de membres (typiquement 4!) pour que leurs dispersions (écarts-type) de vitesses soient fiables.[13] Ainsi, la distribution des $\sigma_{v,\mathrm{gpe}}/\sigma^{\mathrm{min}}_{v,\mathrm{gpe}}$ est similaire à celle obtenue par simulations Monte-Carlo, dans l'hypothèse ou le *vrai* écart-type de chaque groupe est précisément $\sigma^{\mathrm{min}}_{v,\mathrm{gpe}}$.

Toutefois, on peut aller plus loin en considérant le sous-échantillon des 16 groupes compacts pour lesquels de Carvalho et al. (1997), Zabludoff & Mulchaey (1998) et Barton, de Carvalho, & Geller (1998) ont cherché des galaxies peu lumineuses (dont les décalages spectraux suggèrent leur appartenance au groupe), et qui, pour la plupart, ont au moins 7 galaxies. Je trouve alors que 3 groupes sur 16 ont des probabilités de moins de 1.5% d'avoir $\sigma_{v,\mathrm{gpe}} > \sigma^{\mathrm{min}}_{v,\mathrm{gpe}}$, dans le cas défavorable où leur $\sigma^{\mathrm{vrai}}_{v,\mathrm{gpe}} = \sigma^{\mathrm{min}}_{v,\mathrm{gpe}}$, alors que l'on s'attend à $0.015\times16 = 0.2$ groupe. De même, 5 groupes sur 16 ont des probabilités de moins de 6.5%, alors que l'on s'attend à $0.065\times16 = 1$ groupe. On en conclut qu'environ *le quart des groupes compacts ont des dispersions de vitesses trop faibles pour être denses en 3D.*

4.5 La fonction de masse des groupes denses de galaxies

Quelle est la fréquence de groupes compacts attendue par les analyses cosmologiques de la formation des structures de l'Univers? J'ai entrepris de répondre à cette question en adaptant le formalisme de *Press & Schechter étendu* aux groupes compacts. Ainsi, la fonction de masse des groupes denses aujourd'hui peut s'écrire comme l'intégrale sur les époques de formation des taux de formation des groupes avec au moins la moitié de la masse :

$$N_{\mathrm{DG}}(M,t_0) = \int_{t_0-\Delta t}^{t_0} dt \int_{M/2}^{M} dM'\, R_{\mathrm{form}}(M',t)\, P(M,t_0|M',t)\ , \qquad (24)$$

où $t_0-\Delta t$ est l'âge de l'Univers à la formation du groupe, M' sa masse lors de sa formation, $R_{\mathrm{form}}(M',t)$ est le taux de formation des structures de masse M' au temps t (Kitayama & Suto 1996a) et $P(M,t_0|M',t)$ est la probabilité qu'un objet de masse M' au temps t se retrouve à une masse M au temps t_0 (Lacey & Cole 1993).[14]

Si les groupes compacts se sont formés avec leurs tailles actuelles, leurs surdensités de 40 000 par rapport à la densité critique de l'Univers impliquent qu'ils ont dû se former

13. La distribution de $N\,\sigma^2/\sigma^2_{\mathrm{vrai}}$ est distribuée selon une loi de χ^2 avec $N-1$ degrés de liberté, qui est très large, pour $N = 4$, typique des groupes compacts.

14. L'intégrale double de l'équation (24) peut se réduire à une intégrale simple par inversion de l'ordre d'intégration.

à $z \simeq 8$ (quelque soit Ω_0 et λ_0), car c'est à cette époque que le rayon de viriel d'un système de la masse actuelle d'un groupe à la taille d'un groupe compact d'aujourd'hui. Déjà, très peu de structures de la masse des groupes sont déjà formées si tôt. De plus, une telle structure aurait des bonnes chances d'être cannibalisée dans une structure bien plus massive. Finalement, les galaxies devraient coalescer rapidement (Mamon 1987), de sorte que l'on n'aurait plus à faire à un groupe compact, mais à une galaxie elliptique géante. Donc, si on adopte cette hypothèse, alors les groupes compacts observés doivent être des alignements fortuits de galaxies.

L'alternative est que les groupes compacts se forment avec des plus grandes tailles et décroissent en taille par friction dynamique des galaxies contre la matière noire qui domine le potentiel du groupe. Dans le cas extrême, un groupe compact de masse M peut se former récemment avec un rayon similaire à son rayon viriel actuel et les galaxies les plus massives, de masse m, et situées plutôt dans les régions internes du groupe qui vient de virialiser, vont subir un déclin orbital par friction dynamique, qui prend typiquement M/m temps de croisement (e.g. Mamon 1995).

La Figure 7 illustre l'application de l'équation (24) au cas où le groupe se forme récemment (pour survivre un temps compatible avec les temps de survie observés dans les simulations à N-corps de Mamon 1987), puis ses galaxies centrales forment un système de taille décroissante par friction dynamique. D'après la Figure 7, les groupes denses qui ont survécu en tant que groupes compacts (c'est-à-dire avec au moins 4 galaxies brillantes distinctes), sont assez fréquents pour expliquer la grande majorité des groupes compacts observés.[15] On déduit alors que *la plupart des groupes compacts observés sont réels.*

Dans tous les cas, je prédis que *les groupes compacts doivent être beaucoup plus rares que les restes des anciens groupes denses, c'est-à-dire les galaxies elliptiques supergéantes (en dehors des amas)* (Mamon 2000c). Deux équipes (Mulchaey & Zabludoff 1999; Vikhlinin et al. 1999) ont cherché l'émission en rayons X autour de galaxies elliptiques lumineuses et isolées, qui pourraient être le produit de ces coalescences multiples de galaxies dans des ex-groupes compacts. Ils ont trouvé que la plupart avaient bien des halos en X qui ressemblaient bien plus, par leur luminosité X et leur étendue, aux groupes compacts comme HCG 62, qu'aux galaxies elliptiques.

4.6 Epilogue : la nature des groupes compacts de galaxies

Après avoir longtemps poussé l'hypothèse selon laquelle les groupes compacts sont en majorité causés par des alignements fortuits de galaxies le long de la ligne de visée à l'intérieur de groupes diffus, mes travaux récents penchent vers l'hypothèse contraire, selon laquelle les groupes compacts sont bien denses en 3D.

15. On trouve environ 10 fois plus de groupes par unité de volume que les groupes compacts de Hickson. Toutefois, une recherche automatique de groupes compacts par Prandoni et al. (1994) a montré que la complétude de l'échantillon de Hickson n'est que de 20%. Ainsi on trouve 2 fois *trop* de groupes compacts, ce qui est probablement dans les erreurs systématiques de la méthode.

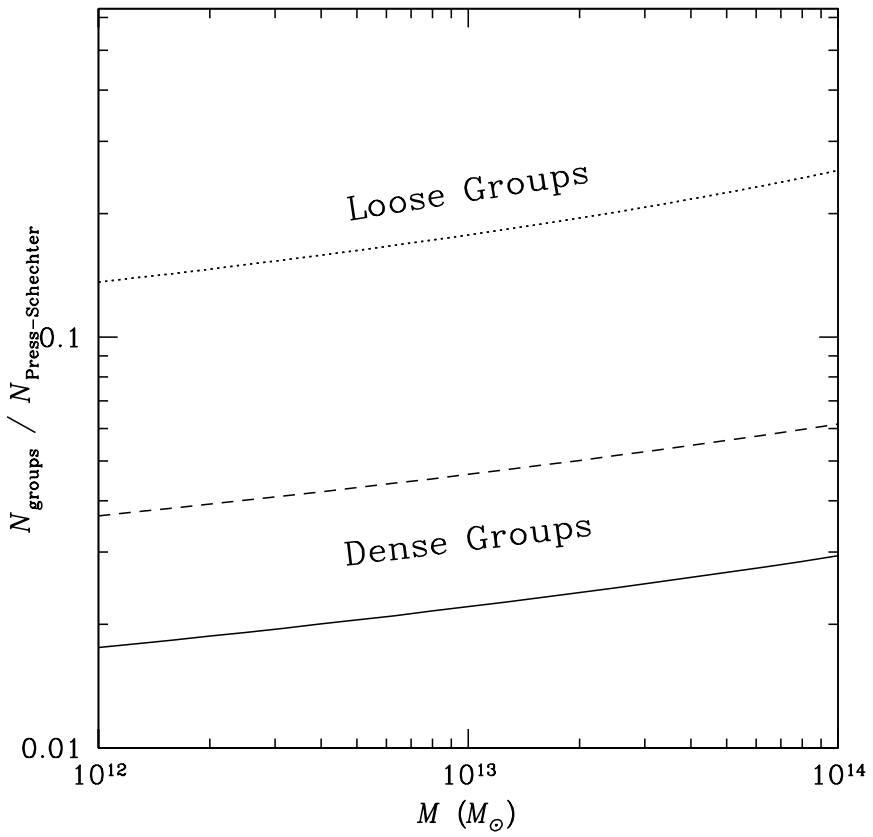

FIG. 7 – *Fonctions de masse des groupes denses (*courbes épaisses*) et diffuses (*courbes fines pointillées*), normalisées à la fonction de masse cosmique de Press & Schechter, tiré de Mamon (2000c). On suppose une cosmologie ΛCDM avec $\sigma_8 = 0.9$. Les* courbes hachurées *et* pleines *correspondent aux groupes denses qui s'effondrent après* 0.9 *et* $0.95\,t_0$*, respectivement.*

Certes, notre étude sur HCG 16 indique que l'on a surestimé la fraction de groupes compacts ayant une composante diffuse de gaz chaud émettant en rayons X. Mais, HCG 16 pourrait être un cas rare.

La distribution des dispersions de vitesses des groupes compacts de Hickson est cohérente avec l'hypothèse que tous sont denses en 3D, mais l'emploi de galaxies naines dans le groupe indique qu'au moins le quart de l'échantillon des groupes est causé par alignements fortuits de galaxies.

L'analyse de la fonction de masse des groupes compacts dépend de l'importance de la friction dynamique subie par les galaxies des groupes compacts. S'ils en ont subi peu, alors les groupes compacts auraient dû se former très tôt et résister aux coalescences des galaxies, ce qui est très improbable et pousse l'idée de alignements fortuits. Si, au contraire, les groupes compacts proviennent de systèmes virialisés de typiquement 200 à $500\,h^{-1}$ kpc, dont certaines galaxies massives ont subi une friction dynamique importante, alors on trouve que de tels systèmes se forment assez fréquemment pour expliquer la plupart des groupes compacts comme systèmes bien denses en 3D.

Au niveau théorique, on peut espérer résoudre le débat à partir d'échantillons de galaxies simulés dans le contexte de l'Univers hiérarchique. Mais cela nécessite que l'évolution dynamique des galaxies dans les groupes et amas soit bien prise en compte, par exemple par les méthodes de la Sec. 3.3.

Au niveau observationnel, on a beaucoup à gagner avec les futures observations Chandra et surtout XMM-Newton (qui est 10 fois plus sensible), qui détermineront la fraction de groupes compacts avec de l'émission diffuse en rayons X.

A plus long terme, on pourra confirmer les analyses X, en les combinant aux cartes de l'effet *Sunyaev-Zel'dovich* (*SZ*), comme cela a été suggéré par Ostriker, Lubin, & Hernquist (1995). En effet, alors que la brillance de surface X est à peu près proportionnelle à $\int n_{\rm gaz}^2\, ds$,[16] l'effet SZ mesure $\int n_{\rm gaz}\, ds$, et la combinaison des deux peut lever la dégénérescence entre effets de projection et fraction de gaz dans les groupes (Ostriker et al.).

D'autre part, la mesure du *cisaillement faible* (*weak shear*), par l'analyse statistique des angles de position des galaxies d'arrière plan, permettra de cartographier le potentiel projeté, et séparer les groupes selon la morphologie de leur potentiel projeté.

16. La proportionnalité est exacte pour un plasma isotherme.

5 L'Univers local en proche IR

5.1 Introduction

Alors que les analyses cosmologiques, basées sur la distribution des galaxies, ont toutes été faites à partir d'échantillons sélectionnés dans le domaine *Visible* (d'ailleurs toute l'astronomie a commencé par là !), le proche infrarouge (IR) est la bande de couleur idéale pour la cosmologie, pour 3 raisons :

1. L'émission proche IR semble être la mieux représentative de la masse en étoiles d'une galaxie, contrairement à la lumière Visible, qui est très accrue par la formation récente d'étoiles, et contrairement aussi à l'IR lointain qui détecte directement les poussières autour d'étoiles jeunes, et est donc aussi très sensible à la formation récente d'étoiles.

2. La lumière proche IR n'est que très peu absorbée (jusqu'à 10 fois moins que la lumière visible) par les poussières ce qui permet une vue propre des galaxies.

3. De même, grâce à cette faible extinction en proche IR, on peut voir pratiquement à travers le plan de la Voie Lactée et on a donc une vision quasi-totale de l'Univers proche (alors que, jusqu'à là, nous avons été limités à des zones au moins 10° au dessus — ou au dessous — du plan de la Voie Lactée).

5.2 Le relevé 2D DENIS

La mise au point récente de détecteurs imageurs performants en proche IR a permis la création du programme européen DENIS (DEep Near-Infrared Southern Sky Survey) de cartographie digitale complète du ciel austral en infrarouge proche. Le relevé DENIS (1995–2000) est en train d'obtenir 4000 Gigaoctets d'images en bandes I ($0.8\,\mu$), J ($1.25\,\mu$) et K_s ($2.15\,\mu$). De ces images, on pense pouvoir tirer près de 10^9 étoiles de notre Galaxie, ainsi que des échantillons complets et fiables d'environ $10^5(K_s)$, $3\times10^5(J)$, et $>10^6(I)$ galaxies. La base de données extragalactique sera donc parmi les plus grandes au monde, avec, en plus tous les avantages de la sélection en proche IR. En particulier, malgré la concurrence du consortium Américain 2MASS, *nous développons le premier échantillon de galaxies en bande I, qui servira de référence pour les années à venir.*

C'est pourquoi je me suis associé au consortium DENIS au début de 1991, et j'en suis devenu le responsable scientifique de l'extraction des galaxies, ainsi que le responsable scientifique de l'équipe extragalactique. En 1991, j'ai convaincu le consortium d'étendre DENIS des voies JK à la voie I.

L'extraction des galaxies des images DENIS représente un défi considérable, pour les raisons suivantes :

1. Les galaxies sont cinq à dix mille fois moins fréquentes que les étoiles.

2. La fonction d'étalement (PSF) est large, en partie parce que les pixels en bandes J et K_s sont de $3''$ (mais de $1''$ en bande I).

3. La PSF varie à travers les images, pour raison de défocalisation et mauvais alignement du télescope, et dans le temps, de sorte qu'il faille modéliser cette PSF, pratiquement image par image.

4. La géométrie du sondage en *strips* très fins ($30°$ par $12'$) empêche la couverture efficace de zones précises.

En 1997–1998, j'ai mis en place une chaîne de traitement préliminaire de galaxies, qui se fait en deux étapes :

1. Les images *corrigées du champ* (flat-fieldées) sont réduites par le logiciel SExtractor de Bertin & Arnouts (1996), qui entreprend les tâches suivantes :

   - calcul du fond de ciel[17] et son écart-type sont calculés localement
   - filtrage des rayons cosmiques[18]
   - lissage de l'image
   - détection des objets : un minimum de pixels connexes dont l'intensité est au dessus d'un seuil égal à $3\,\sigma$ au dessus du fond de ciel[19]

   Les paramètres optimaux d'extraction (nombre d'écarts-type au dessus du fond pour le seuil de détection et nombre de pixels minimum), sont fonctions de la fenêtre de lissage, et ont été déterminés au moyen de nombreuses simulations d'images, avec le but d'éviter que les faux objets dûs au bruit représentent plus que 5% du nombre de galaxies (Banchet, Mamon, & Contensou 1995).

2. Les catalogues d'objets sont analysés avec différents algorithmes classiques de séparation étoiles/galaxies, ainsi que par les *réseaux neuronaux* de SExtractor. Dans chaque cas, la frontière entre étoiles et galaxies est une fonction linéaire de la magnitude, de pente optimisée (Mamon et al. 1998).

J'ai pu mesurer la complétude et la fiabilité des algorithmes en construisant divers *tables de vérité*, basées soit sur des classifications visuelles sur les images I de DENIS, soit sur des catalogues d'objets (étoiles et galaxies) légèrement plus profonds, sélectionnés en bande bleue par la numérisation entreprise par les équipes APM et COSMOS des plaques photographiques du ciel austral prises sur le télescope de *Schmidt* de l'UKST. Ainsi, j'ai pu montrer (Mamon et al. 1998) que l'on obtient avec des méthodes classiques de séparation étoiles/galaxies une extraction à la fois complète et fiable à plus de 95% jusqu'à $I = 16.5$ à hautes latitudes galactiques (alors que les réseaux neuronaux du logiciel SExtractor s'avèrent être bien moins performants).

---

17. L'instrument peut aussi contribuer au fond, par lumière diffusée et en bande K par émission thermique.
18. Nous avons modifié SExtractor pour que les rayons cosmiques soient filtrés.
19. L'écart-type σ est celui de l'image *lissée*.

Durant les 18 derniers mois, j'ai considérablement amélioré les algorithmes de séparation étoiles/galaxies. J'emploie la statistique

$$x = \log\left(\frac{I_{\rm max}}{A_{\rm iso}}\right) \ ,$$

où $I_{\rm max}$ est l'*intensité maximale* de l'objet (l'intensité de son pic), tandis que $A_{\rm iso}$ est l'*aire isophotale* (nombre de pixels à l'intérieur de l'isophote de détection). Cette statistique à l'avantage de cumuler les deux statistiques de concentration/étendue des objets que sont $I_{\rm max}$ en fonction de la magnitude et $A_{\rm iso}$ en fonction de la magnitude. Aujourd'hui, la séparation étoiles/galaxies peut désormais se faire jusqu'à $I = 18$ (mais la limite d'extraction fiable et complète de galaxies reste vers $I = 16.5$).

Pour optimiser la frontière entre étoiles et galaxies, je définis d'abord le *lieu* des étoiles et ensuite le lieu des galaxies. J'emploie le fait que la grande majorité des objets détectés sont des étoiles. Pour cela, j'ajuste (avec rejet des points discordants) un polynôme d'ordre 3 aux médianes des $x = \log[I_{\rm max}/A_{\rm iso}]$, calculées, pour tous les objets, sur une grille fine de magnitudes, pour obtenir une estimation de premier ordre du lieu des étoiles. Puis, je calcule les écarts-type en calculant la racine carrée de la moyenne tronquée des carrés des résidus par rapport au lieu des étoiles. Puis j'itère, en rejetant les points en dehors de $\pm 3\,\sigma$: en recalculant les médianes et moyennes des x dans les intervalles fins de magnitude, j'en déduis les modes avec la relation

$$\text{Mode} = 3 \times \text{Médiane} - 2 \times \text{Moyenne} \ ,$$

et j'ajuste un polynôme d'ordre 3 à ces modes, pour obtenir l'estimation finale du lieu des étoiles. Je recalcule alors les écarts-type en recalculant la racine carrée de la moyenne tronquée des carrés des résidus par rapport au lieu des étoiles.

Pour les galaxies, je ne considère que les objets moins concentrés que $3\,\sigma$ par rapport au lieu des étoiles, et je prends une relation linéaire de pente 0.2, imposée, et de normalisation conforme à la médiane des $x - 0.2\,m$, où m est la magnitude I.

Reste à choisir la frontière des tracés de séparation étoiles/galaxies à fiabilité F donnée, $x_F(m)$. A priori, le choix de $x_F = {\rm Cte} \simeq 2.5$ donne des bons résultats pour les magnitudes pas trop faibles (Mamon et al. 1998, voir aussi Fig. 8 plus bas).[20] Mais cette coupure fixe limite la séparation étoiles/galaxies à faibles magnitudes et il faut adapter la valeur à la qualité des observations (une plus grande PSF donne des lieux d'étoiles avec des plus faibles x — et de même, à moindre mesure, pour les galaxies), et à la densité d'étoiles sur les images.

Alternativement, on pourrait appeler 'galaxies' les objets qui sont à plus de 2 ou 3 écarts-type du lieu des étoiles, comme cela est souvent fait dans la littérature. Mais ce faisant, la fiabilité de l'échantillon des galaxies dépendrait du rapport entre le nombre d'étoiles et le nombre de galaxies. Ainsi, pour une sélection à 95% de fiabilité, il suffirait, au Pôle Galactique Sud, de sélectionner les objets à plus de $2.5\,\sigma$ du lieu des étoiles, alors qu'à quelques degrés du Plan Galactique, le nombre d'étoiles est tel qu'il faudrait se restreindre aux objets à plus de $4.5\,\sigma$ du lieu des étoiles.

20. Cela permet une séparation étoiles/galaxies à l'œil sur les données des catalogues !

Il faut donc prendre en compte le rapport entre le nombre d'étoiles, $f_*(m)$ et le nombre de galaxies, $f_g(m)$ à une magnitude m donnée, qui décroît assez fortement avec la magnitude (car notre Galaxie est de taille finie). Comme la distribution de x, à une magnitude donnée, est à peu près une gaussienne pour les étoiles et une autre gaussienne pour les galaxies, pour une fiabilité de 50%, on mettra la frontière pour la valeur de x pour laquelle le nombre différentiel (par intervalle de x) d'étoiles

$$n_*(x,m) = f_*(m)\, G(x,\bar{x}_*(m),\sigma_*(m)) \ ,$$

où $G(\mu,\sigma)$ est la gaussienne de moyenne μ et d'écart-type σ est égal au nombre différentiel de galaxies

$$n_g(x,m) = f_g(m)\, G(x,\bar{x}_g(m),\sigma_g(m)) \ .$$

Plus généralement, la fiabilité s'écrit

$$F = \frac{f_g(m)\, G(x,\bar{x}_g(m),\sigma_g(m))}{f_g(m)\, G(x,\bar{x}_g(m),\sigma_g(m)) + f_*(m)\, G(x,\bar{x}_*(m),\sigma_*(m))} \ , \qquad (25)$$

et il est aisé de résoudre l'équation (25) pour x, étant donné une fiabilité F donnée. La fonction $f_*(m)$ est déterminée par ajustement, sur les étoiles du strip, d'une relation linéaire, sans à priori de pente, entre le logarithme décimal des comptages et la magnitude. Pour les galaxies, on suppose une pente 0.6, (dite *Euclidienne*, car elle correspond à un Univers homogène, sans effets de corrections k ou d'évolution), et on ajuste simplement la normalisation des comptages $f_g(m)$.

L'an passé, avec mon stagiaire de magistère, Frédéric Giraud, nous avons incorporé des filtres de faux objets (glitchs, objets dans les enveloppes d'étoiles saturées, etc.) dans notre extraction, ce qui a permis d'augmenter sensiblement la fiabilité de l'extraction des galaxies. La Figure 8 illustre notre séparation étoiles/galaxies. Nous avons validé notre séparation étoiles/galaxies par comparaison aux catalogue EDSGC tiré des scans COSMOS des plaques UKST et par visualisation des images dans les cas de désaccord entre le EDSGC et nous. Ainsi, en extrapolant sur le ciel austral, nous devrons obtenir un catalogue, très fiable et à plus de 50% complet, d'environ 5 millions de galaxies (en bande I), dont près d'un million dans un sous-échantillon complet à 95% à $I < 16.5$ (avec une photométrie précise à 0.10 magnitude).

La chaîne d'extraction des galaxies tourne de façon automatique depuis le 12 Avril 2000, au rythme *théorique* de 60 deg^2 par semaine, en employant les images DENIS, corrigées du champ (par J. Borsenberger), qui restent temporairement sur les disques de nos stations de travail.[21] Une version qui lit les données sur bandes DLT, et qui devra traiter 1000 deg^2 par semaine, et par conséquent devra être opérationnelle en Juin 2000, et permettra de rattraper le traitement du flat-field vers la fin de l'été. De plus, le centre parisien de traitement de données DENIS bénéficiera, à partir de l'été 2000, d'un ensemble de disques RAID, permettant de stocker 60% des images DENIS, corrigées du champ (1.7 Téraoctets). L'extraction automatique des galaxies devra alors passer à 2000 deg^2 par semaine, sans aucune intervention manuelle (comme l'insertion de bandes DLT dans les lecteurs).

Vers la fin de l'été 2000, on devrait avoir un catalogue de galaxies sur la quasi-totalité des zones déjà observées par DENIS. En automne 2000, je compte travailler sur l'incorporation des variations spatiales de la PSF (modélisées par C. Alard) dans mon algorithme de séparation étoiles/galaxies.

21. Des pannes fréquentes de disque ont considérablement ralenti la chaîne de traitement.

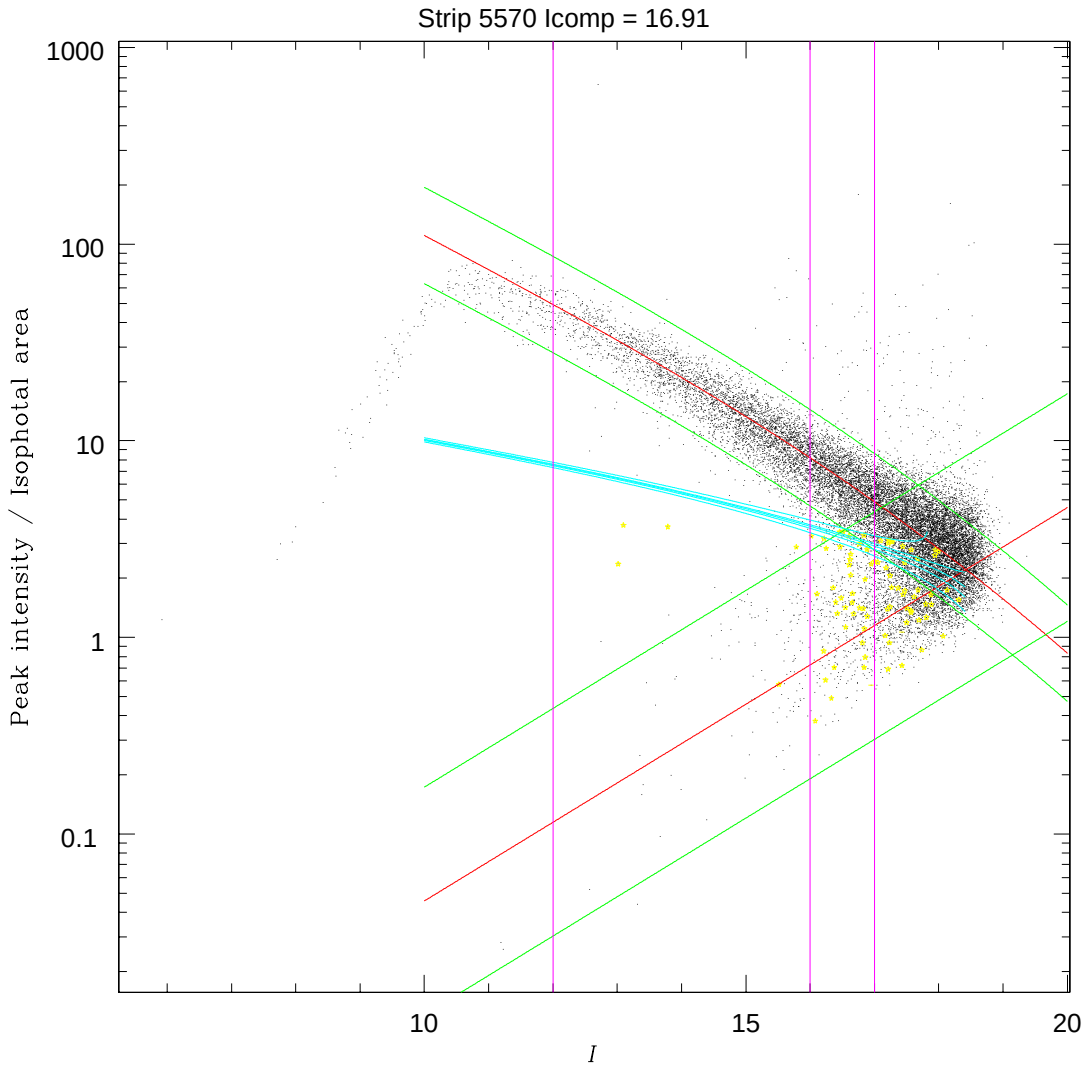

FIG. 8 – *Diagramme de séparation étoiles/galaxies pour un strip de 180 images* DENIS *à relativement haute latitude galactique. La zone dense du haut représente les étoiles (la cassure de pente vers* $I = 10$ *est due à la saturation des détecteurs CCD), tandis que la zone moins dense en bas représente les galaxies. La* courbe rouge *et la* ligne rouge *donnent les moyennes des lieux des étoiles et galaxies, respectivement, tandis que les* courbes *et* lignes vertes *donnent les intervalles de confiance* $\pm 3\sigma$*, pour les étoiles et galaxies, respectivement. Les points au dessus de la zone des étoiles (*$16 \leq I \leq 19$*) sont des rayons cosmiques (qui ont survécu à notre filtrage dans* SExtractor*). Les* courbes turquoises *représentent les limites de séparation étoiles/galaxies à fiabilité donnée. Les* symboles jaunes *indiquent les candidats galaxies qui sont filtrées, généralement parce qu'elles sont trop près d'étoiles très brillantes.*

Nos premiers résultats scientifiques sont les suivants :

- Les comptages de galaxies dans la voie I, à partir d'un sous-échantillon de 50 degrés carrés, sont représentés, sur 5 magnitudes, par une loi Euclidienne, alors que les comptages effectués avec l'APM ou COSMOS donnaient une déficience de galaxies brillantes par rapport à l'extrapolation des comptages de galaxies plus faibles (Mamon et al. 1998; Mamon 1998). Nous estimons que la différence provient de la difficulté de corriger les effets de non-linéarité dans la photométrie sur plaques photographiques. A noter que ces comptages Euclidiens invalident les théories fractales de l'Univers. [22]

- Les premiers comptages en bande J sont Euclidiens aussi (Mamon et al. 1998; Mamon 1998). Ainsi, il n'y a plus besoin d'invoquer une évolution des galaxies à très bas décalage spectral comme ce fut le cas avec les comptages des sondages APM et COSMOS.

- Une comparaison précise et croisée des listes de galaxies COSMOS et DENIS indique que COSMOS a une fiabilité et complétude de moins de 70% à 80% aux magnitudes $15.5 < b_J < 17.5$, et la complétude COSMOS descend à moins de 5% pour $b_J < 14.5$ (Fig. 5.2 et Mamon 2000a). Ainsi COSMOS *manque systématiquement les galaxies très brillantes* (car leur chaîne de traitement sur-compense les effets de la non-linéarité des plaques photographiques).
  En revanche, ces comparaisons révèlent que DENIS *est complet et fiable à plus de 95%* pour $13 < I < 16.5$ (ce qui équivaut à peu près à l'intervalle de magnitudes b_J précédent). Pour cela, nous avons systématiquement visualisé les images de plusieurs centaines d'objets pour lesquels les classifications DENIS et COSMOS sont différentes (galaxie pour l'une, étoile ou non-vue pour l'autre et réciproquement) : nous avons alors trouvé que dans 80% des cas, c'est DENIS qui avait raison et non COSMOS

- La découverte de galaxies sur une petite région dans la Zone d'Obscurcissement (derrière le plan de la Voie Lactée), aux latitudes galactiques $1° < |b| < 5°$ (Schröder et al. 1999).

Frédéric Giraud et moi avons aussi mesuré la fonction de corrélation angulaire des galaxies DENIS, qui mesure l'excès de probabilité de trouver une galaxie à une distance angulaire donnée d'une autre. Le calcul de la fonction de corrélation se fait par comparaison à des échantillons de galaxies tirées au hasard, *sur la même géométrie que les données*. Comme notre échantillon de galaxies DENIS provient d'une zone non-contiguë d'observations DENIS, nous avons pris beaucoup de soins à simuler, image par image, la couverture de notre échantillon de galaxies, et nous avons masqué dans les simulations les zones proches d'étoiles saturées, que nous filtrons de nos catalogues préliminaires de galaxies. Notre première fonction de corrélation, sur 8 strips de $6\,\mathrm{deg}^2$ chacun, est en bon accord avec celle obtenue du catalogue APM (en bande B) et celle de Postman et al. (1998, en bande I). Ma stagiaire de DEA, Effrosyni Rassia, est en train d'améliorer les programmes de Frédéric Giraud et se prépare à recalculer les fonctions de corrélation angulaires, de manière

22. On pourrait s'inquiéter d'un raisonnement circulaire, puisque l'on a adopté des comptages de galaxies de pente Euclidienne dans l'algorithme de séparation étoiles/galaxies. Toutefois, nos comptages de galaxies restent Euclidiens — aux magnitudes brillantes où la séparation étoiles/galaxies est fiable — quand on emploie un algorithme plus simple de séparation étoiles/galaxies, sans faire d'hypothèse, à priori, sur la pente des comptages de galaxies.

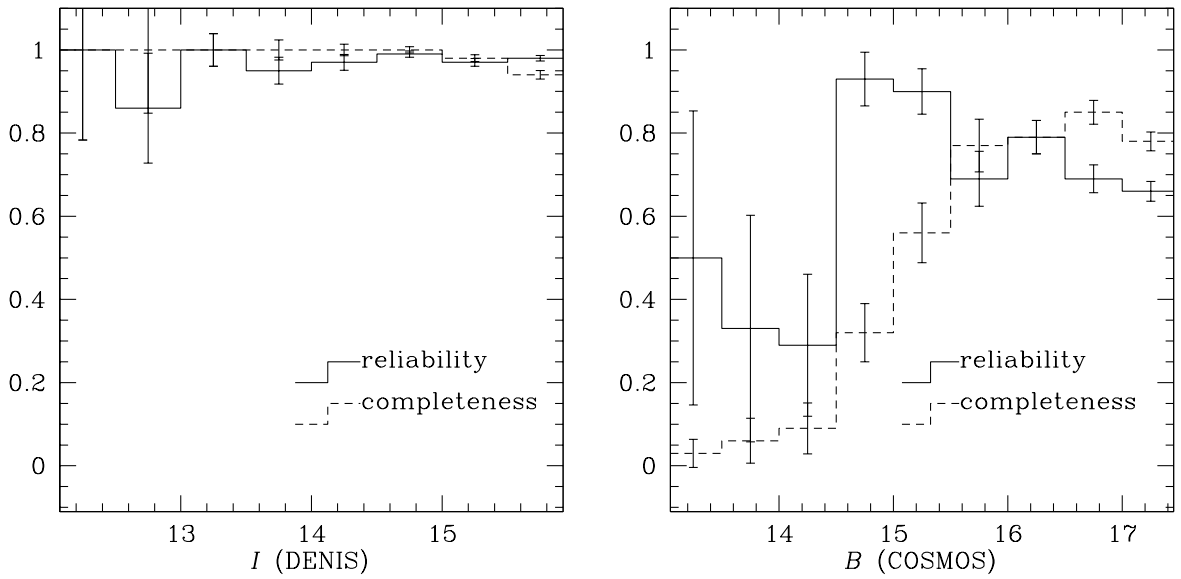

FIG. 9 – *Complétude (histogrammes hachurés) et fiabilité (histogrammes pleins) pour l'extraction de galaxies* DENIS *(gauche) et* COSMOS *(droite), tiré de Mamon (2000a).*

plus précise, grâce, en particulier à l'accès à une meilleure calibration photométrique des images DENIS et à un échantillon de galaxies bien plus grand.

A terme, les applications scientifiques que l'on pourra tirer des catalogues de galaxies DENIS sont les suivants :

- Distribution des galaxies à grande échelle et contraintes sur les paramètres cosmologiques (en particulier, le spectre de fluctuations primordiales de densité)
- Structures de galaxies (paires, groupes, amas)
- Galaxies derrière le plan de la Voie Lactée
- Couleur et concentration des galaxies en fonction de l'environnement (ce qui peut servir de contrainte aux modèles de formation de galaxies [voir Sec. 3.2])
- Cross-identification des galaxies DENIS avec des sondages dans d'autres domaines de longueur d'onde (visible, radio, IR lointain, X)
- Catalogue d'entrée aux suivis spectroscopiques 6dF et DENIS-HI (voir Sec. 5.3).

5.3 Les relevés 3D et 4D du 6dF

C'est bien de faire de la cosmologie avec un catalogue bi-dimensionnel de l'Univers sélectionné en proche IR, mais c'est encore mieux de faire de la cosmologie avec un catalogue tri-dimensionnel ! C'est pourquoi je me suis soucié depuis le début du suivi spectroscopique qui devra être fait sur les échantillons de galaxies sélectionnées en proche IR avec DENIS.

Dans la foulée d'Alain Blanchard (maintenant à l'Obs. de Midi-Pyrénées), qui avait poussé, en 1988–1991, un projet de grand sondage spectroscopique de galaxies en optique, j'ai estimé en 1995 que le meilleur moyen d'accomplir rapidement un tel sondage (mais basé sur un échantillon proche Infrarouge) est avec un instrument multi-fibres monté sur un télescope de Schmidt (qui a le bénéfice d'avoir un champ immense, ce qui permet de paver plus rapidement le ciel).

Je suis allé en Décembre 1996 présenter ce projet au Schmidt Telescope Panel de l'Anglo-Australian Telescope en Australie. Plus précisément, je leur ai proposé de robotiser leur spectroscope FLAIR-II sur le télescope de Schmidt UKST, de doubler le nombre de ses fibres, de dédier l'UKST aux sondages cosmologiques, et de baser ces sondages sur DENIS.

En Juin 1997, l'AAO a présenté à son organisme de tutelle (le AAT Board) le projet 6dF (pour Six Degree Field) de robotisation de FLAIR-II pour la poursuite de sondages cosmologiques du ciel austral comme l'un parmi deux grands projets à moyen terme pour l'UKST. Le AAT Board a sélectionné le 6dF, et en automne 1997, le directeur de l'AAO, Brian Boyle, nous a promis au moins 100 nuits de temps sur l'UKST avec le 6dF par an pour 3 ans, pour entreprendre le sondage de décalages spectraux à partir d'un échantillon de galaxies sélectionnées en proche Infrarouge. Cette promesse vient d'être étendue à *350 nuits sur 2 ans*, c'est-à-dire la grande majorité du temps du télescope en dehors des périodes de pleine Lune. L'instrument 6dF, actuellement en construction, devrait être livré à l'automne 2000 et le sondage de décalages spectraux doit débuter vers Avril 2001.

Brian Boyle a nommé un 6dF Scientific Advisory Group (6dFSAG), composé de M. Colless (PI), G. Mamon (co-PI), J. Huchra, O. Lahav, Q. Parker, W. Saunders & E. Sadler. Pour choisir les cibles des mesures spectroscopiques, le 6dFSAG a choisi d'utiliser un catalogue de galaxies composé d'un échantillon complet en K (2MASS car DENIS est peu sensible en bande K), ainsi que des sous-échantillons complets en I (DENIS), J (DENIS et/ou 2MASS), ainsi que BR (SUPERCOS). Le sondage de décalages spectraux avec le 6dF ressemblerait alors au SDSS, mais avec une extension à l'IR.

Les applications scientifiques du sondage de 10^5 décalages spectraux sont principalement :

- Fonction de luminosité détaillée de l'Univers local et sa variation avec l'environnement
- Structures 3D de l'Univers
- Ségrégation 3D de couleurs et de types spectraux de galaxies
- Fréquence et distribution des galaxies à raies d'émission

Mais ce qui nous motive encore plus est la perspective d'entreprendre un second sondage cosmologique, à plus haute résolution spectrale que le sondage de décalages spectraux, afin de mesurer les largeurs des raies d'environ 15 000 galaxies de type précoce (elliptiques et bulbes de lenticulaires), à l'horizon 2003–2004. En effet, les largeurs de raies permettent de mesurer les distances aux galaxies, indépendamment des décalages spectraux (par les relations du type $D_n - \sigma$, liées au *Plan Fondamental*), et par conséquent nous permettent de

mesurer les *vitesses particulières* des galaxies par rapport au flot de l'expansion de Hubble ($v_{\rm pec} = cz - H_0 D$).

Or la mesure d'environ 15 000 vitesses particulières de galaxies nous fournit une *quatrième dimension* à l'analyse de la distribution des galaxies dans l'espace des phases. L'échantillon de vitesses particulières permettra de cartographier en 3D la densité de masse de l'Univers et par conséquent de mesurer les biais de la distribution de galaxies par rapport à celle de la matière noire. D'autre part, les vitesses particulières nous renseignent sur le paramètre de densité Ω et la constante cosmologique Λ.

Les mesures du second sondage du 6dF devraient permettre de répondre avec précision aux questions suivantes :

- Fonction de masse des galaxies (par la statistique des largeurs de raies)
- Epaisseur et cinématique interne des très grandes structures de galaxies (nappes, filaments)
- Cartographie de la densité de masse de l'Univers austral
- Biais des galaxies par rapport à la matière noire
- Mesures de Ω, Λ et du spectre de fluctuations primordiales de densité $P(k)$

Aujourd'hui, les plus grands échantillons de vitesses particulières ont environ 3000 objets, dont la moitié dans l'hémisphère Sud, ce qui ne donne pas une statistique fiable, et les interprétations sont encore sujettes à débat. De plus, la couverture actuelle est parsemée de grands vides que les analyses de la carte de densité de masse doivent interpoler. La multiplication par plus de 10 de la taille de l'échantillon du ciel Sud doit donc permettre un bond significatif dans les 3 derniers points de la liste ci-dessus.[23]

A noter que la seule concurrence pour le 6dF vient de France, où le consortium DENIS-HI a commencé l'an dernier à mesurer depuis Nançay les largeurs de raies 21cm de spirales tardives inclinées. Le but de ce projet, dont je fais partie, est d'obtenir environ 6000 vitesses particulières d'ici 2006, profitant de la montée en puissance, à partir de la fin 2000, du radiotélescope de Nançay (grâce au projet FORT). Ce projet est complémentaire à 6dF, car il observe les galaxies spirales alors que 6dF se limite aux elliptiques et lenticulaires.

En automne, nous allons simuler des catalogues de vitesses particulières, afin d'estimer la précision avec laquelle que le sondage 6dF de vitesses particulières mesurera les paramètres cosmologiques. Pour cela, nous nous baserons sur les propriétés des galaxies à $z = 0$, issues des simulations cosmologiques faites à l'IAP par Hatton et ses collègues, et qui se base sur une simulation dynamique de l'évolution de la distribution de matière noire, à partir d'un décalage spectral très élevé, et qui incorpore les divers processus de formation des galaxies (voir Sec. 3.2). Il faudra trouver une zone dans la boîte de simulation (de 150 Mpc de côté) qui ressemble à l'environnement du Groupe Local de galaxies, situé environ à mi-chemin entre deux zones de forte densité (*le Grand Attracteur* et *Persée-Poissons*). Puis on simulera des catalogues en 2D, avec les erreurs photométriques, puis les catalogues

23. Le projet 6dF est décrit sur le Web au `http://www.iap.fr/users/gam/6dF`.

de décalages spectraux, avec les erreurs de mesure des z, puis les catalogues de vitesses particulières, avec les erreurs de mesure directe des distances.

6 La densité de masse de l'Univers

6.1 La cinématique interne des groupes hors-équilibre

Plusieurs auteurs (Byrd & Valtonen 1985; Giuricin et al. 1988; Diaferio et al. 1993) ont suggéré que les groupes diffus ne sont pas encore en équilibre, mais s'effondrent encore à partir de leur expansion de Hubble maximale (voir Sec. 4.1). De plus, Giuricin et al. (1988) ont estimé, à partir de simulations simples à N-corps, l'erreur que l'on fait lorsque l'on mesure la masse et le temps dynamique d'un système de particules, en supposant à tort l'équilibre viriel.

La Figure 10 montre l'évolution *cosmo-dynamique* d'un système sphérique de galaxies, schématisée par l'évolution d'une paire de galaxies avec un moment angulaire négligeable, dans l'approximation Newtonienne (Mamon 1993). Comme les galaxies ne sont pas des

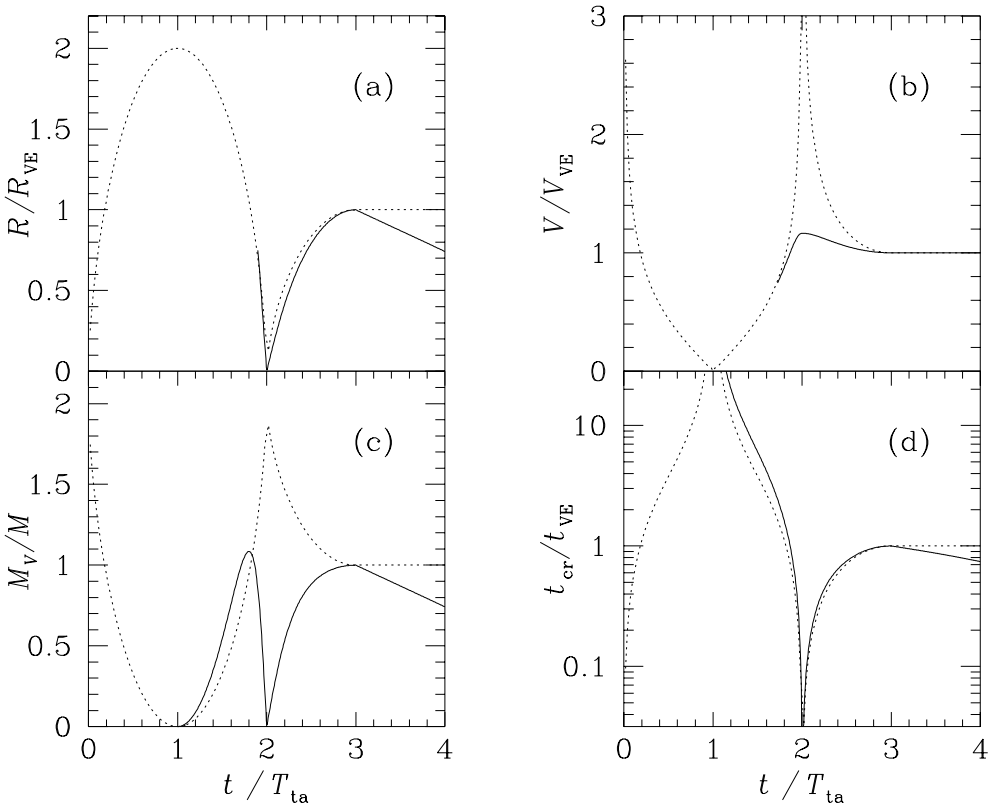

FIG. 10 – *Evolution des biais de rayon (a), dispersion de vitesses (b), masse (c) et temps de croisement (d), relatif aux conditions de l'équilibre viriel final (Mamon 1993).* $T_{\rm ta}$ *est le temps ou la structure atteint son rayon maximal (*turnaround*). Les* courbes pointillées *montre l'évolution pour un système de masse ponctuelles, tandis que les* courbes pleines *incorporent les effets des potentiels adoucis et de la dissipation d'énergie orbitale par friction dynamique (à partir de* $t = 3\,T_{\rm ta}$*).*

objets ponctuels, il faut adoucir leurs potentiels, de sorte que leur vitesse relative au péricentre ne tend plus vers l'infini.

En comparant les biais sur la masse et le temps de croisement, je trouve une trajectoire théorique, que j'appelle *trajectoire fondamentale*, dans l'espace à 2D (biais de masse, biais de temps dynamique) pour les systèmes cosmologiques comme les groupes, moyennant l'hypothèse que l'évolution cosmo-dynamique des groupes peut se calculer dans un cadre sphérique et isolé (Mamon 1993, 1994, 1995). La trajectoire fondamentale est indépendante de la masse du système.

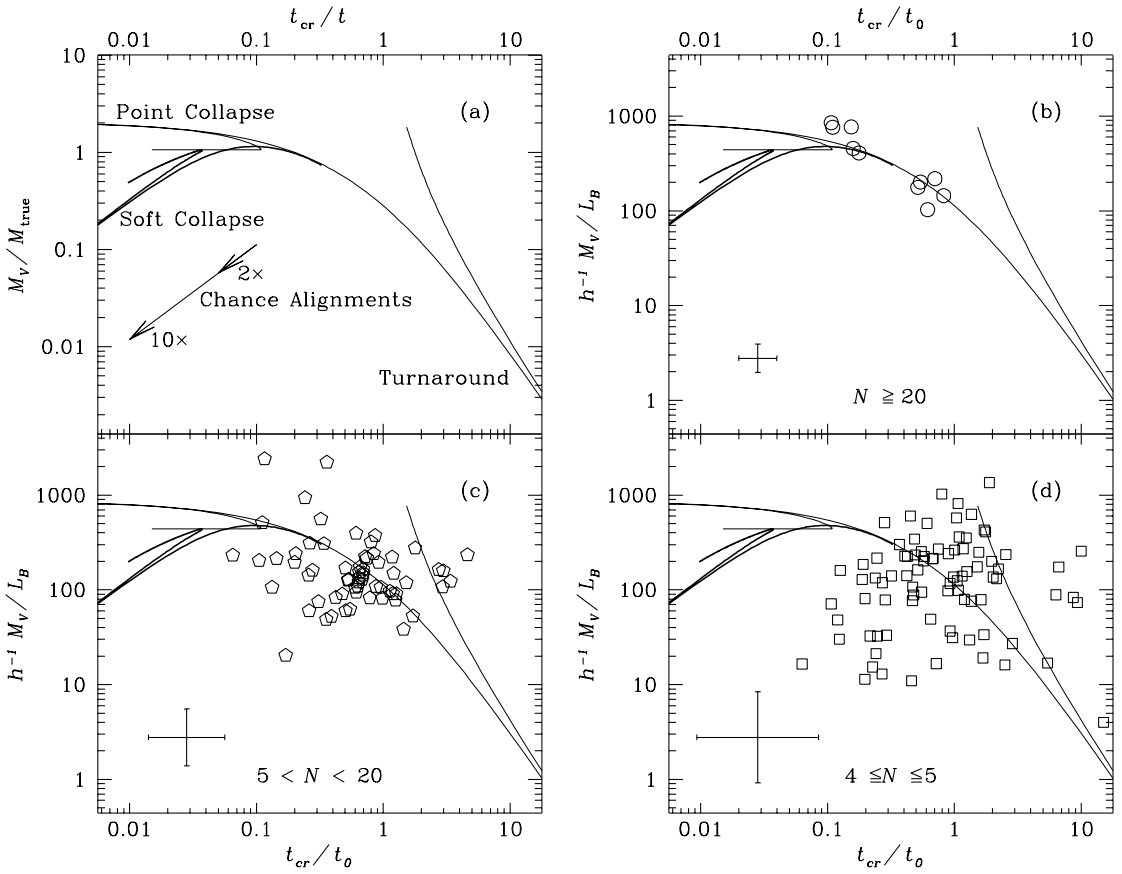

FIG. 11 – *a) : biais de masse (par rapport à celle trouvée par le théorème du viriel) en fonction du biais de temps de croisement, en unités du temps courant. (b, c, et d) : rapport M/L en fonction du temps de croisement, en unités de l'âge présent de l'Univers, pour des groupes rassemblés par multiplicité, pour $\Omega_0 = 1$. Les* polygones *(b, c, and d) représentent les groupes diffus, tirés du catalogue de Gourgoulhon, Chamaraux, & Fouqué (1992). Les* courbes fines *montrent les trajectoires de l'évolution de masses ponctuelles, tandis que les* courbes épaisses *montrent les effets des potentiels adoucis et du déclin orbital par cause de friction dynamique des galaxies contre la matière noire du système. Dans (b, c, et d), les courbes sont ajustées verticalement, en supposant que tous les groupes ont $M_{\rm vrai}/L = 440\,h$. La taille caractéristique des barres d'erreur est indiquée. D'après Mamon (1993).*

Cela est illustré pour les groupes de Gourgoulhon, Chamaraux, & Fouqué (1992) dans la Figure 11, pour le cas $\Omega_0 = 1$.[24] Comme on ne connaît pas les *vraies* masses des groupes, on suppose un même $M_{\rm vrai}/L_B$ pour l'ensemble des groupes.[25] On ajuste la valeur de

24. Pour $\Omega_0 = 0.2$, les symboles doivent être déplacés vers la gauche de 0.1 décade.

25. Ce serait mieux de travailler avec des luminosités en proche-IR (voir Sec. 5.1), mais les catalogues existants de groupes ont une photométrie optique.

$M_{\rm vrai}/L_B$ sur les groupes à haute multiplicité[26] (auxquels sont attachées les plus petites barres d'erreur), ce qui donne $M_{\rm vrai}/L_B = 440\,h$. Ce rapport M/L est 4 fois plus grand que le $M_{\rm vir}/L_B$ médian du catalogue de groupes de Gourgoulhon et al.. Cela traduit le fait que les groupes de Gourgoulhon et al. sont généralement proches de leur expansion maximale, pour laquelle la sous-estimation de masse tend vers l'infini.

En extrapolant à l'Univers tout entier (en supposant que les groupes de galaxies sont des bons traceurs du rapport masse sur luminosité), on en déduit (Mamon 1993, 1994, 1995)

$$\Omega_0 = \frac{M/L_B}{(M/L_B)_{\Omega_0=1}} = 0.34 \ ,$$

avec $(M/L_B)_{\Omega_0=1} = 1300\,h$ pour fermer l'Univers (Zucca et al. 1997). Ω_0 peut être encore plus grand si de la matière noire se cache entre les groupes.

On notera que la trajectoire fondamentale est une coupe d'une *surface fondamentale* dans le diagramme d'observables rapport masse/luminosité versus temps de croisement, c'est-à-dire $RV^2/(GL)$ versus $R/(Vt_0)$, où R, V, L, G, et t_0 représentent respectivement la taille, dispersion de vitesses, luminosité bleue, constante de gravitation, et l'âge de l'Univers.

6.2 La fraction baryonique des groupes de galaxies

Si les groupes ou amas de galaxies sont représentatifs de la fraction de *baryons* dans l'Univers, alors on peut en tirer le paramètre de densité par la simple relation

$$\Omega_0 = \frac{\Omega_b}{f_b} \ , \tag{26}$$

où Ω_b est la densité de baryons de l'Univers, déterminé par les relations entre les abondances de divers éléments (^{2}D, ^{3}He, ^{4}He, ^{7}Li, etc.) par rapport à l'Hydrogène (qui dans l'Univers primordial contient tous les baryons) et la densité d'Hydrogène. Cette idée toute simple a été proposée par White (1992) et White et al. (1993), qui l'ont appliquée aux amas de galaxies, pour trouver $\Omega_0 \simeq 0.3$.

Dans un groupe ou amas de galaxies, la fraction de baryons s'écrit

$$f_b = \frac{M_{\rm gaz} + M_{\rm étoiles}}{M_{\rm total}} \ .$$

Le rapport M/L d'une vieille population stellaire donne la masse en étoiles :

$$M_{\rm étoiles} = 8\,L_B \ .$$

Généralement, on néglige la contributon du gaz dans les galaxies et on ne comptabilise donc que le gaz diffus intergalactique. Alors, la masse de gaz est intégrée sur le profil de densité de gaz diffus,

$$M_{\rm gaz} = \int \mu m_p\, n_{\rm gaz}\, dV \ , \tag{27}$$

26. L'amas de Virgo fait partie de l'échantillon $N \geq 20$.

où μm_p est la masse moyenne des constituants du plasma (électrons compris), m_p étant la masse du proton. La normalisation de $n_{\rm gaz}$ dans l'équation (27) est donnée par la luminosité X :

$$L_X = \Lambda(T) \int n_{\rm gaz}^2 \, dV \ ,$$

où l'on suppose un plasma intergalactique *isotherme*. Finalement, la masse totale est obtenue par l'équation d'équilibre hydrostatique du gaz dans le potentiel du groupe ou amas :

$$M_{\rm tot} = -\frac{kT\,r}{G\mu m_p} \left(\frac{d\log n}{d\log r} \right) \ ,$$

où de nouveau on suppose un gaz isotherme.

Peu de temps après que White ait introduit sa nouvelle méthode pour déterminer Ω_0, Mulchaey et al. (1993) ont découvert, avec le satellite X ROSAT, du gaz intergalactique dans le groupe de galaxies, NGC 2300.[27] Le travail de Mulchaey et al. a généré beaucoup d'enthousiasme : d'abord pour la première découverte de gaz *diffus* dans une groupe, ensuite parce que ce gaz semblait tracer un potentiel plus important que prévu, et finalement parce que la fraction baryonique était similaire à Ω_b, ce qui impliquait, avec l'équation (26), $\Omega_0 = 1$.

Surpris par les résultats de Mulchaey et al. (1993), en particulier par leur très grande masse totale pour le groupe, j'ai refait l'analyse de leurs observations X avec M. Henriksen (alors à l'Université d'Alabama, maintenant à UMBC, Baltimore). Nous avons ajusté le profil de brillance de surface X, en laissant le fond de ciel comme paramètre libre (méthode souvent employée depuis). Nous avons alors trouvé une masse totale 8 fois moins grande, et une fraction baryonique de plus de 20%, ce qui nous a conduits, par l'équation (26), à $\Omega_0 \simeq 0.3$ (Henriksen & Mamon 1994).

Les mesures récentes de la fraction baryonique dans les groupes, à partir d'une analyse couplée des données ROSAT et ASCA, sont de 15–20% (Hwang et al. 1999), ce qui confirme notre analyse.

6.3 La règle comobile étalon appliquée aux quasars

Boud Roukema (postdoc à l'IUCAA, Pune, Inde) et moi avons entrepris une toute nouvelle démarche pour déterminer les paramètres cosmologiques Ω_0 et λ_0 (Roukema & Mamon 2000). Alors que les méthodes de mesures de supernovae lointains se basent sur le concept de *bougie étalon*, nous avons introduit le concept de *règle étalon* dans la mesure de ces paramètres cosmologiques.

S'il n'y avait pas la gravitation, les structures (galaxies, quasars, groupes et amas de galaxies) seraient figées *dans un repère comobile avec l'expansion de l'Univers.*[28] La gravitation agit de telle sorte que les régions denses attirent de préférence la matière

27. NGC 2300 est plus exactement une galaxie elliptique. Le groupe est un triplet diffus, avec une paire serrée au centre, à laquelle est associée l'émission diffuse X.

28. Il faut ajouter que sans gravitation, l'expansion ne serait soumise qu'à l'accélération causée par l'énergie sombre de la constante cosmologique.

avoisinante tandis que dans les régions peu denses, la matière s'échappe vers les régions sur-denses. A petite échelle, l'impression provenant des simulations cosmologiques (et bien sûr prédite par la théorie de la croissance des perturbations de densité dans un Univers en expansion) est que le contraste entre les structures augmente, mais, qu'*à très grande échelle*, les structures restent bien figées dans le repère comobile.

Roukema et moi avons découvert (Roukema & Mamon 2000) une structuration de la distribution des quasars lointains ($z \simeq 2$, c'est-à-dire au moment où le facteur d'expansion de l'Univers n'était que d'un tiers de sa valeur actuelle), sur un échantillon de 800 quasars, découverts par un relevé prisme-objectif, répartis sur une zone contiguë de ciel d'angle solide $200\,\mathrm{deg}^2$ (Iovino, Clowes, & Shaver 1996). On trouve que les quasars sont distribués en bulles (Fig. 12).

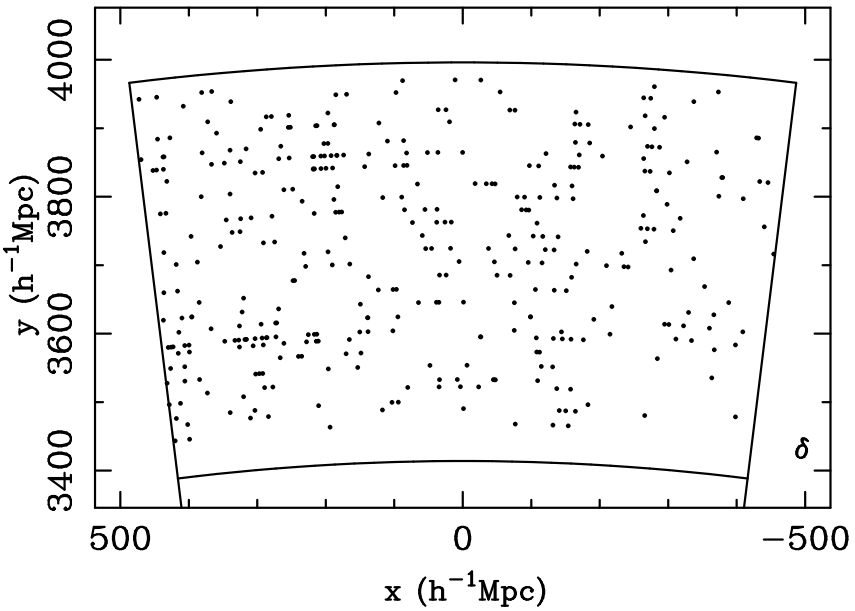

FIG. 12 – *Diagramme déclinaison - décalage spectral de la distribution des quasars d'un sous-ensemble limité en position sur le ciel et en décalages spectraux de l'échantillon de Iovino, Clowes, & Shaver (1996), tiré de Roukema & Mamon (2000).*

Or, on croit savoir (par les sondages spectroscopiques en pinceau de Broadhurst et al. 1990, ainsi, semble t-il, par le sondage large du Las Campanas Redshift Survey) que les galaxies de l'Univers local sont aussi distribuées dans des structures (en bulles) de typiquement $130\,h^{-1}\,\mathrm{Mpc}$.[29] Cette échelle de $L = 130\,h^{-1}\,\mathrm{Mpc}$ correspond au nombre d'onde ($k = 2\pi/L$) auquel le spectre de fluctuations primordiales de densité de *matière noire froide* (CDM) est à son maximum.

Roukema et moi avons appliqué cette *règle étalon comobile* à la distribution des quasars à $z = 2$, *projetée sur une coordonnée tangentielle comobile* (nous ne prenons pas en compte les décalages spectraux afin d'éviter les effets de sélection en z).

29. L'existence de cette échelle caractéristique à $130\,h^{-1}\,\mathrm{Mpc}$ dans l'Univers local est encore sujette à débat, mais voir Guzzo (1999).

La taille angulaire et la taille projetée comobile dépendent du paramètre de densité, Ω_0 et de la constante cosmologique, λ_0. En effet, la coordonnée tangentielle comobile, $d_\perp$ et l'angle sur le ciel sont reliées par les relations (voir Lahav et al. 1991) :

$$\begin{aligned} d_\perp(z,\theta) &\equiv (\theta-\theta_1)\, d_{\rm mp}(z) \\ &= (\theta-\theta_1) \begin{cases} R_C \sinh[d(z)/R_C], & \kappa_0 < 0 \\ d(z), & \kappa_0 = 0 \\ R_C \sin[d(z)/R_C], & \kappa_0 > 0. \end{cases} , \end{aligned} \tag{28}$$

où la coordonnée angulaire θ est mesurée, relativement à une coordonnée angulaire de référence θ_1, $d_{\rm mp}(z)$ est la *distance de mouvement propre*,

$$d(z) = \frac{c}{H_0} \int_{1/(1+z)}^{1} \frac{{\rm d}a}{a\sqrt{\Omega_0/a - \kappa_0 + \lambda_0 a^2}}, \tag{29}$$

est la *distance propre* ,

$$\kappa_0 \equiv \Omega_0 + \lambda_0 - 1 \tag{30}$$

est la courbure (sans dimension) de l'Univers observable, et

$$R_C \equiv \frac{c}{H_0} \frac{1}{\sqrt{|\kappa_0|}} \tag{31}$$

est son rayon de courbure. Donc, si on connait la taille angulaire d'une structure, et que l'on croit connaître sa taille projetée comobile, on obtient, d'après l'équation (28), une contrainte sur le rayon de courbure ainsi que la distance propre, ce qui se traduit par une contrainte sur Ω_0 et λ_0, qui rentrent dans les expressions du rayon de courbure (eqs. [31] et [30]) et de la distance propre (eq. [29]).

Notre analyse conduit à une contrainte forte sur Ω_0 (mais faible sur λ_0). La Figure 13 montre les couples (Ω_0,λ_0) permises si les tailles angulaires des structures de quasars à $z = 2$ (Fig. 12) correspondent à une taille projetée comobile de $130\,h^{-1}$ Mpc. Ainsi, la Figure 13 indique que, pour $\lambda_0 = 0$ on a $\Omega_0 = 0.24^{+0.05}_{-0.15}$, tandis que pour $\Omega_0 + \lambda_0 = 1$ (l'Univers plat), on trouve $\Omega_0 = 0.30 \pm 0.15$ (Roukema & Mamon 2000). L'analyse 3D est en cours.

Avec les très grands échantillons de quasars attendus dans les 3 ans avec les sondages 2dF et surtout SDSS, notre méthode devrait apporter des contraintes bien plus fortes sur Ω_0 et probablement une contrainte sur λ_0.[30]

6.4 Synthèse

Mes trois contributions à la mesure du paramètre de densité Ω_0, par la cinématique hors-équilibre des groupes, par leur fraction baryonique, et par la règle étalon comobile, donnent des valeurs très similaires : $\Omega_0 \simeq 0.3$.

30. Une page Web expliquant, de façon didactique, notre méthode et nos résultats est disponible sur `http://www.iap.fr/users/gam/etalon.html`.

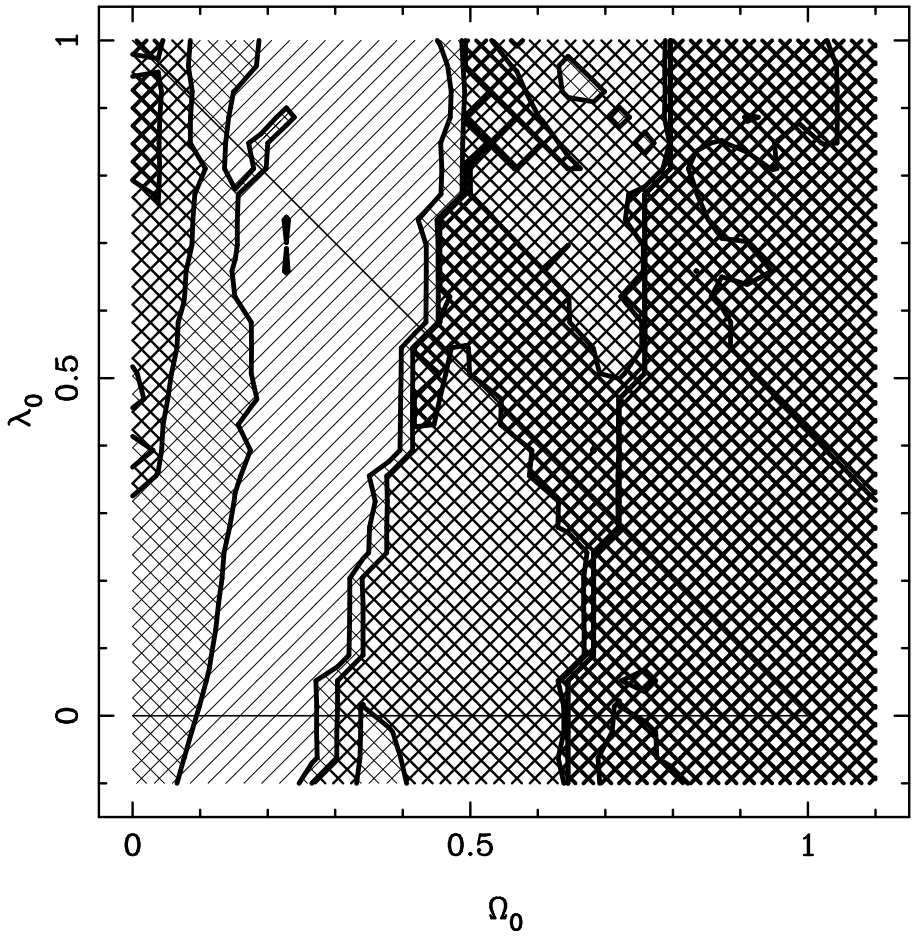

FIG. 13 – *Diagramme Ω_0, λ_0 des zones permises par la présence d'un pic de $L = 130\,h^{-1}\,\mathrm{Mpc}$ (comobile) dans le spectre de puissances des coordonnées tangentielles de l'échantillon de la Figure 12, tiré de Roukema & Mamon (2000). Les zones sombres correspondent à celles qui sont rejetées.*

Il faut noter que la présence de la constante cosmologique devrait affecter légèrement l'analyse hors-équilibre de la cinématique des groupes en effondrement. Une étude est en préparation (avec E. Łokas, CAMK, Varsovie) pour refaire l'analyse dans le contexte de l'analyse cosmologique perturbative.

7 Conclusions et perspectives

Ce mémoire couvre beaucoup de terrain et présente un grand nombre de résultats, qui correspondent à 15 ans de travail.

La modélisation de la photo-chimie des enveloppes circumstellaires a servi de référence pour la compréhension des abondances des divers espèces observées, principalement avec le 30 m et l'interféromètre de l'IRAM. Peut-être le résultat principal de ce travail a été la modélisation des effets sur la photo-chimie des enveloppes enveloppe circumstellaires du transfert de rayonnement en raies de la molécule CO.

Notre étude sur l'origine de la séquence de Hubble est très ambitieuse. Nous avons passé beaucoup de temps à modéliser au mieux l'évolution de la matière noire dans les zones de l'Univers qui, à $z = 0$, se retrouvent dans des amas de galaxies. Nous espérons avoir très bientôt des résultats à partir de la modélisation semi-analytique de la physique des baryons et de l'évolution morphologique des galaxies. Après, on analysera l'*évolution chimique* des galaxies, pour mieux comprendre l'histoire de l'enrichissement du plasma intra-amas.

En attendant, il convient de vérifier la modélisation des taux de collisions rapides et coalescences (après collisions lentes), en comparant avec les données observationnelles, en particulier avec une série de travaux de Moss & Whittle (1993, 1997, 2000), qui apportent des contraintes sur les galaxies d'amas avec des anomalies morphologiques et/ou des voisins proches, et ceux de Lobo et al. (1997), qui montrent comment la pente de la fonction de luminosité des galaxies varie avec la position dans l'amas.

Les modèles semi-analytiques de formation de galaxies développées à l'IAP seront très utiles pour contraindre la nature des groupes compacts. Du point de vue analytique, il faudra quantifier la quantité de déclin orbital par friction dynamique qui est subie par les galaxies des groupes compacts. Au niveau observationnel, les données X du satellite XMM-Newton devront être déterminantes, et le relevé d'un échantillon *homogène* d'une dizaine de groupes compacts sera proposé.

Les observations du relevé DENIS vont se terminer à la fin 2000, et à ce moment, on aura de grands catalogues de galaxies à exploiter avec les avantages de la sélection proche-IR. En particulier, je compte construire des grands catalogues de groupes compacts, à partir de DENIS et 2MASS, couplée aux sondages spectroscopiques du 6dF (au Sud) et du SDSS (au Nord), ce qui apportera un échantillon bien plus important et homogène, et permettra donc de mieux contraindre la nature de ces systèmes. D'autre part, nous espérons tirer une fonction de corrélation angulaire à 2 points des galaxies, qui sera de bonne qualité jusqu'au très grandes échelles angulaires, afin de pouvoir l'inverser pour déterminer le spectre de fluctuations primordiales de densité, $P(k)$. Des comparaisons seront faits avec les catalogues de galaxies provenant du relevé 2MASS.

Dans moins d'un an devront commencer les observations du premier relevé cosmologique du 6dF, avec 120 000 décalages spectraux en moins de deux ans d'observations. Notre ambition principale est de lancer le second relevé cosmologique du 6dF, avec 15 000 vitesses particulières de galaxies elliptiques et lenticulaires (dix fois plus que l'échantillon actuel de l'hémisphère Sud). Nous allons nous y préparer en construisant des échantillons simulés de

catalogues de vitesses particulières, à partir des simulations semi-analytiques de galaxies de l'IAP (en collaboration avec S. Hatton).

Les mesures de la densité de masse de l'Univers, Ω_0, vont continuer sur deux fronts. A partir des groupes, une ré-analyse de la théorie de la trajectoire fondamentale, sur une base cosmologique, auto-cohérente (au lieu de mon approximation Newtonienne) sera entreprise avec E. Łokas. D'autre part, avec B. Roukema, nous poursuivons notre analyse de l'échantillon de quasars à $z = 2$ de Iovino et al. (1996), maintenant directement en 3D, et nous avons commencé l'analyse d'un échantillon de quasars provenant du relevé 2dF. Il faudra se dépêcher, car vers 2002, le satellite MAP aura cartographié le CMB et déterminé Ω_0 avec environ 10% de précision.

A plus long terme, qui sait où mes recherches vont me mener?

Références

Balland, C., Silk, J., Schaeffer, R., 1998, Collision-induced Galaxy Formation, ApJ 497, 541

Banchet, V., Mamon, G.A., Contensou, M., 1995, The detection of DENIS galaxies, ApL&C 31, 37

Barnes, J.E., 1992, Transformations of galaxies. I. Mergers of equal-mass stellar disks, ApJ 393, 484

Barton, E.J., de Carvalho, R.R., Geller, M.J., 1998, Environments of redshift survey compact groups of galaxies, AJ 116, 1573

Baugh, C.M., Cole, S., Frenk, C.S., 1996, Evolution of the Hubble sequence in hierarchical models for galaxy formation, MNRAS 283, 1361

Bertin, E., Arnouts, S., 1996, SExtractor: software for source extraction, A&AS 117, 393

Binney, J., 1977, The physics of dissipational galaxy formation, ApJ 215, 483

Binney, J., Mamon, G.A., 1982, M/L and velocity anisotropy from observations of spherical galaxies, or must M87 have a massive black hole?, MNRAS 200, 361

Blanchard, A., Valls-Gabaud, D., Mamon, G.A., 1992, The origin of the galaxy luminosity function and the thermal evolution of the intergalactic medium, A&A 264, 365

Blumenthal, G.R., Faber, S.M., Primack, J.R., Rees, M.J., 1984, Formation of galaxies and large-scale structure with cold dark matter, Nature 311, 517

Bond, J.R., Cole, S., Efstathiou, G., Kaiser, N., 1991, Excursion set mass functions for hierarchical Gaussian fluctuations, ApJ 379, 440

Bower, R.G., 1991, The evolution of groups of galaxies in the Press-Schechter formalism, MNRAS 248, 332

Broadhurst, T.J., Ellis, R.S., Koo, D.C., Szalay, A.S., 1990, Large-scale distribution of galaxies at the Galactic poles, Nature 343, 726

Byrd, G.G., Valtonen, M.J., 1985, Origin of redshift differentials in galaxy groups, ApJ 289, 535

Catelan, P., Lucchin, F., Matarrese, S., Porciani, C., 1998, The bias field of dark matter haloes, MNRAS 297, 692

Charlton, J.C., Whitmore, B.C., Gilmore, D.M., 1995, Pairs in groups and clusters, in: Richter, O.G., Borne, K. (eds.), Groups of Galaxies, ASP, San Francisco, vol. 70, p. 49

Cherchneff, I., Glassgold, A.E., Mamon, G.A., 1993, The formation of cyanopolyyne molecules in IRC +10216, ApJ 410, 188

Combes, F., 2000, Bar-driven galaxy evolution and timescales to feed AGN, in: Combes, F., Mamon, G.A., Charmandaris, V. (eds.), Dynamics of Galaxies: From the Early Universe to the Present, ASP, San Francisco, vol. 197, p. 15, astro-ph/9908145

Cowie, L.L., Songaila, A., 1977, Thermal evaporation of gas within galaxies by a hot intergalactic medium, Nature 266, 501

de Carvalho, R.R., Ribeiro, A.L.B., Capelato, H.V., Zepf, S.E., 1997, Redshift survey of galaxies around a selected sample of compact groups, ApJS 110, 1

de Vaucouleurs, G., Olson, D.W., 1982, The central velocity dispersion in elliptical and lenticular galaxies as an extragalactic distance indicator, ApJ 256, 346

Devriendt, J., 1999, Une vision panchromatique de la formation hiérarchique des galaxies, Thèse de doctorat, Université de Paris XI

Diaferio, A., Ramella, M., Geller, M.J., Ferrari, A., 1993, Are groups of galaxies virialized systems?, AJ 105, 2035

Dos Santos, S., Mamon, G.A., 1999, Clumpy diffuse X-ray emission from the spiral-rich compact galaxy group HCG 16, A&A 352, 1

Evrard, A.E., Silk, J., Szalay, A.S., 1990, The morphology-density relation for galaxies in a cold dark matter-dominated universe, ApJ 365, 13

Faber, S.M., Jackson, R.E., 1976, Velocity dispersions and mass-to-light ratios for elliptical galaxies, ApJ 204, 668

Fukugita, M., Hogan, C.J., Peebles, P.J.E., 1998, The cosmic baryon budget, ApJ 503, 518

Garcia, A.M., 1993, General study of group membership. II. Determination of nearby groups, A&AS 100, 47

Geller, M.J., Huchra, J.P., 1983, Groups of galaxies. III. The CfA survey, ApJS 52, 61

Gerhard, O.E., 1981, N-body simulations of disc-halo galaxies: isolated systems, tidal interactions and merging, MNRAS 197, 179

Ghigna, S., Moore, B., Governato, F., Lake, G., Quinn, T., Stadel, J., 1998, Dark matter haloes within clusters, MNRAS 300, 146

Giuricin, G., Gondolo, P., Mardirossian, F., Mezzetti, M., Ramella, M., 1988, Groups of galaxies in the Local Supercluster: some hypotheses on the evolutionary stage, A&A 199, 85

Glassgold, A.E., 1996, Circumstellar photochemistry, ARA&A 34, 241

Glassgold, A.E., Mamon, G.A., 1992, Circumstellar chemistry, in: Bohme, D.K., Herbst, E., Kaifu, N., Saito, S. (eds.), Chemistry and Spectroscopy of Interstellar Molecules, Univ. of Tokyo Press, Tokyo, p. 261

Glassgold, A.E., Mamon, G.A., Huggins, P.J., 1989, Molecule formation in fast neutral winds from protostars, ApJ 336, L29

Glassgold, A.E., Mamon, G.A., Huggins, P.J., 1991, The formation of molecules in protostellar winds, ApJ 373, 254

Glassgold, A.E., Mamon, G.A., Omont, A., Lucas, R., 1987, Photochemistry and molecular ions in carbon-rich circumstellar envelopes, A&A 180, 183

Gourgoulhon, E., Chamaraux, P., Fouqué, P., 1992, Groups of galaxies within 80 Mpc. I. Grouping hierarchical method and statistical properties, A&A 255, 69

Gunn, J.E., Gott, J.R.I., 1972, On the infall of matter into clusters of galaxies and some effects on their evolution, ApJ 176, 1

Gunn, J.E., Peterson, B.A., 1965, On the density of neutral hydrogen in intergalactic space, ApJ 142, 1633

Guzzo, L., 1999, Large-scale structure at the turn of the millennium, in: Paul, J., Montmerle, T., Aubourg, E. (eds.), 19th Texas Symposium on Relativistic Astrophysics, astro-ph/9911115

Harmon, R., Mamon, G., 1993, The detection of galaxies in infrared surveys, in: Soifer, B.T. (ed.), Sky Surveys. Protostars to Protogalaxies, ASP, San Francisco, vol. 43, p. 15

Henriksen, M.J., Mamon, G.A., 1994, The baryonic fraction in groups of galaxies from X-ray measurements, ApJ 421, L63

Hernquist, L., Katz, N., Weinberg, D.H., 1995, Physically detached "compact groups", ApJ 442, 57

Hickson, P., 1982, Systematic properties of compact groups of galaxies, ApJ 255, 382

Hickson, P., 1997, Compact groups of galaxies, ARA&A 35, 357

Hickson, P., Mendes de Oliveira, C., Huchra, J.P., Palumbo, G.G., 1992, Dynamical properties of compact groups of galaxies, ApJ 399, 353

Hickson, P., Rood, H.J., 1988, The nature of compact groups of galaxies, ApJ 331, L69

Hubble, E., Humason, M.L., 1931, The velocity-distance relation among extra-galactic nebulae, ApJ 74, 43

Hwang, U., Mushotzky, R.F., Burns, J.O., Fukazawa, Y., White, R.A., 1999, Mass and metallicity of five X-ray-bright galaxy groups, ApJ 516, 604

Iovino, A., Clowes, R., Shaver, P., 1996, A large sample of objective prism quasar candidates, A&AS 119, 265

Jenkins, A., Frenk, C.S., White, S.D.M., Colberg, J.M., Cole, S., Evrard, A.E., Yoshida, N., 2000, Mass function of dark matter halos, MNRAS submitted, astro-ph/0005260

Kitayama, T., Suto, Y., 1996a, Formation rate of gravitational structures and the cosmic X-ray background radiation, MNRAS 280, 638

Kitayama, T., Suto, Y., 1996b, Semianalytic predictions for statistical properties of X-ray clusters of galaxies in cold dark matter universes, ApJ 469, 480

Knapp, G.R., Morris, M., 1985, Mass loss from evolved stars. III. Mass loss rates for fifty stars from CO J = 1-0 observations, ApJ 292, 640

Krivitsky, D.S., Kontorovich, V.M., 1997, Mergers of galaxies in clusters: Monte Carlo simulation of mass and angular momentum distribution, A&A 327, 921

Lacey, C., Cole, S., 1993, Merger rates in hierarchical models of galaxy formation, MNRAS 262, 627

Lahav, O., Rees, M.J., Lilje, P.B., Primack, J.R., 1991, Dynamical effects of the cosmological constant, MNRAS 251, 128

Lanzoni, B., Mamon, G.A., Guiderdoni, B., 2000, Merging history trees for dark matter haloes: tests of the Merging Cell Model in a CDM cosmology, MNRAS 312, 781

Larson, R.B., Tinsley, B.M., Caldwell, C.N., 1980, The evolution of disk galaxies and the origin of S0 galaxies, ApJ 237, 692

Letzelter, C., Eidelsberg, M., Rostas, F., Breton, J., Thieblemont, B., 1987, Photoabsorption and photodissociation cross sections of CO between 88.5 and 115 nm, J. Chem. Phys. 114, 273

Lizano, S., Heiles, C., Rodriguez, L.F., Koo, B., Shu, F.H., Hasegawa, T., Hayashi, S., Mirabel, I.F., 1988, Neutral stellar winds that drive bipolar outflows in low-mass protostars, ApJ 328, 763

Lobo, C., Biviano, A., Durret, F., Gerbal, D., Le Fevre, O., Mazure, A., Slezak, E., 1997, Environmental effects on the Coma cluster luminosity function, A&A 317, 385

Lucas, R., Guélin, M., 1990, Spectroscopy of circumstellar envelopes with the IRAM 30-m telescope, in: Watt, G.D., Webster, A.S. (eds.), Submillimetre Astronomy, Kluwer, Dordrecht, p. 97

Maia, M.A.G., da Costa, L.N., Latham, D.W., 1989, A catalog of southern groups of galaxies, ApJS 69, 809

Makino, J., Hut, P., 1997, Merger rate of equal-mass spherical galaxies, ApJ 481, 83

Mamon, G.A., 1986, Are compact groups of galaxies physically dense?, ApJ 307, 426

Mamon, G.A., 1987, The dynamics of small groups of galaxies. I. Virialized groups, ApJ 321, 622

Mamon, G.A., 1989, A compact group in Virgo, A&A 219, 98

Mamon, G.A., 1992a, Are cluster ellipticals the products of mergers?, ApJ 401, L3

Mamon, G.A., 1992b, Compact group modeling, in: Mamon, G.A., Gerbal, D. (eds.), 2nd DAEC mtg., Distribution of Matter in the Universe, Obs. de Paris, Paris, p. 51

Mamon, G.A., 1993, Dynamical theory of groups and clusters of galaxies, in: Combes, F., Athanassoula, E. (eds.), Gravitational Dynamics and the N-Body Problem, Obs. de Paris, Paris, p. 188, astro-ph/9308032

Mamon, G.A., 1994, The galaxy group/cosmology connections, in: Durret, F., Mazure, A., White, S.D.M., Trânh Thanh Vân, J. (eds.), 14th Moriond Astrophysics Mtg., Clusters of Galaxies, Frontières, Gif-sur-Yvette, p. 291, astro-ph/9406043

Mamon, G.A., 1995, The dynamics of groups and clusters of galaxies and links to cosmology, in: de Vega, H., Sánchez, N. (eds.), 3rd Paris cosmology colloq., p. 95, astro-ph/9511101

Mamon, G.A., 1998, The wide-field DENIS near-IR imaging survey and 6dF redshift and peculiar velocity surveys, in: Mellier, Y., Colombi, S. (eds.), 14th IAP Astrophysics Mtg., Wide Field Surveys in Cosmology, Frontières, Paris, p. 323, astro-ph/9809376

Mamon, G.A., 2000a, Near-infrared galaxy surveys in 2D, 3D & 4D, in: Courteau, S., Strauss, M., Willick, J. (eds.), Cosmic Flows 1999: Towards an Understanding of Large-scale Structure, ASP, San Francisco, vol. 201, p. 103, astro-ph/9908163

Mamon, G.A., 2000b, Theory of galaxy dynamics in clusters and groups, in: Combes, F., Mamon, G.A., Charmandaris, V. (eds.), 15th IAP Astrophys. Mtg., Dynamics of Galaxies: from the Early Universe to the Present, ASP, San Francisco, vol. 197, p. 377, astro-ph/9911333

Mamon, G.A., 2000c, Understanding low and high velocity dispersion compact groups, in: Valtonen, M.J., Flynn, C. (eds.), IAU Coll. No. 174, Small Galaxy Groups, ASP, San Francisco, vol. 209, in press, astro-ph/9909019

Mamon, G.A., Borsenberger, J., Tricottet, M., Banchet, V., 1998, Galaxies with DENIS: Preliminary star/galaxy separation and first results, in: Epchtein, N. (ed.), 3rd DENIS/2MASS Euroconference, The Impact of Near-Infrared Sky Surveys on Galactic and Extragalactic Astronomy, Kluwer, Dordrecht, p. 177, astro-ph/9712169

Mamon, G.A., Glassgold, A.E., Huggins, P.J., 1988, The photodissociation of CO in circumstellar envelopes, ApJ 328, 797

Mamon, G.A., Glassgold, A.E., Omont, A., 1987, Photochemistry and molecular ions in oxygen-rich circumstellar envelopes, ApJ 323, 306

Marzke, R.O., da Costa, L.N., Pellegrini, P.S., Willmer, C.N.A., Geller, M.J., 1998, The galaxy luminosity function at $z \leq 0.05$: dependence on morphology, ApJ 503, 617

Mauron, N., Huggins, P.J., 1999, Multiple shells in the circumstellar envelope of IRC+10216, A&A 349, 203

Merritt, D., 1984, Relaxation and tidal stripping in rich clusters of galaxies. II.: Evolution of the luminosity distribution, ApJ 276, 26

Mo, H.J., White, S.D.M., 1996, An analytic model for the spatial clustering of dark matter haloes, MNRAS 282, 347

Moles, M., del Olmo, A., Perea, J., Masegosa, J., Marquez, I., Costa, V., 1994, Star formation and merging in compact groups of galaxies, A&A 285, 404

Morris, M., Jura, M., 1983, Molecular self-shielding in the outflows from late-type stars, ApJ 264, 546

Moss, C., Whittle, M., 1993, An H-alpha survey of cluster spirals — Comparison of star formation in clusters and the field, ApJ 407, L17

Moss, C., Whittle, M., 1997, Tidally-induced star formation in cluster galaxies, RvMexA&A 6, 145

Moss, C., Whittle, M., 2000, An H alpha Survey of 8 Abell Clusters: the dependence of tidally-induced star formation on cluster density, MNRAS in press, astro-ph/0003337

Mulchaey, J.S., Davis, D.S., Mushotzky, R.F., Burstein, D., 1993, Diffuse X-ray emission from the NGC 2300 group of galaxies: Implications for dark matter and galaxy evolution in small groups, ApJ 404, L9

Mulchaey, J.S., Davis, D.S., Mushotzky, R.F., Burstein, D., 1996, The intragroup medium in poor groups of galaxies, ApJ 456, 80

Mulchaey, J.S., Zabludoff, A.I., 1999, The isolated elliptical NGC 1132: evidence for a merged group of galaxies?, ApJ 514, 133

Navarro, J.F., Frenk, C.S., White, S.D.M., 1995, Simulations of X-ray clusters, MNRAS 275, 720

Navarro, J.F., Frenk, C.S., White, S.D.M., 1997, A universal density profile from hierarchical clustering, ApJ 490, 493

Ninin, S., 1999, Influence de la dynamique gravitationnelle sur la formation des galaxies, Thèse de doctorat, Université de Paris XI

Nolthenius, R., 1993, A revised catalog of CfA1 galaxy groups in the Virgo/Great Attractor flow field, ApJS 85, 1

Ostriker, J.P., Lubin, L.M., Hernquist, L., 1995, Using X-rays to determine which compact groups are illusory, ApJ 444, L61

Pfenniger, D., Norman, C., 1990, Dissipation in barred galaxies: the growth of bulges and central mass concentrations, ApJ 363, 391

Pildis, R.A., Bregman, J.N., Evrard, A.E., 1995, ROSAT observations of compact groups of galaxies, ApJ 443, 514

Ponman, T.J., Bourner, P.D.J., Ebeling, H., Böhringer, H., 1996, A ROSAT survey of Hickson's compact galaxy groups, MNRAS 283, 690

Ponman, T.J., Cannon, D.B., Navarro, J.F., 1999, The thermal imprint of galaxy formation on X-ray clusters, Nature 397, 135

Prandoni, I., Iovino, A., MacGillivray, H.T., 1994, Automated search for compact groups of galaxies in the southern sky, AJ 107, 1235

Press, W.H., Schechter, P., 1974, Formation of galaxies and clusters of galaxies by self-similar gravitational condensation, ApJ 187, 425

Quinn, P.J., Goodman, J., 1986, Sinking satellites of spiral systems, ApJ 309, 472

Ramella, M., Geller, M.J., Huchra, J.P., 1989, Groups of galaxies in the Center for Astrophysics redshift survey, ApJ 344, 57

Ramella, M., Pisani, A., Geller, M.J., 1997, Groups of galaxies in the northern CfA redshift survey, AJ 113, 483

Ramella, M., Zamorani, G., Zucca, E., Stirpe, G.M., Vettolani, G., Balkowski, C., Blanchard, A., Cappi, A., Cayatte, V., Chincarini, G., Collins, C., Guzzo, L., MacGillivray, H., Maccagni, D., Maurogordato, S., Merighi, R., Mignoli, M., Pisani, A., Proust, D., Scaramella, R., 1999, The ESO slice project (ESP) galaxy redshift survey VI. Groups of galaxies, A&A 342, 1

Rees, M.J., Ostriker, J.P., 1977, Cooling, dynamics and fragmentation of massive gas clouds: clues to the masses and radii of galaxies and clusters, MNRAS 179, 541

Rodrigues, D.D.C., Thomas, P.A., 1996, Merger trees and the multiplicity function of haloes, MNRAS 282, 631

Roukema, B.F., Mamon, G.A., 2000, Tangential large scale structure as a standard ruler: curvature parameters from quasars, A&A in press, astro-ph/9911413

Sakai, S., Mould, J.R., Hughes, S.M.G., Huchra, J.P., Macri, L.M., Kenicutt, R.C., Gibson, B.K., Ferrarese, L., Freedman, W.L., Han, M., Ford, H.C., Graham, J.A., Illingworth,

G.D., Kelson, D.D., Madore, B.F., Sebo, K., Silbermann, N.A., Stetson, P, B., 2000, The Hubble Space Telescope key project on the extragalactic distance scale XXIV: The calibration of Tully-Fisher relations and the value of the Hubble constant, ApJ 529, 698

Salvador-Sole, E., Solanes, J.M., Manrique, A., 1998, Merger versus accretion and the structure of dark matter halos, ApJ 499, 542

Saracco, P., Ciliegi, P., 1995, ROSAT observations of compact groups of galaxies, A&A 301, 348

Schechter, P., 1976, An analytic expression for the luminosity function for galaxies, ApJ 203, 297

Schröder, A., Kraan-Korteweg, R.C., Mamon, G.A., 1999, DENIS observations of multibeam galaxies in the Zone of Avoidance, PASA 16, 42

Schweizer, F., 1992, Mergers, in: Thuan, T.X., Balkowski, C., Tran Thanh Van, J. (eds.), 12th Moriond Astrophysics Meeting, Physics of Nearby Galaxies — Nature or Nurture?, Frontières, Gif-sur-Yvette, p. 283

Sheth, R.K., Mo, H.J., Tormen, G., 2000, Ellipsoidal collapse and an improved model for the number and spatial distribution of dark matter haloes, MNRAS submitted, astro-ph/9907024

Sigad, Y., Kolatt, T.S., Bullock, J.S., Kravtsov, A.V., Klypin, A.A., Primack, J.R., Dekel, A., 2000, Velocity and mass functions of galactic halos: evolution and environmental dependence, MNRAS submitted, astro-ph/0005323

Silk, J., 1977, On the fragmentation of cosmic gas clouds. I. The formation of galaxies and the first generation of stars, ApJ 211, 638

Spitzer, L.J., Baade, W., 1951, Stellar populations and collisions of galaxies, ApJ 113, 413

Sulentic, J.W., 1987, Properties of dense galaxy groups and the implications of their existence, ApJ 322, 605

Toomre, A., 1977, Mergers and some consequences, in: Tinsley, B.M., Larson, R.B. (eds.), The Evolution of Galaxies and Stellar Populations, Yale University Press, New Haven, p. 401

Trasarti-Battistoni, R., 1998, Loose groups of galaxies in the Perseus-Pisces survey, A&AS 130, 341

Tully, R.B., 1987, Nearby groups of galaxies. II. An all-sky survey within 3000 kilometers per second, ApJ 321, 280

Tully, R.B., Fisher, J.R., 1977, A new method of determining distances to galaxies, A&A 54, 661

Valageas, P., Silk, J., 1999, The reheating and reionization history of the universe, A&A 347, 1

Vikhlinin, A., McNamara, B.R., Hornstrup, A., Quintana, H., Forman, W., Jones, C., Way, M., 1999, X-ray overluminous elliptical galaxies: a new class of mass concentrations in the Universe?, ApJ 520, L1

Walke, D.G., Mamon, G.A., 1989, The frequency of chance alignments of galaxies in loose groups, A&A 225, 291

Weinberger, R., Temporin, S., Kerber, F., 1999, A new ultra-dense group of obscured emission-line galaxies, ApJ 522, L17

White, S.D.M., 1992, The structure of galaxy clusters, in: Fabian, A.C. (ed.), Clusters and Superclusters of Galaxies, Kluwer, Dordrecht, p. 17

White, S.D.M., Navarro, J.F., Evrard, A.E., Frenk, C.S., 1993, The baryon content of galaxy clusters: a challenge to cosmological orthodoxy, Nature 366, 429

White, S.D.M., Rees, M.J., 1978, Core condensation in heavy halos: a two-stage theory for galaxy formation and clustering, MNRAS 183, 341

Whitmore, B.C., Gilmore, D.M., 1991, On the interpretation of the morphology-density relation for galaxies in clusters, ApJ 367, 64

Whitmore, B.C., Gilmore, D.M., Jones, C., 1993, What determines the morphological fractions in clusters of galaxies?, ApJ 407, 489

Zabludoff, A.I., Mulchaey, J.S., 1998, The properties of poor groups of galaxies. I. Spectroscopic survey and results, ApJ 496, 39

Zepf, S.E., 1993, The frequency of mergers in compact groups, ApJ 407, 448

Zucca, E., Zamorani, G., Vettolani, G., Cappi, A., Merighi, R., Mignoli, M., Stirpe, G.M., MacGillivray, H., Collins, C., Balkowski, C., Cayatte, V., Maurogordato, S., Proust, D., Chincarini, G., Guzzo, L., Maccagni, D., Scaramella, R., Blanchard, A., Ramella, M., 1997, The ESO Slice Project (ESP) galaxy redshift survey. II. The luminosity function and mean galaxy density, A&A 326, 477

A Sélection d'articles publiés en Chimie Circumstellaire

A.1 Photochemistry and molecular ions in carbon-rich circumstellar envelopes

Glassgold, Mamon, Omont & Lucas, 1987, *A&A 180, 183–190*

Astron. Astrophys. 180, 183–190 (1987)

ASTRONOMY
AND
ASTROPHYSICS

Photochemistry and molecular ions in carbon-rich circumstellar envelopes

A.E. Glassgold[1], G.A. Mamon[1], A. Omont[2,⋆], and R. Lucas[2,⋆]

[1] Physics Dept., New York University, New York, NY 10003, USA
[2] Observatoire de Grenoble CERMO, B.P. 68, F-38402 St Martin D'Heres Cedex, France

Received October 22, accepted December 31, 1986

Summary. Our earlier theory of ionization of C-rich circumstellar envelopes based on the photochemical model is extended to include the temperature dependence of ion-molecule reactions with polar molecules, particularly HCN, and line self-shielding of CO dissociating radiation. The results are applied to the abundances of HCO^+ and HNC in C-rich circumstellar envelopes. With standard parameters for IRC + 10216, the model is found to be consistent with the new upper limit to the antenna temperature of the $J = 1 - 0$ line of HCO^+ obtained with the IRAM 30-m telescope. The photochemical model provides a natural explanation of the relatively large ratio of HCN to HNC observed for C-rich circumstellar envelopes, and good agreement is obtained for the $H^{13}CN$/HNC antenna temperature ratio measured for IRC + 10216.

Key words: circumstellar matter – ionization – molecules

1. Introduction

The chemistry of circumstellar envelopes (CSEs) of cool evolved stars is of considerable interest in the context of millimetre and infrared observations of a wide variety of molecules (see, e.g., the reviews by Omont 1985 and by Glassgold and Huggins 1986). In a recent paper (Glassgold, Lucas, and Omont 1986, henceforth referred to as GLO), we developed a theory of ionization of C-rich CSEs with particular reference to the well observed star IRC + 10216. The theory was based on the photochemical model, supplemented by cosmic ray ionization. According to this model, strongly bound molecules entering the CSE (beyond the region of dust formation) are destroyed by penetrating interstellar ultraviolet (UV) radiation. In addition to providing cut-offs in the spatial distributions of circumstellar molecules, photodestruction generates families of strongly interacting radicals, atoms, and ions. It was shown in GLO that ion-molecule reactions are the most important reactions in the cool outer parts of C-rich CSEs. The main ions are $C_2H_2^+$ (produced by photoionization of acetylene), C^+ (produced by photoionization of carbon generated in the photochains of CO, C_2H_2, HCN, etc.), and a series of ions produced by cosmic rays such as H_3^+, HCO^+, HN_2^+, $C_2H_3^+$, and H_2CN^+.

It was suggested in GLO that the $J = 1 - 0$ line of HCO^+ might be detected in IRC + 10216 with a sensitive search near 89.2 GHz. Lucas et al. (1986) obtained an upper limit of 20 mK for the brightness temperature of this line with the new IRAM 30-m telescope, equivalent to almost a factor of 5 less than an earlier limit (Johansson et al., 1984). One objective of this paper is to evaluate this result in terms of our model of circumstellar chemistry and ionization.

In this paper we improve the GLO model by incorporating recent advances in our understanding of ion-molecule reactions and CO line self-shielding. The most important aspect of the new treatment of ionic reactions is the temperature dependence of reactions with polar molecules (Adams et al., 1985) and dissociative recombination of H_3^+ and HCO^+ (Adams and Smith 1987). The temperature is expected to vary by one or two orders of magnitude in the CSE (Kwan and Linke 1982), and ionic reactions are sensitive to the low temperature conditions of the outer envelope. Self-shielding of CO was invoked in GLO to argue that C^+ is not significantly produced from the CO photochain until the radial distance r exceeds the cut-off parameter r_c ($\sim 10^{18}$ cm for IRC + 10216) introduced by Morris and Jura (1983). A more detailed study of CO line self-shielding (Mamon et al., 1987) indicates, however, that C^+ production from CO occurs well before r_c and can compete with ionization produced from the acetylene chain.

The large range in the HCN/HNC ratio measured in interstellar clouds has been a puzzle for interstellar chemistry for some time (see, for example, the review by Irvine et al. 1985). The ratio of unity for cool clouds is consistent with ion-molecule chemistry, as first predicted by Watson (1974). However, the much larger ratios found in OMC-1, about 250 for the plateau source and 20 for the ridge, have no satisfactory explanation at the present time. For IRC + 10216, Olofsson et al. (1982) have derived a value of ~ 250 for the HCN/HNC abundance ratio. This value is small compared to predictions based on thermal equilibrium considerations, and we will show that the HCN/HNC ratios found in C-rich CSEs can be understood in terms of ion-molecule chemistry.

In the next section we describe the various changes in our theory of ionization and chemistry of C-rich CSEs. The main results of these changes will be presented in Sect. 3, which includes a discussion of the new observational limits on HCO^+ for IRC + 10216 and an estimate of the abundance of HNC and its line intensity. The paper is concluded with a brief summary.

Send offprint requests to: A. Omont

⋆ Groupe d'Astrophysique U.A. CNRS No. 708, Université Scientifique, Technologique, et Médicale de Grenoble

2. Developments in the model

The alterations in the GLO model that are described here mainly produce quantitative rather than qualitative changes in the results. We refer to GLO for the physical basis and rationale of the model, except where significant changes are made, and continue to use the "standard" parameter set of GLO, given in Table 1 in abbreviated form.

Adams et al. (1985) have recently pointed out that reaction rates for ion polar molecule reactions decrease with increasing temperature below 300 K, and suggest that rate coefficients as large as $10^{-7}\,cm^{-3}\,s^{-1}$ may be appropriate for cold molecular gas ($T \sim 10$ K). This increase is expected from theory (Clary 1985, and earlier work cited therein and in Herbst and Leung 1986) and has been verified in laboratory experiments (Adams and Smith 1987).

Table 2 gives new and revised reaction rate coefficients; it supplements the first part of Table 3 in GLO (and follows the same numbering system). Ionic reactions with HNC are assumed to be the same as for HCN. The temperature dependence of all ion polar molecule reaction rate coefficients have been represented by

$$k(T) = k(300\,K)(300/T)^n \quad (1)$$

with $n \simeq 0.65$, our fit to the measurements for reaction No. 4. Ion molecule reactions with C_2H were included in order to determine whether they could reduce the abundance of C_2H below the prediction of the photochemical model (Huggins and Glassgold 1982a). Detailed analysis of the radio observations of C_2H lines in IRC + 10216 (Huggins et al., 1984, Truong-Bach et al., 1986) indicates that agreement with the model requires a much smaller abundance of C_2H_2 than is inferred from infrared absorption measurements. The same motivation lay behind the introduction of the neutral reaction No. 21 between C_2H and C_2H_2.

Most other reaction rate coefficients are the same as in GLO, with the following exceptions and additions. The photodissociation rate of HNC is assumed to be the same as for HCN, i.e. $7\,10^{-10}\,s^{-1}$. The recombination rate of HCO^+ is represented by $2.3\,10^{-5}\,T^{-1}\,cm^3\,s^{-1}$, consistent with both old (Leu et al., 1973) and new (Smith and Adams 1984) laboratory measurements. The upper limit to the H_3^+ recombination rate constant, $2\,10^{-8}\,cm^3\,s^{-1}$, has been replaced by the much smaller upper limit recently obtained by Smith and Adams (1985), $2\,10^{-11}\,cm^3\,s^{-1}$, and a temperature dependence $(300/T)^{0.5}$. Recombination of H_3^+ at this level is actually unimportant, even near the edge of the CSE where it is destroyed by proton transfer with CO and then with O.

We have now included photodissociation of CO using a theoretical treatment of CO line self-shielding (Mamon, et al., 1987). The contribution of the CO photochain to C^+ now begins to dominate for $r > 3 \times 10^{17}$ cm. Because this is beyond the region of greatest chemical activity, the qualitative conclusion of GLO holds, i.e. CO line self-shielding makes only a quantitative

Table 1. Standard model for IRC + 10216

Distance	$d = 200$ pc
Expansion velocity	$V = 16\,km\,s^{-1}$
Mass loss rate (total hydrogen)	$\dot{M} = 4\,10^{-5}\,M_\odot\,yr^{-1}$
Gas density, $n = Cr^{-2}$	$C = 7.5\,10^{37}\,cm^{-1}$
Abundances (relative to total hydrogen):	
CO	$3\,10^{-4}$
C_2H_2	$3\,10^{-5}$
HCN	$6\,10^{-6}$
Gas kinetic temperature	$T = 74\,K\,(r_{16})^{-0.79}$

Table 2. New or revised reaction rates[a,b]

Reaction	Rate coefficients at 300 K ($cm^3\,s^{-1}$)	References[d]
4. $H_3^+ + HCN \longrightarrow H_2CN^+ + H_2$	$8.0\,10^{-9}$	ASC 85
6. $HCO^+ + HCN \longrightarrow H_2CN^+ + H_2$	$3.0\,10^{-9}$	AH 84
10. $C_2H_2^+ + HCN \longrightarrow H_2CN^+ + C_2H$	$2.4\,10^{-10}$	AH 84
$\longrightarrow C_3H_2N^+ + H$	$1.2\,10^{-10}$	
11. $C_2H_3^+ + C_2H_2 \longrightarrow C_4H_3^+ + H$	$2.5\,10^{-10}$	AH 84
12. $C_2H_3^+ + HCN \longrightarrow H_2CN^+ + C_2H_2$	$6.0\,10^{-10}$	AH 84
14. $C^+ + HCN \longrightarrow CNC^+ + H$	$3.5\,10^{-9}$	H 77, DKF 86
18. $HCO^+ + C_2H \longrightarrow C_2H_2^+ + CO$	1.0×10^{-9}	
19. $C^+ + C_2H \longrightarrow C_3^+ + H$	1.0×10^{-9}	
20. $C_2H_2^+ + C_2H \longrightarrow C_4H_2^+ + H$	$1.0\,10^{-9}$	
21. $C_2H + C_2H_2 \longrightarrow C_4H_3 + H$	3.0×10^{-11}	LB 79[c]

[a] All ion-molecule reaction rates for HCN and C_2H are assumed to vary as $T^{-0.65}$, as measured for reaction No. 4. (See text.)

[b] All reactions for HNC are assumed to occur with the same rate coefficients as HCN.

[c] Allen et al. (1980) interpret the measured value of the rate coefficient at 300 K to imply an activation energy for this reaction of 360 K.

[d] References to laboratory measurements: ASC 85 – Adams, Smith, and Clary (1985); AH 85 – Anicich and Huntress (1984); DKF 86 – Daniel, Keim, and Farrar (1986); H 77 – Huntress (1977); LB 79 – Laufer and Bass (1979)

difference in the chemistry of C-rich CSEs. This is in contrast to O-rich CSEs, where CO is by far the major source of the C^+ ion (Mamon et al., 1986).

A new feature of the present model is the emphasis on the HCN photochain. Although its abundance is small compared to the dominant neutral molecules in C-rich CSEs, HCN can be important because many molecular ions are destroyed by HCN with large reaction rates, especially at low temperatures. The isomer HNC is produced by dissociative recombination of H_2CN^+,

$$e + H_2CN^+ \longrightarrow \begin{cases} HCN + H & b_1 \\ HNC + H & b_2 \\ CN + H_2 & b_3. \end{cases} \quad (2)$$

The branching ratios b_i have not been measured, and we have used the results of phase space calculations of Herbst (1978), $b_1 = b_2 = 0.25$ and $b_3 = 0.5$. The general considerations of Bates (1986) also support a large value for b_3. The H_2CN^+ ion is produced by proton transfer of other molecular ions with HCN,

$$MH^+ + HCN \longrightarrow H_2CN^+ + M \quad (3)$$

particularly $C_2H_2^+$. Thus, increased destruction of other molecular ions by HCN at low temperatures is accompanied by enhanced production of H_2CN^+, and then of HNC.

3. Results

We now present the results obtained with the revised chemical model, including variations in the standard model that test its stability to changes of parameters and assumptions.

3.1. *Abundance and spatial distribution of molecular ions*

The spatial variation of the abundances are familiar from previous studies (e.g. Huggins and Glassgold 1982, Huggins, et al., 1984, and GLO in particular): progenitor molecules are located toward the inside of the CSE, radicals and molecular ions in the middle (e.g. in the range $10^{16} - 10^{17}$ cm for the standard case), and C^+, N, and O on the outside. The spatial distributions of the *main* C-bearing species in the region of interest ($3\,10^{15} < r < 3\,10^{17}$ cm) are similar to Fig. 5a of GLO, and we only comment briefly on several quantitative changes. In GLO, the peak abundances of C_2H, C_2, and C are all about the same, $\sim 1.5\,10^{-5}$ for the standard model. In the new calculations, these abundances are reduced by about 2/3 and the peak abundance of C_2H is now the smallest, $\sim 9\,10^{-6}$. This reduction is due to the new reactions in Table 2 which destroy C_2H, particularly the neutral reaction No. 21 – if we assume there is no activation energy. Although this decrease is clearly insufficient to explain the radio observations of C_2H in IRC + 10216 in the context of the photochemical model (Huggins et al. 1984, Truong-Bach et al., 1986), it may suggest a possible resolution of the difficulty. The C_2H radical is generally chemically reactive with carbon and hydrocarbon molecules. If a substantial fraction of the carbon not in CO were incorporated into these species in the process of incomplete dust formation in the inner envelope, they might be able to destroy the bulk of the photochemically produced C_2H. However, there is no sign of a large enough abundance of carbon in such species, either in long chain molecules observed in the radio or in polycyclic aromatic hydrocarbons, whose presence would be observed by characteristic IR absorption features.

Figure 1 shows the run of carbon-bearing ions for the standard model of IRC + 10216; also shown are the abundances X_3 and X_4 of neutral hydrocarbon molecules with odd and even numbers of carbon atoms ≥ 3 or ≥ 4, respectively. The results are qualitatively similar to Fig. 5 of GLO, and the general conclusions made in GLO about the formation of complex molecules by ion-molecule reactions remain unchanged. Relative to GLO, the main changes (expressed in terms of peak values) are as follows: $x(HCO^+)$ is decreased by about a factor of 3 to $4.5\,10^{-10}$; $x(C_2H_3^+)$ is decreased by a factor of 2 to $1.8\,10^{-10}$, $x(H_2CN^+)$ is increased by more than a factor of 5 to $5\,10^{-9}$, and H_3^+, X_3^+, and X_4^+ are changed by small amounts ($\pm 30\%$). Thus the main change is the large increase in H_2CN^+, which arises from the low temperature enhancement of ionic reactions with HCN. Ions such as $C_2H_3^+$ and HCO^+, whose destruction is strongly influenced by reactions with HCN, are correspondingly reduced in abundance.

The spatial distribution of H_2CN^+ is broader than all the other molecular ions. At small distances, $r < 10^{16}$ cm, it is produced by the cosmic ray ions and at intermediate distances, $10^{16} < r < 10^{17}$ cm, by hydrocarbon ions, particularly $C_2H_2^+$; it is destroyed by dissociative recombination. The large abundance of H_2CN^+ does not imply that it will replace HCO^+ as a potential observational signature for the ionization of C-rich CSEs. The best calculation of the dipole moment of H_2CN^+ is 0.29 *D* (Botschwina 1986), so that the brightness temperature of the $J = 1 - 0$ transition at 74 GHz (Bogey et al., 1985) will be much less than 1 mK for IRC + 10216. Similarly, the column density of H_2CN^+ is of order 10^{13} cm^{-2}, and its detection in the IR also seems infeasible. There are two additional implications of the

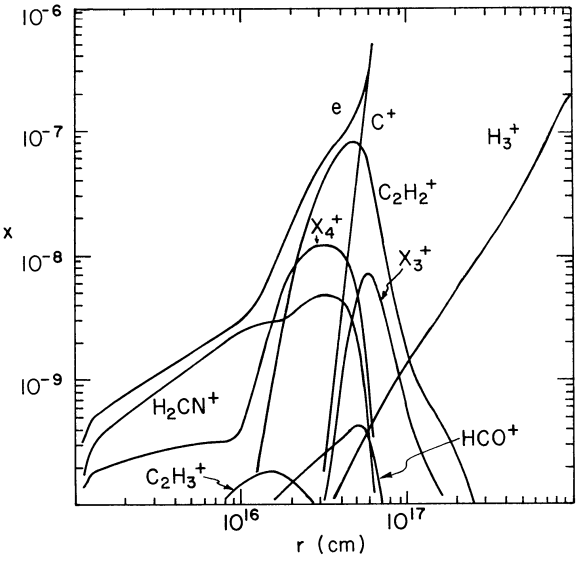

Fig. 1. The spatial distribution of various ions for the standard parameters of Table 1. X_3^+ and X_4^+ represent the total abundance of ions with odd and even numbers of carbon atoms ≥ 3 and ≥ 4, respectively. The abundances refer to the total number of hydrogen nuclei

increased abundance of H_2CN^+, however, which have a bearing on other observable species. The first is an increase in the abundance of HNC implied by Eq. (3), which will be discussed in more detail below. The second is that the production of HC_3N is increased by the low temperature enhancement of reaction No. 10b:

$$C_2H_2^+ + HCN \longrightarrow \begin{cases} H_2CN^+ + C_2H \\ H_2C_3N^+ + H \end{cases}$$

with HC_3N being produced by the dissociative recombination of $H_2C_3N^+$.

In order to test the sensitivity of the results to the kinetic temperature, we have done calculations where the slope and scale of the standard distribution in Table 1 (due to Kwan and Linke 1982) are changed. The main effects come from the temperature dependence of ion-molecule reactions with HCN and of recombination coefficients. The most important observational issue is the peak abundance of HCO^+, which is sensitive to the temperature at the peak. In the standard model, the temperature is 20 K. When it is changed by a factor of two, the peak HCO^+ abundance changes by about 65%, mostly due to the effects of reaction No. 6. If the initial abundance of HCN were reduced (see Sect. 3.3), the change would be smaller. Another ion affected by temperature is $C_2H_3^+$, which is important in the synthesis of C_4H_2 via reaction 11. Again, factor of two changes in temperature lead to abundance changes for $C_2H_3^+$ and for X_4^+ (mainly $C_4H_3^+$) before its peak that are somewhat less than two. It may be noted that the temperature measurement of Sahai and Wannier (1985) for the inner dust envelope ($r = 6\,10^{15}$ cm) are almost a factor of two larger than an extrapolation of the model of Kwan and Linke.

One further point about the chemistry associated with HCN is the substantial rate of production of CNC^+ by reaction No. 14 (Daniel et al., 1986). Using the heats of formation given by these authors, we find that this ion cannot be hydrogenated by reactions with the major H-bearing molecules, H_2, C_2H_2, and HCN. It may undergo condensation reactions with acetylene and produce additional amounts of C_3H and HC_3N. If this is the case, its abundance will be rather small because the reaction with C_2H_2 will dominate dissociative recombination at intermediate distances. Production of C_3H and HC_3N by CNC^+ is unlikely to compete with the more direct channels discussed in GLO which are based on the reactions of C^+ and $C_2H_2^+$ with C_2H_2.

The abundance of C_2H_2 is sufficiently high that it partially shields itself from the external UV radiation. Because photodissociation and photoionization of C_2H_2 are basically continuum processes, the theoretical treatment of self-shielding is relatively straightforward, and the method used by Huggins and Glassgold (1982) for H_2O has been adapted to this case. When C_2H_2 self-shielding is included, some quantitative changes occur in closely related species, e.g. the rise at small distances of C_2H, C_2, X_3, $C_2H_2^+$, and X_3^+ are shifted to slightly larger distances. The abundance of HCO^+ is unaffected. The only species whose peak abundance is changed is $C_2H_3^+$; C_2H_2 self-shielding increases its abundance by about 30%. None of these changes is expected to have any significant observational consequences.

We have also examined the effect of changing the cosmic ray ionization rate ζ. In the standard parameter set of GLO, $\zeta = 5\,10^{-18}\,s^{-1}$, consistent with the high energy cosmic ray flux observed in the solar system and with molecular abundances in dense clouds. On the basis of a recent re-analysis of several well studied diffuse clouds, van Dishoeck and Black (1986) have suggested using a much larger rate, $7\,10^{-17}\,s^{-1}$. We have done a calculation for a C-rich CSE in which the only change in the standard model was to increase ζ by a factor of 10 to $5\,10^{-17}\,s^{-1}$. Substantial changes in the abundances of cosmic ray generated molecular ions are obtained. For an ion that contributes negligibly to the total ionization, such as H_3^+, HCO^+, or $C_2H_3^+$, the abundance increases linearly with ζ. Because H_2CN^+ is the dominant ion for $r < 10^{16}$ cm, its abundance increases only as $\zeta^{0.5}$ in this region. The production rate of HNC is proportional to $x_e x(H_2CN^+)$ and its abundance scales as ζ at small distances and as $\zeta^{0.5}$ near its peak. The observational implications of a cosmic ray ionization rate larger than "standard" for HCO^+ and HNC will be explored further in the following sections.

3.2. *The abundance of HCO^+*

Our new results for the spatial distribution of HCO^+ in C-rich CSEs are given in Fig. 2. The solid curves correspond to Fig. 4 of GLO; the three values for the mass loss rate define a realistic range for IRC + 10216, which remains the best studied C-rich CSE. The abundances have been adjusted for the two non-standard cases of $\dot{M} = 10^{-5}$ and $10^{-4}\,M_\odot\,yr^{-1}$ so that the total loss rates of the progenitor molecules CO, C_2H_2, and HCN are the same as for the standard case, $\dot{M} = 4\,10^{-5}\,M_\odot\,yr^{-1}$. (Thus the initial abundances have been increased relative to Table 1 by a factor of 4 for $\dot{M} = 10^{-5}\,M_\odot\,yr^{-1}$ and decreased by 2.5 for $\dot{M} = 10^{-4}\,M_\odot\,yr^{-1}$.) The peak value and the size of the HCO^+ distribution both increase with mass loss rate, but less rapidly than linearly. The calculated antenna temperatures (main beam brightness temperature of a perfect telescope with a gaussian beam)

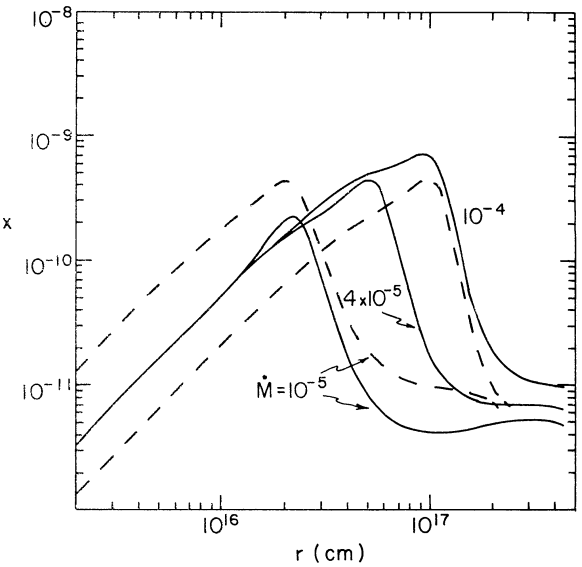

Fig. 2. The spatial distribution of HCO^+ for three values of the mass loss rate. The middle solid curve is the standard model (see Table 1). The other solid curves are for smaller and larger mass loss rates, with the abundances at the base of the envelope scaled as $\dot{M}^{-1}$. The dashed curves are for the same mass loss rates but with the same abundances as in the standard model

Table 3. Main beam brightness temperatures for the $J = 1 - 0$ line of HCO^+ (89 GH z)

Model		T_A(mk) Telescope		
$\dot{M}(M_\odot\,yr^{-1})$	Abundances[a]	20-m	30-m	45-m
10^{-5}	Scaled	1.6	3.4	6.6
$4\,10^{-5}$	Scaled[b]	13	24	38
10^{-4}	Scaled	50	81	114
10^{-5}	Fixed	2.9	6	12
10^{-4}	Fixed	17	28	41

[a] Abundances: scaled means that $\dot{M}$ times the initial abundances of CO, C_2H_2, and HCN are fixed; fixed means the same abundances as in Table 1.
[b] The standard model

for on-source measurements of the $J = 1 - 0$ line of HCO^+ near 89.2 GHz are given in Table 3 for three large mm telescopes. The antenna temperature increases with $\dot{M}$ more rapidly than linearly. The dashed curves in Fig. 2 give the spatial distribution of HCO^+ for two additional values of the mass loss rate but with abundances fixed at the standard values in Table 1; the corresponding antenna temperatures are given in Table 3. These might be applicable to other C-rich CSEs besides IRC + 10216. When the abundances are kept constant, the HCO^+ antenna temperature becomes an even steeper function of mass loss rate.

The HCO^+ antenna temperature calculated with the standard model is 24 mK, consistent with the upper limit of 20 mK obtained for IRC + 10216 by Lucas et al. (1986) with the IRAM 30-m telescope. Of course the actual antenna temperature may well be less than this, but another search with the 30-m telescope would require sensitivities at the mK level. The 45-m Nobeyama telescope would be of some help because its larger dish gives a proportional increase in sensitivity in this case, all other things being equal. It would also be of interest to search for HCO^+ in other C-rich CSEs with mass loss rates comparable to or larger than that for IRC + 10216 using high sensitivity systems.

We have also considered the effects of varying some of the assumptions in the model in the context of the abundance of HCO^+. For example, increasing the cosmic ray ionization rate by 10 (to $5\,10^{-17}\,s^{-1}$), suggested by the analysis of diffuse interstellar clouds by van Dishoeck and Black (1986), increases both the abundance and the antenna temperature by the same factor of 10. Without further adjustments, the model would then be in strong conflict with the IRAM upper limit for HCO^+. The consistency between the model and the observations could be restored by reducing the mass loss rate by a factor of 5. However, a mass loss rate for IRC + 10216 smaller than $10^{-5}\,M_\odot\,yr^{-1}$ would be difficult to reconcile with other molecular measurements, including CO. Another possibility is that the cosmic ray ionization rate varies significantly with position in the Galaxy.

It was emphasized in GLO that the abundance of HCO^+ is strongly affected by the ionization of the CSE. In the standard model, the main source of electrons is photoionization of C produced in the C_2H_2 photochain. Increasing the initial abundance of C_2H_2 leads to a reduction in the HCO^+ abundance, but it also increases C_2H, which is already too abundant in the model. Conversely, trying to solve the C_2H problem for IRC + 10216 by reducing the initial C_2H_2 abundance leads to HCO^+ abundances in conflict with the IRAM upper limit and possibly with IR absorption measurements.

If there were another source of electrons, independent of the C_2H_2 photochain, then HCO^+ could be reduced further without aggravating the C_2H_2/C_2H situation (unless the new species destroys C_2H_2 and C_2H). The CO photochain deserves consideration, but strong self-shielding limits the production of C^+ to beyond the region of large HCO^+ abundance. Yet another possibility is that there is another neutral species entering the outer envelope that is photoionized. To be effective, the abundance of this species must be $>10^{-5}$ in the standard model and its photoionization rate $>10^{-10}\,s^{-1}$. Heavy elements like S, Si, Fe, and Mg are candidates, but they are likely to be depleted onto dust grains. An interesting possibility is free, atomic carbon that might be left as a residue from the process of dust formation in the inner envelope. Our calculations suggest that an initial C abundance of 10^{-5} could reduce the peak HCO^+ abundance by a factor of 2, assuming that C does not react with C_2H_2 and C_2H in the inner CSE. The present upper limit to the abundance of C in IRC + 10216, obtained from attempts to detect the 605 micron line with the NASA 3-m IRTF (Beichman et al., 1983), is an order of magnitude larger. Beichman et al. have reported a detection of this line in another C-rich CSE, CRL 2688 (the Egg Nebula) with the NASA 0.94-m KAO at a level that suggests $C/CO > 4$ in this object. The relation between abundances in CRL 2688 and IRC + 10216 is unclear at present because these two objects are so different in structure and dynamics. For example, CRL 2688 is a bipolar nebula with an embedded star of spectral type F5 Ia (Cohen and Kuhi 1977). The emission at 2.12 microns of the $v = 1 - 0$ S(1) line of H_2 in CR 2688 has been interpreted in terms of shocks produced by a stellar wind (Beckwith et al., 1984). Perhaps a large C/CO ratio is also produced by these shocks. It is noteworthy that the optical spectrum (Cohen and Kuhi 1977), is characterized by emission of the C_2 molecule.

3.3. *The abundance of HNC*

The observed values of the ratio HCN/HNC in C-rich CSEs have been interpreted in terms of a freeze-out model (e.g. McCabe et al., 1979), where $x(HCN)/x(HNC) = \exp(\Delta E/kT)$ and $\Delta E = 0.67$ eV (~ 7800 K) is the energy difference between the ground states of HNC and HCN. Typical values for this ratio are $6\,10^6$, 2500, and 200 for values of the freeze out temperature $T = 500$, 1000, and 1500 K, respectively. If the relatively large HCN/HNC ratio observed for IRC + 10216 is interpreted in this way, the freeze out must occur at a fairly high temperature, $T \sim 1400$ K. However, it is unlikely that freeze out actually occurs at such a high temperature because the reactions.

$$HCN + H \underset{b}{\overset{a}{\rightleftharpoons}} CN + H_2 \underset{d}{\overset{c}{\rightleftharpoons}} HCN + H \qquad (3)$$

are expected to be operative throughout a good part of the outer CSE. Reaction c is known to have a moderate activation energy, $k_c = (1.0 \pm 0.3)\,10^{-11} \exp(-2670/T)\,cm^3\,s^{-1}$ (Albers et al., 1974), but the activation energy of reaction b is unknown. If it is the same as that for reaction c, then the conversion of HNC to HCN through the reactions in Eq. (3) would not freeze out

1987A&A...180..183G

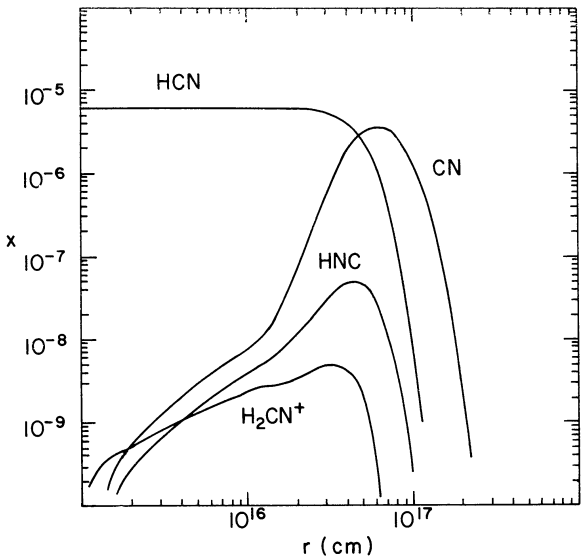

Fig. 3. The spatial distribution of the HCN photochain for the standard parameters of Table 1

until T had decreased to about 500 K, assuming that the ratio of atomic to molecular hydrogen is $\gtrsim 10^{-3}$ (Glassgold and Huggins 1983), which implies a much larger HCN/HNC ratio than is observed for IRC + 10216. Even if the activation energy of reaction a were twice that of reaction c, the freeze-out would not occur until T had decreased to ~ 900 K, which would yield HCN/HNC $\sim$ 6000 if $H/H_2 \gtrsim 10^{-3}$.

The large value of HNC/HCN in IRC + 10216 has a natural interpretation in the photochemical model. As described in Sect. 2, H_2CN^+ is formed by proton transfer from other molecular ions to HCN, and HNC is then produced by dissociative recombination according to Eq. (2). The results of our model calculations are shown in Fig. 3 for the standard parameters and a branching ratio, $b_2 = 0.25$. The abundance ratio varies with distance from the star because HCN and HNC vary in different ways. Thus going across the peak of HNC in Fig. 3, HCN/HNC varies from 200 to 40. It is noteworthy that the spatial distribution of HNC is smaller than that of CN, e.g. the peaks of HNC and CN in Fig. 3 occur at 4 and $6\,10^{-16}$ cm, respectively. There is some observational indication of this effect (Olofsson et al., 1982, Truong-Bach et al., 1986). It would be interesting to test this prediction of the photochemical model by making maps of both HNC and CN with a large telescope or interferometer. The mean abundance ratio is not very sensitive to mass loss rate; it does decrease slowly with $\dot{M}$. More important, the size of the HNC distribution increases with increasing $\dot{M}$.

Table 4 gives the predicted antenna temperatures for $H^{13}CN$ and HNC for the models discussed for HCO^+ in connection with Table 3; HCN is not given because the large optical depths for the relevant mm transitions make it much less useful than its isotopic forms. The calculations are based on the value of 40 given by Wannier (1985) for the $^{12}CO/^{13}CO$ isotope ratio, which is in substantial agreement with more recent measurements by Kahane et al. (1987). The IR lines of $H^{13}CN$ and HNC have also been assumed to be optically thin. It is important to stress that the IR line strengths of HNC are somewhat uncertain and have been represented by a single line with IR dipole moment = 0.16 D. It should also be noted that the $1 - 0$ population of $H^{13}CN$ appears to be inverted in the inner part of the CSE, which makes the calculated T_A sensitive to the model parameters. We first consider the ratio of $H^{13}CN$ to HNC antenna temperatures, in order to reduce the sensitivity of the conclusions to various uncertainties in the analysis. For a 30-m telescope, this ratio is 6.2 for the standard case; it increases with $\dot{M}$, but less rapidly than linearlv. This result is in good agreement with the ratio of 7.0 recently determined for IRC + 10216 with the IRAM telescope (Kahane et al., 1987). The standard model also agrees with the Onsala ratio of ~ 4 (Olofsson et al., 1982). If we consider the absolute antenna temperatures, the model predicts values which are too large by a factor of two for both HNC and $H^{13}CN$. Close agreement with both values could be achieved by reducing the initial abundance of HCN or both b_1 and b_2 by a factor of two, all of which are permitted by the uncertainties in these quantities. Changing the mass loss rate is not called for, because it affects $H^{13}CN$ and HNC differently.

Bieging et al. (1984) have derived a smaller abundance for HCN in IRC + 10216 than our standard model from mm interferometric measurements with a 9″ synthesized beam. They also find a smaller abundance in the interior of the envelope (inside 9″) relative to the outside. Such a decrease in abundance at small distances would have a small effect on the predictions of the photochemical model for the spatial distribution of HNC and

Table 4. Main beam brightness temperatures for the $J = 1 - 0$ lines of $H^{13}CN$ and HNC

Model		T_A(K)			
$\dot{M}(M_\odot\,yr^{-1})$	Abundances[a]	20-m telescope		30-m telescope	
		$H^{13}CN$	HNC	$H^{13}CN$	HNC
10^{-5}	Scaled	1.8	0.8	3.9	1.7
$4\,10^{-5}$	Scaled[b]	6.8	1.4	13.6	2.2
10^{-4}	Scaled	4.1	2.1	10.4	3.2
10^{-5}	Fixed	0.56	0.13	1.2	0.28

[a] See the explanation in Table 3.
[b] The standard model

CN, because these distributions peak at larger distances. When the exterior abundance of Bieging et al. is scaled to our adopted distance of 200 pc, the result is 1/3 of the abundance of the standard model. Taking into account that $\sim 1/2$ of the emission is resolved out in the interferometric measurement, we suggest that the exterior HCN abundance, before it is reduced by photodestruction, is $\sim 3\,10^{-6}$ on the basis of the work of Bieging et al. (1984). As we discussed above, this abundance produces good agreement between the photochemical model and the single dish measurements of $H^{13}CN$ and HNC. Thus our best estimate of the abundance of HCN for the IRC + 10216 CSE is $3\,10^{-6}$, down by a factor of two compared with the standard model. The column density into 10^{15} cm (1/3″ at 200 pc), which might be the beginning of the dust shell is $6\,10^{17}$ cm^{-2}, a factor of 2.5 smaller than the fairly uncertain value obtained by Hall and Ridgway (1978) on the basis of IR absorption measurements.

We conclude this discussion of HNC in C-rich CSEs with a brief comment about the role of the cosmic ray ionization rate. As remarked earlier, the abundance increases as ζ in the interior of the envelope and as $\zeta^{0.5}$ near the peak. We have calculated the change in the HNC antenna temperature when the standard cosmic ray ionization rate is increased by 10, and find that it increases by about a factor of 4. Thus increasing ζ produces a smaller $H^{13}CN$/HNC ratio, and tends to destroy the reasonable agreement of the standard model with the observations of IRC + 10216.

4. Conclusion

In this paper we have given an improved version of the photochemical model for C-rich CSEs. Although strongly founded on our previous work (GLO), our goal here has been to develop a more quantitative model suitable for analyzing data relevant to molecular ions, using IRC + 10216 as a test case. The model has been improved by incorporating new understanding of several basic physical processes, in particular the temperature dependence of ion-molecule reaction rates and the self-shielding of CO. The observational data of interest include the new upper limit to the antenna temperature of the $J = 1 - 0$ line of HCO^+ in IRC + 10216 (Lucas et al., 1986) and the large HCN/HNC ratio observed in C-rich CSEs, particularly the accurate values for IRC + 10216 (Olofsson et al., 1982, Kahane et al., 1987).

The new calculations show quantitative but not qualitative differences with GLO. The largest changes arise from the temperature dependence of ion-molecule reactions with HCN. The final result of the analysis is that both the upper limit for HCO^+ and the HNC/HCN ratio in IRC + 10216 can be accounted for in our standard model for this object, using the same parameters as GLO. This parameter set is based on the analysis of CO observations by Kwan and Linke (1982) and infrared absorption measurements of C_2H_2 and HCN. The general conclusion of GLO, that the chemical activity of the intermediate regions of C-rich CSEs is basically ion-molecule in character, is strengthened by the increased role of HCN, which leads to larger abundances for complex, N-bearing molecules.

The abundance of HCO^+ in IRC + 10216 (peak abundance $4.6\,10^{-10}$ in the standard case) may be still too large. Several possibilities for reducing it have been discussed in this paper and in GLO. The first is decreasing the mass loss rate $\dot{M}$. The HCO^+ antenna temperature is fairly sensitive to $\dot{M}$ (varying as $\dot{M}^{4/3}$) and, reducing $\dot{M}$ by 2 for example, reduces $T_A(HCO^+)$ by a factor of 2.5 to 10 mK. One motivation for considering smaller values for $\dot{M}$ is that IRC + 10216 may be closer than we have assumed (200 pc), e.g. Zuckerman et al. (1986) have recently suggested that the distance might be 100–150 pc. For this distance, $\dot{M}$ would have to be reduced by a factor of a few in order to maintain the HCO^+ brightness temperature at the same value as the standard model. Yet another way of reducing the abundance of HCO^+ is to increase the ionization in the neighborhood of its peak abundance. We suggested one such scenario where a relatively small amount of free atomic carbon (of order 10^{-5}) is left over from the process of dust formation and then photoionized by interstellar radiation. Another possibility is that the cosmic ray flux into the CSE is reduced by the action of strong magnetic fields. Evidence for significant magnetic fields in O-rich CSEs now exists from measurements of the Zeeman effect in OH masers (Cohen 1987). We have also pointed out that increasing the cosmic ray ionization rate to the level used in the recent analysis of diffuse interstellar clouds (van Dishoeck and Black 1986), would lead to serious disagreement between the model and the limits on HCO^+ set by observations with the IRAM 30-m telescope (Lucas et al., 1986).

At the present time, the photochemical model provides the most convincing description of the chemistry of C-rich CSEs. It embodies the well founded ideas of thermal equilibrium for saturated molecules, but includes the inevitable destruction of circumstellar molecules by interstellar UV radiation. The model allows for the fact that radicals do not necessarily freeze out far out in the CSE, and its basic photochemical nature leads to a strong ion-molecule chemistry at intermediate distances, consistent with the low temperatures of these envelopes. One serious problem of the photochemical model is that it predicts about one order of magnitude too much C_2H in IRC + 10216, if IR absorption measurements are used to determine the initial abundance of C_2H_2. It would be of great interest to determine whether a similar problem occurs for other C-rich envelopes. Although C_2H has been detected in the bipolar nebula CRL 2688 (Huggins et al., 1984; Lucas et al., 1986), its abundance relative to C_2H_2 is unknown for this object. Clearly the model requires further careful testing, and many observational opportunities are now becoming feasible with the increasing availability of systems capable of high sensitivity observations with high spatial resolution.

Acknowledgement. The authors wish to thank Dr. C. Kahane and Dr. M. Guélin for making their data available before publication, Dr. M. Jura for numerous helpful comments and suggestions and, at New York University, the support of NASA Grant NAGW-630.

References

Adams, N.G., Smith, D.: 1986 in *Astrochemistry*, eds. S.P. Tarafder, M.S. Vardya, Reidel, Dordrecht, p. 1

Adams, N.G., Smith, D., Clary, D.C.: 1985, *Astrophys. J. Letters* **296**, L31

Allen, M., Pinto, J.D., Yung, Y.: 1980, *Astrophys. J. Letters* **242**, L125

Albers, E.A., Hoyermann, K., Schacke, H., Schmatzko, K.J., Wagner, H.G., Wolfrum, J.: 1974, 15th Symposium on Combustion, Pittsburgh

Anicich, V.G., Huntress, W.T.: 1984, Jet Propulsion Lab. Report

Bates, D.R.: 1986, *Astrophys. J. Letters*, **306**, L45
Beckwith, S., Beck, S.C., Gatley, I.: 1984, *Astrophys. J.* **280**, 648
Beichman, C.A., Keene, J., Phillips, T.A., Huggins, P., Wootten, H.A., Masson, C., Frerking, M.A.: 1983, *Astrophys. J.* **273**, 633
Bogey M., Demuynck, C., Destombes, J.L.: 1985, *J. Chem. Phys.* **83**, 3703
Botschwina, P.: 1986, *Chem. Phys. Letters* **124**, 382
Clary, D.C.: 1985, *Mol. Phys.* **54**, 605
Cohen, M., Kuhi, L.: 1977, *Astrophys. J.* **212**, 79
Cohen, J.M.: 1987, *Symposium No.* **122** *on Circumstellar Matter*, eds. I. Appenzeller, C. Jordan, Reidel, Dordrecht (in press)
Daniel, R.G., Keim, E.R., Farrar, J.M.: 1986, *Astrophys. J.* **303**, 439
van Dishoeck, E., Black, J.H.: 1986, *Astrophys. J.* **62**, 109
Glassgold, A.E., Lucas, R., Omont, A.: 1986, *Astron. Astrophys.* **157**, 35
Glassgold, A.E., Huggins, P.J.: 1983, *Monthly Notices Roy. Astron. Soc.* **203**, 517
Glassgold, A.E., Huggins, P.J.: 1986, in *The M, S, and C Stars*, eds. H.R. Johnson, F. Querci, NASA and CRNS (in press)
Herbst, E.: 1978, *Astrophys. J.* **222**, 508
Herbst, E., Leung, C.M.: 1986, *Astrophys. J.* **312**, 378
Huggins, P.J., Glassgold, A.E.: 1982, *Astron. J.* **87**, 1828
Huggins, P.J., Glassgold, A.E., Morris, M.: 1982, *Astrophys. J.* **279**, 284
Huntress, W.T.: 1977, *Astrophys. J. Suppl.* **33**, 495
Irvine, W.B., Schloerb, P.B., Hjalmarson, A., Herbst, E.: 1985, in *Protostars and Planets II*, eds. D.C. Black, Shapley, M.S., Arizona, p. 579
Johansson, L.E.B., Anderson, C. Elder, J., Friberg, P., Hjalmarson, A., Hoglund, B., Irvine, W.B., Olofsson, H., Rydbeck, G.: 1984, *Astron. Astrophys.* **130**, 227
Kahane, C., Gomez-Gonzalez, J., Cernicharo, J., Guelin, M.: 1987, Astron. Astrophys. (in press)
Kwan, J., Linke, R.A.: 1982, *Astrophys. J.* **254**, 587
Laufer, A.M., Bass, A.M.: 1979, *J. Phys. Chem.* **83**, 310
Leu, M.T., Biondi, M.A., Johnsen, R.: 1973, *Phys. Rev.* **8A**, 413
Lucas, R., Omont, A., Guilloteau, S., Nguyen-Quang-Rieu: 1986 *Astron. Astrophys. Letters* **154**, L12
Mamon, G.A., Glassgold, A.E., Omont, A.: 1987, *Astrophys. J.* (submitted).
Mamon, G.A., Glassgold, A.E., Huggins, P.J.: 1987, (in preparation)
McCabe, E.M., Smith, R.C., Clegg, R.E.S.: 1979, *Nature*, **281**, 263
Morris, M., Jura, M.: 1983, *Astrophys. J.* **264**, 546
Omont, A.: 1985, in *Mass Loss fron Red Giants*, eds. M. Morris, B. Zuckerman, Reidel, Dordrecht, p. 269
Olofsson, M., Johansson, L.E.B., Hjalmarson, A., Nguyen-Quang-Rieu: 1982, *Astron. Astrophys.* **107**, 128
Sahai, R., Wannier, P.G.: 1985, *Astrophys. J.* **299**, 424
Smith, D., Adams, N.G.: 1984, *Astrophys. J. Letters* **284**, L13
Smith, D., Adams, N.G.: 1985, (private communication)
Truong-Bach, Nguyen-Quang-Rieu, Omont. A., Olofsson, H., Johansson, L.E.B.: 1986, *Astron. Astrophys.* (submitted)
Watson, W.D.: 1974, *Astrophys. J.* **188**, 35

A.2 Photochemistry and molecular ions in oxygen-rich circumstellar envelopes

Glassgold, Mamon & Omont, 1988, *ApJ 323, 306–315*

THE ASTROPHYSICAL JOURNAL, 323:306-315, 1987 December 1

PHOTOCHEMISTRY AND MOLECULAR IONS IN OXYGEN-RICH CIRCUMSTELLAR ENVELOPES

G. A. MAMON AND A. E. GLASSGOLD
Department of Physics, New York University

AND

A. OMONT
Groupe d'Astrophysique,[1] Observatoire de Grenoble, Université Scientifique et Médicale de Grenoble
Received 1987 March 9; accepted 1987 May 18

ABSTRACT

A theory for the ionization of the circumstellar envelopes around O-rich red giants is developed from the photochemical model. The main source of ionization is photoionization of H_2O, OH, and C by the interstellar UV radiation field, supplemented by cosmic-ray ionization of hydrogen. Significant amounts of H_3O^+ and HCO^+ are produced, with peak abundances $\sim 10^{-7}$ at intermediate distances from the star. Although H_3O^+ may be difficult to detect with current instrumentation, HCO^+ is probably detectable in nearby O-rich envelopes with large millimeter-wave telescopes.

Subject headings: molecular processes — stars: circumstellar shells — stars: late-type

I. INTRODUCTION

The study of the extended circumstellar envelopes (CSEs) of red giant stars can provide significant information on the late stages of stellar evolution and the chemical reprocessing of the interstellar medium. Basic to the subject is the understanding of the physical and chemical properties of these envelopes. Some of the earliest chemical information was obtained from the detection of infrared spectral features characteristic of dust formation in O-rich and C-rich environments. More recently, the potential for understanding the gas phase chemistry of circumstellar envelopes has been amply demonstrated by the detection of numerous molecules at radio wavelengths. For recent reviews of circumstellar chemistry, see Omont (1985) and Glassgold and Huggins (1986*a*).

Most attention has been focused on the nearby C-rich envelope, IRC +10216, which displays a rich hydrocarbon chemistry. With the help of large new millimeter-wave telescopes and arrays, other C-rich envelopes are now being investigated in detail. The observational study of O-rich CSEs is less well advanced, in part because CO tends to take up all the available gas phase carbon. O-rich envelopes do host astrophysically important OH, H_2O, and SiO masers (e.g., Walmsley 1987). Recent observations suggest that O-rich CSEs have an interesting chemical activity of their own. For example, HCN, SO_2, and SO have now been detected in several cases (Deguchi and Goldsmith 1985; Lucas *et al.* 1986; Guilloteau *et al.* 1986; Nercessian *et al.* 1987) and many molecules have been detected in the bipolar nebula OH 231.8+4.2 (Morris *et al.* 1987). In this paper, we present the first results of our research on the circumstellar chemistry of O-rich CSEs based on the photochemical model.

This model was introduced by Goldreich and Scoville (1976, henceforth GS) to explain the formation of OH masers in terms of the photoproduction of OH from H_2O The model was extended by Scalo and Slavsky (1980, also Slavsky and Scalo 1984) to include S and Si chemistry. Deguchi (1982) and Huggins and Glassgold (1982*a*) refined the GS treatment of photodissociation, and the latter authors showed that the correlation of OH maser position with mass loss rate (Bowers, Johnston, and Spencer 1981) could be interpreted in terms of a dust and H_2O self-shielding of the interstellar radiation field. The photochemical model has also been extensively applied to C-rich CSEs (Huggins and Glassgold 1982*b*, and the reviews by Omont 1985 and Glassgold and Huggins 1986*a*).

We have recently developed a theory of ionization of C-rich CSEs in which atomic and molecular ions produced by cosmic rays and penetrating UV radiation generate a rich ion-molecule chemistry in these envelopes (Glassgold, Lucas, and Omont 1986, hereafter Paper I; Glassgold *et al.* 1987, hereafter Paper II; see also Nejad, Millar, and Freeman 1984). Here, we extend the theory to O-rich CSEs and lay the foundations for a more comprehensive treatment of the chemistry of these envelopes. We restrict our considerations to the photochains associated with the most abundant heavy molecules, CO, H_2O, and N_2, which account for the bulk of the ionization. We also consider the possibilities for detecting particular molecular ions in order to obtain direct confirmation of the theory. In § II, we briefly introduce the photochemical model, emphasizing those features which distinguish O-rich and C-rich chemistry. The results of model calculations and the observability of HCO^+ and H_3O^+ are discussed in § III. A summary is given in § IV.

II. IONIZATION MODEL

a) Physical Basis

According to the photochemical model, interstellar UV radiation penetrates the CSE and dissociates and ionizes the neutral expanding wind. Cosmic rays provide a supplementary source of ionization in the form of hydrogen ions. The ionization and dissociation products then generate an active chemistry in the outer envelope, primarily by ion-molecule reactions.

For purposes of simplicity, we consider a steady spherically symmetric wind with constant expansion velocity V and hydrogen mass-loss rate $\dot{M}$, so that the total hydrogen density

[1] Associated with CNRS UA 708.

TABLE 1

STANDARD PARAMETERS

Parameter	Value
Hydrogen mass loss rate ($\dot{M}$)	$10^{-5}\ M_\odot\ \mathrm{yr}^{-1}$
Expansion velocity (V)	$15\ \mathrm{km\ s}^{-1}$
Gas kinetic temperature [$T(r)$]	$550\ r_{15}{}^{-0.7}$ K
Initial abundances:[a]	
CO	4×10^{-4}
H_2O	3×10^{-4}
N_2	10^{-4}

[a] Relative to hydrogen nuclei; the abundance of atomic hydrogen is assumed to be zero.

varies as

$$n(r) = C/r^2, \tag{1}$$

where r is the distance from the center of the star and $C = \dot{M}/4\pi m_H V$; expressing $\dot{M}$ and V in units of $10^{-5}\ M_\odot\ \mathrm{yr}^{-1}$ and $10^6\ \mathrm{cm\ s}^{-1}$, respectively, $C = 3 \times 10^{37}\ \dot{M}_{-5}/V_6$. The kinetic temperature of the gas is assumed to vary as

$$T(r) = T_0\left(\frac{r_0}{r}\right)^m, \tag{2}$$

where T_0, r_0, and m are fitted to various theoretical temperature calculations. For example, in our "standard model" (whose parameters are given in Table 1), we use the results of GS. By specifying the density and temperature distributions, calculations for the photochemical model are reduced to solving a system of ordinary differential equations for the abundances. The inner boundary conditions are specified at a radial distance r_0, well outside the region of dust formation and evolution.

Just beyond the region of dust formation, the wind is assumed to consist only of hydrogen, carbon, oxygen, and nitrogen, with most of the heavier elements in dust. A more comprehensive treatment of the gas phase chemistry of O-rich CSEs, including heavier elements such as S and Si, is postponed to a later paper. The central star is considered to be sufficiently cool that the hydrogen is mainly molecular. Small amounts of atomic hydrogen can have important selective chemical effects (Slavsky and Scalo 1984), but this goes beyond the scope of the present study. In our standard model, we use for simplicity solar abundances for carbon, nitrogen, and oxygen at radius r_0, with all the carbon in CO, all the nitrogen in N_2, and the residual oxygen in H_2O. Condensation of H_2O onto dust grains (Jura and Morris 1985) is assumed to have been completed by the time the molecules reach the region of active chemical activity, i.e., beyond 10^{16} cm. We ignore the production of atoms and molecules such as HCN that might arise in the inner envelope as the result of shocks or other high-excitation processes. In the present calculations, the only gaseous species at r_0 are thus H_2, CO, H_2O, and N_2, with abundances given in Table 1.

The homogeneous, spherically symmetric wind model adopted in this paper (and also in Papers I and II) is greatly oversimplified. Many envelopes are bipolar, and even spherical ones may manifest asymmetries and inhomogeneities close to the star. Asymmetries in the extended chromosphere and dust shell of Alpha Orionis are particularly well documented (Hebden, Eckart, and Hege 1987; Hebden *et al.* 1986; Cheng *et al.* 1986; Bloemhof, Townes, and Vanderwyck 1984; Bloemhof, Danchi, and Townes 1985). A relatively small degree of asymmetry has also been found in images of its outer envelope made in scattered KI radiation (Honeycutt *et al.* 1980; Mauron *et al.* 1984). Strong evidence for clumping close to red giant stars is also provided by observations of SiO masers (Elitzur 1980; Herman and Habing 1985; Alcock and Ross 1986*b*).

The bulk of the present evidence for clumps in spherical CSEs refers to regions close to the star, but the outer envelope may also be clumped. Alcock and Ross (1986*a*) have recently proposed a model for OH masers in which the mass loss occurs in blobs which evolve into transverse platelets under the action of the radial driving force. Although it would be of considerable interest to investigate the chemistry of clumpy CSEs, the development of the required clump dynamics and radiative transfer is beyond the scope of this paper. However, we will comment in § IIIa on some possible effects of clumping on the chemistry.

b) Ion-Molecule Chemistry

The chemistry of the outer CSE is illustrated schematically in Figure 1; the associated reaction rates are listed in Table 2 (ion-molecule reactions and recombination) and Table 3 (photoprocesses).

The main building blocks of the chemistry are the three photochains which break down H_2O, CO, and N_2. Photoionization occurs in the first two chains and produces C^+, OH^+, and H_2O^+. The last two ions are rapidly hydrogenated into H_3O^+ in an environment containing H_2. We compare the time scale of hydrogenation with that of recombination:

$$\frac{\tau_{ch}}{\tau_{rec}} = \frac{\beta x_e}{k x(H_2)} = 10^4\ T^{-1/2}\ \frac{x_e}{x(H_2)}, \tag{3}$$

using $\beta = 10^{-5} T^{-1/2}\ \mathrm{cm^3\ s^{-1}}$ and $k = 10^{-9}\ \mathrm{cm^3\ s^{-1}}$. For the conditions appropriate to the standard mass-loss rate $\dot{M} = 10^{-5}\ M_\odot\ \mathrm{yr}^{-1}$ ($T \approx 25$ K and $x_e \approx 10^{-6}$ in the region where the ions reach their peak abundance), the requirement $\tau_{ch} < \tau_{rec}$ is satisfied for $x(H_2) \gtrsim 2 \times 10^{-3}$; a similar calculation for $\dot{M} = 10^{-4}\ M_\odot\ \mathrm{yr}^{-1}$ yields $\tau_{ch} < \tau_{rec}$ for $x(H_2) \gtrsim 0.3$. Thus, hydrogenation is more rapid than recombination in any predominantly molecular CSE and in any low to moderate mass-loss CSE in which molecules are detected.

The C^+ ion interacts strongly with H_2O to produce HCO^+ and with OH to produce CO^+, which is hydrogenated to

TABLE 2

PHOTODESTRUCTION RATES

Species	G_{diss}	G_{ion}	d (10^{16} cm)[a]	Reference
CO	1.4 (−10)[b]	...	3.5	1
C	...	3.2 (−10)	3.3	2, 3
H_2O[c]	1.6 (−10)	2.5 (−11)	3.6	4
	2.65 (−10)	...	2.3	
	1.05 (−10)	...	2.4	
OH	2.8 (−10)	1.25 (−11)	2.7	5
O_2	8.9 (−10)	...	2.3	6
N_2	5.0 (−11)	...	2.4	7

[a] Values for $\dot{M} = 10^{-5}\ M_\odot\ \mathrm{yr}^{-1}$; d is proportional to $\dot{M}$.

[b] After blocking of CO bands by H_2 lines (Mamon *et al.* 1987).

[c] H_2O is subdivided into three separate dissociating bands with cross sections 1.75, 0.75, and 0.5 in units of $10^{-17}\ \mathrm{cm^2}$, and an ionizing band with a cross section of 1.75 in the same units.

REFERENCES.—(1) Letzelter *et al.* 1987; (2) Burke and Taylor 1979; (3) Cantu *et al.* 1981; (4) Hudson 1971; (5) van Dishoeck and Dalgarno 1984; (6) Black and Smith 1984; (7) van Dishoeck 1987.

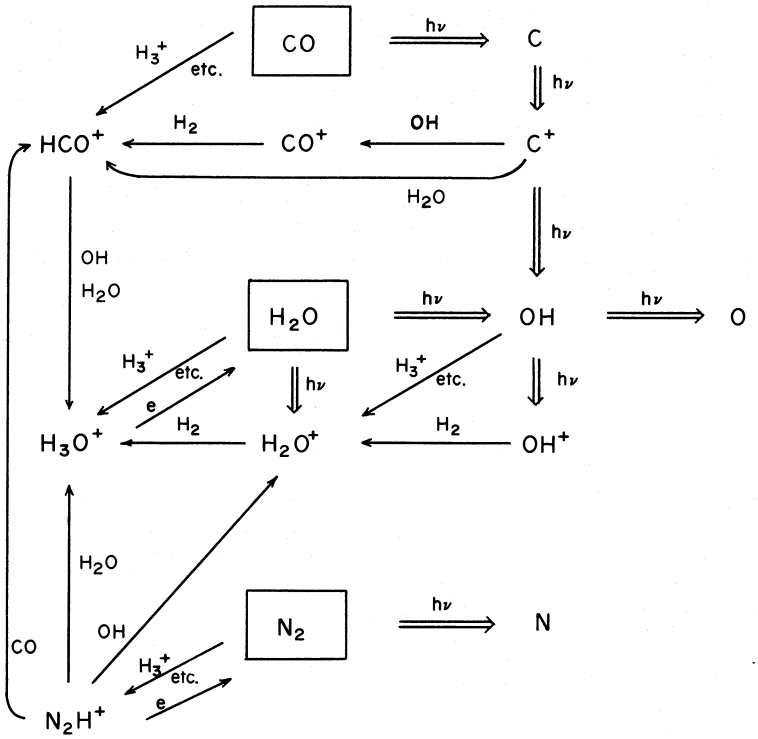

FIG. 1.—Chemical reactions in the model O-rich CSE. The progenitor molecules of the three primary photochains (*double lines*) are shown in *boxes*.

HCO^+; HOC^+ is also produced in the first reaction but is also hydrogenated to HCO^+ (Jarrold *et al.* 1986). The condition for hydrogenation in these cases is similar to that in equation (3). The major mode of destruction of HCO^+ is by proton transfer with H_2O, which yields H_3O^+. The C^+ ion is mainly produced by photodissociation of CO followed by photoionization of C. Thus, the major ions in the model, C^+, HCO^+, and H_3O^+ are all photoproduced.

Cosmic rays generate further ionization by producing H_3^+ from H_2; if the hydrogen were predominantly atomic, the main hydrogen ion would be H^+. The H_3^+ ion undergoes proton transfer with CO, H_2O, and N_2 to yield more HCO^+ and H_3O^+, as well as HN_2^+. These ions undergo further proton transfer, mainly producing more H_3O^+. Cosmic-ray ionization is mainly effective in the inner envelope ($r \lesssim 10^{16}$ cm), where photoprocesses are ineffective due to the shielding of the incoming UV radiation. It is the dominant mechanism for producing H_3^+ and, by interaction with N_2, HN_2^+.

In addition to proton transfer reactions, the main mode of destruction of hydrogenated molecular ions is dissociative recombination; it dominates where $x_e \gtrsim 10^{-6}$ and causes the rapid decrease of these ions at large distances. The only exception is H_3^+, whose recombination rate appears to be characteristic of radiative recombination (Adams and Smith 1987).

Most of the ionic reaction rates listed in Table 3 have been measured in the laboratory. In those cases where experimental values were not available, approximate rates were adopted from simple theoretical considerations, usually from Herbst and Leung (1986). Although the dominant moleculer ions interact with neutral species containing S and Si, their omis-

TABLE 3

REACTION RATES

	Reaction	k (100 K) ($cm^3\ s^{-1}$)	α[a]	Reference
1.	$C^+ + H_2O \rightarrow HCO^+ + H$	4.7 (−9)	−0.5	1
2.	$C^+ + OH \rightarrow CO^+ + H$	9.9 (−9)	−0.5	1
3.	$C^+ + O_2 \rightarrow CO^+ + O$	4.0(−10)	0	2
4.	$C^+ + O_2 \rightarrow O^+ + CO$	6.0(−10)	0	2
5.	$H_3^+ + H_2O \rightarrow H_3O^+ + H_2$	6.9 (−9)	−0.5	1
6.	$H_3^+ + OH \rightarrow H_2O^+ + H_2$	1.6 (−8)	−0.5	1
7.	$H_3^+ + O \rightarrow OH^+ + H_2$	8.0(−10)	0	2
8.	$H_3^+ + CO \rightarrow HCO^+ + H_2$	1.6 (−9)	0	2
9.	$H_3^+ + C \rightarrow CH^+ + H_2$	2.0 (−9)	0	1
10.	$H_3^+ + N_2 \rightarrow HN_2^+ + H_2$	1.8 (−9)	0	2
11.	$HCO^+ + H_2O \rightarrow H_3O^+ + CO$	3.5 (−9)	−0.5	1
12.	$HCO^+ + OH \rightarrow H_2O^+ + CO$	8.1 (−9)	−0.5	1
13.	$HN_2^+ + H_2O \rightarrow H_3O^+ + N_2$	4.5 (−9)	−0.5	2
14.	$HN_2^+ + OH \rightarrow H_2O^+ + N_2$	8.1 (−9)	−0.5	1
15.	$HN_2^+ + O \rightarrow OH^+ + N_2$	1.4(−10)	0	2
16.	$HN_2^+ + CO \rightarrow HCO^+ + N_2$	8.8(−10)	0	2
17.	$O + OH \rightarrow O_2 + H$	3.3(−11)	−0.5[b]	3
18.	$H_3^+ + e^- \rightarrow H_2 + H$	1.7(−11)	−0.5	4
19.	$H_3O^+ + e^- \rightarrow H_2O + H$	8.3 (−7)	−0.5	5, 6
	$\rightarrow OH + H_2$	1.7 (−7)	−0.5	
20.	$C^+ + e^- \rightarrow C$	9.7(−12)	−0.625	7
21.	$HCO^+ + e^- \rightarrow CO + H$	3.3 (−7)	−1	8
22.	$HN_2^+ + e^- \rightarrow N_2 + H$	2.4 (−7)	−1	8
	$\rightarrow N + N + H$	2.4 (−7)	−1	

[a] $k(T) = k(100\ \mathrm{K})T^{\alpha}$.

[b] This reaction has an activation energy of ~80 K.

REFERENCES.—(1) Herbst and Leung 1986; (2) Anicich and Huntress 1986; (3) Black and Smith 1984; (4) Adams and Smith 1987; (5) Mul *et al.* 1983; (6) Bates 1986; (7) Aldrovandi and Pequignot 1973; (8) Smith and Adams 1984.

sion from the model generates only small errors in the molecular ion abundances because of the low abundances of gaseous S and Si. All ion molecule reactions with H_2O and OH have been scaled up by a factor $(300/T)^{1/2}$ relative to their rates measured at 300 K, in accord with theoretical (e.g., Clary 1985) and experimental (Adams, Smith, and Clary 1985; Adams and Smith 1987) studies of reactions of ions with neutral molecules possessing large dipole moments. The branching ratio for dissociative recombination of H_3O^+ is based on the recent work of Bates (1986). Unlike the situation for shielded dense interstellar clouds (Sternberg, Dalgarno, and Lepp 1987), our results do not depend sensitively on this parameter.

Finally, neutral-neutral reactions generally play a negligible role here, because their activation energies are usually too large for the temperatures found in the outer parts of CSEs. The one exception is the reaction $O + OH \rightarrow O_2 + H$, which produces significant ($\sim 10^{-5}$) amounts of O_2; the abundance of O_2 is limited by its destruction by C^+ and by photodissociation in the outer envelope.

b) *Photorates and Shielding*

The most important rates are given in Table 2 with references for the underlying cross sections. The unshielded rates have been calculated with the Jura (1974) interstellar radiation field below 1100 Å and with the "Jura-Habing" interpolation (Glassgold and Langer 1974; curve 3 of Fig. 1) at longer wavelengths. This representation of the interstellar radiation is essentially the same as in Draine (1978) and was also used in Papers I and II. The rate for N_2 is very uncertain (van Dishoeck 1987), and we have adopted her minimum value.

The UV radiation that contributes to the photodissociation and photoionization rates given in Table 2 is shielded by dust and by abundant gas phase species. The dust shielding is approximated by an exponential attenuation factor $e^{-d/r}$, as in Papers I and II. The depth d is the distance at which the incoming radiation reaches an optical depth of order unity for the process and species in question. The values of d given in Table 1 are based on the properties of interstellar dust, but circumstellar dust could be significantly different and d should be varied in attempts to fit the observations.

For continuum photoprocesses, self-shielding is included with the following iterative procedure. Each self-shielding species j is subdivided into wavelength intervals k in which the photodissociation cross section is roughly constant, and the optical depth $\tau_{j,k}$ of species j and wavelength interval k is treated as an additional dependent variable. In the zeroth order, we integrate the system of abundances and optical depths from r_0 to r_{max} assuming no self-shielding, i.e., $\tau_{j,k}^{(0)} = 0$ throughout the envelope. We then iterate using

$$\tau_{j,k}^{(i+1)}(r_0) = \sigma_{j,k} \int_{r_0}^{r_{max}} x_j^{(i)} n(r) dr ,$$

where $\sigma_{j,k}$ is the cross section of the jth species in the kth wavelength interval. The iterations are terminated once the condition

$$|\tau_{j,k}^{(i+1)}(r_0) - \tau_{j,k}^{(i)}(r_0)| < 10^{-3}$$

is satisfied, which usually takes less than 12 steps. Self-shielding is important only for species with large column densities and cross sections, and it is applied here only to H_2O, using three dissociation bands with the cross sections listed in Table 2.

Self-shielding of CO is now understood to occur mainly through absorption by lines, rather than by continuum absorption, as discussed by Glassgold, Huggins, and Langer (1985). Because CO photodissociation provides the main source of C^+ in O-rich envelopes, which itself is the main source for the formation of HCO^+, an accurate treatment of CO line self-shielding is fundamental to this study. Morris and Jura (1983) developed the theory of line self-shielding of CO for CSEs, using the Sobolev approximation, and Mamon, Glassgold, and Huggins (1987) have adapted their formulation to the recent far-UV absorption and fluorescence measurements of Letzelter *et al.* (1987). According to these experiments, there are 34 CO bands which contribute significantly to the dissociation of CO by interstellar UV radiation, with a mean oscillator strength 1.1×10^{-2}. However, a significant number of these bands will be blocked by nearly coincident Lyman and Werner bands of H_2 and Lyman lines of H. The number of blocked bands depends on position but, for the region of primary interest (where H_3O^+ and HCO^+ are abundant), about 16 bands are involved. Thus, our standard model is based upon 23 bands with mean oscillator strength 1.4×10^{-2}, corresponding to an unshielded photodissociation rate of 1.4×10^{-10} s^{-1} (see Mamon, Glassgold, and Huggins 1987, for details).

III. RESULTS AND DISCUSSION

a) *Abundances*

The computed abundances for the standard model (parameters and rates in Tables 1–3) are shown in Figure 2; the N_2 photochain and several minor species have been omitted for clarity. The spatial distribution of CO shown in Figure 2*a* is much more extended than that of H_2O; this reflects the difference between line self-shielding of CO and continuum self-shielding of H_2O. Another consequence of CO line self-shielding is the unusual shape of the C distribution, already noted for C-rich CSEs (Paper II).

A result of immediate interest in the distribution of electrons and ions is the high abundance (up to $\sim 10^{-7}$) of both H_3O^+ and HCO^+ at intermediate distances, as seen in Figure 2*b*. The C^+ ion is also relatively abundant in this region and, consequently, the electron fraction reaches $\sim 5 \times 10^{-6}$ at the HCO^+ peak. In the region where it is rising, the HCO^+ distribution has the unusual property that $x(HCO^+) \approx x(C^+)$. This occurs because HCO^+ is both formed from and destroyed by H_2O (reactions 1, 2, 11, and 12 in Table 3), so that

$$\frac{x(HCO^+)}{x(C^+)} \approx \frac{k_1 + yk_2}{k_{11} + yk_{12}} \approx 1 ,$$

where $y = x(OH)/x(H_2O)$. The abrupt fall of HCO^+ is due to similar decreases in its progenitors, H_2O and OH, accompanied by a rapid increase in x_e, which makes dissociative recombination the main mechanism for its destruction. Further out in the envelope, where $x(H_3^+)$ becomes appreciable, HCO^+ is replenished somewhat by reaction 6, $H_3^+ + CO \rightarrow HCO^+ + H_2$, which is the dominant formation mechanism in C-rich envelopes, but its abundance remains $< 10^{-10}$. Although molecular ions are mainly produced by cosmic rays in the inner envelope, e.g., H_3O^+ (see Fig. 2*b*), their peak abundances, which are reached at intermediate distances, are a consequence of photoionization of H_2O and C (the latter from photodissociation of CO).

It is interesting to compare these results with those obtained recently for C-rich envelopes. The analog of H_3O^+ in C-rich CSEs is $C_2H_2^+$, and its abundance also reaches the 10^{-7} level

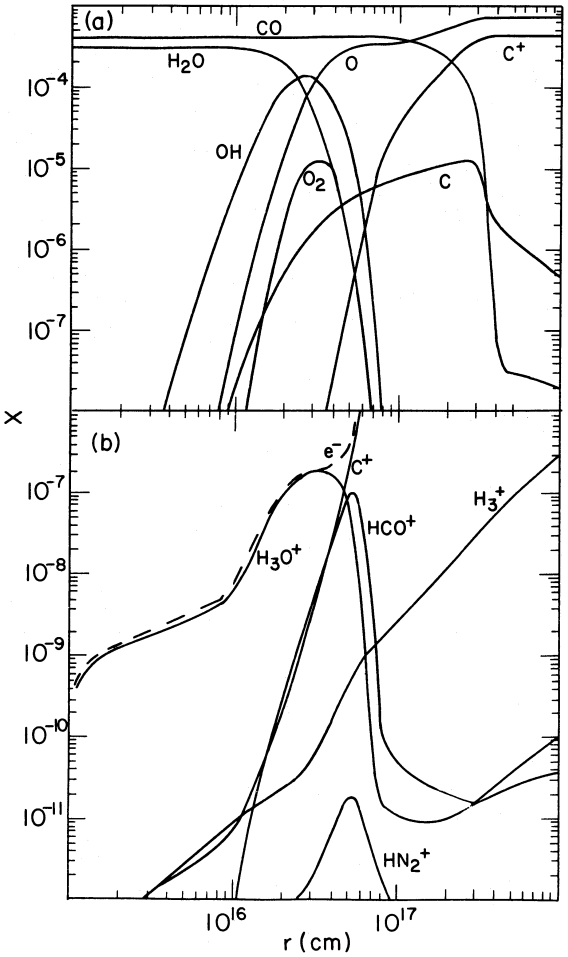

FIG. 2.—Chemical abundances for the standard O-rich CSE (Table 1): (*a*) CO, H_2O, and O_2 photochains; (*b*) ions and electrons.

(see Papers I and II). The smaller photoionization cross section of H_2O is compensated by its larger initial abundance, relative to C_2H_2. In a C-rich envelope, the process analogous to $C^+ + H_2O \rightarrow HCO^+ + H$ is $C^+ + C_2H_2 \rightarrow C_3H^+ + H$. Subsequent hydrogenation by H_2 leads to $C_3H_2{}^+$ and then to C_3H by recombination (Nejad, Millar, and Freeman 1984). In C-rich CSEs, $x(C_3H_2{}^+)$ reaches $\sim 10^{-8}$; the larger abundance of HCO^+, its analog in O-rich envelopes, is due to the polar nature of H_2O and OH, which leads to larger rates for its formation.

As the mass-loss rate is increased, the shielding of both H_2O and CO increases, and the photochains are displaced to larger radii. This is illustrated in Figure 3 for both H_3O^+ and HCO^+. The peak abundances are all of the order of 10^{-7} for the range in $\dot{M}$ used in Figure 3, 10^{-7} to 10^{-4} $M_\odot$ yr^{-1}, and they decrease with increasing $\dot{M}$. The distribution of HCO^+ is more sharply peaked than that of H_3O^+, and its maximum abundance is more affected by the mass-loss rate. These differences arise because the HCO^+ distribution is determined by C^+ and line shielding of CO, whereas the H_3O^+ distribution is determined by H_2O and dust shielding. The electrons that destroy H_3O^+ have an abundance $x_e \approx x(H_3O^+)$, which leads to $x(H_3O^+) \propto n^{-1/2} \approx \dot{M}^{-1/2}$. The dependence on $\dot{M}$ is weaker than this, however, because dust shielding moves the distribution farther out to lower densities. The peak abundance of HCO^+ is essentially the same as that of C^+ at the position where recombination begins to dominate destruction by reactions with H_2O and OH. For line self-shielding of CO, the abundance of C^+ in this region decreases roughly as $\dot{M}^{-1}$, in accord with Figure 3.

Because the HCO^+ abundance in O-rich CSEs depends directly on C^+, it is important to determine how $x(HCO^+)$

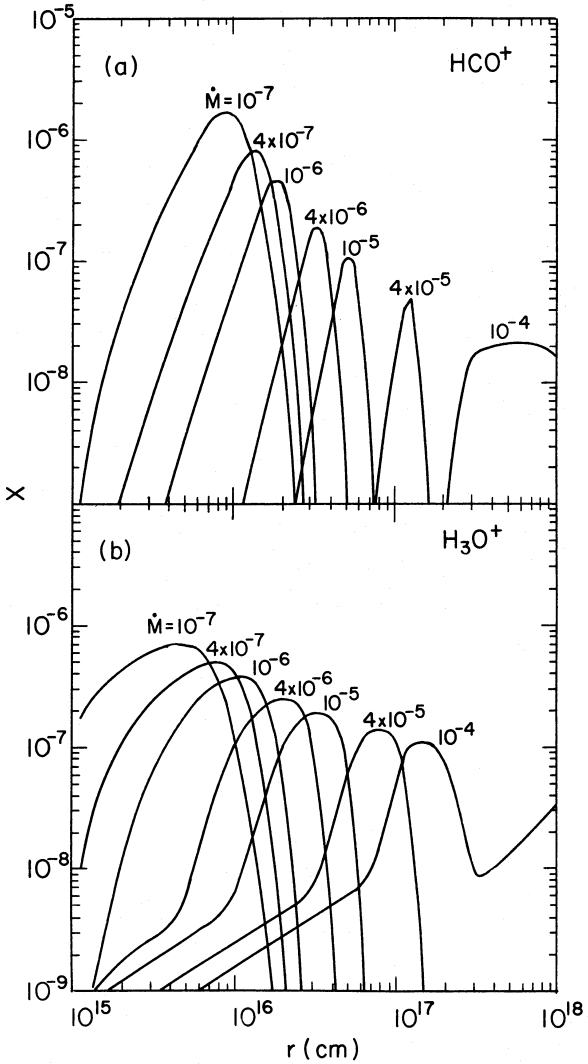

FIG. 3.—Ion abundance distributions for three different mass-loss rates (in units of $M_\odot$ yr^{-1}): (*a*) HCO^+, (*b*) H_3O^+

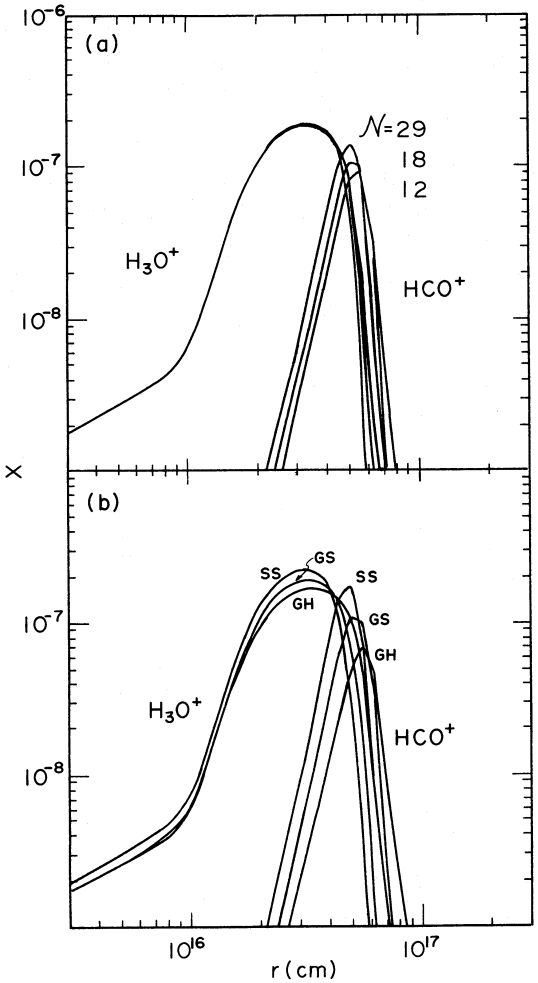

FIG. 4.—Abundance distributions of HCO^+ and H_3O^+ for (*a*) variations in the number $\mathcal{N}$ of bands effective in the photodissociation of CO ($\mathcal{N}$ = 23 is the standard model), and (*b*) three different temperature distributions—GS: $T = 550\, r_{15}^{-0.7}$ K (Goldreich and Scoville 1976); SS: $T = 805\, r_{15}^{-0.6}$ K (Slavsky and Scalo 1984); GH: $T = 800\, r_{15}^{-1.0}$ K (Glassgold and Huggins 1986*b*).

depends on the parameters used in the theory of line-shielding of CO. Figure 4*a* shows the HCO^+ abundance for three values of the number of bands $\mathcal{N}$ and the corresponding unshielded rate of CO photodissociation G(CO): the standard values given in § II*d* ($\mathcal{N}$ = 23, $G = 1.4 \times 10^{-10}$ s^{-1}), the unblocked values ($\mathcal{N}$ = 34, $G(\mathrm{CO}) = 2.0 \times 10^{-10}$ s^{-1}), and the case where more distant bands as well as nearly coincident ones are blocked ($\mathcal{N}$ = 17, $G(\mathrm{CO}) = 1.1 \times 10^{-10}$ s^{-1}). The differences are small and the main effect of decreasing $\mathcal{N}$ is to move the $\mathrm{CO} \rightarrow \mathrm{C}^+$ transition to slightly larger distances where the larger C^+ abundance leads to smaller HCO^+ abundances.

The temperature distribution in the envelope affects the computed abundances mainly through the temperature dependence of the chemical reaction rates. We illustrate in Figure 4*b* the effects of choosing different temperature distributions on the abundances of H_3O^+ and HCO^+. For comparison with the standard temperature distribution of GS, we use those derived by Slavsky and Scalo (1984) for general O-rich CSEs and by Glassgold and Huggins (1986*b*) for α Ori. The changes in the peak abundances of H_3O^+ and HCO^+ correlate with decreasing temperature, and arise mainly from the T^{-1} and $T^{-1/2}$ dependences of the recombination rates of HCO^+ and H_3O^+, respectively.

Although the above results are based on a highly idealized model, qualitative aspects of the generalized photochemical model probably apply to other models such as the clumpy wind mentioned in § II. In particular, ion-molecule reactions should still produce substantial levels of H_2O^+ and HCO^+ in O-rich CSEs, determined in large part by C^+ ions produced by photodissociation of CO. We can attempt to illustrate some of the effects of clumping with an extreme version of the Alcock and Ross (1986*a*) model in which there are a large number of high-density platelets. The most important change in our model probably occurs in the self-shielding of the CO dissociating radiation. The transfer of the continuum radiation responsible for the dissociation and ionization of H_2O will be altered relatively little. Because the UV line radiation traveling in tangential directions is most effective in dissociation, the CO in thin, dense platelets will be more effective in shielding than a uniform wind.

Increased shielding of the CO dissociating radiation would imply that the chemically important C^+ ion occurs further out in this type of clumpy envelope as compared to a uniform one. As a consequence, production of HCO^+ would occur at larger distances as would destruction of both HCO^+ and H_3O^+. We would then expect the peak abundance of HCO^+ distribution to be about the same but its brightness temperature to be decreased because of weaker excitation. The H_3O^+ would extend to larger distances and reach a larger peak abundance, and the chances for detecting this ion in O-rich CSEs might be increased somewhat (see the discussion of observability of molecular ions in § III*b* below). These remarks about the ion-molecule chemistry of clumpy envelopes are very preliminary. They are likely to be sensitive to the physical properties of the clumps. A deeper understanding of the effects of clumping on circumstellar must await detailed calculations.

b) Observability

Consistent with our focus on ionization, we discuss the prospects for observing molecular ions in O-rich CSEs. There are only two real possibilities, H_3O^+ and HCO^+ because, as will be shown below, the other abundant molecular ion, H_3^+, has a peculiar spatial distribution which mediates against its detection.

i) H_3^+

The theory of the abundance of H_3^+ is basically the same for O-rich and C-rich envelopes: production by cosmic rays and destruction by proton transfer reactions with neutrals. Its density is given by the simple expression

$$n(\mathrm{H_3^+}) = \frac{\zeta}{\sum_i k_i x_i},$$

where ζ is the cosmic ray ionization rate of H_2 (per hydrogen nucleus), and k_i and x_i are, respectively, the rate constants and abundances of the neutral species that destroy H_3^+. The denominator does not vary much throughout the envelope

because both progenitor molecules and photofragments react strongly with H_3^+, with rate constants typically $\sim 10^{-9}$ cm^3 s^{-1}. Consequently the abundance of H_3^+ varies roughly as r^2, as is shown in Figure 2 (see also eq. [8] of Paper I). The jump in $x(H_3^+)$ in the region 3–7 $\times 10^{16}$ cm occurs because, according to Table 3, the destruction by O is less effective than by H_2O and OH. The column density is given by

$$N(H_3^+) = \frac{\zeta r_m}{k\bar{x}} = 10^{13} \left(\frac{\zeta_{-17} r_{m18}}{k_{-9} x_{-3}} \right) \text{cm}^{-2} ,$$

where r_m is the outer boundary of the envelope and all parameters are measured in cgs units with powers of 10 indicated by subscripts. The column density is independent of mass-loss rate and, as discussed in Paper I for C-rich envelopes, its order of magnitude is too small for the infrared detection of H_3^+ with present instrumentation.

ii) HCO^+

The lowest $J = 1 \rightarrow 0$ rotational transition of HCO^+ at 89.2 GHz provides the best method for detecting this ion in CSEs, and several detections have been made recently with the IRAM 30 ms telescope (Morris *et al.* 1987; Bachiller, Bujarrabal, and Gomez-Gonzalez 1987; Guilloteau, Omont, and Lucas 1987). Most of the CSEs in which HCO^+ has been detected so far appear to be high-excitation objects such as bipolar and/or young planetary nebulae. In this paper we restrict the discussion to spherically symmetric envelopes without internal sources of ionization. We follow the methods of § III of Paper I for calculating the brightness temperature of this line. There are two important differences in applying the methods of Paper I to O-rich envelopes. First, the large abundance of HCO^+ implies that the line is generally optically thick at the peak of the HCO^+ abundance distribution. The excitation temperature is then a sensitive function of various parameters (e.g., Morris and Alcock 1977), particularly the infrared excitation rate, and population inversion often occurs at some locations. Thus the computed brightness temperatures are less certain than for C-rich envelopes. Second, there is no equivalent of the very luminous C-rich CSE, IRC +10216, among the nearby O-rich envelopes. This situation is partly compensated by the predicted increase of the HCO^+ abundance for small mass-loss rates. The best opportunities for detecting HCO^+ in O-rich CSEs appear to be nearby Mira stars with $\dot{M} \approx 10^{-7}$ to 10^{-6} $M_\odot$ yr^{-1} and $d \approx 100$–200 pc, rather than the massive but relatively distant OH/IR envelopes e.g., IRC +10011 ($\dot{M} \approx 10^{-5}$ $M_\odot$ yr^{-1}, $d = 500$ pc) and NML Tau ($\dot{M} \approx 10^{-6}$ $M_\odot$ yr^{-1}, $d \approx 300$ pc). The case of *o* Cet ($\dot{M} \approx 6 \times 10^{-7}$ $M_\odot$ yr^{-1}, $d = 80$ pc) is interesting, although its bright UV companion may alter the photochemistry.

For IRC +10216, the IR pumping of HCO^+ is dominated by the ν_2 bending mode near 11 μm, with an appreciable contribution of the ν_3 mode near 5 μm (Paper I). The same is probably true for OH/IR stars, but in Miras the ν_1 ($\lambda \approx 3.2$ μm) and the ν_3 modes dominate. For prominent nearby O-rich envelopes (e.g., *o* Cet, R Cas, NML Tau, IRC +10011) we estimate that the IR pumping rate of HCO^+ is a factor 5–10 smaller than the one used in Paper I.

Figure 5 displays the on-source, beam averaged brightness temperature T_{MB} at the center of the $J = 1 \rightarrow 0$ HCO^+ line for a 30 m telescope, as a function of the distance to the star. Values for other telescope diameters D can be easily deduced by scaling because the results depend only on d/D. The calculations have been performed for the IR pumping rate R_0 of Paper I (*dashed curves*), and for the more realistic case $R_0/10$ (*solid curves*).

The results depend only mildly on the mass loss rate for $\dot{M} < 10^{-5}$. The peak density $n(HCO^+)$ decreases slowly with $\dot{M}$ but is compensated to a large degree by the increasing extent of the HCO^+ distribution. However, for $\dot{M}$ approaching 10^{-4} $M_\odot$ yr^{-1}, the large HCO^+ shell can be partially resolved and T_{MB} decreases with decreasing distance d as the observations increasingly sample the hole in the HCO^+ distribution. Compared to C-rich envelopes with the same mass-loss rate (Papers I and II), the emission is much stronger for O-rich CSEs (e.g., by a factor ~ 20 for $\dot{M} = 10^{-5}$ $M_\odot$ yr^{-1}). However, the increase is not proportional to the peak abundance ratios (~ 400), mainly because the line is optically thick. Figure 5 also illustrates the strong dependence on the IR excitation rate, and hence the sensitivity of the results to the precise value of the IR dipole moment and possibly the phase of the star.

The 30 m telescope (FHWM beam size of 25″ at 89 GHz) is unable to resolve the HCO^+ emission expected for most of the familiar O-rich envelopes, including NML Tau and IRC +10011. It could marginally resolve the emission from *o* Cet, where the calculated radius of the HCO^+ distribution is $\sim 15''$, and the beam averaged emission has a FWHM width of 25″. The brightness temperature distribution for a massive envelope ($\dot{M} = 10^{-4}$ $M_\odot$ yr^{-1}) is very extended (the HCO^+ density peaks at 3×10^{17} cm) and, at a typical distance of 1 kpc, the emission is extremely weak (~ 2 mK) and probably presently undetectable.

In summary, the large abundance of HCO^+ in O-rich CSEs does not imply that the brightness temperature of the $J = 1 \rightarrow 0$ line is large. For a typical case of an object with $\dot{M} = 10^{-5}$ $M_\odot$ yr^{-1}, $d = 500$ pc, and $R = R_0/5$, the calculated mean brightness temperature for the 30 m telescope is only about 0.01 K. Thus the present theory is not in contradiction with the recent reports of nondetections of HCO^+ in IRC +10011 and NML Tau with an rms noise temperature of ~ 0.015 mK (Guilloteau, Omont, and Lucas 1987). The line may be stronger in less massive nearby Mira envelopes. The production of HCO^+ in bipolar envelopes probably involves the specific, high-excitation (e.g., shocks) conditions characteristic of these systems, and is beyond the scope of the present investigation.

iii) H_3O^+

The oxonium ion H_3O^+ plays an important role in the synthesis of interstellar molecules based on ion-molecule reactions (Herbst and Klemperer 1973; Watson 1973; Dalgarno, Oppenheimer, and Berry 1973). Hollis *et al.* (1986) and Wootten *et al.* (1986) have detected a line near 1 mm in the Kleinman-Low nebula in Orion which may be from H_3O^+, but a definitive detection requires more than one line. The peak abundances of H_3O^+ (10^{-7}) in our theory of O-rich CSEs are several orders of magnitude larger than obtained in models of interstellar clouds (e.g., Leung, Herbst, and Huebner 1984; Millar and Nejad 1985). The essential difference is that, in CSEs, H_3O^+ is predominantly produced by photoionization of H_2O and OH (see Fig. 1), rather than by cosmic rays.

The oxonium ion is isoelectric with ammonia and has a similar pyramidal structure with four vibrational modes (ν_1, ν_2, ν_3, and ν_4) and with a characteristic inversion spectrum. Only the ν_2 bending-inversion mode is not blocked by Earth's atmosphere, and its splitting in the ground state is 55.34 cm^{-1} (Liu and Oka 1985). Liu, Oka, and Sears (1985) have analyzed the

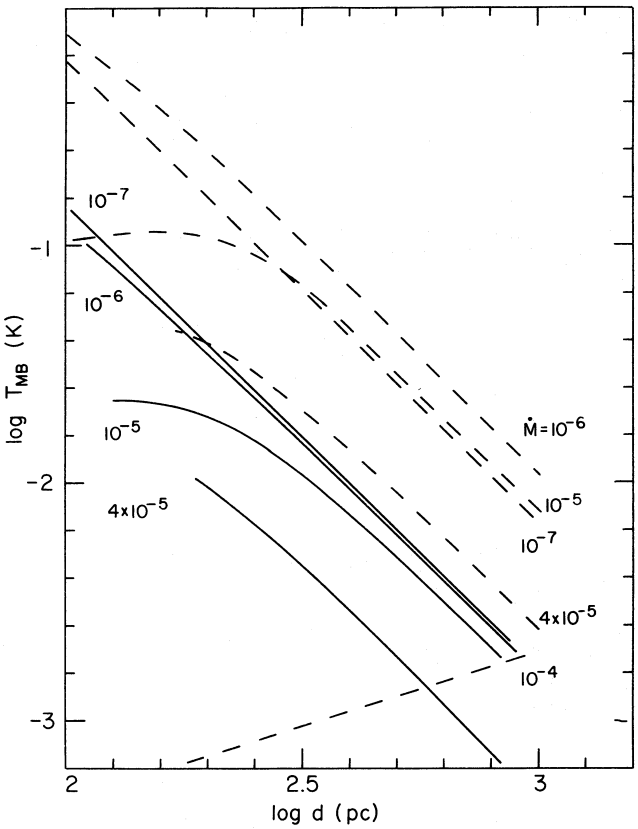

FIG. 5.—Values of the on-source beam-averaged brightness temperature for different mass-loss rates ($M_\odot$ yr^{-1}) and different stellar infrared fluxes ($R = R_0$: *dashed curves* and $R = R_0/10$; *solid curves*) as a function of the distance d to the source for a 30 m telescope. The results depends only on d/D and can thus easily be extended to other values of the telescope diameter D.

recent measurements of the v_2 bands and obtained accurate spectroscopic constants and frequencies for the four lowest ones. The transitions of primary astrophysical interest occur at sub-millimeter and mid-infrared (1^-–0^+ at 10 μm and 1^+–0^- at 17 μm) wavelengths and are shown in Figure 6*a*. Many transitions are observable from the ground.

Figure 6*b* gives the levels which lie less than 200 cm^{-1} above the $J = 1$, $K = 1^+$ ground state; these are the most likely initial states for emission and absorption lines that might be detectable in a CSE. The four transitions marked with double arrows have been measured in the laboratory (Plummer, Herbst, and de Lucia 1985; Bogey *et al.* 1985), and have wavelengths between 0.75 and 1 mm. The transition at 307 GHz ($11^- \rightarrow 21^+$) has been searched for in interstellar clouds (Hollis *et al.* 1986; Wootten *et al.* 1986); the upper level in this case is about 80 K above the ground state. The next lowest transition ($00^- \rightarrow 10^+$), whose upper level is at 56 K, has a frequency of 985 GHz (305 μm), and its detection would have to be attempted from space, e.g., with the Kuiper Airborne Observatory.

The transition dipole moments calculated for the v_2 band are large (Botschwina, Rosmus, and Reinsch 1983); for the transitions of interest $\mu(0^-$–$0^+) = 1.438D$, $\mu(1^-$–$0^+) = 0.302D$, and $\mu(1^+$–$0^-) = 0.673D$. These values imply that the millimeter and submillimeter transitions of H_3O^+ in CSEs are excited by the absorption of infrared radiation rather than by collisions. Because O-rich CSEs emit strongly at 10 μm and 17 μm (Forrest, McCarthy, and Houck 1979), both the 1^+–0^- and 1^-–0^+ v_2 bands are likely to be effective in absorbing infrared radiation. A detailed calculation of the excitation of the rotational bands of H_3O^+ is beyond the scope of this paper, but the underlying physical processes appear to be favorable for relatively strong excitation. Emission in the lowest submillimeter transitions of H_3O^+ is probably stronger than from HCO^+, because the transition dipole moments are larger and because H_3O^+ is located closer to the star.

In principle, H_3O^+ could also be detected by infrared absorption techniques as have other circumstellar molecules, particularly toward IRC +10216 (see Betz 1987 for a recent review). We have estimated the absorption coefficients for transitions from low-lying levels (80 K above the ground state) using the measured frequencies for the 1^-–0^+ and 1^+–0^- bands (Liu, Oka, and Sears 1985), the calculated dipole moments of Botschwina, Rosmus, and Reinsch (1983), the Hönl-London factors in Herzberg (1945), and a turbulent (Doppler) broadened line with FWHM width of 1 km s^{-1}. The typical order of magnitude of the absorption cross section is

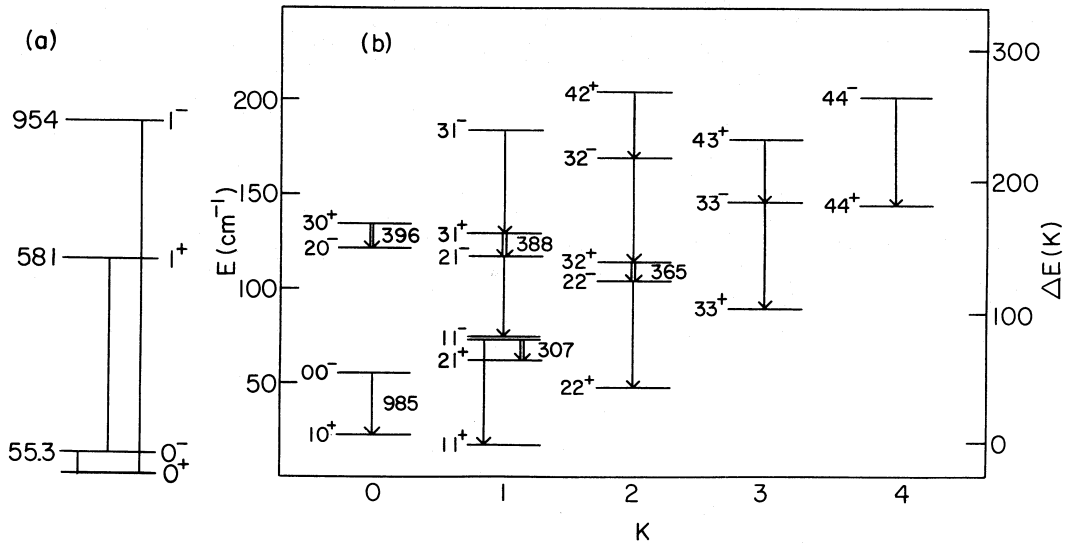

FIG. 6.—Energy levels of the ν_2 mode of H_3O^+: (*a*) four lowest vibrational levels with transitions of astrophysical interest, 0^-–0^+ (mm and sub-mm), 1^+–0^- (10 μm), 1^-–0^+ (20 μm); (*b*) low-lying levels and transitions for the 0^-–0^+ band. Fig. 6*a* is patterned after Liu *et al.* (1985) and Fig. 6*b* after Bogey *et al.* (1985). The energy units are cm^{-1} throughout.

10^{-15} cm^2 and, if the corresponding populations are not too small, a column density of 10^{14} cm^{-2} might be sufficient to give a detectable absorption with a sensitive, high-resolution ($\lambda/\Delta\lambda \approx 3 \times 10^5$) spectrometer. The column densities of H_3O^+ calculated in our model do reach this level, with the major contributions coming from the peak in the H_3O^+ abundance. The excitation of H_3O^+ will change with mass-loss rate because the position of the abundance peak increases with $\dot{M}$, as shown in Figure 3*b*. For small $\dot{M}$, many levels are excited in the interior of the envelope and the absorption coefficients are then very small. For large $\dot{M}$ (10^{-5} to 10^{-4} $M_\odot$ yr^{-1}), the H_3O^+ peak is sufficiently distant that the populations of the two lowest levels may be large enough to produce a detectable amount of absorption. Nonetheless, infrared detection of H_3O^+ column densities of even a few times 10^{14} cm^{-2} will still be difficult. In this context, it is worth noting that the current sensitivity for the detection of circumstellar molecules by infrared absorption in IRC +10216 is $\sim 10^{15}$ cm^{-2} (Betz 1987).

IV. SUMMARY

We have developed a model for the ionization of O-rich CSEs based upon the photochemical model, using the methodology developed for C-rich CSEs (Papers I and II). We again find a rich ion-molecule chemistry that is strongly dependent on position within the envelope. This chemistry is driven mainly by photoprocesses, supplemented by cosmic-ray ionization. The overall spatial distribution of the ionization is similar to that in C-rich CSEs, although it is generated by different chemical species.

An important aspect of O-rich envelopes is that large peak abundances ($\sim 10^{-7}$) are predicted for the polar molecular ions, H_3O^+ and HCO^+. The H_3O^+ ion is produced by photoionization of H_2O and OH, whereas HCO^+ is formed by reactions of H_2O and OH with C^+ (produced in the CO photodissociation chain). The present calculations suggest that the abundance of H_3O^+ is an order of magnitude too low to be detectable at the present time in IR absorption, and probably in millimeter emission as well. However, our understanding of the excitation conditions of H_3O^+ in O-rich CSEs is incomplete at best, and we believe that an effort should still be made to detect its emission in submillimeter lines.

We do find that HCO^+ is abundant enough to be detectable in the $J = 1 \rightarrow 0$ transition at 89.2 GHz as long as the envelope is not too massive ($\dot{M} \lesssim 10^{-5}$ $M_\odot$ yr^{-1}) or distant ($d < 1$ kpc), but its relatively large abundance does not yield particularly strong lines because of optical thickness and excitation effects. It is thus unfortunate that there is no counterpart among O-rich envelopes to the nearby and extremely luminous C-rich envelope, IRC +10216. Nevertheless, our colleagues at the IRAM 30 m telescope have succeeded in detecting this line in a handful of cases. Further observations of molecular ions, as well as theoretical calculations extending the ones presented here, should elucidate their role in determining the physical and chemical properties of red giant winds.

We would like to thank M. Jura for helpful comments and R. Lucas for his help in the use of his molecular excitation and line formation codes. This work was supported in part by NASA grant NAGW 630.

REFERENCES

Adams, N. G., and Smith, D. 1987, in *Astrochemistry*, ed. M. S. Vardya and S. P. Tarafder (Dordrecht: Reidel), p. 1.
Adams, N. G., Smith, D., and Clary, D. C. 1985, *Ap. J. (Letters)*, **296**, L31.
Alcock, C., and Ross, R. 1986*a*, *Ap. J.*, **305**, 837.
Alcock, C. 1986*b*, *Ap. J.*, **310**, 838.
Aldrovandi, S. M. V., and Pequignot, D. 1973, *Astr. Ap.*, **25**, 137.
Anicich, V. G., and Huntress, W. T. 1986, *Ap. J. Suppl.*, **62**, 553.
Bachiller, R., Bujarrabal, V., and Gomez-Gonzalez, J. 1987, in preparation.

Bates, D. R. 1986, *Ap. J. (Letters)*, **306**, L45.
Betz, A. 1987, in *Astrochemistry*, ed. M. S. Vardya and S. P. Tarafder (Dordrecht: Reidel), p. 327.
Black, J. H., and Smith, P. L. 1984, *Ap. J.*, **277**, 562.
Bloemhof, E. E., Danchi, E. E., and Townes, C. H. 1985, *Ap. J. (Letters)*, **299**, L37.
Bloemhof, E. E., Townes, C. H., and Vanderwyck, A. H. B. 1984, *Ap. J. (Letters)*, **276**, L21.
Bogey, M., Demuynck, C., Denis, M., and Destombes, J. L. 1985, *Astr. Ap.*, **148**, L11.
Botschwina, P., Rosmus, P., and Reinsch, E. A. 1983, *Chem. Phys. Letters*, **103**, 299.
Bowers, P. F., Johnston, K. J., and Spencer, J. H. 1981, *Nature*, **291**, 382.
Burke, P. G., and Taylor, K. T. 1979, *J. Phys.*, **B18**, 2971.
Cantu, A. M., Mazzoni, M., Pettini, M., and Tozzi, G. P. 1981, *Phys. Rev. A*, **23**, 1223.
Cheng, A. Y. S., Hege, E. K., Hubbard, E. N., Goldberg, L., Strittmatter, P. A., and Cocke, W. J. 1986, *Ap. J.*, **309**, 737.
Clary, D. C. 1985, *Mol. Phys.*, **54**, 605.
Dalgarno, A., Oppenheimer, M., and Berry, R. S. 1973, *Ap. J. (Letters)*, **183**, L21.
Deguchi, S. 1982, *Ap. J.*, **259**, 634.
Deguchi, S., and Goldsmith, P. F. 1985, *Nature*, **317**, 336.
Draine, B. T. 1978, *Ap. J. Suppl.*, **36**, 595.
Elitzur, M. 1980, *Ap. J.*, **240**, 553.
Forrest, W. J., McCarthy, J. F., and Houck, J. R. 1979, *Ap. J.*, **233**, 611.
Glassgold, A. E., and Huggins, P. J. 1986*a*, in *The M, S, and C Stars*, ed. H. R. Johnson and F. Querci (NASA/CNRS), in press.
———. 1986*b*, *Ap. J.*, **306**, 605.
Glassgold, A. E., Huggins, P. J., and Langer, W. D. 1985, *Ap. J.*, **290**, 615.
Glassgold, A. E., and Langer, W. D. 1974, *Ap. J.*, **193**, 73.
Glassgold, A. E., Lucas, R., and Omont, A. 1986, *Astr. Ap.*, **157**, 35 (Paper I).
Glassgold, A. E., Mamon, G. A., Omont, A., and Lucas, R. 1987, *Astr. Ap.*, **180**, 183 (Paper II).
Goldreich, P., and Scoville, N. Z. 1976, *Ap. J.*, **205**, 144 (GS).
Guilloteau, S., Lucas, R., Nguyen-Q-Rieu, and Omont, A. 1986, *Astr. Ap.*, **165**, L1.
Guilloteau, A., Omont, A., and Lucas, R. 1987, in preparation.
Hebden, J. C., Cheng, A. Y. S., Hege, E. K., Strittmatter, P. A., Beckers, J. M., and Murphy, H. P. 1986, *Ap. J.*, **309**, 745.
Hebden, J. C., Eckart, A., and Hege, E. K. 1987, *Ap. J.*, **314**, 690.
Herbst, E., and Klemperer, W. 1973, *Ap. J.*, **185**, 505.
Herbst, E., and Leung, C. M. 1986, *Ap. J.*, **310**, 378.
Herman, J. and Habing, H. J. 1985, *Phys. Rept.*, **124**, 255.
Herzberg, G. 1945, *Molecular Spectra and Molecular Structure. II. Infrared and Raman Spectra of Polyatomic Molecules* (New York: van Nostrand Reinhold), chap. 4.
Hollis, J. M., Churchill, E. B., Herbst, E., and de Lucia, F. C. 1986, *Nature*, **322**, 524.
Honeycutt, R. K., Bernat, A. P., Kephart, J. E., Gow, C. E., Sandford, M. T., and Lambert, D. L. 1980, *Ap. J.*, **239**, 565.
Hudson, R. D. 1971, *Rev. Geophys. Space Phys.*, **9**, 305.
Huggins, P. J., and Glassgold, A. E. 1982*a*, *A.J.*, **87**, 1828.
———. 1982*b*, *Ap. J.*, **252**, 201.
Jarrold, M. F., Bowers, M. T., DeFrees, D. J., McLean, A. D., and Herbst, E. 1986, *Ap. J.*, **303**, 392.
Jura, M. 1974, *Ap. J.*, **191**, 375.
Jura, M., and Morris, M. 1985, *Ap. J.*, **292**, 487.
Letzelter, C., Eidelsberg, M., Rostas, F., Breton, J., and Thieblemont, B. 1987, *Chem. Phys.*, in press.
Leung, C. M., Herbst, E., and Huebner, W. F. 1984, *Ap. J. Suppl.*, **56**, 231.
Liu, D.-J., and Oka, T. 1985, *Phys. Rev. Letters*, **54**, 1787.
Liu, D.-J., Oka, T., and Sears, T. J. 1985, *J. Chem. Phys.*, **84**, 312.
Lucas, R., Omont, A., Guilloteau, S., and Nguyen-Q-Rieu 1986, *Astr. Ap.*, **154**, L12.
Mamon, G. A., Glassgold, A. E., and Huggins, P. J. 1987, *Ap. J.*, submitted.
Mauron, N., Fort, B., Querci, F., Dreux, M., Fauconnier, T., and Lamp, P. 1984, *Astr. Ap.*, **130**, 341.
Millar, T. J., and Nejad, L. A. M. 1985, *M.N.R.A.S.*, **217**, 507.
Morris, M., and Alcock, C. 1977, *Ap. J.*, **218**, 687.
Morris, M., Guilloteau, S., Lucas, R., and Omont, A. 1987, preprint.
Morris, M., and Jura, M. 1983, *Ap. J.*, **264**, 546.
Mul, P. M., McGowan, J. W., Defrance, P., and Mitchell, J. B. A. 1983, *J. Phys. B*, **16**, 3099.
Nejad, L. A. M., Millar, T. J., and Freeman, A. 1984, *Astr. Ap.*, **134**, 129.
Nercessian, E., Forveille, T., Guilloteau, S., Lucas, R., and Omont, A. 1987, in preparation.
Omont, A. 1985, in *Mass-Loss from Red Giants*, ed. M. Morris and B. Zuckerman (Dordrecht: Reidel), p. 269.
Plummer, G. M., Herbst, E., and De Lucia, F. C. 1985, *J. Chem. Phys.*, **83**, 1428.
Scalo, J., and Slavsky, D. B. 1980, *Ap. J. (Letters)*, **239**, L73.
Slavsky, D. B., and Scalo, J. 1984, preprint.
Smith, D., and Adams, N. G. 1984, *Ap. J. (Letters)*, **284**, L13.
Sternberg, A., Dalgarno, A., and Lepp, S. 1987, preprint.
van Dishoeck, E. F. 1987, in *Astrochemistry*, ed. M. S. Vardya and S. P. Tarafder (Dordrecht: Reidel), p. 51.
van Dishoeck, E. F., and Dalgarno, A. 1984, *Ap. J.*, **277**, 576.
Walmsley, C. M. 1987, in *Astrochemistry*, ed. M. S. Vardya and S. P. Tarafder (Dordrecht: Reidel), p. 369.
Watson, W. D. 1973, *Ap. J. (Letters)*, **183**, L17.
Wootten, A., Boulanger, F., Bogey, M., Combes, F., Encrenaz, P. J., Gerin, M., and Ziurys, L. 1986, *Astr. Ap.*, **166**, L15.

A. E. GLASSGOLD and G. A. MAMON: Department of Physics, New York University, 4 Washington Place, New York, NY 10003

A. OMONT: Groupe d'Astrophysique, Observatoire de Grenoble, CERMO, B.P. 68, 38402 Saint Martin d'Hères Cedex, France

A.3 The photodissociation of CO in circumstellar envelopes

Mamon, Glassgold & Huggins, 1988, *ApJ 328, 797–808*

THE ASTROPHYSICAL JOURNAL, 328:797–808, 1988 May 15

THE PHOTODISSOCIATION OF CO IN CIRCUMSTELLAR ENVELOPES

G. A. MAMON, A. E. GLASSGOLD, AND P. J. HUGGINS
Department of Physics, New York University
Received 1987 August 27; accepted 1987 November 2

ABSTRACT

We calculate the CO photodissociation rate for the unshielded interstellar medium using recent laboratory results which confirm that photodissociation occurs by way of line absorption. The new rate of 2×10^{-10} s^{-1} is an order of magnitude larger than that used in earlier studies and requires that many situations in which CO photodissociation plays a role need to be reexamined. We demonstrate the effects of line photodissociation with calculations of the abundances of the CO photochain in the circumstellar envelopes of cool, evolved stars. For low mass-loss rate, optically thin envelopes, the large photodissociation rate leads to a CO distribution $\sim 10^{16}$ cm in extent; for thicker envelopes, strong line shielding leads to a much larger CO distribution with a steep falloff. These envelope sizes are considerably smaller than commonly discussed in the literature. We show how the results of the full theory can be simulated by a schematic model based on representative bands and provide a simple interpolation formula for the spatial variation of the CO abundance. The distribution of ^{13}CO and the photodissociation products, C and C^+ are also discussed. For ^{13}CO, the selective photodissociation due to its lower abundance tends to be canceled by chemical fractionation. We discuss the important implications of these results for the ion-molecular chemistry of circumstellar envelopes and for observations of circumstellar CO, C, and C^+.

Subject headings: molecular processes — stars: circumstellar shells

I. INTRODUCTION

In many astrophysical situations the transition from molecular to atomic gas occurs as a result of photodissociation. Carbon monoxide is one of the most important molecules in the study of interstellar and circumstellar matter, but in the past there has been no firm understanding of its photodissociation by the interstellar radiation field. Following a suggestion by Bally and Langer (1982), Morris and Jura (1983, hereafter MJ) and Glassgold, Huggins, and Langer, (1985, hereafter Paper I) investigated some of the consequences of CO photodissociation occurring through a line process rather than through a continuum process for circumstellar and interstellar matter, respectively. As a result of the recent laboratory measurements of the far-UV absorption and fluorescence cross sections by Letzelter *et al.* (1987), definitive calculations of the CO photodissociation rate can now be made, and the new photodissociation rate is significantly larger than previous estimates. Consequently, situations in which CO photodissociation plays an important role need to be reevaluated. A particular application discussed here is CO photodissociation in the circumstellar envelopes of cool, evolved stars undergoing substantial mass loss. Not only is CO an important diagnostic for these objects but, at least in the case of spherical envelopes, their simple geometry allows the relevant radiative transfer to be developed in a straightforward way.

It was pointed out in Paper I that the dissociating radiation is absorbed by CO itself ("self-shielding") and by other species such as atomic and molecular hydrogen, atomic carbon, and dust ("mutual shielding"). In the case of ^{13}CO, any near coincident lines of ^{12}CO provide additional shielding. In this paper we treat these processes in the context of the photochemical model (e.g., Huggins and Glassgold 1982*a*) in which the major molecular constituents of expanding red giant winds are destroyed by penetrating interstellar UV radiation. For present purposes we focus on the case of ^{12}CO and ^{13}CO and their dissociation products. Additional applications to circumstellar chemistry are investigated in companion papers on carbon-rich envelopes (Glassgold *et al.* 1987) and oxygen-rich envelopes (Mamon, Glassgold, and Omont 1987). In § II we review the underlying physics, particularly CO line photodissociation, and describe the basis of the model calculations for circumstellar envelopes. The results are described in § III for CO and in § IV for ^{13}CO and the dissociation products, C and C^+; the paper is concluded with a brief summary in § V.

II. THE CO PHOTODISSOCIATION RATE AND ITS APPLICATION TO CIRCUMSTELLAR ENVELOPES

The laboratory experiments of Letzelter *et al.* (1987) show that CO is photodissociated by a line process over the relevant wavelength range extending from the threshold (1120 Å) to the Lyman cutoff (912 Å). The upper limit to any continuum dissociation in this wavelength band is less than 1% of the total rate. Ignoring a small number of partially overlapping bands, the total photodissociation rate is the sum of contributions from individual bands,

$$G = \sum_i g_i \,. \tag{1}$$

For a typical unshielded region of the interstellar medium, the ith band contributes

$$g_i^{(0)} = 0.0265 K_i f_i 4\pi I(\nu_i) \text{ s}^{-1} \,, \tag{2}$$

where f_i is the absorption oscillator strength, K_i is the probability for dissociation, and I is the mean intensity of the interstellar radiation field (measured in photons cm^{-2} s^{-1} Hz^{-1} sr^{-1}). Table 1 lists the dissociating bands for CO for $\lambda > 912$ Å (adapted from Table 1 of Letzelter *et al.* 1987). We have calculated the oscillator strengths, using their integrated cross sections (col. [3]), and the contribution of each band to the rate for the unshielded interstellar medium (col. [5]), using a fit to

TABLE 1

PHOTODISSOCIATION BANDS OF CO

Band[a]	λ (Å)	f[b]	$4\pi I$ (cm^{-2} s^{-1} Hz^{-1})	g (s^{-1})
1	1099.0	3.7 (−5)	5.8 (−8)	5.8 (−14)
2*	1076.1	3.6 (−2)	5.4 (−8)	4.7 (−11)
3	1063.1	2.8 (−3)	5.2 (−8)	2.3 (−12)
4*	1051.7	2.5 (−3)	5.0 (−8)	3.2 (−12)
5	1029.3	4.3 (−5)	4.5 (−8)	5.1 (−14)
6	1017.9	4.4 (−5)	4.3 (−8)	4.9 (−14)
7	1010.9	4.4 (−5)	4.1 (−8)	4.8 (−14)
8*	1002.5	7.9 (−3)	3.9 (−8)	8.2 (−12)
9*	989.3	4.6 (−4)	3.5 (−8)	4.3 (−13)
10*	985.6	1.5 (−2)	3.4 (−8)	1.4 (−11)
11	982.7	4.8 (−4)	3.4 (−8)	4.3 (−13)
12	977.5	1.8 (−3)	3.2 (−8)	1.5 (−12)
13	972.7	1.2 (−2)	3.0 (−8)	9.3 (−12)
14*	970.4	2.1 (−2)	3.0 (−8)	1.6 (−11)
15	968.9	1.2 (−2)	2.9 (−8)	9.6 (−12)
16*	968.4	7.7 (−3)	2.9 (−8)	5.9 (−12)
17	964.4	2.8 (−3)	2.8 (−8)	2.0 (−12)
18	960.5	2.6 (−4)	2.6 (−8)	1.8 (−13)
19*	956.1	1.3 (−2)	2.4 (−8)	8.7 (−12)
20	949.9	2.2 (−2)	2.2 (−8)	1.3 (−11)
21	948.4	2.8 (−3)	2.1 (−8)	1.6 (−12)
22	946.3	7.6 (−3)	2.0 (−8)	4.1 (−12)
23	941.1	2.6 (−2)	1.8 (−8)	1.2 (−11)
24	939.9	2.1 (−2)	1.7 (−8)	9.7 (−12)
25	935.7	3.8 (−3)	1.5 (−8)	1.5 (−12)
26	933.1	4.0 (−2)	1.4 (−8)	1.4 (−11)
27	930.0	6.3 (−3)	1.2 (−8)	2.0 (−12)
28	928.4	6.7 (−3)	1.1 (−8)	1.9 (−12)
29	925.8	1.6 (−2)	9.4 (−9)	4.1 (−12)
30	924.6	5.1 (−3)	8.6 (−9)	1.2 (−12)
31*	922.8	6.3 (−3)	7.5 (−9)	1.3 (−12)
32	917.3	2.8 (−2)	3.8 (−9)	2.9 (−12)
33*	915.8	9.9 (−3)	2.8 (−9)	7.3 (−13)
34	913.5	3.4 (−2)	1.1 (−9)	1.0 (−12)

[a] Bands followed by an asterisk are assumed to correspond to 0–0 transitions with no isotope shift.

[b] Bands 2, 3, and 13 have $K_i = 0.89$, 0.60, and 0.96, respectively. All other bands have $K_i = 1$.

NOTE.—Parentheses indicate multiplication by the power of ten given within the parentheses.

the far-UV interstellar radiation field given by Jura (1974) (col. [4]). The total unshielded rate is then $G^{(0)} = 2.0 \times 10^{-10}$ s^{-1}, and the associated mean oscillator strength (weighted by the radiation field) is 0.0087. This rate is an order of magnitude larger than the earlier value based on a putative continuum process and used in chemical models of diffuse clouds. The rate $G^{(0)}$ is sensitive to the spectrum of the far-UV interstellar radiation field. For example, if the radiation field is represented by the flux at 1000 Å, $G^{(0)} = 3.7 \times 10^{-10}$ s^{-1}. For comparison and later applications, the photoionization rate for atomic carbon with the Jura radiation field is $G^{(0)}(C) = 3.4 \times 10^{-10}$ s^{-1}.

The basis for treating CO photodissociation in circumstellar envelopes has been given previously in Paper I and MJ. In particular, MJ developed the radiative transfer for a typical far-UV line that dissociates CO, using the Sobolev approximation. Consequently, we need only indicate here how to adapt the results of MJ to the full complement of bands measured by Letzelter *et al.* (1987) and to include appropriate mutual shielding (Paper I). For purposes of simplicity, we consider only the effects of the interstellar radiation field and ignore internal radiation sources. Fluorescent line radiation of H_2, induced by cosmic-ray secondary electrons (Prasad and Tarafdar 1983; Sternberg, Dalgarno, and Leep 1987), might add to the photodissociation of CO deep within the most massive and shielded envelopes.

Although the experiment of Letzelter *et al.* (1987) represents an important advance in the measurement of the CO photodissociation cross section, further measurements are needed to clarify the process. More recent experiments by Yoshino *et al.* (1987) at 20 times the spectral resolution indicate that the cross sections for some of the bands below 1000 Å may be larger than reported by Letzelter *et al.* The spectroscopic parameters of the upper states have not been established for most of the bands below 1000 Å. This affects our treatment of the radiation transfer within the circumstellar envelope which requires the Hönl-London factors for the rotational part of the oscillator strength. About one-half of the assignments for the states above 1000 Å are Σ and one-half are Π. In the absence of definitive information, we use the Hönl-London factors for Σ–Σ transitions, i.e., we do not treat Q-branch lines explicitly. This should lead to only small changes in the total CO photodissociation rate inside the circumstellar envelope.

We have also assumed that the line widths are small compared with that associated with the expansion velocity V. The preliminary results of Letzelter *et al.* indicate that some of the lines may be broader than this, in which case improvements to the Sobolev approximation should be implemented. Large line widths and other blending tend to introduce some aspects of continuum self-shielding into the problem, but it is unlikely that the qualitative conclusions of our calculations will be substantially altered by these effects. We ignore them here, pending additional experiments to better establish the photodissociation cross section.

Inside the circumstellar envelope the contribution of each band g_i is modified by optical depth effects and, in the Sobolev approximation, is given by

$$g_i = \langle \beta_i(r) \rangle \gamma_i(r) g_i^{(0)} , \tag{3}$$

where $\langle \beta_i(r) \rangle$ is a mean escape probability and $\gamma_i(r)$ is the continuum attenuation factor for band i. The mean escape probability is an average over the rotational states involved in the transition, weighted by the populations of the initial states. In the Sobolev approximation, the escape probability for each transition is given by a simple function of the optical depth, as discussed in more detail in the Appendix. In evaluating equation (3) for each of the bands in Table 1, we have assumed for simplicity that the populations are given by a Boltzmann distribution with the excitation temperature $T_{ex}(r)$; later we vary $T_{ex}(r)$ to investigate the sensitivity of the results to this quantity. We also use the continuum factor of MJ,

$$\gamma_i(r) = \exp\left[-1.644 \tau_c(\lambda_i)^{0.86}\right] , \tag{4}$$

where $\tau_c(\lambda_i)$ is the radial optical depth for continuum absorption at wavelength λ_i.

The species with the greatest potential for blocking of the CO bands are atomic and molecular hydrogen, but the possibilities for near coincidence of the transitions are different for the two species. The spacing of the Lyman transitions of atomic hydrogen is such that relatively few near coincidences with the CO bands occur. The Lyman and Werner bands of H_2 are roughly uniformly distributed over the 900–1100 Å region, and 11 of these lines with initial rotational quantum numbers in the range $J = 0$–2 coincide with the CO bands within 0.4 Å as do six others within 1 Å. In our treatment of H_2 blocking, we assume that the relevant (outer) parts of the envelope are

cool enough so that only the $J = 0$–2 lines of H_2 are significantly populated. The H_2 lines are highly saturated and one of them can effectively block a CO band even if it is several tenths of an angstrom away.

In this paper we consider circumstellar envelopes whose hydrogen is mainly molecular. This assumption is well justified for cool stars with photospheric temperatures less than 3000 K (Glassgold and Huggins 1983). The envelopes of such stars do have a small amount of atomic hydrogen (Glassgold and Huggins 1983), e.g., between 10^{17} and 10^{18} cm^{-2} for IRC +10216, but the amount is insufficient to produce very much blocking from the (atomic) Lyman lines. The situation would be very different for warmer stars, which are predominantly atomic and for diffuse interstellar clouds with $N(\mathrm{H}) > 10^{19}$ cm^{-2}. It is also appropriate to ignore the shielding due to atomic carbon because the calculated column density and photoionization cross section satisfy the condition $N(\mathrm{C}) \ll \sigma_{\mathrm{ph}}(\mathrm{C})^{-1} = 6 \times 10^{16}$ cm^{-2}.

The H_2 lines become so optically thick that absorption occurs in the radiative wings of the Lyman and Werner transitions. From the point of view of the CO lines, the blocking of the dissociating radiation by a nearby H_2 line can be included in the continuum factor of equation (4). Thus, the optical depth in this equation is a sum of contributions from dust and the wings of those Lyman and Werner lines which originate from the lowest rotational states of H_2. Despite the strong blocking of many CO lines by H_2, the effect on the total CO photodissociation rate inside a circumstellar envelope is only a quantitative one because the CO bands that are distant from H_2 lines still contribute $\sim 50\%$ of the total rate.

The isotope shift of the far-UV transitions of CO is substantial except for $v = 0$–0 transitions. Thus the shielding of ^{13}CO by ^{12}CO occurs only for 0–0 transitions, where the isotope shift is typically 0.01 Å (Paper I). Most of the ^{13}CO bands are shifted by a large amount (>0.5 Å) (Eidelsberg 1987) and there is only a modest amount of mutual shielding of ^{13}CO by the more abundant isotope.

The effects of the most important physical processes that enter into the above theory are illustrated in Figure 1. This shows the variation of the photodissociation rate of CO with radius for the case of a spherically symmetric envelope of steady mass-loss rate with parameters given in Table 2. The total photodissociation rate is given by the solid curve at the top, labeled "Total." Starting at the outside of the envelope, the rate decreases sharply near $r = 5 \times 10^{17}$ cm due to the onset of self-shielding. It then follows the linear law expected at intermediate distances on the basis of the optically thick limit of the theory for the model $1/r^2$ CO density distribution (see eq. [3] and the Appendix). The rate decreases even further at smaller distances due to dust shielding. By $r = 10^{16}$ cm, the

TABLE 2

PARAMETERS FOR THE STANDARD MODEL

Expansion velocity	$V = 15$ km s^{-1}
Mass-loss rate (total hydrogen)	$\dot{M} = 10^{-5}\ M_\odot$ yr^{-1}
Initial CO abundance[a]	$x_0(^{12}\mathrm{CO}) = 4 \times 10^{-4}$; $x_0(^{13}\mathrm{CO}) = 8 \times 10^{-6}$
Temperature distribution[b], $T = 14.6\ \mathrm{K}\ (r/r_0)^{\phi}$	$r_0 = 9 \times 10^{16}$ cm; $\phi = -0.72$, $r < r_0$; $\phi = -0.54$, $r \geq r_0$
Dust shielding[c], $\tau_c^{(d)} = d/r$	$d = 2.67 \times 10^{16}$ cm

[a] Relative to total hydrogen, $n(\mathrm{H}) + 2n(\mathrm{H}_2)$.
[b] For $r > 1.92 \times 10^{18}$ cm, $T = 2.8$ K.
[c] The value of d scales with $\dot{M}/V$.

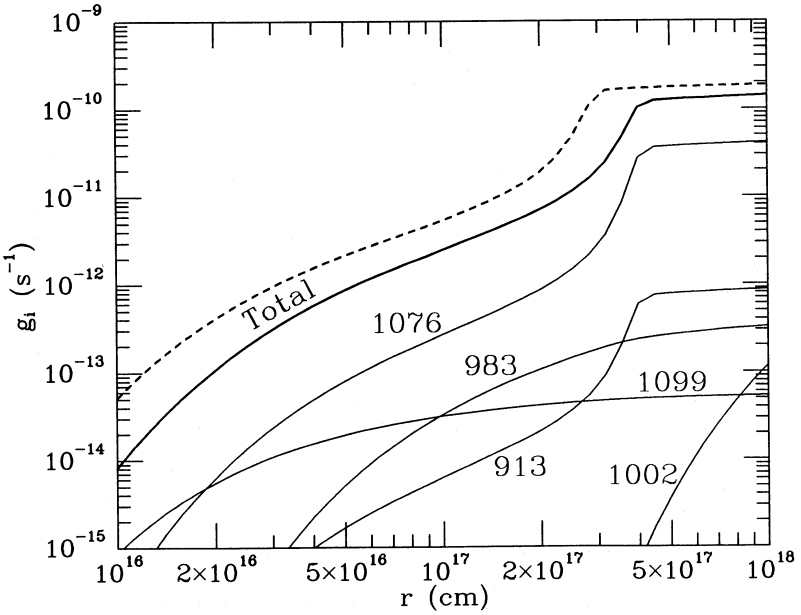

FIG. 1.—Photodissociation rates as a function of radius for the standard model. The total rate is shown, with and without H_2 blocking, by the solid and the dashed curves, respectively. The contributions of representative, individual bands are labeled by the band wavelength in Å.

various shielding mechanisms have reduced the CO photodissociation rate by over 4 orders of magnitude.

The dashed curve gives the total CO photodissociation rate when H_2 line blocking is ignored. Over most of the interior of the envelope, H_2 blocking reduces the photodissociation rate by only a factor of 2 or 3, because a substantial number of CO bands are not blocked. It is interesting that some H_2 blocking occurs even at $r = 10^{18}$ cm in this model, which implicitly assumes that the hydrogen content of the envelope is completely molelcular out to infinity. For an envelope of finite age t, the H_2–H transition near the outer edge ($r = Vt$) will make the total rate approach the unshielded value, $G^{(0)} = 2 \times 10^{-10}$ s^{-1}.

The other curves in Figure 1 give the contributions of a selection of individual CO bands labeled by their wavelengths in angstroms. The properties of the bands in Table 1 help explain the variation of these partial dissociation rates with radius. Thus dissociating band 2 at 1076.1 Å has a large dissociation oscillator strength (0.032) and is strongly self-shielded. It is the single most important band, contributing 23% of the total rate at the outside of the envelope but, because of self-shielding, only 1% in the interior. The variation of the rate for band 2 is typical of the stronger bands which dominate the total photodissociation rate. Band 34 at 913.5 Å is also strongly dissociating, but it contributes little to the total rate because the interstellar radiation field is very small near the Lyman cutoff. Band 8 at 1002.5 Å is moderately strong but it is very effectively blocked by a closely coincident H_2 line. Bands 1 (1099 Å) and 11 (983 Å) are both weak and are not close to any H_2 lines; the former is hardly self-shielded because its oscillator strength is very small (3.7×10^{-5}) and plays a dominant role in the inner part of the envelope.

III. THE DISTRIBUTION OF CO

We now present the results of the theory of the photodissociation of circumstellar CO in terms of the actual distribution of the CO abundance, defined as the ratio of CO density to the total hydrogen density $[n_H = n(H) + 2n(H_2)]$. The abundance of CO can be calculated accurately in terms of the simplest photochain (Huggins and Glassgold 1982*a*),

$$\mathrm{CO} \xrightarrow{h\nu} \mathrm{C} \underset{e}{\overset{h\nu}{\rightleftharpoons}} \mathrm{C}^+ , \qquad (5)$$

in which the backward arrow signifies radiative recombination. The neglect of other reactions is justified by more complete chemical studies (Glassgold *et al.* 1987; Mamon, Glassgold, and Omont 1987). The results for a standard model will be discussed first; the physical parameters are given in Table 2. We use two power laws to fit the calculations by Kwan and Linke (1982) of the kinetic temperature of IRC +10216 in the outer envelope, and cut it off at 2.8 K, the temperature of the cosmic background radiation.

In Figure 2 we compare the spatial variation of CO with and without line shielding. The curve labeled S is the standard calculation (Table 2) which includes all the important shielding processes discussed in § II. In comparison with the case where the only shielding of the dissociating UV radiation is by dust, the CO distribution for the standard case differs substantially in two ways: the CO distribution is shifted outward (by more than a factor of 5) and it decreases more rapidly in the transition region. Inclusion of H_2 blocking shifts the CO distribution outward by 30%. Dust plays a minor role in the presence of strong line shielding. For the standard case, the dust optical depth is only ~ 0.2 in the CO transition region.

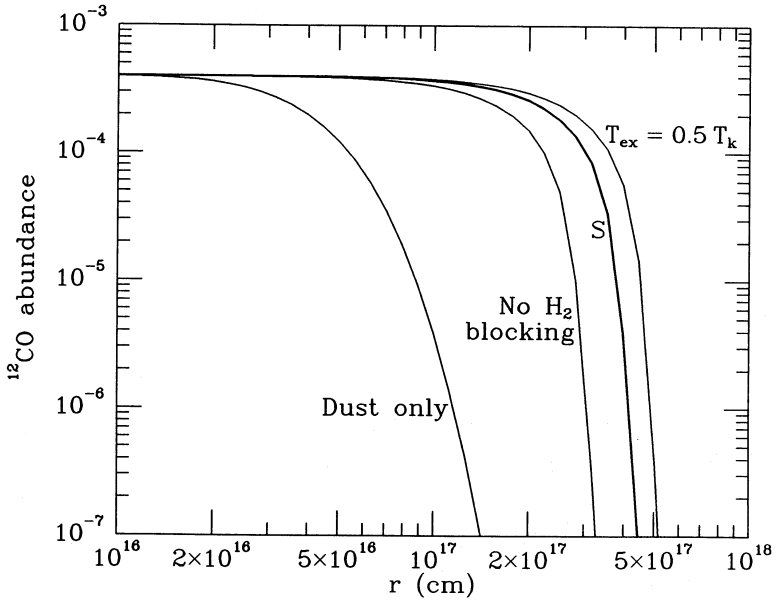

FIG. 2.—The spatial distribution of the CO abundance for the standard case (S) of Table 2. Variational calculations are shown for the cases of no line shielding ("Dust"), no H_2 blocking, and reduced excitation temperature.

The variation of the CO abundance distribution with mass-loss rate, keeping all other parameters fixed, is shown in Figure 3. In the limit of very small $\dot{M}$, the distribution approaches that of "free decay" (Huggins and Glassgold 1982*a*),

$$x = x_0 = \exp\left[-V/G^{(0)}\right] . \quad (6)$$

With increasing $\dot{M}$, dust and especially self-shielding become important, and both the size of the distribution and the steepness of its decline increase. If the size of the distribution is defined by the position where x(CO) has decreased by a factor of 2, $r_{1/2} \propto (x_0 \dot{M})^{0.6}$, reminiscent of the scaling of the OH peak in the H_2O photochain (Huggins and Glassgold 1982*b*).

The excitation of the CO levels in any given circumstellar envelope depends on a number of factors including the gas kinetic temperature and density, the infrared and cosmic background radiation fields, and photon trapping. Increasing the rotational excitation temperature T_{ex} tends to decrease the effective opacity of the absorbing transitions and to reduce the self-shielding of the envelope. For simplicity in the present calculations, we assume that the levels are thermalized at the kinetic temperature, i.e., $T_{ex} = T_k$. In order to investigate the sensitivity of the results to T_{ex}, we have also done calculations with $T_{ex} = 0.5T_k$. These two cases should bracket most situations. The results of setting $T_{ex} = 0.5T_k$ for the standard model are shown in Figure 2; the shifts in the curves are slight. Thus the results are not very sensitive to the level populations.

The curves in Figure 3 for intermediate values of $\dot{M}$ should be considered rather provisional in view of our ignorance of the CO excitation properties in these envelopes. For low and intermediate mass-loss rates, $\dot{M} < 10^{-6}\ M_\odot\ \mathrm{yr}^{-1}$, the excitation of the CO levels is strongly affected by the IR flux from the star and inner dust shell, thereby diminishing the dependence of the photodissociation rate on the kinetic temperature. Of course, for very small $\dot{M}$, the envelopes are almost optically thin and the photodissociation rate is independent of excitation. The excitation and thermal properties of these envelopes deserves further study, but this is beyond the scope of the present paper.

The results shown in Figures 2 and 3 have been obtained from a detailed theory that includes individual treatment of the many bands of CO and the lines of molecular hydrogen as well as the effects of dust. We now discuss two simpler, but approximate, treatments that should be useful in both theoretical modeling and the analysis of observational data. In earlier discussions of CO line self-shielding (e.g., MJ and Paper I), a schematic model was used in which the ensemble of dissociating bands was replaced by a number of identical bands. Now that the physical properties of the bands have been measured, we can investigate whether this approach is a good approximation. The ensemble of CO bands is represented by N_e identical bands of wavelength $\langle\lambda\rangle$, dissociation oscillator strength $\langle f_d\rangle$, and effective total unshielded photodissociation rate G_e. Using $\langle\lambda\rangle = 1000$ Å (the results are insensitive to this value), the approximation is specified by any pair of the quantities G_e, $\langle f_d\rangle$, and N_e; the third is directly related to the others by equations (1) and (2). We find that the schematic model can reproduce the CO abundance distribution to a high degree of accuracy; the difference would barely be visible in the plots used in this paper. For the standard model and $G_e = G^{(0)} = 2 \times 10^{-10}\ \mathrm{s}^{-1}$, $\langle f_d\rangle = 0.029$ or $N_e = 12$; the reduction of N_e from 34 to 12 comes from H_2 blocking and the fact that the transition region is determined mainly by the stronger CO bands with $\langle f_d\rangle \sim 0.01$. (Deep inside the envelope, even very weak bands contribute to the total rate, but their effect on the abundance CO is negligible because the dissociation rate is already very small.) The parameters of the schematic model do not change much when the mass-loss rate is changed. Its main limitation is that the abundance of C^+ becomes inaccurate

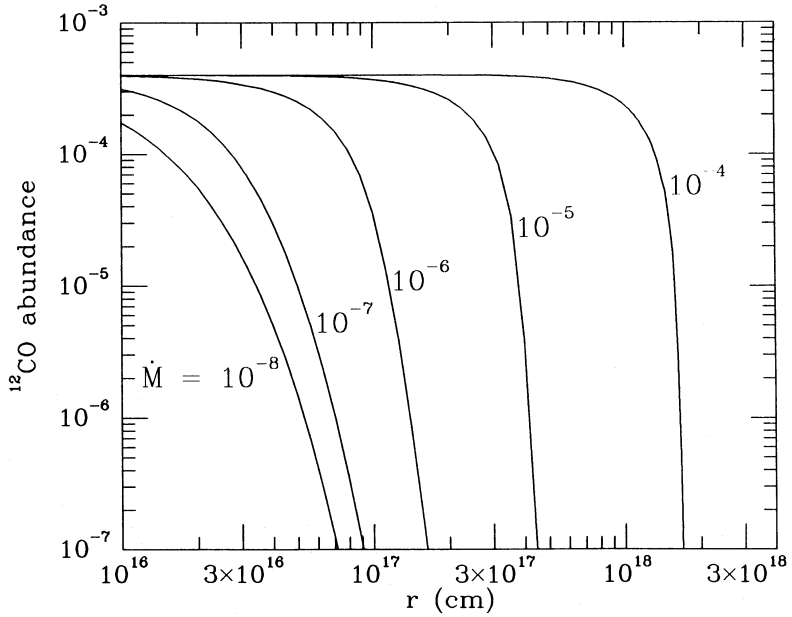

FIG. 3.—The CO abundance distribution for a range of mass-loss rates (units $M_\odot\ \mathrm{yr}^{-1}$). All other parameters are the same as in Table 2.

deep within the envelope. As long as $x(C^+) > 10^{-7}$ however, the errors are usually considerably less than 50%. For applications to detailed chemical modeling, we suggest the use of $\langle f_d \rangle = 0.035$, which improves the fit to the C^+ distribution at the expense of a slightly less accurate representation of the CO distribution.

On the basis of this validation of the schematic model, we recommend its use in many astrophysical applications where the accuracy of the complete multiband theory is not required. This procedure has already proved useful in chemical modeling of circumstellar envelopes (Glassgold *et al.* 1987; Mamon, Glassgold, and Omont 1987) and in a detailed study of CO in IRC +10216 (Huggins, Olofsson, and Johansson 1987). We expect that appropriate schematic models can also be developed for interstellar clouds.

If only the distribution of CO is of interest, it is possible to represent the results of the full theory even more simply by generalizing an approximate form of the CO abundance distribution derived by MJ in the optically thick limit of the Sobolev theory of line self-shielding,

$$x = x_0(1 - r^2/r_c^2) , \tag{6}$$

$$r_c = \left(\frac{3x_0 \dot{M}/m_H}{4\pi V N_b \langle 4\pi I K \lambda^{-1} \rangle} \right)^{1/2} , \tag{7}$$

where the quantity in angle brackets is an average over the N_b bands. The singular behavior of equation (6) near the cutoff radius is an artifact that arises from the assumption that the bands are optically thick, whereas they actually become optically thin in the limit $r \to r_c$ and $x \to 0$. Examination of the numerical solutions of the full theory shows that the real transition is continuous and that the contributing bands have a wide range of optical depths. Nevertheless equations (6) and (7) express some qualitative aspects of the correct solution. For example, equations (6) and (7) imply that $r_{1/2} = 2^{-1/2} r_c \propto \dot{M}^{1/2}$, whereas the numerical solution typically gives $r_{1/2} \propto \dot{M}^{0.6}$, which is not too different. However, the characteristic size of the CO envelope is overestimated by equation (7). For example, in the standard case (Table 2), with $N_b = 34$ and $\langle 4\pi I K \lambda^{-1} \rangle = 2.6 \times 10^{-3}$ cm^{-3} Hz^{-1} s^{-1}, equation (7) gives $r_{1/2} = 3.7 \times 10^{17}$ cm, significantly larger than the value in the complete theory (for the comparable case of no H_2 blocking), where $r_{1/2} = 1.8 \times 10^{17}$ cm. This discrepancy increases with decreasing mass-loss rate.

It is possible to obtain an improved fit to the CO abundance distribution by modifying equation (6) as

$$x = x_0[1 - (r/r_c)^b] \tag{8}$$

and treating b and r_c as empirical parameters; 20% accuracy can be obtained in this way. A much better fit can be obtained with the formula

$$x = x_0 \exp [-\ln 2(r/r_{1/2})^a] , \tag{9}$$

which does not have a sharp cutoff. As shown in Figure 4, the quality of the fits is high as long as x/x_0 is larger than 0.05. The best-fit parameters are shown in Figure 5 as a function of mass-loss rate for the standard velocity of 15 km s^{-1} (*solid curves*) and $\frac{1}{2}$ and 2 times this value (*short and long-dashed curves, respectively*). For convenience in applications, numerical values of the parameters are given in Table 3. It is apparent that the slopes of the $r_{1/2}$ versus $\dot{M}$ curves increase with $\dot{M}$. A good approximation for the mass-loss rate range, 10^{-6}–10^{-4} $M_\odot$ yr^{-1} is $r_{1/2} \propto \dot{M}^{0.6}$. In the limit of vanishing $\dot{M}$, $r_{1/2}$ approaches a constant, in keeping with the fact that the size of the abundance distribution is now determined by $V/G^{(0)}$ (Huggins and Glassgold 1982*a*).

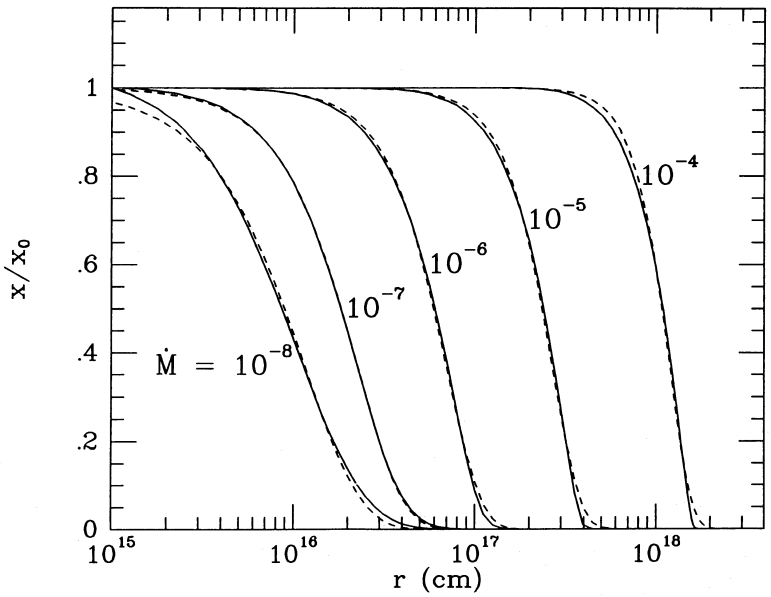

FIG. 4.—Fit of equation (9) for the CO abundance distribution (*dashed curves*) compared with the full theory (*solid curves*) for a range of mass-loss rates. All other parameters are the same as in Table 2.

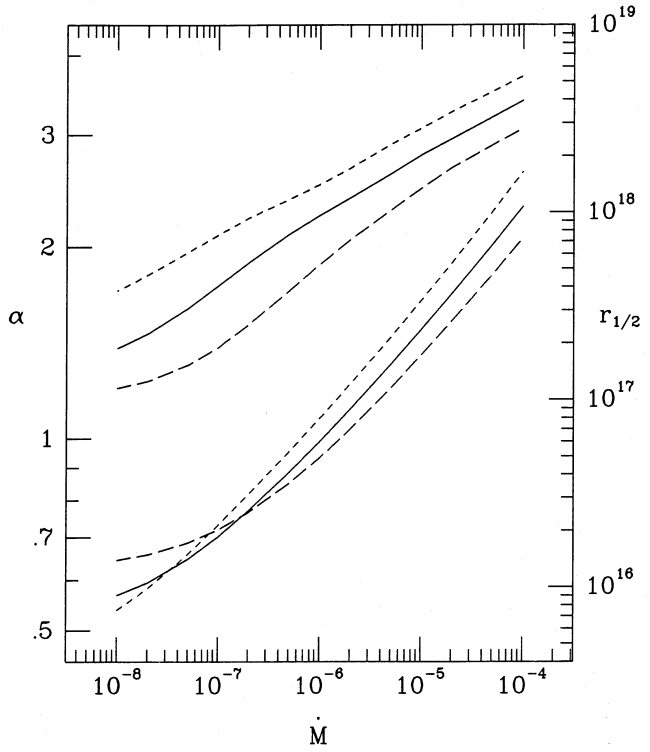

FIG. 5.—Variation of the fitting parameters in equation (9) with mass-loss rate for three values of the expansion velocity, $V = 7.5$ (*short-dashed curve*), 15 (*solid curve*) and 30 km s^{-1} (*long-dashed curve*). The top three curves show α and the bottom three show $r_{1/2}$. All other parameters are the same as in Fig. 2.

One important result of the above calculations is that the characteristic sizes of the CO envelopes are significantly smaller than previous estimates, and this can effect the interpretation of observation of circumstellar CO. For example, in analyzing CO survey data, Knapp and Morris (1985) and Wannier and Sahai (1986) used the old value of the CO photodissociation rate and a two-band approximation (following MJ) which yields envelope sizes that are typically a factor 5 times larger than given here for the same envelope parameter. Application of the new theory indicates that mass-loss rates inferred by these earlier analyses need to be increased in those cases where the angular size of the telescope beam is comparable to, or larger than, the CO envelope. This new result also resolves the problem raised by the above authors concerning the lack of double-peaked spectra in sources whose intensities indicate that the emission is optically thin. These effects have been discussed for the case of α Ori (Huggins 1987), where it was deduced that the source size was significantly smaller than suggested by earlier theory; this result is confirmed by the present results. The prescription given above for calculatng the CO envelope size should enable CO survey data to be interpreted consistently in accord with the new theory of CO photodissociation.

TABLE 3

FIT PARAMETERS OF CO DISTRIBUTION

$\dot{M}$ ($M_\odot$ yr^{-1})	$v = 7.5$ km s^{-1}		$v = 15$ km s^{-1}		$v = 30$ km s^{-1}	
	$r_{1/2}$	α	$r_{1/2}$	α	$r_{1/2}$	α
1 (−8).....	7.50 (15)	1.71	9.01 (15)	1.39	1.39 (16)	1.20
2 (−8).....	9.79 (15)	1.81	1.05 (16)	1.46	1.48 (16)	1.23
5 (−8).....	1.49 (16)	1.96	1.40 (16)	1.60	1.71 (16)	1.31
1 (−7).....	2.12 (16)	2.09	1.85 (16)	1.74	2.01 (16)	1.39
2 (−7).....	3.10 (16)	2.22	2.54 (16)	1.89	2.49 (16)	1.51
5 (−7).....	5.23 (16)	2.38	4.05 (16)	2.09	3.55 (16)	1.71
1 (−6).....	7.91 (16)	2.51	5.95 (16)	2.24	4.88 (16)	1.88
2 (−6).....	1.21 (17)	2.66	8.88 (16)	2.39	6.94 (16)	2.05
5 (−6).....	2.14 (17)	2.90	1.54 (17)	2.61	1.15 (17)	2.29
1 (−5).....	3.35 (17)	3.07	2.35 (17)	2.79	1.72 (17)	2.47
2 (−5).....	5.31 (17)	3.26	3.65 (17)	2.96	2.61 (17)	2.66
5 (−5).....	9.99 (17)	3.51	6.67 (17)	3.20	4.63 (17)	2.89
1 (−4).....	1.64 (18)	3.71	1.07 (18)	3.39	7.26 (17)	3.07

NOTES.—These parameters refer to the distribution given in equation (9). The units of $r_{1/2}$ are cm. Parentheses indicate multiplication by the power of ten given within the parentheses.

IV. THE DISTRIBUTION OF C, C^+, AND ^{13}CO

The products of the CO photochain, C and C^+, are important for circumstellar chemistry and are potentially useful observational probes of the outer regions of the envelopes. Figure 6 shows the spatial variation of the abundances for the standard case. Relative to the predictions of the simplest theory with only dust shielding (Huggins and Glassgold 1982*a*), the main changes are the shift of the CO–C^+ transition to larger distances and the sharpening of the various abundance distributions. The transition is predominantly from CO to C^+: the peak abundance of neutral carbon, x_p(C), is always

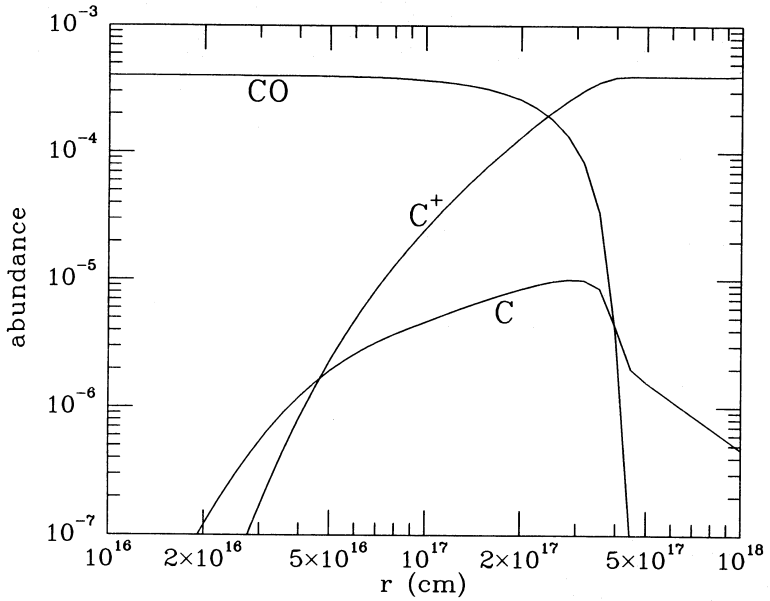

FIG. 6.—The complete CO photochain for the parameters of Table 2

small compared with x_0, the initial abundance of CO. The ratio $x_p(C)/x_0$ does increase with decreasing mass-loss rate but, even for $\dot{M} = 10^{-8}\ M_\odot\ \mathrm{yr}^{-1}$, $x_p(C)/x_0$ is only 0.25. The spatial distribution of neutral carbon is characterized by a long recombination tail that is sensitive to the temperature in the outer envelope. The radial column density of neutral carbon is typically of order $2 \times 10^{15}\ \mathrm{cm}^{-2}$ and fairly independent of $\dot{M}$. The detection of the emission in the fine structure lines of C is expected to be difficult in IRC +10216 because of the problems in exciting the lines far from the star (Omont 1986).

The abundance of C^+ decreases very rapidly going into the interior of the envelope. The details of its spatial distribution are quite important for the ionization of the envelope and for ion-molecule chemistry, particularly in O-rich circumstellar envelopes where CO is essentially the only source of C^+ (Mamon, Glassgold, and Omont 1987). The detection of the 158 μm far-infrared line or the radio recombination lines of C^+ would be of great interest as further tests of the photochemical model, and sensitive new detection systems may make such observations feasible in the near future.

The measurement of the relative abundances of the mass 12 and 13 isotopes of carbon is of considerable importance for understanding stellar evolution. Radio observations of the isotope ratio for several circumstellar envelopes have been carried out (see, e.g., Knapp and Chang 1985). For the C-rich envelope IRC +10216, the most accurate determination of the $^{12}C/^{13}C$ ratio, 50^{+6}_{-4}, is based on the optically thin lines of several molecules (Kahane *et al.* 1987). Chemical fractionation appears to be unimportant for on-source isotope ratio measurements in IRC +10216 because a single isotope ratio is appropriate for all of these molecules. Measurements for other envelopes are generally less accurate, but the ratios for O-rich envelopes are smaller on average than for C-rich envelopes (Knapp and Chang 1985).

The demonstration that ion-molecule reactions are operative in circumstellar envelopes (Nejad, Millar, and Freeman 1984; Glassgold, Lucas, and Omont 1986) suggests that chemical fractionation of CO occurs through the well-known exchange reaction (Watson, Anicich, and Huntress 1976),

$$^{13}C^+ + {}^{12}CO \rightarrow {}^{12}C^+ + {}^{13}CO\ , \qquad (10)$$

which is exothermic by ~ 35 K. Below this temperature, the backward reaction is suppressed and production of ^{13}CO from ^{12}CO is favored. On the other hand, "selective photodissociation" (Bally and Langer 1982) favors ^{12}CO because the lower abundance of ^{13}CO produces relatively less self-shielding and more photodissociation of ^{13}CO. The competition between these processes in interstellar clouds was investigated in Paper I with a schematic treatment of CO photodissociation. Using the new photodissociation rate and the theory described in § II, it is now possible to obtain more definitive results on the chemical and photo fractionation of CO in circumstellar envelopes.

We have calculated the abundances for both the ^{12}CO and ^{13}CO photochains, linking the two by the fractionation reaction equation (10). The properties of this reaction have been well established by laboratory experiments and we follow Paper I in fitting the temperature dependence of the forward and backward rate coefficients given by Langer *et al.* (1984). The unshielded photodissociation rates of ^{12}CO and ^{13}CO are the same, as are the rate coefficients for radiative recombination. According to Table 1, nine ^{13}CO bands coincide with ^{12}CO bands and are strongly shielded. In treating the case of overlapping ^{12}CO and ^{13}CO bands, we replace the optical depth for each isotope by the sum. However, the blocked bands contribute only 30% of the unshielded dissociation rate and so the effect of ^{12}CO blocking is only a quantitative one.

Figure 7*a* shows the spatial distribution of ^{12}CO and ^{13}CO with and without fractionation for the standard case (Table 2), which assumes an initial isotope ratio of 50. Without fractiona-

1988ApJ...328..797M

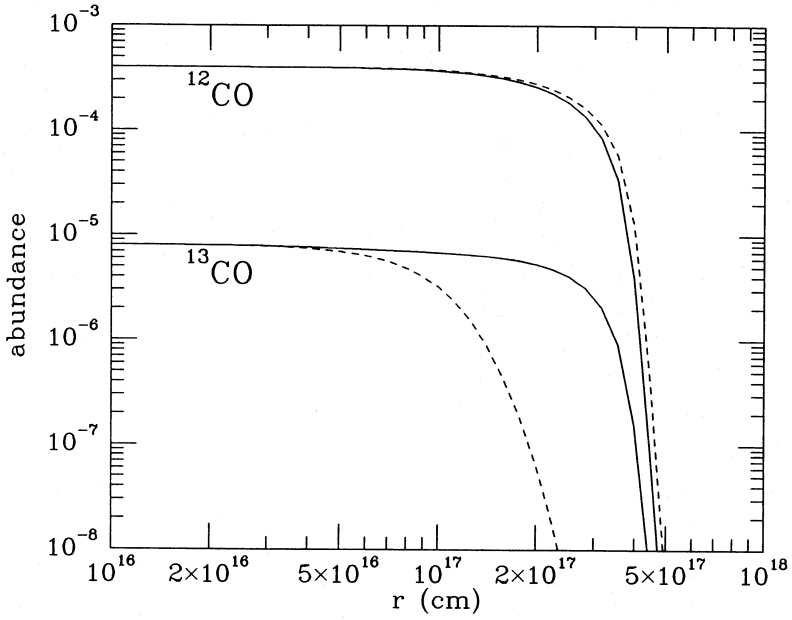

FIG. 7*a*

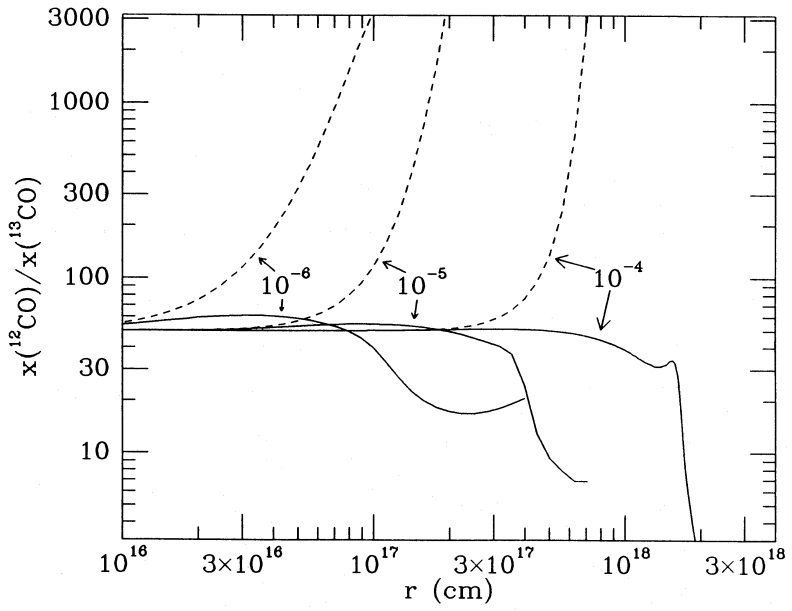

FIG. 7*b*

FIG. 7.—(*a*) The spatial distribution of the ^{12}CO and ^{13}CO abundances with (*solid curves*) and without (*dashed curves*) chemical fractionation for the standard case. (*b*) The same, plotted as a ratio, for a range of mass-loss rates.

tion (*dashed curves*), the transition from ^{13}CO to $^{13}C^+$ occurs at a much smaller radius than the corresponding transition for the more abundant isotope—simply because the smaller abundance of ^{13}CO produces less self-shielding. When fractionation is included (*solid curve*), however, substantial amounts of ^{13}CO are produced in the ^{12}CO transition region and the two distributions become very similar. In other words, fractionation undoes the effects of selective photodissociation. The sizes of the CO distributions can be simply characterized by the one-half radius, defined by $x(r_{1/2})/x_0 = \frac{1}{2}$. For small values of $\dot{M}$ ($< 5 \times 10^{-6}\ M_\odot\ \mathrm{yr}^{-1}$), $r_{1/2}(^{13}CO) < r_{1/2}(^{12}CO)$, whereas for large values of $\dot{M}$ ($> 5 \times 10^{-6}\ M_\odot\ \mathrm{yr}^{-1}$), $r_{1/2}(^{13}CO) > r_{1/2}(^{12}CO)$. However, the difference between the sizes of the ^{12}CO and ^{13}CO distributions is always small, no more than 10% or 20%.

Some of these effects can be seen more clearly in Figure 7*b*, which plots the abundance ratio of the CO isotopes as a function of distance, again with (*solid curves*) and without (*dashed curves*) fractionation. For purposes of clarity, the results for small mass-loss rates are not shown. Without fractionation, the ratio of ^{12}CO to ^{13}CO becomes very large as soon as the ^{13}CO–$^{13}C^+$ transition is reached. This increase is halted by fractionation at a characteristic distance which depends on the mass-loss rate and the temperature distribution. Fractionation reduces the $^{12}CO/^{13}CO$ ratio significantly below its initial value, but only in the tenuous, outer parts of envelopes, where ^{13}CO is difficult to detect. At intermediate distances, where both isotopes can be detected, the theory predicts modest increases in the isotope ratio by up to 20%. For IRC +10216, the theory predicts an essentially constant $^{12}CO/^{13}CO$ ratio out to 3×10^{17} cm (100″ for a distance of 200 pc). Existing measurements of isotope ratios for this envelope have been restricted to on-source observations. It is important to emphasize that the predicted constancy of the $^{12}CO/^{13}CO$ isotope ratio in IRC +10216 is due to the cancellation of strong selective photodissociation (associated with line self-shielding) by strong chemical fractionation.

The results shown in Figure 7 are largely independent of the initial isotope ratio, $R_0 = {}^{12}CO/{}^{13}CO$. When R_0 is varied over the range 5–80 (or greater) keeping $x_0(CO)$ fixed, the ^{12}CO photochain is hardly changed. The shapes of the ^{13}CO and $^{13}C^+$ distributions are only slightly altered, but their absolute values are shifted according to the new value of R_0. The distribution of ^{13}C is affected at intermediate distances but, when R_0 is changed from 5 to 80 for example, the renormalized distributions differ by no more than a factor of 3. The general insensitivity of the distributions to the initial isotope ratio, other than an overall scaling of the ^{13}CO photochain, can be understood in terms of the relevant physical processes and the assumption that $R_0 \gg 1$. At very small distances from the star, there are essentially no carbon ions and the two photochains are independent of one another. At very large distances, the assumption $R_0 \gg 1$ implies that the relatively small abundance of $^{13}C^+$ does not alter the recombination of either $^{12}C^+$ or $^{13}C^+$. Over much of the intermediate range of distances, both the forward and backward rates of equation (10) are fast enough that the fractionation process is equilibrated and the two transitions are locked together.

The above calculations suggest that the CO isotope ratio varies significantly only in the outer parts of circumstellar envelopes where it would be difficult to measure. The effects of selective photodissociation and fractionation might be detected more readily through their effect on species synthesized by ion-molecule reactions initiated by the C^+ ion. The $^{12}C^+/^{13}C^+$ ratio is generally much less than R_0 before the CO to C^+ transitions are complete, i.e., C^+ is fractionated to a significant degree. The most obvious candidates for indirect fractionation by C^+ are hydrocarbon molecules with three carbon atoms such as C_3H and C_3H_2 which are formed by reactions of C^+ and acetylene. In O-rich circumstellar envelopes, the small $^{12}C^+/^{13}C^+$ ratio should have a significant effect on the relative abundances of the HCO^+ isotopes. In this connection, it should also be mentioned that, when R_0 becomes as small as 5, $^{13}C^+$ makes an important contribution to the electron density.

The CO isotope problem can be analyzed with the help of the schematic model of CO photodissociation discussed in § III. However, the lower abundance of ^{13}CO requires the use of a larger oscillator strength, e.g., for the standard parameters $\langle f_d(^{13}CO)\rangle = 0.072$ compared with $\langle f_d(^{12}CO)\rangle = 0.029$. The increase is largely due to the enhanced importance for the rarer isotope of H_2 blocking relative to self-shielding.

V. CONCLUSION

Carbon monoxide is one of the most important constituents of interstellar and circumstellar matter. Its abundance in diffuse interstellar clouds and in the transition regions of dense clouds and circumstellar envelopes is dictated by photodissociation. However, the physics of CO photodissociation by UV radiation has only recently been understood through the new measurements of its absorption and fluorescence cross sections by Letzelter *et al.* (1987). Thus it is now possible to put the theory of these regions on a sound basis.

The transfer of the UV radiation that dissociates CO longward of the Lyman cutoff depends on whether the dissociation occurs by a line or continuum process. The new experiments show that it is lines that dominate, and so the radiation transfer must deal with over 30 CO absorption bands and numerous, nearly coincident lines of atomic and molecular hydrogen. Using the results of Letzelter *et al.*, we find that the CO photodissociation rate in the interstellar medium is $2.0 \times 10^{-10}\ \mathrm{s}^{-1}$, an order of magnitude larger than the rate used in the past. The new rate and a treatment of the radiative transfer and shielding are used to develop a theory for the CO abundance in the circumstellar envelopes of cool, evolved stars, and results are presented on the spatial variation of CO, C, and C^+. As shown in §§ III and IV, these distributions play important roles in determining the observational properties of circumstellar envelopes. Detailed demonstrations of the significance of the new theory of CO photodissociation are given in separate papers dealing with the distribution of CO in IRC +10216 (Huggins, Olofsson, and Johansson 1987) and with circumstellar chemistry (e.g. Mamon, Glassgold, and Omont 1987).

Although substantial progress has been made in understanding the photodissociation of CO on the basis of recent laboratory measurements, considerable additional work still needs to be done. Further experiments are required to identify the spectroscopic properties of the upper states and to measure the widths of the lines. Depending on the precise outcome of these experiments, more accurate treatments of the radiation transfer in circumstellar envelopes may then be required. Considerations similar to those discussed in this paper are also important for the modeling of interstellar clouds (Bally and Langer 1982; Paper I; van Dishoeck and Black 1987). For

example, the recent comprehensive chemical models of diffuse interstellar clouds (e.g., van Dishoeck and Black 1986; Viala, Abgrall, and Roueff 1987) are likely to have difficulty in accounting for the measured column densities of CO when the new and larger CO photodissociation rate is used, and new ways of synthesizing CO may be called for.

We wish to thank M. Eidelsberg and F. Rostas for providing the results of their experimental work on CO before publication and M. Jura, M. Morris, and A. Omont for helpful comments. This research has been supported by NASA grant NAWG-630 (to A. E. G.) and NSF grant AST 86-16646 (to P. J. H.).

APPENDIX

NOTE ON THE MEAN ESCAPE PROBABILITY

The basis for the calculation of the CO photodissociation rate is the mean escape probability introduced in equation (3). In this Appendix we outline its calculation for circumstellar envelopes undergoing steady mass loss. Photodissociation occurs following the absorption of a photon in a transition in which the electronic, vibrational, and rotational quantum numbers change, and we represent such a transition symbolically as $lJ \rightarrow uJ'$. We refer to the set of transitions that occur with fixed values of the initial and final electronic and vibrational quantum numbers as a band and label the band by $i = (l, u)$.

The oscillator strength for the transition $lJ \rightarrow uJ'$ factors into

$$f_{lJ,uJ'} = f_{l,u} f_{J,J'} . \tag{A1}$$

For absorption from the ground state of CO, $f_i \equiv f_{l,u}$ is tabulated in Table 1 and the nonvanishing (normalized) Hönl-London factors are $f_{J,J+1} = (J + 1)/(2J + 1)$ and $f_{J,J-1} = J/(2J + 1)$. The probability for finding the initial rotational state J is specified by a normalized distribution $P(J)$. As discussed in the text, we represent $P(J)$ with a Boltzmann distribution rather than calculating it self-consistently.

The mean escape probability is defined by

$$\langle \beta_i \rangle = \sum_{JJ'} P_J f_{J,J'} \beta_{lJ,uJ'} , \tag{A2}$$

i.e., in terms of the normalized distribution function, $P_J f_{J,J'}$. Following MJ, the escape probability for transition $lJ \rightarrow uJ'$ is approximated simply as

$$\beta_{lJ,uJ'} = f(3/2\tau_{lJ,uJ'}) , \tag{A3}$$

where

$$f(x) = (1 - e^{-x})x^{-1} \tag{A4}$$

and the optical depth is

$$\tau_{lJ,uJ'} = P_J f_{l,u} f_{J,J'} (\pi e^2/mc) \lambda_{lJ,uJ'} V^{-1} C x(r) r^{-1} , \tag{A5}$$

where m is the electron mass, $\lambda_{lJ,uJ'}$ is the wavelength, and $x(r)$ is the CO abundance at radial distance r. This expression is based on the usual formula for the hydrogen density in an envelope with steady mass-loss rate $\dot{M}$ and expansion velocity V,

$$n_{\rm H} = Cr^{-2} \tag{A6}$$

and

$$C = \dot{M}(4\pi m_{\rm H} V)^{-1} . \tag{A7}$$

In the interior of the envelope, where $x(r)$ is constant, the fact that the optical depth is large and inversely proportional to r implies that the mean escape probability and the dissociation rate vary linearly with r, as long as the effects of dust can be ignored.

REFERENCES

Bally, J., and Langer, W. D. 1982, *Ap. J.*, **255**, 143.
Eidelsberg, M. 1987, private communication.
Glassgold, A. E., and Huggins, P. J. 1983, *M.N.R.A.S.*, **203**, 517.
Glassgold, A. E., Huggins, P. J., and Langer, W. D. 1985, *Ap. J.*, **290**, 615 (Paper I).
Glassgold, A. E., Lucas, R., and Omont, A. 1986, *Astr. Ap.*, **157**, 35.
Glassgold, A. E., Mamon, G. A., Omont, A., and Lucas, R. 1987, *Astr. Ap.*, **180**, 183.
Huggins, P. J. 1987, *Ap. J.*, **313**, 400.
Huggins, P. J., and Glassgold, A. E. 1982*a*, *Ap. J.*, **52**, 201.
———. 1982*b*, *A.J.*, **87**, 1828.
Huggins, P. J., Olofsson, H., and Johansson, L. E. B. 1987, in preparation.
Jura, M. 1974, *Ap. J.*, **191**, 375.
Kahane, C., Gomez-Gonzalez, J., Cernicharo, J., and Guelin, M. 1987, *Astr. Ap.*, in press.
Knapp, G. R., and Chang, K. M. 1985, *Ap. J.*, **293**, 281.
Knapp, G. R., and Morris, M. 1985, *Ap. J.*, **292**, 690.
Kwan, J., and Linke, R. A. 1982, *Ap. J.*, **254**, 587.
Langer, W. D., Graedel, T. E., Frerking, M. A., and Armentrout, R. 1984, *Ap. J.*, **277**, 551.
Letzelter, C., Eidelsberg, M., Rostas, F., Breton, J., and Thieblemont, B. 1987, *Chem. Phys.*, **114**, 273.
Mamon, G. A., Glassgold, A. E., and Omont, A. 1987, *Ap. J.*, **323**, 306.
Morris, M., and Jura, M. 1983, *Ap. J.*, **264**, 546 (MJ).
Nejad, L. A. M., Millar, T. J., and Freeman, A. 1984, *Astr. Ap.*, **134**, 129.
Omont, A. 1986, private communication.
Prasad, S. S., and Tarafdar, S. P. 1983, *Ap. J.*, **239**, 151.
Sternberg, A., Dalgarno, A., and Lepp, S. 1987, *Ap. J.*, **320**, 676.
Wannier, P. G., and Sahai, R. 1987, *Ap. J.*, **311**, 335.
Watson, W. D., Anicich, V. G., and Huntress, W. 1976, *Ap. J.* (*Letters*), **205**, L165.
van Dishoeck, E., and Black, J. H. 1986, *Ap. J. Suppl.*, **62**, 109.
———. 1987, in *Physical Processes in Interstellar Clouds*, ed. M. Scholer, in press.
Viala, Y. P., Abgrall, H., and Roueff, E. 1987, in *Astrochemistry*, eds. M. S. Vardya and S. P. Tarafdar (Dordrecht: Reidel), p. 227.
Yoshino, K., Stark, G., Smith, P. L., and Parkinson, W. H. 1987, preprint.

Note added in proof.—As noted above in §§ II and III, large line widths and line blending could introduce aspects of self-shielding that are outside of the theory of radiation transfer used in this paper, which is based on the Sobolev approximation and the assumption that the lines are well separated. We have made a preliminary study of this possibility by representing those bands that appear to be very broadened as uniform absorption continua. According to the qualitative analysis of Viala, Letzelter, Eidelsberg, and Rostas (*Astr. Ap.*, in press [1988]), 13 CO dissociating bands appear to have extremely short lifetimes ($\leq 10^{-12}$). When these bands are treated as dissociating continua, spread over the width of the band, the abundance distributions of the CO photochain are altered somewhat but they retain the essential properties described in this paper. The size of the CO distribution is reduced by $\sim 40\%$ due to the fact that the generally smaller continuum absorption allows the dissociating radiation to penetrate further into the envelope. This effect enhances the conclusion emphasized in the text that the new understanding of CO photodissociation implies considerably smaller circumstellar envelopes than previously considered. Of course this discussion of broadened lines is highly simplified and the conclusions must be regarded as tentative. A more complete investigation must await definitive, high-resolution laboratory studies of the far-UV spectrum of CO.

A. E. GLASSGOLD, P. J. HUGGINS, and G. A. MAMON: Department of Physics, New York University, 2 Washington Place, New York, NY 10003

A.4 The formation of molecules in protostellar winds

Glassgold, Mamon & Huggins, 1991, *ApJ 373, 254–265*

THE ASTROPHYSICAL JOURNAL, 373:254–265, 1991 May 20

THE FORMATION OF MOLECULES IN PROTOSTELLAR WINDS

A. E. GLASSGOLD, G. A. MAMON,[1] AND P. J. HUGGINS
Department of Physics, New York University, 2 Washington Place, New York, NY 10003
Received 1990 September 7; accepted 1990 October 31

ABSTRACT

The production and destruction processes for molecules in very fast protostellar winds are analyzed and modeled with a one-dimensional chemical kinetics code. Radial density and temperature distributions suggested by protostellar theory are explored as are a range of mass-loss rates. The efficiency of in situ formation of heavy molecules is found to be high if the wind temperature falls sufficiently rapidly, as indicated by theory. The degree of molecular conversion is a strong function of the mass-loss rate and of density gradients associated with the acceleration and collimation of the wind. Even in cases where essentially all of the heavy atoms are processed into molecules, a significant fraction of atomic hydrogen remains so that highly molecular, protostellar winds are able to emit the 21 cm line. Although CO has a substantial abundance in most models relevant to very young protostars, high abundances of other molecules such as SiO and H_2O signify more complete association characteristic of winds containing regions of very high density. Although the models apply only to regions close to the protostar, they are in qualitative accord with recent observations at much larger distances of both atomic and molecular emission from extremely high-velocity flow.

Subject headings: molecular processes — stars: pre–main-sequence — stars: winds

1. INTRODUCTION

Both observations and theory support the idea that very high-velocity winds are generated by newly formed protostars. The most direct evidence is the detection of both atomic hydrogen and carbon monoxide at speeds of up to a few hundred km s^{-1} in several low-luminosity protostars (Lizano et al. 1988; Koo 1989). Theoretical notions on the formation of a protostar from an accretion disk also lead to high-velocity winds, generated, for example, by centrifugally driven magnetic stresses (e.g., Shu, Adams, & Lizano 1987). These winds originate close to the protostar and carry fundamental information about the star-formation process out to large distances, where their effects are observed in a variety of phenomena, e.g., in low-velocity, bipolar, molecular outflows (Lada 1985; Snell 1987). Observations also suggest that low-luminosity protostars produce partially recombined winds (Natta et al. 1988). We are thus led to investigate in this paper both the ionization and the molecular properties of the primary winds generated by protostars.

In an earlier paper (Glassgold, Mamon, & Huggins 1989, henceforth Paper I), we concluded that molecular synthesis in protostellar winds can be efficient, in contrast to the work of Rawlings, Williams, & Canto (1988). Our preliminary results were based on ad hoc representations of the wind properties, dictated by the absence of temperature information. Paper I prompted Ruden, Glassgold, & Shu (1990, henceforth RGS) to investigate the heating and cooling of the protostellar winds of very young, low-luminosity protostars, for which the theory is sufficiently developed that the dynamics can be reasonably well-specified (see, e.g., Shu et al. 1987). According to this theory, the protostar and the accretion disk corotate at the protostellar breakup speed so that there is no accretion shock (a condition that is not likely to be satisfied during later stages of protostellar evolution). RGS find that the temperature depends mainly on the chemistry of hydrogen and not on the heavy elements. In principle, the dynamical, thermal, and chemical properties of the wind should be obtained in a completely self-consistent calculation. The complexity of the chemical considerations to be described below and the two-dimensional nature of the hydrodynamics indicate that such calculations would be extremely difficult, if not infeasible, at the present time.

The primary objective of this paper is to describe the physical and chemical considerations that apply in low-luminosity protostellar winds. We illustrate the role of the most important processes with simplified models, especially those suggested by protostellar theory (RGS). In order to develop a basis for applications to other models, we vary the wind parameters and consider particular modifications in the basic model such as the effects of far-UV radiation, which might arise, for example, from an accretion shock. Our results provide insights into the physical conditions that are required for efficient molecular synthesis and on potential molecular diagnostics of protostellar winds.

The organization of the paper is as follows. Section 2 gives a full description of the dynamical model and the underlying physical and chemical processes, including radiation transport. Section 3 presents the results of the calculations, and § 4 summarizes the main conclusions, particularly those relevant to observational studies. The reader interested primarily in the results may wish to first read § 2.1, where the basic models are described, and then skip to § 3.

2. THE MODEL

2.1. *The Physical Model*

We represent the primary wind of a low-luminosity protostar by a steady, spherical flow with density, velocity, and temperature fields, $n(r)$, $v(r)$, and $T(r)$, all *specified* functions of the radial distance r from the center of the protostar. Our objective is to calculate the ionization and the chemical abundances with these functions as "given." This separation of the chemistry from the hydrodynamics is justified in practical terms, i.e., the

[1] Permanent address: DAEC, Observatoire de Meudon, 92195 Meudon Principal Cedex, France.

full problem is too complex. A similar justification underlies the use of one-dimensional flows. However, here we invoke the device of an "equivalent, quasi-spherical" flow (RGS) that incorporates the most important effect of wind collimation, which is to increase the density of the wind near the protostar.

The density $n(r)$ is defined as the volume density of hydrogen nuclei in all species. The velocity is represented as

$$v = u(r)V , \tag{1}$$

where V is the terminal speed of the wind and u describes its acceleration; usually $u < 1$. We assume steady flow and, following RGS, allow for the possibility that, at a distance r, the wind crosses an area $4\pi r^2 A(r)$, with $A < 1$, i.e., only a fraction A of the allowed area. Thus the density $n(r)$ is determined directly by mass conservation and is parametrized by the *hydrogen* mass-loss rate $\dot{M}$ as follows:

$$n(r) = (\dot{M}/4\pi r^2 mV)(1/uA) . \tag{2}$$

In practice we mainly consider three flow cases:

$$\text{Case 1: } A = 1,\ u = 1 , \tag{3a}$$

$$\text{Case 2: } A = 1,\ u = 1 - R_*/r , \tag{3b}$$

$$\text{Case 3: } A = 1 - R_*/r,\ u = 1 - R_*/r . \tag{3c}$$

In Case 1, the flow is started "impulsively" at the stellar radius (R_*) and emerges isotropically; this is the flow assumed in Paper I. Case 2 is more realistic than Case 1 in that the terminal speed is reached over a finite distance of the order of the stellar radius; the flow is still everywhere isotropic. In Case 3, the flow emerges from an infinitesimal (equatorial) region and becomes isotropic at large distances; this case is actually RGS Case 4. The singularities in Case 2 and Case 3 are avoided by starting the integration at the sonic point, as discussed by RGS. The function $1 - R_*/r$ then varies from a/V to 1, where a is the sound speed at R_* and $a \ll V$.

In accord with observations and theory for protostars, (see, for example, the review of Shu et al. 1987 or RGS), typical parameters for low-luminosity protostars are $T_* = 3500$–6500 K, $R_* = 5 \times 10^{11}$–3×10^{12} cm, and $\dot{M} = 10^{-7}$–$10^{-5}\ M_\odot\ \mathrm{yr}^{-1}$. We adopt a "standard" set of parameters suggested by the observationally important protostellar source SSV 13, associated with HH 7 – 11: $T_* = 5000$ K, $R_* = 6.63 \times 10^{11}$ cm, $\dot{M} = 3 \times 10^{-6}\ M_\odot\ \mathrm{yr}^{-1}$; the luminosity is about 50 $L_\odot$. For this set, equation (3) becomes

$$n(r) = 2.4 \times 10^{12}(R_*/r)^2(1/uA)\ \mathrm{cm}^{-3} , \tag{4}$$

and $V/a = 22$. In going from Case 1 to Case 3, the density close to the protostar increases by $(V/a)^2 = 466$ for these parameters and is greater than $10^{15}\ \mathrm{cm}^{-3}$ for Case 3.

Figure 1 shows the RGS temperature distributions for $\dot{M} = 3 \times 10^{-6}\ M_\odot\ \mathrm{yr}^{-1}$. For comparison, we show the ad hoc form introduced in Paper I,

$$\begin{aligned} T &= T_0 \qquad r < R_0 , \\ T &= T_0(R_0/r)^p \quad r > R_0 , \end{aligned} \tag{5}$$

for the choice $p = -4/3$, $T_0 = 5000$ K, and $R_0 = 2R_*$. The RGS distribution for Case 1 has a modest increase at large r, relative to the adiabatic distribution ($T = T_* r^{-4/3}$), due to ambipolar diffusion heating. For Cases 2 and 3, the temperature drops very rapidly at first because of enhanced adiabatic cooling, but then H_2 formation heating and ambipolar diffusion heating reverse this trend. Ambipolar diffusion heating is responsible for keeping the gas warm at large distances and, in Case 3, reheats the gas to 3000 K, high enough to destroy H_2, but not CO, by collisional dissociation.

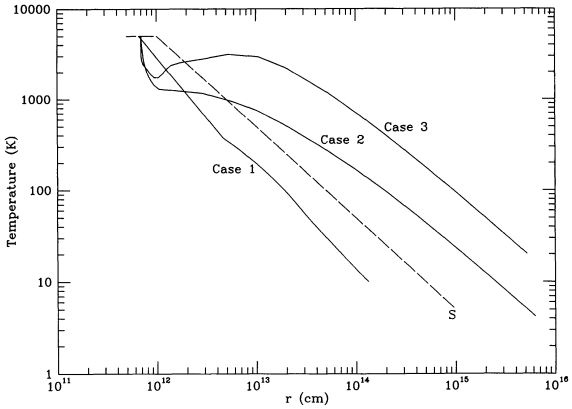

FIG. 1.—Temperature distributions corresponding to the RGS cases defined by equation (3) and $\dot{M} = 3 \times 10^{-6}\ M_\odot\ \mathrm{yr}^{-1}$. The dashed curve, labeled S, is the temperature model used in Paper I.

Another physical property important for the molecular physics of the wind is the radiation field. We assume that the only source of radiation is the protostar, which we treat as a blackbody with (photospheric) temperature T_*. At a distance r, radiative rates are reduced by the standard dilution factor,

$$W(r) = 1/2[1 - (1 - R_*^2/r^2)^{1/2}] \tag{6}$$

and by absorption by various species. We shall take up the calculation of radiative transfer in the wind in § 2.3 and departures from a blackbody in § 3.4.

2.2. *Chemistry and Ionization*

We describe the calculation of the chemical abundances in the wind, assuming that the wind flows from the protostar in the manner described in § 2.1. Electrical neutrality is assumed so that the electron density n_e is the difference between the densities of positive and negative ions. The short dynamical time scale of the flow, typically

$$t_{\mathrm{dy}} = r/v \approx 10^5(r_{12}/v_7)\ \mathrm{s} \tag{7}$$

($r_{12} = r/10^{12}$ cm and $v_7 = v/10^7\ \mathrm{cm\ s}^{-1}$), means that kinetic rather than steady state chemistry is required. Thus the rate equation for species Y has the generic form

$$v\,d/dr\,x(Y) = P(Y) - D(Y)x(Y) \tag{8}$$

where P and D are appropriate production and destruction rates. The initial conditions are calculated for steady state photospheric physical conditions using standard cosmic abundances. Our program reads the input set of chemical reactions and rate coefficients and internally derives the rate equations for each species. The system of rate equations is integrated using Gear's (1971) method for stiff, ordinary differential equations. The integration is performed for the abundances as a function of log r, starting at the stellar surface and integrating outwards. The calculations typically require about 20 minutes of CPU time on a Convex C210 mini-supercomputer.

For the flows in equation (3), the hydrogen density n ranges up to $10^{15}\ \mathrm{cm}^{-3}$ and the temperature T up to 5000 K or more.

Although n and T decrease rapidly with distance, their values in chemically active regions are considerably higher than encountered in interstellar clouds away from star-forming regions. The radiation field and velocity gradient (essentially the inverse of t_{dy} in equation [7]) are also much greater. Thus protostellar wind chemistry involves relatively extreme physical conditions and differs from familiar interstellar chemistry. There are interesting connections with the chemistry of the early universe (Dalgarno & Lepp 1987), with the reformation of molecules behind shocks (Neufeld & Dalgarno 1989a, b), and with the formation of molecules in supernova shells (Lepp, Dalgarno, & McCray 1990; Petuchowski et al. 1989). In the following subsections, we describe the essential aspects of our chemical model. Although the chemistry is reasonably complete, we have had to be judicious in the selection of the included processes because of the heavy computational demands of the radiation transfer.

2.2.1. *Three-Stage Synthesis of Heavy Molecules*

We start with an overview of the chemistry and consider the synthesis of CO, one of the most important molecular diagnostics. Figure 2 is a greatly simplified schematic diagram of the three-stage synthesis of CO described briefly in Paper I. Because the wind is hydrogen-rich and the density and temperature are high, the first step toward molecular synthesis is the formation of H_2, which can be achieved in three ways, which we refer to as the H^-, H_2^+, and three-body routes. The first two dominate for Case 1 (unless $\dot{M} > 10^{-4}\ M_\odot\ \mathrm{yr}^{-1}$) whereas the densities in Cases 2 and 3 are sufficiently high for three-body formation to dominate (unless $\dot{M} < 10^{-7}\ M_\odot\ \mathrm{yr}^{-1}$). In addition to the three progenitor reactions, the full hydrogen chemistry includes reactions that neutralize H^- and H_2^+, that ionize H, and a variety of photo processes to be discussed in § 2.2.3. The ionization of atomic hydrogen occurs by collisional excitation of the $n = 2$ level followed by photoionization from this level by Balmer continuum radiation. The main destruction mechanisms for H^+ are radiative recombination and charge exchange. We forego an extensive discussion of the hydrogen chemistry (other than photo processes) because it is described in full detail in RGS.

Once H_2 is formed, neutral reactions with atomic oxygen produce OH if the wind is warm (the energy barrier is 3940 K) and then CO by reaction of OH with atomic carbon (without any significant energy barrier). A similar three-stage pathway with CH is also shown in Figure 2; it is less effective because of the larger barrier for the formation of CH. Also illustrated in Figure 2 are the fourth-stage molecules O_2 and C_2, each of which can lead to CO by another neutral reaction.

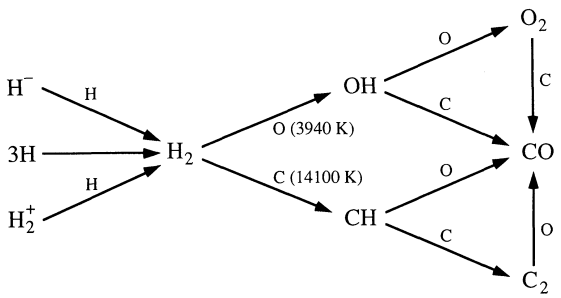

FIG. 2.—Three-stage synthesis of heavy molecules. The numbers under the dashed arrows give the energy barriers for the endothermic reactions, $O + H_2 \rightarrow OH + H$ (3940 K) and $C + H_2 \rightarrow CH + H$ (14,100 K).

Under appropriate circumstances, molecules can also be formed by ion-molecule reactions and by radiative association (for diatomic species). Destruction routes are also critical and we have considered a wide range of processes that include neutral and ionic reactions, collisional dissociation, charge exchange, photoionization and photodissociation, and recombination and neutralization of ions. In the following, we discuss the roles of the different reactions and how we obtained their rate coefficients.

2.2.2. *Neutral Reactions*

The schematic chemistry in Figure 2 indicates the type of neutral reactions that are important in protostellar winds:

$$A + H_2 \rightarrow AH + H\ , \tag{9}$$

$$AH + B \rightarrow AB + H\ , \tag{10}$$

where A, B = O, C, N, S, and Si. The level of laboratory and theoretical information on these types of reactions is mixed, with rather reliable data for reactions of O, C, and S (at and just above $T = 300$ K) and considerably less for N and Si. We rely primarily on the compilations of Baulch et al. (1984) and on the recent theoretical work of Graff and collaborators (Wagner & Graff 1987; Graff & Dalgarno 1987; Leen & Graff 1988; Graff 1989). Even with limited data, some general trends are readily discernible within the set of atoms that we consider. The most important factor is the relatively small energy barrier of the $O + H_2 \rightarrow OH + H$ reaction, which means that reaction (9) leads to the production of much more OH than any other hydride. By contrast, O, C, N, and S all are known to engage readily with OH in reaction (10); Si probably does too, although the rate coefficient has not been measured. The important conclusion here is that OH can be effectively formed from H_2 by reaction (9) and that essentially all of the heavy oxides can be synthesized from OH with reaction (10).

The primary role of three-body, neutral reactions is the synthesis of H_2 (Paper I; RGS). The inverse process of collisional dissociation is potentially important for H_2 and other molecules with vanishing or small dipole moments, notably CO and the homonuclear molecules C_2, N_2, and O_2. This process only occurs rapidly from excited vibrational levels and the rate coefficient k_d is negligible unless the density exceeds some critical value n_{cr} (Roberge & Dalgarno 1982). For H_2, $n_{cr} \approx 10^5$ cm^{-3} (Lepp & Shull 1983), but it is much larger for CO, $\approx 10^{11}$ cm^{-3} (Roberge & Dalgarno 1982). For $n > n_{cr}$, k_d goes over to the high-density, thermal equilibrium limit, presumably also characteristic of laboratory measurements (when they exist).

In practice we use the experimental values for H_2 recommended in the critical review of Cohen & Westburg (1983). We ignore the density dependence of the rate coefficients because $n \gg n_{cr}$ in the chemically active regions of protostellar winds. Furthermore, k_d has a temperature barrier of about 53,000 K in this case, which cuts in before the dependence associated with n/n_{cr}. In the absence of any information on the collisional dissociation rates of other homonuclear molecules, we use the same rates as for H_2 but with barriers determined by the dissociation energies. For CO, we use the high-density theoretical calculation of Roberge & Dalgarno (1982) whenever the initial density is greater than 10^{11} cm^{-3}. The large temperature barrier ($\approx$97,000 K) helps to suppress the effect of CO collisional dissociation as does destruction by the chemical reaction, $H + CO \rightarrow OH + C$, which has a barrier of 77,500 K.

Similar reactions play an even more important role in destroying O_2, C_2, and N_2 because of the smaller energy barriers. Our approximate treatment of CO collisional dissociation overestimates its effect in cases where the density in the region of CO formation is about the same as the critical density. For example, in Case 1 for the standard mass-loss rate, our calculation of the freeze-out abundance of CO may be too small by a factor of 2 because we ignore the cutoff of this process for $n < n_{cr}$.

2.2.3. *Ionic Reactions*

Ion-molecule reactions familiar in interstellar chemistry supplement molecular synthesis in protostellar winds that do not recombine strongly. The primary ions in such winds are atomic rather than molecular and they are produced by the protostellar radiation field. Although H_2^+ is important in the synthesis of H_2, its abundance is generally quite small (usually $< 10^{-10}$). Consequently only a small amount of H_3^+ is made by the reaction

$$H_2^+ + H_2 \rightarrow H_3^+ + H \,. \quad (11)$$

A more important molecular ion is CO^+, which is produced by

$$C^+ + OH \rightarrow CO^+ + H \,, \quad (12)$$

and produces CO by charge exchange with atomic hydrogen

$$CO^+ + H \rightarrow CO + H^+ \,. \quad (13)$$

Some HCO^+ is formed by the reaction

$$CO^+ + H_2 \rightarrow HCO^+ + H \,. \quad (14)$$

The most abundant molecular ion after H_2^+ is generally OH^+, which is formed by the ion-molecule reaction

$$O^+ + H_2 \rightarrow OH^+ + H \,, \quad (15)$$

and, somewhat more efficiently, by charge-exchange

$$H^+ + OH \rightarrow OH^+ + H \,. \quad (16)$$

Where there are enough ions for these processes to be interesting, the H_2 abundance is too small to make much H_2O^+ and the OH^+ is destroyed by dissociative recombination, which is a very rapid process for the ionization levels characteristic of these winds. Thus reaction (15) fails to lead to heavy-molecule synthesis, and reaction (16) effectively destroys OH. This conclusion applies fairly generally because H^+ is able to charge-exchange with many molecules.

In addition to charge exchange with molecules (which leads to their destruction by dissociative recombination following charge exchange), purely atomic charge exchange

$$A^+ + B \rightarrow B^+ + A \quad (17)$$

is crucial for the correct calculation of the ionization of the wind. Only a few of the relevant charge-exchange rate coefficients have been measured or even studied theoretically in any detail. In the absence of any better information, we rely on the educated theoretical guesses of Pequignot & Aldrovandi (1986). We list the charge-exchange reactions in Table 1; the energy barriers for the reverse reactions are taken as the differences in the ionization potentials. The most important charge exchange reactions are H^+ with O and Fe for which, fortunately, some experimental results exist. For the $H^+ + O$ rate coefficient, we use the theoretical temperature variation of Chambaud et al. (1980) which agrees with the room temperature measurement of Fehsenfeld & Ferguson (1972). The

TABLE 1

ATOMIC CHARGE-EXCHANGE CHART[a]

	Atom							
Ion	H	C	S	Si	Fe	Mg	Al	Na
O^+	0.18[b]	0	0	0	2.9[b]	0	0	0
H^+		0	3	0	7.4[c]	0[d]	3	0
C^+			0	1	3	0	0.3	0
S_+					3	0	0	0
Si^+					3	1	3	0
Fe^+						3	1	3
Mg^+							0	0
Al^+								0

[a] Units for rate coefficients are 10^{-9} cm^3 s^{-1}.

[b] Measured value for $H^+ + O$ at 300 K (Fehsenfeld & Ferguson 1972) supplemented by theory (Chambaud et al. 1980) at other temperatures.

[c] Measured value at $T = 300$ K (Rutherford & Vroom 1972).

[d] We use the theoretical result of Allan et al. (1988), $1.25 \times 10^{-9} \exp(-22{,}100\ \mathrm{K}/T)$.

$H^+ + Fe$ charge exchange cross section was measured at high energies (more than 8 eV) by Rutherford & Vroom (1972) and extrapolated by them to much lower energies using theory; we use their $T^{-0.5}$ dependence for $T < 5000$ K. Charge-exchange greatly reduces the abundance of H^+ and causes the ionization to be transferred to heavier atomic ions which can survive longer in the wind. This tendency is assisted by the reduction in the shielding of various ionizing continua that results from the ionization of the atoms. Charge-exchange ensures that the ionization level remains moderately high even for high-density winds.

2.2.4. *Radiative Reactions*

Two-body association accompanied by the emission of radiation can form heavy molecules as well as the progenitor species H^- and H_2^+ (paper I; RGS). Although the characteristic rate coefficients are small, $\approx 10^{-18}$–10^{-17} cm^3 s^{-1}, this process can be effective in the cooler parts of the wind where other production mechanisms are shut off. We list the radiative association reactions in Table 2. Radiative recombination of electrons and ions is a much better studied process, and the rates we adopt are similar to those used by others.

2.3. *Photoprocesses*

Ultraviolet photons from the protostar ionize the atoms and dissociate the molecules of the wind. Because we are concerned with very young, highly embedded protostars, we neglect the interstellar radiation field and Galactic cosmic rays. Table 3 lists the photoprocesses that we consider and the sources for the cross sections, which are mainly for the ground state of the

TABLE 2

ATOMIC RADIATIVE ASSOCIATION RATES

System	Rate (cm^{-3} s^{-1})	Reference
O + H	6.2(−19)	Smith & Zweibel (1976)
C + H	1.5(−18)	Brooks & Smith (1974)
Si + H	1.5(−19)	Adapted from carbon
C^+ + H	1.7(−17)	Graff et al. (1983)
C + O	2.6(−17) exp(−1450 K/T)	Dalgarno, Du, & Yu (1990)
C^+ + O	2(−18)	Dalgarno, Du, & Yu (1990)
Si + O	2(−17)	Adapted from carbon
Si^+ + O	2(−18)	Adapted from carbon

TABLE 3

PHOTO RATES[a]

Reaction	Typical Rate	Reference
$H\ (n=2) \rightarrow H^+$	3.63 (3)	Karzus & Latter (1961)
$H^- \rightarrow H + e$	5.21 (5)	Wishart (1979)
$H_2^+ \rightarrow H^+ + H$	3.87 (3)	Argyros (1974)
$H_2 \rightarrow H + H$	2.10 (−5)	Stephens & Dalgarno (1972)
$CO \rightarrow C + O$	5.43 (−4)	Letzelter et al. (1987)
$SiO \rightarrow Si + O$	0.470	Adapted from CO
$OH \rightarrow O + H$	0.442	van Dishoeck & Dalgarno (1984)
$H_2O \rightarrow OH + O$	2.04	Hudson (1971); Lee (1984)
$O_2 \rightarrow O + O$	0.819	Black & Smith (1984)
$CH \rightarrow C + H$	16.4	van Dishoeck (1987)
$C_2 \rightarrow C + C$	1.74 (−4)	Pouilly et al. (1983)
$C\ (n=1) \rightarrow C^+ + e$	4.89 (−4)	Escalante & Victor (1990)
$C\ (n=2) \rightarrow C^+ + e$	7.90 (−3)	Escalante & Victor (1990)
$C\ (n=3) \rightarrow C^+ + e$	1.88 (−2)	Escalante & Victor (1990)
$C\ (n=4) \rightarrow C^+ + e$	4.66	Escalante & Victor (1990)
$Si \rightarrow Si^+ + e$	0.993	Hudson & Kieffer (1971)
$S \rightarrow S^+ + e$	2.69 (−2)	Tondello (1972)
$Mg \rightarrow Mg^+ + e$	9.98 (−2)	Hudson & Kieffer (1971)
$Fe \rightarrow Fe^+ + e$	0.184	Kelly & Ron (1972)
$Al \rightarrow Al^+ + e$	1.07 (2)	Roig (1975)
$Na \rightarrow Na^+ + e$	0.905	Hudson & Kieffer (1971)

[a] At $1.05R_*$ for a $T_* = 5000$ K blackbody; units are s^{-1}.

species and are well established. The third column of Table 3 gives the rate at the photosphere (R_*) for $T_* = 5000$ K.

Because photoreactions often dominate the ionization of these winds, it is important to treat the transfer of the UV radiation self-consistently. Stellar photons can be absorbed and scattered by atoms and molecules and by dust grains. The corresponding cross sections generally depend on wavelength and a wavelength-dependent treatment of the radiative transfer is called for. In our model, we divide the UV spectrum into a finite number N_{abs} of bands and calculate averages over the photoabsorption cross section for each species in each band. For this purpose, we tabulate the cross sections referred to in Table 3 and fit them with cubic-splines in log-log space for greater accuracy. When necessary, the tabular data is extrapolated assuming a constant slope in log-log space.

Our program allows for the incorporation of dust opacity although we have not included it in the present calculations. RGS did consider the possibility that dust might heat the gas and found that it had little effect. The formation of dust could have some chemical consequences at distances from the protostar of the order of $10R_*$, e.g., it could increase the UV opacity for wavelengths where the atoms are ineffective. Dust might also reduce the ionization of the outer wind by neutralizing the atomic ions that are the dominant source of ionization far from the protostar. We have chosen not to include dust formation at this time because it mainly forms outside the region of rapid molecule formation.

The unshielded photorates are computed from cross sections by integration with the spectral distribution of the flux, most often a blackbody spectrum. Labeling the wavelength bands by k, the photorate for species j at a distance r from the protostar is

$$g_j(r) = W(r)\Sigma_k g_{j,k}^{(0)} \exp\left[-\tau_k(r)\right], \quad (18)$$

where W is the dilution factor of equation (6) and $g_{j,k}^{(0)}$ is the unshielded rate evaluated at the photosphere; the optical depth for band k is a sum over species j:

$$\tau_k(r) = \Sigma_j \tau_{j,k}(r), \quad (19)$$

$$\tau_{j,k}(r) = \int_{R_*}^{r} dr' x_j n(r) \sigma_{j,k}, \quad (20)$$

where $\sigma_{j,k}$ is the average absorption cross-section of species j in wavelength band k.

In principle, the calculation of photorates should take into account the population of excited states. Because of the large computational demands of such calculations in a chemical kinetics program, we generally assume that photodestruction occurs from the ground state, with three exceptions: H, C, and H_2. For atomic hydrogen, most of the photoionization occurs from the first excited level, so we include both the $n = 1$ and $n = 2$ levels (Paper I, RGS). Atomic carbon is the single most important far-UV shielding species and we include photoionization from and recombination to its first three excited electronic levels as well as the ground level. We calculate the population of the levels in a fully kinetic manner, including collisional excitation and de-excitation and chemical reactions as well as the radiative processes just mentioned.

Photodissociation of thermally equilibrated H_2^+ occurs from a large number of excited vibrational levels. Because of the small Einstein A-values, thermal equilibrium is a good approximation in the inner wind where the peak abundances of H_2^+ occur. We have tabulated the thermally averaged cross sections of Argyros (1974) as a function of wavelength and temperature, and have fit log-log cubic splines to these data, extrapolating with a constant slope in log-log space when necessary. The photorates are computed by integrating out to 36,000 Å, which yields an accuracy typically better than 5%. Photodissociation is the most important destruction mechanism for H_2^+ and it is not suppressed very significantly by shielding by other species as are most other molecules. For a protostar with a 5000 K blackbody spectrum, the photodestruction time scale for H_2^+ in gas with a kinetic temperature of 5000 K is 10^{-3} s.

The calculation of the shielding of the ionizing and dissociating radiation is done self-consistently using the method of Mamon, Glassgold, & Omont (1987) where the differential form of equation (20) is integrated for each band simultaneously with the chemical rate equations. If N_{abs} is the number of absorbers, l_{max} the number of bands, and N_{sp} the number of chemical species, then altogether we integrate $N_{sp} + l_{max} N_{abs}$ equations, or about 250 in practice. For purposes of simplicity, we treat all molecular shielding as a continuum process. Although H_2 and CO photodissociation occur through lines, our approximation makes little difference because the relevant 900–1000 Å wavelength band is so heavily blocked by atomic absorption, especially by carbon and sulfur.

3. RESULTS

In this section we present results for the models introduced in § 2. The three cases defined in equation (3) represent a sequence of increasing physical complexity and, presumably, of increasing realism in modeling very young, low-mass protostars. For each case we calculate the abundances for mass-loss rates, $\dot{M} = 3 \times 10^{-7}$, 3×10^{-6}, and $3 \times 10^{-5}\ M_\odot\ yr^{-1}$. Because the three cases differ in their velocity and temperature fields, the grid of nine basic calculations provide a good idea of how the results depend on the most important physical variables: temperature, density, and flow velocity. The asymptotic

TABLE 4

ASYMPTOTIC ABUNDANCES

	CASE 1			CASE 2			CASE 3		
$\dot{M}$	3 (−7)	3 (−6) ($M_\odot$ yr^{-1})	3 (−5)	3 (−7)	3 (−6) ($M_\odot$ yr^{-1})	3 (−5)	3 (−7)	3 (−6) ($M_\odot$ yr^{-1})	3 (−5)
H	1.0	1.0	0.99	1.0	1.0	0.72	1.0	1.0	0.18
H_2	5.0−6	2.1−6	5.2−3	1.1−5	1.5−3	1.4−1	3.5−7	8.2−6	4.1−1
x_e	1.4−4	7.5−5	5.5−6	1.2−4	4.3−5	7.0−6	2.8−4	8.5−5	7.3−6
C	4.0−4	4.0−4	0	3.9−4	0	0	3.8−4	8.5−12	0
C^+	3.8−11	0	0	1.1−11	0	0	2.8−5	0	0
CO	2.8−7	7.9−6	4.0−4	1.1−5	4.0−4	4.0−4	5.9−7	4.0−4	4.0−4
CH	7.0−12	7.2−11	0	6.8−12	0	0	6.7−12	2.9−18	0
C_2	3.1−12	3.6−11	0	3.4−12	0	0	1.9−12	0	0
O	8.0−4	7.9−4	1.6−4	7.9−4	3.6−4	2.2−8	8.0−4	3.8−4	4.4−11
OH	2.2−10	4.1−9	2.6−8	2.2−10	7.3−9	2.6−12	2.2−10	1.1−8	1.3−15
H_2O	0	0	8.2−5	0	6.8−19	3.6−4	0	7.0−12	3.6−4
O_2	4.2−16	2.3−11	5.8−5	1.5−12	9.1−8	6.6−10	2.4−12	6.7−8	3.1−12
Si	1.2−7	2.6−5	0	3.0−8	5.2−16	0	2.4−8	1.3−5	0
Si^+	3.7−5	1.1−5	0	3.7−5	0	0	3.8−5	7.4−6	0
SiO	2.2−14	3.7−10	3.8−5	2.4−14	3.8−5	3.8−5	3.8−15	1.7−5	3.8−5
S^+	1.6−5	0	0	3.8−10	0	0	1.8−6	3.4−10	0
Mg^+	3.8−5	3.6−5	6.0−9	4.0−5	3.7−5	4.6−6	4.0−5	4.0−5	4.9−6
Fe^+	3.3−5	2.2−5	0	3.4−5	2.5−7	0	3.4−5	3.3−5	0
Al^+	3.2−6	3.2−6	3.2−6	3.2−6	3.2−6	9.1−8	3.2−6	3.2−6	9.6−8
Na^+	2.3−6	2.3−6	2.3−6	2.3−6	2.3−6	2.3−6	2.3−6	2.3−6	2.3−6

abundances of representative species for these models are summarized in Table 4. In § 3.4, we investigate the effects of varying the radiation field.

3.1. *Case 1: Isotropic, Impulsive Wind*

Case 1 is similar to the model discussed in Paper I. The wind expands isotropically at constant velocity and the temperature decreases monotonically with distance. The relatively small departures from an adiabatic fall-off calculated by RGS have little effect on the chemistry because they occur at large distances where the chemistry is frozen out. For Case 1 and $\dot{M} = 3 \times 10^{-6}\ M_\odot\ \mathrm{yr}^{-1}$, Figure 3 illustrates the radial variation in the wind of the abundances of representative species. Compared with the corresponding Figure 1 of Paper I, the abundances of H_2 and CO are about the same order of magnitude, 10^{-5}, but now the abundance of SiO is much smaller due to the implementation of a full rather than the earlier, schematic silicon chemistry. Another major difference is the rapid decline in the abundance of H^+ at $2R_*$ due to the inclusion of many more charge exchange reactions. The abundances of the $n = 2$ level of hydrogen and H_2^+ (which are not shown) also decrease rapidly. The bulk of the carbon is atomic throughout the wind and S^+, which is produced by charge-exchange of H^+ and S, recombines as soon as H^+ disappears. Among the other heavy ions, only Si^+ recombines completely (by $200R_*$) so that the electron fraction is of order 10^{-4} throughout much of the envelope. The asymptotic values of many of the calculated abundances are given in the third column of Table 4. The substantial asymptotic abundances of the radical hydrides, OH and CH, and of the molecules synthesized from them are due to radiative association.

Figure 3 describes a wind that is still basically atomic; the density for $\dot{M} = 3 \times 10^{-6}\ M_\odot\ \mathrm{yr}^{-1}$ is too small to produce short chemical time scales, and the chemistry is incompletely developed. Although the asymptotic fraction of carbon atoms in molecules (0.02) is small, it is much larger than that of hydrogen (4×10^{-5}). This difference reflects primarily the difference in binding energy between CO and H_2. For the temperature range expected for young, low-mass, protostellar winds (RGS), collisional dissociation of CO is much more strongly suppressed than for H_2. Table 4 shows the sensitive dependence of the chemistry on the mass-loss rate; the degree

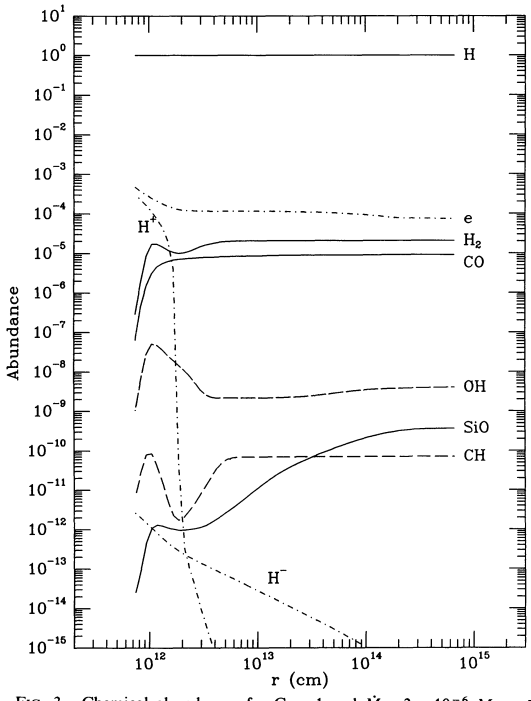

FIG. 3.—Chemical abundances for Case 1 and $\dot{M} = 3 \times 10^{-6}\ M_\odot\ \mathrm{yr}^{-1}$. Ionic abundances are represented by dot-dashed lines; the solid and dashed lines are used to distinguish the neutral species.

of molecular synthesis is smaller for the lower mass-loss rate, $\dot{M} = 3 \times 10^{-7}\ M_\odot\ \mathrm{yr}^{-1}$ [$x(\mathrm{CO})/x_\mathrm{C} \rightarrow 7.5 \times 10^{-4}$], but, for $\dot{M} = 3 \times 10^{-5}\ M_\odot\ \mathrm{yr}^{-1}$, it is almost complete for CO and SiO. For the highest mass-loss rate, none of the carbon or silicon is left in atoms or radicals at large distances, whereas only 0.005 of the hydrogen is in H_2, i.e., the wind is still atomic from the point of view of hydrogen. The situation with oxygen is different, in that the residual oxygen left over from the synthesis of CO is divided among O and H_2O but a significant amount remains in OH [$x(\mathrm{OH}) \simeq 4 \times 10^{-8}$]. The extent to which any oxygen is outside of H_2O measures the incompleteness in the chemical evolution. The ionization fraction is significantly reduced in this case (the highest mass-loss rate, $3 \times 10^{-5}\ M_\odot\ \mathrm{yr}^{-1}$) because all of the heavy ions except Al^+ and Na^+ recombine. These ions are the most resistant to recombination because the corresponding thresholds for atomic photoionization occur at long wavelengths (beyond 2000 Å) where the protostellar flux is relatively large and where other, more abundant atoms, cannot shield the ionizing radiation.

3.2. *Case 2: Isotropic, Accelerated Wind*

This model is more realistic than Case 1 in that it includes wind acceleration. The most important consequences for the chemistry are that the dynamical time scale and the density are each increased by a factor of V/a at the base of the wind (where V = terminal speed and a = sound speed), which is a factor of 22 in these calculations. Because the chemical time scale is decreased and the dynamical time increased by this same factor, molecular synthesis is much more efficient than in Case 1 for the same mass-loss rate. The temperature distribution also changes so there is some potential for lower molecular abundances because the temperature is generally higher than in Case 1. However, the RGS temperature distributions are all monotonically decreasing for this case and, most important, fall even more rapidly near the protostar than in Case 1. Thus, relative to Case 1, the density increase dominates the changes in the chemistry because the photoprocesses remain at about the same rate.

As can be seen from Table 4, the CO abundance reaches a substantial level, $\approx 10^{-5}$, for the lowest mass-loss rate, $\dot{M} = 3 \times 10^{-7}\ M_\odot\ \mathrm{yr}^{-1}$, but the abundances of all the other molecules are low. This calculation illustrates again how a poorly collimated wind with a modest mass-loss rate can be essentially atomic and moderately ionized ($x_e \approx 10^{-4}$) but still have CO as the only molecule with a substantial abundance. Once the mass-loss rate reaches $\dot{M} = 3 \times 10^{-6}\ M_\odot\ \mathrm{yr}^{-1}$, however, all of the available carbon and silicon are in CO and SiO, as shown in Figure 4. Most of the residual oxygen is in O and there is also some in OH, but there is very little in O_2 and H_2O which, under these conditions, are unable to compete with CO and SiO for oxygen. The ionization level is moderate because several ions are unrecombined, as given in Table 4. For $\dot{M} = 3 \times 10^{-5}\ M_\odot\ \mathrm{yr}^{-1}$, illustrated in Figure 5, essentially all of the heavy molecules are processed into their most stable forms. There are few radicals and the ionization level is small, again with only Al^+ and Na^+ unrecombined. It is interesting that the fraction of protons frozen out in H_2 is still only 30% for this mass-loss rate. The large abundance of molecular hydrogen is due to three-body formation, which dominates the other two formation channels (see Fig. 2) because the density close to the protostar is very large, $\approx 10^{14}\ \mathrm{cm}^{-3}$. Ion-molecule reactions are now unimportant in the synthesis of the heavier molecules.

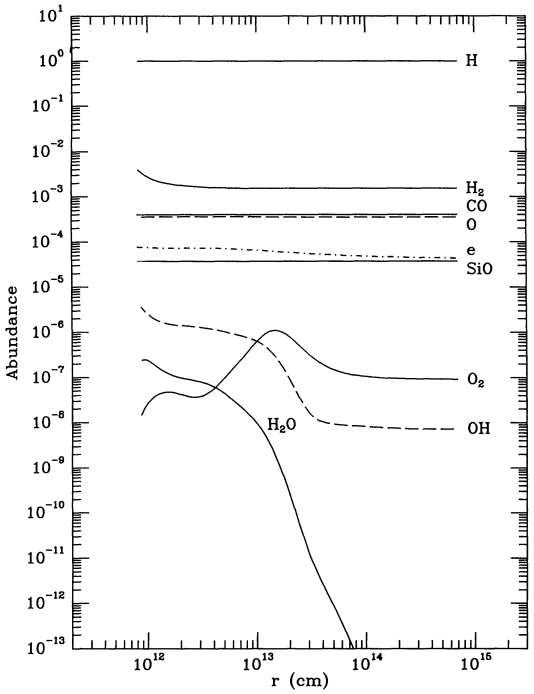

FIG. 4.—Chemical abundances for Case 2 and $\dot{M} = 3 \times 10^{-6}\ M_\odot\ \mathrm{yr}^{-1}$

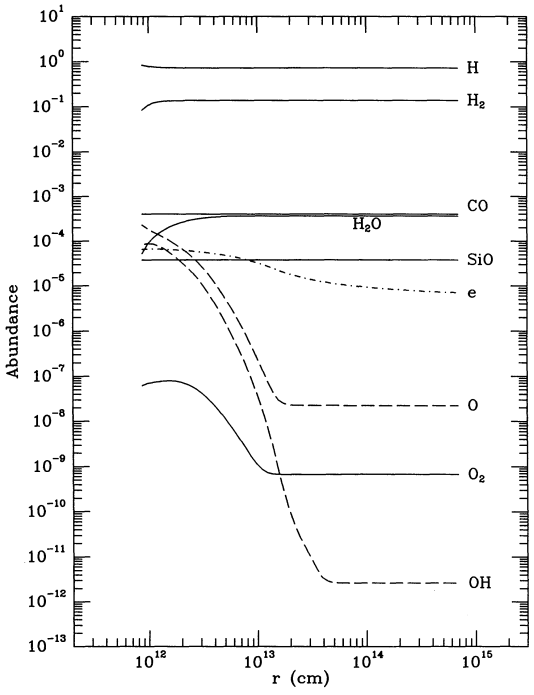

FIG. 5.—Chemical abundances for Case 2 and $\dot{M} = 3 \times 10^{-5}\ M_\odot\ \mathrm{yr}^{-1}$

3.3. *Case 3: Collimated, Accelerated Wind*

This case is closest to the theoretical models of very young, low-mass protostars developed by Shu et al. (1988). Relative to Case 2, the density at the photosphere is another factor of V/a larger due to the area factor in equation (2). Thus the trend toward efficient neutral molecular synthesis is further enhanced. Another implication of the higher density is that the formation and destruction of molecular hydrogen can now have perceptible thermal effects. Collisional destruction of H_2 cools the gas whereas three-body formation heats the gas because the newly formed (vibrationally excited) molecules are collisionally de-excited at high density. The results of the thermal calculations of RGS in Figure 1 for the intermediate mass-loss rate, $\dot{M} = 3 \times 10^{-6}\ M_\odot\ \mathrm{yr}^{-1}$, illustrate these effects. RGS also found that ambipolar heating may reheat the gas sufficiently for the H_2 balance to favor collisional dissociation. The reheating depends on the density and the ionization, the latter because ambipolar heating is inversely proportional to x_e. For the case illustrated in Figure 1, the residual ionization is due to unrecombined Na^+, i.e., $x_e \approx 10^{-6}$, because H^+ recombines close to the protostar. RGS found even greater reheating for $\dot{M} = 3 \times 10^{-7}\ M_\odot\ \mathrm{yr}^{-1}$ (to $\approx$4500 K) but, for $\dot{M} = 3 \times 10^{-5}\ M_\odot\ \mathrm{yr}^{-1}$, ambipolar diffusion heating merely reduces the rate of decrease in the temperature.

A further consequence of the extremely high initial wind densities in this case is that our integration method becomes difficult to use for mass-loss rates greater than $\dot{M} = 3 \times 10^{-6}\ M_\odot\ \mathrm{yr}^{-1}$, corresponding to initial densities greater than $10^{14}\ \mathrm{cm}^{-3}$. As described in § 2, in addition to integrating several hundred chemical rate equations, many with highly disparate time scales, we also implement multiband radiation transfer for each photo-process. The deterioration in our numerical integration capability is manifested by an increased sensitivity to the initial conditions. In order to carry out the calculations for $\dot{M} = 3 \times 10^{-6}\ M_\odot\ \mathrm{yr}^{-1}$, we start the integrations at somewhat larger radial distances than in the previous cases. Starting at 1.0×10^{12} cm, instead of 6.9×10^{11} cm, for example, means that the initial density is reduced by a factor of 2.5. This has little effect on the final results because the density is still so high that steady state conditions apply at the start of the integration. We have checked our results by redoing the calculations for a purely neutral chemistry starting at R_* and find essentially the same asymptotic molecular abundances.

Figure 6 shows our results for $\dot{M} = 3 \times 10^{-6}\ M_\odot\ \mathrm{yr}^{-1}$. In this case, the temperature (shown in Fig. 1) decreases very rapidly to a minimum of $\approx$1750 K at $2R_*$ and, because of H_2 formation and ambipolar diffusion heating, reaches a maximum of $\approx$3130 K at about $10R_*$. As found by RGS, the H_2 abundance is reduced from 0.1 to $\approx 10^{-5}$ by reheating. A similar effect is found for OH and even more so for O_2 and H_2O, which are closely linked to OH. Unlike H_2, the abundances of these three oxygen molecules increase again as the temperature drops, but they are more or less frozen beyond 1000 R_*. On the other hand, CO is unaffected by reheating and SiO is reduced by only a factor of 2; the wind beyond $10R_*$ has roughly equal amounts of SiO and Si.

The results for $\dot{M} = 3 \times 10^{-7}\ M_\odot\ \mathrm{yr}^{-1}$ shown in Figure 7 illustrate the effects of even greater reheating from a temperature minimum of 1350 to 4500 K. In this case, SiO is greatly reduced and even CO has an abundance of only 5×10^{-7}. The high electron fraction in Figure 7 raises the question of whether reheating by ambipolar diffusion really

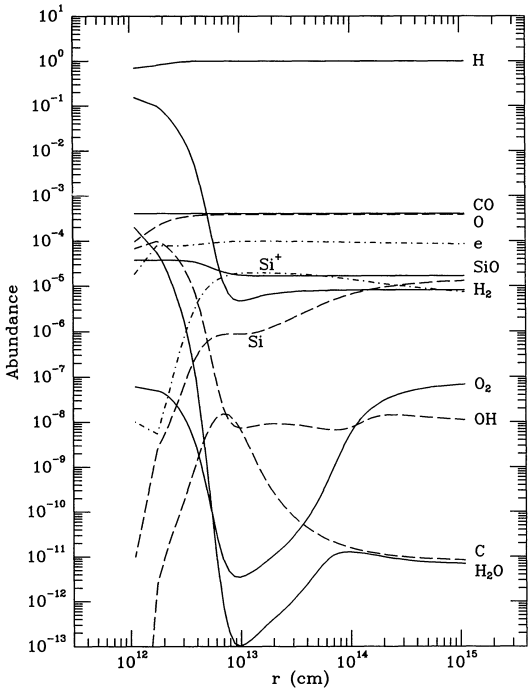

FIG. 6.—Chemical abundances for Case 3 and $\dot{M} = 3 \times 10^{-6}\ M_\odot\ \mathrm{yr}^{-1}$

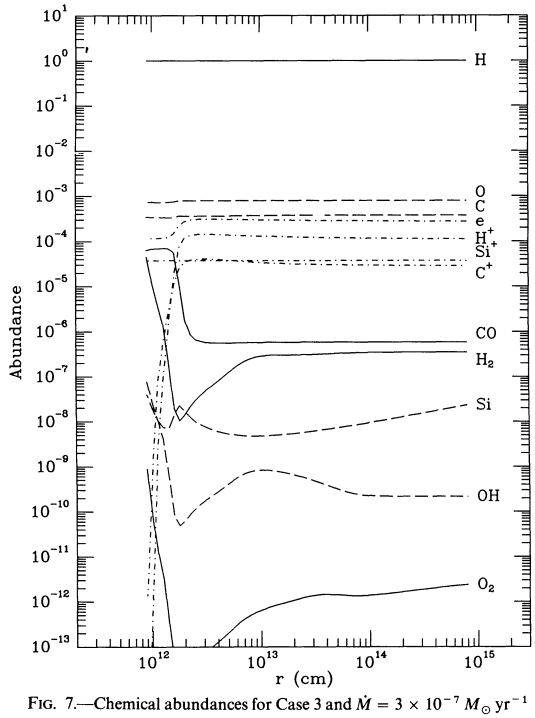

FIG. 7.—Chemical abundances for Case 3 and $\dot{M} = 3 \times 10^{-7}\ M_\odot\ \mathrm{yr}^{-1}$

produces effects as large as those obtained by RGS. In the present calculations, we include the ions of C, S, Si, Mg, Fe, and Al, as well as Na, and find that $x_e \approx 10^{-4}$, in contrast to RGS who assumed $x_e = x_{Na} = 2.3 \times 10^{-6}$. Our large electron fraction arises because only C^+ and S^+ recombine, although Si^+ recombines partially for $\dot{M} = 3 \times 10^{-6}\ M_\odot\ yr^{-1}$. Factors of 40 or 50 in x_e make a big difference in the thermal balance and suggest that the extreme reheating may be an artifact of the low electron fraction assumed by RGS.

In order to further understand the effects of reheating on the chemistry, we calculated the molecular abundances for $\dot{M} = 3 \times 10^{-7}\ M_\odot\ yr^{-1}$ without reheating by assuming that the temperature falls monotonically and joins smoothly onto the asymptotic form given by RGS (Appendix C) appropriate to $x_e = 1.2 \times 10^{-4}$. The abundances shown in Figure 8 show fewer effects of reheating and 20% of the carbon is in CO.

Finally, the results for the largest mass-loss rate, $\dot{M} = 3 \times 10^{-5}\ M_\odot\ yr^{-1}$, using the RGS temperature distribution are shown in Figure 9. Again we start the integration at 10^{12} cm. In this case, RGS predict little reheating and the wind is essentially molecular. All of the heavy atoms are in the molecules, CO, H_2O, and SiO, etc., and 75% of the protons are in H_2. The remaining 25% in atomic hydrogen might, of course, be observable at 21 cm. Most of the atomic ions are recombined; in addition to Na^+, 20% of the magnesium remains ionic. Thus the RGS estimate of x_e is only a factor of 3 too high and the theoretical calculation of the temperature should hold.

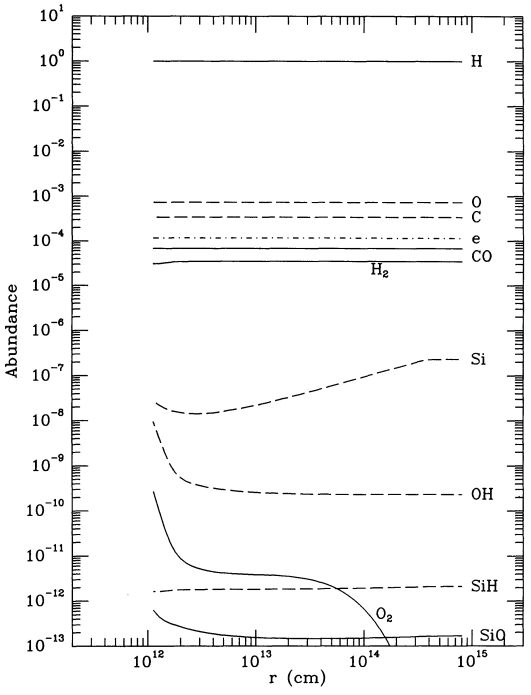

FIG. 8.—Chemical abundances for Case 3 and $\dot{M} = 3 \times 10^{-7}\ M_\odot\ yr^{-1}$ for a modified temperature distribution without reheating.

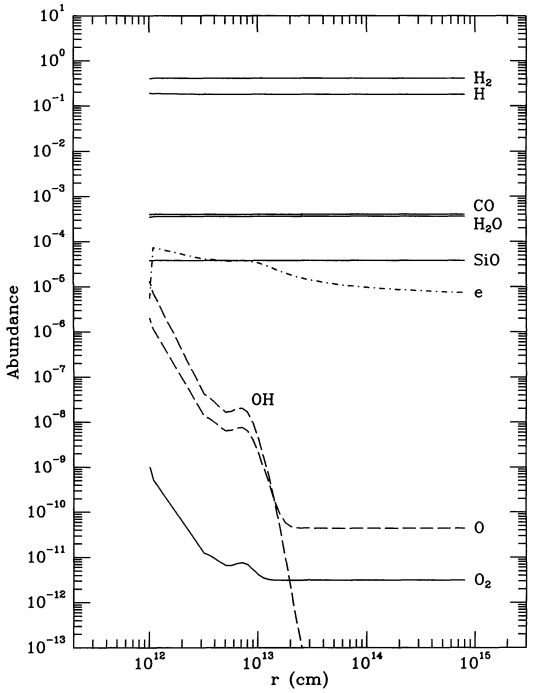

FIG. 9.—Chemical abundances for Case 3 and $\dot{M} = 3 \times 10^{-5}\ M_\odot\ yr^{-1}$

3.4. *Variations in the Radiation Field*

It is obvious that the inner protostellar wind is exposed to a very large radiation field. Its effects can be seen in the occurrence of some very large photorates in Table 3 for a 5000 K blackbody spectrum. Because the density is also large, a proper comparison with other (particle) reaction rates in different astrophysical situations involves the ratio G/n, where G is a photorate and n is the density. In these terms, photo processes that depend on the far-UV band from 900–1100 Å, for example H_2 and CO photodissociation, are weaker than in the diffuse interstellar medium whereas those that depend on the 1200–2000 Å band, for example H_2O photodissociation and heavy element photoionization, are stronger. In this section, we introduce variations in the protostellar radiation to study how departures from the standard 5000 K blackbody spectrum affect our results.

We first consider changes in the blackbody temperature T_*. The first three columns of Table 5 offer a comparison between $T_* = 4000$, 5000, and 6000 K for Case 2 and $\dot{M} = 3 \times 10^{-6}\ M_\odot\ yr^{-1}$. The results for $T_* = 5000$ K have been discussed in § 3.2 and displayed in Figure 4. We have changed only the photospheric temperature in the new calculations. Although the implied changes in the spectral distribution of the radiation and the total luminosity can, in principle, affect the gas temperature, such effects are actually small (RGS). The results in Table 5 indicate that the basic character of the 4000 and 5000 K winds are similar, i.e., hydrogen is mainly atomic and almost all of the carbon is in CO, but there are differences in SiO and other oxygen-bearing molecules. In particular, oxygen is split equally between O and H_2O for $T_* = 4000$ K and all of the

TABLE 5

ASYMPTOTIC ABUNDANCES[a]

X (1)	4000 K (2)	5000 K (3)	6000 K (4)	UV1 (5)	UV2 (6)
H_2	6.4−3	1.4−3	4.5−6	6.3−6	4.7−6
e	4.2−5	4.3−5	1.2−4	1.2−4	1.2−4
O	2.9−4	3.5−4	8.0−4	4.5−4	6.0−4
OH	8.9−9	7.0−9	1.2−10	1.7−10	8.4−12
H_2O	4.1−5	4.7−19	0	0	0
O_2	1.6−5	3.9−6	5.4−13	7.8−13	1.6−15
C	0	0	4.0−4	5.3−5	2.0−4
C^+	0	0	2.8−10	5.6−16	3.2−15
CO	4.0−4	4.0−4	1.0−7	3.5−4	2.0−4
CH	0	0	5.4−12	4.2−12	8.6−12
C_2	0	0	2.7−12	5.0−13	2.8−13
Si	2.6−19	6.2−16	7.5−9	7.5−9	1.8−10
Si^+	0	0	3.8−4	3.8−4	3.8−4
SiO	3.8−5	3.8−5	3.4−15	4.6−15	9.0−15
S	1.8−5	1.8−5	1.6−5	1.8−5	1.8−5
S^+	0	0	1.9−6	4.3−15	5.2−15
Fe	3.4−5	3.0−5	5.1−8	5.0−8	1.4−9
Fe^+	2.0−7	7.5−7	3.4−5	3.4−5	3.4−5
Mg	4.1−6	2.9−8	8.4−8	1.4−7	6.7−9
Mg^+	3.6−5	3.7−5	4.0−5	4.0−5	4.0−5
Al	6.7−9	6.8−11	1.3−11	9.3−11	5.4−12
Al^+	3.2−6	3.2−6	3.2−6	3.2−6	3.2−6
Na	5.3−8	3.3−9	1.2−9	6.5−9	9.5−10
Na^+	2.2−6	2.3−6	2.3−6	2.3−6	2.3−6

[a] Case 2, $\dot{M} = 3 \times 10^{-6}\ M_\odot\ \mathrm{yr}^{-1}$.

silicon remains in SiO; the heavy atoms in this model are also slightly more recombined. By contrast, all molecular abundances are reduced for $T_* = 6000$ K and the ionization is increased by a factor of 3 relative to $T_* = 5000$ K. Even CO is much reduced and, most striking of all, the abundance of SiO is negligible. These substantial changes in going from $T_* =$ 5000 to 6000 K are a consequence of the great sensitivity of the abundances of most oxygen-bearing molecules (other than CO) to the far-UV radiation field, which is markedly "harder" at 6000 K.

Next we consider the possibility that the protostellar radiation field is not a pure blackbody, in particular that there may be a significant excess flux in the far-UV. Such an effect might arise in a natural way as the protostar-disk system evolves and the protostar rotation is braked, giving rise to an accretion shock and associated UV emission. We have carried out calculations in which the protostellar spectral energy distribution is blackbody down to a "cutoff" wavelength and constant below that wavelength. There is some observational evidence of T Tauri stars that is suggestive of this type of short-wavelength continuum (Kenyon et al. 1989). The results presented in columns (5) and (6) of Table 5 correspond to cutoff wavelengths of 2000 and 3000 Å, respectively. Although the total excess UV luminosities are small, 4.0×10^{-3} and 9.8×10^{-2} $L_\odot$, respectively, the flux increases at 1000 Å are very large: 5.5×10^4 and 8.8×10^5 for the cutoffs at 2000 and 3000 Å, respectively. Figure 10 shows the results for the case where the far-UV spectral energy distribution is flat below 2000 Å for Case 2 and $\dot{M} = 3 \times 10^{-6}\ M_\odot\ \mathrm{yr}^{-1}$. Compared with Figure 4 (no UV excess), there are substantial reductions in all molecules but the reduction in the CO abundance is only 15%. The most striking change is that the abundance if SiO is reduced to an extremely low level. Increasing the cutoff wavelength to 3000 Å continues this trend, e.g., the asymptotic CO abundance is reduced by 50%. Although a far-UV excess can be very effective in reducing the abundance of many neutral atoms and molecules, the most easily observed molecule CO is fairly resistant to even quite large UV flux increases.

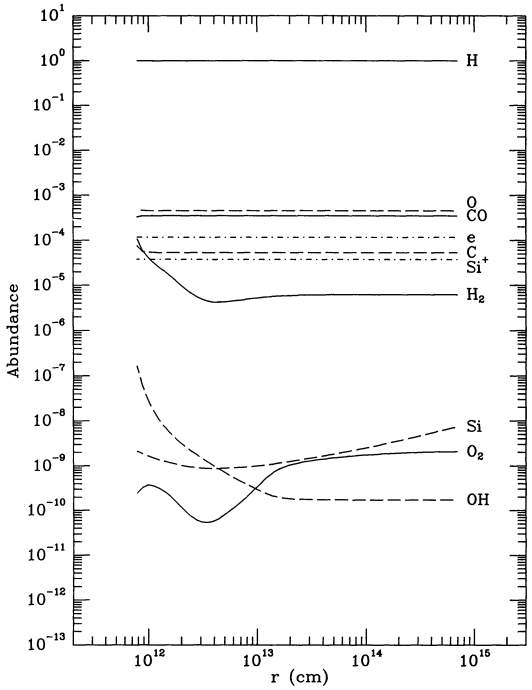

FIG. 10.—Chemical abundances for Case 2 and $\dot{M} = 3 \times 10^{-6}\ M_\odot\ \mathrm{yr}^{-1}$ with constant UV energy flux below 2000 Å equal to that of a blackbody at 2000 Å.

4. DISCUSSION

The results presented in the last section show how molecules can be formed at substantial levels in the very fast, primary winds generated by young, low-mass protostars. The underlying processes proceed efficiently under a wide range of conditions. Even for situations where RGS predicted large reheating, the winds retain a substantial abundance of CO. The most important requirement for molecular synthesis in these winds is that the temperature fall to less than a few thousand K within several protostellar radii. The calculations of RGS are critical in this context because they show how difficult it is to heat the winds in the inescapable presence of cooling associated with adiabatic expansion. We find that the efficiency for molecule formation is greater than in our preliminary report (Paper I), mainly because we now include the density enhancements due to acceleration and collimation. Of course for very low mass-loss rates, such as assumed in the one previous study of the subject by Rawlings et al. (1988), who considered a mass-loss rate, $\dot{M} = 10^{-9}\ M_\odot\ \mathrm{yr}^{-1}$, typical of some T Tauri stars, molecule formation is indeed inefficient.

The calculations also reveal that, given favorable temperatures, molecule formation increases rapidly with the density. Taking into account the effects of expansion, acceleration, collimation, and variations in the mass-loss rate, the calculations span a large range of density. Consequently we have had to implement several types of chemistry, for example

the H^-, H_2^+, and 3H routes to form H_2 and ion-molecule and neutral reactions to form heavy molecules. The proximity to the protostar also implies that photo effects and the shielding of the protostellar radiation are important. Of particular interest is the crucial role played by charge exchange in the rapid destruction of H^+ ions and the concomitant increase in the ionization of the wind. The latter effect is due to the fact that the destruction of H^+ differs from that of the typical heavy atomic ion because it interacts strongly with neutral radicals and molecules. Unfortunately, quantitative results on the ionization of the wind are rendered uncertain by the almost total absence of laboratory measurements of charge exchange reactions in the sub-eV energy range.

The self-shielding of the neutral species subject to photodestruction also plays a crucial role in molecule formation close to the protostar. Most of the shelding is due to the absorption of photoionizing continuum radiation by the abundant neutral atoms. The effectiveness of an atom in this respect is determined by the photoionization threshold as well as by the abundance of the element and the magnitude of its cross section. Thus, the order in which the ions recombine as the density increases is generally C^+, S^+, Si^+, Fe^+, Mg^+, Al^+, and Na^+. For CO, which requires photons shortward of 1100 Å, the shielding is produced primarily by C and S atoms. In this context, it is useful to note that, in the least opaque Case 1, equation (2) implies that the optical depth from R_* to infinity due to C at 1000 Å is more than 3×10^4 (for $\dot{M} = 3 \times 10^{-6}$ $M_\odot$ yr^{-1} and $V = 150$ km s^{-1}).

Although similar considerations apply to molecular hydrogen, its formation proceeds relatively slowly except at the highest densities. In addition, H_2 can be readily destroyed by chemical reactions and by collisional dissociation at intermediate temperatures of the order of a few thousand K. It is for these reasons that fast, protostellar winds usually manifest an atomic hydrogen character even where most of the heavy atoms are incorporated in molecules. It is therefore important to keep in mind that the *mere detection of atomic hydrogen, e.g., by its 21 cm emission, does not imply the wind is completely atomic.* Not only may CO be abundant at relatively low mass-loss rates but, for high mass-loss rates, some hydrogen remains atomic, as shown in Figure 9.

Our calculations are relevant to observations of protostellar winds in the emission lines of various species that can be detected at infrared and radio wavelengths. As we have just mentioned, the short dynamical time scales of protostellar winds ensures that atomic hydrogen is present unless the mass-loss rate is extremely large, i.e., more than 10^{-4} $M_\odot$ yr^{-1}. Being quite robust, CO is usually present unless the mass-loss rate is so low that the formation processes are inefficient. The abundance of SiO is more sensitive to density than CO, and the SiO/CO ratio is a tracer of high-density gas. SiO also appears to be particularly sensitive to the presence of excess UV radiation, largely because it has a relatively low threshold energy for photodissociation. However, we know practically nothing about the SiO photodissociation cross section so our ideas on this point are somewhat provisional.

The hydroxyl radical reaches abundances of the order of 10^{-8} and represents a potential diagnostic for intermediate mass-loss rates. Although O_2 is another indicator of incomplete oxygen chemistry, its abundance is generally small. The abundances of the CH and C_2 radicals are small and their diagnostic potential for these winds appears to be slight. On the other hand, H_2O is a high-density tracer because it can capture almost all of the residual oxygen not in CO.

There is also considerable interest in the atomic component of these winds. Our calculations show that, except for the largest mass-loss rates, the dominant form of oxygen is atomic. Hence the emission in the fine structure lines in the far-infrared at 63 and 146 μm offers potential diagnostic opportunities. Although carbon is more readily incorporated into CO than oxygen is in H_2O, we find that atomic carbon dominates at low mass-loss rates. In this case, the submillimeter lines at 492 and 809 GHz are of potential interest. In contrast to carbon, silicon occurs in the form of Si^+ when it is not in SiO, so here the focus is the Si^+ fine structure line at 35 μm. On the other hand, sulfur will generally be atomic except at the largest mass-loss rates; its fine structure lines are at 25 and 56 μm.

Very high-velocity gas was detected by Lizano et al. (1988) near the highly embedded, protostellar source SSV 13 (with the associated Herbig-Haro objects HH 7 – 11) in both the 21 cm line of atomic H and the 2.6 mm line of CO. They interpreted their observations in terms of a protostellar wind with a mass-loss rate of 3×10^{-6} $M_\odot$ yr^{-1} and suggested that this wind drives the extended, lower velocity bipolar outflow, often observed near young stellar objects (e.g., Lada 1985; Snell 1987). Detections of very high-velocity CO with speeds in the range 100–200 km s^{-1} in other sources (Koo 1989, 1990; Marguiis & Snell 1989; Giovanardi et al. 1990) lend support to this conclusion. High spatial resolution observations of the HH 7 – 11 outflow (Masson, Mundy, & Keene 1990; Bachiller & Cernicharo 1990) show that it is bipolar with correlated clumps on the two sides of the flow. High-resolution, near-infrared observations of more luminous protostars also provide important evidence for such flows (Mitchell et al. 1989).

At the nominal distance of the HH 7 – 11 source (350 pc), the highest-resolution radio observations (12″, Bachiller & Cernicharo 1990), probe regions of linear dimension 6×10^{16} cm (4000 AU). This is a size scale altogether different from the source of the wind, and it is difficult to comprehend which aspects of the primary wind are being observed with current instrumentation. Our chemical models express some of the qualitative features of the above cited observations. Most important, they explain how the primary wind can be primarily atomic hydrogen for mass-loss rates of the same order as measured in HH 7 – 11 and still contain substantial CO. To make further connections with observations, it will be necessary to understand the excitation of the observed lines and to calculate the line fluxes using radiative transfer techniques that are appropriate for these winds. Eventually, a high-speed primary wind will interact with the surrounding material and undergo significant dynamical and physical changes that include channeling of the flow, entrainment of ambient gas, and shock heating and chemistry. A full understanding of the observations requires consideration of these interactions of the primary wind.

The basic concept of the model investigated in this paper is fairly simple, being based on specified one-dimensional flows and temperature distributions. It is important to keep its limitations in mind as well as the fact that even this "simple" model requires rather elaborate calculations. The assumption of only one spatial dimension is a serious limitation in modeling protostellar evolution involving an accretion disk. We have adopted the RGS method for simulating the effects of collimation on the wind density (Case 3). Similar representations of the changes in the shielding of the protostellar radiation field and inclusion of the radiation emanating from the inner regions of the disk could be implemented. In the longer term,

however, it would be preferable to develop a two-dimensional version of the present calculation.

Our discussion of the ionization and reheating for Case 3 indicates that a more consistent treatment of the thermal effects is needed, one that extends the theory of RGS to include the heavy element chemistry of this paper. It should be recalled that we have emphasized the flow models of RGS in the present calculations and found that the molecular abundances are sensitive to density. The results for other flows may well differ quantitatively, but their qualitative properties should not be much different.

Another assumption of the present calculations, that dust does not form, was made primarily for purposes of simplification but also because it probably has little effect on our general conclusions. As discussed by RGS, dust may form at about 10 R_* but at this point most of the critical molecular synthesis has already occurred. Dust formation can actually help molecular synthesis by shielding wavelength bands longward of 1200 Å that are not shielded by neutral carbon and sulfur. On the other hand, the dust will be silicates and therefore reduce the amount of silicon available for SiO and of oxygen for H_2O.

Another chemical simplification in the present report is the omission of sulfur and nitrogen chemistry. We have actually developed a full sulfur chemistry and are investigating its implications. Because it more than doubles the number of chemical equations, a complete study requires further improvements in our numerical methods in order to deal with the problems mentioned in § 3.3.

We have assumed that the flows are both steady in time and vary smoothly with position. Real winds may be variable and thus clumpy. The strong dependence of the chemistry on density would suggest that the denser parts of a clumpy flow would be even more molecular, as long as these regions are also well-shielded, and that the more rarefied parts would be more atomic. Even though our present program is one-dimensional, it could be adapted to simulate some aspects of clumpy protostellar winds. Finally, our calculations must eventually break down when the winds begin to interact with ambient interstellar material, particularly with other portions of the nascent cloud. Again some aspects of these interactions could be incorporated into our program but, in principle, they require a two-dimensional theory and the inclusion of shocks.

5. CONCLUSION

In conclusion, our calculations reveal the presence of a rich chemistry in the primary winds of young, low-mass protostars. The chemical abundances are sensitive to the basic properties of the flow such as the temperature, the mass-loss rate, and the spatial variation of the density due to the acceleration and collimation of the wind. Our calculations indicate that a variety of atomic and molecular diagnostics of these winds may eventually be able to provide direct information on this important aspect of the formation of stars.

This research has been aided substantially by the NYU Academic Computing Facility. The authors would like to express their appreciation to its staff and director, Max Goldstein, for grants of computing time and other assistance. They would also like to thank V. Escalante and G. Victor for early communication of their results on the carbon atom and A. Dalgarno for helpful discussions of charge exchange and other reactions. This work has been supported by grants from NASA (to A. E. G.) and NSF (to P. J. H.).

REFERENCES

Allan, R. J., Clegg, R. E. S., Dickinson, A. S., & Flower, D. R. 1988, MNRAS, 235, 1245
Argyros, J. D. 1974, J. Phys. B, 7, 2025
Bachiller, R., & Cernicharo, J. 1990, A&A, in press
Baulch, D. L., Cox, R. A., Hampson, R. F., Kerr, J. A., Troe, J., & Watson, R. T. 1984, J. Phys. Chem. Ref. Data, 13, 1259
Black, J. H., & Smith, P. L. 1984, ApJ, 277, 562
Brooks, N. H., & Smith, W. H. 1974, ApJ, 194, 513
Chambaud, G., Launay, J. M., Levy, B., Millie, P., Roueff, E., & Tran-Minh, F. 1980, J. Phys. B, 13, 4205
Cohen, N., & Westberg, K. R. 1983, J. Phys. Chem. Ref. Data, 12, 351
Dalgarno, A., Du, M. L., & Yu, J. H. 1990, ApJ, in press
Dalgarno, A., & Lepp, S. 1987, in Astrochemistry, ed. M. S. Vardya & S. P. Tarafdar (Dordrecht: Reidel), p. 109
Escalante, V., & Victor, G. A. 1990, ApJS, in press
Fehsenfeld, F. C., & Ferguson, E. E. 1972, J. Chem. Phys., 56, 3066
Gear, 1971, Numerical Initial Value Problems in Ordinary Differential Equations, (Englewood Cliffs, NJ: Prentice-Hall)
Giovonardi, F., et al. 1990, private communcation.
Glassgold, A. E., Mamon, G. A., & Huggins, P. J. 1989, ApJ, 336, L29 (Paper I)
Graff, M. M. 1989, ApJ, 339, 239
Graff, M. M., & Dalgarno, A. 1987, ApJ, 317,
Graff, M. M., Moseley, J. T., & Roueff, E. 1983, ApJ, 269, 796
Hudson, R. D. 1971, Rev. Geophys. Space Sci. 9, 305
Hudson, R. D., & Kieffer, L. J. 1971, Atomic Data, 2, 205
Karzus, W. J., & Latter, R. 1961, ApJS, 6, 167
Kelly, H. P., & Ron, A. 1971, Phys. Rev. A, 5, 168
Kenyon, S. J., Hartmann, L., Imhoff, C. L., & Cassatella, A. 1989, ApJ, 344, 925
Koo, B.-C. 1989, ApJ, 337, 318
———. 1990, ApJ, in press
Lada, C. 1985, ARA&A, 23, 267
Lee, L. C. 1984, ApJ, 282, 172
Leen, T. M., & Graff, M. M. 1988, ApJ, 325, 41
Lepp, S., Dalgarno, A., & McCray, R. M. 1990, ApJ, in press
Lepp, S., & Shull, J. M. 1983, ApJ, 270, 578
Letzelter, C., Eidelsberg, M., Rostas, F., Breton, J., & Thieblemont, B. 1987, Chem. Phys. 114, 273
Lizano, S., Heiles, C. F., Rodriguez, L. F., Koo, B.-C., Shu, F. H., Hayashi, S., & Mirabel, I. F. 1988, ApJ, 328, 763
Mamon, G. A., Glassgold, A. E., & Omont, A. 1977, ApJ, 323, 306
Margulis, M., & Snell, R. L. 1989, ApJ, 343, 779
Masson, C. R., Mundy, L. G., & Keene, J. 1990, ApJ, in press
Mitchell, G. F., Curry, C., Maillard, J.-P., & Allen, M. 1989, ApJ, 341, 1020
Natta, A., Giovanardi, F., Palla, F., & Evans II, N. J. 1988, ApJ, 327, 817
Neufeld, D. A., & Dalgarno, A. 1989a, ApJ, 340, 869
———. 1989b, ApJ, 344, 251
Pequignot, D., & Aldrovandi, S. M. V. 1986, A&A, 161, 169
Petuchowski, S. J., Dwek, E., Allen, J. A., & Nuth, J. A. 1989, ApJ, 342, 406
Pouilly, B., Robbe, J. M., Schamps, J., & Roueff, E. 1983, J. Phys. B, 16, 437
Rawlings, J. M. C., Williams, D. A., & Canto, J. 1988, MNRAS, 230, 695
Roberge, W., & Dalgarno, A. 1982, ApJ, 255, 176
Roig, R. A. 1965, J. Phys. B, 8, 2939
Ruden, S. P., Glassgold, A. E., & Shu, F. H. 1990, ApJ, 361, 546 (RGS)
Rutherford, J. A., & Vroom, D. A. 1972, J. Chem. Phys., 57, 3091
Shu, F. H., Adams, F. C., & Lizano, S. 1987, ARA&A, 25, 23
Shu, F. H., Lizano, S., Ruden, S. P., & Najita, J. 1988, ApJ, 328, L19
Smith, W. H., & Zweibel, E. G. 1976, ApJ, 207, 758
Snell, R. L. 1987, in Star Forming Regions, ed. M. Peimbert & M. Jugaku (Dordrecht: Reidel), p. 213
Stephens, T. L., & Dalgarno, A. 1972, J. Quant. Spectros. Rad. Transf., 12, 569
Tondello, G. 1972, ApJ, 172, 771
van Dishoeck, E. F. 1987, J. Chem. Phys., 86, 196
van Dishoeck, E. F., & Dalgarno, A. 1984, ApJ, 227, 576
Wagner, A. F., & Graff, M. M. 1987, ApJ, 317, 423
Wishart, A. W. 1979, MNRAS, 187, 50P

B Sélection d'articles et proceedings publiés en Formation & Evolution des Galaxies

B.1 The origin of the galaxy luminosity function and the thermal evolution of the intergalactic medium

Blanchard, Valls-Gabaud & Mamon, 1992, *A&A 264, 365–378*

Astron. Astrophys. 264, 365–378 (1992)

ASTRONOMY AND ASTROPHYSICS

The origin of the galaxy luminosity function and the thermal evolution of the intergalactic medium

A. Blanchard[1,2], D. Valls-Gabaud[3,4], and G.A. Mamon[1]

[1] DAEC, Observatoire de Paris-Meudon, F-92195 Meudon Cedex, France
[2] Université de Paris VII, Place Jussieu, F-75005 Paris, France
[3] Institut d'Astrophysique de Paris, 98 bis, Bld. Arago, F-75014 Paris, France
[4] Institute of Astronomy, Madingley Road, Cambridge CB3 0HA, England

Received January 2, accepted February 27, 1992

Abstract. We study the mass function of cosmic structures that arise from gravitational instability in an expanding Einstein-de Sitter Universe. Assuming that fragmentation processes are negligible and the transition from the linear to non-linear regime is controlled by the linear density contrast, we derive a general formal expression for the mass function for any kind of fluctuations, whether gaussian or not. Rather than counting objects directly, we count the mass entering in objects that become non-linear, which avoids the problems met in the peak approach. For scale-invariant initial density fluctuations the asymptotic low-mass slope can be in principle calculated. With general assumptions, we find that the slope can only be shallower than that predicted by the Press and Schechter prescription. As tidal effects are unlikely to affect the low-mass slope, we argue that the smaller observed slope of the galaxy luminosity function is related to processes of galaxy formation, rather than a change in the primordial index. Examining the thermal evolution of gas during galaxy formation, we estimate the instantaneous fraction of gas able to cool at any epoch, and find that almost all the baryons should have cooled by the present time. This causes an "overcooling" problem: assuming efficient conversion of cooled gas into stars, too much star formation occurs. Since gas is unlikely to remain in the form of cold dense systems a reheating phase is required to solve this problem. We also showed that the existence of hot gas in clusters of galaxies does provide a strong evidence for such a reheating phase. We therefore assume the existence of a feedback mechanism, leading to hot uniform gas, which then slows down the rate of galaxy formation. The cooling of intergalactic gas, coupled with its collapse inside galaxy halos leading to star formation is restricted to halos with virial temperatures greater than the gas temperature. The faint-end slope of the luminosity function is then modified and agrees with the observed slope. In addition, we predict a turnover in the galaxy luminosity function, corresponding to the absence of halos with circular velocity smaller than 20–50 km s^{-1} and the existence of two populations of dwarf galaxies, well separated in morphology, gaseous and stellar content, ages and large-scale clustering. Contrary to the standard hierarchical picture, our model implies that bright galaxies form before most dwarves.

Key words: cosmology – galaxy formation – luminosity function – dark matter – intergalactic medium – galaxy halos

Send offprint requests to: A. Blanchard (Meudon address)

1. Introduction

A common idea in cosmology is that the present galaxy distribution results from the gravitational growth of initial small fluctuations in the density field (Lemaître 1933). This is indeed the simplest way to reproduce the remarkable isotropy of the cosmic microwave background and the present inhomogeneous distribution of galaxies at small scales, in which gravitation nowadays plays a major role. It is usually assumed that the fluctuations are generated in the early Universe (e.g. inflation) although other mechanisms suggest that the seeds of galaxy formation may have been produced much later (e.g. explosions, cosmic strings, a late phase transition). Much effort has been concerned with the relation of the present properties of the galaxy distribution to the initial spectrum of the fluctuations (Peebles 1974; Gott & Rees 1975) and indeed most predictions of any theory are based on the knowledge of the spectrum. In the context of gravitational instability, Press & Schechter (1974, hereafter PS) have proposed a prescription to derive the mass function of cosmic structures in a gaussian density field. More recently, other theoretical efforts have used the peak approach (Bardeen et al. 1986; Peacock & Heavens 1985), or various other mechanisms (e.g. Henriksen & Lachièze-Rey 1990; Newman & Wasserman 1990) to study the link between the initial fluctuations and the mass function. However, numerical simulations have shown that the PS formalism describes the mass multiplicity function remarkably well (Efstathiou et al. 1988b; Efstathiou & Rees 1988; Carlberg & Couchman 1989), although it is not clear whether this is merely a coincidence or whether the original approach of PS is indeed physically motivated. It is often stated that the original PS derivation does not integrate most of the difficulties in the determination of the mass function in a hierarchical scenario, and several other approaches have recently been put forward to

1992A&A...264..365B

understand the origin of the mass function (Silk & White 1978; Schaeffer & Silk 1985; Carlberg & Couchman 1989; Lucchin & Matarrese 1988; Colafrancesco et al. 1989; Bower 1991; Bond et al. 1991; Bernardeau & Schaeffer 1991; Cavaliere et al. 1991).

This problem is far from academic, as the main purpose of these studies is to explain the observed luminosity function of cosmic structures: clusters, groups and individual galaxies. Many investigations have shown that the PS formalism combined with the CDM scenario successfully reproduces the observed cluster and group luminosity function with a constant M/L (Schaeffer & Silk 1985; Martınez-González & Sanz 1988), while the galaxy luminosity function remains difficult to account for unless M/L increases rapidly with decreasing galaxy luminosity (Frenk et al. 1990; Evrard 1989; White & Frenk 1991). The galaxy luminosity function is determined by processes that affect the baryonic gas, mainly star formation (Larson 1974; White & Rees 1978). Indeed, the cooling criterion for star formation is able to explain the origin of the turnover L_* of the luminosity function (Binney 1977; Rees & Ostriker 1977; Silk 1977).

In this paper, we analyze the origin of the luminosity function of galaxies, taking into account the thermal *evolution* of gas in the Universe. In Sect. 2, we present a formal derivation of the mass function from very general arguments. We outline the hypotheses that are necessary for such a derivation, and stress the motivation of the PS formalism. For the case of scale-invariant initial fluctuations, the asymptotic behavior of the mass function at the low-mass end can also be derived from generic assumptions, independently of the details of the non-linear regime. We go on to compare the calculated mass function with the observed luminosity function of cosmic structures and argue that the discrepancy at low luminosities, on galactic scales, does not reflect a real feature of the mass function. Since dynamical processes, such as tidal limitation or disruption of small halos, do not seem efficient, we analyze in Sect. 3 the evolution of gas during galaxy formation, relating its fate to the origin of the shape of the luminosity function of galaxies. This paper considers in more detail the preliminary study of Blanchard et al. (1990).

The success of the Cold Dark Matter scenario in reproducing galactic-scale properties (clustering, halos, flat rotation curves) makes it the most attractive theory of galaxy formation today (e.g. Frenk et al. 1990); and we apply our scenario to this model, although any scale-invariant model can be used. Nevertheless, the standard CDM model, i.e. with a bias parameter b of the order of 2), has several problems, among which (1) too little clustering predicted at large scales (e.g. Maddox et al. 1990; Saunders et al. 1991; but see also Couchman & Carlberg 1991), (2) the bulk of galaxy formation occurring at too recent epochs (Cole 1991; White & Frenk 1991), (3) the discrepancy between the expected number of low mass halos and the observed slope of the faint end of the luminosity function (White & Frenk 1991), (4) the absence of luminosity segregation in the galaxy distribution, contrary to what is expected in a biased theory (Valls-Gabaud et al. 1989) (5) the large number of hot X-ray clusters as well as the shape of their distribution function (Blanchard & Silk 1991). In Sect. 3, we estimate the amount of gas able to cool in a CDM cosmogony, and find that far too many stars must have been formed by now, unless some process has efficiently prevented galaxy formation in the past. In addition, we show that such a process should exist in any hierarchical picture to allow for hot gas in clusters. We interpret this process as a feedback mechanism that injects energy into the cosmological gas at relatively high redshifts ($z \approx 10$). This energy feedback alters substantially the history of galaxy formation. Assuming that reheating leads to a *nearly homogeneously* hot IGM at intermediate redshifts, which later cools adiabatically as the source of the feedback fades, we show that faint-end slope of the luminosity function of galaxies is flattened to a slope that agrees with the observed one.

2. Derivation of the cosmological mass function

2.1. Basic theory

In hierarchical models, initial fluctuations are present on all scales and at any epoch. For example, at high redshifts, when the Universe appears linear on some scale, there are smaller scales on which the Universe shows non-linear fluctuations (this is the consequence of a diverging fluctuation variance on small scales, for a CDM or any power-law perturbation density spectrum). Several problems arise in the derivation of the mass function of cosmic structures from the initial conditions. First, it is necessary to understand how a structure becomes non-linear. Although the full details of non-linear collapse are complicated, exact solutions (one-dimensional Zel'dovich solution, spherical solution) as well as numerical studies indicate that the collapse is mainly driven by the density contrast δ in the linear phase: matter evolves in a non-linear fashion (e.g. collapses and rapidly virializes) when δ reaches a value of order unity. Furthermore, a given mass that becomes non-linear may fragment into smaller structures, as expected in the pancake scenario for example (Sunyaev & Zel'dovich 1972; Jones et al. 1981). The mass function is then entirely dominated by the fragmentation process. A basic assumption here is the neglect of fragmentation. This common assumption is necessary for the derivation of the mass function, but the implications are essential as will be shown below. A final important question is the the so-called *cloud-in-cloud* problem: a given mass scale might merge into a larger mass scale that is becoming non-linear. We now show how one can derive the cosmic mass function from initial conditions with the two assumptions of density contrast based non-linearity and the absence of fragmentation.

Let $\mathscr{F}_{\rm NL}(>m)$ be the present fraction of mass in the Universe that is in *non-linear* structures with masses greater than m (the theory detailed below is independent of whether "non-linear" refers to *collapsing*, *collapsed*, or *virialized*). The mass function is, by definition, related to $\mathscr{F}_{\rm NL}(>m)$ by

$$n(m) = -\frac{\bar{\rho}}{m}\frac{\mathrm{d}\mathscr{F}_{\rm NL}(>m)}{\mathrm{d}m}, \tag{1}$$

where $\bar{\rho}$ is the present mass density of the Universe. Recall that in hierarchical models, non-linear fluctuations are present on all scales, and hence any piece of matter in the Universe is in some non-linear fluctuation; the integrated mass function is then

$$\int_0^\infty n(m) m \,\mathrm{d}m = \bar{\rho}\,\mathscr{F}_{\rm NL}(0) = \bar{\rho}. \tag{2}$$

In the standard Friedmann–Lemaître cosmology with $\Omega = 1$, it is well known that the transition from the linear to non-linear regime is controlled by the linearly extrapolated density contrast $\delta = \delta\rho/\bar{\rho}$. For instance, in the top-hat model, the virialization of

a sphere is determined by whether the mean linear density contrast δ within the sphere is greater than some threshold value δ_S.[1] In fact, the collapse should also depend on the shape and perhaps the density profile. It is possible to write a general form for $\mathcal{F}_{NL}(>m)$ in terms of the initial fluctuations as follows.
Let

$$\int_{\nu_S}^{\infty} F_R(\nu)\,d\nu \tag{3}$$

be the fraction of volume in the Universe, in which each point can be embedded in a sphere of radius greater than R, whose *mean* density satisfies the threshold criterion $|\delta|>\delta_S=\nu_S/\sigma(R)$, where $\sigma(R)$ is the rms linear density contrast at scale R. Note that a top-hat filtering is different, since each point is then at the *center* of a sphere of radius R satisfying the mean density criterion above. Therefore F_R is *not* expected to be gaussian, even if the underlying density field *is* gaussian. On the other hand, for a non-gaussian field the following approach holds as well. From this definition, we clearly have

$$\int_0^{\infty} F_R(\nu)\,d\nu=1, \tag{4}$$

as this represents the fraction of volume embedded in spheres with $|\delta|>0$. As we are dealing with linearly extrapolated initial conditions, the matter is uniformly distributed, and the fraction of mass included in a volume is just proportional to this volume. Without loss of generality, we can introduce a selection function $s(\delta, \nu)$ that gives the fraction of mass in between δ and $\delta+d\delta$ that ends up in a non-linear object of mass $>m$ for a threshold ν. For example, a sharp threshold ($|\delta|>\delta_S$), corresponding to the spherical model, will result in $s(\delta)$ being the Heaviside function centered on δ_S, independently of ν. We may expect some dispersion around δ_S. Also the intrinsic properties of the density field, for instance the non-sphericity of the non-linear regions, might imply that $s(\delta)$ varies also with ν. We can then write

$$\mathcal{F}_{NL}(>m)=\int_0^{\infty} s(\nu\sigma, \nu)\,F_R(\nu)\,d\nu. \tag{5}$$

Equation (5) is *exact* and solves the *cloud-in-cloud* problem, as long as the unknown behavior of the non-linear evolution is described by the selection function $s(\delta, \nu)$. It is straightforward to verify that this automatically ensures global mass conservation. Note that in Eq. (5) the smoothing scale R is related to the mass m by $m=aR^3$, where a is some constant of order unity (not necessarily $4\pi/3$).

In the gravitational instability scenario, negative fluctuations are expected to lead to voids, the matter content of this region is therefore pulled away. For instance, the formation of a void could be surrounded by a thin shell of matter. This material should be counted in the non-linear objects. If the matter in the void could form objects of arbitrarily low mass, then fragmentation processes are important. By neglecting fragmentation one assumes that the matter in non-linear underdense regions ends up in objects of mass greater than some value related to the scale of the void. Although this approximation is crude, it is necessary to take this material into account, as it clearly is "non-linear", a point omitted in most derivations of the mass function. Accordingly, the selection function should therefore tend towards 1 when $|\delta|$ tends towards infinity, so that the derivative $\partial s/\partial\delta$ is zero outside a finite domain in δ. In Sect. 2.2.2 below, we relax the assumption of non-fragmentation and allow for a different treatment of underdense regions.

We have thus formally obtained a general expression for the mass function, Eqs. (1) and (5), based on two general hypotheses. First, fragmentation processes are negligible and, second, the selection function $s(\delta, \nu)$ varies from zero to one on the scale that satisfies a criterion $|\delta|\approx\delta_S$, i.e. the transition from linear to non-linear regime is essentially controlled by the *amplitude* of the density fluctuations. The self-consistency of this approach comes from the fact that we directly count the non-linear mass and derive in a second step the corresponding number of objects. Our approach helps to clarify the establishment of the low mass regime. Unfortunately the function $F(\nu)$ is difficult to estimate, even for a gaussian field, and therefore we cannot provide the full shape of the mass function even in the sharp threshold approximation. Note that any approximation should be used with the integral constraint [Eq. (2)] in mind.

2.2. *Scale-invariant fluctuations*

It is not possible, in general, to derive a practical expression for the mass function based upon the formal solution given by Eq. (5), as the dependence of the integrand of Eq. (5) with the smoothing scale is unknown a priori. However, in the special case of scale-invariant density fluctuations, the distribution function F and the selection function s do not depend on the smoothing scale. Therefore, with Eqs. (1) and (5), the mass function becomes

$$n(m)=-\frac{\bar\rho}{m}\frac{1}{\sigma^2}\frac{d\sigma}{dm}\int_0^{\infty}\delta\frac{\partial s}{\partial\delta}(\delta, \nu)\,F(\nu)\,d\delta, \tag{6}$$

where we have dropped the subscript R.

The mass behavior can be qualitatively described from Eq. (6) as long as $\partial s/\partial\delta$ is non-zero, outside a small range in δ, i.e. assuming that the selection function is close to a Heaviside function centered on some threshold δ_S. Equation (6) then yields

$$n(m)\approx-\frac{\bar\rho}{m}\frac{1}{\sigma^2}\frac{d\sigma}{dm}F(\nu)\,\delta_S. \tag{7}$$

When the mass is large enough, ν becomes large and F becomes negligible, producing a high mass cut-off.

2.2.1. The low-mass regime

The formal expression (6) allows one to study the behavior of the mass function in the low-mass regime, independently of the form of both functions s and F. Indeed, in hierarchical models, $\lim_{m\to0}\sigma=\infty$, so that $\lim_{m\to0}\nu=0$, the functions F and s can be developed around $\nu=0$ and $\partial s/\partial\delta$ is zero outside a finite domain. The mass function in the low-mass limit then becomes

$$n(m)\to-\frac{\bar\rho}{m^2}\frac{1}{\sigma}\frac{d(\ln\sigma)}{d(\ln m)}F(0)\int_0^{\infty}[1-s(\delta, 0)]\,d\delta \quad \text{as } m\to0. \tag{8}$$

Consequently, the mass function for small masses is determined uniquely (up to a constant factor) by the dependence of the rms

[1] For the spherical top-hat model, $\delta_S=(3/5)(3\pi/4)^{2/3}(1+z)$ $=1.062\,(1+z)$ at turnaround (Peebles 1969), and $1.686\,(1+z)$ at collapse, as well as for virialization if the collapse generates violent relaxation. The actual density contrast at virialization is then $\Delta=178$ assuming a collapse factor of 2.

density fluctuation $\sigma(m)$ with mass. For scale-invariant fluctuations with $\sigma(m) \propto m^{-\alpha}$ the mass function of small masses takes the form given by PS, provided that $F(0) \neq 0$, namely,

$$n(m) \sim m^{-(2-\alpha)}.$$

However, the normalization cannot be precisely determined unless the function F is known.

We have seen above that *the low-mass dependence of the mass function is correctly given by the PS formalism* and the expression depends essentially on our three assumptions: (1) fragmentation is not important, (2) the linear amplitude of density controls non-linearity, and (3) density fluctuations are scale-invariant; although this third assumption should not be critical, and we expect the basic behavior to be correct in any hierarchical model.

Such hypotheses are implicitly assumed in previous work, but not always explicited. However, this result holds only if $F(0)$ is a non-vanishing constant (Eq. 8). Although it seems that the exact derivation of $F(\nu)$ is intractable, it is still possible to see how the low mass behavior can be modified: noticing that the volume of the Universe occupied by all the points lying inside non-linear spheres of radius $\geq R$ is greater than the corresponding volume, considered by PS, occupied by the points at the centers of such spheres, we have the inequality:

$$\int_{\nu_S}^{\infty} F(\nu)\,d\nu \geq \sqrt{\frac{2}{\pi}} \int_{\nu_S}^{\infty} e^{-\nu^2/2}\,d\nu,$$

implying (Eq. 4) that

$$\int_0^{\nu_S} F(\nu)\,d\nu \leq \sqrt{\frac{2}{\pi}} \int_0^{\nu_S} e^{-\nu^2/2}\,d\nu \leq \sqrt{\frac{2}{\pi}}\,\nu_S. \tag{9}$$

Therefore, for small ν_S, F is a power law of index μ greater than zero

$$F(\nu) \simeq c\nu^{\mu}, \text{ with } \mu \geq 0 \text{ and } \nu_S \ll 1.$$

The mass function in the low-mass regime becomes (Eq. 6)

$$n(m) = -\frac{c\rho}{m^2} \frac{d(\ln\sigma)}{d(\ln m)} \frac{1}{\sigma^{1+\mu}} \int_0^{\infty} \partial s/\partial\delta\, \delta^{\mu}\,d\delta,$$

and the asymptotic behavior is

$$n(m) \sim m^{-[2-\alpha(1+\mu)]}. \tag{10}$$

Hence, the asymptotic mass slope can only be *shallower* than the standard PS slope. The CDM spectrum yields $\alpha \leq 0.1$ for $z=0$ and $m < 10^{10} h_{50}^{-1} M_{\odot}$, where h_{50} is the Hubble constant in units of $50\,\mathrm{km\,s^{-1}\,Mpc^{-1}}$. So for reasonably low values of μ, the correction is small. It is clear from Eq. (10) that it is possible to escape this conclusion if μ is negative, implying that F diverges at $\nu=0$. It is difficult to see how this could be physically motivated. However, it is possible to give a general argument for the validity of this regime.

2.2.2. Underdense regions

Despite its generality, the prescription given above lacks a consistent treatment of non-linear underdense regions, which is often not addressed in the literature. As we have emphasized, when a negative fluctuation becomes non-linear, its material content has to be counted as collapsed. Some fraction of this mass is actually embedded in non-linear positive fluctuations with larger smoothing radii, but some could lie outside any such positive fluctuations. We can therefore decompose the fraction of non-linear mass into two parts:

$$\int_{\nu_S}^{\infty} F(\nu)\,d\nu = \int_{\nu_S}^{\infty} F_+(\nu)\,d\nu + \int_{\nu_S}^{\infty} F_-(\nu)\,d\nu,$$

where $F_+(\nu)$ corresponds to the mass that is embedded in at least one positive fluctuation satisfying the threshold criteria ($\delta \geq \delta_S$), while $F_-(\nu)$ corresponds to the mass satisfying the threshold, but only for negative fluctuations ($\delta \leq -\delta_S$). This means that $F_-(\nu)$ counts only the matter in non-linear underdense regions not embedded in any positive fluctuations (for any radius larger than the smoothing radius). We have assumed until now that this matter entirely ends up in objects with mass directly associated with the smoothing radius. However, it is not obvious that this matter should end up in this way. On the other hand, the neglect of this non-linear fraction amounts to assume that some fragmentation occurs. To our knowledge, this question has not been addressed previously.

It is still possible to relax the above assumptions in order to treat underdense regions in a more satisfactory way. Assume that the mass associated with underdense regions ends up in existing objects independently of their mass. This could be written in the following way:

$$\mathscr{F}_{NL}(>m) = \int_0^{\infty} s_+(\nu\sigma) F_+(\nu)\,d\nu + \mathscr{F}_{NL}(>m) \int_0^{\infty} s_-(\nu\sigma) F_-(\nu)\,d\nu. \tag{11}$$

In this case, it is straightforward to verify that the integral constraint of Eq. (2) automatically holds, so that the normalization is naturally obtained. Furthermore the mass function still has the same form. A similar limit to Eq. (9) can be obtained:

$$\int_0^{\nu_S} [F_+(\nu) + F_-(\nu)]\,d\nu \leq \sqrt{\frac{2}{\pi}} \int_0^{\nu_S} e^{-\nu^2/2}\,d\nu.$$

This leads to the same constraint on the slope of the low-mass regime. We conclude that the low mass end of the mass function should be shallower or equal than the PS one.

2.3. Comparison with other theoretical approaches

In their classical paper, PS derive the cosmic mass function by applying a threshold criterion to a smoothed density field. When the smoothing filter is a top-hat (as it usually is) the PS prescription amounts to assuming that $\mathscr{F}_{NL}(>m)$ corresponds exactly to the centers of the spheres of radius R that satisfy the criteria for the overdense part and $F(\nu)$ is gaussian. Note that this approach clearly underestimates the actual $F(\nu)$. The sharp threshold assumption then leads to

$$n(m) = -\left(\frac{1}{2\pi}\right)^{1/2} \delta_S \frac{\bar{\rho}}{m} \frac{1}{\sigma^2} \frac{d\sigma}{dm} \exp\left(-\frac{\delta_S^2}{2\sigma^2}\right). \tag{12}$$

Now their sphere-centered prescription neglects regions below the density threshold that yet belong to overdense regions, and PS correct this by multiplying their number by a fudge factor of two. The factor of two discrepancy in the normalization is therefore caused by the use of an approximation for $F(\nu)$. The cloud-in-cloud problem is dealt by PS in a crude way: they basically assume that any center of a non-linear sphere of a given radius is also the center of a non-linear sphere for any arbitrary *smaller* radius. Although the density of non-linear substructures is

strongly enhanced in the presence of a positive background fluctuation (Bardeen et al. 1986), some region inside this region may have a density contrast smaller than the threshold value, so the cloud-in-cloud problem is not adequately treated in PS. From our analysis it is clear that without the factor for two their formula gives an underestimation. Nevertheless, the low mass regime is recovered in a very general case (Sect. 2.2) and it is therefore not very surprising that the low mass slope derived from numerical simulations is in good agreement with the PS formula. In the high mass regime the agreement is more surprising and could probably be looked at only as a coincidence. Peacock & Heavens (1990) set out to compute the probability that, for smoothing radius R, an underdense region might be "promoted" to an overdense region in the PS approach. Many small regions are promoted in their scheme into non-linear structures, and their resultant mass function has a significantly steeper low-mass asymptotic slope than in PS, whereas our low-mass asymptotic slope is shallower.

In the gravitational instability theory, objects are likely to form near the maxima of the density field, and one expects that there is a direct relation between the mass function and the statistics of peaks in the initial density field (Bond et al. 1991). However, the cloud-in-cloud problem has to be solved. A crude way to derive the mass function is to assume that peaks above the threshold correspond to the total number of objects:

$$N(>m)=\int_{\nu_S}^{\infty}\mathcal{N}_{pk}(\nu)\,d\nu, \tag{13}$$

where $N(m)=\int_m^{+\infty} n(m)\,dm$.

For a scale invariant spectrum, $\mathcal{N}_{pk}(\nu)$ is of the form $R^{-3}F_{pk}(\nu)=m^{-1}F_{pk}(\nu)$, and the mass function is then:

$$n(m)=\frac{1}{m^2}\int_{\nu_S}^{\infty}F_{pk}(\nu)\,d\nu+\frac{d\nu_S}{dm}\frac{F_{pk}(\nu)}{m}.$$

The second term has the form of the PS mass function, while the first term leads to a logarithmic divergence in the mass integral [Eq. (2)], regardless of the index of the spectrum. This problem occurs because the cloud-in-cloud problem is not dealt with at all in Eq. (13). For a peak on a scale R to be identified with a structure of mass m, it must not be merged into a larger structure. Writing this condition explicitly is very difficult, as an infinite number of constraints appear (from a continuous range of smoothing scales), and thus critically limit the peak approximation. A first step to the solution of this problem has been proposed by Appel & Jones (1990). Rather than starting from the number of peaks above the threshold $\nu_S=\delta_S/\sigma$, they compute the number of peaks at some threshold value for radii greater than some scale R. However, this approach does not handle the cloud-in-cloud problem and consequently their formula leads to the same divergence.

It is possible, however, to merge the PS approach with the peak formalism by writing

$$\int_{\nu_S}^{\infty}F_R(\nu)\,d\nu=\int_{\nu_S}^{\infty}\mathcal{N}_{pk}(\nu,R)m_{pk}(\nu,R)\,d\nu,$$

where $\mathcal{N}_{pk}$ is the differential number of peaks (Bardeen et al. 1986). The mass function can be derived as

$$n(m)=\mathcal{N}_{pk}(\nu_S,R)\frac{d\nu_S}{dm}$$

(Efstathiou & Rees 1988; Bond 1989) and has obviously the same low-mass behavior as the standard PS function. However, this approach implicitly assumes that the mass in non-linear peaks of any scale larger than R is exactly included in non-linear peaks at scale R. This is the most worrisome approximation in the original PS derivation, as noted by Peacock & Heavens (1990). In the peak approach, one needs to understand precisely how low mass scales are damped as larger and larger structures form. The exact shape then depends on the way the low peaks actually merge and can eventually be determined by careful numerical simulations.

2.4. *Tidal effects*

As we emphasized in Sect. 2.2.1, we expect the PS formalism to be appropriate for small scales. A possible mechanism that may change the low-mass end of the mass function is the tidal disruption of small halos. Their mass content could then be lost and the integral mass constraint [Eq. (2)] would no longer be satisfied. From tidal theory (e.g. King 1962; Mamon 1987; Allen & Richstone 1988), an object of mass m lying at a distance R of a larger object of mass M is limited in its extent to a scale r, given by

$$\frac{r}{R}\approx\left(\frac{m}{M}\right)^{1/3}$$

to within a constant factor of order unity that depends on the relative orbit of the two objects and the internal velocity structure of the smaller one. In other words, a small halo is tidally limited to a scale within which its mean density roughly matches the mean density in a sphere centered on the larger halo and just barely containing the center of the smaller one. Now for spherical cosmological infall, all objects have, at a given time, the same mean density out to their turnaround radius. Therefore, only objects that lie within the turnaround radius of a larger object will be tidally limited inside their own turnaround radius. Now, in our mass function prescription of Sect. 2.1, the mass corresponding to an object embedded in a larger object will be counted as within the larger object only. Therefore, tidal processes should have little effect on the cosmic mass function.

2.5. *Discussion*

In the previous section we have shown that the low mass slope should be close to the value given by the PS formalism. The slope is directly related to the index of the spectrum of primordial fluctuations, while the characteristic mass depends on both the nature of density fluctuations (gaussian or non-gaussian) and on the details of the non-linear collapse.

In addition to the caveats mentioned in Sect. 2, and to the various improvements that have claimed better agreement with CDM simulations (Cole 1991; Bower 1991), the precise value of the turn-over mass is not easily measured in numerical simulations (Bond et al. 1991), and the faint-end slope determination is hampered by the limited dynamic range of the numerical codes. Therefore, the range of validity of the theory cannot yet be tested precisely.

It is nevertheless interesting to compare the calculated slope with the observed one. The observed *luminosity* function of cosmic structures (groups and clusters) scales as L^{-2} in the range corresponding to groups, i.e. $10^{11}-10^{13}L_{\odot}$ (Bahcall 1979), in agreement with the prediction of CDM theory (Moore et al. 1991). This slope, however, cannot hold at low luminosities for

the integrated luminosity to remain finite. Assuming a constant M/L ratio, this slope, taken at face value, indicates that in a hierarchical model the primordial index for the fluctuations should be close to -3.

The slope of the faint-end galaxy luminosity function is in the range -1.3 to -1 (Efstathiou et al. 1988a), thus different from the -2 slope of the group luminosity function. This difference in slopes could be explained by faint galaxies having larger mass-to-light ratios than bright galaxies and groups. If the luminosity function varies as $L^{-1-\varepsilon}$, one then requires $m \propto L^{\varepsilon}$, i.e. the masses of galaxies barely depend on their luminosities. However, this is inconsistent with the Faber–Jackson and Tully–Fisher relations: Because the velocity dispersion scales as $\sigma^2 \propto M/R \propto \rho^{1/3} M^{2/3}$, and at a given time all objects have the same density, $\bar{\rho} \propto (1+z)^3$ (see Sect. 2.4), one has

$$M \propto \sigma^3 (1+z)^{-3/2}. \tag{14}$$

Now the Faber–Jackson and Tully–Fischer relations are $L \sim \sigma^{\beta}$, where $\beta = 3$ to 4 (Faber & Jackson 1976; Tully & Fischer 1977; Tonry 1982). One would then require that $M/L \propto L^{\gamma}$, with $\gamma = -0.25$–0 instead of $\gamma = \varepsilon - 1 = -1$ to -0.7 from the observed luminosity function. In addition, it is worth noting that, if $\Omega = 1$, the existence of a large number of small halos is inevitable, at least within hierarchical scenarios: groups and clusters contain most of the galaxies, contributing 10–20% of the critical density, isolated galaxies represent at most a few percent, therefore, most of the remaining dark matter should reside in small halos (to satisfy the integral constraint of Eq. 2).

3. Thermal evolution of the gas

We now discuss the evolution of the gas and its link to the galaxy luminosity function. To interpret the galaxy luminosity function within the PS context, one must understand the conditions under which the primeval gas is processed into stars, and its impact on the luminosity of galaxies. It is commonly believed that galaxies correspond to the objects able to cool in a dynamical time or a Hubble time (Binney 1977; Rees & Ostriker 1977; Silk 1977) leading to the correct characteristic luminosity for the brightest galaxies. White & Rees (1978) included cooling and dynamical arguments in the derivation of the luminosity function, but predicted too many faint galaxies. The luminosity where the luminosity function of *cosmic structures* changes slope (galaxy to group transition) corresponds to the luminosity of the break in the *galaxy* luminosity function. This suggests that the change in slope is related to the physics of galaxy formation. As mentioned above, it is unlikely that this break corresponds to a change in the M/L relation. In the last sub-section we propose a new explanation for the slope of the faint-end of the galaxy luminosity function.

3.1. *History of galaxy formation in the absence of a reheating phase*

In this section, we sketch how galaxy formation may have occurred, assuming that any gas able to cool will turn into stars. As soon as gas is able to cool in a potential well, it is no longer thermally supported, it contracts, and the cooling is more and more efficient, leading to a cooling runaway. It is likely that this process will slow down, or even stop, when enough energy is injected into the gas, suggesting that only star formation and its feedback could actually prevent further cooling (Larson 1974). There is little hot gas in present day galaxies, and galaxies contain little cold gas, except HI dwarfs. This strongly suggests that, as gas settles in a potential satisfying the cooling criterion, it should either turn into stars or be reheated and expelled from the galaxy. On the other hand, if the gas temperature is larger than the virial temperature of the halo, the halo will not retain its gas and will therefore not turn into a luminous galaxy. We explore below the implications of this mechanism in the context of the hierarchical picture. The applications are computed for the CDM spectrum, assuming the PS mass function.

Let us assume that when objects form, the collapse of dark matter is followed by the associated baryonic gas. This is a reasonable assumption as long as $T_{\rm gas}$ is less than $T_{\rm vir}$. In the top-hat model for spherical collapse, the virial temperature $T_{\rm vir}$ can be derived from the final scale of the structure as (see Eq. 23 in the Appendix)

$$T_{\rm vir} = 5.73\,10^5 \left(\frac{f_{\rm v}}{0.5}\right)^{-1} \left(\frac{g_{\rm v}}{2}\right)^{2/3} \left(\frac{\gamma}{1.5}\right) \times \left(\frac{\mu}{0.59}\right) \left(\frac{M}{10^{12} M_{\odot}}\right)^{2/3} h_{50}^{2/3} (1+z)\,{\rm K},$$

where the parameters $f_{\rm v}$, $g_{\rm v}$, γ, and μ are given in the Appendix, and the first four terms in parenthesis are of order unity. Numerical simulations by Evrard (1990) give temperatures smaller by about 20%. The cooling criteria basically set two well-defined regimes: structures that virialize below 10^4 K and structures that collapse at larger temperatures. For the latter, the cooling is almost instantaneous, except for the massive objects that formed recently.

The thermal evolution of the gas can be followed on the D–T diagram of Fig. 1, where D is the density in units of the present-day virial density (see Appendix). The cooling region is enclosed by the thick curves that represent our cooling criteria (see below). At a given epoch, all objects have the same density (see e.g. Sect. 2.5), so that the entire population at one epoch lies on a horizontal line. The turn-over mass m_* of the mass function for given z leads to a maximum temperature T_* for the halo temperature distribution at a given epoch. Figure 1 displays such T_* vs. z curves. As the mass function of the CDM spectrum is spread over a wide range of masses, different values of m_* are shown, corresponding to different mass fractions (i.e. equal rms fluctuations). Almost all the halos are situated to the left of these curves. Also shown in Fig. 1 is the temperature of the cosmological gas assuming that it cools adiabatically after recombination. Numerical simulations of the evolution of the IGM (Shapiro 1991) show that this is a good approximation.

As long as the temperature of the gas is higher than the temperature of the isothermal halo, the gas remains uniformly distributed while the dark matter halos agglomerate to build up the mass hierarchy. At a later stage, gas falls into those halos whose virial temperature is higher than the gas temperature, and from Fig. 1, it can be seen that this occurs for a temperature of few K. The star formation rate at this point is quite uncertain. Gas can cool rapidly because molecular cooling may be efficient if the density is high enough, at least in the cores. However, because of the flatness of the CDM fluctuation spectrum on these scales, the temperature T_* rapidly reaches 10^4 K, the gas in potentials is ionized and a regime of very fast cooling is attained.

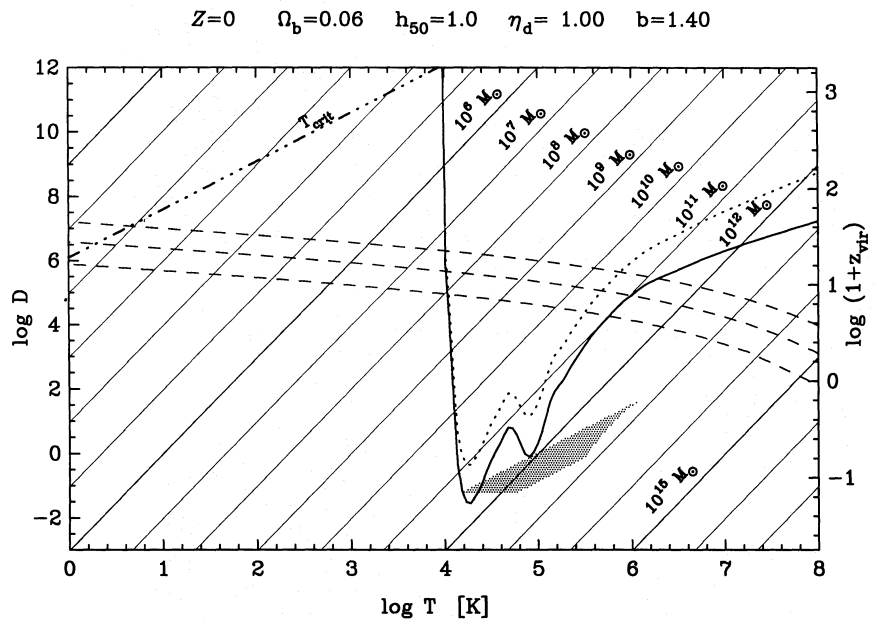

Fig. 1. Density-temperature diagram for the primordial gas (no metals). D is the dimensionless ratio of the local density to the present-day critical density, and z_{vir} gives the virialization redshift of the structure. Note that the redshift scale applies to virialized objects only. T is the temperature of the gas lying in the potentials. Thin lines are constant *total* mass, while the thick dash-three-dotted line gives the evolution of the cosmological gas after the recombination. The thick dotted curve is the D–T relation for the dynamical local cooling criterion ($t_{cool} \leq \eta_d t_{dyn}$) while the thick full line corresponds to our criterion $t_{cool} \leq \eta \kappa_\alpha t_H$, with $\eta = 1$ (Eq. 16). Thin dashed lines represent the mass above which lie 50%, 10%, 1% of the structures, with a bias parameter of $b = 1.4$. The relevant formulae are given in the Appendix. The shaded area indicates the region where gas cools adiabatically once re-heating terminates

At this stage, initial star formation begins. Once the gas has sufficiently cooled, it settles down into a disk, and it has been argued that star formation is triggered by tidal interactions (e.g. Lacey & Silk 1991). Due to the rapid variation of T_*, we in fact expect the halos to be strongly merging and the star formation rate to be enhanced. As long as important reheating does not take place, the cooling criterion is directly related to star formation. The case of a reheating phase is dealt in the following section.

Let $B(z)$ be the fraction of baryons in gas, $B_*(z) = 1 - B(z)$ the fraction of baryons in stars, $\Gamma(z)$ the rate at which gas is transformed into stars, and $\Gamma_*(z)$ the rate at which stars eject gas in the medium. The time evolution of B is

$$dB = -B\Gamma(z)\,dt + (1-B)\Gamma_*(z)\,dt. \quad (15)$$

The gas ejected in by a supernovae is extremely metal-rich and cannot therefore represent a large fraction of the total mass in the IGM. This leads to a much simpler picture, in which the evolution of B is controlled by the amount of gas that is processed into stars. The mass in forming stars per unit time is

$$-\rho_b(z)\frac{dB}{dt} = B\Gamma(z)\rho_c^0\Omega_b(1+z)^3,$$

where ρ_c^0 is the present-day mean (critical) density of the Universe.

We first wish to calculate for each epoch, the fraction $g(z)$ of mass in cosmic structures that is able to cool, either in a fraction η_H of the age of the Universe at epoch z, hereafter abusively called Hubble time ($t_c < \eta_H t_H(z)$, where $t_H(z) = 2/3H(z)$), or a fraction η_d of their dynamical time ($t_c < \eta_d t_d$, see the Appendix for the precise values of these time scales). The usual criterion is that all the gas able to cool in less than one of these time scales turns into stars. However, as the intergalactic gas can be heated by the dissipation of orbital energy of the virialized objects (galaxies) and not cool before the object merges into a larger one. Therefore, one must estimate the timescale of the variation of the gas temperature as the hierarchy grows. This effect will depend on the index of the spectrum. For a flat mass fluctuation spectrum ($n \approx -3$), the rate of change of the characteristic mass of halos M_* is large, i.e. we are in a regime of fast merging.

The characteristic time scale t_* of the temperature T_* of the halos is computed as follows: $\sigma_0(m_*)/(1+z) = \delta_S/v$ yields $d(\ln m_*)/d(\ln t) = 2/(3\alpha)$, where as usual $\alpha = -d(\ln\sigma)/d(\ln m)$ (evaluated here at $m = m_*$). Then $T_* \propto m_*^{2/3}(1+z)$ [Eq. (23)] leads to $d(\ln T_*)/d(\ln t) = (4-6\alpha)/(9\alpha)$, and hence

$$t_* = \frac{T_*}{\dot{T}_*} = \kappa_\alpha t_H(z), \quad \text{with } \kappa_\alpha = \frac{9\alpha}{4-6\alpha}.$$

The CDM spectrum has $\alpha \sim 0.1$ on the relevant scales implying that merging and therefore shock heating are efficient. This provides a minimal criterion for the gas to be able to cool :

$$t_{cool} \leq \eta t_* = \eta\kappa_\alpha t_H, \quad (16)$$

where η is expected to be of the order of one. In the relevant scales, for the CDM spectrum, this criteria is more stringent than the usual ones. When the structures are in the regime where:

$$\eta t_* \leq t_{cool} \leq t_H\ ,$$

the gas radiates energy, but its temperature is maintained by the shocks arising from the fast merging of the structures. It seems reasonable that such structures lead to disk systems, as the gas is within the cooling region.

We determine $g(z)$ by estimating the range in mass for which cooling actually occurs and then integrating over the PS mass function. The general derivation is given in the Appendix. Figure 2 presents the evolution of $g(z)$ for different values of the normalization of the CDM spectrum, where the bias parameter

b_ρ is defined as

$$\frac{1}{b_\rho}=\left(\frac{\delta M}{M}\right)_{8h^{-1}\,\mathrm{Mpc}}$$

The *solid curves* represent the case where the gas cools in less than the timescale defined above ($\eta\kappa_\alpha=0.35$). The resultant value of $g(z)$ is an underestimate of the actual fraction of the gas able to cool as the gas can be ionized by shocks in potential wells of lower temperature and because other coolants might exist, such as molecules. We have also plotted the fraction $g(z)$ when one requires that the cooling time is less than the dynamical time (dash–dotted curves). This criterion is used to identify systems that will end up as ellipticals.

As seen in Fig. 2, the maximum of the instantaneous fraction of gas able to cool depends only slightly on the values of the bias parameter, although its dependence on redshift is sensitive to b_ρ. With our criteria, the cooling time is always much shorter than the Hubble time, the gas therefore cools very rapidly and is quickly processed into stars. In this regime, we have :

$B_*(z)\geq g(z)$.

as long as the gas is the dominant form of baryons. The fraction $g(z)$ is then the minimal fraction of the gas that *has been able to cool*. The maximum value $g_{\max}$ of g over the different redshifts represents a *minimal* fraction of gas that has been presently processed into stars. As expected, the cooling is more efficient at high redshift for low values of the bias b. Changes of the parameters that comes in the determination of $g(z)$ are equivalent to changes in the value of η: taking η ten times smaller leads to values half as large, illustrating that $g(z)$ is insensitive to the parameters. From this we can set a firm limit on B_*

$$B_*^{\min}\approx g_{\max}\geq 0.2\,2^{\pm 1}. \qquad (17)$$

A further step in the process lies in the determination of $B_*(z)$, the total (integrated) fraction of the gas that has cooled (i.e. turn into stars) at some epoch z. In particular, $B_*(0)$ provides the total baryonic fraction that has been processed into stars at the present time. In the regime where cooling occurs in less than a Hubble time $t_{\mathrm{H}}(z)$, the gas that lies in the cooling region is depleted and there is no more gas available for cooling, until the next generation of potentials form. Therefore, the time scale relevant to the gas evolution is t_* and the fraction of hot gas follows

$$\mathrm{d}B\approx -Bg\frac{\mathrm{d}t}{t_*(z)}$$

so that the fraction of gas that had cooled by the redshift z is

$$B_*(z)=1-\exp\left(-\frac{3}{2}\int_z^\infty \frac{g(z)}{\eta_\alpha}\frac{\mathrm{d}z}{1+z}\right),$$

where it is assumed that the scales on which cooling occurs at different redshifts are independent. Note however, that there should be some correlation between different mass scales, as structures that satisfy the cooling criteria at a given epoch are likely to satisfy them at some later epoch. This means that a more precise determination of $B_*(z)$ requires the knowledge of the merging history of halos at each step of the hierarchy. Although calculations have been attempted to determine this merging history (Bower 1991; Cole 1991; Bond et al. 1991), a simple argument will be given to estimate directly $B_*(z)$ without requiring a detailed calculation.

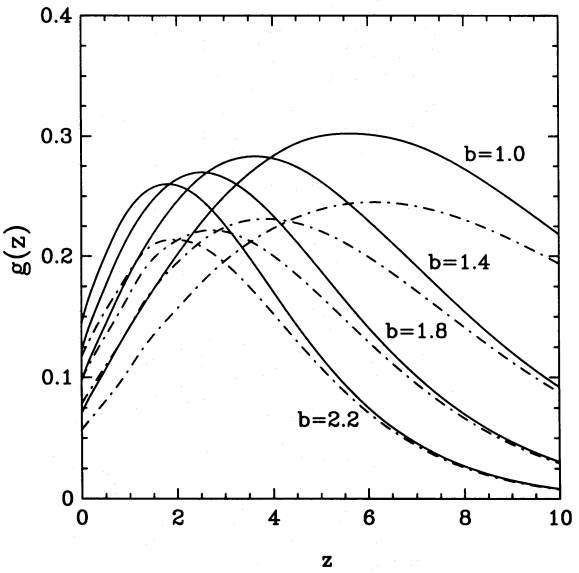

Fig. 2. Evolution with redshift of the instantaneous fraction of gas $g(z)$ that is able to cool for different values of the bias parameter $b_\rho=1$, 1.4, 1.8, and 2.2. The solid curves correspond to our criterion of Eqs. (16), (31) and (32), where $\eta_{\mathrm{H}}=\eta\kappa_\alpha$ in Eq. (31). The dash-dotted curves corresponds to the dynamical time criterion (Eq. 27) defined in Eqs. (28) and (32)

Consider in Fig. 1 the gas in a given structure with $T_{\mathrm{vir}}>10^4$ K but below the cooling region, i.e. on the lower right part of the diagram. After recombination, the gas was at ≈ 3000 K on the upper left part of the diagram. For the gas to reach its present state, *it must have crossed the cooling region, independently of which path it took in the* (D, T) *diagram* (of course its density must remain above $D=1$). Therefore, the total fraction of gas that has been able to cool corresponds essentially to the fraction of mass in halos with virial temperatures greater than 10^4 K. Note that we neglect here halos with a virial temperature greater than 10^4 K, which are later embedded within halos of smaller temperature. Such a process is likely to be unimportant, especially in the CDM scenario, due to the fast growth of the temperature of typical halos, as we pointed out above. This integrated fraction has been represented in Fig. 3. The value reached at present is of the order of 80%, almost independently of the parameters. This comes from the fact that any piece of gas should at some stage lie in a potential well within the cooling region. Note that CDM is believed to lead to very late galaxy formation (White & Frenk 1991). However, from our curves it is clear that all the present stars (see below) can form by a redshift of 5, even if $b_\rho=2.2$. The actual difficulty is the large late cooling, and clearly the main problem is to prevent this "overcooling", which is expected to occur in any hierarchical picture.

On the observational side, $B_*(0)$ can be compared with two measured quantities. The first constraint comes directly from the observed number density of stars

$\Omega_*=B_*(0)\Omega_{\mathrm{b}}$,

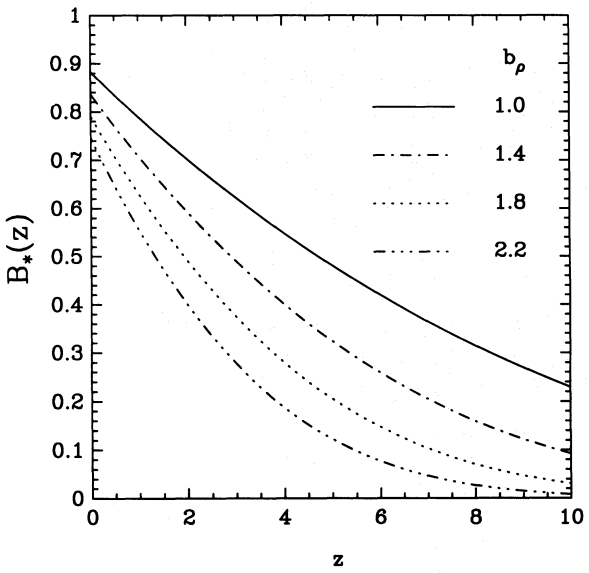

Fig. 3. Evolution with redshift of the integrated fraction of gas $B_*(z)$ that cools for different normalizations of the CDM spectrum. This quantity represents the fraction of baryons expected to have been processed into stars by the epoch z. The present value $B_*(0)$ is insensitive to the adopted bias parameter

yielding

$$B_*(0)=\frac{(M/L)_*}{\Omega_b(M/L)_{close}},$$

where $(M/L)_{close}$ is the mass-to-light ratio that closes the Universe, and is equal to $750^{+350}_{-200}\,h_{50}$ (Efstathiou et al. 1988a), with $\Omega_b=0.04-0.06h_{50}^{-2}$ (Olive et al. 1990; Walker et al. 1991). The fraction of gas that has been cooled by now is essentially provided by the baryonic content of galaxies, i.e. the mass-to-light ratio of the stellar component. Population synthesis does not provide adequate estimate of this quantity because the low mass star content of galaxies is uncertain (Jablonka & Arimoto 1991). However, upper limits to $(M/L)_*$ can be obtained by estimating the maximum disk mass for spirals and the dynamical mass for ellipticals. Depending on type and color, the maximum disk produces $M/L_B\approx 3\pm 2h_{50}$ (from Athanassoula et al. 1987). For elliptical galaxies, the dynamical blue mass-to-light ratio of the central regions is $M/L_B\approx 7\pm 2.5h_{50}$ (from Lauer 1985). Thus we adopt an upper-limit of $(M/L)_*=5\pm 2h_{50}$, which leads to a $\Omega_*\leq 0.003-0.013$ and

$$B_*(0)\leq 0.05-0.3h_{50}^2.$$

We can also infer a similar constraint: as stars and cold gas lie only in galaxies, $B_*(0)$ is equal to the fraction of mass in galaxies times the star to gas ratio in galaxies. Analyses of EINSTEIN and EXOSAT X-ray observations, respectively by David et al. (1990) and Edge & Stewart (1991), indicate that in clusters of galaxies there is 1–8 times more mass in gas than in stars [both studies assume $(M/L)_*=8$], where the ratio increases with cluster richness (in fact with T_{gas}). Thus, $B_*(0)$ must be smaller than the fraction of gas in the Universe lying in galaxies, and, if the ratio of baryonic matter to non-baryonic matter is the same in galaxies and in the IGM, then $B_*(0)$ represents a lower limit to the fraction of mass associated with galaxies, (there might be baryons that have not yet cooled, at least at large distances from the core), one can write this as

$$B_*(0)\leq\Omega_{gal},$$

where Ω_{gal} is the contribution of galaxies to Ω_0 . This leads to the constraint

$$B_*(0)\leq(M/L)_{gal}/(M/L)_{close},$$

where $(M/L)_{gal}$ is the typical mass-to-light ratio of galaxies. Depending on how far out one considers the extent of galaxies, one gets $h_{50}^{-1}(M/L)_{gal}$ in the range 2–50 (Faber & Gallagher 1979), thus yielding

$$B_*(0)\leq 0.002-0.09,$$

independent of the Hubble constant.

The calculated value $B_*(0)=0.8$ is much larger than the observed one. In addition, we have clearly underestimated the fraction of gas able to cool in the cosmic history. If cooling in potential wells with $T<10^4$ K is taken into account, almost all baryons should end up today in stars. One can possibly argue that this cooling does not lead to normal stars, implying that, even in a non-baryonic model, the dark matter contains most of the baryons. For example, one can imagine that 90% of the primordial gas able to cool is turned into low-mass stars, the remaining baryons corresponding to visible stars. However, as we will see in the following section, such a scheme is difficult to reconcile with the fraction of gas in clusters. We conclude that in CDM model, *the galaxy formation rate expected from simple cooling arguments produces far too many galaxies.* From our argument on the amount of total cooling we expect the same conclusion to hold in any hierarchical picture. Numerical checks of this "overcooling problem" are difficult. While hydrodynamical treatments of the cosmological gas are beginning (Carlberg & Couchman 1989; Evrard 1990; de Araujo & Opher 1991; Cen et al. 1991; Kates et al. 1991), the dynamical range will be extremely difficult to achieve (Buchert & Bastelmann 1991). With a cubic box size of 10 Mpc, a resolution of 10^3 in length and 10^9 in mass are required to follow the first halos in which cooling occurs.

3.2. Evidence for a reheating phase

The existence of a large amount of hot gas in clusters indicates that a substantial fraction of baryons should be in the form of gas. X-ray data imply a gas to star ratio in the range 1–8 (David et al. 1990; Edge & Stewart 1991). Now it is difficult to imagine that baryonic gas exists only in clusters. In a hierarchical picture, clusters form after the galaxies, and the difference in the environment at the time of galaxy formation should be representative of the average situation (this is no longer true in "biased" or "anti-biased" scenarios, but this could be taken into account in the following analysis) and thus a significant fraction of baryons in the Universe should lie in intergalactic gas. In rich clusters, X-ray observations provide an estimate of the contribution of gas to the density of the Universe. If the intergalactic gas to star ratio in clusters is representative of the whole Universe, then the IGM

1992A&A...264..365B

density is

$$\Omega_{\rm IGM} \approx \left(\frac{M_{\rm gas}}{M_*}\right)_{\rm clusters} b_{\rm L}\Omega_*,$$

where $b_{\rm L}$ is the luminosity bias of clusters which should be of the order of $\approx 4-5$ to be consistent with $\Omega_0 = 1$. With a gas to star mass ratio of 1–8 in rich clusters (David et al. 1990; Edge & Stewart 1991), $\Omega_{\rm IGM}$ can easily contain all the baryonic content of the universe predicted from primordial nucleosynthesis (see above). Here, by IGM we mean any gas that is not in stars. The amount of diffuse neutral gas ($T_{\rm gas} < 10^4$ K) is well constrained by the limits from the Gunn–Peterson (Gunn & Peterson 1965) test, implying that the gas must be highly ionized at large redshifts (Steidel & Sargent 1987). QSO absorption line systems do not provide a significant contribution to $\Omega_{\rm b}$, except may be the damped systems. This implies that small halos with $T_{\rm vir} < 10^4$ K are *not* the sites of large amounts of baryons.

The Gunn–Peterson test is usually explained by assuming the existence of a strong UV background. In fact, photoionization from QSOs is not sufficient to maintain the observed ionization degree (Shapiro & Giroux 1987). Recent constraints from the He Gunn–Peterson test indicate that if the IGM is shock-heated the temperature should be larger than $10^{5.3}$ K (Tripp et al. 1990). Collisional heating by supernovae winds from protogalaxies may be the source of such heating (Larson 1974; Dekel & Silk 1986), but other sources are also possible. Collin–Souffrin (1991) has suggested that Compton heating in the pre-QSO period can reach a temperature of the order of 10^5 K. The mechanism is very efficient if the X-ray background is produced at high redshift ($z \approx 10$).

The existence of hot gas in clusters does however provide direct evidence that the cosmological gas should not have been efficiently converted into stars in the past: as we already pointed out above, the gas in structures that lie under the cooling curve on the right part of Fig. 1 must originate from the left part of the diagram (at recombination the gas temperature is ≈ 3000 K). Therefore, this gas must have crossed at some epoch into the cooling region and then been converted into stars. As this argument applies to any piece of hot gas, it would imply that clusters should contain almost no hot gas! To overcome this difficulty, *cluster gas must have gone through a stage of strong reheating.* The relatively high metallicity of cluster gas (David et al. 1991) directly supports this scenario.

The reheating of gas can be well explained by some feedback mechanism (Chiang et al. 1989). The existence of such a feedback mechanism has been advocated in several contexts. For example, Dekel & Silk (1986) argue that galaxies with circular velocity $V_{\rm c} < 100$ km s^{-1} essentially form no stars, because supernova winds expel their gas content. In our model, we find that the fraction of cooled gas in potentials with $V_{\rm c} > 100$ km s^{-1} remains of the order of 50%, too high to be consistent with the observations (see Sect. 3.1 above). A temperature of $T \approx 10^6$ K is required to get as little as 10% of the gas converted into stars. This value is well constrained as, on one hand, the temperature has to be high enough to prevent efficient cooling, while on the other hand, cooling must not be canceled.

Another argument for a hot IGM comes from the formation of spiral galaxies. Their collapse must be highly dissipative if they are to form a gaseous-stellar disk, which means that a large fraction of their baryons must be in gaseous form before collapse. This implies that too high a star-formation rate (hereafter, SFR) before collapse is not allowed, otherwise an essentially stellar system would form. Kinematic analyses of the spheroid of our Galaxy (e.g. Bienaymé et al. 1987) indicate that the mass of the stars in the spheroid is small in comparison with the mass of the dark halo, so that most baryons are in gas phase at collapse. If this gas were cold, it would have sunk towards the center and cooled, forming too many stars. On the other hand, the gas cannot be too hot, otherwise it would not be confined to the dark matter potential. Therefore, we conclude that the gas in protogalactic systems that lead to spiral galaxies should lie at a temperature close to the virial temperature of the potential i.e. $T_{\rm spiral} \approx 10^6$ K, the same temperature as found above with the previous line of reasoning.

The existence of a hot IGM at a temperature of the order of 10^6 K and containing most of the baryons at high redshift is thus coupled with a re-heating mechanism associated with galaxy formation. Note that recent limits obtained with COBE on the comptonization parameter [$y \leq 10^{-3}$ (Mather et al. 1991; Gush et al. 1991], require that the IGM cannot be too hot ($T < 10^7$ K, Barcons et al. 1991), however the COBE limit does not seriously constrain the IGM history (Bartlett & Stebbins 1991).

However, the existence of a hot IGM substantially changes the cooling history. Gas cannot fall into a potential with $T_{\rm vir} < T_{\rm gas}$. Figure 4 presents the cooling history as in Fig. 2, assuming that the gas is kept hotter than some temperature by some heating mechanism. We used $b_\rho = 1.4$ as suggested by a cluster temperature distribution function (Blanchard & Silk 1991). We see from this figure that "overcooling" is prevented if the gas is heated at a temperature of the order of 10^6 K. The advocacy of a heating mechanism in a CDM scenario has also

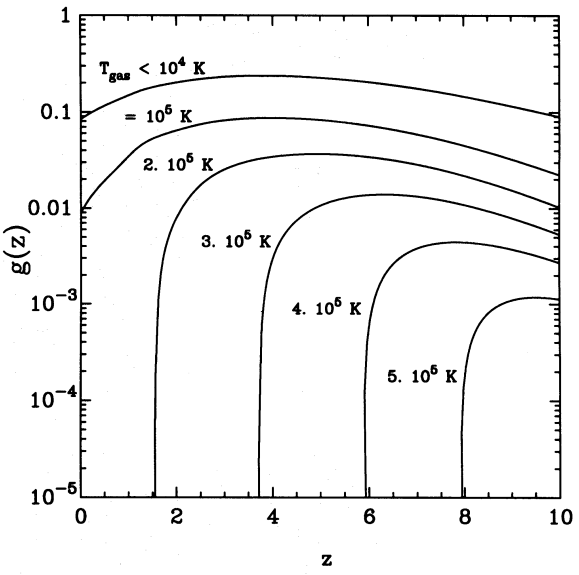

Fig. 4. Evolution with redshift of the instantaneous fraction of gas $g(z)$ that cools when the IGM is heated before collapsing in potential wells. The normalization of the CDM spectrum is $b_\rho = 1.4$, and the other parameters are the same as in Fig. 3. The temperature (which thus corresponds to the minimum virial temperature of the galaxies) is indicated for each curve

been pointed out by White & Frenk (1991) and Cole (1991). However, in our model we assume that the heating is mainly homogeneous, rather than local. Of course, the main problem remains the nature of the heating mechanism, although the Compton heating suggested by Collin-Souffrin (1991) fits nicely in our scenario and is close to what seems necessary. Other possibilities include the product of the decay of exotic dark matter (Asselin et al. 1987), or, perhaps more likely, mechanisms coupled to the SFR history (Silk 1985), for which case gas is maintained at a temperature close to T_*. From Fig. 4, we see that when the gas is hot, cooling is not very efficient after a redshift z_* of the order of 4. By this time, the gas temperature should have reached a value of the order of a few 10^6 K, and gas cools adiabatically once the heating mechanism terminates (shaded area in Fig. 1).

3.3. *The faint-end luminosity function*

As discussed in the preceding section, a halo becomes a galaxy only if its virial temperature is larger than the gas temperature. This implies that forming protogalaxies with a virial temperature lower than the gas temperature will basically lead to dark halos (i.e. without any luminous component). If the temperature of the gas remains constant, then the luminosity function should display a low luminosity cut-off, associated with the gas temperature. In other words, galaxies with circular velocity smaller than some value, will not form "bright galaxies". However, as already mentioned above, a high velocity cut-off (corresponding to L_* galaxies) is then required to prevent efficient cooling, forbidding the formation of low circular velocity galaxies. Nevertheless, re-heating is feedback-driven by the star formation rate (see Fig. 4) and stops when this rate falls below a certain value.

A fraction of this gas sinks into the deep potentials of groups and clusters, and is prevented from subsequent cooling by gravitational heating, while the remaining fraction, outside most dark matter potential wells, follows the adiabatic cooling of a dilute gas

$$T(z)=T_*\left(\frac{1+z}{1+z_*}\right)^2,$$

and, assuming no other heating mechanism, its present temperature should be of a few 10^4 K. As the redshift decreases, a smaller fraction of gas is able to fall into shallower potentials which are forming at a virial temperature equal to the gas temperature. In the dark matter potential wells, the gas density increases and enters the cooling region, giving rise to gaseous systems. The number of such systems at their formation epoch is therefore determined by the number of halos at the epoch at which the gas temperature is equal to their virial temperature.

We can estimate the galaxy luminosity function, assuming that halos are not destroyed by subsequent evolution of the clustering hierarchy. As seen in Sect. 2, the slope of the mass function of cosmic structures is very close to -2. Therefore, the low-mass tail of the mass function of halos is

$$N(m,z)\sim\frac{1+z}{m^2}.$$

From Eq. (18), the velocity dispersion associated with the temperature of the gas is $\sigma=\sigma_0(1+z)$ and thus the mass-velocity dispersion relation gives the typical mass of the *galaxies* forming at the redshift z as $m\sim\sigma^3(1+z)^{-3/2}\sim(1+z)^{3/2}$ (see Eq. 14). The number density of galaxies varies then as

$$N(m)\sim m^{-4/3}.$$

Assuming an L–σ relation of the form $L\sim\sigma^\beta$, we can infer the present-day observed luminosity function. The luminosity function has a power-law dependence at faint magnitudes

$$\phi(L)\sim L^{-(1+1/\beta)}.$$

From the observed values of $\beta\sim 2.7$–4.0, the resulting theoretical slope is interestingly close to the observed one.

We also predict that the faint end of the luminosity function should present a cut-off at a luminosity corresponding to the present temperature of the IGM, i.e. at a velocity dispersion in the range 20–50 km s^{-1} (more precisely we expect a cut-off in the circular velocity distribution function of galaxies; the consequences for the luminosity function depend on the details of star formation in its early stages). In our scenario, low-luminosity galaxies form late[2], and galaxy formation is still occurring in potentials of the above velocity dispersion. It is not easy to calculate whether star formation occurs in these systems in such a short time. It is tempting to identify these systems with gas-rich dwarf galaxies like DDO154 (Carignan & Freeman 1989) or HI 1225+01 (Giovanelli & Haynes 1990) where the star to gas ratio is very small. As hot gas in clusters no longer falls in shallow potentials as the cluster forms, we expect that such faint galaxies form preferentially in the field, so that at least the gas rich dwarfs should lie outside well-defined "old" structures that have virialized at higher redshift. Binggeli et al. (1989) show that dwarf ellipticals are at most as clustered as bright galaxies. Vader & Sandage (1991) claim that dwarf ellipticals are the most clustered population. On the other hand, Thuan et al. (1991) show that irregular dwarfs are almost absent of clusters although they find that the correlation function of these dwarfs is similar to that of bright galaxies. In our model, the low velocity halos naturally separate into two very different populations. The first population corresponds to the first bound objects that crossed the cooling area, and can be identified as the dwarf elliptical systems, while a second population, of recent formation, contains the gas-rich dwarfs. As we expect the dwarf ellipticals to be in higher density regions, there should be a segregation effect in the clustering of the two populations, as observed, and their stellar content should be older than for normal galaxies, although the difference is small. Normal lower luminosity galaxies should be younger, the youngest ones being the HI dwarfs.

4. Conclusions

We have investigated in detail the derivation of the mass and luminosity functions, giving a general formal expression for the cosmic mass function, based on two assumptions: (1) fragmentation processes are negligible and (2) the transition from the linear to the non-linear regime is controlled by the linear overdensity δ. Assuming, in addition, that the initial density fluctuations are scale-invariant, we have shown that the asymptotic low-mass slope can be derived.

Although our mass function can be shallower at low masses than the Press-Schechter mass function, we argue that this is

[2] Note that in the hierarchical scenario, low mass objects form preferentially earlier as illustrated in Eq. (12).

1992A&A...264..365B

probably not an explanation for the observed shallow slope of the galaxy luminosity function. Dynamical processes such as tidal effects cannot be responsible either. Instead, we suggest that the galaxy luminosity function is related to the rate of galaxy formation, coupled to the cosmological evolution of intergalactic gas. We find that most of the present day stars should form at large redshift (as high as 5 for $b=2.2$, and larger than 10 for $b\leq 1.4$), although this leads to the very serious "overcooling" problem, that is the model predicts far too much cold gas by now. We also find that the existence of a re-heating mechanism is *necessary* to account for the hot gas in clusters of galaxies.

Instead of assuming "local" reheating, we assume the cosmological gas to be uniformly reheated. The main point to notice is that in such a case the gas will not fall in potentials with virial temperature smaller than the temperature of the cosmological gas. It is important to keep in mind the fact that the IGM is necessarily at temperature larger than 10^4 K and therefore this mechanism should work at some level. Our analysis has revealed several interesting aspects of the way galaxy formation may proceed within such a hot IGM. First, we have presented several lines of argument pointing to the existence of such a hot IGM with a temperature of 10^6K at the time of galaxy formation. Second, we find that the bulk of galaxy formation takes place at a reasonable redshift, of the order of 5–20, depending on the value of the bias parameter. Third, the luminosity function is strongly affected by the existence of such a hot phase and flattens to values such that the luminosity function has a faint-end slope close to the observed one. We predict the existence of a turn-over in the luminosity function at low magnitudes, related to the present temperature of the IGM. Our model provides a natural explanation for the different properties (morphologies, gaseous and stellar content, ages, and large-scale clustering) of dwarf ellipticals and dwarf irregulars. In this model the HI dwarfs are the present-day forming galaxies, corresponding to the smallest potentials in which the gas can fall.

Our model provides some relief to the problems of the Cold Dark Matter scenario of galaxy formation. First, the shape of the luminosity function is easily explained. Second, galaxy formation is strongly modulated by the temperature of the gas the IGM should probably not have a homogeneous temperature, and the local rate of galaxy formation will vary accordingly, leading to inhomogeneities in the galaxy distribution that will be loosely correlated to the underlying density field. Recently, Babul & White (1991) has suggested that the activity of QSO's could induce such a modulation. A hot inhomogeneous IGM should induce similar variations. Still, a major problem for the CDM model remains the shape of the temperature distribution of clusters (Blanchard & Silk 1991).

We suggest several tests for this scenario. The ongoing large surveys of the galaxies may reveal the cutoff in the luminosity function. In clusters, this cut-off should occur at a brighter luminosity. The high degree of ionization revealed by the Gunn-Peterson test should be caused by collisions (high temperature), rather than by radiation (photo-ionization), and the determination of the mean temperature of the IGM is a crucial test of our model.

Acknowledgements. We thank Suzy Collin-Souffrin and Joe Silk for useful comments. DVG was partially supported by a predoctoral grant from the European Doctoral Network in Astrophysics.

Appendix

In this appendix, we give a detailed derivation of the mean fraction of gas that cools as a function of redshift. For this, we compute, for given redshift and object mass M, the ratio of the mass within which the cooling time is *locally* smaller than either the *local* free-fall time or the Hubble time, to the total mass in gas $\Omega_g M$. A similar local analysis of the various cooling times can be found in Evrard (1989). The mass dependence has been presented by Peacock & Heavens (1985) and analyzed by Ashman & Carr (1991). The global fraction of gas is then obtained by averaging over the Press–Schechter mass function. This method has been introduced by Blanchard et al. (1990), and subsequently used by Ashman & Carr.

We assume that structures are singular isothermal spheres

$$\rho=\frac{\sigma^2}{2\pi G r^2}, \tag{18}$$

where σ is the 1-D velocity dispersion. The virial theorem gives

$$\sigma^2=\frac{GM}{2R}, \tag{19}$$

Now writing energy equipartition as $kT=\mu m_p\sigma^2$ we obtain

$$\rho=\frac{2}{\pi}\left(\frac{kT}{G\mu m_p}\right)^3\frac{1}{M^2}. \tag{20}$$

Writing the total mass of the structure as

$$M=\tfrac{4}{3}\pi R^3\bar{\rho} \tag{21}$$

gives a mean density and temperature

$$\bar{\rho}=\frac{9\pi^2}{16}f_v^{-3}g_v^2\rho_0(1+z)^3, \tag{22}$$

$$T_{vir}=\left(\frac{\pi^2}{96}\right)^{1/3}f_v^{-1}g_v^{2/3}\frac{\gamma\mu m_p}{k}(GM)^{2/3}H_0^{2/3}(1+z), \tag{23}$$

where $\rho_0=3H_0^2/8\pi G$, f_v is the ratio of final virialized scale to turnaround scale (usually 1/2) and g_v is the ratio of virialized time to turnaround time (usually 2, sometimes 3). Now eliminating the scale R of the structure with Eqs. (19), (21), and (22), one finally gets

$$M=\frac{16}{3\pi\sqrt{3}}\frac{f_v^{3/2}}{g_v}(GH_0)^{-1}(\mu m_p)^{-3/2}\left(\frac{kT}{1+z}\right)^{3/2}. \tag{24}$$

The cooling time of a primordial ionized gas of temperature T, with helium mass abundance Y is

$$t_c=\frac{3}{2}\frac{nkT}{n_p^2\Lambda(T)}=\frac{3}{2}\frac{\mu_1^2 m_p}{\mu\Omega_g\rho}\left[\frac{kT}{\Lambda(T)}\right], \tag{25}$$

where n, n_p, and ρ are the respective particle (including electrons), proton, and total mass densities, m_p is the proton mass, k is Boltzmann's constant, Λ is the cooling function (in erg cm^3 s^{-1}), Ω_g is the ratio of gas density to critical density, and finally $\mu=\rho/nm_p=4/(8-5Y)$ and $\mu_1=\rho/n_p m_p=1/(1-Y)$.

The free-fall (dynamical) time for a singular isothermal sphere is locally

$$t_d(r)=[8G\rho(r)]^{-1/2}. \tag{26}$$

The cooling time is shorter than a fraction η_d of the free-fall time

if

$$\rho(r) > \rho_{\rm cool}^{(1)} = \frac{18 G \mu_1^4 m_{\rm p}^2}{\mu^2 \Omega_{\rm g}^2 \eta_{\rm d}^2} \left[\frac{kT}{\Lambda(T)} \right]^2 . \quad (27)$$

Now combining Eqs. (20), (24), and (27) the fraction of gas that cools in less than a fraction $\eta_{\rm d}$ of the free-fall time is

$$w_1 = {\rm Min}\left[1, \frac{\sqrt{3\pi}}{16} \frac{g_{\rm v}}{f_{\rm v}^{3/2}} \frac{\eta_{\rm d} \Omega_{\rm g} \mu H_0}{G \mu_1^2 m_{\rm p}} \left(\frac{\Lambda(T)}{kT} \right) (1+z)^{3/2} \right]. \quad (28)$$

The second cooling criterion is derived from the current Hubble time

$$t_{\rm H}(z) = \left(\frac{2}{3H_0} \right) (1+z)^{-3/2} . \quad (29)$$

Using Eqs. (25) and (29), we find that the cooling time is shorter than a fraction $\eta_{\rm H}$ of the local Hubble time for densities

$$\rho(r) > \rho_{\rm cool}^{(2)} = \frac{9}{4} \frac{\mu_1^2 m_{\rm p}}{\mu \Omega_{\rm g} \eta_{\rm H}} \left[\frac{kT}{\Lambda(T)} \right] H_0 (1+z)^{3/2} , \quad (30)$$

and the fraction of gas that cools in less than a fraction $\eta_{\rm H}$ of the "local" Hubble time is

$$w_2 = {\rm Min}\left[1, \left(\frac{3\pi}{32} \right)^{1/2} \frac{g_{\rm v}}{f_{\rm v}^{3/2}} \left(\frac{\eta_{\rm H} \Omega_{\rm g} \mu H_0}{G \mu_1^2 m_{\rm p}} \right)^{1/2} \left(\frac{\Lambda(T)}{kT} \right)^{1/2} (1+z)^{3/4} \right]. \quad (31)$$

We show in Fig. 1, a local density-temperature diagram, in which we display the critical cooling densities $\rho_{\rm cool}^{(1)}$ and $\rho_{\rm cool}^{(2)}$ [Eqs. (27) and (30)], where the latter density is plotted for $z = 0$.

We now estimate the mean fraction of gas that is able to cool as a function of redshift, by averaging over the Press–Schechter mass function.

$$g_i(z) = \frac{1}{\rho} \int_0^\infty M \phi(M, z) w_i(M, z) {\rm d}M , \quad (32)$$

where M is related to ν through $\nu = 1.69(1+z)/\sigma_0(M)$ and the rms density fluctuation is given by

$$\sigma_0^2(M) = \frac{1}{2\pi} \int_0^\infty |\delta_k|^2 k^2 {\rm e}^{-k^2 R^2} \, {\rm d}k . \quad (33)$$

We plot the resultant mean cooled fractions in Fig. 2.

References

Allen A.J., Richstone D.O. 1988, ApJ 325, 583
Appel L.A., Jones B.J.T., 1990, MNRAS 245, 522
Ashman K.M., Carr, B.J., 1991, MNRAS 249, 13
Asselin X., Girardi G., Salati P., Blanchard A., 1987, Nucl. Phys. B310, 669
Athanassoula E., Bosma A., Papaioannou S., 1987, A&A 179, 23
Babul A., White S.D.M., 1991, MNRAS 253, 21P
Bahcall N.A., 1979, ApJ 232, 689
Barcons X., Fabian A.C., Rees M.J., 1991, Nat 350, 685
Bardeen J.M., Bond J.R., Kaiser N., Szalay A.S., 1986, ApJ 304, 15
Bartlett J.G., Stebbins A., 1991, ApJ 371, 8
Bernardeau F., Schaeffer R., 1991, A&A 250, 23
Bienaymé O., Robin A., Crézé M., 1987, A&A 180, 94
Binggeli B., Tarenghi M., Sandage A., 1989, A&A 228, 42
Binney J., 1977, ApJ 215, 483
Blanchard A., Silk J., 1991, "Diffuse Backgrounds", Proceedings of the XXIst Rencontres de Moriond in Astrophysics, ed. B. Rocca-Volmerange, J.-M. Deharveng and Editions Frontières, Gif-sur-Yvette, p. 93
Blanchard A., Valls-Gabaud D., Mamon G., 1990, in "Particle Astrophysics, the early Universe and cosmic structures", Proc. XXth Rencontres de Moriond in Astrophysics, ed. J.-M. Alimi, A. Blanchard, A. Bouquet, F. Martin de Volnay J. Trân Thanh Vân, Editions Frontières, Gif-sur-Yvette, p. 403
Bond J.R. 1989, in Large-Scale Motions in the Universe, ed. V.C. Rubin & G.V. Coyne, Princeton, Princeton University Press, p. 419
Bond J.R., Cole S., Efstathiou G., Kaiser N., 1991, ApJ 379, 440
Bower R.G., 1991, MNRAS 248, 332
Buchert T., Bastelmann M., 1991, A&A 251, 389
Carignan C., Freeman K.C., 1989, ApJ 332, L33
Carlberg R.G., Couchman H.M.P., 1989, ApJ 340, 47
Cavaliere A., Colafrancesco S., Scaramella R., 1991, ApJ 380, 15
Cen R.Y., Jameson A., Liu F., Ostriker J., 1991, ApJ 362, L41
Chiang W.-H., Ryu D., Vishniac E.T., 1989, ApJ 339, 603
Colafrancesco S., Lucchin F., Matarrese S., 1989, ApJ 345, 3
Cole S., 1991, ApJ 367, 45
Collin-Souffrin S., 1991, A&A 243, 5
Couchman H.M.P., Carlberg R.G., 1991 (preprint)
David L.P., Arnaud K.A., Forman W., Jones C., 1990, ApJ 356, 32
David L.P., Forman W., Jones C., 1991, ApJ 380, 39
de Araujo J.C.N., Opher R., 1991, ApJ 379, 461
Dekel A., Silk J., 1986, ApJ 303, 39
Edge A.C., Stewart G.C., 1991, MNRAS 252, 428
Efstathiou G., Rees M.J., 1988, MNRAS 230, 5P
Efstathiou G., Ellis R.S., Peterson B.A., 1988a, MNRAS 232, 431
Efstathiou G., Frenk C.S., White S.D.M., Davis M., 1988b, MNRAS 235, 715
Evrard A., 1989, ApJ 341, 26
Evrard A., 1990, ApJ 363, 349
Faber S.M., Gallagher J.S., 1979, ARA&A 17, 135
Faber S.M., Jackson R.E., 1976, ApJ 204, 668
Frenk C.S., Efstathiou G., White S.D.M., Davis M., 1990, ApJ 327, 507
Giovanelli R., Haynes M.P., 1989, ApJ 346, L5
Gott J.R., Rees M.J., 1975, A&A 45, 365
Gunn J.E., Peterson B.A., 1965, ApJ 142, 1633
Gush H., Halpern M., Wishnow E., 1991, Phys. Rev. Lett. 65, 537
Henriksen R.N., Lachièze-Rey M., 1990, MNRAS 245, 255
Kates R.E., Kotok E.V., Klypin A.A., 1991, A&A 243, 295
King I.R., 1962, AJ 67, 471
Jablonka P., Arimoto N., 1992, A&A, (submitted)
Jones B.J.T., Palmer P.L., Wyse R.F.G., 1981, MNRAS 197, 967
Lacey C., Silk J., 1991, ApJ 381, 14
Lauer T.R., 1985, ApJ 292, 104
Larson R.B., 1974, MNRAS 169, 229
Lucchin F., Matarrese S., 1990, ApJ 330, 535
Maddox S.J., Efstathiou G., Sutherland W.J., Loveday J., 1990, MNRAS 242, 43P
Mamon G.A., 1987, ApJ 321, 622
Martínez-González J., Sanz J., 1988, ApJ 332, 89
Mather J.C., et al., 1990, ApJL, 354, L37
Moore B., Frenk C., White S.D.M., 1991, (preprint)
Newmann W.I., Wasserman I., 1990, ApJ 354, 411

Olive K.A., Schramm D.N., Steigman G., Walker T.P., 1990, Phys. Lett. B 236, 454
Peacock J.A., Heavens A.F., 1985, MNRAS 217, 805
Peacock J.A., Heavens A.F., 1990, MNRAS 243, 133
Peebles P.J.E., 1969, JRASC 63, 4
Peebles P.J.E., 1974, ApJ 189, L51
Press W.H., Schechter P., 1974, ApJ 187, 425 (PS)
Rees M.J., Ostriker J.P., 1977, MNRAS 179, 541
Saunders W., Frenk C., Rowan-Robinson M., Efstathiou G., Lawrence A., Kaiser N., Ellis R., Crawford J., Xia X.-Y., Parry I., 1991, Nat 349, 32
Schaeffer R., Silk J., 1985, ApJ 292, 319
Shapiro P.R., 1991, in: Deharveng J.-M., Rocca-Volmorange B. (eds.) Diffuse Backgrounds, Proc. XXIst Rencontres de Moriond in Astrophysics. Editions Frontières, Gif-sur-Yvette (in press)
Shapiro P.R., Giroux M.L., 1987, ApJ 321, L107
Silk J., 1977, ApJ 211, 638
Silk J., 1985, ApJ 297, 9
Silk J., White S.D.M., 1978, ApJ 223, L59
Steidel C.C., Sargent W.L.W., 1987, ApJ 318, L11
Sunyaev R.A., Zel'dovich Ya.B., 1972, A&A 20, 14
Thuan T.X., Alimi J.-M., Gott III J.R., Schneider S.E., 1991, ApJ 370, 25
Tonry J.L., 1982, ApJ 251, L1
Tripp T.M., Green R.F., Bechtold J., 1990, ApJ 364, L29
Tully R.B., Fischer J.R., 1977, A&A 54, 661
Vader J.P., Sandage A., 1991, ApJ 379, L1
Valls-Gabaud D., Alimi J.-M., Blanchard A., 1989, Nat. 341, 215
Walker T.P., Steigman G., Schramm D.N., Olive K.A., Kang K.A., 1991, ApJ 376, 51
White S.D.M., Frenk C.S., 1991, ApJ 379, 52
White S.D.M., Rees M., 1978, MNRS 183, 341

B.2 Are cluster ellipticals the products of mergers?

Mamon, 1992, *ApJ 401, L3–L7*

THE ASTROPHYSICAL JOURNAL, 401:L3–L6, 1992 December 10

ARE CLUSTER ELLIPTICALS THE PRODUCTS OF MERGERS?

GARY A. MAMON
DAEC, Observatoire de Paris-Meudon, 92195 Meudon, France
Received 1992 August 3; accepted 1992 September 24

ABSTRACT

The rates of evolution of galaxy morphologies in clusters are integrated within an analytical collision model where merger remnants have elliptical morphologies. Cluster and galaxy properties are set by cosmological spherical infall in an $\Omega = 1$ universe, and once galaxies fall into the cluster, they are severely tidally stripped by the cluster potential. Mergers become efficient as galaxies rebound out of the cluster core. The local merger rate is constant in time. The precise shape of the morphology-density and morphology-radius relations for ellipticals is in fine agreement with the observational data, including the sharp increase in elliptical fraction recently found by Whitmore and Gilmore within the central 100 kpc of clusters. No recourse need be made for increased merging within low velocity dispersion subclusters. The normalization of the relation is fit for galaxies satisfying $M/L \simeq 60\ h$.

Subject headings: cosmology: theory — galaxies: clustering — galaxies: elliptical and lenticular, cD — galaxies: kinematics and dynamics

1. INTRODUCTION

Although simulations of merging galaxies yield elliptical-like remnants (Barnes 1988, 1993) questions have been raised as to whether *most* elliptical galaxies could be formed by mergers (Ostriker 1980; Tremaine 1981; van den Bergh 1982), one objection (Ostriker 1980) being that the large velocity dispersion in clusters ought to prohibit merging. In this *Letter*, a merger model is presented to test whether or not galaxy mergers can produce the observed morphology-density and morphology-radius relations in clusters of galaxies, respectively given by Postman & Geller (1984) and Whitmore (1993). The mix of morphologies is evolved in time, assuming mergers yield ellipticals and initially nearly all the galaxies are non-elliptical. This morphological evolution is placed in the context of galaxies falling into a cluster and being tidally stripped by the cluster potential as they pass through its center. A similar attempt has been performed by Silk & Norman (1981), but they assumed that all the merging occurs *before* galaxies fall into clusters, whereas there is probably not enough time for this. Although it is often assumed that merging in clusters occurs in low velocity dispersion subclusters, the model presented here assumes the cluster to be smooth. This is in line with the realization by Sanromà & Salvador-Solé (1990) that the morphology-density relation remains the same when one performs an angular scrambling of the galaxy positions, as well as the observation by Whitmore & Gilmore (1991) that galaxy morphologies are at least as dependent on their clustocentric radius than on the density of their environment.

2. COSMOLOGICAL INFALL

Figure 1 shows the schematic time evolution of the radius of three shells of matter with their initial Hubble expansions, their subsequent infall into a cluster, and final virialization. At a given time the regions beyond the turnaround radius of the cluster are expanding with the universe, the outer regions of the cluster situated between the turnaround radius and the mixing radius are infalling, while the inner regions of the cluster, within the mixing radius are the sites of shell crossing.

For $\Omega = 1$, top hat spherical infall (Gunn & Gott 1972) leads to simple scaling relations for the turnaround radius, mass, and mean density:

$$R_{\rm ta} \sim t^{8/9}\ , \quad M_{\rm ta} \sim t^{2/3}\ , \quad \bar{\rho}(R_{\rm ta}) \sim t^{-2}\ . \tag{1}$$

As shells spend most of their time at a fixed fraction of their initial turnaround radius, one obtains a "pile-up" model of successive shells, where one can relate the properties of shells at different radii from the laws in equation (1) above (Gott 1975):

$$M(R) \sim R^{3/4}\ , \quad \rho(R) \sim R^{-9/4}\ , \quad v_{\rm cl}(R) \sim R^{-1/8}\ . \tag{2}$$

Galaxies will possess huge halos before they fall into a cluster: the turnaround radius of a galaxy today is $r_{\rm ta} = (8Gmt_0^2/\pi^2)^{1/3} = 0.68\ h^{-1}\ (hm/10^{12}\ M_\odot)^{1/3}$ Mpc. Before galaxies enter a cluster, mergers should be insignificant, as the galaxy densities are low, and most galaxies deep in clusters today will have spent a negligible fraction of their lives outside of clusters. Once a galaxy falls in, the merger rate remains low because it moves too rapidly in the cluster. When the galaxy bounces back to its apocenter, it loses most of its huge halo in a tidal shock, its velocity relative to the cluster galaxies becomes small, and only then will the merger rate be important. This occurs a little before 3 times the turnaround time $T_{\rm ta}$, and to be conservative, mergers are assumed to start precisely at $3T_{\rm ta}$.

3. CLUSTER TIDES

As galaxies fall into the cluster, their outer halos will be stripped from the tides emanating from the cluster potential itself (White & Rees 1978). The tidal acceleration felt by a star in an infalling galaxy can be written

$$\begin{aligned} \boldsymbol{a}_{\rm tid} &= -\frac{GM(S)}{S^3}\boldsymbol{S} + \frac{GM(R)}{R^3}\boldsymbol{R} \\ &= \frac{GM(R)r}{R^3}\left\{3(\hat{\boldsymbol{R}}\cdot\hat{\boldsymbol{r}})\left[1-\frac{\rho(R)}{\bar{\rho}(R)}\right]\hat{\boldsymbol{R}} - \hat{\boldsymbol{r}}\right\}, \end{aligned} \tag{3}$$

where $\boldsymbol{R}$ and $\boldsymbol{S}$ give the positions of the galaxy center and the star in the frame of the cluster center, respectively, while $\boldsymbol{r} = \boldsymbol{S} - \boldsymbol{R}$ gives that of the star relative to the center of its galaxy, and where the second equality is obtained by expand-

1992ApJ...401L...3M

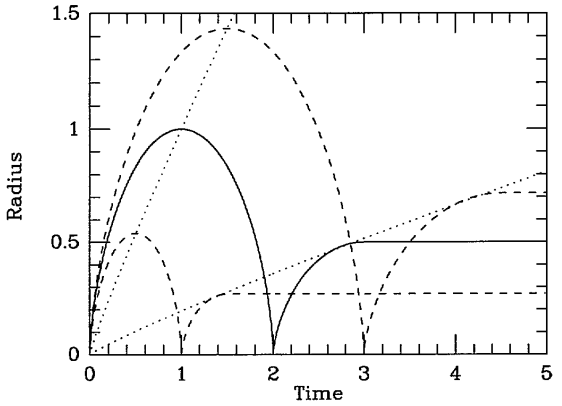

FIG. 1.—Time evolution of the radii of three shells (*solid and dashed curves*). The locus of turnaround radii (eq. [1]) is given by the upper dotted curve, while that of the "mixing" radii is given by the lower dotted curve.

ing $M(S)/S^3$ into power series around R. Each star then feels an impulse $\Delta \boldsymbol{v}_{\rm tid} = \int_{-\infty}^{\infty} \boldsymbol{a}_{\rm tid}\, dt$. Then integrating equation (3), for the case of a scale-free density distribution $\rho \sim R^{-\alpha}$ and assuming an impulse approximation of constant velocity of the galaxy $\boldsymbol{V}$ yields after some algebra

$$|\Delta v_{\rm tid}| = \text{constant} \times \frac{GM(R_p)r}{R_p^2 V} = \text{constant} \times f(\epsilon)\left[\frac{GM(R_p)}{R_p^3}\right]^{1/2} r\,, \quad (4)$$

where R_p is the pericentric distance, r is the distance of the star to the center of the galaxy, ϵ is a measure of the ellipticity of the galaxy's orbit, and $f(\epsilon) = V_{\rm circ}/V(R_p)$.

Now, following White (1983) and Mamon (1987), identify the tidal radius with the radius of the last bound shell after the passage of the galaxy through the cluster center. Thus, $|E| \simeq Gm(r)/r \simeq \Delta E \simeq (\Delta v)^2/2$, and equation (4) yields $\tilde{\rho}_{\rm gal}(r_t) = \text{constant} \times \tilde{\rho}_{\rm cl}(R_p)$. From cosmological infall, $\rho \sim r^{-9/4}$ for both galaxy and cluster (eq. [2]), which leads to $r_t \sim R_p$. Now galaxies acquire angular momentum through interactions with other galaxies outside and within the cluster and will thus avoid disruption by missing the cluster center. Because the evolution of clusters is self-similar in the $\Omega = 1$ cosmology, one has $r_t \sim R_p \sim R_{\rm ta}$.

4. MERGER RATE

The merger rate is $k(t) = \int_0^\infty s(v, t) v f(v, t) dv$, where $s(v, t)$ is the merger cross section at time t, while $f(v, t)dv$ is the probability that the relative velocity of two merging galaxies is between v and $v + dv$ at time t. The merger cross section is a simplified version of that of Roos & Norman (1979) with a critical impact parameter that falls linearly with velocity:

$$s = \pi p^2\,,$$

$$p = \begin{cases} \alpha_p r_h \left(1 - \dfrac{v}{\alpha_v v_g}\right) & v < \alpha_v v_g\,, \\ 0 & v \geq \alpha_v v_g\,, \end{cases}$$

where r_h and v_g are the average half-mass radius and the one-dimensional internal velocity dispersion of the two colliding galaxies, respectively, while α_p and α_v are dimensionless numbers. If the cluster is virialized, then $f(v)$ should describe a Maxwellian velocity distribution of dispersion $2^{1/2} v_{\rm cl}$, where $v_{\rm cl}$ is the one-dimensional velocity dispersion of the cluster. After some algebra, the merger rate turns out to be

$$k = 2\pi^{1/2} \alpha_p^2 \alpha_v r_h^2 v_g K(v_{\rm cl}/v_g)\,,$$

where K is a dimensionless merger rate given by

$$K = \left[\frac{1}{x} + \frac{2}{x^3} - \frac{2\exp(-x^2)}{x^3} - \frac{3\pi^{1/2}}{2}\frac{\operatorname{erf} x}{x^2}\right], \quad (5a)$$

$$x = \frac{\alpha_v v_g}{2 v_{\rm cl}}\,. \quad (5b)$$

As illustrated in Figure 2, K is maximum for $v_{\rm cl} \simeq 0.7 v_g$ and falls off as $(v_{\rm cl}/v_g)^{-3}$ for $v_{\rm cl} \gg v_g$ to values roughly 25 times lower for ratios typical of clusters. With $\alpha_p = 4$ (Aarseth & Fall 1980) and $\alpha_v = 3.1(3)^{1/2} = 5.4$ (Roos & Norman 1979) one gets the merger rate

$$k \simeq 8 \frac{G^2 m^2}{v_{\rm cl}^3}\,. \quad (6)$$

5. SIMPLE MODEL

Consider the reaction between disks (D) and ellipticals (E): D + D → E, evolving with rate k. The elliptical fraction follows $df_{\rm E}/dt = nk(1 - f_{\rm E})^2$, which integrates to

$$\frac{f_{\rm E} - f_i}{(1 - f_{\rm E})(1 - f_i)} = \int_{t_i}^{t_0} nk\, dt\,, \quad (7)$$

where f_i is the initial elliptical fraction when a shell enters the cluster.

Consider now a shell at given radius R. In the cosmological pile-up model (§ 2) the local properties of the cluster are fixed. This implies that *the local merger rate is constant in time*. Then $\int_{t_i}^{t_0} nk\, dt = nk(t_0 - t_i) \simeq nkt_0$. Now from § 3, tides limit the galaxies to $r_t \sim R_{\rm ta} \sim R$. If, in general, $\rho \sim R^{-\alpha}$, then $m \sim R^{3-\alpha}$ and $v_g \propto v_{\rm cl} \sim R^{1-\alpha/2}$. Hence $v_{\rm cl} \gg v_g$ at all times, and from equation (2), $k \sim R^{3-\alpha/2}$. Now, $n \sim \rho(R)/m \sim R^{-3}$ (e.g., eq. [2]), hence $nk \sim R^{-\alpha/2} \sim n^{\alpha/6}$. For $\alpha = -9/4$ (eq. [2]), the

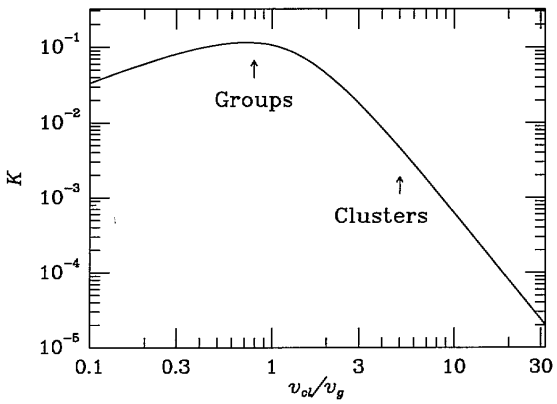

FIG. 2.—Dimensionless merger rate K (eq. [5]) vs. ratio of cluster to galaxy velocity dispersions. Here $\alpha_v = 5.4$.

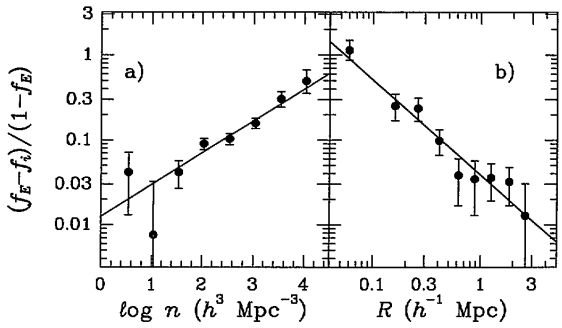

FIG. 3.—(*a*) Morphology-density relation, with best fit field elliptical fraction (f_i) of 7.3%. *Points:* observed relation (Postman & Geller 1984). *Lines:* power-law predictions from eq. (8). (*b*) Morphology-radius relation, with best-fit field elliptical fraction of 13.0%. *Points:* observed relation (Whitmore 1993) restricted to $R < 3\ h^{-1}$ Mpc. *Lines:* power-law predictions from eq. (8).

merger model therefore predicts

$$(1-f_i)nkt_0 \simeq \frac{f_E-f_i}{1-f_E} \sim n^{3/8} \sim R^{-9/8} . \quad (8)$$

6. COMPARISON WITH OBSERVATIONS

6.1. *Shape and Normalization*

As shown in Figure 3, the observed morphology-density relation of Postman & Geller (1984), derived from Dressler's (1980) cluster data, yields an excellent fit to the power law of slope 3/8 of equation (8) (with a best-fit elliptical fraction of 7.3%), giving $\chi^2 = 4.69$ for 6 degrees of freedom, where this fit and the following one are obtained to

$$f_E = (f_i + cx^\beta)/(1 + cx^\beta) ,$$

where x is either number density or radius, giving the relations of equation (8).

Whereas a recent reanalysis by Whitmore & Gilmore (1991) and Whitmore (1993) of Dressler's cluster data shows a sharp increase of the elliptical fraction within 100 kpc from the cluster cores, this increase is consistent with the $-9/8$ slope of equation (8). Indeed, the fit in Figure 3*b* gives $\chi^2 = 4.32$ for 7 degrees of freedom. Although Whitmore (and Gilmore) consider *projected* radius, one can easily show that, if $\rho(R)$ and $(f_E - f_i)/(1 - f_E)$ (eq. [7]) are power laws of physical radius, then $(f_E - f_i)/(1 - f_E)$ must also be a power-law of projected radius with the same power. Therefore, the points in Figure 3*b* should be shifted to the right, but the slope is unaltered. Hence, *this simple merger model predicts the shape of the observed morphology-density and morphology-radius relations in the inner cores of clusters.*

The normalization to the fit of the Postman and Geller's morphology-density relation is

$$f_E - f_i = 1.25 \times 10^{-2}[n/(h^3\ \mathrm{Mpc}^{-3})]^{3/8} ,$$

which matches equation (8) if

$$8G^2nm^2t_0/v_{cl}^3 = 0.43[n/(10^4\ h^3\ \mathrm{Mpc}^{-3})]^{3/8} .$$

For galaxies in cluster cores (adopting $v_{cl} = 1000$ km s^{-1}) this yields $m \simeq 2.1\ h^{-1}\ 10^{11}[n/(10^4\ h^3\ \mathrm{Mpc}^{-3})]^{-5/16}\ M_\odot$. Now Postman and Geller normalized their morphology-density relation to absolute magnitudes brighter than $-17.5 + 5 \log h$. This corresponds to $0.174L_*$ or $0.134L_*$ depending on whether $M_* = -19.40$ (Postman and Geller) or -19.68 (Efstathiou, Ellis, & Peterson 1988). Now the harmonic mean luminosity is then $\bar{l} = 0.38L_*$ or $0.31L_*$, respectively, giving a mean galaxy mass-to-light ratio $m/l \simeq 60h[n/(10^4\ h^3\ \mathrm{Mpc}^{-3})]^{-5/16}$, in both cases, a reasonable value for galaxy halos. Note that once the halos of galaxies merge, the luminous components merge soon thereafter (Barnes 1993).

6.2. *Groups versus Clusters*

Table 1 shows how the *global* effect of mergers should compare in different environments. As the elliptical fraction is roughly given by the product nk (eq. [7]), one sees from Table 1 that in loose groups ellipticals should be less frequent than in rich clusters. On the other hand, the fraction of ellipticals in Hickson's (1982) compact groups should saturate to a value near unity. Numerical simulations of dense groups of galaxies have indeed shown that a merging instability occurs within a few crossing times (Carnevali, Cavaliere, & Santangelo 1981; Mamon 1987). In fact, compact groups have much fewer ellipticals than rich clusters of comparable *apparent* density (Mamon 1986), which seems best explained by the hypothesis that compact groups are merely chance alignments of galaxies within larger loose groups (Mamon 1986) and clusters (Walke & Mamon 1989).

The Postman & Geller (1984) hypothesis of a universal morphology-density relation for groups and clusters is not validated by this merger model and for the intermediate densities appearing in both loose groups and rich clusters, the loose group elliptical fraction should be much larger. The continuity found by these authors may be caused by the Virgo and Coma clusters contaminating the densest bin in their loose group sample (Whitmore 1992).

6.3. *Differences among Clusters and Compact Groups*

The analysis by Edge & Stewart (1991a, b) of X-ray data from *EXOSAT* reveal interesting constraints on cluster properties: the spiral fraction in clusters *decreases* with cluster gas temperature as $f_S \sim T^{-1.2}$, whereas rich clusters tend to be hot as measured by $n(<250\ h^{-1}\ \mathrm{kpc}) \sim T^{0.9}$. From equation (6), one predicts $f_E \sim nm^2/T^{3/2}$. If the numerator were independent of cluster temperature, then one would expect *fewer* ellipticals in hot clusters, contrary to what is seen by Edge and

TABLE 1

MERGERS IN DIFFERENT ENVIRONMENTS

Environment	$n(h^3\ \mathrm{Mpc}^{-3})$	k (Relative Units)	nk (Relative Units)
Rich clusters	10^3–10^4	1/25	4
Loose groups	10–100	1	1
Compact groups	10^3–10^4	1	100

Stewart. The metric galaxy number density n helps towards the opposite trend but is not sufficient. The mean galaxy mass is then the crucial variable, and one has

$$\begin{cases} f_E \sim T^{1.4} & \text{if } m \sim L_1 , \\ f_E \sim T^{-0.6} & \text{if } m \text{ independent of } L_1 , \end{cases}$$

where L_1 is the luminosity of the brightest cluster member, and scales as $L_1 \sim T$ (Edge & Stewart 1991a). Hence the merger model cannot work unless the mean mass in galaxies scales as the luminosity of the brightest cluster member.

Note that in compact groups a similar trend exists (Hickson, Kindl, & Huchra 1988): f_S decreases with increasing v_{cl}. Here, equation (5) shows that the merger rate is roughly independent of the system's velocity dispersion (Fig. 2). Now, there is some question on how real the morphology-velocity dispersion relation is in compact groups. Indeed, compact group properties are strongly dependent on redshift (Tikhonov 1990; Mamon 1990; Whitmore 1990) and the most distant groups tend to be elliptical rich, luminous, large, and with high-velocity dispersions. These trends may be interpreted as being caused by the contamination of the distant compact groups in Hickson's catalog by the bright ends of clusters (Mamon 1993).

In summary, *despite their high velocity dispersions, clusters of galaxies should witness enough mergers to explain the high fraction of ellipticals seen in them.* These mergers occur from the low-end tail of the distribution of collision velocities in clusters. This result has been obtained without recourse to low velocity dispersion substructures, in which merging may be enhanced. Nevertheless, the trend of increasing elliptical fraction with increasing cluster velocity dispersion may signify that processes other than mergers may contribute significantly to elliptical morphologies. In a following paper in preparation, the present model will be refined to include: (i) a more self-consistent "chemistry" (adding the "reactions" $D + E \rightarrow E$ and $E + E \rightarrow E$); (ii) a multimass model with a maximum cannibal to victim mass ratio to produce ellipticals; (iii) the treatment of internal cluster kinematics; (iv) $\Omega < 1$.

I wish to thank Cedric Lacey for a thorough reading of a preliminary version of this manuscript, as well as useful comments by Alain Blanchard, Avishai Dekel, Henry Ferguson, Daniel Gerbal, Joe Silk, and Brad Whitmore.

REFERENCES

Aarseth, S., & Fall S. M. 1980, ApJ, 236, 43
Barnes, J. 1988, ApJ, 331, 699
———. 1993, in Physics of Nearby Galaxies: Nature or Nurture?, ed. T. X. Thuan, C. Balkowski, & J. Trân Thanh Vân (Gif-sur-Yvette: Editions Frontières), in press
Carnevali, P., Cavaliere, A., & Santangelo, P. 1981, ApJ, 249, 449
Dressler, A. 1980, ApJ, 236, 351
Edge, A. C., & Stewart, G. C. 1991a, MNRAS, 252, 414
———. 1991b, MNRAS, 252, 428
Efstathiou, G., Ellis, R. S., & Peterson, B. A. 1988, MNRAS, 232, 431
Gott, J. R. 1975, ApJ, 201, 296
Gunn, J. E., & Gott, J. R. 1972, ApJ, 176, 1
Hickson, P. 1982, ApJ, 255, 382
Hickson, P., Kindl, E., & Huchra, J. P. 1988, ApJ, 331, 64
Mamon, G. A. 1986, ApJ, 307, 426
———. 1987, ApJ, 321, 622
———. 1990, in Paired and Interacting Galaxies, ed. J. W. Sulentic & W. C. Keel (Washington: NASA), 619
———. 1993, in Distribution of Matter in the Universe, ed. G. Mamon & D. Gerbal (Paris: Obs. Paris), 51
Ostriker, J. P. 1980, Comm. Astrophys., 8, 177
Postman, M., & Geller, M. J. 1984, ApJ, 281, 95
Roos, N., & Norman, C. A. 1979, A&A, 95, 349
Sanromà, M., & Salvador-Solé, E. 1990, ApJ, 360, 16
Silk, J., & Norman, C. 1981, ApJ, 247, 59
Tikhonov, N. A. 1990, in Paired and Interacting Galaxies, ed. J. W. Sulentic & W. C. Keel (Washington: NASA), 105
Tremaine, S. D. 1981, in The structure and Evolution of Normal Galaxies, ed. S. M. Fall & D. Lynden-Bell (Cambridge: Cambridge Univ. Press), 67
van den Bergh, S. 1982, PASP, 94, 459
Walke, D. G., & Mamon, G. A. 1989, A&A, 295, 291
White, S. D. M. 1983, in Morphology and Dynamics of Galaxies, ed. L. Martinet & M. Mayor (Sauverny: Geneva Obs.), 289
White, S. D. M., & Rees, M. J. 1978, MNRAS, 183, 341
Whitmore, B. C. 1990, in Clusters of Galaxies, ed. W. R. Oegerle, M. J. Fitchett, & L. Danly (Cambridge: Cambridge Univ. Press), 139
———. 1992, private communication
———. 1993, in Physics of Nearby Galaxies: Nature or Nurture? ed. T. X. Thuan, C. Balkowski, & J. Trân Thanh Vân (Gif-sur-Yvette: Editions Frontières), in press
Whitmore, B. C., & Gilmore, D. 1991, ApJ, 367, 64

B.3 Merging history trees for dark matter haloes: tests of the Merging Cell Model in a CDM cosmology

Lanzoni, Mamon & Guiderdoni, 2000, *MNRAS 312, 781–793*

Mon. Not. R. Astron. Soc. **312**, 781–793 (2000)

Merging history trees for dark matter haloes: tests of the Merging Cell Model in a CDM cosmology

B. Lanzoni,[1] G. A. Mamon[1,2] and B. Guiderdoni[1]
[1]*Institut d'Astrophysique de Paris, (CNRS UPR 0341), Paris, France*
[2]*DAEC (CNRS UMR 8631), Observatoire de Paris, Meudon, France*

Accepted 1999 October 15. Received 1999 September 17; in original form 1999 June 7

ABSTRACT

The merging history of dark matter haloes is computed with the Merging Cell Model proposed by Rodrigues & Thomas. While originally discussed in the case of scale-free power spectra, it is developed and tested here in the framework of the cold dark matter cosmology. The halo mass function, the mass distribution of progenitors and child haloes, as well as the probability distribution of formation times, have been computed and compared with the available analytic predictions. The halo autocorrelation function has also been obtained (a first for a semi-analytic merging tree), and tested against analytic formulae. An overall good agreement is found between results of the model, and the predictions derived from the Press & Schechter theory and its extensions. More severe discrepancies appear when formulae that better describe *N*-body simulations are used for comparison. In many instances, the model can be a useful tool for following the hierarchical growth of structures. In particular, it is suitable for addressing the issue of the formation and evolution of galaxy clusters, as well as the population of Lyman-break galaxies at high redshift, and their clustering properties.

Key words: galaxies: clusters: general – galaxies: formation – galaxies: haloes – cosmology: theory – dark matter.

1 INTRODUCTION

In the basic picture of the formation of cosmic structures, the Universe is dominated by a dark matter (DM) component, and small perturbations in the initial density field grow in amplitude proportionally to a linear growth factor, until they approach unity. Then, non-linear effects dominate their evolution, and the regions stop expanding with the Universe, collapse, and virialize, thus forming DM haloes. In hierarchical scenarios, like the cold dark matter (CDM) model, small-scale inhomogeneities collapse first and then aggregate via merging to generate larger structures. Since galaxies form by the collapse and cooling of baryonic gas within DM haloes, and their history is greatly influenced by that of their surrounding haloes (e.g. Lemson & Kauffmann 1999), it is important to understand how these objects form and evolve with time.

The most realistic way for following the history of DM haloes is by means of *N*-body simulations, but they require huge amounts of RAM memory and are computationally expensive. Therefore, they are often limited to a modest dynamic range, and to few different cosmological scenarios.

The simplest alternative approach is to consider only the linear regime of growth of density fluctuations, and describe the non-linear evolution and collapse by means of the spherical 'Top-Hat' model (Gunn & Gott 1972). In this formalism, the formation of a DM halo of mass M at redshift z is described by identifying in the initial density field smoothed on a scale M, and *linearly* extrapolated to redshift z, a region having overdensity equal to a given threshold value. Starting with Gaussian initial conditions, Press & Schechter (1974, hereafter PS) interpreted the probability of finding such regions as the number density of haloes of mass M, that formed at redshift z (see Section 3.1). The PS mass function has been extensively tested against *N*-body simulations, and has been found to be in reasonably good agreement with numerical results (e.g. Efstathiou et al. 1988; Carlberg & Couchman 1989; Lacey & Cole 1994; Gelb & Bertschinger 1994). However, systematic deviations both at small and high masses have been recognised, with the PS formula predicting too many low-mass haloes, and underestimating the number of massive objects (e.g. Jain & Bertschinger 1994; Gross et al. 1998; Somerville, Primack & Faber 1998; Tormen 1998; Lee & Shandarin 1999; Sheth & Tormen 1999; and references therein). A better agreement with numerical results is obtained when ellipsoidal rather than spherical collapse models are considered (Monaco 1995, 1997a,b; Bond & Myers 1996; Audit, Teyssier & Alimi 1997, 1998; Lee & Shandarin 1998, 1999, hereafter LS98 and LS99; Sheth & Tormen 1999; Sheth, Mo & Tormen 1999; and references therein).

Extensions of the PS theory (Bower 1991; Bond et al. 1991) follow the redshift evolution of the halo population as a whole, by deriving the conditional probability of finding progenitors of mass M_p at redshift z_p, given their child haloes of mass M_o at z_o, and vice versa (see Section 3.2). By means of the extended Press & Schechter (EPS hereafter) theory, the distribution of halo formation and survival times, as well as their merger rate, can also be obtained (Lacey & Cole 1993, 1994, hereafter LC93 and LC94; see also Section 3.3). The few comparisons between these analytic predictions and numerical results reveal a general good agreement, even if discrepancies similar to those of the mass function have been pointed out (LC94; Somerville et al. 1998; Tormen 1998).

Still based on the EPS theory, analytic predictions for halo bias in the Lagrangian space of initial conditions have been obtained (Mo & White 1996, MW96 hereafter; Catelan et al. 1998, CLMP hereafter; Porciani et al. 1998; Sheth & Lemson 1999b; Sheth & Tormen 1999; Sheth et al. 1999; and references therein). The halo autocorrelation function $\xi_{hh}(r)$ is then the product of the halo bias with the correlation function of the underlying matter. The predicted ξ_{hh} is in good agreement with that in *N*-body simulations for massive objects, but its amplitude is too large for low-mass haloes (Porciani, Catelan & Lacey 1999, PCL hereafter; Jing 1999; Sheth & Tormen 1999). However, Jing (1999) propose an empirical fitting formula (see Section 3.5) that provides a good description of halo clustering on the whole range of masses (see also Sheth & Tormen 1999; Sheth et al. 1999).

While the PS and EPS formalisms describe the mean statistical properties of the population as a whole, several models of the individual merger history of DM haloes have been proposed (Cole & Kaiser 1988; Kauffmann & White 1993, KW93 hereafter; Rodrigues & Thomas 1996, RT96 hereafter; Somerville & Kolatt 1999; Sheth & Lemson 1999a). Each model presents some advantages and some drawbacks with respect to the others. For example, the 'block model' of Cole & Kaiser (1988) partly retains the spatial information, but it is affected by the discretization of both halo masses (in powers of two), and positions. The KW93 merging tree presents a more continuous spectrum of masses, but a grid of collapse redshifts is imposed, and the relative positions of haloes are unknown. Moreover, it reproduces exactly the mean progenitor mass distribution, but mass conservation is enforced only approximately, while the opposite holds in the model of Somerville & Kolatt (1999).

In this paper, we focus on the 'Merging Cell Model' (MCM)[1] proposed by Rodrigues & Thomas (1996), which has the same characteristics of simplicity and speed as the other merging tree algorithms, but also presents some major advantages. Since it is based on an actual realization of the initial density field, it is much closer to the spirit of *N*-body simulations, thus allowing direct comparisons with numerical results, and it also seems to take into account the spatial correlations of density fluctuations (Nagashima & Gouda 1997). Moreover, no specific collapse times are imposed a priori, and haloes form with a continuous spectrum of masses, and a variety of (Lagrangian) shapes. Also the spatial information about the relative location of haloes is retained by construction, thus allowing study of their clustering properties. While in the original paper, the authors only discuss the halo mass function in the case of scale-free power spectrum, here we consider the more realistic standard CDM (SCDM) cosmology (see Section 3). Moreover, we test the model reliability also in terms of the mass distribution of progenitor and child haloes, the behaviour of the largest progenitor mass as a function of redshift, and the probability distribution of formation times. For the first time for a semi-analytic merging tree, the halo two-point correlation function is also computed, and we test it against theoretical predictions. We outline the method in Section 2, define these quantities and compare them to the analytic predictions in Section 3. Discussion and conclusions are presented in Sections 4 and 5, respectively.

[1] As first coined by Nagashima & Gouda (1997).

2 THE ALGORITHM

2.1 Basic principles

At an 'initial time' t_i, consider the density field $\rho(\boldsymbol{x}, t_i)$ of the Universe characterized by a mean value $\bar{\rho}(t_i)$, and small perturbations $\delta(\boldsymbol{x}, t_i) = \rho(\boldsymbol{x}, t_i)/\bar{\rho}(t_i) - 1$. Through gravitational instability, the amplitude of density fluctuations start growing proportionally to a linear growth factor $D(t)$, i.e. $\delta(\boldsymbol{x}, t) = \delta(\boldsymbol{x}, t_i) \times D(t)/D(t_i)$. Such a linear growth law strictly holds only when perturbations are much smaller than unity, but it is useful to extrapolate it also into the non-linear regime. In fact, the 'Top-Hat' model (Gunn & Gott 1972) shows that the formation of a bound virialized object of mass M occurs at the time t_f when the density contrast of a spherical region in the initial density field, smoothed at a scale M, reaches a critical value δ_c. This in turn corresponds to a value $\delta_c^{\rm lin}(t_f)$ of the density field *linearly* extrapolated to that time, or to a value $\delta_c^{\rm lin}(t_0)$ if the extrapolation is carried on until the present epoch t_0. For an Einstein–de Sitter Universe, $D(t) \propto (1+z)^{-1}$, $\delta_c \simeq 178$, $\delta_c^{\rm lin}(z_f) \simeq 1.686$, and $\delta_c^{\rm lin}(z=0) \simeq 1.686(1+z_f)$. It is therefore sufficient to know the values of the density field linearly extrapolated to $z = 0$, for determining the formation epochs of DM haloes.

Because this is the approach we adopt in the paper, we choose henceforth to change the notation and we denote the density field linearly extrapolated to $z = 0$ as δ. Therefore, $\delta_c = 1.686$, and the collapse redshift of haloes is $z_f = \delta/\delta_c - 1$.

2.2 The method

The MCM is based on an actual realization of the density field, obtained with a standard initial condition generator, by Fourier transforming waves of random phase and amplitude drawn from a Gaussian distribution of zero mean, and variance given by the chosen power spectrum.

A value of the density contrast δ is assigned to each of the L^3 base cells (bcs) composing a periodic cubic box of side L (for simplicity, $L = 2^l$, where l is a positive integer). Density fluctuations are then averaged within cubic *blocks* of side 2, 4, 8, …, L. At each of these smoothing levels, a set of 8 overlapping grids, displaced one relative to another by half a block length in each coordinate direction, is used. This ensures that the density peaks are always approximately centred within one of the blocks in each smoothing hierarchy. At this point, one has a total of $(15L^3 - 8)/7$ base cells and cubic blocks, with side ranging from 1 to L, mutually overlapping in the volume of the box. Each of them is characterized by a value of the density contrast δ.

All base cells and blocks are then ordered in a single list in terms of decreasing δ (or, correspondingly, decreasing collapse redshift). The largest value of δ in the list fixes the earliest z_f of the realization. It usually corresponds to a base cell, which thus becomes the first collapsed object (i.e. the first *halo*). All the

elements of the list are then analysed one after the other from early times to the present, and the specific base cell or cubic block under investigation is called *investigating region*. Whether the investigating region can collapse and give rise to a new halo or not is decided by the following rules:

(i) an investigating region that does not overlap with any other pre-existing halo collapses and forms a new halo;

(ii) if there exist two haloes, each of them containing half of the investigating region, the latter cannot collapse. This is to avoid the formation of very elongated structures in linking together adjacent haloes without the collapse of any new matter. If instead there exists only one halo containing half (or more) of the investigating region, the latter collapses and merges with it, thus forming a new halo;

(iii) after taking into account condition (ii), if the investigating region overlaps with at least half of one (or more) pre-existing halo(s), it collapses and merges with it (them), thus forming a new halo.

Note that in the Lagrangian space of initial conditions, mass and volume are equivalent quantities ($M = \bar{\rho} V$), and 'merging' together the investigating region with one or more pre-existing haloes does not mean summing up their masses. Instead, the mass (volume) of the new resulting halo is that of the old ones plus the fraction of the investigating region that does not overlap with any already pre-existing object.

Thanks to the use of overlapping grids and merging criteria, haloes of a large variety of shapes and masses are obtained. The model also contains information on the relative locations of haloes, since their positions within the box are known, and the effects of discretization are expected to be smaller than in the block model. Moreover, because halo formation times are given by the density contrasts in the list, they span a continuous range of values. As a drawback, the overdensity of the investigating region (which fixes the collapse redshift of the new forming object) is not necessarily equal to the mean overdensity ($\bar{\delta}_{\rm h}$) of the resulting halo. Therefore, the position of an object in the merging tree occasionally differs from that predicted by the linear theory, i.e. the assigned $z_{\rm f}$ is not exactly equal to $\bar{\delta}_{\rm h}/\delta_{\rm c} - 1$, as it should be (see section 3.2 in RT96). Finally, the 'linking' and the 'overlapping' conditions [criteria (*ii*) and (*iii*), respectively] are reasonable but arbitrary, and different choices would result in different mass functions, as discussed by Nagashima & Gouda (1997). Yet, it is not clear which are the 'best' criteria. Thus, we will adopt the original conditions (*ii*) and (*iii*) throughout the paper.

3 TESTS OF THE ALGORITHM

The MCM is based on the linear theory of growth of density fluctuations, and it uses simplified criteria to describe the formation and merging history of DM haloes. It is therefore necessary to test its reliability by comparing its results against those of *N*-body simulations that directly take into account the gravitational interactions between DM particles, and are much more realistic in following the dynamics in the non-linear regime.

The model is required to correctly describe not only the population of haloes at a given redshift, but also how this population evolves with time.

As a first test, the cumulative and the differential mass functions in the case of a scale-free power spectrum with spectral index $n = 0$, and -2 have been computed and compared to those in the original paper (figs 4 and 5 in RT96). A remarkable agreement has been found.

Here we consider the SCDM cosmology, and perform several tests against the available analytic formulae, to verify the reliability of the model results. We set the Hubble constant to $H_0 = 100\,h\,{\rm km\ s^{-1}\,Mpc^{-1}}$, $h = 0.5$. The total and baryonic density parameters are $\Omega_0 = 1$ and $\Omega_{\rm b} = 0.05$ respectively, while that corresponding to the cosmological constant is $\Omega_\Lambda = 0$. The transfer function of Bardeen et al. (1986) is adopted, and the power spectrum is normalized so that the mass variance on scale $8\,h^{-1}\,{\rm Mpc}$ is equal to $\sigma_8 = 0.67$.

For a 256^3 base cell realization in a cubic box of $L = 100\,{\rm Mpc}$ side (i.e. $50\,h^{-1}\,{\rm Mpc}$, and a total mass of about $3.5 \times 10^{16}\,h^{-1}\,{\rm M_\odot}$), the base cell mass is about $2 \times 10^9\,h^{-1}\,{\rm M_\odot}$, and the resulting most massive halo typically has a mass of about $5 \times 10^{14}\,h^{-1}\,{\rm M_\odot}$ (but see Section 3.1). The CPU time on a 500 MHz DEC Alpha workstation is only roughly 25 min, and typically 700 MB of RAM memory are required.

In the following sections, results averaged over 10 different realizations are presented, and error bars correspond to the standard deviations of the 10 run sample.

3.1 Mass function

The differential mass function of haloes, is defined as the comoving number density of haloes with mass in the range [M, $M + {\rm d}M$] at redshift z. This is shown for logarithmic mass interval in the histograms of Fig. 1 (left-hand panels), for $z = 0$ and $z = 3$.

Also shown for comparison as dotted lines are the corresponding predictions of the PS theory (e.g. LC94):

$$\frac{{\rm d}n}{{\rm d}\ln M}(M,z) = \sqrt{\frac{2}{\pi}}\,\bar{\rho}\,\frac{\delta_{\rm c}(z)}{\sigma^2(M)}\left|\frac{{\rm d}\sigma}{{\rm d}M}\right| \exp\left[-\frac{\delta_{\rm c}^2(z)}{2\sigma^2(M)}\right], \qquad (1)$$

where $\delta_{\rm c}(z) = \delta_{\rm c} \times (1+z)$, and $\sigma(M)$ is the mass variance of the linearly extrapolated (to $z = 0$) density field smoothed on scale M. In this paper, $\sigma(M)$ is always computed by a fitting formula analogous to that proposed by White & Frenk (1991), with errors smaller than 8 per cent on mass scales ranging from $10^9\,{\rm M_\odot}$ to $10^{15}\,{\rm M_\odot}$.

Right panels show the cumulative mass fraction for the same redshifts, i.e. the fraction of the total mass which is in haloes of mass above M, at redshift z.

At $z = 0$ the overall agreement is good over a large range of masses, but a lack of objects at the two ends of the mass function is evident. At small masses, the problem seems to be inherent to the method, since this is also the case for scale-free power spectra (RT96; Nagashima & Gouda 1997). This is a drawback of the model, which limits the reliable dynamical range, and it is probably due to the adopted criteria for the formation and merging of haloes. In fact, as detailed in Section 2, the 'bricks' for the construction of haloes are base cells and blocks composed by 8^i bcs ($i = 1, 2, \ldots$). Thus, an object of less than 8 bcs can only result if an *investigating region* partly overlaps with a pre-existing halo, but does not merge with it, and the fraction of its non-overlapping volume (which gives rise to the new halo) is less than 8 bcs. In practice, the model requires that some 'particular' conditions happen in order to form haloes of mass between 2 and 7 bcs, thus explaining the underproduction of these kind of objects in the resulting mass function. The lack of high-mass structures instead, is partly inherent to the method, partly due to a statistical fluctuation (in different realizations in fact the problem is more or less severe). At high redshift the model always tends to produce a

larger number of intermediate mass haloes, and less massive objects than predicted by the PS theory.

These discrepancies appear to be even more severe if compared to results of *N*-body simulations. It has been recently shown that the PS mass function already tends to predict fewer high-mass haloes, and more low-mass objects than those found in the simulations (e.g. Jain & Bertschinger 1994; Gross et al. 1998; Somerville et al. 1998; Tormen 1998; LS99; Sheth & Tormen 1999). An analytic formula which better agrees with numerical results has been obtained by LS98, based on a nonspherical model for the collapse of a perturbation, in the frame of the Zel'dovich approximation (but see also Monaco 1995, 1997a,b; Audit, Teyssier & Alimi 1997; Bond & Myers 1996; Sheth & Tormen 1999; Sheth et al. 1999).

In this formalism, the displacement of a particle due to the surrounding density field, is simply computed from the perturbation potential Ψ generated by the distribution of particles in the *initial* conditions. The mass density can therefore be expressed as a function of the three eigenvalues of the deformation tensor (defined as the second derivative of Ψ), and a virialized bound object forms when the smaller one (λ_3) is positive. The idea is therefore to substitute the collapse condition of the spherical Top-Hat model ($\delta = \delta_c$), with an analogous one for λ_3: a DM halo of mass M forms when this eigenvalue reaches a critical value λ_{3c} in a region of the linearly extrapolated density field, smoothed on a scale M. The resulting mass function is:

$$\frac{\mathrm{d}n_{\mathrm{LS}}}{\mathrm{d}\ln M}(M,z) = \frac{25\sqrt{10}}{2\sqrt{\pi}}\frac{\bar{\rho}}{M}\left|\frac{\mathrm{d}\ln\sigma}{\mathrm{d}\ln M}\right|\frac{\lambda_{3c}(z)}{\sigma}\times f[x], \qquad (2)$$

with $x = \lambda_{3c}(z)/\sigma$, and:

$$f[x] = \left[\frac{5}{3}x^2 - \frac{1}{12}\right]\exp\left[-\frac{5}{2}x^2\right]\mathrm{erfc}[\sqrt{2}x] + \frac{\sqrt{6}}{8}\exp\left[-\frac{15}{4}x^2\right]\mathrm{erfc}\left[\frac{\sqrt{3}}{2}x\right] - \frac{5\sqrt{2\pi}}{6\pi}x\exp\left[-\frac{9}{2}x^2\right],$$

where $\sigma = \sigma(M)$, erfc(x) is the complementary error function, and the critical value for λ_3 has been empirically chosen to be $\lambda_{3c}(z) = 0.37(1+z)$.

Fig. 1 shows that in comparison to the LS98 mass function (solid curves), the MCM presents an excess of small objects, and a significant underproduction of high-mass haloes, especially at high redshift.

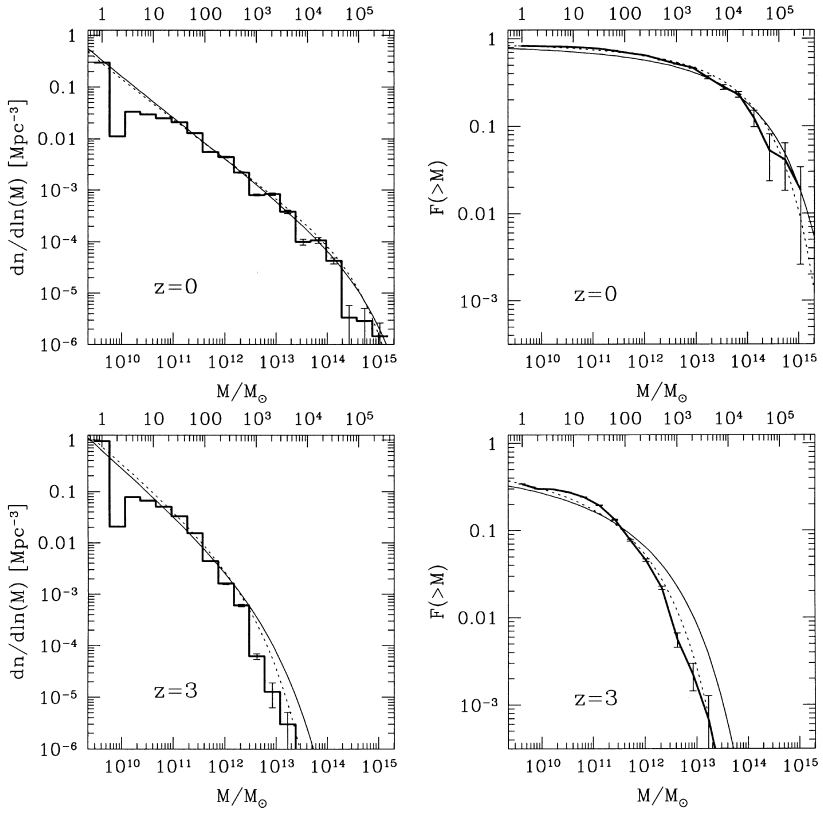

Figure 1. *Left panels*: comoving number density in units of Mpc^{-3}, per logarithmic mass interval, of haloes of mass M at redshifts $z = 0$ (*upper panel*) and $z = 3$ (*lower panel*), as a function of $M/M_\odot$. Masses are also shown in units of base cells on the top of the figure. Results averaged over 10 realizations of the MCM are displayed in the histograms. Error bars show the standard deviations of the 10 run sample. The Press & Schechter (1974) predictions [equation (1)] and the Lee & Shandarin (1998) mass function [equation (2)] are plotted as *dotted* and *solid* curves, respectively. *Right panels*: cumulative mass fraction of haloes with mass larger than M at redshifts $z = 0$ and $z = 3$, as a function of M. Results from the MCM (*thick solid* line) are compared to the PS and the LS98 predictions (*dotted* and *solid* curves, respectively).

3.2 Conditional mass functions

In this section we analyse how the population of haloes identified at a given time has changed with respect to a different epoch.

Fig. 2 shows the mass fraction of haloes of mass M_o at redshift z_o, that has already settled at redshift z_p in progenitors with masses between M_p and $M_p + dM_p$. Child haloes have been selected at $z_o = 0$ and have masses M_o in the range $M_o/M_\odot = [10^i,\ 10^{i+1}[$, where, from the top to the bottom panel, $i = 11, 12, 13, 14$. The mass distribution of their progenitors at $z_p = 1$ is shown in the left panels, that for $z_p = 3$ is plotted on the right-hand panels.

The analytic prediction for the distribution of progenitor masses is given by (e.g. Bower 1991; Bond et al. 1991):

$$\frac{df}{d\ln M_p}(M_p, z_p | M_o, z_o) = \frac{M_p}{\sqrt{2\pi}} \frac{\delta_{cp} - \delta_{co}}{(\sigma_p^2 - \sigma_o^2)^{3/2}} \left|\frac{d\sigma_p^2}{dM_p}\right| \times \exp\left[-\frac{(\delta_{cp} - \delta_{co})^2}{2(\sigma_p^2 - \sigma_o^2)}\right], \quad (3)$$

where $\delta_{cj} = \delta_c(z_j)$, $\sigma_j = \sigma(M_j)$.

Because numerical results shown in Fig. 2 have been obtained for ranges of M_o, the analytic formula has been computed in two different ways for an accurate comparison. In the MCM, the mass of a halo corresponds to the number of base cells that compose it. Thus, when expressed in these units, the mass M_o can only assume $\mathcal{N}$ integer values in the range $[M_i, M_s]$, with $\mathcal{N} = (M_s - M_i + 1)$: i.e. $M_o = \{M_{ok} = M_i + k - 1,\ k = 1, \mathcal{N}\}$. Given the number $N(M_{ok})$ of child haloes with mass equal to M_{ok} for each of its possible $\mathcal{N}$ values, the mean weighted mass in the range is:

$$\bar{M}_o = \frac{\sum_{k=1}^{\mathcal{N}} N(M_{ok}) M_{ok}}{N_o}, \quad (4)$$

where N_o is the total number of haloes in the chosen range of M_o. Dotted curves in Fig. 2 show results from equation (3) computed for $M_o = \bar{M}_o$ (whose numerical values are listed in the figure caption). The abrupt fall down of dotted curves occurs at values of M_p near $\bar{M}_o$, because the progenitor mass obviously cannot be larger than that of its child halo. Since $\bar{M}_o$ is lower than M_s in each panel, this explains why dotted curves are not as extended in M_p as the histograms are.

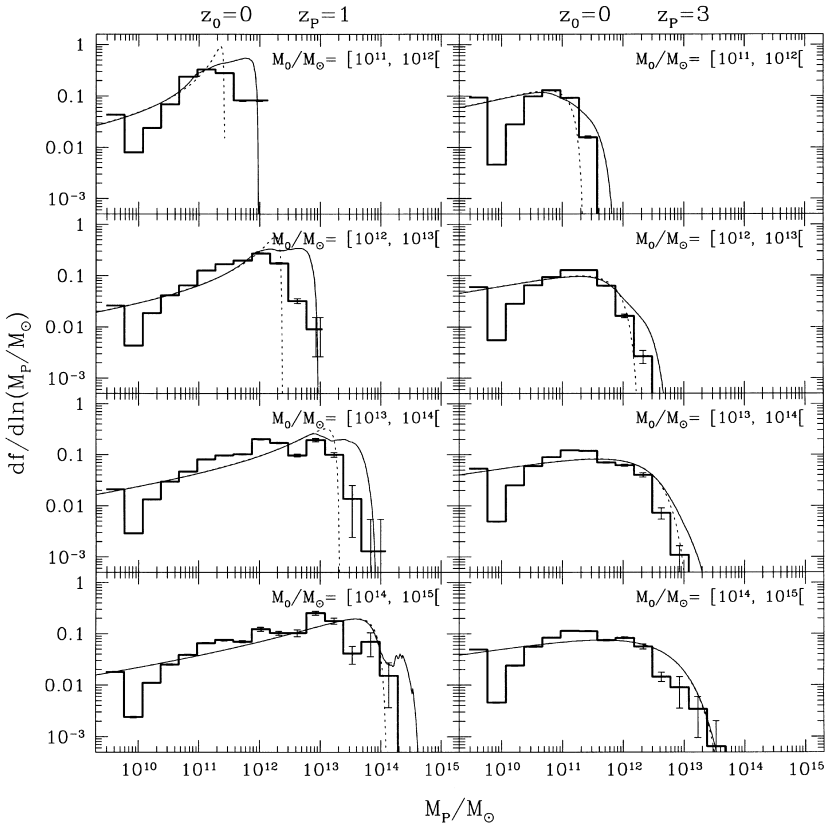

Figure 2. Progenitor mass distribution at redshifts $z_p = 1$ (*left panels*), and $z_p = 3$ (*right panels*), for child haloes in four different mass ranges M_o at $z_o = 0$ (*from top to bottom*: $M_o/M_\odot = [10^i,\ 10^{i+1}[,\ i = 11,\ 12,\ 13,\ 14$). Average results from 10 realizations of the MCM are displayed in the histograms, and their standard deviation is shown as error bars. The average number of child haloes found in each mass range is, from top to bottom: $N_o = 34839$, 5545, 822, and 67. *Dotted* curves correspond to the progenitor distribution computed from equation (3) for M_o equal to the mean mass in the corresponding range ($M_o = \bar{M}_o \simeq 2.7 \times 10^{11}$, 2.5×10^{12}, 2.3×10^{13}, and $1.5 \times 10^{14}\ M_\odot$). *Solid* curves are the average distributions in each mass range, computed from equation (5).

For a better comparison between numerical and analytic results, we have also computed the *average* progenitor mass distribution by summing up the $\mathcal{N}$ single-mass distributions, each weighted with the fraction of mass in haloes of mass M_{ok}:

$$\left\langle \frac{\mathrm{d}f}{\mathrm{d}\ln M_\mathrm{p}} \right\rangle = \frac{\sum_{k=1}^{\mathcal{N}} f(M_{ok}) N(M_{ok}) M_{ok}}{\sum_{k=1}^{\mathcal{N}} N(M_{ok}) M_{ok}}, \quad (5)$$

where $f(M_{ok}) = (\mathrm{d}f/\mathrm{d}\ln M_\mathrm{p})$ is the single-mass progenitor distribution for child haloes of mass M_{ok} as given in equation (3). M_p is obviously also a function of M_o, and it is required that $M_\mathrm{p} \leq \mathrm{M_o}$. The average progenitor mass distribution is plotted in Fig. 2 as solid curves. By construction, $\langle \mathrm{d}f/\mathrm{d}\ln M_\mathrm{p} \rangle$ is a sum of curves of the same kind as the dotted lines, with the sharp cut-off at progenitor masses very similar or equal to those of their child haloes. This is the reason for the oscillations in the solid curves for values of M_p between M_i and M_s.

A lack of objects with masses between 2 and about 7 bcs is apparent, just as was the case for the mass function. The MCM also appears to systematically underproduce progenitors with mass similar to that of their child haloes. At intermediate masses, an overall good agreement between the MCM results and the analytic predictions is found, with a possible slight overproduction of haloes in the model. When compared to *N*-body simulations, these discrepancies may become more severe, since simulations appear to have fewer/more haloes than predicted by EPS theory in the intermediate/high-mass range (Somerville et al. 1998; Tormen 1998). For the less massive child haloes (top panels), numerical and analytic results only agree over a small range of M_p. This is due to the lack of low-mass objects, and to the fact that the minimum mass in the model is limited to 1 base cell, thus not allowing to accurately follow back in time the past history of small haloes.

The reverse conditional probability that a halo of mass M_p at z_p is incorporated at a later time z_o in a halo of mass between M_o and $M_\mathrm{o} + \mathrm{d}M_\mathrm{o}$, is shown per logarithmic mass interval in the histograms of Fig. 3. Progenitors of mass $M_\mathrm{p}/\mathrm{M}_\odot = [10^i,\ 10^{i+1}[$, with $i = 11, 12, 13$, are selected at $z_\mathrm{p} = 1$ (left panels) and $z_\mathrm{p} = 3$ (right panels), and the mass distribution is computed for their child haloes at redshift zero. No results for progenitors with masses

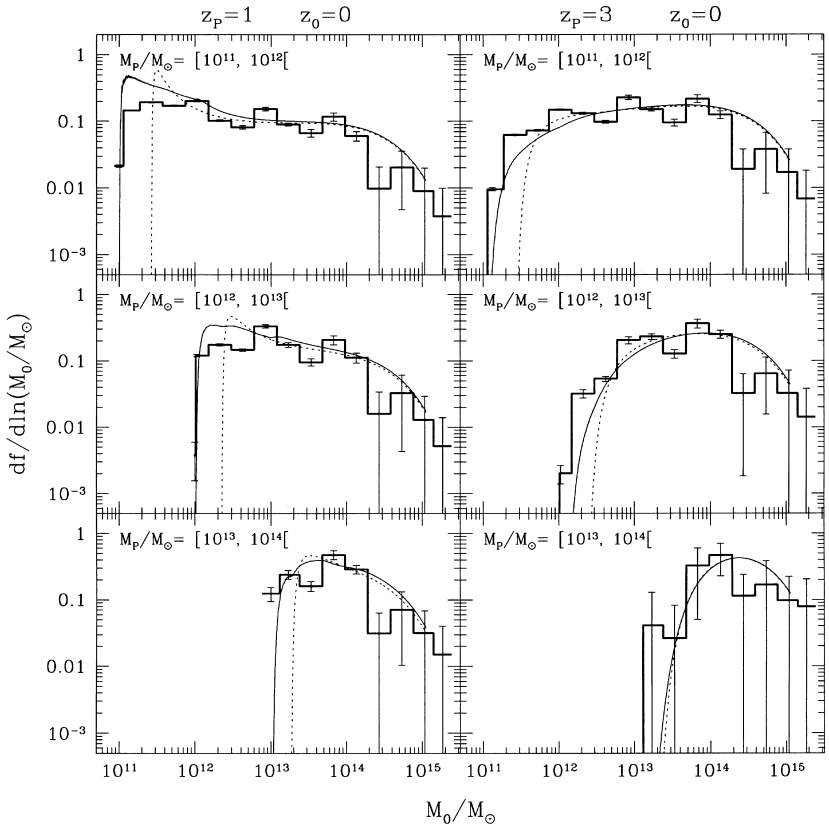

Figure 3. Mass distribution of child haloes at redshifts $z_\mathrm{o} = 0$, given the progenitors at $z_\mathrm{p} = 1$ (*left panels*), and $z_\mathrm{p} = 3$ (*right panels*) with masses $M_\mathrm{p}/\mathrm{M}_\odot = [10^i,\ 10^{i+1}[,\ i = 11,\ 12,\ 13$, from *top to bottom*. Average results from 10 realizations of the MCM are plotted as histograms, and their standard deviation is shown as error bars. The number of progenitors found in each mass range at $z_\mathrm{p} = 1$ is, from top to bottom: $N_\mathrm{p} = 59898$, 6696, and 431, while at $z_\mathrm{p} = 3$, $N_\mathrm{p} = 52213$, 1724, and 8. *Dotted* curves refer to the children mass distribution computed from equation (6) for the mean progenitor mass in the corresponding range (from top to bottom): $\bar{M}_\mathrm{p} \simeq 2.6 \times 10^{11}$, 2.2×10^{12}, and $1.7 \times 10^{13}\,\mathrm{M}_\odot$ for progenitors at $z_\mathrm{p} = 1$; $\bar{M}_\mathrm{p} \simeq 2.3 \times 10^{11}$, 1.9×10^{12}, and $1.5 \times 10^{13}\,\mathrm{M}_\odot$ in the right panels. *Solid* curves are the average distribution in each mass range, computed in the same way as in equation (5), as detailed in the text.

between 10^{14} and $10^{15}\,M_\odot$ are shown, because too few of them have already formed at redshifts 1 and 3.

Given all the objects of mass M_p at z_p, the analytic prediction from the EPS theory for the mass distribution of their child haloes at z_o, when expressed per mass logarithmic interval, is given by (e.g. LC94):

$$\frac{df}{d\ln M_o}(M_o, z_o|M_p, z_p) = \frac{M_o}{\sqrt{2\pi}}\frac{\delta_{co}(\delta_{cp}-\delta_{co})}{\delta_{cp}}\left|\frac{d\sigma_o^2}{dM_o}\right| \times \left[\frac{\sigma_p^2}{\sigma_o^2(\sigma_p^2-\sigma_o^2)}\right]^{3/2}\exp\left[-\frac{(\delta_{co}\sigma_p^2-\delta_{cp}\sigma_o^2)^2}{2\sigma_p^2\sigma_o^2(\sigma_p^2-\sigma_o^2)}\right], \quad (6)$$

where the notation is the same as in equation (3).

As before, equation (6) has been computed in two different ways, in order to get an accurate comparison with the numerical distributions. Results for $M_p = \bar{M}_p$, the mean weighted progenitor mass in the range $[M_i, M_s]$ (analogous to $\bar{M}_o$), are plotted in Fig. 3 as dotted lines. A sharp cut off occurs for values of M_o near to $\bar{M}_p$, because child haloes cannot be less massive than their progenitors. Since $\bar{M}_p$ is larger than M_i in each panel, this explains why dashed lines are not as extended in M_o as histograms are. A more appropriate comparison between numerical and theoretical results is obtained if the *average* child mass distribution $\langle df/d\ln M_o\rangle$ is considered, instead of that relative to progenitors with mean mass $\bar{M}_p$: $df(\bar{M}_p)/d\ln(M_o)$. The computation of $\langle df/d\ln M_o\rangle$ is analogous to that in equation (5), and results are plotted in Fig. 3 as solid lines.

An overall agreement is found between MCM results and the EPS theory predictions, that in turn fit reasonably well *N*-body simulations (LC94). However an oscillating behaviour of the child haloes mass distribution can be recognised in the histograms. Actually it is more evident when a different binning is used (here results are binned on a mass grid $M_o = 2^i$ bcs, $i = 0, 1, 2\ldots$), and it seems inherent to the method. Also the halo mass function and the progenitor distribution present analogous features, and oscillations appear to occur with peaks corresponding to the block masses of 8^i, $i = 1, 2, \ldots$bcs, and with troughs in between. Moreover, the same trend is found in the halo mass function for the scale free power spectrum (in particular for the spectral index $n = -2$, that fits the CDM spectrum over a significant range of masses; see RT96).

3.3 Largest progenitor history

By analysing the variation with redshift of the largest progenitor mass, information can be obtained on how haloes build up in time, whether they preferably form via a continuous and slow accretion of small objects, or whether their mass suddenly increases because of nearly equal-mass merging events, or by mergers of several sub-units at the same time. A different behaviour is expected for haloes of different masses, with larger objects preferably assembling at recent epochs, and smaller haloes showing a more

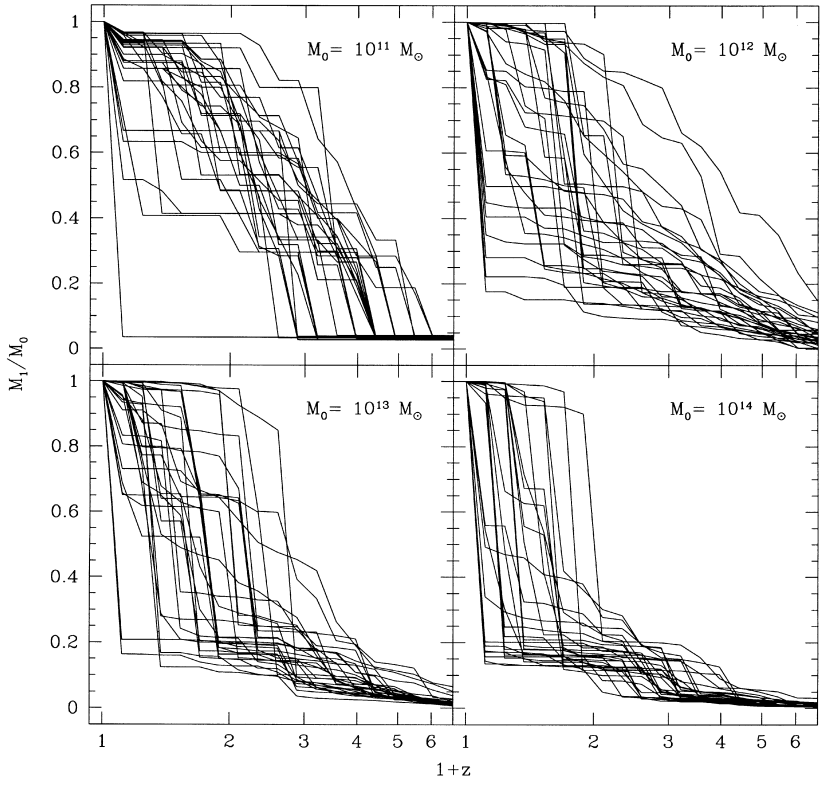

Figure 4. History of the most massive progenitor of 30 haloes selected at $z_o = 0$. The *y*-axis represents the ratio of progenitor mass M_1 to final halo mass M_o. The four panels refer to four different values of $M_o/M_\odot$: 10^{11}, 10^{12}, 10^{13}, 10^{14}.

delayed and smooth evolution with time. This is shown for instance, in KW93, both from their merging tree model, and from *N*-body simulations (their Figs 5 and 6, respectively).

We have looked at the past history of haloes with current mass $M_o = 10^{11}, 10^{12}, 10^{13}, 10^{14}\,M_\odot$, randomly selecting 30 objects for each value of M_o to show the scatter in the merging histories. The ratio between the mass of the largest progenitor M_1, and that of its child halo M_o is plotted in Fig. 4, as a function of $1+z$. For all the masses, the expected trends are obtained, with larger haloes preferably assembling through major mergers at low z, and smaller objects gradually forming in a smoother way by accreting small mass objects over a larger interval of time. A qualitative good agreement of both trends and scatters is also found between the present results and those of KW93. Moreover, halo collapse occurs at more recent epochs here, as expected when a SCDM cosmology is considered instead of an open model ($\Omega_0 = 0.2$ in KW93).

3.4 Formation redshift

In the hierarchical clustering scenario, massive haloes form by accretion of lower mass structures. Therefore, their formation redshift is expected on average to be lower than that of small objects. Actually, because of the continuous evolution in mass due to the hierarchical nature of the process, the definition of 'halo formation time' is not straightforward. In this paper, we adopt the definition of LC93, as the time when half the mass of the halo is assembled, i.e. when a progenitor with mass equal to half or more that of its child halo appears for the first time.

Fig. 5 shows the distribution of formation redshift for haloes with mass $M_o = [10^i,\ 5\times10^i]\,M_\odot$, $i = 11, 12, 13, 14$ at $z = 0$. In agreement with results of the previous section, high-mass objects tend to form at more recent epochs, while lower mass haloes typically collapse earlier and over a larger interval of time. The mean formation redshifts for haloes in the four mass ranges, from lower to higher M_o, are: $\bar{z}_f = 1.55, 1.03, 0.66, 0.46$.

As discussed in LC93 and LC94, the probability that a halo of mass M_o at redshift z_o has a progenitor with mass between $M_o/2$ and M_o at z_p, gives the probability that its formation epoch was earlier than z_p. In differential form, the probability distribution of formation redshifts is therefore given by:

$$\frac{dp}{dz_f}(z_f|M_o,z_o) = \int_{M_o/2}^{M_o} \frac{M_o}{M_p}\left[\frac{\partial}{\partial z_f}\left(\frac{df}{dM_p}\right)\right] dM_p, \qquad (7)$$

where $df/dM_p = df(M_p, z_f|M_o, z_o)/dM_p$ is the progenitor mass distribution (see Section 3.2). Formation times computed by means of the previous formula are found to be in good agreement with *N*-body simulation results, except for haloes on cluster scales

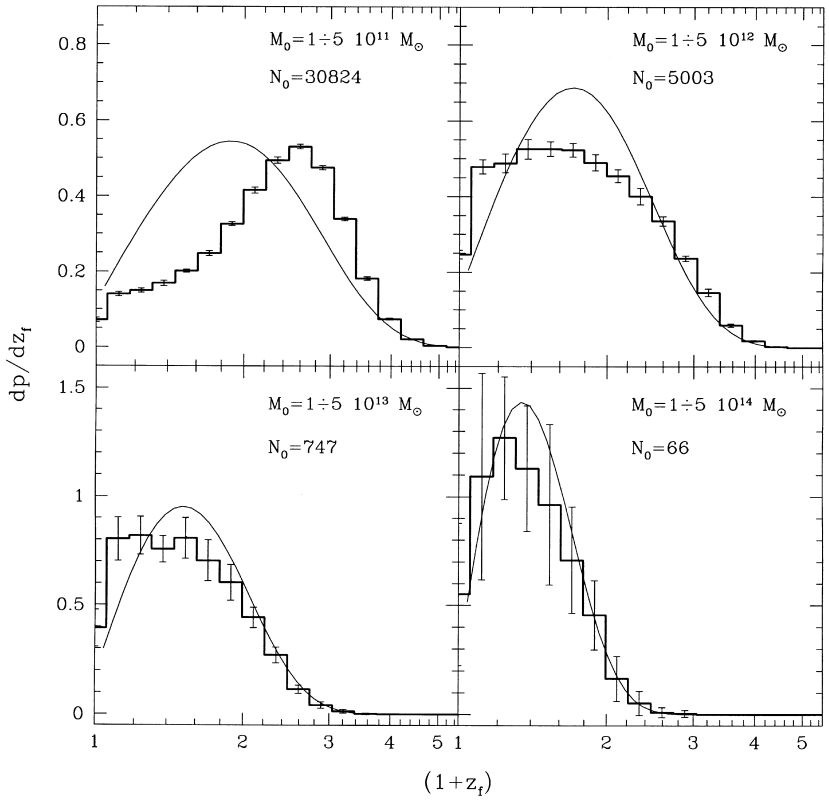

Figure 5. Differential probability distribution of formation redshifts z_f for haloes at $z_o = 0$ with masses $M_o/M_\odot = [10^i,\ 5\times10^i]$, $i = 11, 12, 13, 14$ (see labels), as a function of $(1+z_f)$. Histograms and error bars result from the average over 10 realizations of the MCM. N_o labels the number of haloes found at $z_o = 0$ in the corresponding mass range. *Solid curves* refer to the analytic prediction of the EPS theory computed from equation (7), for $M_o = \bar{M}_o \simeq 2\times10^{11}$, 2×10^{12}, 1.7×10^{13}, $1.4\times10^{14}\,M_\odot$.

that form earlier than predicted by the EPS theory (LC94; Tormen 1998; note however that these conclusions are drawn for scale-free power spectra only).

Once again numerical results are derived for ranges of masses M_o, thus the analytic prediction for z_f has been computed in the same way as discussed in Section 3.2. In this case however, the probability distribution for the average mass $dp(z_f|\bar{M}_o, z_o)/dz_f$, and the *average* probability distribution $\langle dp/dz_f \rangle$ are almost indistinguishable in the chosen range of M_o. Only the former is therefore shown in Fig. 5, where solid curves correspond to equation (7) solved for $M_o = \bar{M}_o \simeq 2.2\times10^{11},\ 2\times10^{12},\ 1.7\times10^{13},\ 1.4\times10^{14}\,M_\odot$. Within the error bars, a very good agreement is found for the most massive objects. For intermediate mass haloes, the epoch when they first appear, as well as the rising of the probability distribution with decreasing z, is well reproduced by the MCM. However, they do not present the expected peak of formation epoch, but instead still form at very recent times, in contradiction with the expectations of the EPS theory. A severe disagreement is found for small objects, with the departure of MCM relative to the EPS theory going in the opposite sense. Low-mass haloes in fact preferentially collapse and stop forming at earlier epochs than predicted, with a peak of formation at about $z_f = 1.6$, instead of $z_f = 0.85$. No significant improvements are obtained if different values for the collapse threshold δ_c are adopted. This confirms once more that the history of low-mass objects is not well followed in the model.

3.5 Two-point correlation function

Since the relative positions of haloes within the box are known by construction, the MCM also contains information about their spatial distribution. We have computed the two-point autocorrelation function of DM haloes, by counting the number of objects separated by a distance r, and comparing it with the value expected for a Poissonian distribution:

$$\xi(r) = \frac{N_{DD}(r)}{N_{RR}(r)} - 1, \tag{8}$$

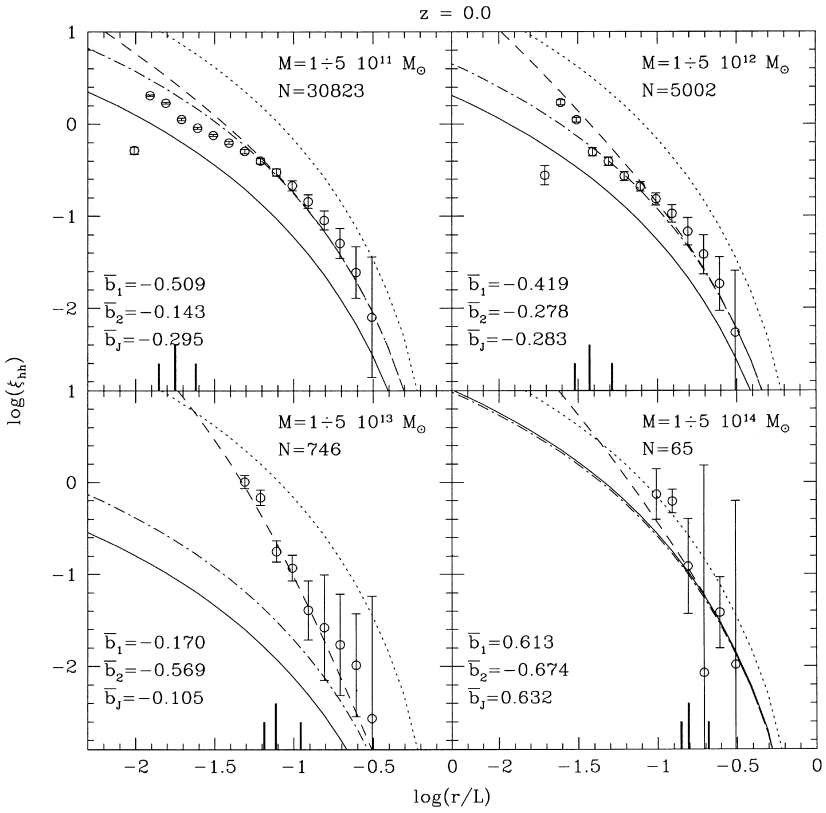

Figure 6. Autocorrelation function of haloes with mass M selected at redshift $z = 0$. Each panel refers to a different mass range: $M/M_\odot = [10^i,\ 5\times10^i]$, with $i = 11, 12, 13, 14$ (see labels). Average results and standard deviation from 10 MCM realizations are plotted as *circles* and error bars, and the average number of haloes found for each mass range is also indicated as N. Separations are in units of the box length (L = 100 Mpc = 256 bcs). The three *vertical thick lines* mark the typical Lagrangian radius R of haloes in the given range of M: the two shorter ones correspond to the minimum and the maximum mass in the range, while the longer one refers to the mean mass in the interval, weighted by the mass function. *Long-dashed* curves have been computed by use of the linear and the second order bias factors [Catelan et al. 1998; see equations (9)–(12)], and the values of $\bar{b}_1$ and $\bar{b}_2$ are labelled in each panel. Also shown are the linear mass correlation function at the given redshift (*dotted* curves), and ξ_{hh} computed with the linear bias only, as first discussed by Mo & White (1996; *dashed–dotted* lines). *Solid* curves corresponds to the correlation functions computed as $\xi_{hh} = \bar{b}_J^2\xi_m$, where the value of $\bar{b}_J$ (see label) is derived from Jing's formula [equation (13)], which provides a good fit to N-body simulations. The first order bias vanishes at $M_* \simeq 3.4\times10^{13}\,M_\odot$.

where $N_{DD}(r)$ is the number of pairs whose geometric centres are separated by a distance between r and $r + dr$, and $N_{RR}(r)$ is the same quantity if haloes were randomly distributed in the same volume: $N_{RR}(r) = (1/2)N_o^2(dV/V)$, where N_o is the total number of haloes, dV is the volume of the shell at r with thickness dr, and V is the total volume of the box.

Results for haloes selected in four mass ranges at $z = 0$, 1 and 3 are shown as circles in Figs 6, 7 and 8, respectively. Note that

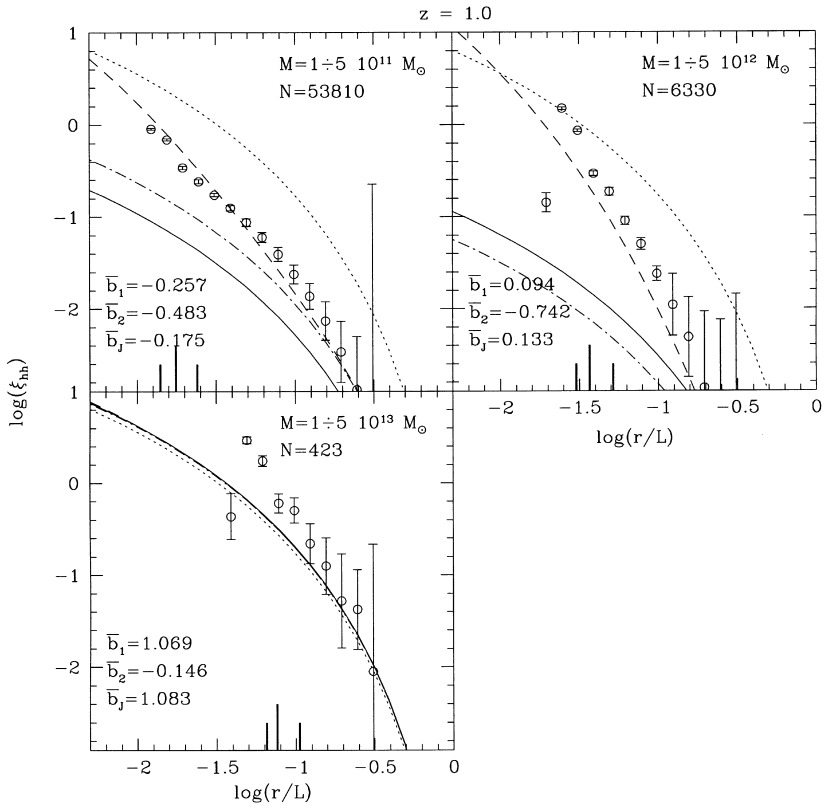

Figure 7. The same as in Fig. 6, but for haloes selected at $z = 1$. No results for haloes with mass in the range $[10^{14},\ 5\times10^{14}]\,M_\odot$ are shown because only 5 of them have already formed at this epoch. At $z = 1$, $M_* \simeq 1.2\times10^{12}\,M_\odot$.

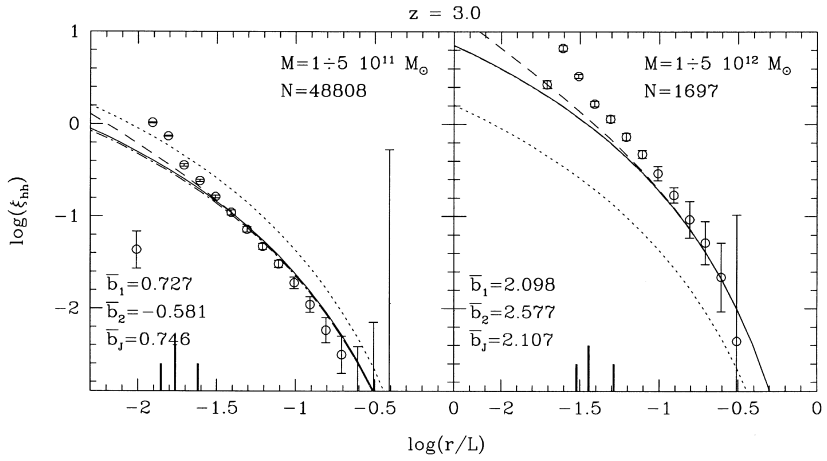

Figure 8. The same as in Fig. 6, but for haloes selected at $z = 3$. No results for larger masses are shown because too few, or no high-mass haloes, have already formed at this redshift. Here, $M_* \simeq 6.2\times10^9\,M_\odot$.

points are found at separations smaller than the typical halo sizes (marked by the vertical thick lines in plots). This is a consequence of the non-spherical shape of haloes in the MCM, allowing the distance between two centres to be smaller than the spherical radius R artificially attributed to each object in this computation.

Using an approach based on the EPS theory, CLMP give an analytic formula for the halo two-point correlation function, which is valid for separations r larger than R. In particular, when $r \gg R$, the correlation function of objects of mass M identified at redshift z, can be expressed as:

$$\xi_{hh}(r, M, z) = b_1^2(M, z)\xi_m(r, z) + \tfrac{1}{2}b_2^2(M, z)\xi_m^2(r, z) + \ldots, \qquad (9)$$

where $\xi_m(r, z)$ is the matter correlation function (the Fourier transform of the power spectrum) linearly extrapolated to redshift z. The linear bias function $b_1(M, z)$ was already obtained by MW96 using a different approach still based on the EPS theory. It is given by:

$$b_1(M, z) = \frac{\delta_c}{\sigma^2(M, z)} - \frac{1}{\delta_c}, \qquad (10)$$

where $\sigma(M, z)$ is the mass variance linearly extrapolated to redshift z: $\sigma(M, z) = \sigma(M)(1 + z)^{-1}$. CLMP show that the second order bias factor is:

$$b_2(M, z) = \frac{1}{\sigma^2(M, z)}\left[\frac{\delta_c^2}{\sigma^2(M, z)} - 3\right]. \qquad (11)$$

If the typical non-linear mass $M_*(z)$ for dark matter haloes is defined as $\sigma[M_*(z), z] = \delta_c$, it results from equation (10) that the first order bias vanishes for $M = M_*$, and ξ_{hh} is then determined by the second order term only. For redshifts $z = 0$, 1, 3, the values of M_* are 3.4×10^{13}, 1.2×10^{12}, and $6.2 \times 10^9\ \mathrm{M}_\odot$, respectively.

When a finite range of halo masses is considered instead of a single value of M, the theoretical halo correlation functions can still be estimated by equation (9), with the two bias factors replaced by their mean values in the mass interval, weighted by the mass function $n(M, z) = \mathrm{d}n/\mathrm{d}M$:

$$\bar{b}_i = \frac{\int_{M_i}^{M_s} b_k(M, z)n(M, z)\,\mathrm{d}M}{\int_{M_i}^{M_s} n(M, z)\,\mathrm{d}M} \qquad k = 1, 2. \qquad (12)$$

Long-dashed curves in Figs 6, 7 and 8 have been computed by means of equations (9)–(12) for the corresponding mass ranges and redshifts. Also shown for comparison are the linear mass correlation function at each redshift (dotted lines), and ξ_{hh} computed with the linear term in equation (9) only (dashed-dotted lines). For all redshifts and halo masses, the autocorrelation function derived from the MCM is in a remarkable good agreement with the predictions of the EPS theory. Even if the analytic formula for ξ_{hh} has been obtained in the limit of separations much larger than R, a reasonable agreement is also found when this condition is not exactly satisfied. Moreover, results of the MCM are well described by the linear bias relation also in the (slightly) non-linear clustering regime (i.e. for separations where $\xi_m(r)$ is slightly larger than unity), and thanks to the second order term, equation (9) still provides a very good description of the model correlation function, even for masses near M_*, where b_1 vanishes.

Such an agreement between the MCM results and analytic predictions derived from the EPS theory only ensures the reliability of the model in correctly taking into account the clustering of high-mass ($M \gtrsim M_*$) haloes, but it also highlights its limitations for small objects. Indeed, accurate comparisons with N-body simulations show that the correlation function given by equations (9)–(12) correctly describes numerical results for haloes with masses larger than M_*, but significantly overestimates the clustering of small-mass objects (PCL; Jing 1999; Sheth & Tormen 1999; Sheth et al. 1999). For $M < M_*$, the analytic bias factor b_1 is significantly lower (more negative) than that found in numerical simulations, whereas a better fit to the N-body Lagrangian correlation function (with errors within the 15 per cent for a CDM cosmology) is obtained by means of the linear term in equation (9), with b_1 replaced by (Jing 1999; but see also Sheth et al. 1999):

$$b_J(M, z) = \left[\frac{\sigma^4(M, z)}{2\delta_c^4} + 1\right]^{(0.06-0.02n)} [1 + b_1(M, z)] - 1, \qquad (13)$$

where n is the index of the power spectrum $P(k)$, computed as:

$$n = \frac{\mathrm{d}\ln P(k)}{\mathrm{d}\ln k}\Big|_{k=2\pi/R}. \qquad (14)$$

The correlation functions computed as $\xi_{hh} = \bar{b}_J^2\xi_m$ are plotted in Figs 6–8 as solid curves. Relative to these N-body based correlation functions, the MCM overestimates the clustering of haloes on the low-mass ($M < M_*$) regime.

4 DISCUSSION

As far as the halo mass function, and the conditional probability distribution of progenitor and child haloes are concerned, a good general agreement between MCM results and PS and EPS analytic formulae is found, but an underproduction of low-mass objects in the model is apparent. This limits the mass resolution of the MCM to a minimum of 8 base cells ($3 \times 10^{10}\ \mathrm{M}_\odot$, for the present choice of cosmological parameters and box size). Compared to the mass function from N-body simulations (well described when a non-spherical model for the collapse of density fluctuations is considered; see LS98; LS99; Sheth et al. 1999, and references therein), the MCM produces a significantly lower number of high-mass haloes, especially at early times. Since a finite box is used for representing the Universe, the effective amplitude of the mass variance on large scales is smaller than that expected from the input power spectrum, used in the computation of the analytic formulae. Such an effect may in part be responsible for the underproduction of high-mass haloes in the MCM with respect to theoretical predictions. Also changing the *linking* and the *overlapping* conditions (see Section 2.2) helps to obtain larger mass haloes, especially at high z, but it is not clear which are the best criteria (see also Nagashima & Gouda 1997). Moreover, oscillations in the mass functions occurring at block masses of 8^i base cells, $i = 1, 2, \ldots$, are apparent, but may possibly disappear if different criteria are adopted when deciding whether or not to merge pre-existing haloes and form a new structure, as well as if a set of grids displaced in a different way (no longer by half a block-length) are used.

The distribution of formation redshifts is in good agreement with analytic predictions for high-mass haloes, even if the peak of formation is systematically shifted towards more recent epochs. For intermediate mass objects, the MCM correctly reproduces the analytic expectations only at high redshifts, then it keeps forming haloes also at very recent times, in contradiction to the EPS theory. Once more, a failure of the model in describing the history

of low-mass haloes is evident, since they systematically form at earlier epochs than predicted.

Finally, a remarkable agreement of the two-point correlation function is found with respect to the predictions derived from the EPS theory (MW96; CLMP), for all considered masses and redshifts. This ensures that the model reliably retains information about the spatial correlation of high-mass haloes ($M \gtrsim M_*$), but it also overestimates the clustering of small objects (as do all analytic formulae). The amplitude of their correlation function in fact is significantly (2–3 times) higher than that predicted by the fitting formula recently proposed by Jing (1999), that correctly describes the correlation function found in numerical simulations. As discussed by Jing (1998, 1999) and PCL, this difference between *N*-body and EPS results in Lagrangian space, suggests that the criteria adopted in the PS theory for identifying bound virialized objects in the initial conditions are inadequate. The assumption of spherical symmetry for the collapse is certainly a strong simplification, and it also affects both the mass function and the typical formation epoch of structures. Considering that haloes in the MCM are produced with a large variety of shapes, we intend to adopt a nonspherical condition and study its effects on the resulting mass function and formation redshift distribution in a future paper.

The physical processes ruling gas cooling, dissipative collapse, star formation, evolution and feedback (as well as interactions and merging between galaxies) are currently implemented in merging history trees of DM haloes, so far obtained through two main approaches. In semi-analytic models (KW93; Kauffmann, White & Guiderdoni 1993; Kauffmann, Guiderdoni & White 1994; Cole et al. 1994; Baugh et al. 1998; Somerville & Primack 1999; and papers in these series), the merging history of DM haloes is built through Monte Carlo realizations of the block model or EPS formalism, with no (or not accurate) spatial information. More recently (Kauffmann, Nusser & Steinmetz 1997; Governato et al. 1998; Benson et al. 1999), DM haloes have been selected from cosmological *N*-body simulations, but their merging trees are still computed with the Monte Carlo technique. In a 'fully' hybrid model (Roukema et al. 1997; Kauffmann et al. 1999), merging trees are also computed from the output of large *N*-body simulations, and as a consequence they retain the spatial and dynamical information of the parent simulation, but they suffer from its limited mass resolution and expensive CPU cost.

The interest of the MCM is that it represents an intermediate approach. It is very fast, and it partly retains spatial information in the linear or weakly non-linear regime. A priori, it suffers from the same resolution problem as merging trees built from *N*-body simulations. For the same choice of cosmological parameters and box length, the 256^3 base cells have the same mass as the 256^3 particles, and reliable haloes cannot be obtained below $\sim$8 base cells or 10 particles. However, its low cost in terms of CPU time allows to run realizations of sub-boxes, thus improving the mass resolution. Moreover, many choices of the cosmological parameters, shape and normalization of the power spectrum of linear fluctuations can be tested. So the MCM appears as a versatile and rapid method to test physical ideas about galaxy, group and cluster formation in various cosmologies, mostly when some degree of spatial information can be useful.

In particular, the MCM can be suitable for studying galaxy clusters, mainly at low redshifts, where a good agreement between MCM and analytic results is found, not only in terms of mass functions, but also in the distribution of formation redshifts, as well as in the halo two-point correlation function. Also the population of Lyman-break galaxies at $z = 3$ can be reasonably well studied by means of the MCM. In fact, these objects are often interpreted as star-forming galaxies located at the centre of haloes of about $10^{12}\,M_\odot$ (e.g. Steidel et al. 1996; Giavalisco, Steidel & Macchetto 1996; Steidel et al. 1998; Giavalisco et al. 1998; Baugh et al. 1998; but see also Somerville, Primack & Faber 1998). For these masses and redshifts, the model provides a reasonably good description of both the mass distribution and the formation history. Moreover, the correlation function fairly matches the numerical results over a large range of halo separations, thus allowing in principle to investigate the clustering properties of Lyman-break galaxies.

5 CONCLUSIONS

The Merging Cell Model originally proposed by Rodrigues & Thomas (1996) for a scale-free power spectrum, has been developed in the case of the SCDM cosmology. Its reliability has been tested not only in terms of the halo mass function, but also comparing the distributions of the progenitor and child masses, as well as that of halo formation times, to the analytic predictions derived by the Press & Schechter theory and its extensions.

For the first time in the case of a semi-analytic merging tree model, we have also computed the halo two-point correlation function, and compared it to the available theoretical predictions.

We have stressed the major successes of the model, as well as its main weakness, and several possible solutions to improve it have been proposed.

Two main fields where the use of this method can be of particular interest have been recognized. It appears to be a suitable tool for studying the properties of cluster-scale objects, mainly at low redshift, as well as the population of Lyman-break galaxies, and their clustering at high z.

We intend to apply the method in a more realistic cosmological scenario (as the open and the lambda CDM), and directly test it against *N*-body simulations in a forthcoming work.

ACKNOWLEDGMENTS

BL is very grateful to S. Colombi, S. Matarrese, L. Moscardini, C. Porciani, and G. Tormen for many useful discussions. We also thank D. Pogosyan for having kindly provided us with its code for the generation of initial conditions. BL is supported by a Marie Curie Training Grant (category 20), under the TMR Activity 3 of the European Community Program.

REFERENCES

Audit E., Teyssier R., Alimi J. M., 1997, A&A, 325, 439
Audit E., Teyssier R., Alimi J. M., 1998, A&A, 333, 779
Bardeen J. M., Bond J. R., Kaiser N., Szalay A. S., 1986, ApJ, 304, 15
Baugh C. M., Cole S., Frenk C. S., Lacey C. G., 1998, ApJ, 498, 504
Benson A. J., Cole S., Frenk C. S., Baugh C. M., Lacey C. G., 1999, MNRAS, in press, astro-ph/9903343
Bond J. R., Myers S. T., 1996, ApJS, 103, 41
Bond J. R., Kaiser N., Cole S., Efstathiou G., 1991, ApJ, 379, 440
Bower R. G., 1991, MNRAS, 248, 332
Carlberg R. G., Couchman H. M. P., 1989, ApJ, 340, 47
Catelan P., Lucchin F., Matarrese S., Porciani C., 1998, MNRAS, 297, 692 (CLMP)
Cole S., Kaiser N., 1988, MNRAS, 233, 637

Cole S., Aragon-Salamanca A., Frenk C. S., Navarro J. F., Zepf S. E., 1994, MNRAS, 271, 781
Efstathiou G., Frenk C. S., White S. D. M., Davis M., 1988, MNRAS, 235, 715
Gelb J. M., Bertschinger E., 1994, ApJ, 436, 491
Giavalisco M., Steidel C. C., Macchetto F. D., 1996, ApJ, 470, 189
Giavalisco M., Steidel C. C., Adelberger K. L., Dickinson M. E., Pettini M., Kellogg M., 1998, ApJ, 503, 543
Governato F., Baugh C. M., Frenk C. S., Cole S., Lacey C. G., Quinn T., Stadel J., 1998, Nat, 392, 359
Gross M. A. K., Somerville R. S., Primack J. R., Holtzman J., Klypin A., 1998, MNRAS, 301, 81
Gunn J. E., Gott J. R., 1972, ApJ, 176, 1
Jain B., Bertschinger E., 1994, ApJ, 431, 495
Jing Y. P., 1998, ApJL, 503, L9
Jing Y. P., 1999, ApJL, 515, L45
Kauffmann G., White S. D. M., 1993, MNRAS, 261, 921 (KW93)
Kauffmann G., White S. D. M., Guiderdoni B., 1993, MNRAS, 264, 201
Kauffmann G., Guiderdoni B., White S. D. M., 1994, MNRAS, 267, 981
Kauffmann G., Nusser A., Steinmetz M., 1997, MNRAS, 286, 795
Kauffmann G., Colberg J. M., Diaferio A., White S. D. M., 1999, MNRAS, 303, 188
Lacey C., Cole S., 1993, MNRAS, 262, 627 (LC93)
Lacey C., Cole S., 1994, MNRAS, 271, 676 (LC94)
Lee J., Shandarin S. F., 1998, ApJ, 500, 14 (LS98)
Lee J., Shandarin S. F., 1999, ApJ, 517, L5 (LS99)
Mo H. J., White S. D. M., 1996, MNRAS, 282, 347 (MW96)
Monaco P., 1995, ApJ, 447, 23
Monaco P., 1997a, MNRAS, 287, 753
Monaco P., 1997b, MNRAS, 290, 439
Nagashima M., Gouda N., 1997, MNRAS, 287, 515
Porciani C., Matarrese S., Lucchin F., Catelan P., 1998, MNRAS, 298, 1097
Porciani C., Catelan P., Lacey C., 1999, ApJ, 513, L99 (PCL)
Press W. H., Schechter P., 1974, ApJ, 187, 425(PS)
Rodrigues D. D. C., Thomas P. A., 1996, MNRAS, 282, 631 (RT96)
Roukema B. F., Peterson B. A., Quinn P. J., Rocca-Volmerange B., 1997, MNRAS, 292, 835
Sheth R. K., Lemson G., 1999a, MNRAS, 304, 767
Sheth R. K., Lemson G., 1999b, MNRAS, 305, 946
Sheth R. K., Tormen G., 1999, MNRAS, 308, 119
Sheth R. K., Mo H., Tormen G., 1999, MNRAS, submitted, astro-ph/9907024
Somerville R. S., Kolatt T. S., 1999, MNRAS, 305, 1
Somerville R. S., Primack J. R., 1999, MNRAS accepted, astro-ph/9802268
Somerville R. S., Lemson G., Kolatt T. S., Dekel A., 1998, MNRAS submitted, astro-ph/9806228
Somerville R. S., Primack J. R., Faber S. M., 1998, MNRAS submitted, astro-ph/9806228
Steidel C. C., Giavalisco M., Pettini M., Dickinson M., Adelberger K. L., 1996, ApJ, 462, L17
Steidel C. C., Adelberger K. L., Dickinson M., Giavalisco M., Pettini M., Kellogg M., 1998, ApJ, 492, 428
Tormen G., 1998, MNRAS, 297, 648

This paper has been typeset from a TEX/LATEX file prepared by the author.

B.4 Theory of galaxy dynamics in clusters and groups

Mamon, 2000, *in XVth IAP Meeting, Dynamics of Galaxies: from the Early Universe to the Present, ed. F. Combes, G. A. Mamon & V. Charmandaris, San Francisco, ASP (vol. 197), pp. 377–387, arXiv:astro-ph/9911333*

Dynamics of Galaxies: from the Early Universe to the Present
ASP Conference Series, Vol. 197, 2000
F. Combes, G. A. Mamon and V. Charmandaris, eds., p. 377

Theory of galaxy dynamics in clusters and groups

Gary A. Mamon

Institut d'Astrophysique, F–75014 Paris, FRANCE

Abstract. Analytical estimates of the mass and radial dependence of the rates of galaxy mergers and of tidal interactions are derived for clusters and groups of galaxies, taking into account the tides from the system potential that limit the sizes of galaxies. Only high mass galaxies undergo significant major merging before being themselves cannibalized by more massive galaxies. Strong tides from the group/cluster potential severely limit the merger/tide cross-sections in the central regions, and while tides are most efficient at the periphery, one should see merging encounters further inside rich clusters.

1. Introduction

Mergers of galaxies in slow collisions and tidal interactions in rapid collisions are two key dynamical processes that occur in groups and clusters of galaxies. Cosmological N-body simulations are beginning to approach the resolution necessary to study galaxy dynamics in groups and clusters (see Moore, in these proceedings). Moreover, mergers and tidal collisions leave significant observational signatures, in the form of tidal tails, asymmetries and generally disturbed morphologies and internal kinematics (see Amram, in these proceedings). Also, galaxy merging is an essential mechanism for driving elliptical galaxy morphologies given disk-like progenitors. As such, an understanding of galaxy merging is very important for semi-analytical modeling of galaxy formation.

In this review, I compute analytically the rates at which a galaxy of given mass and position within a cluster or group with a Navarro, Frenk, & White (1995, NFW) potential undergoes slow major mergers with lower mass galaxies and rapid tidal encounters. Since the collision cross-sections are strongly modulated by the tides from the group/cluster potential, I begin with a simple formalism for estimating the tides from the system potential. Note that I will not consider ram pressure stripping on galaxies.

2. Tides from the cluster/group potential

The potential of a cluster can exert a strong differential force on a galaxy orbiting within it, but these tides are strongly dependent on the galaxy orbit.

A galaxy on a nearly circular orbit is likely to be tidally locked, as the Moon is with respect to the Earth. In this case, the tidal force is simply (King, 1962)

$$F_{\rm tide} = \Delta \left[\frac{GM(R)}{R^2} - \Omega^2(R) \right] \tag{1}$$

and equating $F_{\rm tide}$ in eq. (1) to the force, $f = Gm(r)/r^2$ that a galaxy exerts on one of its stars yields for $r \ll R$ a galaxy tidal radius r_t that satisfies a velocity modulated density criterion (see Mamon, 1995):

$$\bar\rho_g(r_t) = \bar\rho_{\rm cl}(R) \left[2 - \frac{3\rho_{\rm cl}(R)}{\bar\rho_{\rm cl}(R)} + \frac{V_p^2(R)}{V_{\rm circ}^2(R)} \right] \ , \tag{2}$$

where V_p and $V_{\rm circ}$ are respectively the galaxy's velocity at pericenter and the cluster's circular velocity. The term in brackets in eq. (2) is 2 for circular orbits. Moreover, for a singular isothermal law $\rho \sim r^{-2}$ for both galaxy and cluster, one finds (see White, 1983) that for circular orbits the galaxy size is proportional to its clustocentric radius: $r_t = 2^{-1/2}(v_{\rm circ}/V_{\rm circ})R$, where $v_{\rm circ}$ is the circular velocity of the galaxy. For general density profiles, writing $\bar\rho(r) \sim v_{\rm circ}^2(r)/r^2$, one obtains

$$\frac{r_t/R}{v_{\rm circ}(r_t)/V_{\rm circ}(R)} = \left(2 - 3\,\frac{\rho}{\bar\rho} + V_p^2/V_{\rm circ}^2(R) \right)^{-1/2} \ . \tag{3}$$

Merritt (1984) used a similar circular-tide criterion to argue that galaxies are strongly tidally limited by the cluster potential.

However, cosmological infall imposes elongated orbits. A galaxy on an elongated orbit experiences a strong tide during its rapid, hence short, passage at pericenter, prompting Ostriker, Spitzer, & Chevalier (1972) to introduce the term *tidal shock*. During this shock, a star in the galaxy experiences a velocity impulse

$$\Delta v \sim F_{\rm tide} \Delta t \sim \frac{GM(R_p)\,r}{R_p^3} \left(\frac{R_p}{V_p} \right) = {\rm cst} \frac{GM(R_p)\,r}{R_p^2 V_p} \ , \tag{4}$$

where we neglected the centrifugal term in $F_{\rm tide}$, because the galaxy falls in too fast to be phase locked. A more precise calculation by Spitzer (1958), who introduced the *impulsive approximation* where the point-mass perturber moves at constant $\mathbf{V}$, produces the same relation as in eq. (4) with a constant of order unity. The impulse approximation can also be applied to extended perturbers (Aguilar & White, 1995; Mamon, 1987). Recently, Gnedin, Hernquist, & Ostriker (1999) applied the impulsive approximation to the more realistic Hernquist (1990) potential and found a dependence of Δv matching that of eq. (4), with a very small dependence on R_p and again the constant is found to be of order unity for elongated orbits (with order of unity changes when they performed orbit-integrated — instead of straight-line — tidal calculations).

The tidal radius can then be defined as that where the energy increment caused by the tidal perturbation is equal to the binding energy (White, 1983).

With $E \sim Gm(r_t)/r_t$ and $\Delta E \sim (\Delta v)^2/2$, one obtains another velocity modulated density criterion

$$\bar{\rho}_g(r_t) \simeq \bar{\rho}_{\rm cl}(R_p) \left(\frac{V_{\rm circ}(R_p)}{V_p} \right)^2 , \tag{5}$$

which for any density profile yields

$$\frac{r_t/R}{v_{\rm circ}(r_t)/V_{\rm circ}(R)} = \frac{V_p}{V_{\rm circ}} . \tag{6}$$

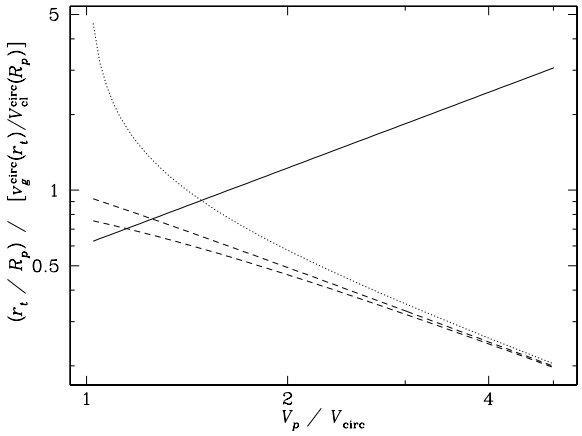

Figure 1. Velocity modulation of normalized tidal radii for given orbit pericenter. The *solid curve* shows impulsive tides for elongated orbits (eq. [6]). The *dashed curves* show circular tides (eq. [3]) in a Navarro, Frenk, & White potential for 0.1 (*upper curve*) and 1 (*lower curve*) scale radii. The *dotted curve* shows the circular tide within a homogeneous core.

Figure 1 shows the effects of velocity modulation on the tidal radii. The effective tidal radius should be taken as the largest of the circular and impulsive regimes (otherwise one would be left with discontinuities in the transition V_p from near-circular to elongated orbits). Hence, with homogeneous cores, circular tidal theory produces increasingly smaller tidal radii for orbits of increasing but low elongation, as Merritt & White (1987) found in their N-body simulations. With cuspy cores as in the NFW profile, low-elongation non-circular orbits experience tidal shocks instead. The orbit elongation, $R_p/R_a \simeq 0.2$, found in Ghigna et al.'s (1998) high-resolution cosmological simulations corresponds to $V_p/V_{\rm circ}(R_p) \simeq 1.5 - 2.7$, roughly yielding

$$r_t \simeq (1.2 - 1.5)\, R_p \left(\frac{v_{\rm circ}}{V_{\rm circ}} \right) \approx (1.2 - 1.5)\, R_p \left(\frac{v_g}{v_{\rm cl}} \right) \tag{7}$$

as for singular isothermal models, where v_g and $v_{\rm cl}$ are the mean galaxy and cluster velocity dispersions, respectively. If $V_p \simeq V_{\rm circ}(R_p)$ and if galaxy and cluster density profiles are self-similar, then tides from the cluster potential would force the simple relation $m(r_t)/m(r_{\rm vir}) = M(R_p)/M(R_{\rm vir})$. In fact, using $V_p/V_{\rm circ}(R_p)$ expected for the NFW profile, assuming $\langle R \rangle \simeq 4R_p$, and adopting the departures from self-similarity in the NFW profiles noted by Navarro, Frenk, & White (1997, lower mass NFW profiles are more centrally concentrated), one finds

$$\frac{m(r_t)}{m(r_{\rm vir})} \simeq \left[\frac{M(R)}{M(R_{\rm vir})}\right]^{b_m} \simeq a_r \left(\frac{R}{R_{\rm vir}}\right)^{b_r} , \qquad (8)$$

where for clusters ($v_{\rm cl} = 1000\,{\rm km\,s^{-1}}$) and groups ($v_{\rm cl} = 300\,{\rm km\,s^{-1}}$) we respectively have $b_m = 0.50$ and 0.82, $a_r = 0.58$ and 0.52, and $b_r = 0.57$ and 0.78 (eq. [8] is accurate to better than 5% for $R > 0.05\,R_{\rm vir}$).

3. Galaxy merger rates in clusters and groups

3.1. Global merger rates for equal mass galaxies

The rate of mergers is obtained by integrating over velocities the merger cross-sections:

$$k \equiv \frac{1}{n^2}\frac{d^2N}{dt\,dV} = \langle vs(v)\rangle = \int_0^\infty dv f(v) v s(v) , \qquad (9)$$

where $s(v) = \pi[p_{\rm crit}(v)]^2$ is the merger cross-section and $f(v)$ is the distribution of relative velocities (with $\int_0^\infty f(v)\,dv = 1$). Hence, $nk \equiv dN/dt$ is the rate at which a galaxy suffers a merger. Within the virialized regions of clusters with 1D velocity dispersion $v_{\rm cl}$, the velocity distribution is a gaussian with standard deviation $2^{-1/2}v_{\rm cl}$: $f(v) = 2^{-1}\pi^{-1/2}v_{\rm cl}^{-3}v^2\exp[-v^2/(4\,v_{\rm cl}^2)]$.

Roos & Norman (1979), Aarseth & Fall (1980) and Farouki & Shapiro (1982) have established merger cross-sections from very small N-body simulations of galaxy collisions, that were based upon the parameters at closest approach. The maximum distance of closest approach, $r_p^{\rm max}$, was 4 (Aarseth & Fall) or 11 (Farouki & Shapiro) times the mean galaxy half-mass radius, r_h. Mamon (1992) used the Roos & Norman cross-section with the Aarseth & Fall scaling to derive a merger rate.

However, the gaussian approximation for the relative velocity distribution implies that the cross-sections used in eq. (9) are based upon impact parameters (at infinity) and not at closest approach. Makino & Hut (1997) derived merger cross-sections using high resolution N-body simulations of colliding galaxies with more realistic density profiles. Their cross-sections are expressed in terms of impact parameters.

Krivitsky & Kontorovich (1997) used a simple gravitational focusing recipe to connect the cross-section at closest approach (which they assumed to be independent of pericentric velocity), in units of the velocity at infinity, to the cross-section at infinity (without making any assumption on the potential energy of interaction of the colliding pair). Note that Makino & Hut show that $r_p^{\rm max} > 10\,r_h$, while Krivitsky & Kontorovich argue that it is approximately the sum of the galaxy *radii* (which are ill-defined).

Figure 2 shows the dimensionless merger rates $k/(r_h^2 v_g)$, where v_g is the mean galaxy internal velocity dispersion, derived from Mamon (1992), Makino & Hut (1997), and Krivitsky & Kontorovich (1997). I rescale the rates of Krivitsky & Kontorovich in terms of half-mass radii using $R = 9\,r_h$ (to obtain merger rates similar to those of Makino & Hut), *i.e.*, $r_p^{\max}/r_h = 18$.

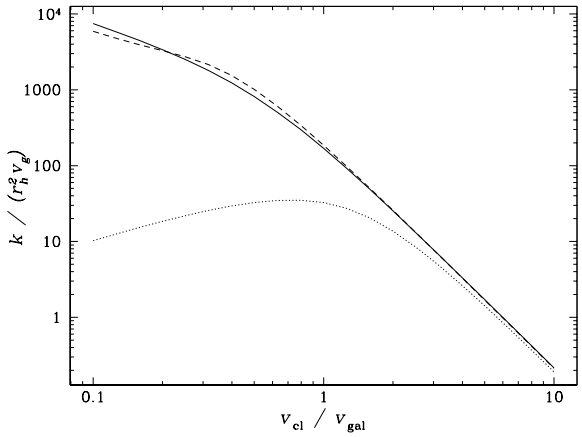

Figure 2. Dimensionless merger rates $k/(r_h^2 v_g)$ (see eq. [9]) as a function of the ratio of cluster to galaxy velocity dispersion. The *dotted*, *solid* and *dashed* curves respectively correspond to the rates of Mamon (1992), Makino & Hut (1997, using Hernquist, 1990 model galaxies) and Krivitsky & Kontorovich (1997, rescaled vertically, because they reason in terms of galaxy radii rather than galaxy half-mass radii).

The agreement between the merger rates of Krivitsky & Kontorovich and Makino & Hut is remarkable, given the very simple analytical formulation of the former authors (but again this required a rescaling, or, in other words, a choice of $r_p^{\max}/r_h = 18$). The very low merger rate of Mamon (1992) in the group regime ($v_{\rm cl} \approx v_g$) is a consequence of the lack of gravitational focusing in that model.

The merger rates of Mamon (1992) and Makino & Hut agree to within 15% in the cluster regime ($v_{\rm cl} \gtrsim 4\,v_g$). This agreement is almost fortuitous since Mamon shows that the merger rate with the Roos & Norman cross-section scales as $(r_p^{\max}/r_h)^2$, while this ratio is very different in Makino & Hut's cross-section. In any event, in the cluster regime the merger rate can then be written

$$k = b\,\frac{r_h^2 v_g^4}{v_{\rm cl}^3} = a\,\frac{G^2 m^2}{v_{\rm cl}^3}\ , \tag{10}$$

where $a \simeq 8$ (Mamon, 1992). With $3\,v_g^2 \simeq 0.4\,Gm/r_h$ (Spitzer, 1969), appropriate for the Hernquist model, the Makino & Hut rate translates to $a = 12$. Figure 2 shows that $k \sim v_{\rm cl}^{-3}$, whichever merger cross-section is used. In fact,

it is easy to show that *for any merger cross-section rapidly decreasing with increasing velocity*, the merger rate should scale as $v_{\rm cl}^{-3}$ for $v_{\rm cl} \gg v_g$, as first found by Mamon (1992) for the Roos & Norman cross-section.

The important conclusion of Figure 2 is that *for given galaxy parameters, the merger rate is roughly 100 times lower in rich clusters than in poor groups of galaxies.*

3.2. Merger rates for different masses

If the critical merging velocity $v_{\rm crit}$ is a function of r_p/r_h (Aarseth & Fall, 1980; Farouki & Shapiro, 1982), it is easy to show that $k \sim r_h^2$, and if $v_{\rm crit}$ is a function of $r_p/\langle r_h \rangle$, then $k \sim \langle r_h \rangle^2$ (see Mamon, 1992). Similarly, it is reasonable to expect that $k \sim \langle v_g^2 \rangle^2$. Then, given eq. (10) and that $m \sim r_h^3$, the rate of mergers of a galaxy of mass m with a galaxy of mass λm

$$k(m, \lambda m) = \frac{aG^2 m^2}{v_{\rm cl}^3} \left(\frac{1+\lambda^{1/3}}{2} \right)^2 \left(\frac{1+\lambda^{2/3}}{2} \right)^2 . \tag{11}$$

A given galaxy undergoes mergers with other galaxies at a rate

$$\mathcal{R} \equiv n \bar{k}(m) = \int_{\lambda_{\rm min}}^{\lambda_{\rm max}} k(m, \lambda m)\, n(\lambda m)\, d(\lambda m) , \tag{12}$$

where for major mergers with smaller galaxies (that transform disk galaxies into ellipticals), $\lambda_{\rm min} \simeq 1/3$ and $\lambda_{\rm max} = 1$, while for destruction by mergers with larger galaxies, $\lambda_{\rm min} = 1$ and $\lambda_{\rm max} \to \infty$. Adopting a Schechter (1976) form for the mass function of galaxies, $n(m) = (n_*/m_*)\, x^{-\alpha} \exp(-x)$, where $x = m/m_*$, eqs. (11) and (12) yield

$$\mathcal{R} = n \bar{k} = \frac{aG^2 n_* m_*^2}{16\, v_{\rm cl}^3} K(m/m_*) , \tag{13}$$

$$K_{\rm major}(x) = x^{3-\alpha} \sum_{j=0}^{6} {\rm Min}(j, 7-j)\, [\Gamma(1+j/3-\alpha, x/3) - \Gamma(1+j/3-\alpha, x)] , \tag{14}$$

$$K_{\rm destr}(x) = x^{3-\alpha} \sum_{j=0}^{6} {\rm Min}(j, 7-j)\, \Gamma(1+j/3-\alpha, x) . \tag{15}$$

Figure 3 shows the expected number of major mergers with smaller galaxies and destruction by mergers with larger galaxies that a galaxy of a given mass should expect in a Hubble time if it sits in a typical location of a rich cluster, assuming a constant rate in time. The rise in merger rates at low mass reflects the rise of merger cross-section with mass, while the decrease at high mass is caused by the sharp decrease in the galaxy mass function yielding few galaxies to merge with. Figure 3 clearly indicates that *the probability of merger for a given galaxy is always small.* Moreover, *low and intermediate mass galaxies ($m < m_*$) are usually cannibalized before undergoing major mergers.*

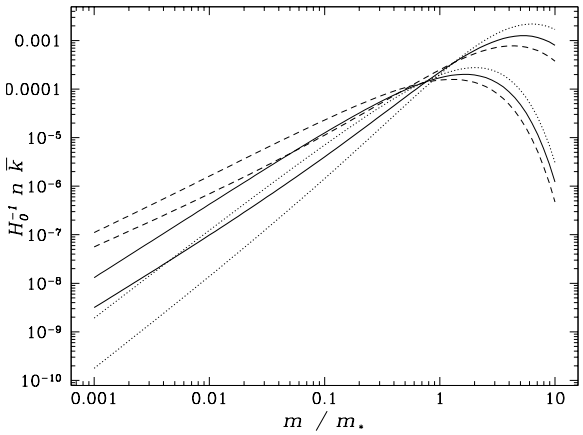

Figure 3. Number of major mergers with lower mass galaxies (eqs. [13] and [14], *thick curves*) and higher mass galaxies (eqs. [13] and [15], *thin curves*) extrapolated to one Hubble time versus galaxy mass. *Dotted*, *solid* and *dashed curves* are for $\alpha = -1.1$, -1.3 and -1.5, respectively. The normalization assumes $a = 12$, $v_{\rm cl} = 1000\,{\rm km\,s^{-1}}$, $n_* = 200\, n_*^{\rm field}$, with $n_*^{\rm field} = 0.013\, h^3{\rm Mpc}^{-3}$ (Marzke et al., 1998), and $m_* = 0.1\,(M/L)_{\rm cl}\,\ell_* = 3\times10^{11}h^{-1}M_\odot$.

3.3. Variation of merger rates with position in cluster

One can go one step further and predict the variation of the merger rate with position in the cluster. From eq. (13), the merger rate scales with radius as

$$\mathcal{R}(R,m) = \frac{a\,G^2\,m_*\,\mu^2(R)\,\rho_{\rm cl}(R)}{16\,\Gamma(2-\alpha,x_m)\,v_{\rm cl}^3(R)}\,K(m/m_*)\ , \qquad (16)$$

where $\mu(R) = m(r_t)/m(r_{\rm vir})$ (see eq. [8]), m_* is the mass at the break of the *field* galaxy mass function and x_m is the minimum galaxy mass in units of m_*.

Assuming a mass density profile $\rho \sim R^{-\beta}$ and arguing that cluster galaxies are severely tidally truncated by the cluster potential as $r_{\rm gal} \sim R$ (i.e. with eq. [7] and assuming constant R_p/R_a), Mamon (1992) showed that if galaxies also follow the law $\rho \sim r^{-\beta}$, then their masses obey $m \sim R^{3-\beta}$. Note that this sharp scaling of galaxy size with clustocentric distance is now confirmed in high resolution cosmological simulations of clusters (Ghigna et al., 1998). Hence, *the radial variation of merger rates are strongly modulated by potential tides.*

By writing $n(R) \sim \rho(R)/m(R) \sim R^{-3}$, I derived $nk \sim R^{-\beta/2}$, hence a higher merger rate inside the cluster, with a slope agreeing perfectly with the observed elliptical fraction (Whitmore, Gilmore, & Jones, 1993), given $\beta = 9/4$ as predicted in early models of cluster formation (Bertschinger, 1985). The derivation above has one flaw: although galaxy masses were correctly scaled to increase with R, I forgot to scale the fraction of cluster mass lying within

galaxies in the same way. Therefore, one really expects $n(R) \sim \rho(R) \sim R^{-\beta}$ and $nk \sim R^{3-3\beta/2}$ yielding a slope $d\ln(nk)/d\ln R = -3/8$ for $\beta = 9/4$ and a null slope for $\beta = 2$, both in disagreement with the logarithmic gradient of elliptical fraction found by Whitmore et al..

One can use the more realistic NFW density profiles to estimate the radial dependence of the merger rates. An essential parameter is $\langle R_p/R \rangle$, which measures the effectiveness of the tides from the cluster potential. Because the dynamical friction time scales as M/m times the orbital time (Mamon, 1995), *orbit circularization*, which to first order operates on a dynamical friction time scale, should be very slow for galaxies falling onto clusters, but fairly effective for galaxies falling into small groups.

Figure 4 shows the predicted number of major mergers in rich clusters and small groups, extrapolated over a Hubble time, using the non-self-similarity of the NFW profiles, an exact scaling of the typical galaxy mass m_* with radius (see eq. [8]), and partial orbit circularization in groups.

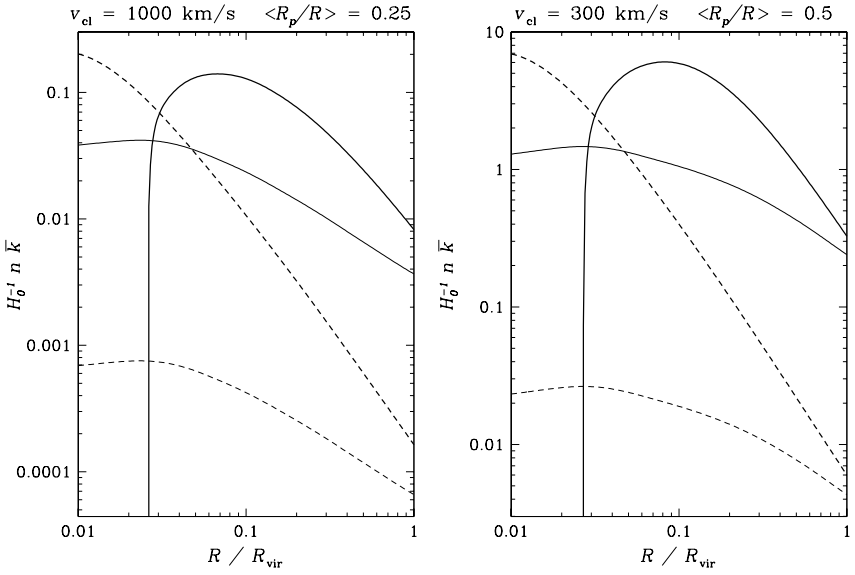

Figure 4. Number of major mergers a given galaxy undergoes with lower mass galaxies (eq. [16], with eqs. [13] and [14]), extrapolated to one Hubble time, versus clustocentric radius in (*left*) an NFW cluster with $v_{\rm cl} = 1000\,{\rm km\,s^{-1}}$ and (*right*) a group with $v_{\rm cl} = 300\,{\rm km\,s^{-1}}$, where the galaxy mass function has $\alpha = 1.3$. The *solid thick* and *dashed thick curves* represent the expected number of major mergers for galaxies of mass $m = m_*^{\rm field} = \Omega_0\rho_c/[n_*^{\rm field}\Gamma(2-\alpha, x_m)] = 5\times10^{12}h^{-1}M_\odot$ and $m = 0.1\,m_*^{\rm field} = 5\times10^{11}h^{-1}M_\odot$, respectively. The *solid thin* and *dashed thin curves* refer to galaxy masses $m = m_*(R)$ and $m = 0.1\,m_*(R)$, respectively.

The merger rates for constant mass galaxies fall off sharply at small clustocentric radii, simply because tidal truncation of galaxies is so severe that there are no galaxies left that are massive enough to produce a major merger with our test galaxy. In general, the merger rates are maximum for intermediate radii for given test galaxy masses, and at low radii for fixed $m/m_*(R)$ (recall though that low mass galaxies get cannibalized before they can undergo a major merger with a smaller galaxy). In any event, Figure 4 confirms that *mergers are ineffective in clusters, but very effective in small groups.* Note that without resorting to partial orbit circularization within groups, the expected number of mergers in groups is somewhat less than expected from the $v_{\rm cl}^{-3}$ scaling, because, relative to clusters, the more concentrated NFW profiles in groups lead to stronger modulation of the merger rate by the potential tides.

4. Collisional tidal stripping in clusters and groups

Because non-merging galaxy collisions are by essence rapid, they can be treated as tidal shocks, and it is reasonable to assume that for tidal features to be visible, one requires $\Delta E \geq \gamma |E|$, where $\gamma \lesssim 1$. Hence, $\Delta v \geq (3\gamma)^{1/2} v_g$. Denoting p and V the separation and relative velocity at pericenter, and $v_{\rm circ,p}(p)$ the circular velocity of the perturbing galaxy out to p, eq. (4) leads to a critical impact parameter

$$p_{\rm crit} = \frac{r}{(3\gamma)^{1/2}} \frac{v_{\rm circ,p}^2}{v_g V} \ , \tag{17}$$

where we note that $v_{\rm circ,p}$, is almost independent of p for realistic density profiles for the perturbing galaxy. Then, integrating the cross-sections derived from eq. (17), the rate of tidal interactions is

$$k = \langle vs(v) \rangle = \frac{\pi^{1/2}}{3\gamma} \left(\frac{r}{v_g} \right)^2 \frac{v_{\rm circ,p}^4}{v_{\rm cl}} \ , \tag{18}$$

and is virtually independent of the test galaxy parameters. Integrating eq. (18) over perturber mass and remarking that both the galaxy and the perturbers are tidally limited by the cluster potential, one obtains using eq. (5)

$$n\bar{k} = \frac{\Gamma(7/3-\alpha, x_m)}{4\pi^{1/2}\gamma\, G\, \Gamma(2-\alpha, x_m)} \left(\frac{v_{\rm circ}}{v_g} \right)^2 \frac{v_{\rm circ,*}^4}{m_*} \frac{\rho_{\rm cl}(R)\, \mu^{7/3}(R)}{\bar{\rho}_{\rm cl}(R_p)\, v_{\rm cl}(R)} \left[\frac{V_p}{V_{\rm circ}(R_p)} \right]^2 \ , \tag{19}$$

where again $\mu(R) = m(r_t)/m(r_{\rm vir})$ (see eq. [8]), $v_{\rm circ,*}$ is the circular velocity at the virial radius for a field m_* galaxy. Again, *the rate of tidal encounters is independent of the galaxy mass.* Note that the $\mu^{7/3}(R)$ dependence of the rate of tidal encounters illustrates the strong modulation of this rate by the tides from the cluster potential.

Figure 5 shows the expected (eq. [19]) number of strong tidal collisions for galaxies in clusters and groups, with $\langle R/R_p \rangle$ as in Figure 4. Although groups are preferential sites for strong tidal encounters, galaxies in the outskirts of clusters should also witness such interactions. However, the signature of tidal interactions lasts of order $1\, h^{-1}\,$Gyr, so that the fraction of galaxies in clusters

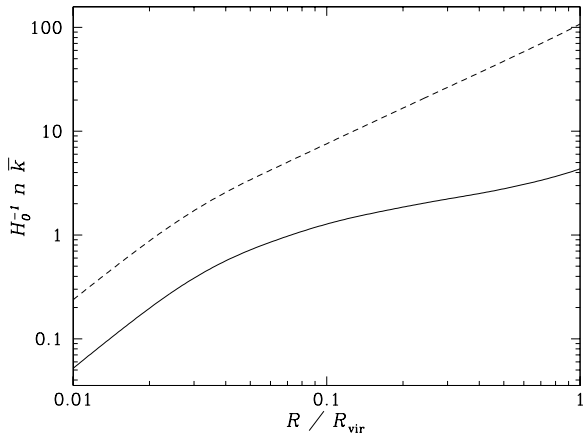

Figure 5. Number of strong ($\gamma = 1/3$) tidal encounters a given galaxy undergoes (eq. [19]), extrapolated to one Hubble time, versus clustocentric radius in an NFW cluster with $v_{\rm cl} = 1000\,{\rm km\,s^{-1}}$ (*solid curve*) and a group with $v_{\rm cl} = 300\,{\rm km\,s^{-1}}$ (*dashed curve*). The galaxy mass function has $\alpha = 1.3$ with field $m_* = 5 \times 10^{12}\,h^{-1}\,M_\odot$.

and groups that are currently undergoing tidal interactions is roughly one-tenth of what is displayed in Figure 5.

5. Discussion

The strong radial dependence of galaxy masses, predicted by the tidal theory (eq. 8), is clear in the cosmological simulations of Ghigna et al. (1998). Should we then witness *inverse luminosity segregation* in clusters where, outside of the core, galaxies become more luminous towards the cluster periphery? Indeed, Adami, Biviano, & Mazure (1998) found a weak trend of mean galaxy magnitude versus radius for an ensemble of clusters, although they worry that this trend is caused by observational bias. It may be that incompleteness of the observational samples is washing out the trend rather than creating it.

The lack of mergers in present-day rich clusters has been noted in cosmological simulations of clusters (Ghigna et al., 1998). Figure 4 shows that in rich clusters, mergers are at best marginally probable for high mass galaxies lying in the cluster body. Given that high mass galaxies are rare, such merging will be difficult (but not impossible) to detect observationally or in simulations.

From their Hα prism surveys of galaxies in clusters, Moss and co-workers (Moss & Whittle, 1993; Moss, Whittle, & Pesce, 1998; Bennett & Moss, 1998) note $\simeq 30\%$ of spiral galaxies in rich clusters exhibit a *compact* Hα morphology and roughly half of these tend to be morphologically disturbed *and* have nearby neighbors. Another half of these compact Hα emission galaxies are in the cluster

core, and presumably those have no tidal companions, suggesting that they are harassed by the cluster potential. But the first half, outside the core are probably *bona fide* cases of strong tidal interactions within clusters, leading to an overall frequency of 20% of all galaxies outside the cores of clusters. It remains to be seen if they are associated to substructures such as infalling groups. Correcting Figure 5 for the 1 Gyr duration of these tidal features produces an absolute frequency of tidally interacting galaxies in clusters in rough agreement with that found by Moss and co-workers.

References

Aarseth, S. J., & Fall, S. M. 1980, ApJ, 236, 43

Adami, C., Biviano, A., & Mazure, A. 1998, A&A, 331, 439

Aguilar, L. A., & White, S. D. M. 1985, ApJ, 295, 374

Bennett, S. M., & Moss, C. 1998, A&AS, 132, 55

Bertschinger, E. 1985, ApJS, 58, 39

Farouki, R. T., & Shapiro, S. L. 1982, ApJ, 259, 103

Ghigna, S., Moore, B., Governato, F., Lake, G., Quinn, T., & Stadel, J. 1998, MNRAS, 300, 146

Gnedin, O. Y., Hernquist, L., & Ostriker, J. P. 1999, ApJ, 514, 109

Hernquist, L. 1990, ApJ, 356, 359

King, I. 1962, AJ, 67, 471

Krivitsky, D. S., & Kontorovich, V. M. 1997, A&A, 327, 921

Makino, J., & Hut, P. 1997, ApJ, 481, 83

Mamon, G. A. 1987, ApJ, 321, 622

Mamon, G. A. 1992, ApJ, 401, L3

Mamon, G. A. 1995, in 3rd Paris cosmology colloq., ed. H. de Vega, & N., Sánchez (Singapore: World Scientific), 95, astro-ph/9511101

Marzke, R. O., da Costa, L. N., Pellegrini, P. S., Willmer, C. N. A., & Geller, M. J. 1998, ApJ, 503, 617

Merritt, D. 1984, ApJ, 276, 26

Merritt, D., & White, S. D. M. 1987, in IAU Symp. 117, Dark Matter in the Universe, ed. J. Kormendy & G. R. Knapp (Dordrecht: Reidel), 283

Moss, C., & Whittle, M. 1993, ApJ, 407, L17

Moss, C., Whittle, M., & Pesce, J. E. 1998, MNRAS, 300, 205

Navarro, J. F., Frenk, C. S., & White, S. D. M. 1995, MNRAS, 275, 720

Navarro, J. F., Frenk, C. S., & White, S. D. M. 1997, ApJ, 490, 493

Ostriker, J. P., Spitzer, L., & Chevalier, R. A. 1972, ApJ, 176, L51

Roos, N., & Norman, C. A. 1979, A&A, 76, 75

Schechter, P. 1976, ApJ, 203, 297

Spitzer, L. 1958, ApJ, 127, 17

Spitzer, L. 1969, ApJ, 158, L139

White, S. D. M. 1983, in Morphology and Dynamics of Galaxies, ed. L. Martinet & M. Mayor (Sauverny: Geneva Obs.), 289

Whitmore, B. C., Gilmore, D. M., & Jones, C. 1993, ApJ, 407, 489

C Sélection d'articles et proceedings publiés sur les groupes compacts de galaxies

C.1 The frequency of chance alignments of galaxies in loose groups

Walke & Mamon, 1989, *A&A 225, 291–302*

Astron. Astrophys. 225, 291–302 (1989)

ASTRONOMY AND ASTROPHYSICS

The frequency of chance alignments of galaxies in loose groups

D.G. Walke[1,2] **and G.A. Mamon**[1,3,4]

[1] Department of Physics, New York University, 4 Washington Place, New York, NY 10003, USA
[2] Raritan Valley Community College, P.O. Box 3300, Somerville, NJ 08876, USA
[3] DAEC, Observatoire de Meudon, F-92195 Meudon Cedex, France
[4] UFR de Physique, Université de Pairs VII, Place Jussieu, F-75005 Paris, France

Received November 8, 1988; accepted April 17, 1989

Summary. We derive semi-analytical expressions for the frequency of chance occurrence of isolated subgroups (using Hickson's 1982 definition) within groups of galaxies. Our analysis is checked with Monte-Carlo simulations that are 1000 times costlier. We generalize our model to investigate the issues of contamination by interlopers and compactness of the subgroups. Using the NBG galaxy and grouping catalog as a reference, we show that contamination has a small effect on the frequency of isolated subgroups, but explains the relatively large fraction of discordant redshifts in Hickson's compact groups. We confirm the high frequencies of chance alignments found in earlier dynamical simulations of groups. We also find that the typical NBG group will contribute enough to produce, by chance alignments of galaxies, compact groups strictly meeting Hickson's selection criteria. However, since Hickson's sample is incomplete at its compactness limit, the typical NBG group will contribute negligibly to producing compact groups as compact as Hickson's by chance alignments. Nevertheless, we show that a few loose groups, as well as small clusters and the Virgo cluster contibute disproportionately more than the typical NBG group. Furthermore, we show that binaries are important in NBG groups. We argue that the combination of these two effects account for roughly half of Hickson's compact groups as chance alignments of galaxies within intermediate density groups and small clusters.

Key words: analytical methods – clusters of galaxies

1. Introduction

The lack of accurate depth perception has often led astronomers to question whether aparently tight associations of astronomical objects are not just chance alignments along the line of sight. For groups and clusters of galaxies (in fact, for any virialized system of galaxies whose mean density is larger than the critical density of the Universe), the accuracy of the redshift as a distance indicator is at best of the order of the radius of the system: groups and clusters have velocity dispersions $\sigma > 100\,\mathrm{km\,s^{-1}}$, giving relative distance uncertainties of $\sigma/H_0 \gtrsim 2\,h_{50}^{-1}\,\mathrm{Mpc}$, where $h_{50} = H_0/50\,\mathrm{km\,s^{-1}\,Mpc^{-1}}$, while their sizes are usually smaller than $2h_{50}^{-1}$ Mpc. This problem is critical in assessing the nature of the so called compact groups of galaxies, whose typical projected sizes are only $70h_{50}^{-1}$ kpc (see, e.g., Hickson and Rood, 1988). Whereas many authors have argued that compact groups are in fact bound dense systems (e.g., Williams and Rood, 1987; Sulentic, 1987; Hickson and Rood, 1988), numerous arguments suggest that most of the compact groups catalogued by Hickson (1982) are caused by chance alignments of galaxies within loose groups (Mamon, 1986, hereafter Paper I).

A major argument in Paper I was that compact configurations that satisfy all of Hickson's selection criteria occur in significant numbers when simulated loose groups are viewed in projection. The frequencies of occurrence of compact configurations ranged from 2% to 10% in preliminary simulations (Paper I), and from 3% to 25% in later simulations (see Table 4 of Mamon, 1987, hereafter Paper II). These numbers were shown to be large enough to account for the number of compact groups relative to that of loose groups (after correcting for different sky coverage and limiting magnitude). Recently Hickson and Rood (1988), using static Monte-Carlo simulations, showed that typical loose groups should yield less than 0.1% of chance alignments on average, and concluded against compact groups being mostly caused by chance alignments.

The present paper reconciles these two opposing views. We derive semi-analytically the frequency at which isolated subgroups (in Hickson's 1982 sense) occur by chance within parent groups generated in 2D by a Poisson homogeneous distribution. Although, in reality, galaxy positions are strongly correlated (e.g., Peebles, 1980), the assumption of homogeneity will lead to a *lower* limit of the frequency of such subgroups.

We present in Sect. 2 our static semi-analytical derivation of the frequency of occurrence of isolated subgroups. The results from these calculations are presented in Sect. 3 and are shown to agree with static 2D Monte-Carlo simulations of a similar type as those performed by Hickson and Rood (1988). In Sect. 4, we consider three refinements to our model: We consider the effects of a uniform background of galaxies, we add a compactness criterion, and we generate Monte-Carlo estimates using more realistic radial density distributions. We apply our model to the data from published group catalogs in Sect. 5, check the basic validity of the frequencies given in Papers I and II, and make predictions on the frequency of compact groups with discordant redshifts. In Sect. 6 we discuss the results from our model, and compare them with those from Hickson and Rood (1988), and although we are in good agreement on the frequencies, we reach

Send offprint requests to: G. Mamon (Meudon address)

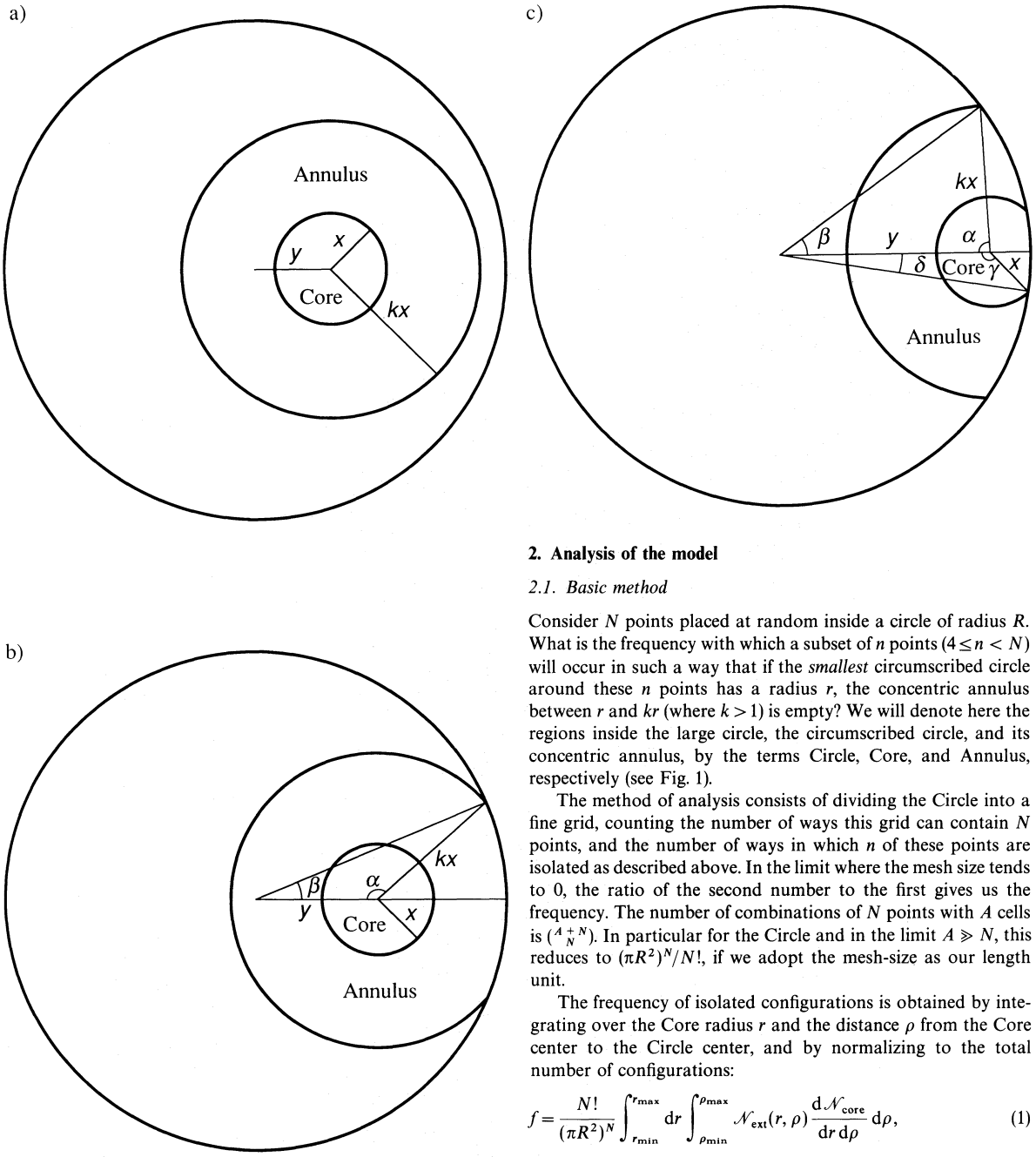

Fig. 1a–c. Geometry of Case 1(**a**), Case 2(**b**), and Case 3(**c**). The large circle delimits the "Circle", which has unit radius

the opposite conclusion: chance alignments should be frequent enough in groups of galaxies to produce an important fraction of Hickson's (1982) compact groups (hereafter HCGs). We also argue that small clusters of galaxies are also efficient at compact group formation.

2. Analysis of the model

2.1. Basic method

Consider N points placed at random inside a circle of radius R. What is the frequency with which a subset of n points ($4 \leq n < N$) will occur in such a way that if the *smallest* circumscribed circle around these n points has a radius r, the concentric annulus between r and kr (where $k > 1$) is empty? We will denote here the regions inside the large circle, the circumscribed circle, and its concentric annulus, by the terms Circle, Core, and Annulus, respectively (see Fig. 1).

The method of analysis consists of dividing the Circle into a fine grid, counting the number of ways this grid can contain N points, and the number of ways in which n of these points are isolated as described above. In the limit where the mesh size tends to 0, the ratio of the second number to the first gives us the frequency. The number of combinations of N points with A cells is $\binom{A+N}{N}$. In particular for the Circle and in the limit $A \gg N$, this reduces to $(\pi R^2)^N/N!$, if we adopt the mesh-size as our length unit.

The frequency of isolated configurations is obtained by integrating over the Core radius r and the distance ρ from the Core center to the Circle center, and by normalizing to the total number of configurations:

$$f = \frac{N!}{(\pi R^2)^N} \int_{r_{\min}}^{r_{\max}} \mathrm{d}r \int_{\rho_{\min}}^{\rho_{\max}} \mathcal{N}_{\mathrm{ext}}(r, \rho) \frac{\mathrm{d}\mathcal{N}_{\mathrm{core}}}{\mathrm{d}r\,\mathrm{d}\rho}\,\mathrm{d}\rho, \tag{1}$$

where $\mathcal{N}_{\mathrm{ext}}(r, \rho)$ is the number of ways of placing $N - n$ points in the regions external to the Annulus, and where $\mathrm{d}\mathcal{N}_{\mathrm{core}}$ is the number of configurations of Cores of radius between r and $r + \mathrm{d}r$, and distance to the center of the Circle between ρ and $\rho + \mathrm{d}\rho$. From the discussion of the preceding paragraph, the number of ways of placing $N - n$ points in the region external to the Annulus is

$$\mathcal{N}_{\mathrm{ext}} = \frac{A_{\mathrm{ext}}^{N-n}}{(N-n)!}, \tag{2}$$

where A_{ext} is the area of the external region. We will return to the computation of $\mathcal{N}_{ext}$ in Sect. 2.3.

2.2. Number of ways of delimiting Cores

A Core can be delimited either by two points diametrically opposed or by three points forming an acute triangle. There are $n-2$ points inside two-point Cores and $n-3$ points inside three-point Cores. Then, the number of ways of forming Cores is

$$d\mathcal{N}_{core} = \frac{A_{core}^{n-2}\, d\mathcal{N}_2}{(n-2)!} + \frac{A_{core}^{n-3}\, d\mathcal{N}_3}{(n-3)!}, \tag{3}$$

where $d\mathcal{N}_2$ and $d\mathcal{N}_3$ are the number of two-point and three-point Cores, respectively. We now analyze in turn both types of Core.

2.2.1. Two-point Cores

For an arbitrary point (cell) P, the number of partners it can be paired with to form the diameter of a circle of radius between r and $r + dr$ is $2\pi \times 2r \times 2dr = 8\pi r dr$. Over a sufficiently large region there will then be $\int 4\pi r dr dA$ such *pairings*, dA being an element of area. Thus the number of pairings forming circles whose *centers* are contained in an area dA with radius between r and $r + dr$ is:

$$d\mathcal{N}_2 = 4\pi r dr dA. \tag{4}$$

2.2.2. Three-point cores

Given an arbitrary point P_1, how many three-point circles can be drawn with radii between r and $r + dr$, with P_1 as one of the vertices? Denote by P_2 a point a distance s_{12} away, and call ϕ the angle $\widehat{(P_2 P_1 P_3)}$ where P_3 is the third vertex (see Fig. 2). The requirement that the triangle formed by P_1, P_2, P_3 is acute imposes the restrictions $0 < \phi < \pi/2$ and $\cos\phi < s_{12}/2r < 1$, where r is the radius of the circle that circumscribes the triangle.

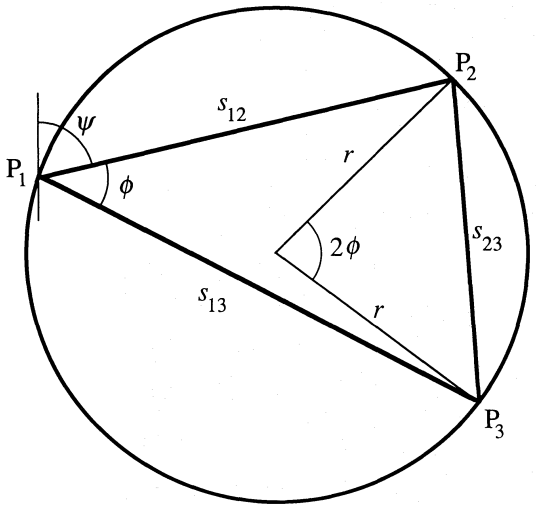

Fig. 2. Geometry of a three-point Core

The distance s_{13} between P_1 and P_3, can be found from simple geometry using the relation

$$\sin\phi = \frac{s_{23}/2}{r} = \frac{(s_{12}^2 + s_{13}^2 - 2 s_{12} s_{13}\cos\phi)^{1/2}}{2r}.$$

Solving the resulting quadratic for s_{13} yields $s_{13} = s_{12}\cos\phi + \sin\phi\,(4r^2 - s_{12}^2)^{1/2}$, where the plus sign forces the angle at P_3 to be acute.

For small variations of r and ϕ, the number of cells at P_3 forming circles radius between r and $r + dr$ is,

$$d\mathcal{N} = (s_{13}\, d\phi)\left(\frac{\partial s_{13}}{\partial r} dr\right)$$

$$= 4r\sin\phi\, d\phi dr\left(\sin\phi + \frac{s_{12}\cos\phi}{(4r^2 - s_{12}^2)^{1/2}}\right).$$

The number of acute triangles that can be constructed with P_1 at one vertex is then

$$\frac{d\mathcal{N}_{total}}{dr} = \int_0^{2\pi} d\psi \int_0^{\pi/2} d\phi 4r\sin\phi \int_{2r\cos\phi}^{2r} s_{12}\, ds_{12}$$

$$\left(\sin\phi + \frac{s_{12}\cos\phi}{(4r^2 - s_{12}^2)^{1/2}}\right) = 6\pi^2 r^3,$$

where ψ is the polar angle of $\overrightarrow{P_1 P_2}$ and the area around P_2 is $s_{12}\, d\psi ds_{12}$ [the integral is easily solved with the substitution $\theta = \cos^{-1}(s_{12}/2r)$]. Thus, the number of three-point circles per unit area is $2\pi^2 r^3 dr$, and for circles whose centers are contained within an element area dA, the number is:

$$d\mathcal{N}_3 = 2\pi^2 r^3 dr dA. \tag{5}$$

2.3. Detalied computation

We now compute $d\mathcal{N}_{core}$ and $d\mathcal{N}_{ext}$ by distinguishing between the three following cases. 1) Both the Core and Annulus are completely inside the Circle (Fig. 1a). 2) The Core is completely inside the Circle, but the Annulus overlaps the boundary of the Circle (Fig. 1b). 3) Both the Core and Annulus overlap the boundary of the Circle (Fig. 1c). The total frequency of occurrence of isolated subgroups is then $f = f_1 + f_2 + f_3$, where f_i is the frequency for case i.

For the first two cases the total number of possible Core configurations is

$$d\mathcal{N}_{core} = \frac{2n\pi^{n-1} r^{2n-3} dr dA}{(n-2)!}, \tag{6}$$

using Eqs. (3), (4), and (5), and with the Core area $A_{core} = \pi r^2$. From Eqs. (1), (2), and (6), the frequency of isolated configurations is then

$$f = \frac{4nN!\pi^{n-N}}{(N-n)!(n-2)!} \int_{x_{min}}^{x_{max}} x^{2n-3}\, dx \int_{y_{min}}^{y_{max}} \tilde{A}_{ext}^{N-n}(x, y)\, y dy, \tag{7}$$

where $dA = 2\pi\rho d\rho$, $x = r/R$, $y = \rho/R$, and $\tilde{A}_{ext} = A_{ext}/R^2$.

2.3.1. Case 1: Core ⊂ Circle and Annulus ⊂ Circle

Here we have $0 < x < 1/k$, $0 < y < 1 - kx$, and $\tilde{A}_{ext} = \pi(1 - k^2 x^2)$ (see Fig. 1a). Using Eq. (7) and setting $u = kx$

yields

$$f_1 = \frac{2nN!}{(N-n)!(n-2)!k^{2n-2}} \int_0^1 u^{2n-3}(1-u^2)^{N-n}(1-u)^2\,du \tag{8a}$$

$$= \frac{n}{k^{2n-2}}\left(N+n-1-2^{N-n+2}\frac{N!(2n-3)!!}{(n-2)!(2N-1)!!}\right), \tag{8b}$$

where the integral in Eq. (8a) is solved by successive integration by parts.

2.3.2. Case 2: Core $\subset$ Circle but Annulus $\not\subset$ Circle

The constraints $x + y < 1$ (preventing case 3), $kx + y > 1$ (preventing case 1), and $kx - y < 1$ (required by $n < N$) lead to $0 < x < 2/(k+1)$, $|1 - kx| < y < 1 - x$, and now:

$$\tilde{A}_{\text{ext}} = \pi - k^2x^2\alpha - \beta + y\sin\beta, \tag{9}$$

where

$$\alpha = \cos^{-1}\left(\frac{k^2x^2 + y^2 - 1}{2kxy}\right)$$

and

$$\beta = \cos^{-1}\left(\frac{1 + y^2 - k^2x^2}{2y}\right)$$

(see Fig. 1b). Then, using Eq. (7), isolated configurations in case 2 will occur with a frequency

$$f_2 = \frac{4nN!\pi^{n-N}}{(N-n)!(n-2)!}\int_0^{\frac{2}{k+1}} x^{2n-3}\,dx \times \int_{|1-kx|}^{1-x} [\pi - k^2x^2\alpha - \beta + y\sin\beta]^{N-n}\,y\,dy. \tag{10}$$

2.3.3. Case 3: Core $\not\subset$ Circle and Annulus $\not\subset$ Circle

Though the Core extends outside the Circle, half of the Core must be contained inside the Circle if its delimiting points are diametrically opposed or form an acute triangle. If γ is the angle that the Core center subtends between the Circle center and one of the two intersections of the boundaries of the Core and Circle, then

$$\gamma = \cos^{-1}\left(\frac{x^2 + y^2 - 1}{2xy}\right) \geq \pi/2$$

(see Fig. 1c). Using Eq. (4), the number of two point circles is now reduced to

$$d\mathcal{N}'_2 = (2\gamma - \pi)4r\,dr\,dA. \tag{11}$$

For three-point circles, if we specify the angular coordinates of the three vertices as x, y, and z, with $x < y < z$, we note the following restrictions: $-\gamma < x < \gamma - \pi$, $x + \pi < z < \gamma$, and $z - \pi < y < x + \pi$. The total number of three point circles is hence proportional to

$$\int_{-\gamma}^{\gamma-\pi} dx \int_{x+\pi}^{\gamma} dz \int_{z-\pi}^{x+\pi} dy = \frac{(2\gamma-\pi)^2(2\pi-\gamma)}{3}.$$

The constant of proportionality is obtained by setting $\gamma = \pi$, for which we recover $d\mathcal{N}_3$ of Eq. (5). So in general, the total number of three-point circles is

$$d\mathcal{N}'_3 = \frac{2}{\pi}(2\gamma-\pi)^2(2\pi-\gamma)r^3\,dr\,dA. \tag{12}$$

The area of the Core is now $A'_{\text{core}} = R^2\tilde{A}'_{\text{core}}$, with

$$\tilde{A}'_{\text{core}} = x^2\gamma + \delta - y\sin\delta, \tag{13}$$

where

$$\delta = \cos^{-1}\left(\frac{1 + y^2 - x^2}{2y}\right)$$

(see Fig. 1c). Thus, in analogy with Eq. (3), the total number of Core configurations is

$$d\mathcal{N}'_{\text{core}} = \frac{A'^{n-2}_{\text{core}}}{(n-2)!}d\mathcal{N}'_2 + \frac{A'^{n-3}_{\text{core}}}{(n-3)!}d\mathcal{N}'_3 = \frac{4(2\gamma-\pi)R^{2n}x\,dx\,y\,dy\,\tilde{A}'^{n-3}_{\text{core}}}{(n-2)!}[2\pi\tilde{A}'_{\text{core}} + (n-2) \times (2\gamma-\pi)(2\pi-\gamma)x^2], \tag{14}$$

using Eqs. (11) and (12), and where again $dA = 2\pi\rho\,d\rho$.

The constraints $x + y > 1$ (forcing case 3), $y < (1 - x^2)^{1/2}$ (required by $\gamma > \pi/2$), and again $kx - y < 1$ lead to $0 < x < 2k/(k^2+1)$, $y_1 < y < (1-x^2)^{1/2}$, where $y_1 = \max(1-x, kx-1)$. Then, the frequency of case 3 configurations is

$$f_3 = \frac{4N!}{\pi^N(N-n)!(n-2)!}\int_0^{2k/(k^2+1)} x\,dx \int_{\max(1-x,\,kx-1)}^{(1-x^2)^{1/2}} (2\gamma-\pi) \times (x^2\gamma + \delta - y\sin\delta)^{n-3}[2\pi(x^2\gamma+\delta-y\sin\delta) + (n-2)(2\gamma-\pi)(2\pi-\gamma)x^2][\pi - k^2x^2\alpha - \beta + \gamma\sin\beta]^{N-n}\,y\,dy, \tag{15}$$

where we have used Eqs. (1), (2), (9), (13), and (14).

3. Model results

Table 1 shows the results obtained from the theory described in Sect. 2 [Eqs. (8b), (10), and (15)], using $k = 3$ as in Hickson's (1982) isolation criterion, where the integrals in Eqs. (10) and (15) are solved numerically by Rhomberg integration, and finally summing over n (from 4 to $N - 1$), and over the three cases. For comparison, Monte-Carlo estimates were obtained for the same model, where polar coordinates of two-dimensional positions were generated from two sets of [0–1] uniform pseudo-random numbers, with the modulus taken as the square root of the first number, and the argument as 2π times the second number (the radius of the Circle is set here and below to unity). The Hickson

Table 1. Frequency of isolated groups for $N = 9$

	Analytical (%)	Monte-Carlo (%)
Case 1	1.14	1.05±0.10
Case 2	7.04	7.23±0.27
Case 3	3.42	3.19±0.18
Total	11.60	11.47±0.34

(1982) isolation criterion was implemented in the same manner as in Papers I and II. The agreement between the analytical and Monte-Carlo methods (using 10 000 trials) is within the counting errors of the Monte-Carlo estimates (Table 1).

Figure 3 shows how the total frequency and the frequency for each of the cases outlined in Sect. 2 vary as functions of N. Case 1 dominates only for very large N, while case 2 is the dominant case up to $N \lesssim 45$, and case 3 becomes relatively unimportant at large N. This can be understood as follows. At low N, most of the isolated subgroups are close enough to the boundary of the Circle for their Annulus to extend out, hence the relative importance of case 2, and to a lesser extent of case 3. For large N, the galaxies are so crowded that if a subgroup appears isolated, it is likely to be small, and so its Annulus will also be relatively small, and a proportionately larger fraction of subgroups will have their Annulus completely enclosed within the Circle.

In Fig. 4 we show the frequencies for different subgroup membership n, again as functions of the parent group membership N. The quarters account for at least 77% of all the subgroups, and for each increase of n by 1, the frequency of subgroups decreases by roughly a factor 5.

4. Refinements to the model

4.1. Background of field galaxies

Because groups of galaxies are not isolated in space, we embed them in a diffuse homogeneous background of field objects, with density equal to λ times the mean density of the loose group, i.e., $\lambda N/\pi R^2$. The background galaxies act in two opposite ways: A subgroup will no longer be isolated if a background galaxy falls inside its Annulus. On the other hand, an isolated triplet will be promoted into an isolated quartet if a background galaxy falls inside or near its Core.

We now estimate the effects of the background of field galaxies arising from these two effects. The analysis below will provide a *lower limit* to the frequency of isolated subgroups because we will neglect the case where several background galaxies can form their own isolated subgroup of 4 or more, with or without the help of 1 or 2 galaxies in the group, as well as well as the cases where background galaxies fall outside but close to the Core of a triplet, while at the same time the new Annulus, which now extends further, remains empty.

The contamination effects that we are considering do not modify the radius x of the Core and its distance y to the group center. So we choose to sum first over n, and later integrate over x and y. Let $g(x, y)\,\mathrm{d}x\mathrm{d}y$ be the frequency of isolated subgroups of radius between x and $x + \mathrm{d}x$, and distance to the group center between y and $y + \mathrm{d}y$, before background contamination, so that

$$f = \iint g(x, y)\,\mathrm{d}x\,\mathrm{d}y = \iint \sum_n g_n(x, y)\,\mathrm{d}x\,\mathrm{d}y .$$

Define similarly $g'(x, y)\mathrm{d}x\mathrm{d}y$ for the frequency of isolated subgroups after background contamination. Then from Poisson statistics, we have

$$g'(x, y) = g(x, y)\mathrm{e}^{-(k^2-1)t} + g_3(x, y)\mathrm{e}^{-(k^2-1)t} \sum_{j=1}^{\infty} \frac{t^j}{j!}\mathrm{e}^{-t}, \qquad (16)$$

where $t = \lambda N x^2$. The first term on the right-hand-side of Eq. (16) represents the number of original subgroups that survive contamination, while the second term represents the triplets promoted

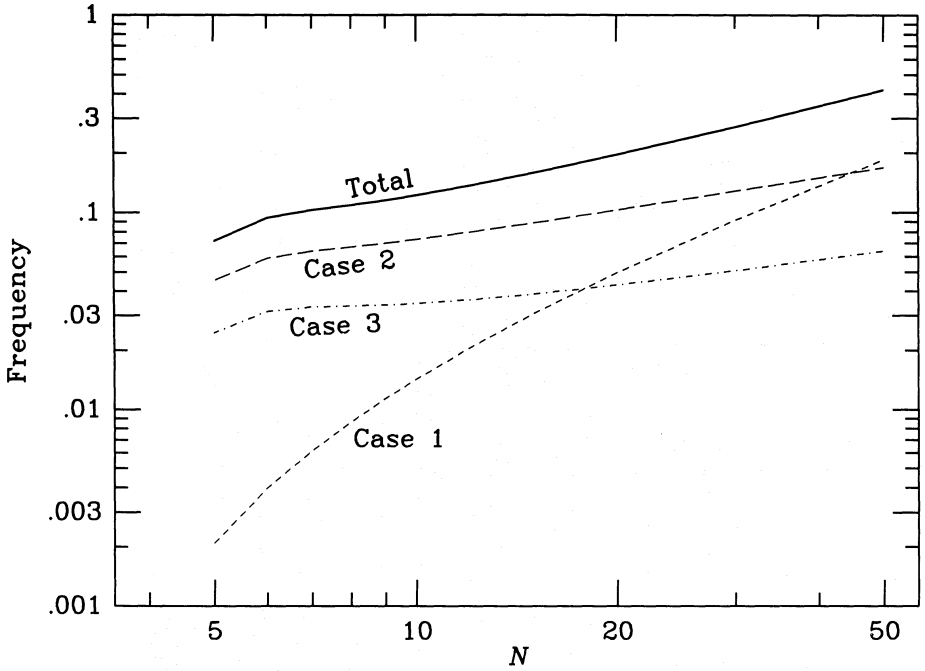

Fig. 3. Frequency of isolated subgroups versus parent group membership N, for Case 1 (*short dashed curve*), Case 2 (*long dashed curve*), Case 3 (*dashed-dotted curve*), and all three cases (*solid curve*)

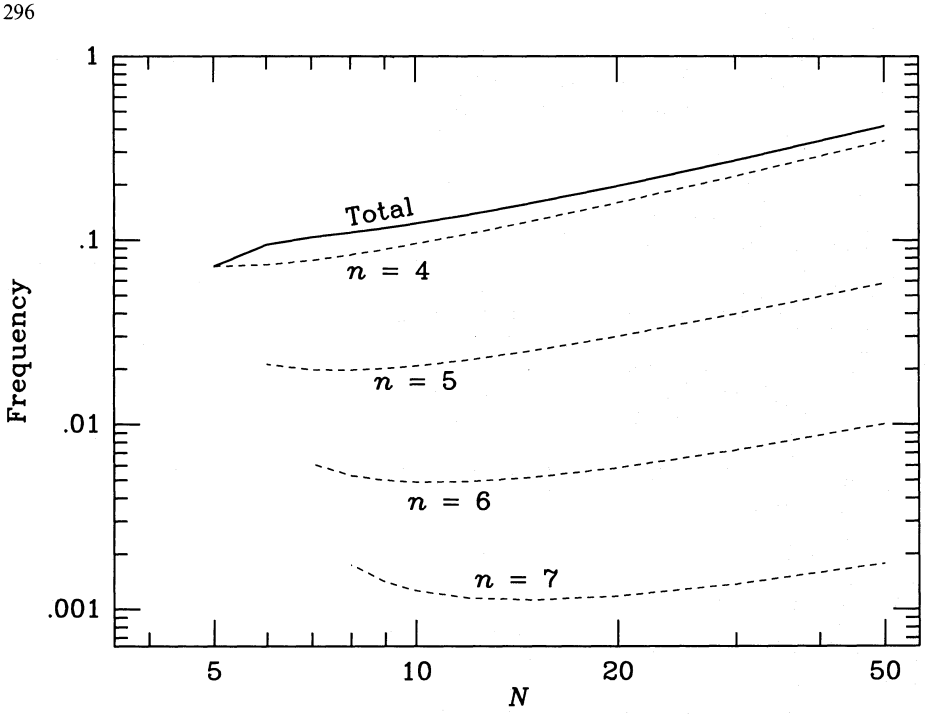

Fig. 4. Frequency of isolated subgroups versus parent group membership N, for different values of the subgroup membership n (*dashed curves*) and the total frequency (*solid curve*)

into isolated subgroups by j background galaxies. Equation (16) can be written

$$g'(x, y) = e^{-(k^2-1)\lambda N x^2}\left[\sum_{n=4}^{N-1} g_n(x, y) + g_3(x, y)(1 - e^{-\lambda N x^2})\right]. \quad (17)$$

The first exponential in Eq. (17) represents the fraction of Annuli that survive contamination, while the other factor containing the exponential represents the fraction of triplets that are promoted to higher multiplicity subgroups. We compute the total frequency f' of isolated subgroups after contamination by background field galaxies, by integrating Eq. (17) over x and y, taking g_n (including g_3) from the integrands of Eqs. (8a), (10), and(15), and using the same integration limits as in these three equations.

Figure 5 shows the lower limits for the total frequencies as a function of N, for three choices of λ, as well as $\lambda = 0$ (no field galaxies). The effect of background field galaxies is to reduce the frequency of isolated subgroups, i.e., there are more losses by contamination than there are promotions of triplets. For $\lambda = 0.1$ the frequency of isolated subgroups is reduced by less than 30% (recall that we are estimating lower limits to the frequency here). This factor is not very sensitive to N, except for a slight decrease in the effect of contamination for lage N. This trend arises because at larger N, as the galaxies are more crowded, the Cores and Annuli are smaller, hence contamination is less important.

4.2. Compactness criteria

Although isolated subgroups tend to be small and compact, they do not necessarily satisfy Hickson's (1982) compactness criterion for compact groups. We include here a compactness criterion by limiting the size of subgroup relative to that of the parent loose group, i.e., by putting an upper limit on x (defined in Sect. 2) of x_m. The model described in Sect. 2 must then be modified so that x in Eqs. (10) and (15) does not exceed x_m, while u in Eq. (8a) does not surpass kx_m.

The frequencies plotted in Fig. 6 are very sensitive to the compactness criterion: they are virtually unchanged for $x_m \geq 0.4$, but are reduced to up to three orders of magnitude for $x_m = 0.1$. Furthermore, inclusion of the compactness criterion is most effective at low N, because for groups with large membership, the low mean separation between galaxies (see Sect. 4.1.) makes the isolation criterion an effective compactness limit.

4.3. Radial density distribution

We now introduce radial distributions that are more likely to be representative of real groups. While surface number density for groups of galaxies have not been well established (owing to problems with small number statistics and with the definition of the group center), it is likely to be a decreasing function of distance to the center. For comparison, the Coma cluster of galaxies has a surface number density profile that is nearly homogeneous within its core, and falls off as $1/r^2$ in its outer regions (see, e.g., Fig. 6 of Kent and Gunn, 1982). We consider here two alternatives to the homogeneous model, a power-law distribution with surface number density falling as $1/r$, and the modified Hubble distribution:

$$\sum(r) = \frac{\sum_0}{\left[1 + \left(\frac{r}{r_c}\right)^2\right]}. \quad (18)$$

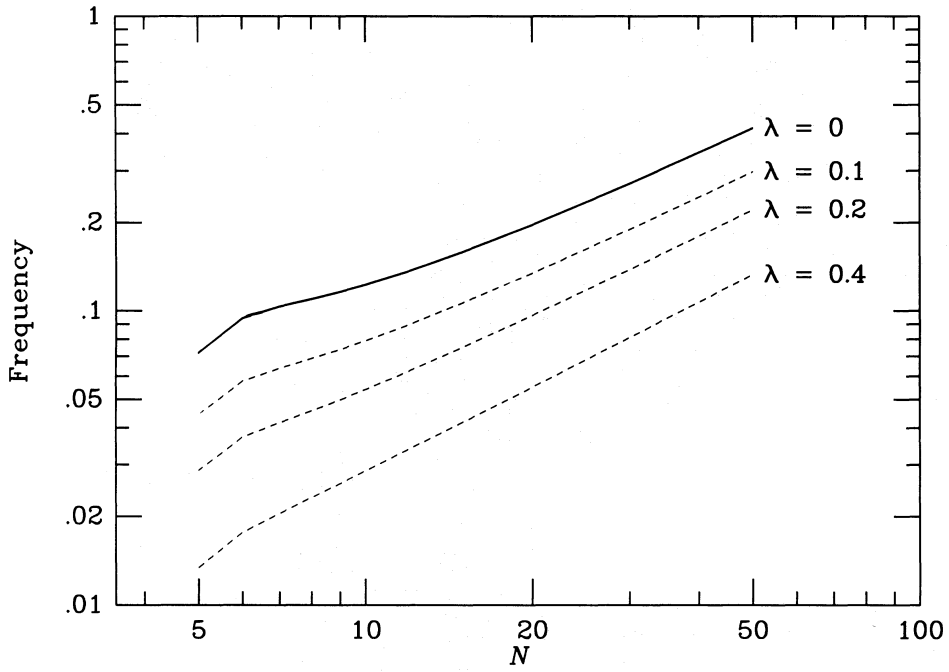

Fig. 5. Frequency of isolated subgroup versus parent group membership N for different choices of the contamination parameter λ (*dashed curves*), and for no contimation (*solid curve*)

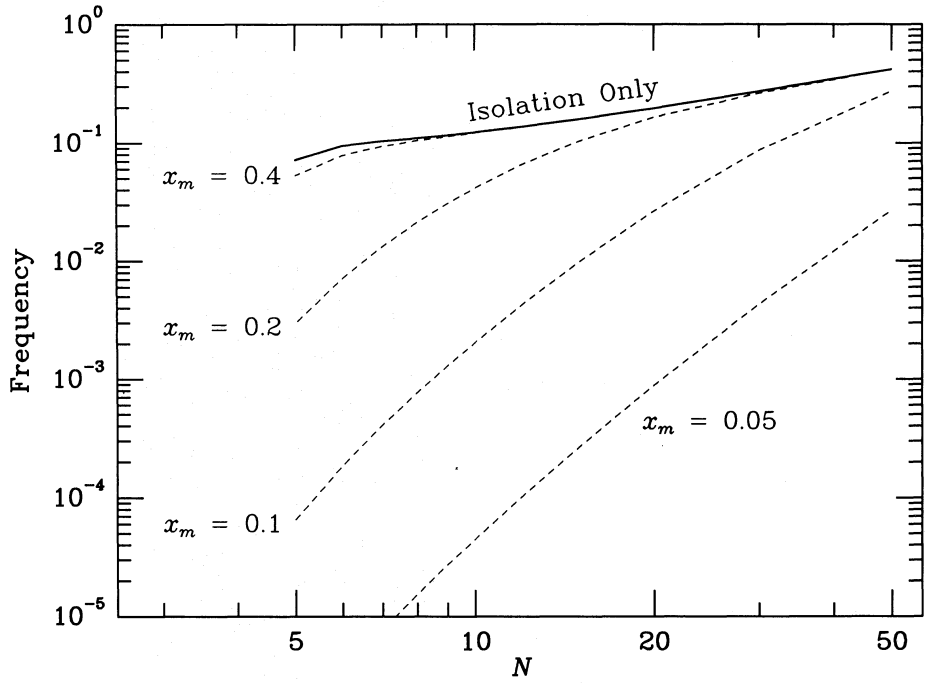

Fig. 6. Frequency of isolated compact subgroups versus parent group membership N for different choices of the compactness parameter x_m (*dashed curves*), and of isolated subgroups with no compactness criterion (*solid curve*)

If q is the first random deviate, the modulus of the polar coordinate of the galaxy is just q for the $1/r$ distribution, and $r_c[(1+r_c^{-2})^q - 1]^{1/2}$ for the modified Hubble distribution (note that r_c is expressed in units of the Circle radius).

Figure 7 shows the total frequencies of isolated subgroups using these number density profiles. For the modified Hubble distribution we use $r_c = 0.1$ and 0.35 (the latter value sets to 0.5 the radius containing half of the galaxies on the average). For low N, the decreasing profiles allow for concentration of galaxies near the center and thus facilitate the appearance of isolated subgroups. This is especially true for the modified Hubble distribution with the small "core" radius $r_c = 0.1$, as high densities are achieved in its central regions. However, as N gets larger, the center gets too crowded and a larger fraction of subgroups will be situated in the outer regions. Since the densities in the outer regions of the modified Hubble distribution are low, the total fraction of isolated subgroups becomes smaller than in the case of a homogeneous distribution.

5. Application to observed groups

5.1. Loose group data

We use the loose group data from the NBG group catalog of Tully (1987a), which we prefer to the CfA group catalog (Geller and Huchra, 1983), because Tully's (1987b) grouping algorithm is more physical, while the CfA groups are artifically stretched near the magnitude limit (in order to preserve the multiplicity function). The NBG catalog has been generated from a galaxy catalog nearly complete in volume. We scale the distances given in the NBG catalog (obtained from a model of virgocentric flow, see Tully, 1987b, and references therein) to $H_0 = 50\ \mathrm{km\,s^{-1}\,Mpc^{-1}}$

5.2. Contamination

The contamination parameter λ is estimated by comparing the mean surface number density of each NBG group, averaged over the smallest circumscribed circle containing the centers of the member galaxies (hereafter referred to as the "Hickson circle"), to the mean surface number density of galaxies in the parent galaxy catalog down to a limit of 3 mag fainter than the median galaxy magnitude in the group, or the magnitude limit of the catalog, whichever comes first (Hickson's compact group membership criterion imposes a maximum magnitude range of 3). Note that in the latter case, although the field surface number density obtained from the catalog must be corrected by some factor larger than unity, the group surface number density must be corrected by the same factor, hence λ is unaffected by the completion limit of the catalog.

For the 75 groups with $N \geq 5$ in the NBG catalog (excluding the Local group) the median λ is 0.065. These medians do not change significantly if one only considers groups with $N \leq 20$.

The contamination parameter must be corrected because it is measured relative to the Hickson circle, rather than the Circle used in Sect. 2. Using Monte-Carlo simulations, we find that if N galaxies are placed at random within a unit circle, the smallest circumscribed circle around these N galaxies has a typical (median) radius of 0.79 for $N = 5$ increasing to 0.89 for $N = 9$. So the λ values above must be divided by $\sim 0.85^2$ yielding $\langle \lambda_{\mathrm{NBG}} \rangle \simeq 0.09$. From Fig. 5, these numbers are small enough

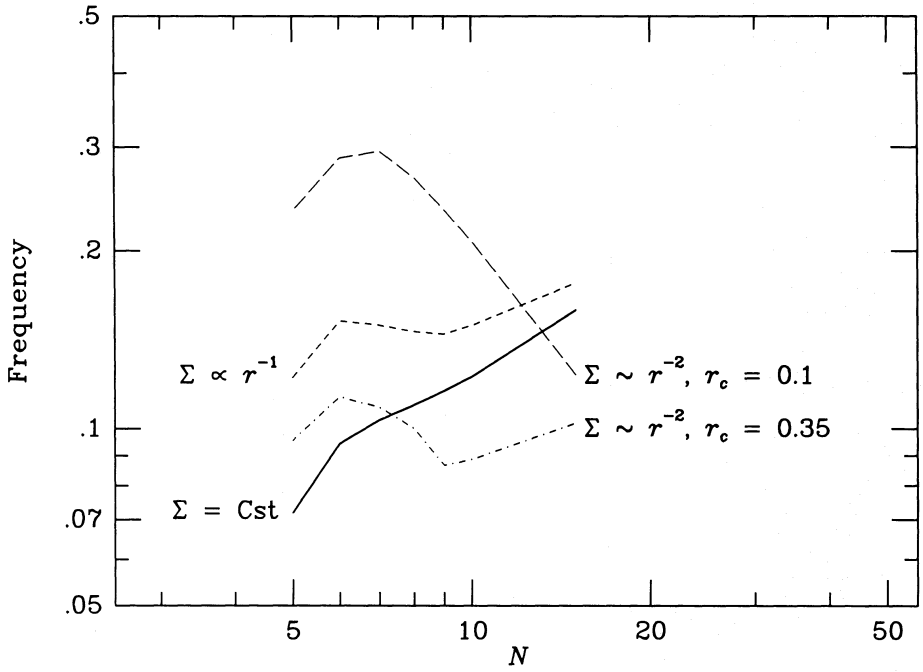

Fig. 7. Frequency of isolated subgroups versus parent group membership N, for the uniform model (*solid curve*), the $1/r$ model (*dashed curve*), the modified Hubble model (Eq. [18]) with $r_c = 0.1$ (*short dash-dotted curve*), and with $r_c = 0.35$ (*long dash-dotted curve*)

that *contamination of the Annulus from foreground and background galaxies is small.*

5.3. Discordant redshifts

The contamination methodology described here can be used to estimate the fraction of discordant redshifts within compact groups. From the analysis in Sect. 2 and 4.2. we can write the probability of having one single discordant redshift in subgroups of n members as

$$\frac{\int\int g_{n-1}(x, y) t e^{-t} e^{(k^2-1)t} dx\, dy}{\int\int g_n(x, y) e^{-t} e^{(k^2-1)t} dx\, dy},$$

using Eq. (16) and again $t = \lambda N x^2$, and where the integration limits and the g's are taken from Eqs. (8a), (10), and (15). In Table 2 we show the probability of quartets and quintets having one discordant redshift, as a function of the parent group membership N, for $\lambda = 0.09$ (Sect. 5.2), and for two choices of x_m (see Sect. 5.4 below). The fraction of discordant redshifts among HCG quintets are consistent with the fraction of 35% predicted by Hickson et al. (1988b), and the 4 out of 10 found by these authors. Similarly, the fraction of discordant redshift quartets in roughly 20%, again consistent with the 4 out of 30 found by Hickson et al. (1988b) for HCG quartets.

These results should be taken as lower limits, because a background galaxy can be strongly amplified through the gravitational lensing by the group members, and thus its magnitude can appear within three mags from that of the brightest member. In fact such a case has been made by Hammer and Nottale (1986) for the discordant redshift in the VV 172 compact group (H55). Note that these results are in disagreement with the conclusion of Sulentic (1987) that discordant redshifts ought to be rare within the HCGs.

5.4. Compactness

We now consider the effects of Hickson's (1982) compactness on the frequency of chance alignments. For given x_m, the maximum subgroup surface magnitude will be

$$\mu_B = 32.14 + 5\log x_m + 5\log\left(\frac{R_H h_{50}}{1\,\mathrm{Mpc}}\right) - 2.5\log\left(\frac{\langle L\rangle h_{50}^2}{10^{10} L_\odot}\right) - 2.5\log\left(\frac{n}{4}\right), \quad (19)$$

where $\langle L\rangle$ is the mean B-band galaxy luminosity, R_H is the radius of the Hickson circle, and where we have corrected from Circle to Hickson circle. Hickson's (1982) compactness criterion is $\mu_E \leq 26$, where E is a color band corresponding to the E (red) POSS plates. He gives color transformations of $B - E = 1.5$ for spiral galaxies, and 1.9 for ellipticals. Adopting $B - E = 1.7$, and using Eq. (19), Hickson's compactness criterion corresponds to

$$x_m = 0.13\left(\frac{R_H h_{50}}{1\,\mathrm{Mpc}}\right)^{-1}\left(\frac{\langle L\rangle h_{50}^2}{10^{10} L_\odot}\right)^{1/2}\left(\frac{n}{4}\right)^{1/2}. \quad (20)$$

For the 75 NBG groups considered above, we find a median group size of $\langle R_H\rangle = 1.18\, h_{50}^{-1}$ Mpc, while the median galaxy luminosity in the NBG groups is $\langle L\rangle = 2.1\, 10^{10}\, h_{50}^{-2}\, L_\odot$. With these numbers and assuming compact quartets, we get $x_m = 0.16$ from the NBG groups. From this value of x_m, we obtain a frequency of chance alignments of 0.82% for the NBG groups of $N = 8$ (the median size of the 75 groups). This can be understood as a lower limit as discussed below in Sect. 6.5. Hence, *in roughly one percent of NBG groups, there should appear chance alignments of galaxies strictly meeting Hickson's selection criteria.*

Table 2. Probability of one discordant redshift for compact quartets and quintets

	Quartets		Quintets	
N	$x_m = 0.06$	$x_m = 0.20$	$x_m = 0.06$	$x_m = 0.20$
5	0.33	0.26	—	—
6	0.26	0.21	0.63	0.49
8	0.21	0.17	0.42	0.33
12	0.18	0.15	0.32	0.25
20	0.16	0.14	0.26	0.22

Notes: The results above are for a contamination parameter $\lambda = 0.09$, as estimated for the NBG groups.

We can also apply this analysis to the loose groups simulated in Paper II. These started within a Circle of radius $800\, h_{50}^{-1}$ kpc and $\langle L\rangle = 3.4\, 10^{10}\, h_{50}^{-2}\, L_\odot$ (mean). From Eq. (20) and correcting back from Circle to Hickson circle, we get $x_m = 0.35$, for which case nearly all isolated quartets meet Hickson's (1982) compactness criterion. One then expects 3.6% and 9.3% of chance alignments for parent groups of five[1] and eight members, respectively. These numbers are consistent with the lage frequencies of chance alignments found in Paper II (3 to 25%), although radial density falloffs and clumpiness must be taken into account to explain that upper limit (see Sect. 6 below).

6. Discussion

6.1. General points

The analysis described in Sect. 2 produces frequencies of isolated subgroups in excellent agreement with Monte-Carlo estimates based upon the same static homogeneous model, giving us strong confidence that both methods are error-free. Note that the "semi-analytical" method has the advantage of computational speed (by a typical factor of 1000). For even more speed (at the expense of less accuracy) one can simply limit the computation to $n = 4$ and normalize to all values of n by multiplying by 5/4 (see Sect. 3). We showed in Sect. 4 how our analytical model could be generalized to incorporate contamination by field galaxies and a compactness criterion. Unfortunately, we are not able to generalize our analytical model to non-homogeneous models such as those presented in Sect. 4.3, for which we had to resort to less elegant and considerably more costly Monte-Carlo methods. In Sect. 5 we found that interloper contamination does not reduce appreciably the frequency of chance isolated configurations. However, the inclusion of a compactness criterion produces a

[1] Although, the simulated loose groups of Paper II initially had eight galaxies, mergers could have depleted their membership down to five while they were still showing compact configurations in projection.

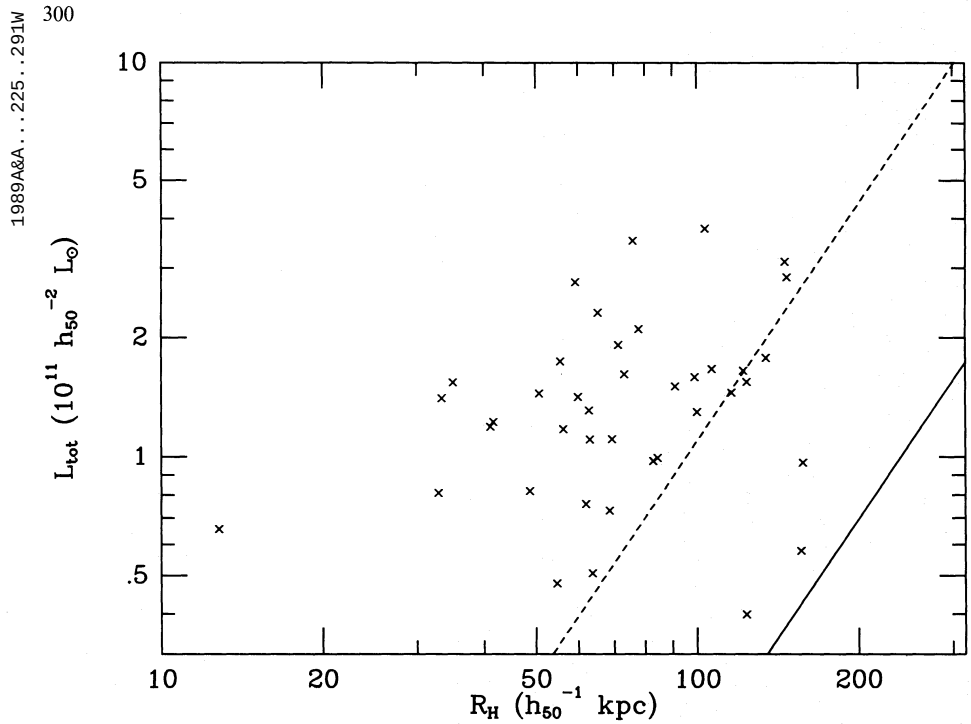

Fig. 8. Total group luminosity versus radius of the smallest circumscribed circle containing the centers of the group members ("Hickson circle") for 40 accordant redshift compact groups. The *solid line* represents Hickson's (1982) compactness criterion, $\mu_B = 27.7$ corresponding to $\mu_E \simeq 26.0$. The *dashed line* represents Hickson's (1982) surface magnitude completion limit, $\mu_B = 25.7$ ($\mu_E \simeq 24.0$)

significantly lower frequency of chance compact and isolated configurations, but roughly enough to explain half of the HCGs.

Hickson and Rood (1988) have independently performed a similar analysis on the frequencies of chance alignments based upon Monte-Carlo simulations. Their frequencies of chance alignments are comparable with ours (to within 20% or better), once the conversion from Hickson circle to Circle is made. And yet their conclusion is that their frequencies of chance alignments are far too small for compact groups to be caused by such projection effects. What causes this discrepancy?

In Fig. 8 we plot for 40 accordant redshift (see Paper I) Hickson groups the physical radius of the Hickson circle versus the total ground luminosity. One immediately notices the paucity of compact groups near the compactness criterion: this translates into a median surface magnitude that is much lower than the critical value $\mu_B = 27.7$ (plotted as the thin solid line). In fact, all but three groups have $\mu_E \leq 24$, which Hickson (1982) pointed out was the near-completion surface magnitude limit of the HCG catalog. Matching this new surface magnitude limit, produces the new compact group maximum size of

$$x_m = 0.051 \left(\frac{R_H h_{50}}{1\,\mathrm{Mpc}}\right)^{-1} \left(\frac{\langle L \rangle h_{50}^2}{10^{10} L_\odot}\right)^{1/2} \left(\frac{n}{4}\right)^{1/2}. \quad (21)$$

Using Eq. (21) the NBG sample has a median x_m of 0.063. Such a low value strongly reduces the frequency of chance alignments expected in the NBG groups to below $5.8\,10^{-5}$ for $N \leq 8$ (and 0.30% for $N = 20$). Therefore, *chance alignments can clearly contribute to forming compact groups that strictly meet Hickson's (1982) selection criteria, but may not be sufficient to create compact groups as compact as Hickson's groups.* Moreover, because Hickson's sample is probably incomplete for the faintest two surface magnitudes (Hickson, 1982), there are most likely more compact groups within the surface magnitude limit than counted by Hickson (1982), hence the need for even larger frequencies of chance alignments.

6.2. *Loose to compact group ratio per unit volume*

We now discuss various points to reconcile the idea of compact groups as chance alignments. First, we note that the incompleteness in magnitude and distance in Hickson's compact group sample and various loose group samples makes it difficult to estimate the fraction of loose groups required to explain half or all of Hickson's compact groups as chance alignments within loose groups. In Paper I, the number of compact groups in a given area of sky and up to a given limiting magnitude was estimated at 2.5% of the number of CfA groups. We now estimate the same ratio between Hickson's groups and the NBG groups. The NBG catalog covers the full sky, and is essentially complete in volume out to $25\,h_{75}^{-1}$ Mpc (Tully, 1987b), or approximately out to 1510 km s^{-1} (the median velocity of the galaxies in the NBG catalog in the distance range $24\,h_{75}^{-1}$ Mpc to $26\,h_{75}^{-1}$ Mpc).[2] Up to that distance there are 49 NBG groups of 5 members or

[2] Recall that Tully (1987a) corrected the galaxy distances in his NBG catalog for the non-uniform Hubble flow caused by the Virgo cluster.

more. Plotting $N(<v)$ for HCG galaxies we estimate that Hickson's catalog is close to complete out to 8000 km s^{-1}, but only covers $\delta > -33°$ (or 77% of the full sky). Combining the data from Hickson (1982) and Hickson et al. (1988a), we find that within that velocity and the surface magnitude completion limit of $\mu_E \leq 24$ (see above) there are 28 groups with accordant redshift (and probably less, had we used the stronger accordant redshift criterion of Paper I). Assuming a homogeneous Universe in this distance range, the total number of galaxies receding from us at velocity v or less is $N(v) \sim v^3$. One then obtains 5600 NBG-type groups out to 8000 km s^{-1} and in the area of sky surveyed by Hickson (1982). So the ratio of HCG groups to NBG groups within that velocity is 28/5600 = 0.5%. This number is really a lower limit, because $N(<v)$ may not rise as fast as v^3 for galaxies between 1510 and 8000 km s^{-1} in the Palomar sky survey.

A second approach is to consider the very close compact groups. Within the velocity limit of 3000 km s^{-1} of the NBG catalog there are 61 groups with $N \geq 5$ and $\delta > -33°$. There are also four HCGs in this region of space: H44, H54, H68, and H90 with accordant redshifts (Hickson et al., 1988a). Of these four groups, three are contained within NBG groups (see Table 3), while the fourth (H54) was probably too faint to be included in the NBG catalog (from Table 1 of Hickson et al., 1988a, it is 7 times fainter than any other compact group – it is also the group with the largest number density). This gives a ratio of HCG groups to NBG groups of $5 \pm 3\%$ (Poisson errors) within the volume of space sampled by the NBG catalog. Altogether, these two arguments set this ratio in between 0.5% and 8% and we adopt the geometric mean of 2%.

Note that, as stated in Paper I, if a compact group is included insde a loose group, this does not imply that the compact group is due to a chance alignment: the group can in fact be physically dense and bound, since such groups are expected to form by two-body relaxation processes inside lager loose groups. Nevertheless, all three of the groups that could fit in the NBG catalog are within lager groupings rather than being fully isolated entities.

From the discussion above, for *half* of the compact groups in Hickson's complete sample ($\mu_E \leq 24.0$) to be caused by chance alignments within loose groups (as advocated in Papers I and II) we require from the discussion above a frequency of chance alignments of at least 0.25% and perhaps as much as 4%. How can these relatively large frequencies be reconciled with the very low ones found in Sect. 6.1. for $N = 8$? We answer this below.

6.3. Binaries

Can clumpiness and non-homogeneous radial distributions push up the frequencies of chance alignments high enough to account for the properties of Hickson's groups? Hickson and Rood (1988) find that for groups of 8 galaxies including one tight binary the frequencies of chance alignments are increased by at least one order of magnitude, but still remain at the 0.1% level or less. They note however that their reference loose group sample (Rood, 1988) contains on the average less than 0.5 binaries (defined as pairs with separation less than 140 h_{50}^{-1} kpc) per group. We checked the NBG catalog and find that the 69 groups with $5 \leq N \leq 20$ have 1.6 binaries on the average (this number would increase to 3 if we had included the clusters of 21 or more members). Therefore the NBG groups should have enough binaries to significantly boost the frequency of chance alignments that are on the average as compact as Hickson's groups above the very small fractions found in Sect. 6.1.

Table 3. Nearby Hickson compact groups

HCG number	N_{HCG}	$\bar{v}_{HCG}$	NBG number	N_{NBG}
H44	4	1380	21–6	12
H54	4	1410	—	—
H68	5	2400	42–1	15
H90	4	2580	63–1	6

Notes: The mean velocity $\bar{v}_{HCG}$ of Hickson groups is expressed in km s^{-1}.

6.4. Central concentration

We also checked the central concentration of NBG groups using a statistic similar to that proposed by Hickson and Rood (1988), but more robust: we compute $\langle R^{med}/\frac{1}{2} R_{ij}^{max} \rangle$, where R^{med} is the median distance to the center of luminosity of the group (Hickson and Rood use the mean), and R_{ij}^{max} is the maximum separation between galaxies in the group. Because the latter quantity is not equal to the radius of the Circle, we performed Monte-Carlo simulations to compute the above ratio for homogeneous groups and for groups with $\Sigma(r) \sim r^{-1}$, and found that the corresponding median ratio for NBG groups was in between the two values found for simulations (for all N) but always closer to the homogeneous value. Hence *we confirm Hickson and Rood's (1988) finding that loose groups have negligible central concentration.* Note that repeating this exercise for HCGs, we found that these were even more consistent with no central concentration.

6.5. Clusters and intermediate density groups

We finish this discussion by the crucial point. From Fig. 6, the frequencies of chance alignments are very sensitive to two parameters: group membership (N) and the maximum ratio of compact group radius to Circle radius (x_m). It is therefore dangerous to compute a *median* frequency of chance alignments using the median values of N and x_m for the chosen loose group catalog. Since we are interested in the sum of the frequencies over a loose group sample, we compute instead the *mean* over all groups of the frequency of chance alignments. Although the median frequency of chance alignments in NBG groups of eight members is only $5.8\,10^{-5}$ (Sect. 6.1.), the mean frequency over the 48 groups in the complete NBG sample is 7%. However, since most of this is contributed by the Virgo cluster, we also checked the subsample of 42 groups of 5 to 20 members (closer than 25 h_{75}^{-1} Mpc) and found a mean frequency of 0.9%. A closer look reveals that because of the strong sensitivity of the frequency of chance alignments to the compactness parameter x_m (and to a lesser extent to the membership N) *the large majority of the compact configurations are generated by a small set of the loose groups: the Virgo cluster and other small clusters ($N > 20$), and the intermediate density groups.* In fact, an automated search in Virgo has yielded such a subgroup that fulfills Hickson's selection criteria (Mamon, 1989). Since compact configurations are more frequent for large membership (Fig. 6), more compact

groups fulfilling Hickson's criteria should be found in clusters of galaxies.

Considering the fact that these groups have 1.5 binaries on the average (see Sect. 6.3.) and that Hickson and Rood find that one binary per group for their $\xi = 0.85/0.06 = 14$ provides an enhancement of the frequency of chance alignments by a factor of 34 (see their Table 1), we conclude that *overall, loose groups are efficient in generating compact groups of high compactness ($\mu_E \leq 24$), although the typical loose group is not.*

The issues presented here could be verified with much deeper, magnitude limited, well-defined catalogs of groups of galaxies. With the recent advent of multi-slit spectroscopy, such catalogs should become available in the not too distant future.

Acknowledgements. We wish to thank Paul Hickson for providing compact group velocities years before publication, Ed Shaya for providing a digital copy of the NBG catalog, and Brent Tully for permission to use it.

References

Geller, M.J., and Huchra, J.P.: 1983, *Astrophys. J. Suppl.* **52**, 61
Hammer, F., and Nottale, L.: 1986, *Astron. Astrophys.* **155**, 420
Hickson, P.: 1982, *Astrophys. J.* **255**, 382
Hickson, P., Kindl, E., Huchra, J.P.: 1988a, *Astrophys. J.* **331**, 64
Hickson, P., Kindl, E., Huchra, J.P.: 1988b, *Astrophys. J. Letters* **329**, L65
Hickson, P., Rood, H.J.: 1988, *Astrophys. J. Letters* **331**, L69
Kent, S.M., Gunn, J.E.: 1982, *Astron. J.* **87**, 945
Mamon, G.A.: 1986, *Astrophys. J.* **306**, 426 (Paper I)
Mamon, G.A.: 1987, *Astrophys. J.* **321**, 622 (Paper II)
Mamon, G.A.: 1989, *Astron. Astrophys.* **219**, 98
Peebles, P.J.E.: 1980, *The Large-Scale Structure of the Universe*, Princeton University Press, Princeton, Chap. 3
Rood, H.J.: 1988, *Astron. J.* (submitted)
Sulentic, J.W.: 1987, *Astrophys. J.* **322**, 605
Tully, R.B.: 1987a, *Nearby Galaxies Catalog*, Cambridge University Press, Cambridge
Tully, R.B.: 1987b, *Astrophys. J.* **321**, 280
Williams, B., Rood, H.J.: 1987, *Astrophys. J. Suppl.* **63**, 265

C.2 A compact group in Virgo

Mamon, 1989, *A&A 219, 98–100*

Astron. Astrophys. 219, 98–100 (1989)

ASTRONOMY AND ASTROPHYSICS

Research Note

A compact group in Virgo

G.A. Mamon [1,2]

[1] Department of Physics, New York University, 4 Washington Place, New York, NY 10003, USA
[2] DAEC, Observatoire de Meudon, F-92195 Meudon Principal Cedex, France*

Received January 9, accepted February 14, 1989

Summary. An automated search for subgroups in the Virgo cluster that strictly satisfy Hickson's (1982) compact group selection criteria is performed. The data is taken from Tully's (1987) recent survey. The algorithm returns a single compact group, whose brightest member is M 60 (NGC 4649). No interloping galaxies are found to spoil the isolation of the group. The group would be the closest known compact group. Its nature (dense system or chance alignment of galaxies) is discussed. The presence of a compact group in Virgo suggests that other clusters may also be the sites of such systems.

Key words: clusters of galaxies – numerical methods

1. Introduction

The nature of the tightest groupings of galaxies in the sky, known as "compact groups", such as those cataloged by Hickson (1982), has been a topic of some recent controversy. One group of authors sees compact groups as dense and bound systems of galaxies (Sulentic, 1987; Williams and Rood, 1987; Hickson and Rood, 1988), in which case their density ressembles that of rich cluster cores. Other authors however, have argued that compact groups are the product of chance configurations within loose groups, either as 3 D transient unbound cores (Rose, 1979) or as 2 D chance alignments (Rose, 1977 for chainlike compact groups; Mamon, 1986, 1987, and Walke and Mamon, 1989 for the majority of Hickson's compact groups).

While testing the chance alignment model, Walke and Mamon (1989) noted that chance alignments become more probable as the number of galaxies in the parent loose group is larger; hence, their suggestion that clusters of galaxies ought to show compact groups within them.

In this paper, I perform an automatic search of compact groups within the Virgo cluster that satisfy Hickson's (1982) selection criteria. The search algorithm is explained in Sect. 2. The results are listed in Sect. 3, and discussed in Sect. 4.

* Present address

2. Method

The algorithm searches for groups within the Virgo cluster satisfying Hickson's selection criteria: 1) At least 4 galaxies in the group within 3 mag from the brightest one (membership). 2) A mean surface magnitude smaller than the limit prescribed by Hickson (compactness), where the mean is computed within the smallest circumscribed circle containing the centers of the galaxies in the group (hereafter, "Hickson circle"). 3) No galaxies within 3 mag of the group's brightest member or brighter outside of the group but within 3 Hickson circle radii from the center of this circle (isolation).

The algorithm is as follows: 1) Start with a test galaxy in the cluster. 2) Build a group with the next three closest galaxies. 3) Make sure that all galaxies are within 3 mag of the brightest one; if not then remove the faint galaxies, and add the next nearest ones until one has four galaxies within 3 mag of the brightest. 4) Compute the radius of the Hickson circle and the coordinates of its center. 5) Check that there are no other galaxies within 3 Hickson circle radii from the center of the Hickson circle, and within 3 mag from the brightest group member. If there are such galaxies, then add the closest one to the test galaxy (making sure that the group has at most $N-1$ members) and go to step 3). 6) Repeat this exercise by starting with all the different galaxies in the cluster. When an isolated group of n members is found, check that there are no subgroups with between 4 and $n-1$ members within it. 7) Check whether the "isolated" groups found statisfy Hickson's compactness criterion (see above).

The galaxy data is taken from Tully's (1987) NBG galaxy catalog (the Virgo cluster in his group number 11-1, and contains 130 galaxies).

3. Results

Figure 1 shows the positions of the galaxies in Virgo, relative to M 87. One compact group was found by the algorithm and it is shown by the thick circles. It lies at roughly 3° from M 87 (the adopted cluster center) in the E-SE direction. Table 1 lists the

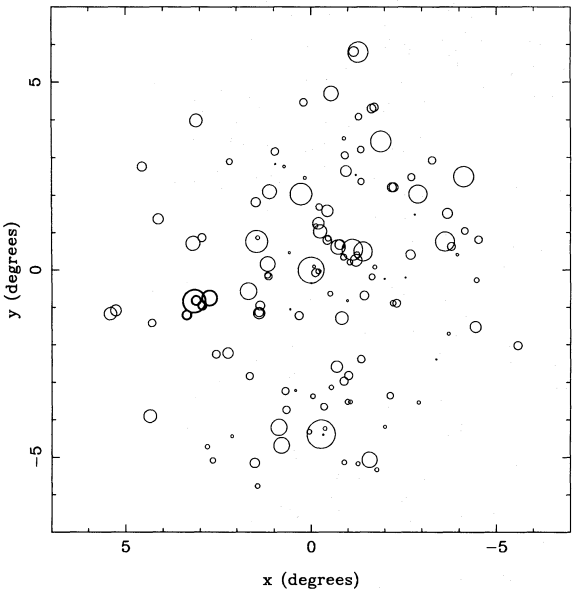

Fig. 1. Galaxy positions in the Virgo cluster, in degrees from M 87 (the large circle in the center – the even larger center at the bottom is NGC 4472), where the map is a projection onto the plane perpendicular to the line of sight to M 87. The sizes of the circles are scaled to the square root of the galaxy luminosities, and for this figure, the galaxies with no measured magnitudes were assumed to have $B = 16$. The thick circles represent the compact group

galaxies in this group. The center of its Hickson circle is located at RA = $12^h40^m45^s$ and Dec = 11°41′30″. The radius of the Hickson circle is 0°.380. The nearest outlying galaxy within 3 mag of the brightest group member (M 60) is NGC 4694 at 3.46 group radii. The group has a total magnitude of 9.09 in the B band, which yields 26.01 for the mean blue surface magnitude of the group. In the E band used by Hickson (1982), with his color transformations of $B-E = 1.9$ for ellipticals and 1.5 for spirals, and adopting $B-E = 1.7$ for the lenticular galaxy, one gets a total E magnitude of 7.23 and a mean surface magnitude $\mu_E = 24.15$. The group thus clearly satisfies Hickson's compactness criterion ($\mu_E \leqq 26.0$).

From its low relative velocity, the first galaxy in the group (NGC 4621) may be a foreground object (its velocity is 726.5 km s^{-1} lower than the median of the other four velocities – but this hypothesis is contradicted by the rough distance estimate given for this galaxy in Sect. 4). Without this galaxy, the group satisfies the compactness criterion, this time with a mean surface magnitude of $\mu_E = 23.49$.

Had I relaxed Hickson's membership criterion (at least 4 galaxies within 3 mag form the brightest one) I would have picked up two more groups, both quartets, dominated by a galaxy much brighter than its neighbors: NGC 4472 (M 49) in one case, and NGC 4486 (M 87) in the other. These two groups resembe the "evolved cores" seen in simulations of dense groups of 20 galaxies (Mamon, 1987).

Another group (formed by NGC 4365, NGC 4342, UGC 7513, and UGC 7557) just failed the selection criteria as it has a neighbor (NGC 4472) at 2.98 radii from the center of its Hickson circle.

Since M 60 has a magnitude of $B_T = 9.77$, I checked that the annulus surrounding the compact group contained no galaxies brighter than $B_T = 12.77$. I first searched for interloping galaxies in the NBG catalog that are not members of the Virgo cluster (NBG group 11-1), and none were found.

Then I searched in the extensive compilation of Virgo cluster galaxies by Binggeli, Sandage, and Tammann's (1985), and found 9 galaxies brighter than $B_T = 12.77$ that were not present in the NBG catalog. [1] Among these galaxies, only one, NGC 4606, is located near the M 60 group. Its distance to the center of the Hickson circle surrounding the compact group is only 1.98, assuming all 5 galaxies in the group. However this relative distance becomes 3.64 if NGC 4621 is omitted.

The differences in the magnitudes published in various catalogs complicate the picture. If the difference in magnitude between M 60 and NGC 4606 were less than 2.6 in the blue (to reach 3.0 in the E band, since NGC 4606 is a spiral), then NGC 4606 would spoil the compact group's isolation criterion. This is not the case in all the recent compilations of galaxy magnitudes (e.g., in de Vaucouleurs and Pence, 1979, the difference in corrected blue total magnitude is 2.88), so the M 60 group can in fact be safely considered compact. However, the difference in the UGC magnitudes (Nilson, 1973) used by Hickson (1982) is only 2.4, which explains why Hickson missed seeing this compact group in Virgo.

4. Discussion

The occurrence of compact groups by chance alignments within clusters is to be expected from the work of Walke and Mamon (1989). The parameters for Virgo ($N = 130$, $R_H = 1.74\, h_{75}^{-1}$ Mpc giving $x_m = 7.82\ 10^{-2}$) yield an expected frequency of chance alignments of 89% satisfying $\mu_E \leqq 26.0$. Poisson statistics then give respective probabilities of 41%, 37%, and 22% of having zero, one, or more than one chance alignments in Virgo. Thus the presence of a compact group does not imply it being formed by a chance alignment, although the odds are for it (especially con-

[1] The NBG catalog shows 87 galaxies in Virgo with measured magnitudes brighter than $B_T = 12.77$. Hence at this magnitude, one could infer that the NBG catalog in the direction of Virgo is only 90% complete

Table 1. Compact group data

Galaxy	R.A.	Dec.	Type	Velocity (km s^{-1})	Magnitude (B_T)	Name(s)
1	$12^h39^m30^s$	11°55′	E	340	10.68	NGC 4621, M 59
2	$12^h40^m18^s$	11°43′	L	1006	11.94	NGC 4638
3	$12^h41^m00^s$	11°51′	S	1285	11.79	NGC 4647
4	$12^h41^m12^s$	11°50′	E	1127	9.77	NGC 4649, M 60
5	$12^h42^m00^s$	11°28′	E	943	11.83	NGC 4660

sidering that the homogeneous model of Walke and Mamon underestimated the frequency of chance alignments).

An argument against the chance alignment hypothesis here is that the compact group contains the third brightest galaxy in Virgo. This is easily understood if the massive galaxy (M 60) is either attracting its neighbors more efficiently than other galaxies, or is sitting in a local potential well. Furthermore, the group shows luminosity segregation from the central location of M 60 in both position space and velocity space. Note also that NGC 4647 seems disturbed by its more massive companion M 60, and as such the pair figures in the Arp (1966) atlas of peculiar galaxies.

However, it could be that gravitational attraction and chance alignments are occurring simultaneously in these systems. Gravity would account for some but not all of the galaxies physically lying in the vicinity of M 60, while the remaining galaxies in the compact group would be chance alignments.

The compact group found here is closer to the Local Group than all of the Hickson (1982) compact groups for which at least one velocity is known (using the data in Hickson et al., 1988). Unfortunately, the group is still too far for a determination of its nature from separate distance estimates to its member galaxies, since such estimates with 10% relative accuracy are not possible for ellipticals.

Nevertheless, one can check whether or not one of the group's members (M 59) lies much closer to us than the other galaxies in the group. Using the distance indicator given by Lynden-Bell et al. (1988) with internal velocity dispersions from Dressler et al. (1987) and D_n parameter from Burstein et al. (1987) one finds a "distance" of 1372 km s^{-1} for M 59 compared to 1414 km s^{-1} for M 60. Although these "distances" may contain calibration errors it seems clear that M 59 is roughly at the same distance as M 60, hence in the Virgo cluster.

A final point is that since a compact group exists in the Virgo cluster, and that the analysis of Walke and Mamon (1989) predicts that other clusters are expected to contain chance alignments appearing as Hickson compact groups, it is worth checking whether such groups are present in clusters.

Acknowledgements. I wish to thank Lucienne Gouguenheim for a useful discussion on distance indicators, as well as Ed Shaya for providing a digital copy of the NBG catalog, and Brent Tully for permission to use it.

References

Arp, H.: 1966, *Atlas of peculiar Galaxies*, Pasadena, Caltech
Binggeli, B., Sandage, A., Tammann, G.A.: 1985, *Astron. J.* **90**, 1681
Burstein, D., Davies, R.L., Dressler, A., Faber, S.M., Stone, R.P.S., Lynden-Bell, D., Terlevich, R.J., Wegner, G.: 1987, *Astrophys. J. Suppl.* **64**, 601
Davies, R.L., Burstein, D., Dressler, A., Faber, S.M., Lynden-Bell, D., Terlevich, R.J., Wegner, G.: 1987, *Astrophys. J. Suppl.* **64**, 581
de Vaucouleurs, G., Pence, W.D.: 1979, *Astrophys. J. Suppl.* **40**, 425
Hickson, P.: 1982, *Astrophys. J.* **255**, 382
Hickson, P., Kindl, E., Huchra, J.P.: 1988, *Astrophys. J.* **331**, 64
Hickson, P., Rood, H.J.: 1988, *Astrophys. J. Letters* **331**, L 69
Lynden-Bell, D., Faber, S.M., Burstein, D., Davies, R.L., Dressler, A., Terlevich, R.J., Wegner, G.: 1988, *Astrophys. J.* **326**, 19
Mamon, G.A.: 1986, *Astrophys. J.* **306**, 426
Mamon, G.A.: 1987, *Astrophys. J.* **321**, 622
Nilson, P.: 1973, *Uppsala General Catalogue of Galaxies*, Uppsala, Uppsala Observatory
Rose, J.A.: 1977, *Astrophys. J.* **211**, 311
Rose, J.A.: 1979, *Astrophys. J.* **231**, 10
Sulentic, J.W.: 1987, *Astrophys. J.* **322**, 605
Tully, R.B.: 1987, *Nearby Galaxies Catalog*, Cambridge, Cambridge University Press
Walke, D.G., Mamon, G.A.: 1989, *Astron. Astrophys.* (in press)
Williams, B., Rood, H.J.: 1987, *Astrophys. J. Suppl.* **63**, 265

C.3 Clumpy diffuse X-ray emission from the spiral-rich compact galaxy group HCG 16

Dos Santos & Mamon, 1999, *A&A 352, 1–18*

Astron. Astrophys. 352, 1–18 (1999)

ASTRONOMY AND ASTROPHYSICS

Clumpy diffuse X-ray emission from the spiral-rich compact galaxy group HCG 16

S. Dos Santos[1] **and G.A. Mamon**[1,2]

[1] Institut d'Astrophysique (CNRS UPR 341), 98 bis Bd Arago, 75014 Paris, France (santos,gam@iap.fr)
[2] DAEC (CNRS UMR 8631), Observatoire de Paris, 92195 Meudon, France

Received 18 November 1998 / Accepted 21 July 1999

Abstract. We carefully reanalyze the ROSAT PSPC X-ray spectro-photometric observations of HCG 16 (Arp 318), and compare them to optical and radio data. Its X-ray morphology resembles its morphology at 20 cm, seen by the NVSS. In particular, we detect diffuse emission in eight regions filling half of the $200\,h_{50}^{-1}\,\mathrm{kpc}$ $(8\farcm7)$ radius circle around the optical center of the group: one region encompassing galaxies a & b, two regions surrounding the group galaxies c & d, a clumpy region roughly $140\,h_{50}^{-1}\,\mathrm{kpc}$ from the group galaxies, which may be gas ejected from one of the galaxies, plus regions respectively associated with a background radio-source, a probable background radio-source, a foreground star and a background group or cluster. The bolometric X-ray luminosity of the diffuse emission, excluding the regions associated with radio galaxies, is $L_X^{\mathrm{bol}} = 2.3 \times 10^{41}\,h_{50}^{-2}\mathrm{erg\,s^{-1}}$, *i.e.,* half of the luminosity found by Ponman et al. (1996). The region that is offset from the galaxies contributes half of the diffuse X-ray luminosity of the group. The diffuse emission is cool ($T < 0.55\,\mathrm{keV}$ with 90% confidence with a best fit $T = 0.27\,\mathrm{keV}$). At these low temperatures, the correction for photoelectric absorption in the estimate of bolometric luminosity is a factor 3.5 and varies rapidly with temperature, hence an uncertain bolometric luminosity.

The clumpy distribution of hot diffuse gas in HCG 16 is illustrated by the low mean X-ray surface brightness and hot gas density of the regions of undetected emission within $8'$ (at most 1/4 and 1/6 of those of the detected gas, assuming both have same temperature, metallicity and clumpiness). The irregular X-ray morphology of the diffuse emission rules out a (nearly) virialized nature for HCG 16, unless intergalactic gas had sufficiently high specific entropy to be unable to collapse with the group. In any event, the clumpy gas distribution, and high luminosity given the low temperature suggest that most of the diffuse gas originates from galaxies, either through tidal stripping or through galactic winds driven by supernova remnants. Therefore, no spiral-only HCGs are known with regular diffuse emission tracing a gravitational potential.

Our results highlight the need for a careful 2D spatial analysis and multi-wavelength study of the diffuse X-ray emission from groups, suggesting that other compact groups could be significantly contaminated by superimposed X-ray sources.

Send offprint requests to: S. Dos Santos

Key words: galaxies: clusters: general – galaxies: clusters: individual: HCG 16 – X-rays: galaxies – X-rays: general

1. Introduction

The extreme apparent density of compact groups of galaxies makes them ideal sites for the study of multiple interactions of galaxies, and more generally, another dense environment to be compared with rich clusters. Indeed, compact groups (of typically 4–5 bright galaxies) such as those (hereafter, HCGs) cataloged by Hickson (1982) appear as compact in projection onto the plane of the sky as the cores of rich clusters, and are moreover selected to be isolated.

The discovery of numerous signs of galaxy-galaxy interaction within HCGs (see Hickson, 1997 for a review) suggest that most HCGs are indeed dense in 3D. However, the very short crossing times derived from galaxy spectroscopy (Hickson et al., 1992) suggest rapid galaxy merging and coalescence into a single giant elliptical galaxy (Carnevali et al., 1981; Barnes, 1985; Mamon, 1987; Barnes, 1989; Bode et al., 1994; Governato et al., 1996) if indeed they correspond to the low-mass end of clusters of galaxies, forming at high redshift, unless the group is constantly replenished through accretion of surrounding galaxies (Diaferio et al., 1994; Governato et al., 1996). In fact, a variety of arguments have been put forth suggesting that compact groups are mostly chance alignments of galaxies along the line of sight within larger systems: loose groups (Rose, 1977 for chain-like groups; Mamon, 1986 for the majority of compact groups), clusters (Walke & Mamon, 1989) or cosmological filaments (Hernquist et al., 1995). Thanks to gravity, these chance alignments tend themselves to be binary-rich (Mamon, 1992), and it is very difficult to tell whether the interaction seen in HCGs are caused by a system of 4 or more bright galaxies or simply by binaries, well-separated along the line-of-sight.

Recently, there has been much hope that the debate on the nature of HCGs could be resolved by X-ray observations. The ROSAT, ASCA and Beppo-SAX X-ray satellites are sensitive enough in the soft X-ray band to be able to detect the diffuse intergalactic plasma within (nearly) virialized galaxy systems with potential wells with depth corresponding to a 1D velocity dispersion of $\sim 250\,\mathrm{km\,s^{-1}}$. Most sensitive of these is the Po-

sition Sensitive Proportional Counter (PSPC) of ROSAT, which discovered diffuse intergalactic emission from large numbers of compact groups (Ebeling et al. 1994; Pildis et al. 1995; Saracco & Ciliegi 1995; Mulchaey et al. 1996; Ponman et al. 1996, hereafter PBEB).

But there has been a debate on whether the fraction of compact groups detected by ROSAT is 40% (Mulchaey et al., 1996) or 75% (PBEB, taking into account the selection effects on distance). There is also controversy on the luminosity-temperature relation: Mulchaey & Zabludoff (1998) derive a relation that is consistent with the extrapolation from rich clusters, while PBEB find a luminosity-temperature relation for compact groups with a much higher slope, with the hottest groups lying on the cluster extrapolation.

Moreover, the morphology of the diffuse X-ray emission of compact groups is very diverse, as attested by the PSPC maps provided by Pildis et al. (1995), Saracco & Ciliegi (1995), Ponman & Bertram (1993) (only for HCG62) and PBEB (only for HCG 16). In some cases, such as HCG 62 (Ponman & Bertram), diffuse intergalactic emission extends well beyond the group, not centered on any galaxy of the group, with regular circular isophotes, just as is to be expected in a well relaxed galaxy system. But in other cases, the emission is only attached to individual galaxies, see e.g. HCG 44 (PBEB). And there are intermediate cases, such as HCG 16, where the diffuse emission does not appear as extended as the galaxy system nor as regular as in HCG 62.

In fact, HCG 16 (also known as Arp 318) is an unusual galaxy system. First, because the six brightest galaxies of the group (Hickson's original 4 plus two more outside the group isolation annulus, see de Carvalho et al., 1994) are starburst, LINERs or AGNs (Ribeiro et al., 1996, hereafter RdC3Z). Moreover, the X-ray properties of HCG 16 are controversial and possibly extreme. It was first detected with the EINSTEIN satellite (Bahcall et al., 1984), which did not have the angular resolution to resolve the emission between the group galaxies and an intergalactic medium. However, Ponman et al.'s analysis of ROSAT PSPC observations made it the coldest detected group ($T = 0.30 \pm 0.05\,\mathrm{keV}$), and there are no other spiral-only compact groups with diffuse X-ray emission (Mulchaey, 1999; see also Ponman et al.). HCG 16 is thus an abnormal group given the very strong correlations between X-ray luminosity and group spiral fraction found by Pildis et al. (1995) and Mulchaey et al. (1996). Moreover, whereas diffuse X-rays were clearly detected by PBEB, Saracco & Ciliegi (1995) failed to detect such diffuse emission at an upper limit 16 times lower,[1] whereas only a factor 2.3 (which we find by simulating a MEKAL plasma with temperature, abundance and absorbing column as quoted by PBEB) is attributable to the wider ("bolometric") energy range in which PBEB compute their luminosities. Given the low temperature that PBEB derive for HCG 16, their derived X-ray luminosity places it two orders of magnitude above their compact group luminosity-temperature relation and roughly a factor of two above the extrapolation of the cluster trend. It thus seems difficult to reconcile HCG 16 with a low temperature extrapolation of regular X-ray emitting compact groups. Indeed, PBEB note that HCG 16 is "probably not fully virialized".

In this article, we present a detailed analysis of the ROSAT PSPC observations of HCG 16. The data reduction is presented in Sect. 2, our spatial analysis in Sect. 3, and our spectral analysis in Sect. 4. In Sect. 5, we compare our results with previous X-ray analyses of HCG 16, perform a mass budget of the group and ask if it is virialized. In a following paper (Mamon & Dos Santos, 1999, hereafter Paper II), we discuss at length the cosmological and dynamical constraints on the nature of HCG 16.

2. Observations and data reduction

2.1. Observations and preliminary reduction

HCG 16 was observed in January 1992 with the PSPC (in its low-gain state), on board the ROSAT satellite, for a total observing time of $14\,634\,\mathrm{s}$. We obtained the data from the ROSAT archives. Snowden et al. (1994)'s PSPC Extended Source Cookbook software was used to perform the first-pass data reduction, *i.e.*, rejection of high-background times, energy-dependent (in 7 bands) background subtraction, exposure and vignetting corrections. We adopted a conservative value of $170\,\mathrm{cts\,s^{-1}}$ for the maximum Average Master Veto rate allowed (see Snowden et al., 1994). Even with this low threshold, only 6% of the total observing time was rejected, leaving an effective observational time of $13\,748\,\mathrm{s}$. We then carefully examined the light curves of the total counts in the entire image per energy band as defined by Snowden et al. (1994), and checked that no short time scale glitches were present. Point sources were detected using a sliding box algorithm, with the improvement that the box is a circle with a radius varying with off-axis angle, to model the varying point spread function. Each point source detected at a level exceeding $3\,\sigma$ was removed, *i.e.* a circle centered on the source, of radius 1.5 times the $90\,\%$ encircled energy radius, was excised. Unless otherwise stated, we limited our analysis to the $[0.2, 2.0]\,\mathrm{keV}$ energy band, because at lower energies, the background is too high to be adequately subtracted from the data, while at high energies the same occurs because our sources happen to be relatively cold, and moreover the calibration of the PSPC is uncertain. This preliminary reduction produced an image with 512×512 pixels, $15''$ wide (roughly the FWHM of the PSPC's PSF at $1\mathrm{keV}$).

2.2. Background estimation

The definition of the background region, whose counts are subtracted to each pixel within some region, is of crucial importance for the spatial detection of sources with very low signal-to-noise ratio (hereafter S/N), as well as for spectral analyses.

The shadowing by the supporting ring of the PSPC (situated at $\simeq 20'$ from the center of the field) is visible in the images, even after the vignetting correction. Thus, we measure

[1] Given the fluxes measured by Saracco & Ciliegi (1995) for HCG 16 and their adopted value for H_0, their quoted upper limit for their luminosities were underestimated by a factor 2 for all undetected groups in their Table 4 except HCG 3.

Table 1. Background from different annular regions

Region	Radii	Pixels	Counts/pixel
BG1	$30' - 48'$	25930	0.593 ± 0.005
BG2	$26' - 40'$	17630	0.577 ± 0.006
BG3	$26' - 34'$	9832	0.565 ± 0.008

Table 2. Tests of background subtraction

Region	$r < 8'$		$8' < r < 17'$	
	Net counts	Significance	Net counts	Significance
BG1	222 ± 48	$4.6\,\sigma$	-250 ± 78	$-3.2\,\sigma$
BG2	271 ± 49	$5.5\,\sigma$	-121 ± 82	$-1.5\,\sigma$
BG3	308 ± 51	$6.0\,\sigma$	-26 ± 91	$-0.3\,\sigma$

the background well outside of the ring. In practice, we choose three annular regions to measure the background, each centered on HCG 16, with inner and outer radii of $30' - 48'$ (BG1), $26' - 40'$ (BG2), and $26' - 34'$ (BG3). The radial structures of the PSPC supporting ring were removed in each case. Table 1 shows the background counts in the three regions within the $0.2 - 2.0\,\mathrm{keV}$ energy range. We note that BG3 has a slightly lower value than the other two.

To decide which is the best background, we measure the *net* counts in two regions within the inner ring support, using each of the three background regions for measuring the background. The latter have been vignetting corrected and normalized to the number of pixels of each region. Our two test regions are the $8'$ radius circle centered on the group optical center and the annulus surrounding this circle, with inner and outer radii of $8'$ and $17'$. Both are in the inner $20'$ of the field of view, thus avoiding problems with the supporting ring of the PSPC and with somewhat uncertain vignetting correction outside of this ring. Table 2 gives the background subtracted data and errors for both regions and for each background.

While we find positive net counts within the inner $8'$ of HCG 16, whatever three of the background regions is used to estimate the background, only BG3 is compatible with the near zero net counts within the $8' - 17'$ annulus. The negative net counts with the other two background regions are difficult to understand, unless there happens to be X-ray absorption by Galactic or intergalactic neutral hydrogen merely in this $8' - 17'$ annulus. This appears to be ruled out by HI observations with the VLA (Williams, 1998; Verdes-Montenegro et al., 1999) and by the spectral analysis (Sect. 4). We thus infer that BG1 and BG2 are contaminated by sources or suffer from uncertain (large) vignetting corrections. In fact, Pildis et al. (1995) had also encountered a PSPC field with a background that rose with distance to the field center. We therefore use BG3 ($26' < r < 34'$) to measure the background, which then amounts to $B = 6.6 \pm 0.1 \times 10^{-4}\,\mathrm{s^{-1}\,arcmin^{-2}}$ (in the $[0.2 - 2.0]\,\mathrm{keV}$ energy range).

3. Spatial analysis

3.1. Preliminary spatial analysis

Ponman et al. (1996) claimed a $3\,\sigma$ detection of diffuse emission within a radius $\simeq 8\farcm5$ surrounding HCG 16 (corresponding to $\simeq 195\,h_{50}^{-1}\,\mathrm{kpc}$, given HCG 16's redshift of 0.0132[2]). The net counts shown in Table 2 confirm PBEB's global detection of diffuse emission in HCG 16. We detect diffuse emission at $6\,\sigma$ within $8'$ and fail to detect significant counts between $8'$ and $17'$. Hence, to first order, the extent of the diffuse emission is very roughly $8'$, or $190\,h_{50}^{-1}\,\mathrm{kpc}$, similar to what is inferred from PBEB's surface brightness profile of HCG 16.

But we wish to go further: what is the spatial distribution of this excess of photons within $8'$ of the group center? Here we are confronted with the low number of detected photons ($\simeq 300$). We applied three different methods to analyze the photon distribution within $8'$. First, we count the photons in a grid encompassing the $8'$ radius circle. Then, in order to obtain the best S/N ratio, we adaptively smooth the image and detect diffuse emission. Finally, we apply a wavelet-based method to detect structures at all scales and verify that emission is present on more than one scale as a confirmation of its diffuse nature.

3.2. Analysis on a grid

The simplest way to spatially analyze HCG 16 is to define a grid encompassing the whole group. We divide the field of view of the group in sixteen 16×16 pixel $(92\,h_{50}^{-1}\,\mathrm{kpc})$ squares. The grid overlaid on a smoothed X-ray image of HCG 16 is displayed in Fig. 1. After removing the point sources (including group galaxies), we counted the background-subtracted number of photons in each square of the grid. The net counts and their statistical significance are given in Table 3.

The analysis of Table 3 shows that 7 regions over the 16 selected are detected at a $2\,\sigma$ level above the background. We count regions from East (left) to West (right) and North (top) to South (bottom). Fig. 1 shows that the regions of excess counts are concentrated East, West and South of the four bright galaxies of the group: regions 9, 13 and 14 in the East contain 114 net counts, while regions 8, 11, and 12, contain 149 net counts. Moreover, half of the cells in the grid (if we don't take into account cell 6, detected at a $1.8\,\sigma$ level) are compatible with no excess emission over the background, and most of these are North of the four galaxies (regions 1, 2, 3, 4, 5, 10, 15 and 16). Hence, the diffuse emission is located in two distinct regions as well as around the galaxies. This could be seen in PBEB's Fig. 2, but they gave no quantitative analysis of the spatial distribution of photons, except for their radial surface brightness profile.

Is it possible to detect more precisely these excess counts regions, without degrading the S/N ratio? Indeed, the grid we used was arbitrarily set on the HCG 16 image, and some cells, especially cells 10, 11, 13 and 14, overlap two regions where the photon densities differ. Using a smaller grid would not help

[2] Distances throughout this paper are derived assuming a Hubble constant $H_0 = 50\,h_{50}\,\mathrm{km\,s^{-1}\,Mpc^{-1}}$, with $h_{50} = 1$, unless explicitly given.

Table 3. Net counts within a square grid

Region	Pixels	Net counts	Significance (σ)
1	106	-4 ± 9	-0.5
2	252	-9 ± 13	-0.7
3	204	-3 ± 12	-0.2
4	217	17 ± 13	1.3
5	256	-8 ± 13	-0.6
6	198	23 ± 13	1.8
7	**167**	$\mathbf{31 \pm 13}$	**2.5**
8	**256**	$\mathbf{57 \pm 16}$	**3.7**
9	**200**	$\mathbf{50 \pm 14}$	**3.6**
10	203	15 ± 13	1.2
11	**194**	$\mathbf{34 \pm 13}$	**2.5**
12	**256**	$\mathbf{58 \pm 16}$	**3.8**
13	**200**	$\mathbf{36 \pm 14}$	**2.7**
14	**256**	$\mathbf{28 \pm 15}$	**2.0**
15	196	18 ± 13	1.4
16	201	-18 ± 11	-1.6

The regions, shown in Fig. 1, are numbered from East to West, looping North to South. Cells with a statistical significance of detection greater than $2\,\sigma$ are shown in bold. Errors are $1\,\sigma$ and on the total (background + net) counts.

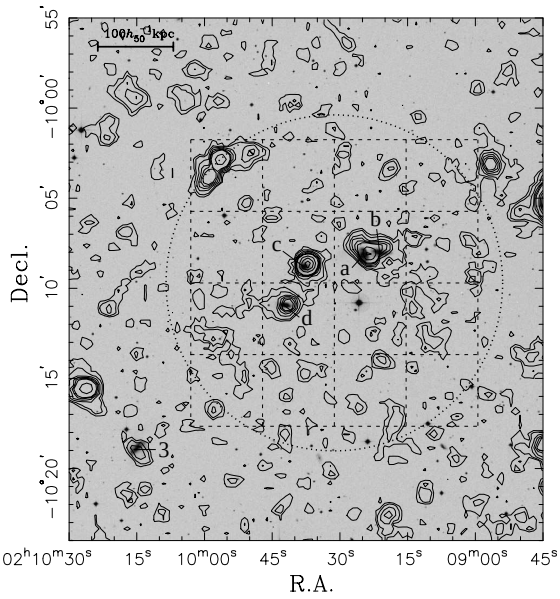

Fig. 1. Contour map of smoothed (by a Gaussian of FWHM = $45''$) ROSAT-PSPC X-ray emission from HCG 16 superimposed on an optical image of the group provided by the Digital Sky Survey (DSS). Coordinates are for epoch J2000. This figure and the following ones do not mask the detected point sources (which are masked in the subsequent X-ray photometry and spectral analyses). Contours are drawn at $1\,\sigma, 2\,\sigma, 3\,\sigma, 4\,\sigma, 5\,\sigma, 10\,\sigma, 15\,\sigma, 20\,\sigma, 30\,\sigma,$ and $50\,\sigma$ above the background level, where σ is the standard deviation of the smoothed background. The scale (*upper left*) is for the plane at the distance of HCG 16. The four original galaxies discovered by Hickson (1982) are marked 'a', 'b', 'c' and 'd', together with galaxy HCG 16-3 (de Carvalho et al., 1994), marked '3', which is at the same distance as the group. The *dotted circle* centered on the group optical center is $8.'7$ wide, *i.e.*, $200\,h_{50}^{-1}$ kpc at the distance of HCG 16. The *dashed square grid* used for the preliminary spatial analysis has cells 16 pixels wide ($92\,h_{50}^{-1}$kpc). Cells are counted from left to right then from top to bottom.

because we are at the limit of sensitivity. Since we are principally interested in mapping the *diffuse intergalactic gas*, we can smooth the image, looking for large-scale features. But we need to be careful with the level of smoothing: indeed, regions with low count numbers must be smoothed on larger scales than the bright regions (e.g. , the bright galaxies), so as to keep a good statistical significance of the regions of diffuse emission. Consequently, we choose an adaptive filter algorithm, which automatically adapts the smoothing length to the local density of photons. PBEB already used adaptive smoothing to detect diffuse gas in HCG 16 (see their Fig. 2), but did not make a quantitative use of the information obtained with this technique.

3.3. Adaptive filtering of the image

3.3.1. Spatial resolution

In a classical (top-hat) smoothing filter, the filtering radius is fixed, the smoothed intensity is the mean (unweighted) counts within this radius, and the total counts within this radius varies across the image. Hence, every pixel will have a S/N directly proportional to the local photon density. The pixels in low surface brightness regions will then have poor statistics.

In an adaptive filter, the filter size is adapted to contain a fixed number of counts. Let C_0 be this fixed number of (background + net) counts per smoothing region of size P pixels. The intensity of a given pixel will typically be $I = C_0/P$, hence $S/N = I/\delta I = P/\delta P$. Now, if the cumulative counts rise with radius $1\,\sigma$ faster than on average, they will reach C_0 at $P - \delta P$, where the typical counts are $C_1 = I(P - \delta P)$. Since the count curve of growth, $C(P)$, is a Poisson process, one has $C_0 = C_1 + C_1^{1/2}$. Then, in the limit $\delta P \ll P$, one obtains $\delta P = (P/I)^{1/2}$, hence $S/N = C_0^{1/2}$ (we check that $\delta P/P = C_0^{-1/2} \ll 1$). Therefore, *every pixel will have the same S/N*.

Refining the grid analysis, we define polygonal regions with much greater S/N than in the grid cells. Contrary to the grid, there will be no regions half overdense and half-underdense in photons. We produce adaptively smoothed images using ADAPT in the PSPC Extended Source Cookbook (Snowden et al., 1994), with $C_0 = 25$, 50 and 100. Before smoothing, we masked point sources detected at the $3\,\sigma$ level, so as to better highlight the diffuse emission. The adaptively smoothed images are shown in Fig. 2. For esthetical reasons, the point sources detected by DETECT are not cut in these images.

Our smoothing resolution is easily computed. Calling B the mean background, since $I > B$, our smoothing radius, equal to $(P/\pi)^{1/2}$, must be smaller than

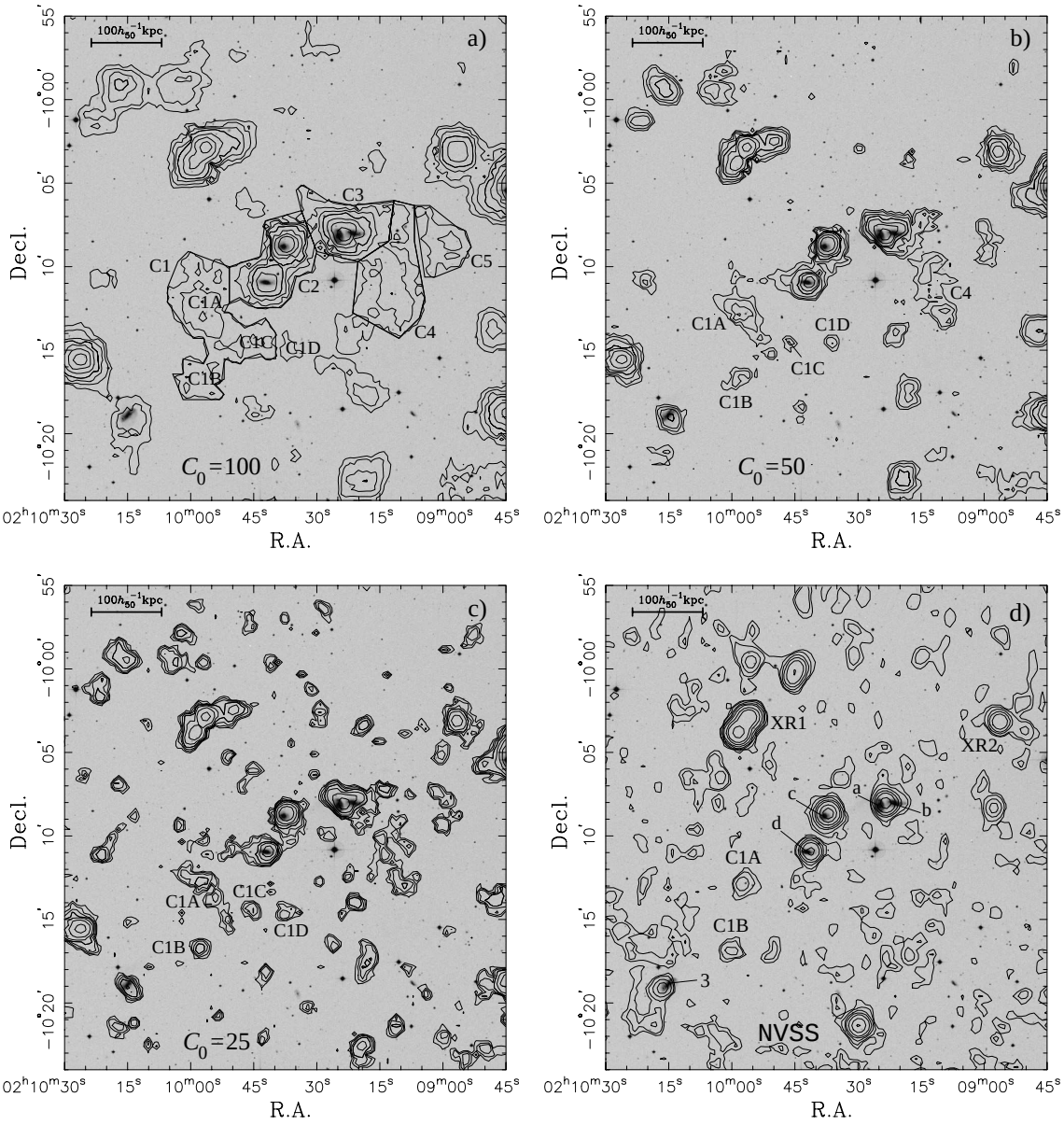

Fig. 2a–d. Contour maps of the adaptively smoothed X-ray emission ($C_0 = 100$ (**a**), 50 (**b**), and 25 (**c**), see Table 4 and Eq. 1) superimposed on an optical DSS image. The five polygonal regions (C1–C5) dividing the emission region in HCG 16 are also shown, as well as the different components of region C1 (C1A, C1B, C1C and C1D, see text). Lower right plot (**d**) shows a contour map of a 20 cm radio image from the NVSS (see Condon et al., 1998).

$$R_{\rm sm} = \left(\frac{C_0}{\pi B}\right)^{1/2} . \quad (1)$$

With a mean background of $B = 0.565\,{\rm counts/pixel}$ (see Sect. 2.2), we obtain the smoothing resolutions listed in Table 4.

The grid we used in Sect. 3.2 was made of 16×16 pixel cells. Table 4 shows that the lowest resolution varies with C_0 from 1/4 square cell ($R_{\rm sm} \simeq 4$ pixels) for $C_0 = 25$ to 1/2 square cell ($R_{\rm sm} \simeq 8$ pixels) for $C_0 = 100$. This shows that our adopted values of C_0 are well suited to the size of the group, and

Table 4. Adaptive smoothing parameters

C_0	$R_{\rm sm}$			S/N
(cts)	(pixels)	(arcmin)	(h_{50}^{-1}kpc)	
25	3.8	0.9	22	5.5
50	5.3	1.3	31	7.6
100	7.5	1.9	43	10.5

The smoothing radii are obtained through Eq. (1) with a mean background of $B = 0.565\,{\rm counts/pixel}$ (see Sect. 2.2).

Table 5. Net counts in regions defined after adaptive filtering

Region	Pixels	Net counts	Significance (σ)
C1	447	96 ± 19	5.1
C2	261	44 ± 14	3.2
C3	206	45 ± 13	3.5
C4	306	83 ± 16	5.2
C5	175	28 ± 11	2.5
C6	1697	10 ± 31	0.32

The counts are computed from the unsmoothed images, within the 0.2–2.0 keV energy interval and are rounded to the nearest integer. Errors are $1\,\sigma$ on the total (background + net) counts.

will not smear out intermediate scale structures by smoothing on too large a scale.

3.3.2. Results

Consider first the image smoothed with $C_0 = 100$ (Fig. 2a), which has the largest features of the three images. Within the single contour encompassing the group galaxies are two overdensities, SE and SW of the group. They correspond respectively to part or all of cells 9, 13, 14 for the SE overdensity and cells 8, 11, 12 and 15 for the SW one, in the grid of Sect. 3.2. These cell numbers correspond to the cells detected at a level higher than $2\,\sigma$ (see Table 3). We divide this closed region in 5 different polygonal regions (C1-C5) filling the contours of the X-ray image adaptively smoothed with $C_0 = 100$, as shown in Fig. 2. The exact cut between different regions is arbitrary, but we tried to be consistent with what we know about HCG 16: C1 is the South-Eastern overdensity, C2 and C3 are the regions around galaxies c & d and a & b of the group (but with these galaxies cut out), C4 is the South-Western overdensity, and C5 is a somewhat disjointed region, to the West of C4. The source to the South of C4 is detected as a point-like X-ray source, and also appears as a double point-like radio-source (Fig. 2d). Finally, C6 is the region within the $8'$ radius circle minus the closed region (C1+C2+C3+C4+C5), *i.e* the part of this circle (53% of it) with no obvious excess counts over the background.

Table 5 shows the net counts in each region. Regions C1 and C4 are detected at $\sim 5\,\sigma$, much higher than regions C2 and C3 surrounding the bright galaxies (detected at $\sim 3\,\sigma$). This shows that the adaptive smoothing has targeted regions of high S/N ratio more efficiently than the spatial detection on the square grid. But the most important feature, which fully justifies the use of adaptive filtering, is that the emission of region C6 is fully compatible with the background. Hence, *half of the region within $8'$ of the group center contains negligible emission from diffuse hot gas*. In Sect. 4.1 below, we confirm the different nature of the two halves of the $8'$ circle.

3.3.3. Detailed spatial analysis

Nothing has yet been said about the nature of the X-ray photon overdensities detected. We have intentionally called them with the vague denomination "regions". Are these photons emitted by diffuse gas linked to the group? If so, is this gas primordial, or mainly ejected by the galaxies? Or does the diffuse emission originate from foreground or background sources, not necessarily linked with the group? Indeed, looking at PBEB's Fig. 2, the position angle of the northern overdensity seems to be well-correlated with the alignment of three optical sources. The spatial and spectral capabilities of ROSAT are certainly insufficient to answer these questions, but the careful analysis of the images and spectra can provide some useful insight. Observations of HCG 16 at other wavelengths can also help to specify the dynamical state of the gas. In particular, deep optical images and radio surveys can precise the interactions between the diffuse gas, the galaxies and the radio sources.

We can now estimate the number of independent smoothing regions within our regions of excess counts. If our region has area A pixels and E excess counts, the number of independent smoothing regions within it is

$$N = \frac{A}{P} = \frac{AB + E}{C_0}\,. \qquad (2)$$

Using Table 5 and Eq. (2), we find that, for $C_0 = 100$ (our worst spatial resolution), our regions C1, C2, C3, C4, and C5 consist of 3.6, 2.0, 1.7, 2.7, and 1.3 independent smoothing regions, respectively. Hence, the correlation among neighboring pixels introduced by adaptive smoothing may connect several local maxima in the X-ray surface brightness map, which are close in the plane of the sky, but not necessarily linked, neither among them nor with the group.

This is illustrated by comparing the adaptively smoothed images with different parameters C_0. Comparing Figs. 2a and 2c, (with $C_0 = 100$ and 25 respectively), we see that region C1 is composed of an elongated structure, almost perpendicular to the group (marked C1A), together with three point sources (marked C1B, C1C and C1D). This substructure remains at $C_0 = 50$, but is smoothed out at $C_0 = 1000$ (Fig. 2a) into the entire C1 region. All these structures can be seen in Fig. 1, although with a worse S/N. On the contrary, region C4 seems to be extended, even with the lightest smoothing.

3.3.4. Spatial positioning of the images

We have obtained an optical image of HCG 16 from the Digitized Sky Survey (DSS), as well as a 20 cm continuum radio image from the NRAO VLA Sky Survey (NVSS), which we superpose on a ROSAT PSPC image. The FWHMs are $\simeq 2''$

(DSS), $30''$ (PSPC) and $45''$ (NVSS). The radio and X-ray images both have $15''$ pixels, while the optical image has $1.8''$ pixels. Fig. 2d shows the NVSS radio contours overlaid on a DSS optical greyscale image. Both optical and radio images were centered at the center of the X-ray image. To ensure a correct superposition, we aligned the three images using the bright sources detected in the three wavebands. Comparison of Figs. 2b,c and 2d clearly shows that *the X-ray and 20 cm morphologies are remarkably similar.*

In their spectroscopic survey of HCG 16, Ribeiro et al. (1996) found that six galaxies among the seven belonging to the dynamical group were emission-line galaxies, AGN, LINERs or starburst galaxies. These galaxies are good candidates for detection in all three wavebands. Indeed, we find four sources detected in the three images: they are all HCG 16 galaxies and are marked a, b, c and d in Fig. 2d. Galaxies HCG 16a and HCG 16b seem to share a common X-ray and radio halo, thus enhancing the probability of tidal interaction between these galaxies suggested by optical tails seen in galaxy HCG 16a. The differences between the optical, radio and X-ray positions are less than $5''$, much less than the radio and X-ray PSFs. Moreover, we find two objects exactly coincident in radio and X-rays, ensuring good correspondence between X-rays and radio images independently. Both were first detected in the X-rays by Saracco & Ciliegi (1995), who called them XR1 and XR2, with no optical counterparts. We found two radio sources within a radius of less than $5''$ around them, and XR1 has *the same* bimodal structure in X-rays and in radio.

The probability of finding an NVSS source within a given radius around an arbitrary position is less than 10^{-3} when this radius is $\simeq 5''$ (see Condon et al., 1998). This means that the coincidences between six sources in the whole image cannot have occurred by chance, and this ensures that the superposition of the three images is quite perfect, given the positioning uncertainties. We are now able to compare small-scale structure in the three wavebands and attempt to elucidate the nature of the three regions of excess X-ray counts.

3.4. Finalizing the regions of diffuse emission of HCG 16

The problem is now to separate local maxima due to interloping X-ray sources (point or extended sources) from those due to the presence of diffuse gas. The regions C2 and C3, surrounding the four group galaxies, are certainly related to the group. We must then analyze the *small scale X-ray structure* of regions C1, C4 and C5 and compare it to optical and radio images. For this, we use a wavelet transform of the image to search for structures simultaneously at all scales.

3.4.1. Wavelet transform of the X-ray image

Since its invention in the early 80s, the wavelet transform (hereafter, WT) has proven its capabilities in numerous astronomical applications, such as the detection of the large scale structure (e.g., Slezak et al., 1993), galaxy detection and counts (Slezak et al., 1990), and structure detection in low-intensity X-ray images (Starck & Pierre, 1998). We used the TRANSWAVE *à trous* (Shensa, 1992; Starck & Murtagh, 1994) wavelet package kindly provided by E. Slezak. In the *à trous* implementation of the discrete WT, an $N \times N$ image is transformed into i wavelet planes (hereafter WPs) of $N \times N$ pixels, each being the difference between two consecutive wavelet smoothings at scales i and $i+1$ (with 2^i and 2^{i+1} pixels respectively). The pixel values in these planes are called the wavelet coefficients at scale i. The main advantage of this algorithm is that each WP has the same number of pixels, and thus, the reconstruction of the image (for example, after thresholding in the wavelet planes) is a straightforward process of addition. However, there is redundancy in the full set of wavelet coefficients. The main difficulty with the *à trous* wavelet filtering is the estimation of the statistical significance of the pixels in each WP, which should not follow Poisson nor gaussian statistics.

Fig. 3 shows the wavelet contours of WPs 2, 3, 4 and 5, respectively. We do not take WP1 into account, since it is highly contaminated by small-scale noise in the original image, nor WP6 and higher, which smooth the group on too large a scale to prove useful. Structures seen only at the $1\,\sigma$ level should mostly be artefacts.

There are two ways we can ensure that a detected source is real: First, if a source is detected in more than one WP, its probability of being true is enhanced. Indeed, random noise is not correlated between WPs and cannot produce large spatial overdensities. Moreover, it cannot produce pixels high enough to leave some power on larger scales. Second, the probability of a false X-ray detection being randomly superimposed on an optical or radio source is very low. Consequently, we will search for small-scale X-ray sources in regions C1, C4 and C5, detected in several WPs and roughly superimposed on optical and/or radio sources.

3.4.2. Nature of region C1

The multiple nature of region C1 (Sect. 3.3.3) is confirmed by the inspection of the Wavelet Planes. Four of the sources present in WP2 are also detected in WP3 (marked C1A, C1B, C1C and C1D in Fig. 3b). The first two are still detected in WP4, where the smoothing is so strong that only an extended region remains, comparable to C1, with two local maxima (at C1A and C1B) and an evidence of distortion by C1C. Note that sources C1A and C1B were detected at $\sim 3.5\,\sigma$ and cut using the local detection algorithm DETECT provided in the PSPC Extended Source Cookbook. Thus, the excess photons measured in Sect. 3.3.2 do not take these sources into account. But, it is very likely that the majority of the diffuse gas is related to these sources.

We now examine sources C1A, C1B, and C1C and compare with their optical and radio counterparts:

– **Source C1A:** Fig. 4a shows a zoomed optical image of C1A, together with WP3 contours (*solid*) and radio contours (*dashed*). There is an NVSS radio source less than $10''$ away from this X-ray source. Both sources are coincident with two optical sources. Moreover, in Fig. 4a, we verify

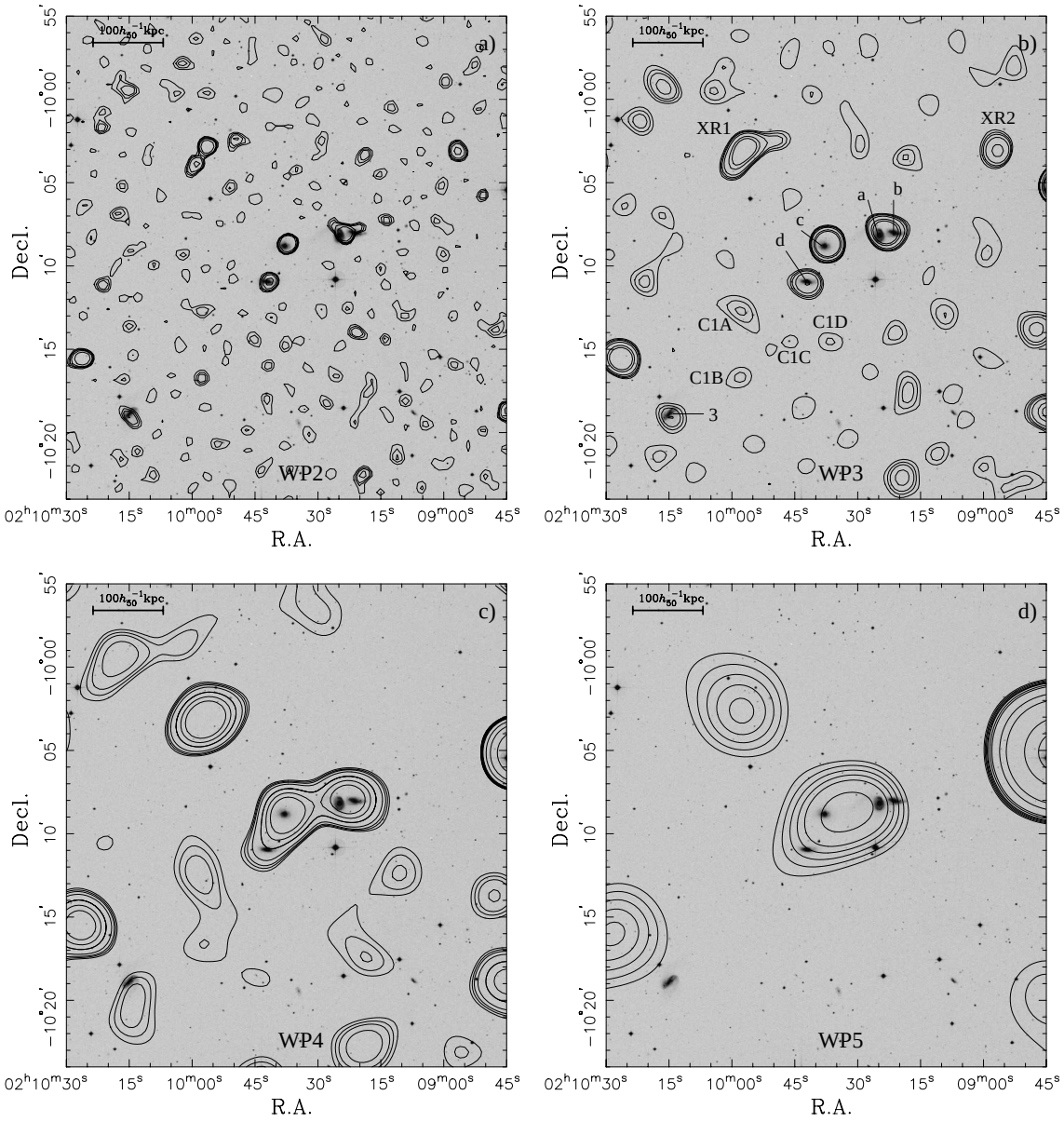

Fig. 3a–d. Contour map of the wavelet planes WP2 (**a**), WP3 (**b**), WP4 (**c**), and WP5 (**d**) superimposed on an optical DSS image. Contours are drawn at $1\,\sigma, 2\,\sigma, 3\,\sigma, 5\,\sigma, 10\,\sigma$ and $50\,\sigma$, where σ^2 is the $3-\sigma$ clipped variance of the whole WP (see Sect. 3.4.1). Structures in WP2, WP3 and WP4 are resolved at 1, 2, 4, and $8'$ (23, 46, 92, and $184\,h_{50}^{-1}\,\mathrm{kpc}$), respectively. In Fig. 3b, the objects XR1 and XR2, detected by Saracco & Ciliegi (1995) are also shown, as well as the different components of region C1.

that the western part of the radio source is aligned with the elongated X-ray source and with the direction defined by the two optical sources. The second of these optical sources is an emission line galaxy, HCG 16-9, observed spectroscopically by RdC3Z. Its recession velocity was measured as more than $20\,000\,\mathrm{km\,s^{-1}}$, *i.e. it is a background galaxy superimposed on the group*. The other optical source is comparable in size and magnitude to HCG 16-9, and although we don't have any spectroscopic evidence for this, it is unlikely that this galaxy lies at the redshift of HCG 16.

that this excess is linked to the group, even if this seems a reasonable assumption. Indeed, the two interacting galaxies HCG 16a and 16b lie at $\simeq 140\,h_{50}^{-1}\,\mathrm{kpc}$ in projected distance from C4. This gas could have been ejected by these galaxies (see Sect. 5).

– **Region C5:** Figs. 5a and b show the superposition of optical, radio and X-ray wavelet planes WP2 and WP3, respectively. Region C5 has a complex X-ray structure, and several local maxima can be seen in WP2, which merge into a single structure in WP3. An $8.2\,\mathrm{mJy}$ NVSS radio source is superposed with the extended structure in WP3, and the prominent three X-ray sources are situated at distances of 35, 80, and $95''$ from the peak of the radio emission. Given cumulative source counts of 10^6 and 4×10^5 for 1.4 GHz radio fluxes greater than 5 and $15\,\mathrm{mJy}$ respectively (Condon et al., 1998), and the 82% NVSS coverage of the celestial sphere, we infer 20.7 NVSS sources brighter than $8.2\,\mathrm{mJy}$ per square degree. Therefore, Poisson statistics yield respective probabilities of 0.6%, 3.2% and 4.5% of having each of the three X-ray sources as close as they are to the radio-source.
Likewise, at least six optical sources are clearly visible within the outer WP3 isophotes of C5, of which two are COSMOS galaxies brighter than $B_J = 20.1$, and there is an additional COSMOS galaxy lying just $10''$ outside of the outer WP3 isophote (to the East). Within the $16'\times16'$ box centered on the group, there are 34 galaxies in COSMOS with $B_J \le 20.1$. Poisson statistics then yield a 3.6% probability of having as least 3 COSMOS galaxies within $10''$ of the WP3 outer contour (in a $5.5\,\mathrm{deg}^2$ region).
If these 3 galaxies were at the distance of HCG 16, their typical separations would be $20\,h_{50}^{-1}\,\mathrm{kpc}$ and they would all be less luminous than the SMC. We would then have a very compact subgroup of very faint dwarfs detached from Hickson's original compact group of 4 bright galaxies.
The alternative of a background group or cluster appears much more plausible, given that subgroups of very faint dwarfs have never been discussed, and that there is X-ray emission apparently associated with this group or cluster.
Therefore, the concordance of the radio source with 3 X-ray sources, *coupled with* the large galaxy surface number density in C5, strongly suggests that C5 is not associated with diffuse emission from HCG 16.

3.5. Summary

We have shown that the detection of diffuse gas within a radius of $\sim 200\,h_{50}^{-1}\mathrm{kpc}$ around HCG 16 reduces to the significant detection of five regions of diffuse X-ray emission, filling less than half of the circle. The small-scale structure of these regions, together with associations with optical and radio point sources, allows us to reject two of these regions (C1 and C5) as related to point sources or background extended sources. There thus remains three diffuse emission regions, two (C2 and C3) surrounding the four bright galaxies and the other (C4) $\sim 140\,h_{50}^{-1}\mathrm{kpc}$ away from the two interacting galaxies HCG 16a and HCG 16b.

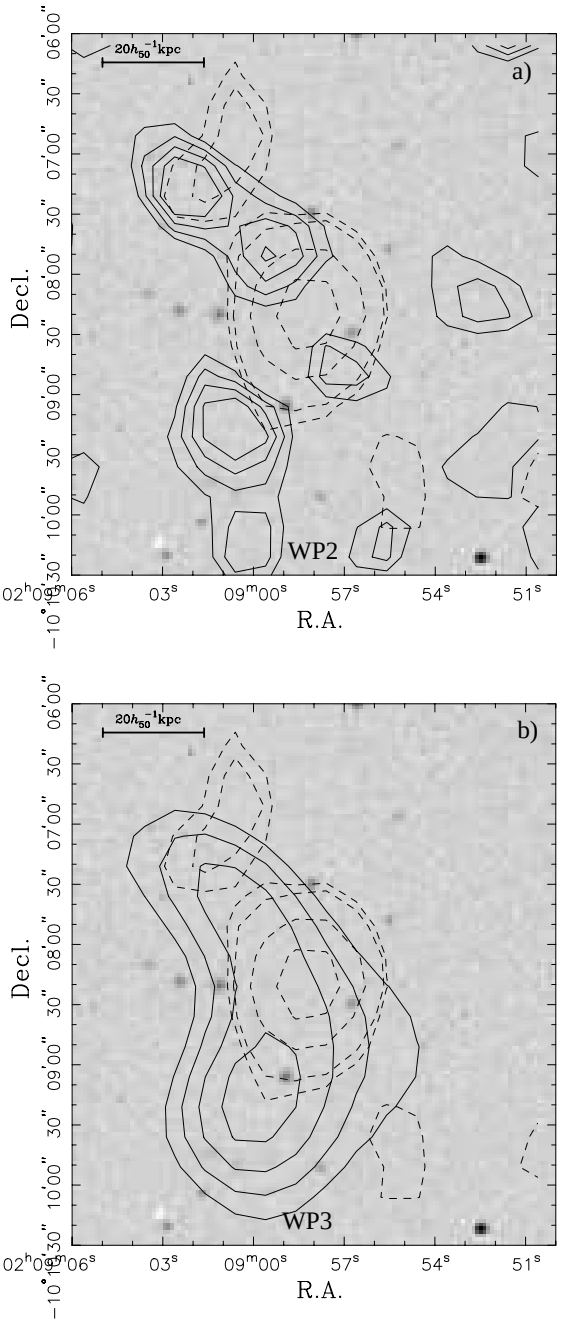

Fig. 5a and b. Radio (*dashed*) and WP2 (**a**), WP3 (**b**) wavelet plane (*solid*) contours of C5 superimposed on an optical image. Note the several maxima comprising the X-ray emission, and the numerous unidentified optical sources present in this area.

A better understanding of the gas physics in these regions requires an examination of their spectra.

4. Spectral analysis

The spectra are extracted using the QPSPEC task in the IRAF/PROS environment. Again, we restrict our analysis to the energy range 0.20–$2.01\,\mathrm{keV}$ unless otherwise noted. We first compare the shapes of the spectra (before background subtraction) of different regions with that of the background.

4.1. Spectral shapes

The shapes of the spectra, C_k, in specific regions are compared to the shape of the background spectrum, B_k, renormalized to the total counts of the spectrum of the region of interest. For this, we use likelihoods with Poisson statistics:

$$\ln\mathcal{L} = \sum C_k \left[\ln\left(\frac{\sum C_k}{\sum B_k}\right) - 1\right] + \sum C_k \ln B_k - \sum_k \sum_{j=2}^{C_k} \ln j \,,$$

where k is the spectral channel. We resort to sets of $10\,000$ Monte-Carlo trials to derive probabilities that the $\ln\mathcal{L}$s of simulated background spectra drawn from the observed background, measured relative to the normalized background spectrum are smaller than the observed $\ln\mathcal{L}_{\rm obs}$ measured between the spectra of a given region and of the normalized background. The simulated spectra are drawn from a Poisson distribution to match the normalized background spectrum in each energy channel, i.e. with expected simulated counts $B_k\,(\sum C_k/\sum B_k)$.

Table 6 shows the resultant probabilities that each spectral region has a spectrum with the same shape as that of the background. Not only does the region of excess emission, C2+C3+C4 present an excess of counts, but it also has a spectrum whose shape is significantly different from that of the background, while region C6 with negligible *net* counts has a spectral shape consistent with that of the background. Hence, *the spectral shape analysis confirms that the regions of excess counts are indeed the locations of X-ray emission and not caused by poor background subtraction.*

4.2. Spectral fits

The background-subtracted, point-source excised spectra were then fit to a hydrogen absorbed (Balucinska-Church & McCammon, 1992) MEKAL (Mewe et al., 1985, 1986, with Fe L calculations by Liedahl et al., 1995 and the ionization balance from Arnaud & Rothenflug, 1985) plasma, using XSPEC version 10, with χ^2 minimization. A vignetting correction of the background was performed before the background-subtracted spectrum was analyzed.

Table 7 shows the parameters we used for extracting the galaxy spectra. Table 8 presents the results of our spectral fitting to different regions within HCG 16. There remains many instances where energy channels have fewer than 10 net counts, and the Poisson statistics do not resemble gaussians, hence our χ^2 spectral fits are not fully appropriate. Therefore, the reduced χ^2 values and the 90% error bars given in Table 8 should not be over-interpreted.

The low net counts in our background-subtracted spectra (Table 8) make it difficult to perform reliable spectral fits for temperature, metal abundance, and absorbing column. Indeed, decent spectral fits require at least 500 net counts, whereas we have typically 2 to 7 times less. Nevertheless, the spectra often do have sufficient counts to provide decent constraints on the gas temperature, as well as on the bolometric luminosity, once metal abundance and absorbing Hydrogen column are fixed to reasonable values. Note the large absorption corrections on the bolometric luminosity, especially for the lower best fit temperatures, where the emission is peaked at low energies, which are the most seriously affected by absorption.

The temperature of the diffuse emission is well constrained: *the diffuse emission is cool* at $kT = 0.27^{+0.28}_{-0.10}$ (with much narrower 90% confidence intervals for fixed metal abundance). All fits produce an upper-limit (90% confidence level) of 0.56 keV. The metallicity is completely unconstrained.

The spectral fits from region C4 (offset from the group galaxies) are similar to that of the total diffuse emission, and C4 accounts for roughly half of the total luminosity of the diffuse emission. However, C4 could be hot if its metal abundance is low. Fig. 6 shows the best-fit MEKAL spectrum for region C2+C3+C4 together with the residual error per bin. The fit is adequate, hence no additional galactic absorption nor additional component is required by the spectrum.

The galaxy pair HCG 16a&b and galaxy HCG 16c both emit more X-ray luminosity, before correction for absorption, than the group, illustrating the difficulty of absorption corrections in low temperature spectra.

Table 6. Comparison of spectral shapes with the background spectral shape

Region	Total counts	$\ln\mathcal{L}$	$P(\ln\mathcal{L} < \ln\mathcal{L}_{\rm obs})$
C2+C3+C4	663	-77.7	0.026
C6	974	-77.1	0.258

The fourth column represents the probability (from Monte-Carlo simulations) that the region has a spectral shape consistent with that of the background.

Table 7. Extraction parameters for galaxy spectra

Galaxy	RA	Dec	radius
	(J2000)		(arcmin)
HCG 16a&b	$2^{\rm h}09^{\rm m}24\overset{\rm s}{.}0$	$-10°07'49''$	1.5
HCG 16c	$2^{\rm h}09^{\rm m}38\overset{\rm s}{.}2$	$-10°08'49''$	1.2
HCG 16d	$2^{\rm h}09^{\rm m}43\overset{\rm s}{.}9$	$-10°10'58''$	1.1
HCG 16-3	$2^{\rm h}10^{\rm m}16\overset{\rm s}{.}5$	$-10°19'11''$	1.1-0.9

The spectrum of HCG 16-3 was extracted from an ellipse.

Table 8. Spectral fits

Region	Energy range (keV)	Net Counts	kT (keV)	Z ($Z_\odot$)	N_H ($10^{20}\mathrm{cm}^{-2}$)	h_{50}^2 VEM ($10^{63}\mathrm{cm}^{-3}$)	χ^2 (/d.o.f.)	$h_{50}^2\,L_X^{[0.5-2.3]}$ ($10^{41}\,\mathrm{erg\,s}^{-1}$)	$h_{50}^2\,L_{\rm bol}^{\rm unc}$ ($10^{41}\,\mathrm{erg\,s}^{-1}$)	$h_{50}^2\,L_{\rm bol}$ ($10^{41}\,\mathrm{erg\,s}^{-1}$)
C2+C3+C4	0.20–1.40	125	$0.27^{+0.28}_{-0.10}$	(0.05)	galactic	31.4	0.64	0.39	0.68	2.13
			$0.24^{+0.17}_{-0.07}$	0.1	galactic	24.5	0.61	0.43	0.69	2.32
			$0.19^{+0.11}_{-0.06}$	1	galactic	4.5	0.69	0.48	0.71	3.31
			$0.19^{+0.10}_{-0.06}$	10	galactic	0.5	0.71	0.48	0.72	3.69
C4	0.20–1.31	71	$0.26^{+31.7}_{-0.11}$	0.1	galactic	11.9	0.30	0.23	0.36	1.03
			$0.20^{+0.27}_{-0.07}$	1	galactic	2.3	0.33	0.26	0.38	1.53
			$0.20^{+0.22}_{-0.07}$	10	galactic	0.3	0.33	0.27	0.38	1.69
HCG 16a&b	0.20–2.01	232	$0.72^{+0.24}_{-0.19}$	$0.17^{+0.43}_{-0.09}$	galactic	16.5	0.58	0.97	1.21	1.99
			$0.72^{+0.25}_{-0.18}$	0.1	galactic	21.8	0.63	0.96	1.27	2.30
			$0.70^{+0.25}_{-0.23}$	1	galactic	4.0	0.74	0.90	0.99	1.40
HCG 16c	0.20–2.01	213	$0.53^{+0.16}_{-0.15}$	$0.79^{+\infty}_{-0.55}$	galactic	7.3	0.39	0.93	1.01	1.42
			$0.65^{+0.19}_{-0.13}$	0.1	galactic	20.3	0.90	0.86	1.13	2.00
			$0.53^{+0.17}_{-0.14}$	1	galactic	4.0	0.37	0.94	1.02	1.42
HCG 16d	0.20–2.01	83	$0.67^{+\infty}_{-0.31}$	0.1	galactic	7.2	0.32	0.31	0.41	0.71
			$0.39^{+\infty}_{-0.14}$	1	galactic	1.5	0.27	0.31	0.35	0.53
			(0.12)	0.1	(41)	(123)	0.19	0.14	0.16	190
			(0.11)	1	(44)	(240)	0.19	0.14	0.16	1770
HCG 16-3	0.20–2.01	32	(0.49)	0.1	galactic	2.3	0.23	0.08	0.11	0.21
			(0.29)	1	galactic	0.6	0.21	0.10	0.12	0.23

Column (1): region. Column (2): energy range used for the spectral fit. Column (3): net counts in the given energy band (hence lower than the net counts in Table 5). Column (4): temperature. Column (5): metal abundance. Column (6): absorbing hydrogen column density (the galactic value is $N_H = 2.02 \times 10^{20}\,\mathrm{cm}^{-2}$, Stark et al., 1992). Column (7): volume emission measure, defined as $\int_V n_e n_p dV$. Column (8): reduced χ^2 (per degrees of freedom) of fit. Their values are low because the noise is not gaussian. Column (9): X-ray luminosity in the 0.5–$2.3\,\mathrm{keV}$ band. Column (10): bolometric X-ray luminosity, uncorrected for absorption. Column (11): bolometric X-ray luminosity, corrected for absorption. The error bars are 90% confidence levels for one interesting parameter. Values in parentheses provide the best fit when the fit was unconstrained (*i.e.,* when the 90% confidence levels could not be determined). Values of the metal abundance without error bars nor parentheses were frozen in the fit.

With only 83 photons the spectrum of HCG 16d produces virtually no constraints on temperature or metallicity. Nevertheless, careful inspection of the spectrum reveals that the 6 first energy channels (between 0.2 and $0.5\,\mathrm{keV}$) have very low net counts, even taking into account the great error bars, suggesting strong hydrogen absorption, as confirmed by the best fits with variable absorption, which produce a column density 20 times the galactic value. However, the absorption correction to luminosity then becomes enormous and produces unreasonably high absorption-corrected bolometric luminosities.

4.3. Comparison with other X-ray results on HCG 16

4.3.1. Group diffuse emission

The EINSTEIN satellite pointed for $3217\mathrm{s}$ at HCG 16 with the IPC detector. The analysis of these observations by Bahcall et al. (1984) led to 26 ± 12 counts for the entire group (galaxies plus intergalactic medium), corresponding to a luminosity of $2 \times 10^{41}\,h_{50}^{-2}\,\mathrm{erg\,s}^{-1}$. But the limited sensitivity and angular resolution of the IPC didn't allow separating the galactic and intergalactic components.

Saracco & Ciliegi's (1995) analysis of the ROSAT PSPC observation of HCG 16 led to the conclusion that the X-ray emission was due to point sources associated to the galaxies and not to a diffuse intra-group medium. By assuming $kT = 1.0\,\mathrm{keV}$ and $Z = 0.1\,Z_\odot$, they obtained a $5\,\sigma$ upper limit on diffuse emission of $3.0 \times 10^{40}\,h_{50}^{-2}\,\mathrm{erg\,s}^{-1}$ in the 0.5–$2.3\,\mathrm{keV}$ band, after converting this flux to luminosity correctly (see footnote in Sect. 1 and Table 8), i.e., $\simeq 30\%$ below our fitted luminosity in the same energy band.[3]

On the other hand, PBEB, who analyzed the same data as Saracco & Ciliegi, but in the full 0.1–$2.4\,\mathrm{keV}$ PSPC energy band, found an excess of photons in an $8'$ radius circle corresponding to a bolometric luminosity of $4.8 \times 10^{41}\,h_{50}^{-2}\,\mathrm{erg\,s}^{-1}$. Their factor of 16 discrepancy with Saracco & Ciliegi can be subdivided into three terms: 1) a factor 3.4 caused by the correction for Hydrogen (and Helium) absorption, 2) a factor 1.6

[3] adopting $kT = 0.3\,\mathrm{keV}$ instead of $1.0\,\mathrm{keV}$ produces roughly the same upper limit.

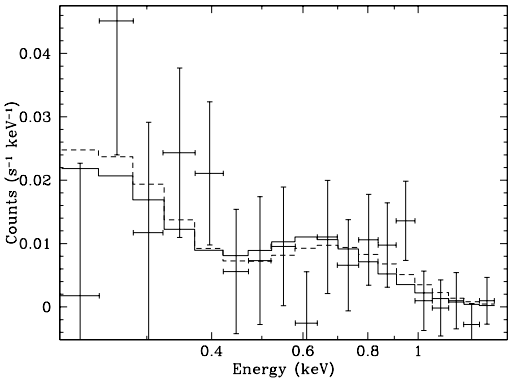

Fig. 6. Spectral fits to the diffuse emission in HCG 16 (regions C2+C3+C4). The *solid* and *dashed histograms* represent the best fit MEKAL models for solar and one-tenth solar metallicity plasmas, with a galactic absorbing column ($N_H = 2.0 \times 10^{20}\,\mathrm{cm}^{-2}$).

caused by the narrower energy band used by Saracco & Ciliegi, and 3) a factor 3.0 unexplained residual term. The adaptive smoothing of the image (PBEB's Fig. 2) indeed showed two diffuse extensions on both sides of the group galaxies, roughly corresponding to the regions C1 and C4 defined in Sect. 3.3.1.

Our spatial analysis is performed over an intermediate energy band ($[0.2, 2.0]\,\mathrm{keV}$, see Sect. 2.1). From our spectral fit to the diffuse emission (regions C2+C3+C4), we find $L_X[0.5 - 2.3\,\mathrm{kev}] = 3.9 \times 10^{40}\,\mathrm{h}_{50}^{-2}\,\mathrm{erg\,s^{-1}}$, only slightly higher than the upper limit of Saracco & Ciliegi. Our bolometric luminosity is $L_{\rm bol} = 2.3 \times 10^{41}\,h_{50}^{-2}\,\mathrm{erg\,s^{-1}}$ (after adding 9% extra luminosity to include region C1D, assuming that it has the same spectrum as the rest of the group emission). Thus *our derived bolometric luminosity for the diffuse emission is half that of Ponman et al. (1996)*.

Summing up from our Table 5, our $8'$ circle around HCG 16 has 306 net counts. In comparison, we infer from the surface brightness profile of PBEB (their Fig. 1) that they measure 281 net counts within a circle of radius $0.^\circ14 = 8.'4$ around HCG 16. In both cases, the group galaxies and point sources exceeding a 3σ threshold were excised. Thus, the difference (although within the error bars) between PBEB's net counts and ours can be attributed to a different background region. Indeed, their background region was chosen to be an annulus of radii between $36'$ and $42'$, while ours was taken between $26'$ and $34'$ (see Table 1). We showed in Sect. 2.2 that the mean background value increases with off-center radius, which explains our higher net counts. But this can certainly not explain the discrepancy in luminosity. Hence, *the discrepancy between the high luminosity measured by Ponman et al. (1996) and our low luminosity for the diffuse emission is not caused by different background subtraction or different removal of the emission from bright galaxies, but by Ponman et al.'s inclusion of regions associated with radio or optical galaxies, some of which are definitely background objects*.

We do agree with PBEB that this diffuse emission is cool, as they find $kT = 0.3 \pm 0.05 (1\,\sigma)\,\mathrm{keV}$, consistent with our values. Note that the correction for absorption is as large as 3.5 at temperatures as low as $0.3\,\mathrm{keV}$ and increases rapidly for decreasing temperature. Hence, while our bolometric luminosity, uncorrected for absorption, depends little on the fit, the absorption corrected luminosity is less certain.

From Table 5, region C6 has 10 ± 31 net counts. Hence the 90% confidence ($1.28\,\sigma$) and $3\,\sigma$ confidence upper limits for diffuse emission in C6 are 50 and 103 net counts, respectively. We convert these net counts to luminosities assuming the same spectrum as region C2+C3+C4, which has 172 net counts according to Table 5. After correction for galactic absorption, this yields $L_{\rm bol}^{\rm C6} < 6.1 \times 10^{40} h_{50}^{-2}\,\mathrm{erg\,s^{-1}}$ (90%) and $1.3 \times 10^{41} h_{50}^{-2}\,\mathrm{erg\,s^{-1}}$ ($3\,\sigma$). Hence, region C6 contributes little to the diffuse X-ray emission of the group (unless it is much cooler, hence more absorbed).

4.3.2. X-ray emission from the group galaxies

Our 0.5–$2.3\,\mathrm{keV}$ luminosities for the galaxies match fairly well those of SC95, who had simply assumed the galaxies to have $1\,\mathrm{keV}$ temperature and solar metallicity: our luminosities are 1%, 12% and 28% lower for HCG 16a&b, HCG 16c, and HCG 16d respectively.

The extent of the diffuse X-ray emission around each galaxy or pair in HCG 16 is fairly large ($\simeq 40\,h_{50}^{-1}\,\mathrm{kpc}$) in comparison with the extent of the X-ray emission detected by Henriksen & Cousineau (1999) around spiral pairs or by Read & Ponman (1998) around most interacting pairs. Fig. 15 of Read & Ponman shows that only the pairs closest to maximum interaction show such large extents of their diffuse X-ray emission, but their diffuse-X-ray to optical luminosity ratio are factors of 5 larger than for the HCG 16ab pair.

5. Discussion

We estimate below the total dynamical mass of the group, the baryonic fraction together with the separation of the baryonic mass into its different components (namely, hot gas, HI, H_2 and stars) and the possibility of virialization of HCG 16.

5.1. Mass budget of HCG 16

5.1.1. Total dynamical mass

The total mass of the group can be estimated, to first order, assuming that the group is in dynamical equilibrium (we will return below to the relevance of this assumption). Table 9 presents the estimates for the total mass of the group using either the 4 original galaxies (Hickson, 1982) of HCG 16, or adding to them the three additional galaxies that were found by de Carvalho et al. (1994) in the close environment of HCG 16, and confirmed spectroscopically by RdC3Z. We apply the mass estimates of Heisler et al. (1985) relevant to self-gravitating systems as well as the projected mass of Bahcall & Tremaine (1981), relevant to test objects orbiting within an underlying potential. We use the

Table 9. Dynamical mass estimates

Group	N	θ	R	σ_v	$M_{\rm vir}^{\rm HTB}$	$M_{\rm proj}^{\rm HTB}$	$M_{\rm avg}^{\rm HTB}$	$M_{\rm med}^{\rm HTB}$	$M_{\rm proj}^{\rm BT}$
		(arcmin)	(h_{50}^{-1} kpc)	(km s^{-1})	($h_{50}^{-1}\,10^{12} M_\odot$)				
Hickson (1982)	4	3.2	74	99	1.1	1.1	0.9	0.7	0.4
Ribeiro et al. (1996)	7	16.9	389	76	2.0	2.0	2.0	1.9	0.8

Column (2): number of galaxies. Columns (3) and (4): radius of the smallest circumscribed circle containing the N galaxies, in arcmin and in kpc respectively. Column (5): unbiased sample velocity dispersion (corrected for the measurement errors, see Eq. [3]). Columns (6), (7), (8), and (9): virial, projected, average and median mass estimates from Heisler et al. (1985), respectively. Column (10): projected mass estimate for isotropic orbits from Bahcall & Tremaine (1981). These mass estimates do not include correction for measurement errors, and are thus slight overestimates.

radial velocity v_i measurements and errors δv_i from RdC3Z. For the velocity dispersion, we computed

$$\sigma_v = \left[\frac{1}{N-1} \sum_i (v_i - \bar{v})^2 - \frac{1}{N} \sum (\delta v_i)^2 \right]^{1/2} . \quad (3)$$

We adopt the median of the four Heisler et al. mass estimates, as we deem it unlikely that the galaxies are test particles in a potential, since we do not detect this potential in diffuse X-rays. Interpolating the total mass at $8'$, within which we have constraints on the gas content of the group, then yields $M_{\rm tot} \simeq 1.4 \times 10^{12} h_{50}^{-1} M_\odot$. For a spherical group, this yields a density that is 256 times the critical density of the Universe or 770 times the mean density if $\Omega_0 = 0.3$.

Of course, the reliable estimation of the total gravitating mass of the group is difficult with only four to seven galaxies. Moreover, the group may not be in virial equilibrium (see Sect. 5.2.1 below). Mamon (1993, 1995) has quantified the effects of departures from virial equilibrium on the estimation of the masses of groups, initially following the Hubble expansion, taking into account the softened nature of galaxy potentials. If the galaxies were point masses, the mass of a galaxy system near full collapse should be half of the mass inferred from dynamical equilibrium (hereafter virial mass), as is well known. But since galaxies have softened potentials, the velocity at closest approach is only a little larger than for the future virialized system (before it coalesces). So, *the virial mass should provide an adequate estimate of the mass — within the apparent radius of a galaxy system near full collapse*. Hence the masses given in Table 9 are probably roughly correct, unless projection effects are important in HCG 16.

5.1.2. Mass in hot gas

An upper limit to the *observed* mass of the diffuse intergalactic gaseous medium (IGM) can be estimated from the normalization of the MEKAL plasma model, which is the Volume Emission Measure (VEM) defined by

$$\mathrm{VEM} = \int_V n_e n_p \, dV = \overline{n_e n_p} V \quad (4)$$

where V is the volume of the emitting region, n_e and n_p are the electron and proton densities. Including the contribution from Helium, the gas mass is

$$M_{\rm hot} = m_p \overline{n_p} [1 + Y/(1-Y)] V \quad (5)$$

where m_p is the proton mass and Y the Helium mass fraction. Since $\overline{n_p}^2 \le \overline{n_p^2} = \overline{n_e n_p}/[1 + Y/(2-2Y)]$ (the equality being reached for a plasma of uniform density), Eqs. (4) and (5) lead to

$$\begin{aligned} M_{\rm hot} &\le \frac{m_p V^{1/2} \mathrm{VEM}^{1/2}}{(1-Y)^{1/2}(1-Y/2)^{1/2}} \\ &= 1.2 \times 10^9 \, h_{50}^{-5/2} \\ &\times \left[\left(\frac{\theta}{1'}\right)^3 - \left(\frac{\theta_g}{1'}\right)^3 \right]^{1/2} \left(h_{50}^2 \frac{\mathrm{VEM}}{10^{63}\,\mathrm{cm}^{-3}} \right)^{1/2} M_\odot \, , \end{aligned} \quad (6)$$

where we took a distance $D = 79.2\, h_{50}^{-1}$ Mpc and $Y = 0.24$, and where θ is the angular radius of the extended emission, and θ_g is the angular radius at which the emission from a possible group galaxy was cut.

Eq. (6) is valid for spherical diffuse regions. Whereas, C3 and C4 are nearly circular, C2 is close to being comprised of two circles. The VEM of C4 is taken from Table 8, while that of C2 and C3 are each taken as half the difference of the VEM of C2+C3+C4 in Table 8 minus the VEM of C4. Moreover, both circular regions of C2 are assumed to have the same VEM. Table 10 presents the estimates of the upper limit to the mass in diffuse intergalactic gas $M_{\rm hot}^{\rm max}$ for the various regions of diffuse emission. Summing up the contributions of the different regions of diffuse X-ray emission, we obtain $M_{\rm hot} < 2.1 \times 10^{10} h_{50}^{-5/2} M_\odot$.

One does not gain much in attempting to fit a β model to each diffuse region. Indeed, if the gas density profile is $n(r) = n_0/[1 + (\theta/\theta_c)^2]^{1/2}$, as in the isothermal β model with $\beta = 1/3$ (close to the slope found by Ponman & Bertram, 1993, for HCG62), then Eqs. (4) and (5) lead to

$$\frac{M_{\rm hot}}{M_{\rm hot}^{\rm uniform}} = \frac{\overline{n_p}}{\left(\overline{n_p^2}\right)^{1/2}} = \frac{3^{1/2}}{2} \frac{x(x^2+1)^{1/2} - \sinh^{-1} x}{x^{3/2}(x - \tan^{-1} x)^{1/2}} \, ,$$

where $x = \theta/\theta_c$. $M_{\rm hot}/M_{\rm hot}^{\rm uniform}$ is always greater than 0.87 for $\theta_c > \theta/100$. If, on the other hand, one assumes $\beta = 1$ as

Table 10. Upper limits to the observed gas content of diffuse regions

Region	h_{50}^2 VEM	θ	θ_g	$h_{50}^{5/2}\,M_{\rm hot}^{\rm max}$	$\rho_{\rm hot}^{\rm max}$
	($10^{63}\,{\rm cm}^{-3}$)	(arcmin)		($10^{10}\,M_\odot$)	($h^{-3/2}\rho_c$)
C2A	4.9	1.7	1.2	0.24	212
C2B	4.9	1.7	1.2	0.24	212
C3	9.8	1.9	1.2	0.49	269
C4	11.9	2.0	0.0	1.2	412
C2+C3+C4	31.5			2.2	309
C6 (face value)	2.5	8.0	0.0	4.3	24
C6 (90%)	12.6	8.0	0.0	9.6	53
C6 ($3\,\sigma$)	25.9	8.0	0.0	13.8	76

The last column is the upper limit to the density of hot gas in units of the critical density of the Universe.

found by Mulchaey & Zabludoff (1998), Eqs. (4) and (5) lead to

$$\frac{M_{\rm hot}}{M_{\rm hot}^{\rm uniform}} = 24^{1/2}\,\frac{x^{-3/2}\left[\sinh^{-1}x - x/(x^2+1)^{1/2}\right]}{\left[\tan^{-1}x + x/(x^2{+}1) - 2x/(x^2{+}1)^2\right]^{1/2}}\,,$$

which falls to 0.47 for $\theta_c = \theta/5$ (close to what we infer was derived by Mulchaey & Zabludoff), but to 0.25 for $\theta_c = \theta/10$. Hence, the uniform approximation for the mass of diffuse gas is probably valid to within a factor of two or at worst four.

An upper limit to the gas mass from region C6 can be estimated, assuming that it is a sphere of $200\,h_{50}^{-1}\,{\rm kpc}$ radius, and that its temperature and metal abundance are the same as the best fit case for regions C2+C3+C4. The upper limits for C6 are provided in Table 10, with the face value counts, the 90% upper limit or the $3\,\sigma$ upper limit. The gas mass of C6 is poorly constrained in contrast with its diffuse X-ray luminosity. However, Table 10 shows that *if the undetected region (C6) has similar temperature, metallicity and clumpiness as the detected regions (C2+C3+C4), then its mass-density is at most ($3\,\sigma$ limit) one-quarter that of the detected regions*. Similarly, its mean X-ray surface brightness is at most one-sixth that of C2+C3+C4. Hence, *the low emission of C6 is not merely a statistical fluctuation in X-ray counts, but indicative of a true underdensity in the distribution of hot diffuse gas*.

In summary, we obtain four upper limits to the mass in diffuse hot gas within $8'$ from the group center: $M_{\rm hot} < 2.1\times10^{10}h_{50}^{-5/2}$ (if the 10 counts in C6 are just noise), $6.4\times10^{10}h_{50}^{-5/2}$ (taking the 10 counts in C6 at face value), $1.2\times10^{11}h_{50}^{-5/2}$ (with 90% upper limit on C6), and $1.6\times10^{11}h_{50}^{-5/2}$ (with $3\,\sigma$ limit on C6).

5.1.3. Baryonic fraction

Within an $8'$ radius from the group center, the molecular gas mass is $M_{\rm H_2} = 7.4\times10^{10}h_{50}^{-2}M_\odot$ (Leon et al., 1998), while the mass in cold HI gas is slightly less than $M_{\rm HI} = 4.5\times10^{10}h_{50}^{-2}M_\odot$ (Williams, 1998, whose VLA map shows that a small fraction of the diffuse HI emission extends beyond the $4'$ radius circle around the group). Note that the contributions of dust and ionized hydrogen (estimated by Mendes de Oliveira et al. 1998), though important in comparison with other galaxies, are negligible within the mass budget of HCG 16. Thus, if the 10 counts measured in region C6 are just noise or taken at face value, the mass in diffuse hot gas is much smaller than the mass in cold gas and fairly negligible within the total mass budget of HCG 16.

The fraction f_b of baryons within $8'$ of the optical center of HCG 16 is

$$f_b = \frac{M_* + M_{\rm HI} + M_{\rm H_2} + M_{\rm hot}}{M_{\rm tot}} = \left(\frac{M_*/L_B}{6.4} + 0.085\right)h_{50}^{-1} + f_{\rm hot}\,h_{50}^{-3/2}\,, \quad (7)$$

where M_*/L_B is the mean stellar mass-to-light ratio for the group and $f_{\rm hot}$ is the mass fraction of the group in hot gas, and is 1.5%, 5%, 8% or 11% depending on the interpretation of the 10 net counts in region C6 (noise, face-value, 90% limit and $3\,\sigma$ limit, respectively).

Because the galaxies in HCG 16 have probably all undergone fairly recent bursts of star formation (e.g. Ribeiro et al., 1996), their stellar mass to blue luminosity ratios are probably much lower than for normal spirals (*i.e.* $M_*/L_B < 2.5$). There are two ways to estimate M_*/L_B for each of the four bright galaxies in HCG 16.

First, MPABB mentioned that galaxies HCG 16a and 16c have rotation velocities consistent with the Tully-Fisher (1977, hereafter TF) relation, whereas galaxy HCG 16d has a rotational velocity at most half of what is expected by the TF relation. This translates to a luminosity that is at least 16 times larger than expected from the TF relation. Assuming that such was also the case for galaxy HCG 16b (its low rotation velocity on one side is also half of what is expected from the TF relation, although its high rotation velocity on the other side is consistent with the TF relation), this leads to $M_*/L_B = 1.19$ assuming $(M_*/L_B)_{\rm normal} = 2.5$ for the group of 4 galaxies.

Alternatively, M_*/L_B can be constrained by the times since the last bursts of star formation in each of the 4 bright galaxies of HCG 16. These times can be inferred from the optical colors of the galaxies or from their X-ray properties. Table 11 provides the values of M_*/L_B inferred from the colors of the 4 bright galaxies, using Fioc and Rocca-Volmerange's (1997) PEGASE spectral evolution model, assuming a single burst, a Rana & Basu (1992) initial mass function, and solar metallicity.

The stellar masses in Table 11 yield $M_*/L_B = 0.53$ for the group of 4 galaxies. With this value of M_*/L_B, Eq. (7) yields a baryonic fraction of 18% or 21% if the emission from C6 is respectively noise or taken at face value, and as much as 25% (90% limit on C6) or 28% ($3\,\sigma$ limit on C6).

Note that if significant star formation occurred before the last burst, the mean colors of the galaxies would be redder than with the most recent starburst. Therefore, blue colors indicate even more recent starbursts than listed in Table 11. This in turn leads to lower M_*/L_B and an even lower baryonic fraction. Moreover, if $M_*/L_B \le 0.55$, then there is more mass in cold (HI+H_2) gas than in stars.

Table 11. Colors, ages and stellar masses of the HCG 16 galaxies

Galaxy	B_T	B_T^0	$B-R$	$(B-R)^0$	Age (Gyr)	M_*/L_B	$h_{50}M_*$ ($10^{10}M_\odot$)
HCG 16a	12.99	12.76	0.82	0.72	0.50	0.39	3.0
HCG 16b	13.74	13.27	1.07	0.86	0.68	0.52	2.5
HCG 16c	13.40	13.10	1.04	0.91	0.71	0.57	3.2
HCG 16d	13.90	13.42	1.29	1.08	0.95	0.75	3.1

Column (1): Galaxy name. Columns (2), (3), and (4): Asymptotic blue magnitude before and after correction for Galactic and internal extinction, and mean color within the $\mu_B = 24.5\,\mathrm{mag\,arcsec^{-2}}$ isophote, all from Hickson et al. (1989). Column (5): Color corrected for galactic and internal reddening using $(B-R)^0 = B-R+0.54\,(B_T^0-B_T)$. Columns (6) and (7): age and M_*/L_B from the PEGASE spectrophotometric evolution model of Fioc & Rocca-Volmerange (1997). Column (8): Mass in stars.

5.2. The dynamical state of HCG 16

The knowledge of the dynamical state of the HCGs is primordial to assess the reality of these close associations of galaxies on the sky. In paper II, we show that the low velocity dispersion of HCG 16 is indicative of a non-virialized dynamical state, but show that the alternative scenario of chance alignments is even less likely for HCG 16. Here, we just want to briefly emphasize two points: is the peculiar X-ray morphology found in HCG 16 compatible with virialization, and are the X-ray properties deduced from ROSAT data reduced here compatible with chance alignment models?

5.2.1. Can a virialized group have an irregular X-ray morphology?

If HCG 16 were in a (nearly) virialized state, the galaxy halos should have merged, and thus the global group potential should be fairly smooth. Moreover, the diffuse gas associated with these halos should have also merged, and reached hydrostatic equilibrium within this smooth potential. For example, HCG 62 is the archetype of such a virialized group, as its X-ray morphology is smooth and the diffuse X-ray emission extends well beyond the HCG galaxies (Ponman & Bertram, 1993). The significant gas density at the group center is attested by the presence of a cooling flow, as witnessed by the increase in surface brightness and the cooler temperature of the inner $50\,h_{50}^{-1}\,\mathrm{kpc}$ (Ponman & Bertram, 1993).

The X-ray morphology of HCG 16 is very different from that of HCG 62. The diffuse X-ray emission is situated within $\simeq 50\,h_{50}^{-1}\,\mathrm{kpc}$ around the galaxies, plus in one clump (C4) at $140\,h_{50}^{-1}\,\mathrm{kpc}$ from the nearest galaxy. This clumpy X-ray morphology strongly suggests that HCG 16 is far from virialization.

This argument against virialization supposes that intergalactic gas, at the time of formation of the group, was able to settle in hydrostatic equilibrium in the shallow potential of HCG 16. This point of view can be challenged if the specific entropy of the intergalactic gas at this epoch is high enough to prevent the gas from collapsing with the dark matter (Ponman, private communication). Indeed, assuming the infalling gas has the density of the Universe at the epoch of group collapse, there is a maximum temperature above which the specific entropy of the infalling gas will be higher than the specific entropy of the gas settled in equilibrium in the potential of the group. Since the gas entropy cannot decrease (unless the gas radiates), this constraint gives a maximum temperature above which the gas cannot settle in the dark matter potential.

This (relatively) high specific entropy intergalactic gas still lacks direct observation, but it is indirectly inferred from the changes in the X-ray surface brightness profiles from clusters to groups (Ponman et al., 1999). Also, the high temperature level is required in the interpretation of a number of observational facts. For example, the negative result of the Gunn-Peterson effect implies that the Universe had an overall reionization (and therefore probably reheating) phase before $z \simeq 5$. Moreover, the steepening of the $L_X - T$ relation from clusters to groups (PBEB) has so far only been explained in models where the infalling gas was preheated at a temperature of $\simeq 0.5\,\mathrm{keV}$ (Cavaliere et al., 1997, 1998; Balogh et al., 1999). Thus, provided that HCG 16 is forming today, we can understand its irregular X-ray morphology as a consequence of its low virial temperature, which does not exclude that the underlying dark matter potential is relaxed. Finally, hydrodynamical cosmological simulations indicate that most of the intergalactic gas is in the 10^5–$10^7\,\mathrm{K}$ temperature range (Cen & Ostriker, 1999).

If intergalactic gas cannot collapse onto the group, then the diffuse gas observed in the group originates primarily from the galaxies of the group, in the form of shock-heated tidally stripped gas or hot winds from collective supernovae ejecta. In the latter case, the diffuse hot gas should be metal-rich. Our spectral fits do not constrain the metallicity of the group, whereas PBEB found $Z < 0.17$ for the diffuse gas that they detected. Since half of their detected emission arises from the radio sources in regions C1 and C5, we cannot confirm the low metallicity of the HCG 16 diffuse gas. Better signal-to-noise observations are required to answer this question, in particular better constraints on metallicity and its spatial variation in the group.

Whether or not the group is near virial equilibrium, *the hot gas appears too clumpy to be itself in hydrostatic equilibrium within a nearly spherical potential*.

5.2.2. Chance alignment models

Difficulties in the understanding of the properties of HCGs (in particular their short crossing-times) have led some authors to the conclusion that most of these objects are chance alignments along the line-of-sight within larger structures, namely loose groups (Mamon, 1986), clusters (Walke & Mamon, 1989) or cosmological filaments (Hernquist et al., 1995).

Loose groups are obviously not dense enough to be globally near full collapse (although their cores may have already collapsed and formed interacting binaries), and are more likely to be in their early phases of collapse (Diaferio et al., 1993; Mamon, 1993, 1994, 1995), as is our Local Group, or even in the

late stages of their Hubble expansion before their turnaround (Valtonen & Byrd, 1986). Thus, one does not expect to see diffuse gas in a compact group caused by a chance alignment within a collapsing near-spherical loose group. Indeed, if loose groups have diffuse intergalactic gas, this gas is too tenuous to be observed. Moreover, this gas should remain fairly cold until it relaxes with the group potential, and this re-heating must await the virialization of the group. Therefore, the gas that one expects to observe in X rays within loose groups will be associated with the dense substructures within these groups, *i.e.*, galaxies and interacting binaries (which are expected in chance alignments, Mamon, 1992), and with gas ejected by supernovae near interacting galaxies (e.g., Read & Ponman, 1998; Henriksen & Cousineau, 1999).

The X-ray properties of chance alignments within cosmological filaments depend strongly on the dynamical and thermal state of the cosmological filament. Such filaments appear clearly in cosmological simulations. For example, the hydrodynamical simulations of Cen & Ostriker (1999) show that most of the intergalactic gas is not only at temperatures of 10^5–10^7 K, but also within filamentary structures. Cen & Ostriker argue that this gas was shock-heated mainly by structure collapse and possibly also by supernovae.

It presents a major challenge to detect gas, either within filaments of loose groups, at temperatures well below $0.3\,\mathrm{keV}$, since the gas in these systems should be too tenuous to be an efficient emitter or an efficient absorber. Moreover, its typical temperature is too cool to observe in X-rays, and its detection is difficult in the EUV because of contamination from emission from the galactic corona and strong absorption from galactic HI. *Hence, one does not expect to detect widespread diffuse X-ray emission in compact groups caused by chance alignments within loose groups or cosmological filaments.* Therefore, in these chance alignments scenarios, the diffuse X-rays detected in HCG 16 are associated with interacting pairs of galaxies, perhaps emitted by gas that was stripped by tidal interactions or ejected by galactic winds generated by supernova explosions.

Our revised X-ray luminosity for HCG 16 brings the group closer to the extrapolation of the cluster luminosity-temperature relation and to the the group $L_X - T$ relation of Mulchaey & Zabludoff (1998). Moreover, if there is a universal luminosity-temperature relation spanning the range from individual galaxies to binaries to real compact groups such as HCG 62 to rich clusters, then one expects that a chance alignment of N equal luminosity systems along the line-of-sight will produce a group that will be located a factor N in luminosity above this universal luminosity-temperature relation. This is consistent with the position of HCG 16 in the L_X-T diagram relative to the relation of Mulchaey & Zabludoff, but the X-ray luminosity of HCG 16 is 300 times too large for its low temperature in comparison with PBEB's $L_X - T$ relation, and chance alignments cannot explain such a large luminosity excess.

In Paper II, we investigate in more detail the possibility that HCG 16 occurs as a chance alignment within a looser group or a cosmological filament.

5.3. Concluding remarks

Due to their low virial temperature ($T \simeq 1\,\mathrm{keV}$), groups of galaxies and their X-ray emission are of extreme importance in the study of processes affecting the baryonic diffuse content of systems of galaxies, such as reheating and early energy injection (Cavaliere et al., 1997, 1998; Balogh et al., 1999; Ponman et al., 1999). Earlier analyses of ROSAT PSPC observations of Hickson Compact Groups (Pildis et al., 1995; Saracco & Ciliegi, 1995; Ponman et al., 1996) were based on counting photons in a circle surrounding the optical center of the group. The present detailed spatial analysis of X-ray emission in HCG 16 highlights the importance of a multi-wavelength study, in particular for rejecting point sources identified in the optical and radio wavebands. The clumpy nature of the hot gas in HCG 16 appears quite different from the more regular diffuse emission seen in other compact groups, and HCG 16 loses its previous characteristic of being the sole spiral-only compact group with hot gas tracing a fairly regular potential well (see Ponman et al., 1996; Mulchaey, 1999). Our study raises nevertheless the question that other compact groups previously detected in X-rays may be significantly contaminated by superimposed X-ray (point or extended) sources.

Another question raised by this study is the inclusion of HCG 16 in the $L_X - T$ relation of groups and clusters. Indeed, this relation measures the trend between dark matter total mass and mean baryonic density *in systems where the diffuse gas is in equilibrium within the dark matter potential*. Since the diffuse hot gas of HCG 16 appears to lie in several (N) clumps, one would then expect that the group luminosity be a factor N above the $L_X - T$ relation, for given temperature. If PBEB's $L_X - T$ relation is correct, then the factor of 300 excess luminosity for its temperature in comparison with the extrapolation of the PBEB's trend is too large to be consistent with the idea that most of the X-ray emission originates from a few clumps of hot gas in equilibrium within an underlying potential. Moreover, in the frame of theories explaining the $L_X - T$ relation in groups (Cavaliere et al., 1997, 1998; Balogh et al., 1999), gas cannot settle in hydrostatic equilibrium into a system with a virial temperature smaller than $\simeq 0.5\,\mathrm{keV}$ (see Sect. 5.2.1). These two arguments naturally lead to the conclusion that the diffuse gas observed in HCG 16 originates mostly from the galaxies, either through tidal stripping or in galactic winds driven by supernova explosions.

The launch of new X-ray satellites (Chandra) with its high spatial and spectral resolution and XMM with its greatly enhanced sensitivity and spectral resolution will eventually allow to answer these questions. The precise nature of the diffuse emission seen in HCG 16 is still difficult to constrain, because of the low signal-to-noise of the ROSAT/PSPC observations. We expect to pursue our study of HCG 16 using archival ASCA data, as well as a Chandra observation, which we have obtained on this compact group.

Acknowledgements. This research constitutes part of the PhD thesis of S.D.S. We acknowledge useful discussions with Joel Bregman, Malcolm Bremer, Florence Durret, Daniel Gerbal, Mark Henriksen,

Stéphane Leon, Gastão Lima Neto, Claudia Mendes de Oliveira, Vincent Pislar, and Trevor Ponman. We are most grateful to Trevor Ponman for his excellent refereeing, which led to substantial improvement of our work. Thanks also to Michel Fioc for providing us digital output from his PEGASE spectro-photometric evolution model, Gastão Lima Neto for use of his graphics package, Eric Slezak for his TRANSWAVE *à trous* wavelet package, and Barbara Williams for sending us her VLA 21cm maps and mass estimates in advance of publication. This research was supported in part by a grant from the French GdR Cosmologie (awarded to G.A.M.). We have made use of the NASA/IPAC Extragalactic Database (NED) which is operated by the Jet Propulsion Laboratory, California Institute of Technology, under contract with the National Aeronautics and Space Administration, the SIMBAD database operated by the Centre de Données Stellaires in Strasbourg, France, the ROE/NRL COSMOS UKST Southern Sky Object Catalog, the NRAO VLA Sky Survey (NVSS) and NASA's Astrophysics Data System (ADS) Abstract Service.

References

Arnaud, M., Rothenflug, R., 1985, A&AS 60, 425
Bahcall, J.N., Tremaine, S., 1981, ApJ 244, 805
Bahcall, N.A., Harris, D.E., Rood, H.J., 1984, ApJ 284, L29
Balogh, M., Babul, A., Patton, D., 1999, MNRAS 307, 463
Balucinska-Church, M., McCammon, D., 1992, ApJ 400, 699
Barnes, J., 1985, MNRAS 215, 517
Barnes, J.E., 1989, Nature 338, 123
Bode, P.W., Berrington, R.C., Cohn, H.N., Lugger, P.M., 1994, ApJ 433, 479
Carnevali, P., Cavaliere, A., Santangelo, P., 1981, ApJ 249, 449
Cavaliere, A., Menci, N., Tozzi, P., 1997, ApJ 484, L21
Cavaliere, A., Menci, N., Tozzi, P., 1998, ApJ 501, 493
Cen, R., Ostriker, J.P., 1999, ApJ 514, 1
Condon, J.J., Cotton, W.D., Greisen, E.W., Yin, Q.F., Perley, R.A., Taylor, G.B., Broderick, J.J., 1998, AJ 115, 1693
de Carvalho, R.R., Ribeiro, A.L.B., Zepf, S.E., 1994, ApJS 93, 47
Diaferio, A., Geller, M.J., Ramella, M., 1994, AJ 107, 868
Diaferio, A., Ramella, M., Geller, M.J., Ferrari, A., 1993, AJ 105, 2035
Ebeling, H., Voges, W., Böhringer, H., 1994, ApJ 436, 44
Fioc, M., Rocca-Volmerange, B., 1997, A&A 326, 950
Governato, F., Tozzi, P., Cavaliere, A., 1996, ApJ 458, 18
Heisler, J., Tremaine, S., Bahcall, J.N., 1985, ApJ 298, 8
Henriksen, M., Cousineau, S., 1999, ApJ 511, 595
Hernquist, L., Katz, N., Weinberg, D.H., 1995, ApJ 442, 57
Hickson, P., 1982, ApJ 255, 382
Hickson, P., 1997, ARA&A 35, 357
Hickson, P., Kindl, E., Auman, J.R., 1989, ApJS 70, 687
Hickson, P., Mendes de Oliveira, C., Huchra, J.P., Palumbo, G.G., 1992, ApJ 399, 353
Leon, S., Combes, F., Menon, T.K., 1998, A&A 330, 37
Liedahl, D.A., Osterheld, A.L., Goldstein, W.H., 1995, ApJ 438, L115
Mamon, G.A., 1986, ApJ 307, 426
Mamon, G.A., 1987, ApJ 321, 622
Mamon, G.A., 1992, in: Mamon, G.A., Gerbal, D. (eds.), 2nd DAEC mtg., Distribution of Matter in the Universe, Obs. de Paris, Paris, p. 51
Mamon, G.A., 1993, in: Combes, F., Athanassoula, E. (eds.), Gravitational Dynamics and the N-Body Problem, Obs. de Paris, Paris, p. 188, astro-ph/9308032
Mamon, G.A., 1994, in: Durret, F., Mazure, A., White, S.D.M., Trânh Thanh Vân, J. (eds.), 14th Moriond Astrophysics Mtg., Clusters of Galaxies, Frontières, Gif-sur-Yvette, p. 291, astro-ph/9511101
Mamon, G.A., 1995, in: de Vega, H., Sánchez, N. (eds.), 3rd Paris cosmology colloq., p. 95, astro-ph/9511101
Mamon, G.A., Dos Santos, S., 1999, A&A to be submitted (Paper II)
Mendes de Oliveira, C., Plana, H., Amram, P., Bolte, M., Boulesteix, J., 1998, ApJ 507, 691
Mewe, R., Gronenschild, E.H.B.M., Van Den Oord, G.H.J., 1985, A&AS 62, 197
Mewe, R., Lemen, J.R., Van Den Oord, G.H.J., 1986, A&AS 65, 511
Motch, C., Guillout, P., Haberl, F., Krautter, J., Pakull, M.W., Pietsch, W., Reinsch, K., Voges, W., Zickgraf, F.J., 1998, A&AS 132, 341
Mulchaey, J.S., 1999, in: Valtonen, M.J., Flynn, C. (eds.), IAU Coll. No. 174, Small Galaxy Groups, ASP, San Francisco, in press
Mulchaey, J.S., Davis, D.S., Mushotzky, R.F., Burstein, D., 1996, ApJ 456, 80
Mulchaey, J.S., Zabludoff, A.I., 1998, ApJ 496, 73
Pildis, R.A., Bregman, J.N., Evrard, A.E., 1995, ApJ 443, 514
Ponman, T.J., Bertram, D., 1993, Nature 363, 51
Ponman, T.J., Bourner, P.D.J., Ebeling, H., Böhringer, H., 1996, MNRAS 283, 690 (PBEB)
Ponman, T.J., Cannon, D.B., Navarro, J.F., 1999, Nature 397, 135
Rana, N.C., Basu, S., 1992, A&A 265, 499
Read, A.M., Ponman, T.J., 1998, MNRAS 297, 143
Ribeiro, A.L.B., de Carvalho, R.R., Coziol, R., Capelato, H.V., Zepf, S.E., 1996, ApJ 463, L5 (RdC3Z)
Rose, J.A., 1977, ApJ 211, 311
Saracco, P., Ciliegi, P., 1995, A&A 301, 348
Shensa, M.J., 1992, Proceedings IEEE 40, 2464
Slezak, E., Bijaoui, A., Mars, G., 1990, A&A 227, 301
Slezak, E., de Lapparent, V., Bijaoui, A., 1993, ApJ 409, 517
Snowden, S.L., McCammon, D., Burrows, D.N., Mendehall, J.A., 1994, ApJ 424, 714
Starck, J.L., Murtagh, F., 1994, A&A 288, 342
Starck, J.L., Pierre, M., 1998, A&AS 128, 397
Stark, A.A., Gammie, C.F., Wilson, R.W., Bally, J., Linke, R.A., Heiles, C., Hurwitz, M., 1992, ApJS 79, 77
Tully, R.B., Fisher, J.R., 1977, A&A 54, 661
Valtonen, M.J., Byrd, G.G., 1986, ApJ 303, 523
Verdes-Montenegro, L., Yun, M.S., Williams, B.A., et al., 1999, in: Valtonen, M.J., Flynn, C.(eds.), IAU Coll. No. 174, Small Galaxy Groups, ASP, San Francisco, in press
Walke, D.G., Mamon, G.A., 1989, A&A 225, 291
Williams, B.A., 1998, private communication

C.4 Understanding low and high velocity dispersion compact groups

Mamon 2000, dans IAU Colloquium 174, *Small Galaxy Groups*, sous presse, arXiv:astro-ph/9909019

Contribution to IAU Colloq. 174 on Small Galaxy Groups, held in Turku, FINLAND, June 13–18, 1999, ed. M. Valtonen & C. Flynn, ASP series

Understanding low and high velocity dispersion compact groups

G. A. Mamon

IAP, F-75014 Paris, FRANCE

Abstract. A galaxy system must have a minimum velocity dispersion for its mass to be greater than the sum of the masses of its galaxies. Nearly half of the nearby Hickson compact groups (HCGs) have too low a velocity dispersion in comparison with the rotational velocities of their spiral galaxies and internal velocity dispersions of their early types.

A detailed study of the low velocity dispersion group, HCG 16 — the only known group of late-type galaxies with diffuse intergalactic X-ray emitting hot gas — reveals that half of the diffuse X rays are associated with foreground/background sources and the remaining gas is clumpy and mostly associated with the bright galaxies of the group. The large-scale environment of the group suggests that HCG 16 lies where a cosmological filament falls perpendicularly onto a large-scale sheet.

The observed frequency of compact groups is lower than predicted from the extended Press-Schechter formalism, which also predicts that most $10^{13}\,M_\odot$ objects in the Universe must be fairly old and hence have already coalesced into single objects, reminiscent of elliptical galaxies over-luminous in X-rays that are now being discovered.

Thus, the low survival time of dense groups against the merging instability is no longer a worry for compact groups, as they form in large enough numbers. I show why other arguments against the reality of HCGs no longer hold, partly because of the biases of Hickson's sample.

1. Introduction

Compact groups (hereafter CGs) have been puzzling astronomers for a number of years. How can a few bright galaxies coexist within less than 100 kpc? CGs may have formed early, and have managed to survive the merging instability (Governato et al. 1991; Athanassoula, in these proceedings) or else formed just recently (Hickson 1982). Alternatively, CGs may be not be truly dense in 3D, but caused instead by chance alignments of galaxies along the line of sight within larger loose groups (Mamon 1986), clusters (Walke & Mamon 1989) and cosmological filaments (Hernquist et al. 1995, hereafter HKW).

In this contribution, we provide new light on this debate by studying the group velocity dispersions, X-ray, optical and continuum radio emission, and by predicting the frequency of dense groups as compact as Hickson's (1982, hereafter HCGs) appear to be, using the (Press & Schechter 1974) cosmological formalism. We conclude on the nature of HCGs.

2. Low velocity dispersion compact groups

For near spherical virialized systems, mass increases with some power (near 3, as is easily shown by combining the virial theorem with a critical mean density for virialization) of the velocity dispersion of virialized systems. One therefore expects that *there must be a minimum velocity dispersion for a virialized galaxy system to be more massive than the sum of the masses of its member galaxies.* Systems near full collapse should have even larger velocity dispersions.

For a tighter constraint, within a given radius R, the sum of the masses of the galaxies *before they they got close to one another* must be smaller or equal to the mass within the same radius that the group would have *once it virializes*: $M(R) \geq \sum_j m_j(R)$. Assuming Navarro, Frenk, & White (1995) profiles for groups and halos of galaxies, one can show (Mamon 1999) that the velocity dispersion σ_v of a given dense group must satisfy:

$$\sigma_v^2 \geq 0.16 \sum_{\text{spirals}} v_{\text{rot}}^2 + 1.0 \sum_{\text{ellipticials}} \sigma_{v,E}^2 \ , \qquad (1)$$

where the sums are over the deprojected maximum rotation velocities of spirals and the internal velocity dispersions of ellipticals.

Table 1. Hickson compact group minimum velocity dispersions

Group	N_S	σ_v^S	N_E	σ_v^E	$\sigma_v^{\min}$	N	σ_v
HCG 16	4	151/166	0	—	151/166	4	99
HCG 23	2	123	0	—	123	4	180
HCG 33	1	93	0	—	93	4	172
HCG 34	1	83	0	—	83	4	365
HCG 37	1	93	2	266	282	5	445
HCG 40	3	124	1	199	234	5	160
HCG 44	2	98	1	158	186	4	145
HCG 57	3	166	2	195	256	7	275
HCG 79	1	42	0	—	42	4	150
HCG 88	2	118	0	—	118	4	24
HCG 89	2	79	0	—	79	4	35
HCG 90	3	106	0	—	106	4	108

Columns (2) and (4): number of spirals and ellipticals used; columns (3) and (5): minimum group velocity dispersion (in $\mathrm{km\,s^{-1}}$) from spirals and from ellipticals; column (6): global minimum group velocity dispersion ($\mathrm{km\,s^{-1}}$), *i.e.*, $\left(\sigma_v^{\min}\right)^2 = \left(\sigma_v^{\mathrm{S}}\right)^2 + \left(\sigma_v^{\mathrm{E}}\right)^2$; column (7) number of accordant redshift galaxies in group; column (8) measured group velocity dispersion ($\mathrm{km\,s^{-1}}$).

Although there is still little data on the internal kinematics of HCG galaxies, Table 1 above shows that 5 HCGs out of 12 (HCGs 16, 40, 44, 88 and 89) have abnormally low velocity dispersions, and two others (HCGs 57 and 90) have just marginal velocity dispersions. We expect to measure by chance low velocity dispersions in roughly 20% of dense groups (those with chance tangential velocity vectors). Still, most of the 5 HCGs mentioned above have too low velocity dispersions to be dense systems near virialization. The simplest alternative is that they are chance alignments within loose groups near turnaround, since at turnaround the velocity dispersion of galaxy systems is expected to be small. Another possibility is that *tidal friction* has been effective in slowing down the

galaxies, although this is only expected in much more compact groups near full coalescence (Weinberger et al. 1999; Temporin, in these proceedings).

The two groups with $\sigma_v \simeq \sigma_v^{\rm min}$ may simply have little intergalactic matter. Given that the internal kinematics data on HCG galaxies is very incomplete (only one group has data for all its members, *i.e.,* $N = N_S + N_E$), some of the groups with high velocity dispersions may turn out to have only marginal velocity dispersions and thus possess little intergalactic matter, while some of the marginal ones may in fact be non-real. In any event, *There seems to be 3 classes of compact groups, following decreasing velocity dispersion: groups with substantial intergalactic matter, groups will little intergalactic matter and chance alignments within loose groups (or clusters or cosmological filaments).*

Finally one may be tempted to secure more precise velocity dispersions by including the galaxies from the environment of HCGs with the data of de Carvalho et al. (1994) and Zabludoff & Mulchaey (1998), but these spectroscopic surveys show that the velocity dispersion usually increases with inclusion of the environment galaxies, and it is not clear that one is not increasingly affected by interlopers.

3. HCG 16

We now focus on HCG 16, the prime, example of a low velocity dispersion, spiral-rich compact group.

3.1. X-ray emission

The X-ray properties of HCG 16 are controversial and possibly extreme. In their ROSAT/PSPC X-ray survey of HCGs, Ponman et al. (1996) (hereafter PBEB), HCG 16 was the coldest detected group ($T = 0.30 \pm 0.05\,$keV), and there are no other spiral-only compact groups with diffuse X-ray emission (Mulchaey in these proceedings; see also PBEB). Moreover, whereas diffuse X-rays were clearly detected by PBEB, Saracco & Ciliegi (1995) failed to detect such diffuse emission at an upper limit 16 times lower,[1] whereas only a factor 2.3 is attributable to the wider ("bolometric") energy range in which PBEB compute their luminosities. Given the low temperature that PBEB derive for HCG 16, their derived X-ray luminosity places it two orders of magnitude above their compact group luminosity-temperature relation and roughly a factor of two above the extrapolation of the cluster trend. It thus seems difficult to reconcile HCG 16 with a low temperature extrapolation of regular X-ray emitting compact groups.

Dos Santos & Mamon (1999) have re-analyzed the ROSAT/PSPC observations of HCG 16 with the hopes of resolving the discrepancy between Saracco & Ciliegi and PBEB and establishing if an irregular morphology is caused by clumpiness or fluctuations in signal-to-noise ratios. Figure 1a below shows the X-ray emission of HCG 16 as contours overlayed on a greyscale map of the group. The emission beyond the galaxies is indeed significant in a few compact regions:

[1] Given the fluxes measured by Saracco & Ciliegi (1995) for HCG 16 and their adopted value for H_0, their quoted upper limit for their luminosities were underestimated by a factor 2 for all undetected groups in their Table 4 except HCG 3.

around the galaxies a&b, c and d, as well as a few clumpy regions outside the galaxies denoted C1 (comprised of 4 sub-clumps), C4 and C5.

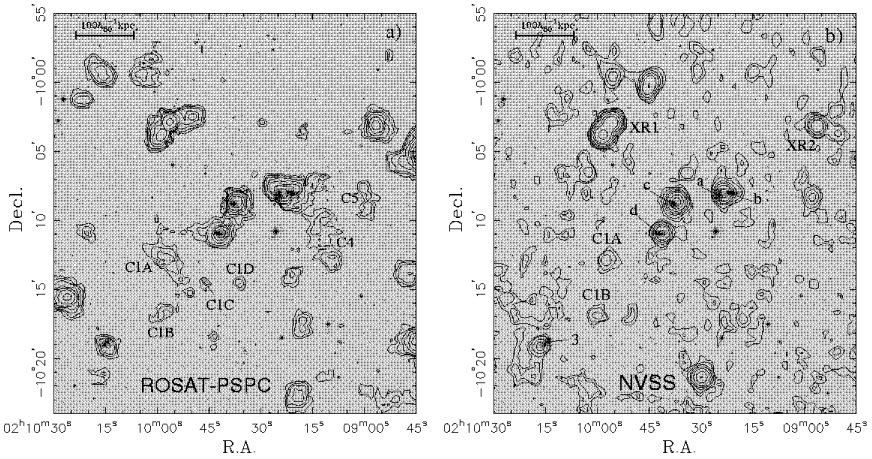

Figure 1. Contour maps of (a): the adaptively smoothed (50 counts per smoothing circle) ROSAT/PSPC X-ray emission, b): the NVSS 20 cm radio emission of HCG 16, both superimposed on an optical DSS image. The five polygonal regions (C1–C5) dividing the emission region in HCG 16 are also shown, as well as the different components of region C1 (C1A, C1B, C1C and C1D, see text).

Figure 1b shows the 20 cm continuum radio contours, measured with the NVSS survey, and illustrates *the similarity between the X-ray and 20 cm continuum radio morphologies of HCG 16.* A closer look (Dos Santos & Mamon 1999) reveals that C1A is connected with a radio-galaxy, which turns out to have a redshift (Ribeiro et al. 1996) that clearly places it in the background, C1B is connected with a radio-source, C1C is related to a foreground star, and C5 is connected to a radio-source and to a background group or cluster. This reduces the X-ray luminosity of the diffuse hot gas connected with HCG 16 by 50% to $L_X^{\rm bol} = 2.3 \times 10^{41}\, h_{50}^{-2} {\rm erg\,s^{-1}}$. In the regions without significant X-ray emission, the upper limits to the counts correspond to at most 1/4 the the space density of hot gas in the detected regions. Hence, *the hot gas in HCG 16 is clumpy.*

3.2. Large-scale environment

If HCG 16 is part a cosmological filament viewed nearly end-on (HKW), one should see this filament in its large-scale environment. We have searched with NED a roughly cubical region around HCG 16 of $40\, h_{50}^{-1}$ Mpc size. HCG 16 is close enough ($cz = 3899\,{\rm km\,s^{-1}}$) that NED should be fairly complete around it.

The projected environment of HCG 16 within $\pm 1000\,{\rm km\,s^{-1}}$ from the group distance (Fig. 2a) suggests concentration of galaxies along 4 projection angles. Figure 2b shows the wedge diagrams in each of these position angles, and one can guess a filament at PA = 31°, stopping at HCG 16 and a wide sheet visible

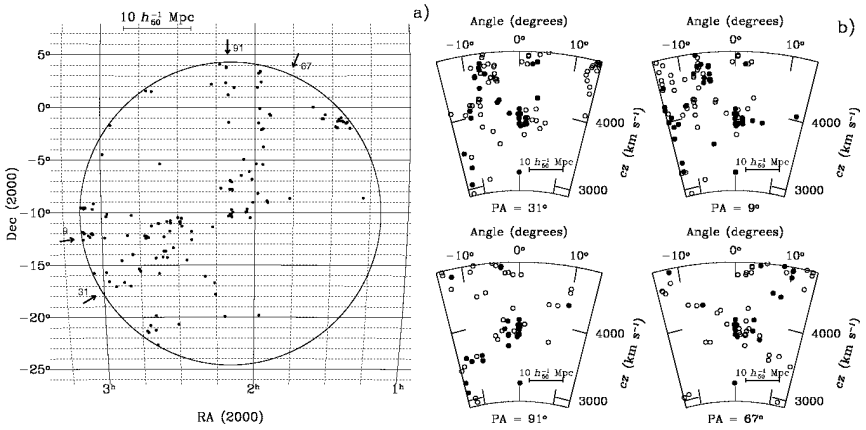

Figure 2. Environment of HCG 16, limited to $cz = 3899 \pm 1000\,\mathrm{km\,s^{-1}}$. a) Projected environment (HCG 16 in center). b) Line-of-sight environments from wedge diagrams at 4 position angles. *Filled* and *open* symbols refer to galaxies within projected distances of respectively 1 and $5\,h_{50}^{-1}$ Mpc from the major axis of the projected wedge. HCG 16 and its 3 neighboring galaxies appear as the *finger of God* of filled symbols at the center of each diagram.

at PA = 91° and 67°. *There are no filaments closely aligned to the line-of-sight* as would have been favored by HKW.

4. Cosmological predictions on the mass functions of groups

Although loose groups have generally not yet collapsed, one can apply the Press & Schechter (1974, hereafter, PS) formalism to these systems, assuming that when they will collapse, their mass is what we infer today ($t = t_0$). We then obtain

$$N_{\rm LG}(M, t_0) = \int_{t_0}^{2\,t_0} dt\, R_{\rm form}(M, t)\ , \qquad (2)$$

where $R_{\rm form}$ is the rate of formation of structures derived by Kitayama & Suto (1996) from the PS formalism.

N-body simulations suggest that compact groups cannot survive (with at least 4 members) for over $\Delta t = 0.05 - 0.10\,t_0$ (Bode et al. 1993; Athanassoula et al. 1997; Athanassoula in these proceedings), the fraction increasing with mass. Assume therefore that compact groups must have undergone their cosmological collapse within that time. One then obtains

$$N_{\rm DG}(M, t_0) = \int_{t_0-\Delta t}^{t_0} dt \int_{M/2}^{M} dM' R_{\rm form}(M', t) P(M, t_0 | M', t)\ , \qquad (3)$$

where P is the probability that a dense group of mass M exists today given that it collapsed with a mass $M' < M$ at time $t < t_0$ (given by Lacey & Cole 1993).

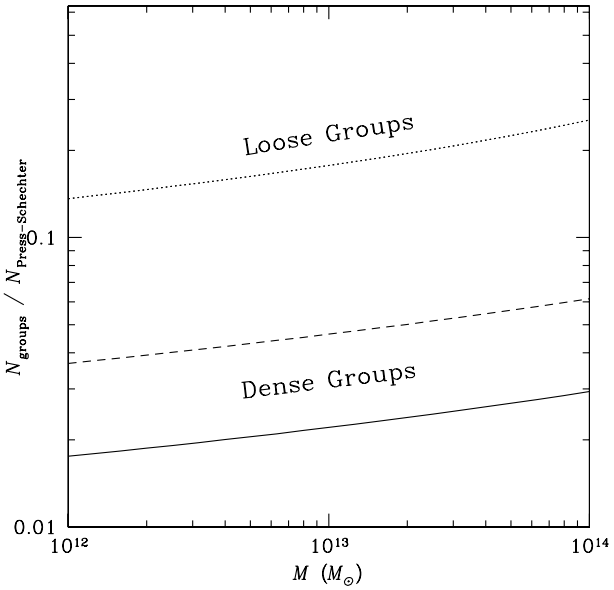

Figure 3. Loose (*thin dotted curve*) and dense (*thick curves*) group mass functions scaled to the Press-Schechter cosmic mass function, derived from extended Press-Schechter theory (eqs.[2] and [3]), assuming a ΛCDM cosmology with $\sigma_8 = 0.9$. *Dashed* and *solid curves* refer to dense groups collapsing later than 0.9 and $0.95\,t_0$, respectively.

Figure 3 shows the resulting loose and dense group mass functions, both normalized to the PS cosmic mass function, for a ΛCDM cosmology (SCDM and OCDM with reasonable values for σ_8 yield roughly similar curves). Massive dense groups survive longer simply because they have more galaxies, so the figure should be interpreted by adopting the recent collapse (*solid curve*) for the lower mass end and the earlier collapse for the high mass end. The ratio of dense to loose groups then varies with increasing group mass from 12 to 20%. If compact groups are replenished by infalling galaxies (Governato et al. 1996), they collapse even earlier and we would predict even more compact groups today.

In contrast, the estimates of the ratio of HCGs to loose groups range from 0.5–8% (Walke & Mamon 1989; see also Mamon 1986, 1992). Comparison of the HCG sample with a similar compact group sample automatically selected from COSMOS/EDSGC galaxies (Prandoni et al. 1994; Iovino in these proceedings) shows that the HCG sample is severely incomplete: inspection of Prandoni et al.'s Fig. 7 suggests that the incompleteness of the HCG sample is a factor of 3 at the bright-end and increasingly worse at fainter magnitudes.

Now if dense groups represent only a few percent of the cosmic mass function, where are the remaining virialized cosmic structures with masses near $10^{13}\,M_{\odot}$? The answer is simple: *the remaining structures collapsed too early to be visible as compact groups today, and must then be in different stages of the final coalescence of groups.* This includes quartets with massive dominant members (thus failing Hickson's 1982 magnitude concordance criterion: $m - m_1 < 3$), as well as triplets, and binaries. But since the cosmic multiplicity function decreases with increasing galaxy number, one is led to conclude that most of the missing structures are fully coalesced, single galaxies, which harbor large X-ray halos, as discovered by Mulchaey & Zabludoff (1999, see Mulchaey, in these proceedings) and Vikhlinin et al. (1999). Therefore, we predict that *X-ray overluminous ellipticals should be more common than compact groups.*

5. Why Hickson's compact groups are dense in 3D after all

It is very difficult to decide whether the numerous signatures of galaxy interactions in CGs are proofs of their reality or alternatively simply binary interactions within binary-rich chance alignments of galaxies within the line of sight (Mamon 1992; Hernquist et al. 1995). The high fraction of HCGs with diffuse X-ray emission (PBEB) should be reduced when only considers groups with *regular* diffuse X-rays (§ 3.1). However, the combination of HI (Verdes-Montenegro, in these proceedings) and optical (Mendes de Oliveira, in these proceedings) data on HCGs suggests that most of these are real interacting systems. In view of this beautiful data, the arguments spelled out by Mamon (1986) against the reality of HCGs must be reappraised.

The large predicted cosmic rate of production of dense groups (§ 4 above) implies that the low survival time of dense groups is no longer a good argument against the reality of most compact groups. Moreover, the end products of dense groups — isolated bright elliptical galaxies with huge X-ray halos — are now being seen (Mulchaey & Zabludoff 1999; Vikhlinin et al. 1999).

Whereas mergers tend to increase rapidly the difference in first and second ranked magnitudes, the low $\langle m_2 - m_1 \rangle$ of HCGs (Mamon 1986, 1987) is simply caused by Hickson's strong bias (Prandoni et al. 1994) against groups with dominant members still satisfying the magnitude concordance criterion. This bias probably also causes the absence of significant luminosity segregation in comparison with simulated groups (Mamon 1986, 1987).

The morphology-density relation of HCGs is offset (Mamon 1986) relative to the cluster / loose group / field morphology-density relation (measured by Postman & Geller 1984): at a given galaxy number density, HCGs have too many spirals. However, HCGs have too *few* spirals given their velocity dispersions in comparison with the cluster morphology-velocity dispersion trend (PBEB).

There happens to be virtually no low velocity dispersion HCGs beyond $10{,}000\,\mathrm{km\,s^{-1}}$, therefore the number of HCGs whose low velocity dispersion (§ 2) suggests they are non-real is limited to roughly 10 out of 69 accordant redshift HCGs with at least 4 members.

Therefore, *there are few arguments left against the reality of HCGs.* However, the samples of automatically defined compact groups (Iovino, in these proceedings) will be much looser on average (given the same compactness crite-

rion as originally used by Hickson), since the HCG sample is severely incomplete for marginally compact groups (Walke & Mamon 1989; Prandoni et al. 1994), hence one would expect that *automatically selected compact groups will be more prone to chance alignments* (see Walke & Mamon 1989).

Acknowledgments. The work on HCG 16 was performed in collaboration with Sergio Dos Santos. I thank Trevor Ponman for useful discussions.

References

Athanassoula, E., Makino, J., Bosma, A., 1997, MNRAS 286, 825

Bode, P.W., Cohn, H.N., Lugger, P.M., 1993, ApJ 416, 17

de Carvalho, R.R., Ribeiro, A.L.B., Zepf, S.E., 1994, ApJS 93, 47

Dos Santos, S., Mamon, G.A., 1999, A&A in press, astro-ph/9811271

Governato, F., Bhatia, R., Chincarini, G., 1991, ApJ 371, L15

Governato, F., Tozzi, P., Cavaliere, A., 1996, ApJ 458, 18

Hernquist, L., Katz, N., Weinberg, D.H., 1995, ApJ 442, 57 (HKW)

Hickson, P., 1982, ApJ 255, 382

Kitayama, T., Suto, Y., 1996, MNRAS 280, 638

Lacey, C., Cole, S., 1993, MNRAS 262, 627

Mamon, G.A., 1986, ApJ 307, 426

Mamon, G.A., 1987, ApJ 321, 622

Mamon, G.A., 1992, in 2nd DAEC mtg., Distribution of Matter in the Universe, G.A. Mamon, D. Gerbal, Paris: Obs. de Paris, p. 51, ftp://ftp.iap.fr/pub/from_users/gam/PAPERS/daec92-cg.dvi.Z

Mamon, G.A., 1999, to be submitted to A&A

Mulchaey, J.S., Zabludoff, A.I., 1999, ApJ 514, 133

Navarro, J.F., Frenk, C.S., White, S.D.M., 1995, MNRAS 275, 720

Ponman, T.J., Bourner, P.D.J., Ebeling, H., Böhringer, H., 1996, MNRAS 283, 690 (PBEB)

Postman, M., Geller, M.J., 1984, ApJ 281, 95

Prandoni, I., Iovino, A., MacGillivray, H.T., 1994, AJ 107, 1235

Press, W.H., Schechter, P., 1974, ApJ 187, 425

Ribeiro, A.L.B., de Carvalho, R.R., Coziol, R., Capelato, H.V., Zepf, S.E., 1996, ApJ 463, L5

Saracco, P., Ciliegi, P., 1995, A&A 301, 348

Vikhlinin, A., McNamara, B.R., Hornstrup, A., Quintana, H., Forman, W., Jones, C., Way, M., 1999, ApJ 520, L1

Walke, D.G., Mamon, G.A., 1989, A&A 225, 291

Weinberger, R., Temporin, S., Kerber, F., 1999, ApJ in press, astro-ph/9907304

Zabludoff, A.I., Mulchaey, J.S., 1998, ApJ 496, 39

D Sélection de proceedings publiés sur l'Univers Local en Proche-IR

D.1 Galaxies with DENIS: preliminary star/galaxy separation and first results

Mamon, Borsenberger, Tricottet & Banchet, 1998, dans *The Impact of Near-Infrared Surveys on Galactic and Extragalactic Astronomy, p. 177, arXiv:astro-ph/9712169*

Invited review to appear in "The Impact of Near-Infrared Surveys on Galactic and Extragalactic Astronomy", meeting held in Meudon, France, June 1997, ed. N. Epchtein (Dordrecht: Kluwer, p. 177)

GALAXIES WITH DENIS:

Preliminary star/galaxy separation and first results

GARY A. MAMON
Institut d'Astrophysique de Paris & DAEC, Obs. de Paris
98 bis Bd Arago, F–75014, Paris, FRANCE

AND

JEAN BORSENBERGER, M. TRICOTTET AND V. BANCHET
Institut d'Astrophysique de Paris

Abstract. The numerous extragalactic and cosmological motivations of the DENIS and 2MASS near infrared surveys are outlined. The performance of the DENIS survey is estimated from $50\,\mathrm{deg}^2$ of high galactic latitude data ($20° < |b| < 60°$). Simple star/galaxy separation methods are presented and comparison with 300 visually classified objects as well as COSMOS and APM classifications. We find that the peak intensity over isophotal area is an excellent star/galaxy separation algorithm, fairly robust to variations of the PSF within the frames, achieving 98.5% completeness and 92.5% reliability for $I < 16.5$, in comparison with visual classification. A new estimate of the photometric accuracy for galaxies is presented. The limiting factors for homogeneous galaxy extraction at high galactic latitudes are completeness and photometric accuracy in K, photometric accuracy in J and star/galaxy separation in I (also used for classification in J and K). Galaxy counts are presented on $50\,\mathrm{deg}^2$. The I counts are in excellent agreement with a Euclidean extrapolation of the published counts around $I = 16 - 17$ (more so than in all previous studies), and thus point to a high normalization at the bright end, in contrast with the counts published from the APM and COSMOS plate scans. The J-band differential galaxy counts follow the relation $N(J) = 12 \pm 1\,\mathrm{dex}(0.6\,[J-14])\,\mathrm{deg}^{-2}\mathrm{mag}^{-1}$. Extrapolation of these high latitude counts suggest that DENIS will produce highly homogeneous catalogs of $\simeq 6000$ ($K < 11$), $\simeq 700\,000$ ($J < 14.8$) and, $\simeq 1\,000\,000$ ($I < 16.5$) galaxies, respectively with photometric accuracy of 0.08^m in I and 0.20^m in J and K. Larger highly homogeneous samples are expected with improvements to the camera and the algorithms.

1. Introduction

The DENIS consortium has been imaging the southern sky in the I (0.8μm), J (1.25μm) and K_s (2.15μm) wavebands since December 1995. When the survey is complete, around 2000–2001, we expect to have extracted tens of thousands of galaxies in K, roughly one million in J, and a few million in I (see § 7 below for our estimated sizes of homogeneous, highly complete, reliable and photometrically accurate galaxy catalogs).

Much of the information in this review has been given elsewhere (Mamon et al. 1997b). The notable improvements here are improved reliability estimates from a much larger visually classified sample, a first-order optimization of star/galaxy separation yielding a one-half magnitude improvement in the high completeness/reliability magnitude limit and a more accurate estimate of the photometric accuracy.

2. Prospective scientific impact

Wide-angle near infrared (hereafter NIR) galaxy surveys, such as DENIS and 2MASS (see Schneider, Jarrett, Rosenberg and Cutri, all in these proceedings) will have a wide array of scientific prospects, of which a few are listed below. The two important advantages of NIR selection are 1) the near transparency of interstellar dust in our foreground Galaxy and within external galaxies, and 2) the low sensitivity of NIR light to recent star formation in galaxies (see Mamon et al. 1997b), hence a better estimation of the stellar mass content of galaxies in the NIR.

Statistics of NIR properties of galaxies: DENIS and 2MASS will provide the first very large galaxy databases with NIR photometry. Photometry of the brighter galaxies will be coupled with redshift measurements, either already made, or performed during spectroscopic followups (see, e.g., Mamon 1996; Paturel, in these proceedings) to be used for distance estimates and computation of precise parameters of the fundamental plane and Tully-Fisher relations (see Vauglin et al. 1997; Rosenberg, in these proceedings).

Cross-identification with other wavelengths: The extragalactic objects extracted by DENIS and 2MASS will be cross-identified with analogous samples at other wavelengths, such as optical galaxy samples, for example in the Zone of Avoidance (see Kraan-Korteweg et al., in these proceedings), IRAS galaxies (Saunders et al. 1997), quasars (see Cutri, in these proceedings), radio-galaxies, galaxies found in blind HI surveys (see Kraan-Korteweg et al., in these proceedings), etc. The NIR properties (mainly their location in color-color diagrams) of such objects will be targeted for discovering new

large samples of such objects. One should expect followups at non-NIR wavelengths of DENIS and 2MASS galaxies.

Galaxy counts: There has been a debate on the level of galaxy counts at the bright end, as first estimates (Heydon-Dumbleton et al. 1989; Maddox et al. 1990) found a depletion relative to the extrapolation of the faint-end counts, while later work (e.g. Bertin & Dennefeld 1997) disputed this. This debate has consequences on galaxy evolution and on whether the environment of the Local Group is underdense on very large scales ($z \lesssim 0.1$).

Zone of avoidance There are two main applications for studying galaxies behind the Galactic Plane (see Kraan-Korteweg et al., in these proceedings): 1) Mapping the large-scale distribution of galaxies in this still poorly known region. Indeed, the Zone of Avoidance contains interesting structures such as the largest large-scale concentration of matter in the local Universe, the Great Attractor (at the intersection of the Supergalactic Plane and the Galactic Plane, Kolatt, Dekel & Lahav 1995) and within the Great Attractor, the Norma cluster, Abell 3627, richer and closer than the Coma cluster (Kraan-Korteweg et al. 1995). 2) The fluxes and angular sizes of galaxies are affected by extinction from dust in the Galactic Plane, and one can measure this extinction from galaxy counts (Burstein & Heiles 1982), colors (Mamon et al. 1997a), and color-color diagrams (Schröder et al. 1997, and Kraan-Korteweg et al., in these proceedings).

Small-scale structures of galaxies Only a few catalogs of clusters (Lumsden et al. 1992; Dalton et al. 1997; Escalera & MacGillivray 1995, 1996) and compact groups (Prandoni, Iovino & MacGillivray 1994) are based upon automatically selected galaxy samples, which happen to be optical and photographic (hence subject to photometric non-linearities). Because star formation is probably enhanced by galaxy interactions, one expects that the statistical properties of pairs, groups and clusters of galaxies built from NIR selected galaxy catalogs will be different from those built from optical catalogs. DENIS and 2MASS will thus have the double advantage of using a NIR galaxy sampled based upon linear (non-photographic) photometry. The applications of such NIR-based samples of structures of galaxies are numerous (e.g. Mamon 1994) and include understanding the dynamics of these structures, their bias to projection effects, their constraints on Ω_0 and the primordial density fluctuation spectrum, their use as distance indicators, and the environmental influences on galaxies.

Large-scale structure of the Universe: The NIR selection and the linear photometry will also benefit the measurement of statistics (two-point

and higher-order angular correlation functions, counts in cells, topological genus, etc.) of the large-scale distribution of galaxies in the Universe. For example, the (3D) primordial density fluctuation spectrum of galaxy clustering can be obtained from the two-point angular correlation function (Baugh & Efstathiou 1993) or from the 2D power spectrum (Baugh & Efstathiou 1994). Moreover, by the end of DENIS and 2MASS, large-scale cosmological simulations with gas dynamics incorporated (thanks to which galaxies are properly identified) will provide adequate galaxy statistics in projection that will be compared with those obtained from the surveys, iterating over the cosmological input parameters of the simulations.

3. Galaxy extraction and current galaxy pipeline

The current galaxy pipeline consists of the following steps:

1) Bias subtraction, flat-fielding, bad pixel mapping and astrometric calibration (standard DENIS Paris Data Analysis Center pipeline, Borsenberger 1997); 2) Cosmic ray removal; 3) Extraction of photometric zeropoints and airmasses from relevant files; 4) Galaxy extraction using the *SExtractor* (Bertin & Arnouts 1996) object extraction software, version 1.2b6a (which includes a neural-network star/galaxy separator, Bertin 1996, whose input parameters are 8 isophotal areas, the maximum intensity and as a control parameter, the FWHM of the PSF), with detection and Kron (1980) photometry parameters optimized from simulated images.

4. Star/galaxy separation

Nevertheless, star/galaxy separation is intrinsically difficult because, at the galaxy extraction limits $I \simeq 16.5$ (see below), DENIS will extract roughly 5.5 times as many stars as galaxies in I, at very high galactic latitude ($|b| \simeq 70°$, see Lidman & Peterson 1996), and the ratio worsens considerably at lower galactic latitudes and at brighter magnitudes.

We discuss below the steps towards an efficient star/galaxy separation method. For this, we extracted in the I band (which has the best angular resolution) classical star/galaxy separation diagnostics such as isophotal area, peak intensity, and FWHM, as well as the neural-network based stellarity parameter, in a direct fashion, or using a suitably modified version of SExtractor that includes a two-dimensional modeling of the PSF that is used as input to the neural network.

Figure 1 shows how these quantities vary with magnitude for all objects at least 20 pixels from the frame edges on a high latitude strip.

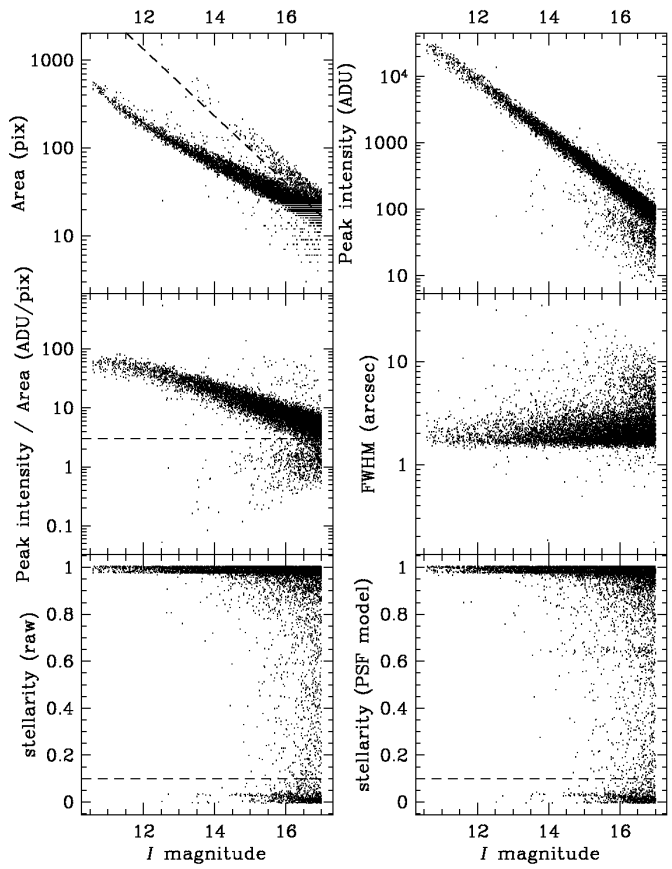

Figure 1. Diagnostics of star/galaxy separation over one DENIS (6 deg^2) strip. The *dashed lines* are the critical lines for selection of candidates for visual classification (see § 4.1).

4.1. TESTS OF AUTOMATIC STAR/GALAXY SEPARATION

One of us (G.A.M.) has classified by eye a set of 329 galaxy candidates on 109 DENIS I band images (of which 33 appeared on consecutive images, leaving 296 unique candidates). These candidates were chosen with $I \leq$

16.5, centers at least 20 pixels from the image borders. Furthermore, they met *at least one* of the following loose (to ensure completeness) galaxy criteria (*dashed lines* in Fig. 1):

- Isophotal area: $A \geq 40\,\mathrm{dex}[-0.38(I-16)]$ pixels
- Pseudo surface brightness: $\Sigma = I_{\rm peak}/A \leq 3$ ADU/pixels
- Neural-network stellarity before PSF modeling: $s_0 \leq 0.1$
- Neural-network stellarity after PSF modeling: $s \leq 0.1$

We've used 5 sets of truth tables:

- Visual DENIS I (see above)
- COSMOS b_J
- APM b_J
- APM r_F
- A mix of the previous 4

The COSMOS and APM lists were obtained through the World Wide Web (`telnet://catalogues apm3.ast.cam.ac.uk` for the APM and `telnet://cosmos cosmos.aao.gov.au` for COSMOS).

We've optimized each of the 6 algorithms plotted in Figure 1 for a linear star/galaxy separator in these plots (slope and normalization, except that we forced a zero slope for the two neural network algorithms). The results are showed in Figure 2, which plots the completeness-reliability plots for 4 of the 5 truth tables. The different points in Figure 2 for a given algorithm correspond to different cuts through the algorithm versus magnitude diagram and we only plotted the optimal slope, varying the normalization.

Figure 2 shows that the pseudo-surface brightness criterion is slightly superior to the peak intensity, which, in turn, is slightly superior to the isophotal area (except for the COSMOS-based truth table, for which isophotal area does best). The other three algorithms (FWHM, and neural network stellarity before and after PSF modeling), are far inferior to the first three algorithms. For the visually classified DENIS I sample, we achieve 92.5% reliability at 98% completeness, and for the global sample we obtain 96% reliability at 96% completeness. The poor results of the neural networks is probably due to the variations of the PSF across the frames, and for this particular DENIS strip (number 5570), PSF modeling worsened the results!

4.2. COSMOS AND APM VERSUS VISUAL STAR/GALAXY SEPARATION

Table 1 shows the comparison between the visual classification and the classification obtained from the COSMOS and APM lists.

Of the 11 objects termed as junk, 3 were fragments of a bright galaxy, two were deemed optical flaws, but according to both APM and COSMOS, one of those was a star.

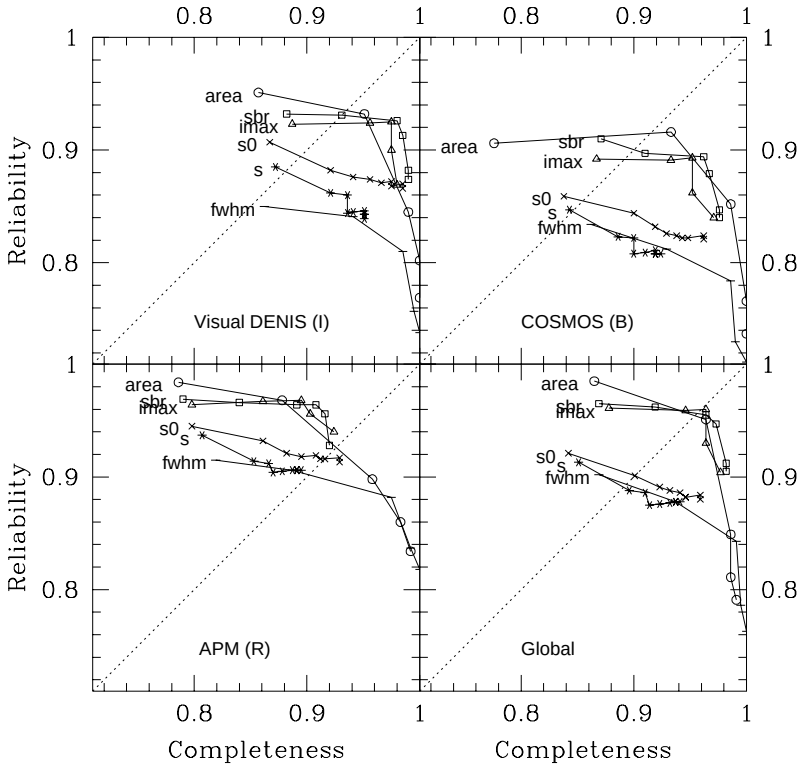

Figure 2. Completeness versus reliability of different automatic star/galaxy separation algorithms using 4 different truth tables. The algorithms are isophotal area (`area`), peak intensity (`imax`), pseudo-surface brightness (`sbr`), star/galaxy separation without PSF modeling (`s0`), star/galaxy separation with PSF modeling (`s`), and full-width half maximum (`fwhm`).

The numbers in Table 1 do not permit to establish which star/galaxy separation is best between visual DENIS, APM or COSMOS. However, if one assumes that visual DENIS star/galaxy separation is perfect, one would then conclude that APM and COSMOS both have a completeness of $193/203 = 95\%$ at $I = 16.5$ (this also assumes that the DENIS I extraction is 100% complete, which remains to be proven). The reliability of the extraction would then be $193/210 = 91\%$ for COSMOS and $193/218 = 89\%$ for APM.

TABLE 1. Visual DENIS I versus COSMOS and APM star/galaxy separation

Visual DENIS I		COSMOS b_J			APM b_J			
Type	Total	Galaxy	Star	Notfound	Galaxy	Star	Faint	Notfound
Galaxy	203	193	10	0	193	5	3	2
Star	53	6	46	1	9	42	1	1
Star+Star	8	4	3	1	4	3	0	1
Faint	21	7	11	3	10	10	0	1
Junk	11	0	2	9	2	3	3	3
Total	296	210	72	14	218	63	7	8

If one assumes that APM or COSMOS are complete, than the incompleteness of the DENIS galaxy extraction can be estimated from the objects too faint for DENIS visual classification but called galaxies by the optical surveys. One obtains completeness levels of 95% or 97% at $I = 16.5$ using APM or COSMOS, respectively. Of course, if the visual classification were imperfect and that objects classified as stars or double stars are in fact galaxies, the completeness of DENIS visual classification would decrease to levels of 90% or 92% using APM or COSMOS, respectively. Moreover, DENIS may not have detected objects at $I = 16.5$ that are seen in the optical surveys, and this issue will be addressed in a forthcoming publication.

4.3. QUICK AND DIRTY AUTOMATIC STAR/GALAXY SEPARATION

Since the pseudo-surface brightness criterion seems to produce the best star/galaxy separation, we have adopted the following preliminary algorithm for each DENIS strip:

We adopt a constant critical pseudo surface brightness (independent of magnitude — the optimal slope with respect to the visual DENIS I, COSMOS B, APM B, and global classifications was 0.05), by fitting with a cubic polynomial the histogram of the values of $\Sigma = I_{\rm peak}/A$ for $I \leq 16.5$, in a range chosen to exclude the peak due to the stars. Although $k\sigma$ curves down from the stellar locus have negative slope, the higher slope of the galaxy counts relative to the star counts leads us to believe that a given reliability will be achieved with a cut of k that decreases with magnitude, *i.e.,* with a lower slope for $\Sigma_{\rm crit}$. This may explain why the optimal slope is non-negative.

For the J and K bands, we rely on the star/galaxy separation performed in the I band. Because the I band has better angular resolution and is more

sensitive than J or K (except at very low galactic latitudes, corresponding to visual extinction $A_B > 3$, see Kraan-Korteweg et al., in these proceedings), using I-band star/galaxy separation is superior to doing star/galaxy separation directly in J or in K.

Our star/galaxy separation, relying only on pseudo surface brightness is simpler than in our previous work (Mamon et al. 1997b), where we required out galaxies to satisfy both neural network stellarity (after PSF modeling) and isophotal area algorithms, and our former star/galaxy separation method had the disadvantage of using a fixed critical isophotal area line, whereas strip to strip variations of the PSF lead to variations of this critical line from one strip to another.

We have thus analyzed a little over $50\,\mathrm{deg}^2$ of DENIS data, restricting ourselves here to $I < 17$.

5. Photometry

We estimate below the accuracy of DENIS galaxy photometry using objects within image overlaps and comparing with APM and COSMOS, and we use color-magnitude diagnostics as an additional test on the reliability of star/galaxy separation.

5.1. PHOTOMETRIC ACCURACY FROM OVERLAPS

Figure 3 shows the magnitude differences on unflagged overlap objects extracted from $50\ \mathrm{deg}^2$ of high galactic latitude data.

Contrary to the analogous figure in Mamon et al. (1997b), we have high certainty on the extragalactic nature of the J-band and K-band overlap objects (since again, we rely on I-band star/galaxy separation). For this reason, the photometric accuracy is worse than given in Mamon et al. (1997b): The rms error on a single measure is 0.05 at $I = 15$, 0.10 at $I = 17$, 0.10 at $J = 13.7$, and 0.20 at $J = 14.8$. There are too few K overlaps to conclude strongly, but indications (based upon only 4 points!) are that the rms photometric accuracy for a single measure is roughly 0.20 at $K \simeq 12.2$. The J-band photometric accuracy was considerably better in our previous study (Mamon et al. 1997b), but unreliable direct (using neural network stellarity in J lower than 0.2) star/galaxy separation had been used for the photometric accuracy study of that work, and the inclusion of stars tends to improve the photometric accuracy.

5.2. COMPARISON OF DENIS GALAXY PHOTOMETRY WITH COSMOS

For the $3.6\,\mathrm{deg}^2$ region in which we visually classified our extracted objects, we plot in Figure 4 the color-magnitude relation obtained with COSMOS

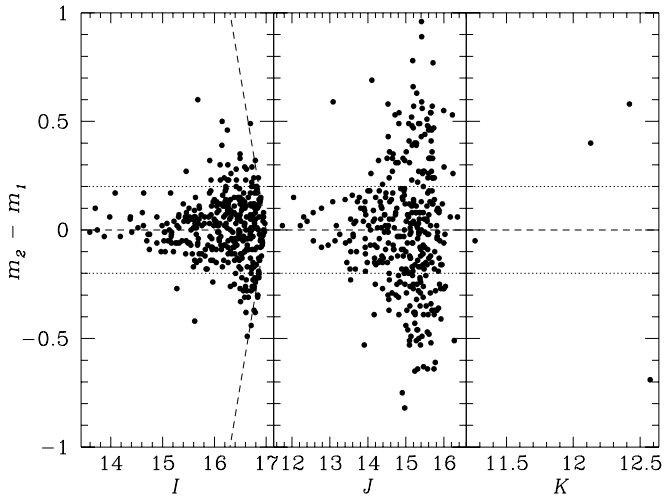

Figure 3. Photometric accuracy for galaxies lying within overlaps of 2 images, extracted within 50 deg^2 of high galactic latitude ($20° < |b| 60°$) DENIS data. Objects closer than 20 pixels to the frame edges are excluded). The *tilted dashed line* represents an $I \leq 17$ selection, whose effects are also seen in the J band.

b_J photometry, taken from the World Wide Web. This figure shows the difficulties in star/galaxy separation, as a number of points lie far off the $B - I \simeq 2 - 3$ region. Part of this difficulty lies in poor star/galaxy separation from COSMOS. Moreover, there is a trend for bluer galaxy colors at brighter magnitudes, which we interpret as poor photometry on the COSMOS side, because of inaccurate compensation for plate saturation.

We also attempted the same with APM data from the World Wide Web, but that photometry suffers from unusually strong systematic errors at the bright end (up to 6 mag difference with COSMOS!), as the photometric calibration has been optimized for stars that saturate at these magnitudes (Maddox, private communication).

5.3. COLORS OF DENIS GALAXIES

Figure 5 shows the color-magnitude diagram for the galaxies. The bluest two points turn out to be galaxies! Visual inspection shows that they are low surface brightness galaxies that are barely visible in J (and invisible in K). The use of adaptive aperture photometry to define colors makes such objects appear very blue. We checked that their central colors are normal.

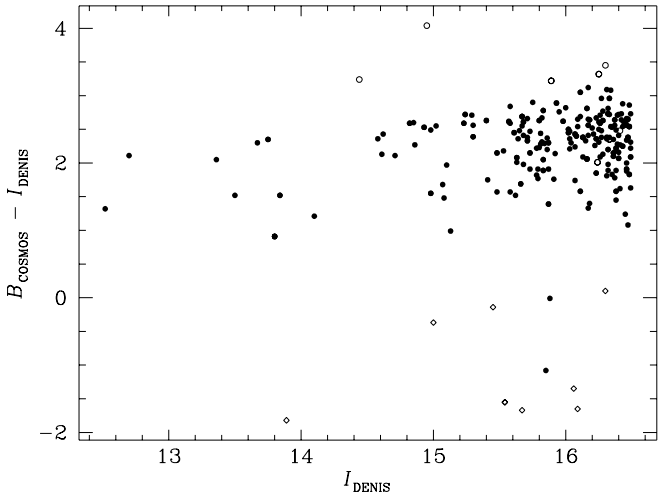

Figure 4. Color-magnitude diagram for galaxies extracted within 3.6 deg^2 of high galactic latitude ($20^\circ < |b| 60^\circ$) DENIS data. *Diamonds* refer to objects classified as stars by COSMOS, but as galaxies by APM, DENIS visual inspection and all DENIS automatic star/galaxy separation algorithms. *Open circles* are objects classified as galaxies with low certainty by the DENIS visual classification and that were not stars in COSMOS.

Figure 5 shows that at the limit $J = 14.8$ for $\Delta J = 0.20$ mag photometric accuracy, the star/galaxy separation performed in I should be roughly as reliable as at $I = 16.5$, and could be made even more reliable by culling out the reddest objects for which $I > 16.5$.

In Figure 6, we plot the color-color diagram for extracted galaxies. The galaxy colors cluster around $I - J = 1.2 \pm 0.3$, $J - K = 1.1 \pm 0.5$, but there are indications for fairly bright objects with red $J - K \simeq 2$ colors, which upon visual inspection are confirmed as galaxies. An important fraction of the points off the central cluster lie near the frame edges where the PSF is larger. The large open circle refers to an object too faint in I for reliable star/galaxy separation, and indeed, visual inspection shows it to be a star blended with a faint galaxy.

6. Galaxy counts

Figure 7 illustrates our IJK galaxy counts. The K-band counts become incomplete at $K \simeq 11$, in comparison to both published counts by Gardner et al. (1996) and to the expected Euclidean 0.6 slope (the completeness is still roughly 50% at $K = 12$).

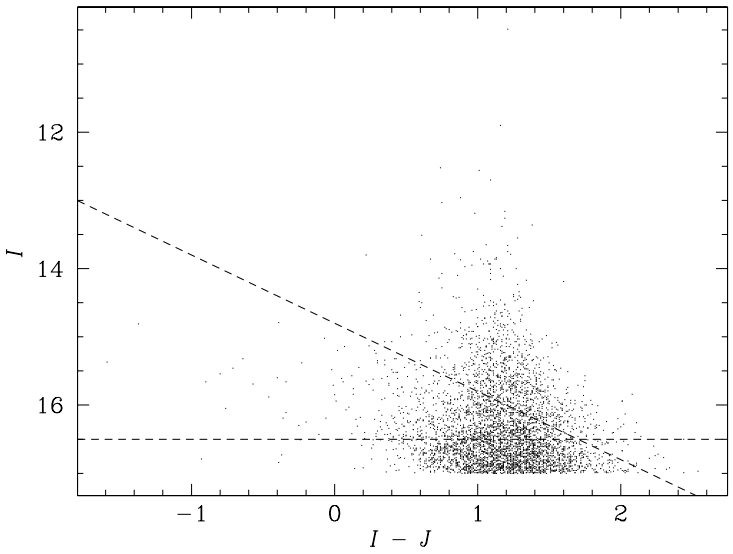

Figure 5. Color-magnitude diagram for galaxies extracted within 50 deg^2 of high galactic latitude ($20° < |b| < 60°$) DENIS data. Objects closer than 20 pixels to the frame edges are excluded. The *horizontal line* represents $I = 16.5$ (the and the dashed line represents $J = 14.8$ (the limit for 0.20 mag J-band photometry and reliable star/galaxy separation).

The I band counts match well the published data, although Lidman and Peterson (1996) find fewer counts at the bright end, while Gardner et al. find more counts at the bright end (the two sets of published data differ by a factor of 3 at $I < 15$). Note that DENIS, Gardner *et al.* and Lidman & Peterson all work with the Cousins I band, so no conversion was made from another I filter. Also, our survey has smaller error bars at the bright end as it covers 4 to 5 times the solid angle of the two cited surveys. Our bright-end I-band counts are more consistent with the extrapolation of the faint counts with a Euclidean slope than either two sets of published data (our high value at $I = 16.5$ is caused by important stellar contamination in the fainter half of the bin; also, at $I > 18$, the published counts become lower than the Euclidean line because of significant k-correction at these magnitudes). In this sense, although not as high as Gardner et al.'s counts, *the DENIS I-band counts argue for a high bright-end normalization, consistent with little galaxy evolution at the bright end*, in line with analogous findings by Bertin and Dennefeld (1997) using blue counts.

The J counts are new (although they were already shown in Mamon

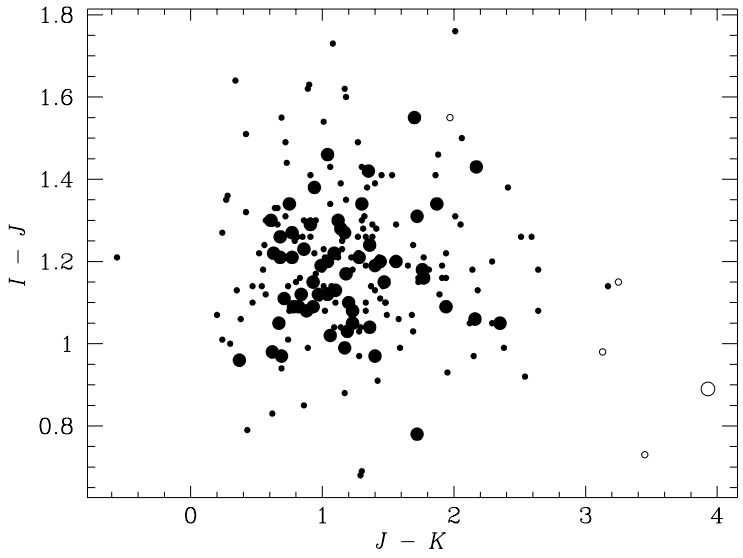

Figure 6. Color-magnitude diagram for galaxies extracted within 50 deg^2 of high galactic latitude ($20° < |b| < 60°$) DENIS data. Objects closer than 20 pixels to the frame edges are excluded. *Large* and *small circles* are for objects brighter or fainter than $K = 12$ (the limit for fairly accurate K photometry, see § 5.1), respectively. *Filled* and *open circles* correspond to objects brighter and fainter than $I = 16.5$ (the rough limit for reliable star/galaxy separation, see § 4.1), respectively.

et al. 1997b). They are highly complete to $J = 15$, follow very well the Euclidean slope of 0.6, and are well described by the relation $N(J) \simeq 12 \times \mathrm{dex}[0.6\,(J-14)]\,\mathrm{deg}^{-2}\,\mathrm{mag}^{-1}$.

7. Discussion

From the results of the preceding sections, we can establish limits for the homogeneous extraction of galaxies from DENIS, as given in Table 2.

The limiting factors turn out to be star/galaxy separation in I, photometry and star/galaxy separation in J, and detection in K (assuming that I-band star/galaxy separation is used to classify objects detected in the other bands).

Using the counts from Figure 7 to extrapolate to the entire survey area (roughly a hemisphere), we infer that our homogeneous catalogs will have sizes of 6000 at $K < 11$ (0.2 mag photometry), 100 000 to 500 000 at $J <$ 13.7 and 14.8 (with 0.2 and 0.1 mag photometry, respectively), and 900 000

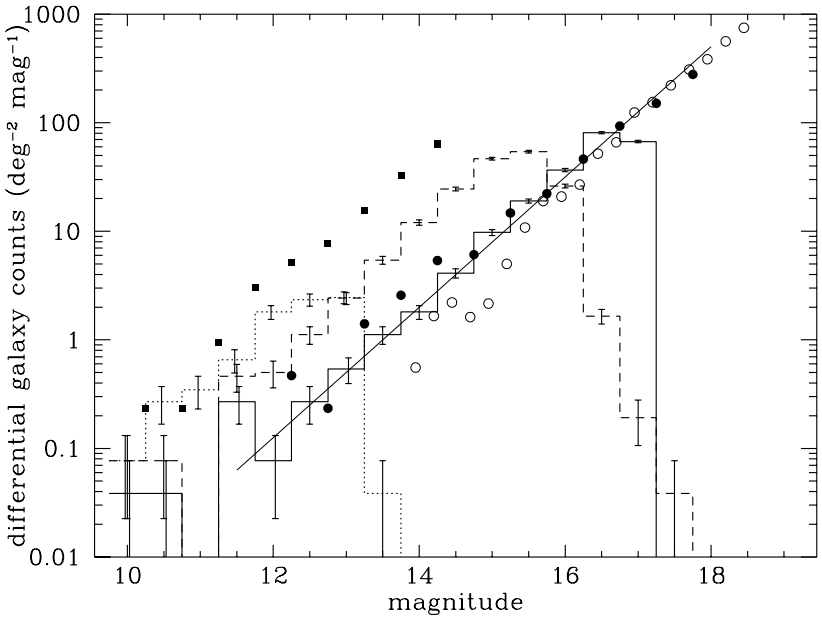

Figure 7. Differential galaxy counts over 50 deg^2 of high galactic latitude ($20° < |b| 60°$), $I < 17$ DENIS data. Objects closer than 20 pixels to the frame edges are excluded. *Solid*, *dashed*, and *dotted histograms* refer to the DENIS I, J, and K counts, respectively. The *squares* represent K-band counts from Gardner et al. (1996), while the *open* and *filled circles* represent the I-band counts from Lidman and Peterson (1996), and Gardner et al. (1996), respectively. The *thin oblique line* represents an eye-fit Euclidean count function (0.6 slope).

TABLE 2. Estimated DENIS limits from 50 deg^2 of reduced data

	I_c	J	K
completeness ($\simeq 80\%$)	17.25	15.25	11
star/galaxy separation (90% reliability, from I)	16.5	14.8	13.5
photometry (0.20 mag accuracy)	>18?	14.8	12.2?
photometry (0.10 mag accuracy)	17.4	13.7	<11?

galaxies at $I < 16.5$ (0.1 mag photometry). The recent installation of an air conditioning system on the K band optics has decreased the instrumental background by 0.7 magnitude, which should bring the extraction limit to

$K \simeq 11.7$, and thus increase the size of the homogeneous K sample to roughly 15 000 galaxies.

Moreover, there is still room for progress on star/galaxy separation. C. Alard has devised a new algorithm to accurately model the variations of the PSF across the frame, which need no longer be an elliptical gaussian (fitting the asymmetric coma of the images), and tests on visually classified data are about to be performed.

Acknowledgements

We thank Emmanuel Bertin for supplying recent updates of his SExtractor software package, Steve Maddox for useful comments on the APM data, Nicolas Epchtein for a careful reading of the manuscript, and Pascal Fouqué and the DENIS operations team.

References

Baugh C.M. & Efstathiou G. (1993) *MNRAS*, **Vol. no. 265**, pp. 145–332
Baugh C.M. & Efstathiou G. (1994) *MNRAS*, **Vol. no. 267**, pp. 323–332
Bertin E. (1996) *PhD thesis*, University of Paris 6
Bertin E. & Arnouts S. (1996) *A&AS*, **Vol. no. 117**, pp. 398–404
Bertin E. & Dennefeld M. (1997) *A&A*, **Vol. no. 317**, pp. 43–53
Borsenberger J. (1997) in *The Impact of Large-Scale Near-IR Surveys*, eds F. Garzón *et al.*, Kluwer, pp. 181–186
Burstein D. & Heiles C. (1982) *AJ*, **Vol. no. 87**, pp. 1165–1189
Dalton G.B., Maddox S.J., Sutherland W.J. & Efstathiou G. (1997) *MNRAS*, **Vol. no. 289**, pp. 263–284
Epchtein N. *et al.* (48 authors) (1997) *ESO Messenger*, **Vol. no. 87**, pp. 27–34
Escalera E. & MacGillivray H.T. (1995) *A&A*, **Vol. no. 298**, pp. 1–21
Escalera E. & MacGillivray H.T. (1996) *A&AS*, **Vol. no. 117**, pp. 519–555
Gardner J.P., Sharples R.M., Carrasco B.E. & Frenk C.S. (1996) *MNRAS*, **Vol. no. 282**, pp. L1–L6
Heydon-Dumbleton N.H., Collins C.A. & MacGillivray H.T. (1989) *MNRAS*, **Vol. no. 238**, pp. 379–406
Kolatt T., Dekel A. & Lahav, O. (1995) *MNRAS*, **Vol. no. 275**, pp. 797–811
Kraan-Korteweg R.C., Woudt P.A., Cayatte V., Fairall A.P., Balkowski C. & Henning P.A. (1995) *Nature*, **Vol. no. 379**, pp. 519–521
Kron R.G. (1980) *ApJS*, **Vol. no. 43**, pp. 305–325
Lidman C.E. & Peterson B.A. (1996) *MNRAS*, **Vol. no. 279**, pp. 1357–1379
Lumsden S.L., Nichol R.C., Collins C.A. & Guzzo L. (1992) *MNRAS*, **Vol. no. 258**, pp. 1–22
Maddox S.J., Sutherland W.J., Efstathiou G., Loveday J. & Peterson B.A. (1990) *MNRAS*, **Vol. no. 247**, pp. 1P–5P
Mamon G.A. (1994) *Astrophys. & Sp. Sci.*, **Vol. no. 217**, pp. 237–242
Mamon G.A. (1996) in *Dark Matter in Cosmology, Quantum Measurements, Experimental Gravitation*, eds. R. Ansari, Y. Giraud-Héraud & J. Trân Thanh Vân, Frontières, pp. 225-232 (astro-ph/9608076)
Mamon G.A., Banchet V., Tricottet M. & Katz D. (1997a) in *The Impact of Large-Scale Near-IR Surveys* eds. F. Garzón *et al.*, Kluwer, pp. 239–248 (astro-ph/9608077)
Mamon G.A., Tricottet, M., Bonin, W. & Banchet, V. (1997b) in *Extragalactic Astronomy*

in the Infrared, eds. G.A. Mamon, T.X. Thuan & J. Trân Thanh Vân, Frontières, pp. 369–380 (astro-ph/9711281)
Monet D. (1997) *Bull. A.A.S.*, **Vol. no. 188**, 54.04
Prandoni I., Iovino A. & MacGillivray H.T. (1994) *AJ*, **Vol. no. 107**, pp. 1235–1244
Saunders W. et al. (15 authors) (1997), in *Extragalactic Astronomy in the Infrared*, eds. G.A. Mamon, T.X. Thuan & J. Trân Thanh Vân, Frontières, pp. 415–424
Schröder A., Kraan-Korteweg R.C., Mamon G.A. & Ruphy S., (1997) in *Extragalactic Astronomy in the Infrared*, eds. G.A. Mamon, T.X. Thuan & J. Trân Thanh Vân, Frontières, pp. 381–386 (astro-ph/9706093)
Vauglin I., Paturel G., Marthinet M.C., Petit C. & Borsenberger J. in *Extragalactic Astronomy in the Infrared*, eds. G.A. Mamon, T.X. Thuan & J. Trân Thanh Vân, Frontières, pp. 387–392

D.2 The wide-field DENIS near-IR imaging survey and 6dF redshift and peculiar velocity surveys

Mamon, 2000, dans XIVth IAP Astrophysics Meeting, *Wide-Field Surveys in Cosmology, p. 323, arXiv:astro-ph/9809376*

Contributed talk at XIVth IAP meeting "Wide-Field Surveys in Cosmology", Paris, May 1998, ed. Y. Mellier & S. Colombi (Paris: Frontières)

The Wide-Field DENIS Near-IR Imaging Survey and 6dF Redshift and Peculiar Velocity Surveys

Gary A. Mamon[1,2]

[1] *Institut d'Astrophysique de Paris, 98 bis Boulevard Arago, F–75014 Paris, France*
[2] *DAEC, Observatoire de Paris, F–92195 Meudon, France*

Abstract. The DENIS survey is currently imaging the entire southern sky in the I, J, and K wavebands. The current star/galaxy separation algorithm is presented and the galaxy counts are nearly perfectly Euclidean. 95% complete and reliable galaxy samples with better than 0.2 magnitude photometry should include 50 000 ($K < 12.0$), 500 000 ($J < 14.8$), and 900 000 ($I < 16.5$) galaxies, respectively, over the full hemisphere. Two spectroscopic followups of DENIS and 2MASS galaxies are planned on the 6dF robotic multi-object spectroscopic unit, currently under construction at the AAO, and which will be mounted on the UKST Schmidt telescope: a redshift survey of roughly 120 000 NIR selected galaxies and a peculiar velocity survey of roughly 15 000 galaxies (both early-types and inclined spirals) at $cz < 10\,000$ km s^{-1}.

1 Importance of Near-IR selected nearby galaxy samples

The Near-IR (NIR) wavebands are considered to provide galaxy catalogs that optimally trace the distribution of matter in the Universe. Indeed, cosmological studies have all been based upon optical (*e.g.,* [7]) or far-IR (*e.g.,* [12]) surveys, and the optical wavebands are severely affected by extinction from interstellar dust, while both optical and far-IR wavebands tend to pick up galaxies undergoing recent starbursts. For this reason, the European DENIS IJK survey of the southern hemisphere [1] and the American 2MASS JHK survey of the entire sky [5] have important cosmological implications [9]. In essence, all the cosmological analyses of the distribution of matter in the local Universe, performed in the optical or the far-IR, need to be redone in the NIR.

2 DENIS galaxy extraction

The current DENIS galaxy pipeline is based upon fairly standard procedures, described elsewhere [10][11]. Star/galaxy separation is performed in the I band, even for J and K-selected objects, because the I-band is the most sensitive (except at $|b| < 3°$) and has the best spatial resolution.

Excellent star/galaxy separation is crucial, because, at the fairly bright magnitude limits of DENIS, stars vastly outnumber galaxies, and also because the point spread function (PSF) of the DENIS images varies in space and in time. We have studied various star/galaxy separation algorithms, by comparing their output to visual classification of 329 galaxy candidates and to

the output of the APM [13] and EDGSC [14] galaxy catalogs. This led us to abandon neural networks, which were improperly trained for PSF variations in space and time. The ratio of peak intensity to isophotal area (hereafter RATIO) turns out to be perhaps the simple star/galaxy separation algorithm that is the most robust to variations of the PSF [10][11].

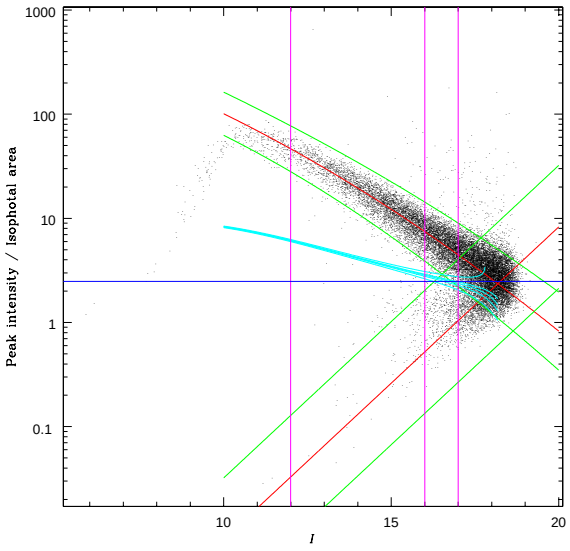

Figure 1: Star/galaxy separation plot for 180 consecutive DENIS I-band images at high galactic latitude. The *upper locus* shows the foreground stars, and shows saturation at $I \leq 11$. The *lower locus* shows the galaxies. The *curved* and *straight lines* around the star and galaxy locii respectively represent our estimates of their mean and 3σ envelopes. The *horizontal line* shows a 1st-order star/galaxy separation, which works well for $I \leq 16.5$. The family of *nearly horizontal curves* represent our 2nd-order star/galaxy separation, as described in the text, with reliabilities of 50%, 84%, 90%, 95% and 99% (see eq. [1]) from top to bottom. The *vertical lines* show the magnitude intervals where the stellar locus is defined (*outer two lines*) and where the star counts are estimated (*left two lines*). Note that this star/galaxy separation is not meant to work beyond where our estimates of the star and galaxy locii cross.

Figure 1 above shows our star/galaxy separation on a sequence of 180 consecutive DENIS I-band images at high galactic latitude. A constant RATIO threshold works well for $I \leq 16.5$, but poorly at fainter magnitudes. A better

star/galaxy separation is obtained by computing critical curves for

$$R = \frac{f_g(m)N(x,\bar{x}_g(m),\sigma_g(m))}{f_g(m)N(x,\bar{x}_g(m),\sigma_g(m)) + f_s(m)N(x,\bar{x}_s(m),\sigma_s(m))} \ , \qquad (1)$$

where $N(x,\mu,\sigma)$ is the gaussian of mean μ and standard deviation σ, f are the number counts, x is our star/galaxy separation statistic, and subscripts 'g' and 's' refer to galaxies and stars, respectively. We've tested the reliability of our two methods, by comparing with visual classifications from DENIS images and with APM and COSMOS classifications, and by checking the very low frequency of very blue or red colors for our galaxies [10][11] and we have begun to test the spatial uniformity along the image frames of our extraction.

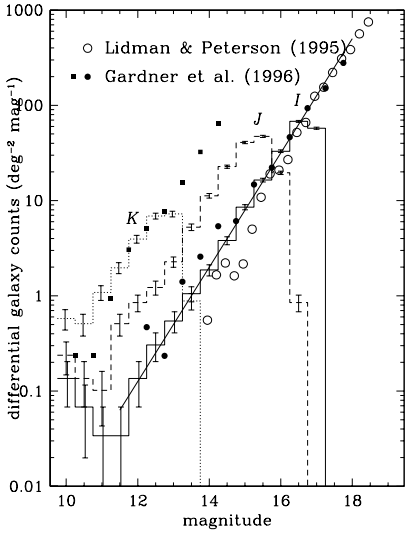

Figure 2: I (*solid*), J (*dashed*) and K (*dotted histogram*) galaxy counts from $50\,\mathrm{deg}^2$ of high galactic latitude DENIS images. The *solid line* is an eye-ball fit of the I counts to a Euclidean (0.6) slope.

Comparing our resulting galaxy counts in Figure 2 to the previous published counts, we infer $> 90\%$ completeness limits of $I \simeq 16.5$, $J \simeq 14.8$, and $K \simeq 12.0$. These yield homogeneous samples of 900 000 (I), 500 000 (J), and 50 000 (K) galaxies over the southern sky. The nine-fold increase of our estimated K sample, relative to our previous estimates (*e.g.,* [10]), is the consequence of the much wider smoothing filter we now use to detect galaxies in the K band. Our counts show Euclidean slopes and no lack of bright objects, in contrast with the APM [8] and EDGSC [4] counts.

3 Spectroscopic followups with 6dF

Simulations [9] of the duration time of a NIR-selected full redshift survey show that a wide field telescope is necessary to tile the sky efficiently. Based upon these findings, we've been able to convince the AAO to robotize its currently highly inefficient FLAIR-II multi-object spectrograph on the UKST, increasing from 92 to 150 its number of fibers. The new instrument, currently under construction, is called 6dF for Six Degree Field. The AAO is suggesting dedicating 100 nights per year during 2001–2003 to obtain roughly 120 000 redshifts. Our input catalog will consist of a combination of magnitude-limited subcatalogs from DENIS IJK, 2MASS [5] JHK, and hopefully SUPERCOS [3] B and R.

We are also planning a peculiar velocity survey of roughly 15 000 galaxies. The sample will be NIR flux-limited, and restricted to distances $cz < 10\,000\,\mathrm{km\,s^{-1}}$ (determined from the redshift survey). We will measure the distances to both early-types and inclined spirals and infer the peculiar velocities by subtracting the Hubble expansion velocity from the radial velocity.

Our main scientific aim is to map the mass density field of the local southern Universe and to infer Ω, Λ and the primordial density fluctuation spectrum. For the first time, we will provide complete and uniform coverage, multiplying by 10 the current sample of peculiar velocities in the southern hemisphere.

References

[1] Epchtein, N. et al. 1997, Messenger 87, 27
[2] Gardner, J.P., Sharples, R.M., Carrasco, B. & Frenk, C. 1996, MNRAS 282, L1
[3] Hambly, N.C., Miller, L., MacGillivray, H.T., Herd, J.T. & Cormack, W.A. 1998, MNRAS 298, 897
[4] Heydon-Dumbleton, N.H., Collins, C.A. & MacGillivray, H.T. 1989, MNRAS 238, 379
[5] Kleinmann, S.G. et al. 1994, Ap&SS 217, 11
[6] Lidman, C.E. & Peterson, B.A. 1996, MNRAS 279, 1357
[7] Maddox, S.J., Efstathiou, G., Sutherland, W.J. & Loveday, J. 1990, MNRAS 242, 43P
[8] Maddox, S.J., Sutherland, W.J., Efstathiou, G., Loveday, J. & Peterson, B.A. 1990, MNRAS 247, 1P
[9] Mamon, G.A. 1996, ed Ansari, R. et al., in *Dark matter in cosmology, quantum measurements, and experimental gravitation*, p. 225 (astro-ph/9608076)
[10] Mamon, G.A., Borsenberger, J., Tricottet, M. & Banchet, V. 1998, ed Epchtein, N., in *The impact of near-infrared sky surveys on galactic and extragalactic astronomy*. Kluwer, Dordrecht, p. 177 (astro-ph/9712169)
[11] Mamon, G.A., Bertin, E., Borsenberger, J., Epchtein, N., Fouqué, P. & Tricottet, M. 1998, to be submitted to A&A
[12] Saunders, W., Frenk, C., Rowan-Robinson, M., Lawrence, A. & Efstathiou, G. 1991, Nature 349, 42
[13] `telnet://catalogues@apm3.ast.cam.ac.uk`
[14] `telnet://cosmos@cosmos.aao.gov.edu.au`

D.3 Near-infrared galaxy surveys in 2D, 3D & 4D

Mamon, 2000, dans *Cosmic Flows 1999: Towards an Understanding of Large-Scale Structure, p. 103, arXiv:astro-ph/9908163*

Contribution to Workshop on Cosmic Flows, held in Victoria, BC, CANADA, July 13–17, 1999, ed. S. Courteau, M. Strauss & J. Willick, ASP series

Near-Infrared Galaxy Surveys in 2D, 3D & 4D

G. A. Mamon[1]
IAP, F-75014 Paris, FRANCE

Abstract. The completeness and reliability of the DENIS IJK survey and the EDSGC (derived from the COSMOS scans of USKT plates) are obtained by detailed cross-identifications and systematic visual inspections of conflictual classifications. The DENIS galaxy extraction turns out to be over 95% complete and reliable out to $I < 16$, while the COSMOS/EDSGC galaxy catalogue is less than 80% complete and reliable at $B_J = 17.5$, and even less than 10% complete at $B_J < 14.5$.

Spectroscopic followups of DENIS and the similar Near-IR 2MASS survey are described: 1) a redshift survey of 120,000 galaxies using the 6dF robotic multi-fiber spectrograph, currently under construction at the UKST, and for which a total of 300 nights are guaranteed for 2001-2003, 2) a peculiar velocity survey of 12,000 early-type galaxies with the 6dF, and 3) the DENIS-HI peculiar velocity survey of 5000 inclined spirals visible from Nançay ($\delta > -38°$), which has just begun. The DENIS-HI and 6dF peculiar velocity samples will have the strong advantage of covering entire regions of the southern sky, and combined, will multiply by 10 and 4 respectively the projected and space number densities of objects in the Southern sky. These two surveys should thus provide considerably more accurate estimates of the bulk flow, $\Omega^{0.6}_{\rm matter}$/bias, $\Omega_{\rm matter}$ itself, and the primordial density fluctuation spectrum.

1. Near-infrared surveys and cosmology

As is well known, near-infrared (NIR) photons are up to 10 times less affected by dust extinction than their visible counterparts. Hence, cosmological surveys based upon NIR-selected galaxy samples can probe the Universe almost completely through the Zone of Avoidance in the Galactic Plane, and moreover have a clearer view of galaxies, virtually unobscured by dust (especially important for the central regions of spirals and for edge-on spirals).

The other main advantage of NIR-selected galaxy samples is that they are not biased towards recent star formation, contrary to optically-selected samples (especially in blue light), and hence the NIR-selected galaxies are more weighed by their mass, or at least their stellar mass.

However, the IRAS galaxy samples, heavily weighted towards galaxies with recent star formation, appear to be better tracers of the mass in the Universe

[1]also DAEC, Observatoire de Paris, F-92195 Meudon, FRANCE

than are early-type galaxy samples. The first spectroscopic followups of NIR selected galaxy samples show fairly small fractions of galaxies with emission lines in their spectra: 37% in $J < 13.7$ samples (Mamon et al. 1999) and 30% in $K < 12.2$ samples (Huchra, 1999), in comparison with 60% in similar depth B-selected samples. Hence, DENIS and 2MASS will be more weighted towards early-type galaxies and may lead to stronger biases relative to the dark matter than the IRAS samples, but this remains to be seen (especially because, contrary to the IRAS samples, they will have a mix of early- and late-type galaxies).

2. DENIS

The DENIS (DEep Near Infrared Southern Sky Survey) consortium is undertaking a complete imaging survey of the southern sky ($-88° < \delta < +2°$) in the Gunn $I\,(0.8\,\mu)$, Johnson $J\,(1.25\,\mu)$, and $K_s\,(2.15\,\mu)$ bands (Epchtein et al. 1997), and at this writing, 62% of the southern sky has been observed (see http://www.iap.fr/users/gam/DENIS/slots.html). The completion date is planned for January 2001. The DENIS team has built an IR camera and mounted it on the ESO 1m telescope (which had previously only done optical aperture photometry). The I, J, and K images are obtained simultaneously through the use of dichroics with integration times of 9 sec. The pixel sizes are $1''$ in I and $3''$ in J and K, and the latter two are dithered in 9 sub-exposures of 1 sec each to yield images with a pseudo-resolution of $1''$.

Star/galaxy separation is performed with classical estimators, and except in the Zone of Avoidance ($|b| < 2°$), the much higher sensitivity and spatial resolution of the I band allow us to base our star/galaxy separation on the I images for objects detected in the J or K images.

3. Comparison of DENIS and COSMOS/EDSGC galaxy extractions

We have performed detailed cross-identifications of the DENIS extractions with the COSMOS extractions from B_J photographic plates (obtained over the World Wide Web), over 8 DENIS strips, corresponding to $50\,\mathrm{deg}^2$. These strips were randomly selected at typically high galactic latitudes ($\langle|b|\rangle \simeq 50°$) from the great majority of strips that are not flagged as poor quality.

To compare the quality of the two surveys, we performed two cross-identifications: 1) relative to all DENIS objects; and 2) relative to COSMOS objects ($B_J < 20.5$) in the exact geometry of the 8 DENIS strips. We assumed that all objects, on which both DENIS and COSMOS agreed were galaxies, were indeed galaxies. We systematically inspected visually the DENIS I-band images for all cases with $I < 16$ (our estimated limit for 95% reliable visual classification) where one of the surveys identified a galaxy while the other called it a star or did not detect it altogether. Objects that both DENIS and COSMOS classify as galaxies have $\langle B - I\rangle = 2.3$ and 95% have $B - I > 1.5$. Hence, our estimates of COSMOS completeness are limited to $B < 17.5$.

Figure 1 shows the resulting DENIS (*left*) and COSMOS (*right*) completeness (*dashed*) and reliability (*solid*) as a function of magnitude. While DENIS achieves better than 95% completeness and reliability over the full range $13 < I < 16$, COSMOS has worse than 80% completeness and reliability at

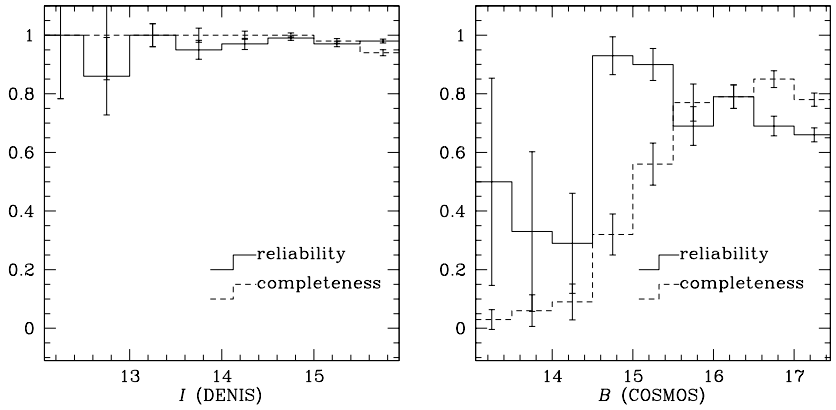

Figure 1. Completeness (*dashed*) and reliability (*solid histograms*) for DENIS (*left*) and COSMOS (*right*) galaxy extraction.

$B = 17.5$, and the numbers get even worse at brighter magnitudes: in particular the completeness falls to below 10% at $B < 14.5$. At bright magnitudes, COSMOS suffers from the non-linearity of the plate photometry. Its reliability suffers from the blending of low non-linear peaks of double stars, while its strong incompleteness is caused by systematic over-compensation of the photometric non-linearity, thus bright galaxies are classified as even brighter stars.

4. The 6dF redshift survey

The strong case for spectroscopic followups of near-IR selected galaxy samples, coupled with the realization that Schmidt telescopes offer wide enough fields to sample most efficiently the sky for shallow samples of 5–10 galaxies deg^{-2}, has led the AAO to replace its existing manually-configured FLAIR II 92-fiber system on the UKST with a robotized, 150-fiber system, called 6dF (for Six Degree Field). The 6dF instrument, currently under construction uses an $r-\theta$ positioner, adapted to the curved focal surface of the UKST.

The AAO has suggested granting 300 nights of dark/grey time during 2001–2003 to a Scientific Advisory Group (6dFSAG, see Acknowledgments, below), to conduct a redshift survey based upon near-IR selected galaxy samples. The 6dFSAG is envisioning a complete spectroscopic followup of $\simeq$ 120,000 DENIS/2MASS selected southern galaxies. The primary sample should be a 2MASS-K or DENIS-J selected sample. Moreover, we will add galaxies to form complete subsamples in DENIS I and 2MASS H, as well as SuperCOSMOS B and R.

Because fibers cannot be placed closer than $5'$ to one another, we envision an adaptive tiling scheme, with typically 2 exposures per effective field to minimize the losses due to crowding. At a galaxy density of 7 deg^{-2}, our 27 deg^2 field will have an average of 189 galaxies. If 10 fibers are reserved for sky, we will have

$2 \times (150 - 10) = 280$ fibers available for objects per field, hence an average of $280 - 189 = 91$ spare fibers, which we intend to use for other classes of objects such as quasars and/or IRAS galaxies, as well as allow for cosmic variance of the field density.

5. The 6dF and DENIS-HI peculiar velocity surveys

The principal motivation of the 6dFSAG is to perform a peculiar velocity survey in the full ($|b| > 10°$) southern hemisphere. Assuming 3/4 dark or grey UKST telescope time and two 4 hours exposures per night, we expect to measure 1 Å resolution spectra for roughly 12,000 ellipticals and lenticulars at $cz < 15{,}000\,\mathrm{km\,s^{-1}}$. To limit the survey duration, only the densest half of the fields will be observed. The line-widths will be coupled with surface photometry (using DENIS I or 2MASS K images), to yield distances (with the $D_n - \sigma$ relation) and hence peculiar velocities. We hope to be awarded the time to pursue the peculiar velocity survey during the period 2003–2005.

In the meanwhile, the DENIS-HI consortium has just begun a spectroscopic followup of DENIS southern galaxies with the Nançay radio-telescope. We estimate that given one-sixth the Nançay time, we can reach the estimated 5000 inclined spiral galaxies at $-38° < \delta < +2°$ with $I < 14.5$ and $cz < 10{,}000\,\mathrm{km\,s^{-1}}$ in 2000–2004, thanks to the 5-fold increase in sensitivity and velocity coverage that Nançay should obtain in the fall of 1999. So far, a hundred spectra have been obtained.

6. Perspectives

The DENIS-HI and 6dF peculiar velocity surveys should increase the coverage of the southern hemisphere from 1500 to 17,000 galaxies, and within $cz = 6000\,\mathrm{km\,s^{-1}}$, the space density of objects will be 4 times higher than today. Therefore, the problems related to the sparseness of the current peculiar velocity samples should disappear with these two surveys, leading to more accurate estimates of bulk flow, $\Omega^{0.6}_{\mathrm{matter}}$/bias, Ω_{matter} itself, and especially the primordial density fluctuation spectrum.

Acknowledgments. I thank members of the DENIS team, especially N. Epchtein, P. Fouqué, and J. Borsenberger. Thanks also to F. Giraud who participated in the comparison of DENIS and COSMOS, and E. Bertin for useful discussions on the matter. I also acknowledge my colleagues on the 6dF Science Advisory Group: M. Colless, J. Huchra, O. Lahav, J. Lucey, Q. Parker, E. Sadler, W. Saunders, and F. Watson and on the DENIS-HI team: G. Theureau, I. Vauglin, G. Paturel, L. Bottinelli, J.-M. Martin, and W. van Driel.

References

Epchtein, N. et al. 1997, Messenger, 87, 27

Huchra, J. P., 1999, in these proceedings

Mamon, G. A., Parker, Q. A., Proust, D. 1999, PASA in prep.

E Sélection d'articles et proceedings publiés sur la densité de l'Univers

E.1 Dynamical theory of groups and clusters of galaxies

Mamon, 1993, dans *N-Body Problems and Gravitational Dynamics, astro-ph/9038032*

DYNAMICAL THEORY OF GROUPS AND CLUSTERS OF GALAXIES

Gary A. Mamon

DAEC, Observatoire de Paris-Meudon, F 92195 Meudon, FRANCE

Abstract. The different dynamical processes (relaxation, dynamical friction, tides and mergers) operating in groups and clusters are reviewed. The small-scale substructure observed in clusters is argued to be the remnants of the cores of rich clusters that merged together, rather than large groups falling into the cluster. The *ROSAT* X-ray observations of two groups of galaxies are discussed, and, contrary to a previous claim, the baryon fraction is high, relative to the constraints from baryonic nucleosynthesis. A general theory of the fundamental surface of groups is presented, allowing one to determine with reasonable confidence the precise cosmo-dynamical state of a given group of galaxies. The data from groups is then consistent with a universal true M/L of $440\,h$, roughly 4 times larger than previous estimates, the discrepancy occurring because most groups are still relatively near cosmological turnaround. This high M/L and the young cosmo-dynamical state of groups suggests a density parameter $\Omega > 0.3$. Hickson's compact groups are explained as a mixture of virialized groups, loose groups near full collapse, and chance alignments from collapsing loose groups. Finally, the level of projection effects contaminating samples of binary galaxies within groups is shown to be important.

1. Introduction

Thanks to gravity, galaxies like to congregate in groups and clusters. As seen in Table 1 below, only a minority of galaxies seem to live in isolation. From the general hierarchical clustering of galaxies in the Universe, one can separate the various systems of galaxies, according to richness (number of galaxies within given magnitude interval and distance from the system's center), *i.e.,* groups vs. clusters, compactness (mean surface brightness), *i.e.,* compact vs. loose groups, with an isolation criterion (compact groups and binaries). Note that with Abell's definition, one has $N_{\rm gal} = 4$, 44, and 106 for the Local Group (Milky Way, M31, M33 and the LMC), Virgo and Coma clusters, respectively.

Despite their relatively rare occurrence in the Universe, there has been plenty of studies of clusters of galaxies. Indeed, clusters are popular because they are the largest objects whose cores are in dynamical equilibrium, hence *virialized* (they obey the virial theorem), as contamination by interlopers is not too significant. In contrast, the outer regions of clusters are thought to still be feeling the effects of their *infall* onto the virialized cores, and to complicate matters even further, clusters often display substructure, as is well shown in pictures of the hot gas traced by the *ROSAT* satellite (*e.g.,* White, Briel & Henry 1993). This substructure is a tracer of cosmological parameters such as the density parameter, Ω, and the spectrum of primordial density fluctuations (see §3).

Table 1: 2D definitions of structures

	Criteria	$N_{\rm gal}$	$\langle M/L \rangle$	$f_{\rm gal}$
Clusters	$m < m_3 + 2$ $hR < 1.5\,{\rm Mpc}$	$30 - 300$	$300\,h$	10%
Loose Groups	$m < m_3 + 2$ $hR < 1.5\,{\rm Mpc}$	$3 - 30$	$150\,h$	50%
Compact Groups	$m < m_1 + 3$ $\theta_n > 3\theta$	$4 - 7$	$50\,h$	0.1%
Binaries	$m < m_1 + 3$ $\theta_n > 5\theta$	2	$100\,h$ $(100\,{\rm kpc})$	10%
Isolated		1		30%

NOTES: The criteria are taken from Abell (1958), Hickson (1982), Turner (1976a), for the clusters, compact groups and binaries, respectively. Here, $N_{\rm gal}$ is the number of galaxies per system, $f_{\rm gal}$ is the fraction of galaxies in the Universe that belong to the type of system under consideration, and $h = H_0/(100\,{\rm km\,s^{-1}\,Mpc^{-1}})$.

Also, as dense systems near equilibrium, clusters represent an excellent laboratory to study dynamical interactions between galaxies, with the caveat that since their potential wells are deep, the relative encounter velocities are large, hence the interactions are short and not very damaging to the galaxies. One would then like to understand the segregation in morphologies, with elliptical galaxies predominantly occurring in the dense regions such as the cluster cores (see Mamon, in these proceedings), and the recent inference of high central concentration of dark matter relative to gas in clusters.

Loose groups have the advantage of being numerous, and for this reason, are often used as distance indicators, since if one knows that the distance to one object is known to some accuracy ΔD, the distance obtained from N galaxies believed to be all lying in the same group ought to be $\Delta D/\sqrt{N}$. Also, although not as extreme as clusters, loose groups can be thought to be good tracers of the Universe, and for many years, astronomers have tried to link the group mass-to-light ratios to Ω by simple extrapolation: $\Omega \simeq (M/L)/(1500h)$. And the distribution of their properties is again related to both Ω and the primordial density fluctuation spectrum, see §§4 and 5.

There are three serious problems with loose groups: 1) They suffer from important contamination from interlopers. 2) They are rarely virialized at best, so that the true mass-to-light ratio is a function of both the mass-to-light ratio obtained by assuming virial equilibrium and the cosmo-dynamical state of the group (expanding, collapsing, collapsed, virialized ...), see §5. 3) Groups could be biased M/L tracers, if significant amounts of dark matter bound to the group lurk beyond the galaxies.

Compact groups appear so dense in projection that they would be the highest density isolated systems of galaxies, denser than the cores of rich clusters. Unfortunately they are very rare (see Table 1), and they may suffer from serious contamination from a surrounding loose group. This last point is a matter of debate (§6). If this contamination is low, then

compact groups would indeed be extremely dense, and as such would serve as the ideal sites for strong galaxy evolution, by dynamical interaction, and by the star formation which this interaction may trigger. They would then also be extreme cosmological tracers, a little bit like the clusters, and thus allow one to determine Ω and the primordial density fluctuation spectrum. If, on the other hand, contamination by surrounding loose groups were indeed important, one still expects that the resulting chance alignments within loose groups will be binary-rich (Mamon 1992b), thus making compact groups interesting sites for galaxy evolution.

One could go on and state that binary galaxies are potential sites of strong galaxy evolution. Moreover, they are used to trace the matter distribution in galactic halos of dark matter, in particular the extent of these halos. The difficulty here is that again, contamination by chance alignments of galaxies within surrounding loose groups may be very important (see §7). Finally, one should state that isolated galaxies are very interesting as they serve as reference galaxies to which to compare the galaxies in denser environments.

2. Dynamical Processes

The reader is encouraged to read the excellent reviews on the details on the different dynamical processes by White (1983) and Richstone (1990), and the classic books by Saslaw (1985) and Binney & Tremaine (1987).

The dynamics of groups and clusters are set by their cosmological initial conditions. An homogeneous isolated system will first expand with the local Hubble flow. Then its high density will force it to decouple from the Hubble flow and it will reach its maximum expansion *turnaround*, collapse, and subsequently virialize. This equilibrium does not last forever, as virialization is followed by dissipation of orbital energy, caused by dynamical friction against an intergalactic background, and by tidal friction during collisions and merging. An inhomogeneous system will evolve in the same way, except that the denser regions will collapse and virialize first, and the low-density regions will later collapse onto the virialized core of the system (*secondary infall*) and subsequently virialize at a larger radius. Conservation of energy then yields a relation between the epoch of turnaround and the crossing time in virial equilibrium (Gunn & Gott 1972): $T_{\rm ta} = \pi t_{\rm cr}$ where the crossing time is defined as $t_{\rm cr} = (3/5)^{3/2} R_V/V_V$, where R_V and V_V are the virial radius and velocity dispersion, respectively.

This can be adapted to the circular orbital time:

$$\tau_{\rm circ} = \frac{2\pi R}{V_{\rm circ}(R)} = \left[\frac{3\pi}{G\bar{\rho}(R)}\right]^{1/2} .$$

As a test particle undergoes scattering collisions within a sea of field particles, it will progressively forget its initial conditions. This *two-body relaxation* time can be defined in at least three ways:

$$\tau_{2-{\rm rel}} \equiv \left\langle \frac{1}{v^2}\frac{dV^2}{dt} \right\rangle^{-1} \text{ or } \left\langle \frac{1}{E}\frac{dE}{dt} \right\rangle^{-1} \text{ or } \left\langle \frac{d\sin^2\Delta\alpha}{dt} \right\rangle^{-1} ,$$

where $\Delta\alpha$ is the deflection angle in an encounter. Chandrasekhar (1942) has shown that this can be written as

$$\tau_{2-\rm rel} = \frac{v^3}{G^2 m_f^2 n f(v/\sigma_v) \ln\Lambda} \ ,$$

where v is the velocity of the test particle, m_f, n, and σ_v are the mass, number density, and 1D velocity dispersion of the field particles, respectively, f is a function of order unity, and $\ln\Lambda$, also of order unity is called the Coulomb logarithm, where Λ is the ratio of maximum to minimum impact parameter. For a system of galaxies and dark matter particles, one finds that the galaxies relax by galaxy-galaxy collisions, but not by collisions with individual dark matter particles (whose masses are too low). Similarly, the dark matter particles relax mainly by collisions with individual galaxies.

Gurzadyan & Savvidy (1984, 1986) estimated the *collective* relaxation time, obtained not by summing up the encounters but by computing the collective response of the system. They obtain

$$\tau_{N-\rm rel} = {\rm Cst}\ \frac{v}{G m_f n^{2/3}} \ .$$

This collective relaxation turns out to be somewhat more efficient than two-body relaxation in clusters and loose groups but not in dense groups. In general, only the cores of rich cluster are relaxed.

Lynden-Bell (1967) has shown that particles can rapidly forget their initial conditions if they evolve in a rapidly time varying potential:

$$\tau_{\rm v-rel} \sim \tau_{\rm ff} \sim \tau_{\rm dyn} \quad \text{when} \quad |\frac{\partial\phi}{\partial t}| > |\mathbf{v}\cdot\nabla\phi| \ ,$$

where $\tau_{\rm ff}$ is the free-fall time, and ϕ is the global potential. This applies for example to collapsing systems, as is often the case in cosmology, and thus explains why the cores of elliptical galaxies appear relaxed although their 2-body (and collective) relaxation times are much longer than the age of the Universe.

Chandrasekhar (1943) also considered the effects of many scattering encounters on the forward velocity of a test particle. Because field particles are scattered in such a way that in the frame of the test particle, the field particle density is higher behind the test particle than in front of it. This leads to a drag force known as *dynamical friction*, which plays a major role in group and cluster dynamics. The timescale for dynamical friction can be written

$$\tau_{\rm df} \equiv \left(\frac{1}{v_\parallel}\frac{dv_\parallel}{dt}\right)^{-1} = \frac{v^3}{G^2(m+m_f)\rho f(v/\sigma_v)\ln\Lambda} \ ,$$

where ρ is the local mass density of field particles, f is another function of order unity, and $\ln\Lambda$ is again the Coulomb logarithm. In principle, one could also compute a collective frictional timescale in a manner analogous to the collective relaxation timescale (Gurzadyan 1993, private communication). Maoz (1993) has recently computed the orbital energy dissipation from dynamical friction in inhomogeneous media, but his methodology does not return the actual force, which in general is not opposite to the motion of the test particle.

Perhaps more physical is the timescale for *orbital decay* defined as

$$\tau_{\rm od} \equiv \left(\frac{1}{R}\frac{dR}{dt}\right)^{-1} = \left(\frac{RdE/dR}{mv^2}\right)\tau_{\rm df} = \frac{3}{2}\left(\frac{\rho}{\bar{\rho}}+\frac{1}{3}\right)\tau_{\rm df} \ .$$

Unfortunately, this timescale does not always provide correct answers: 1) No orbital decay is predicted in zero density environments, whereas a satellite galaxy sitting just outside its parent galaxy will see its orbit decay, because of resonances with its parent (Lin & Tremaine 1983); 2) Although orbital decay should be slowed by tidal effects that reduce the test particle's mass, the contrary may occur with a satellite galaxy circling its parent, as the tides from the latter remove stars from the former, and these carry off energy and angular momentum, thus accelerating the orbital decay (Prugniel & Combes 1992). 3) If one throws a satellite right through a parent galaxy, the resultant energy loss by dynamical friction requires an unusually high Coulomb logarithm (10 or so) to match the results from PM simulations (Seguin, in these proceedings). In any event, the timescale for orbital decay in rich clusters is greater than a Hubble time for galaxies with $m < 10^{12}M_\odot$ (see Mamon 1985, §III), but starts to become important for groups of galaxies falling into these clusters.

Another outgrowth of dynamical friction is *orbital circularization*, whose timescale can be defined as

$$\tau_{\rm oc} = \left(\frac{1}{J_{\rm circ}(E)}\frac{dJ}{dt}\right)^{-1} \ ,$$

which Merritt (1985) finds to be shorter than the orbital decay time outside of the core radius of a cluster.

Tidal forces act on particles in a system *relative* to the full system itself. As such there are two types of tides acting on galaxies in groups and clusters: those caused by close encounters with other galaxies and those caused by variations in the gradient of the global group/cluster potential. The first type of tides (*collisional stripping*) has a timescale

$$\tau_{\rm cs} \equiv \left(\frac{1}{m}\frac{dm}{dt}\right)^{-1} = \langle(\Delta m/m)n\langle\sigma v\rangle\rangle^{-1} = \frac{\rm Cst}{nr_g^2 v_g} \ ,$$

where σ is the collisional stripping cross-section, and the outer stars are assumed to follow elongated orbits (Richstone 1975; Dekel, Lecar & Shaham 1980).

Global potential tides depend strongly on the galaxy's orbit around the cluster. If the galaxy is phase locked in a nearly circular orbit around the cluster, it will feel a roughly constant tidal shear, and its tidal radius will be obtained by equating the tidal shear at a given radius in the galaxy with the gravitational pull that the full galaxy exerts on a star at that radius, plus an inertial term:

$$\Delta\left(\frac{GM(r)}{R^2}\right) = -\frac{Gm(r)}{r^2} + \Omega^2 r \ , \qquad (1)$$

yielding for $r \ll R$

$$\bar{\rho}_g(r_t) = \bar{\rho}_{\rm cl}(R)\left[2 - 3\,\frac{\rho_{\rm cl}(R)}{\bar{\rho}_{\rm cl}(R)} + \frac{V_p^2(R)}{V_{\rm circ}^2(R_p)}\right] \ , \qquad (2)$$

i.e., the galaxy is tidally truncated at a radius r_t where its mean density is of the order of the mean cluster density within the radius R_p of closest approach of the galaxy (where V_p and $V_{\rm circ}$ are the pericentric and circular velocities, respectively). Merritt (1984) has argued that central cD galaxies could not have spiralled in from outside the cluster cores, for otherwise these global potential tides would have seriously limited their sizes.

If the orbits are elongated, the instantaneous tide obtained from equation (1) is short lived and the galaxy experiences a *tidal shock* (Ostriker, Spitzer & Chevalier 1972). Using the impulse approximation (Spitzer 1958), in which the perturber moves with a constant relative velocity $\mathbf{V}$, one can show (Mamon 1992a) that again for $r \ll R$

$$\bar{\rho}_g(r_t) = {\rm Cst}\, \bar{\rho}_{\rm cl}(R_p) f(\epsilon) \ ,$$

where R_p is the pericentric of the galaxy's orbit, and $f(\epsilon)$ is a function of order unity of the galaxy's orbital eccentricity. This criterion is similar to that for circular orbits, but the constants are higher, because at given pericenter, a galaxy in a circular orbit must feel a more effective tide, since it is long-lived (Mamon 1987). Numerical simulations by Allen & Richstone (1988) confirm this result although other simulations by Merritt & White (1987) suggest that the tide is most efficient for some intermediate elongation at given pericenter, when this is within the nearly homogeneous region of the cluster. Note that the timescales for global potential tides are basically the orbital timescales divided by the typical mass-loss per passage through the cluster core.

The effectiveness of a tide is related to the maximum strength of the tide times the duration of this maximum tide. So, from equation (2) one gets

$$\begin{aligned} \Delta v \sim F_{\rm tid} \Delta t \sim \bar{\rho}_g \Delta t &\sim \frac{2 - 3\rho_{\rm cl}/\bar{\rho}_{\rm cl} + V_p^2/V_{\rm circ}^2}{V_p/V_{\rm circ}} \\ &\sim 3\left(1 - \frac{\rho_{\rm cl}}{\bar{\rho}_{\rm cl}}\right) - \left(1 - 3\frac{\rho_{\rm cl}}{\bar{\rho}_{\rm cl}}\right)\left(\frac{V_p}{V_{\rm circ}} - 1\right) \qquad \text{for } V_p \gtrsim V_{\rm circ} \ . \end{aligned}$$

Hence, the results of Merritt & White are understood, since when the cluster region is nearly homogeneous, the effective tide increases with increasing pericenter velocity, but not when the cluster density profile decreases sharply as outside the core of the Modified Hubble model used by Merritt & White.

The timescale for merging may be estimated from a merging cross-section, again as

$$\tau_m = n \left\langle \sigma v \right\rangle^{-1} \ .$$

Using Roos & Norman's (1979) numerically experimental cross-section, the merger time can be written (adapted from Mamon 1992a)

$$\tau_m = {\rm Cst}\, \left[n r_g^2 v_g K(v_{\rm cl}/v_g) \right]^{-1} \ , \qquad (3)$$

where n is the number density of galaxies, r_g and v_g are the galaxy half-mass radius and internal velocity dispersion, respectively, and where the merging efficiency K is optimum for groups ($v_{\rm cl} \simeq v_g$), while for clusters it falls off as $v_{\rm cl}^3$. In groups as dense as Hickson's (1982) compact groups appear to be, merging ought to be extremely efficient, and the

relatively low fraction of ellipticals indicates that chance alignments are contaminating the Hickson compact group catalog (Mamon 1992a). Despite their high velocity dispersions, rich clusters seem to be able to produce the right amount of mergers to produce elliptical morphologies, and moreover, merging is able to account for the morphology-density (Postman & Geller 1984) and morphology-radius (Whitmore & Gilmore 1991) relations (Mamon 1992a, and in these proceedings).

The physical processes described above compete in the evolution of the galaxy system. For example, merging leads to increased merger cross-sections, hence to a merging instability (Ostriker & Hausman 1977; see also the simulations of Carnevali, Cavaliere & Santangelo 1981 and the analytical formulation by Cavaliere, Colafrancesco & Menci 1992). However, this instability is slowed down by tidal processes which are usually thought to truncate galaxies of their outlying particles which become unbound (Mamon 1987). Yet, if the merging cross-section is related to galaxy half-mass radius (Aarseth & Fall 1980), and since the tidal processes for galaxies on elongated orbits or from collisions pump energy into the system, then the half-mass radius of those particles that remain bound to the galaxy should increase. The question remains whether the new half-mass radius is then greater or smaller than the old value, but this reviewer is not aware of any numerical study that has addressed this question yet.

In any event, it becomes necessary to run numerical simulations to see how groups and clusters evolve. The reader is referred to Athanassoula, Friedli, and Scholl (all three in these proceedings) for presentations of the numerical techniques, and to Mamon (1990) for comparison of the results on merging in dense groups from different techniques.

The principal results are as follows: The dynamics of clusters is now understood to depend strongly on the primordial density fluctuation spectrum (West, Oemler & Dekel 1988). Galaxies *overmerge* in clusters and possibly in dense groups, when simulated with collisionless particles (*e.g.,* White *et al.* 1987) and this overmerging seems to be caused by the fact that the particles in the halos of galaxies relax rapidly with the intergalactic particles within the core of the system (Villumsen 1993). This is not seen in simulations where gas is included (Evrard, Summers & Davis 1992; Katz & White 1993), presumably because the gas sinks to the bottom of the halo potential wells and deepens these wells, which thus avoid merging with one another. Dense groups of galaxies witness rapid merging and coalesce into a single elliptical galaxy (Carnevali *et al.* 1981; Barnes 1985; Mamon 1987; Barnes 1989; Lima Neto, in these proceedings).

A detailed comparison of the results on groups (Mamon 1990) showed that the different numerical studies of groups produced comparable rates of merging. In an interesting study, Garcia & Athanassoula (in these proceedings) have gone one step further by simulating the same groups by the various methods (*explicit-physics* with one particle per galaxy and the physics of interactions [§2] explicitly included, and the *self-consistent* methods in which galaxies are constituted of many particles). They point out a discrepancy between the merging cross-section of Roos & Norman (1979) which seems too high, whereas that of Aarseth & Fall (1980), curiously derived from the former, seems to give decent results.

Whereas simulations by Cavaliere *et al.* (1982), Barnes (1985) and Mamon (1987) all show that dense groups survive longer if the dark matter is distributed in a common envelope, the contrary as been found in recent simulations by Athanassoula & Makino (1993). What causes this discrepancy? If galaxies have individual halos, merging is direct (Mamon 1987), and the merging rate is proportional to the merger cross-section, and hence

to the square of the galaxy half-mass radius (eq. [3]). Usually, the individual halos of dark matter are more extended by construction than the luminous matter, and the merging cross-section is increased by a factor of nearly 100, more than compensating the positive effects of dynamical friction on the merging rate when the dark matter is in a common envelope (Mamon 1987). But in Athanassoula & Makino's simulated galaxies, the dark matter halos have the same matter distribution as the luminous matter (simply scaled up), hence the presence of dark matter halos did not increase the merger cross-sections, while the runs with a common envelope merged faster thanks to dynamical friction.

3. Substructure in Clusters

Although perhaps 30% of clusters exhibit *large-scale* substructure (*e.g.,* Jones & Forman 1992), various statistical studies on optical data (Salvador-Solé, Sanromà & González-Casado 1993; Salvador-Solé, González-Casado & Solanes 1993) and recent *ROSAT* observations (*e.g.,* White, Briel & Henry 1993) show that *small-scale* substructure is present in a majority of clusters. Three recent studies (Richstone, Loeb & Turner 1992; Lacey & Cole 1993; Kauffmann & White 1993) have attempted to obtain constraints on the density parameter Ω from the frequency of substructure in clusters. The idea is that if $\Omega < 1$, then structures in the Universe collapse from their initial Hubble expansion at epochs $z \simeq 1/\Omega$, while if $\Omega = 1$, structures keep collapsing today (Gott & Rees 1975; Richstone, Loeb & Turner 1992). The first two of the three studies conclude to $\Omega_0 > 0.5$, while as noted in the third (Kauffmann & White), the problem is that the dynamical survival time of substructures is only guessed (Richstone *et al.*) or treated too simplistically (Lacey & Cole).

In fact, one can do better, and consider as two extreme cases the accretion of a group into a cluster, and the merging of two similar-mass clusters with the decoupling of their dense cores. One can then compare the ability of these two extreme scenarios to produce small-scale substructure of a mass-fraction of say 5 or 10%. Preliminary calculations indicate that groups are destroyed by tides from the global cluster potential in one passage through the cluster core, whereas the stripped cores of clusters are able to survive such tides for a few orbital periods. The difference arises simply because groups have lower mean density than the detached cores of clusters, and thus are easier to destroy (see González-Casado, Mamon & Salvador-Solé 1993). Moreover, while the more massive substructures survive tides better at first passage through the cluster core, their orbits decay faster by dynamical friction, thus reducing their lifetime Δt. One thus expects a small range of mass fractions, which is consistent with the observations (González-Casado, Mamon & Salvador-Solé 1993).

4. X-ray Observations of Groups

Very recently, a diffuse hot intergalactic background has been discovered in two groups with pointed observations of the *ROSAT* satellite: the loose group NGC 2300 (Mulchaey *et*

al. 1993) and the compact group HCG 62 (Ponman & Bertram 1993). In both groups, the diffuse IGM has a temperature of about 1 keV (to within 15%) although the compact group has a dip in its central temperature, probably caused by a cooling flow, since the cooling time in the center is found to be short. Also, both groups have low metallicity compared to clusters, consistent with nearly primordial gas, rather than enriched by supernova ejecta.

The NGC 2300 group is claimed to have a rather high dynamical mass within a radius of $165\,h^{-1}$ kpc (Mulchaey *et al.* 1993), and consequently a very low baryonic fraction, 4%, consistent with the constraints from big-bang nucleosynthesis. Note that the NGC 2300 group has very uncertain parameters: the X-ray surface brightness profile is so poorly constrained out to $R = 45'$ that its background-subtracted asymptotic slope is uncertain to at least a factor of three (Henriksen & Mamon 1993). This implies an uncertainty of a factor two in the total mass within a radius of $25'$, and the resultant gas fractions range between 14% and 24% (Henriksen & Mamon), thus higher than the limits obtained from nucleosynthesis. Moreover, for low asymptotic slope, the baryonic fraction increases with radius, and conversely for high slopes (Henriksen & Mamon 1993). Hence the need for more extended X-ray observations with, for example off-center pointings, which are indeed planned (Burstein 1993, private communication).

5. A Unified Scheme for Groups

Groups of galaxies have often been used to argue for low values of the cosmological density parameter Ω, since their mass-to-light ratios are $\lesssim 10\%$ of the required value to close the Universe. However, these mass analyses assume that groups are virialized entities. It has been shown that groups are rarely virialized (Byrd & Valtonen 1985; Giuricin *et al.* 1988). Diaferio *et al.* (1993) go further and say that the observational properties of the groups that Ramella, Geller & Huchra (1989) extracted from the CfA slice are compatible with a single collapsing group observed from different viewing angles.

Simple cosmological theory provides more insight into the evolution of the observable properties of groups. A homogeneous isolated group should see its size evolve as shown in Figure 1a. It first follows the Hubble expansion, then decouples from this expansion and turns around, collapses and subsequently virializes. Applying the virial theorem, one derives a virial mass $M_V = R_V V_V^2/G$ and crossing time $t_V = R_V/V_V$ to within known constants of order unity. In an important paper, Giuricin *et al.* (1988) have shown how to compute the observable mass and crossing time of a group in terms of its cosmo-dynamical state. Figures 1b, 1c, and 1d show the biases in observable velocity dispersion, mass, and crossing time using their analysis to the idealized evolution depicted in Figure 1a. The dotted track is for groups made of point mass galaxies, while the solid track is for extended galaxies, which reach a terminal velocity at group collapse (because the smoothed potential is flat at the center), and after virialization, dissipate their orbital energy by dynamical friction against their common massive halo (merged from their individual halos after group collapse).

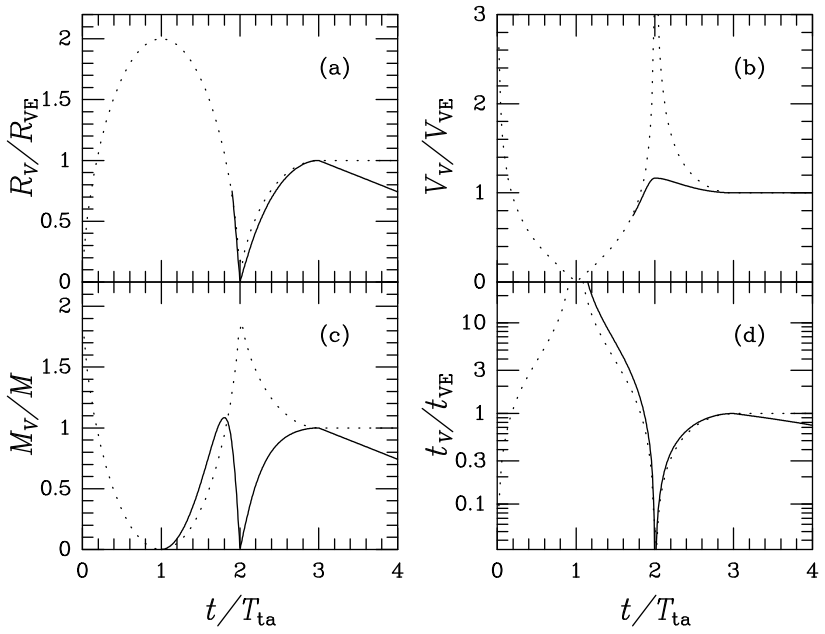

Figure 1. Time evolution of bias in observed virial radius (a), velocity dispersion (b), mass (c), and crossing time (d), relative to virial equilibrium (VE), where T_{ta} is the turnaround time. The *dotted curves* show the evolution for point-masses, while the *full curves* show the effects of softened potentials and orbital energy dissipation by dynamical friction (starting at $t = 3\,T_{ta}$).

In Figure 2a is shown the theoretical evolution of a group in the space (M_V/M versus t_V/t_0), which can be understood to be analogous to an evolutionary track in a Hertzprung-Russell diagram for stars. To compare with parameters from observed groups, we must link the groups to a same mass scale, and do so by assuming that the *true* M/L is constant from group to group and independent of its cosmo-dynamical state. In Figures 2b, c, and d, we plot the observed group parameters (M_V/L vs. $H_0 t_{cr}$, for groups of different multiplicities, and superpose the theoretical evolutionary track, adjusting the y-axis with the high multiplicity groups of Figure 2b, while the x-axis scaling is imposed by theory. The groups are taken from the Gourgoulhon, Chamaraux & Fouqué (1992) catalog of groups, the largest available in the literature, but the results below have been checked with Tully's (1987) groups.

The high-multiplicity groups fit the theoretical tracks very well. A one proceeds to lower multiplicities, the statistical noise in the mass-to-light ratio and crossing time estimates increases, but so does the probability for chance alignments, which make the groups appear smaller while conserving on the average their velocity dispersion. Although precise assignments of group cosmo-dynamical states is difficult because of statistical noise, one can nevertheless get a handle on which groups are unbound (above theoretical track), which are still in their expansion phase (upper-right handle of track), which are near turnaround (lower-right handles of track), which are collapsing (central handle), which are near maximum collapse (first lower-left handle), and those that are virialized (second lower-left handle). The theoretical track thus represents a slice through the *fundamental surface* (which is curved) of groups, where the third axis is total group luminosity.

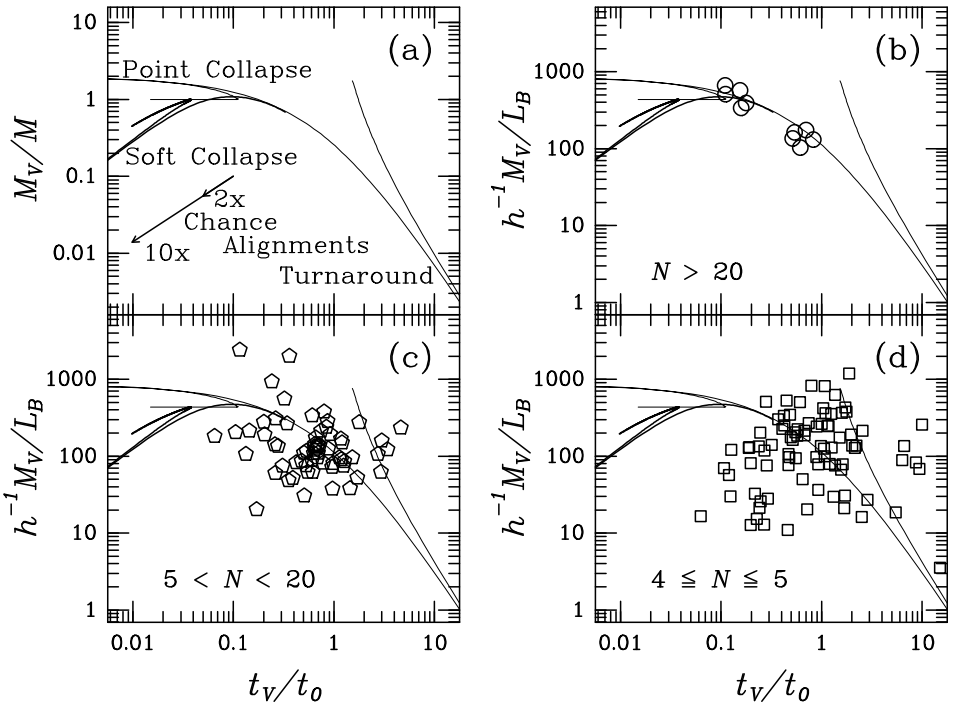

Figure 2. Mass, scaled to total mass (a) or total blue luminosity (b, c, and d), versus crossing time (in units of the age of the Universe for $\Omega = 1$, while for $\Omega = 0.2$ the points should be displaced to the left by 0.1 decade). The *polygons* (b, c, and d) represent the loose groups from Gourgoulhon, Chamaraux & Fouqué (1992). The *thin curves* are the theoretical point-mass evolutionary tracks, while the *thick curves* are the same for softened potentials and allowing for orbital energy dissipation after virialization. In (b, c, and d), these curves are scaled to mass-to-light ratios assuming that all groups have a true $M/L = 440\,h$.

The true M/L is obtained by extrapolating to the early virialized state (before dissipation of orbital energy, which occurs at nearly constant velocity dispersion since the common halo should have near constant circular velocity). The Gourgoulhon *et al.* groups then have $M_{\rm true}/L = 440\,h$, much higher than the median $M/L = 130\,h$, for the groups of $N \geq 4$ members (the mass estimate used here is the median of the non-weighted virial, weighted virial, and projected masses). In other words, *the mass-to-light ratios of groups are severely underestimated because most groups are still relatively near their turnaround phase.* This points to $\Omega \simeq 0.3$ obtained by extrapolating Loveday *et al.*'s (1992) galaxy luminosity function to $(M/L)_{\rm closure} = 1560\,h$. Barnes (1985) showed similar plots as in Figure 2 for simulated groups of 5 galaxies starting from turnaround and also concluded for mass estimates of observed groups too low by a factor three or more, but attributes this to mass segregation between galaxies and dark matter at group collapse instead of the bias near turnaround advocated here.

In any event, *no groups in the loose group catalog has yet completed its collapse*, not even the Virgo cluster included in the catalog, whose outer members are still collapsing onto the virialized core. Although this conclusion is in accord with the single collapsing

state advocated by Diaferio *et al.* (1993), the present analysis allows a range in cosmo-dynamical states. Now, if $\Omega = 0.1$, then structures would form at $z \simeq 10$, and there should be few collapsing groups today (Gott & Rees 1975). *The fact that all groups are in a young cosmo-dynamical state, thus points to a high* Ω*, perhaps close to unity.* Details of this analysis will be found in Mamon (1993b).

6. Real vs. Accidental Compact Groups

The nature of the compact groups such as those cataloged by Hickson (1982) has been a matter of much debate. On one hand, the high level of galaxy-galaxy interaction is becoming increasingly evident as the numerous observational studies of compact groups progress. To summarize briefly, compact group galaxies are often morphologically (Hickson 1990; Mendes de Oliveira 1992) or kinematically (Rubin, Hunter & Ford 1991) disturbed.

However, various theoretical and statistical arguments point against the 3D high density of *the majority* of Hickson's compact groups (once the obvious interlopers with discordant redshifts are culled out). Indeed, 1) It is hard to understand how bound dense groups form in sufficient numbers, given their short survival times against depletion from galaxy mergers (see Mamon 1987 for a statistical appraisal of the survival of dense groups against mergers). 2) Simulations of virialized dense groups (Mamon 1987) show rapid evolution of the bright-end of the luminosity function, in sharp contrast with what is observed for the ensemble of Hickson groups (Mamon 1986). This argument implies that most compact groups could not have been dense in 3D for over 1 or 2 Gyr.

The alternative to compact groups that are dense in 3D are compact groups caused by chance alignments of loose group galaxies along the line of sight. Simulations of *virialized* loose groups have shown that such 1D chance alignments are roughly 10 times more frequent than the formation of 3D dense groups by 2-body processes (Mamon 1992b). Moreover, these chance alignments are binary-rich as only one-quarter is composed of 4 or more unrelated galaxies (Mamon 1992b). A rule of 3 on the frequency of binaries in chance alignments, shows that the fraction of interacting galaxies in groups is consistent with the observed high frequency of 63% (Rubin *et al.* 1991) of compact group galaxies with abnormal internal kinematics, once one folds in a fraction of 10% of truly dense groups in Hickson's sample (Mamon 1992b).

A recent detailed morphological analysis of compact group galaxies (Mendes de Oliveira 1992) shows that 35% of Hickson's compact groups have 3 or more interacting galaxies, whereas the prediction from *only* chance alignments is 19% to 27% (Mamon 1993a). The discrepancy gets worse once the subsample of 16 compact groups with kinematical data is considered, as Mendes de Oliveira finds that 75% of these groups have 3 or more interacting galaxies, combining her morphological analysis with Rubin *et al.*'s (1991) kinematical analysis. But if one-third of the accordant-redshift Hickson compact groups are real while the remainder are binary-rich chance alignments, one then obtains 55% of Hickson's compact groups showing 3 or more interacting galaxies (assuming that dense triplets and quartets *always* show morphological or kinematical interactions). Considering that some of the interactions seen in the sample of 16 could be caused by accretion of dwarf galaxies rather

than interaction between galaxies bright enough to be listed in Hickson's catalog, the discrepancy is not strong enough, in this reviewer's opinion, to rule out that the majority of compact groups are caused by chance alignments.

Where do compact groups lie in the M_V/L vs. $H_0 t_{\rm cr}$ diagram (see Mamon 1993b for details)? This is shown in Figure 3, for the accordant redshift compact groups of four or more members (Hickson *et al.* 1992), which lie within three regions: 1) The low-velocity dispersion compact groups (lower right) are mostly chance alignments within collapsing loose groups. 2) The intermediate velocity dispersion compact groups are mostly loose groups near full cosmological collapse. 3) The high velocity dispersion compact groups (upper left) are mostly virialized loose groups. The previously unexplained morphology-velocity dispersion relation in compact groups (Hickson, Kindl & Huchra 1988) is then attributable to the fact that only the high velocity dispersion compact groups have had enough time to reach virialization and hence witness rapid merging within them to form ellipticals.

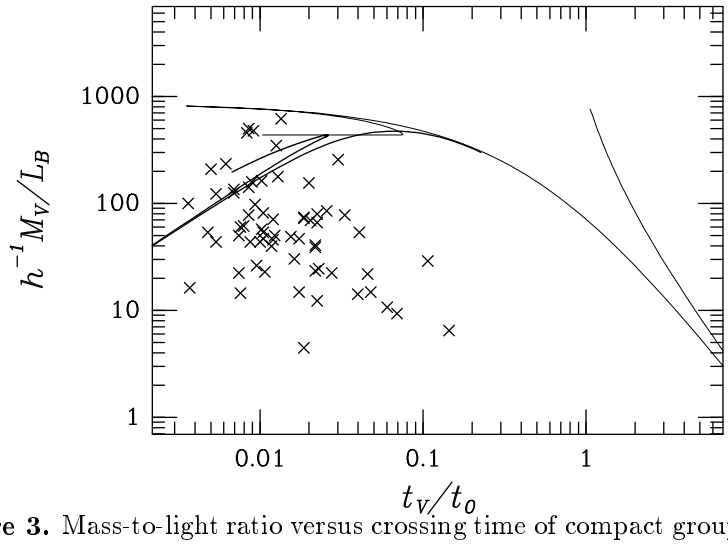

Figure 3. Mass-to-light ratio versus crossing time of compact groups (*crosses*) and theoretical evolutionary tracks (see fig. 2).

7. Real vs. Accidental Binaries

Binary galaxies have been often used to probe the existence and extent of galaxy halos (Turner 1976b; White *et al.* 1983; Schweizer 1987; Charlton & Salpeter 1991), with contradictory results. Indeed, if binary halos overlap, their global kinematics should be altered relative to non-overlapping halos, which orbit in the same manner as point masses. Because a substantial fraction ($\simeq 40\%$) of binaries reside within groups, it is important to assess what fraction of the binaries within groups are caused by chance alignments and which fraction are truly bound pairs. Brieu & Mamon (1993) have employed simulations of virialized groups looking for pairs in projection meeting the binary isolation criteria

of Turner (1976a) or Schweizer (1987). They find that the fraction of accidental binaries is between 40% and 80%, depending on whether galaxies have individual halos or not. Moreover, the correlation of the observational quantities that are the physical projected separation and the radial velocity difference are similar between real and accidental pairs. There is no way to distinguish between the two sets by selecting binaries with small projected separation or small radial velocity difference. Thus, *the isolation criteria used to select binaries are insufficient to select real binaries*, and one has to completely cull out the binaries within group to avoid being swamped by accidental pairs. The weak point of this analysis is that it is based upon virialized groups, whereas loose groups are not virialized (see §5), which should in principle alter the internal kinematics of groups and hence of the binaries appearing in projection.

References

Aarseth S. & Fall S.M.: 1980, ApJ 236, 43
Abell G.O.: 1958, ApJS 3, 211
Allen A.J. & Richstone D.O.: 1988, ApJ 325, 583
Athanassoula E. & Makino J.: 1993, in *Groups of Galaxies*, ed. O. Richter (San Francisco: A.S.P.) in press
Barnes J.: 1985, ApJ 215, 517
Barnes J.: 1989, Nature 338, 123
Binney J. & Tremaine S.D.: 1987, *Galactic Dynamics* (Princeton: Princeton Univ. Press)
Brieu Ph. & Mamon G.A.: 1993, in preparation
Byrd G.G. & Valtonen M.J.: 1985, ApJ 289, 535
Carnevali P., Cavaliere A. & Santangelo P.: 1981, ApJ 249, 449
Cavaliere A., Colafrancesco, S. & Menci, N.: 1992, ApJ 376, L37
Cavaliere A., Santangelo P., Tarquini G. & Vittorio N.: 1982, in *Clustering in the Universe*, ed. D. Gerbal & A. Mazure (Gif-sur-Yvette: Frontières) 25
Chandrasekhar S.: 1942, *Principles of Stellar Dynamics* (New York: Dover)
Chandrasekhar S.: 1943, ApJ 97, 255
Charlton J.C. & Salpeter E.E.: 1991, ApJ 375, 517
Dekel A., Lecar M. & Shaham J.: 1980, ApJ 241, 946
Diaferio A., Ramella M., Geller M.J. & Ferrari A.: 1993, AJ 105, 2035
Evrard A., Summers F. & Davis M.: 1992, preprint
Giuricin G., Gondolo P., Mardirossian F., Mezzetti M. & Ramella M.: 1988, A&A 199, 85
González-Casado G., Mamon G.A. & Salvador-Solé E.: 1993, in preparation
Gott J.R. & Rees M.: 1975, A&A 45, 365
Gourgoulhon E., Chamaraux P & Fouqué P.: 1992, A&A 255, 69
Gunn J.E. & Gott J.R.: 1972, ApJ 176, 1
Gurzadyan V.G. & Savvidy G.K.: 1984, DAN SSSR 277, 69
Gurzadyan V.G. & Savvidy G.K.: 1986, A&A 160, 203
Henriksen M.J. & Mamon G.A.: in preparation
Hickson P.: 1982, ApJ 255, 382
Hickson P.: 1990, in IAU Coll. 124 *Paired and Interacting Galaxies*, ed. J.W. Sulentic & W.C. Keel (Washington: NASA) 77
Hickson P., Kindl E. & Huchra J.P.: 1988, ApJ 331, 64

Hickson P., Mendes de Oliveira C., Huchra J.P. & Palumbo G.G.C.: 1992, ApJ 399, 353
Jones C. & Forman W.: 1992, in *Clusters and Superclusters of Galaxies*, ed. A.C. Fabian (Dordrecht: Kluwer) 49
Katz N. & White S.D.M.: 1993, ApJ 412, 455
Kauffmann G. & White S.D.M.: 1993, MNRAS 261, 921
Lacey C.G. & Cole S.: 1993, MNRAS 262, 627
Lin D.N.C. & Tremaine S.D.: 1983, ApJ 264, 364
Loveday J., Peterson B.A., Efstathiou G. & Maddox S.J.: 1992, ApJ 390, 338
Lynden-Bell D.: 1967, MNRAS 136, 101
Mamon G.A.: 1985, PhD thesis, Princeton University
Mamon G.A.: 1986, ApJ 307, 426
Mamon G.A.: 1987, ApJ 321, 622
Mamon G.A.: 1990, in IAU Coll. 124 *Paired and Interacting Galaxies*, ed. J. Sulentic, W.C. Keel & J.M. Telesco (Washington: NASA) 609
Mamon G.A.: 1992a, ApJ 401, L3
Mamon G.A.: 1992b, in 2nd DAEC meeting *Distribution of Matter in the Universe*, ed. G.A. Mamon & D. Gerbal (Meudon: Obs. de Paris) 51
Mamon G.A.: 1993a, in STScI workshop on *Groups of Galaxies*, ed. O. Richter (San Francisco: A.S.P.) in press
Mamon G.A.: 1993b, in preparation
Maoz E.: 1993, MNRAS 263, 75
Mendes de Oliveira C.: 1992, PhD thesis, University of British Columbia
Merritt D.: 1984, ApJ 276, 26
Merritt D.: 1985, ApJ 289, 18
Merritt D. & White S.D.M.: 1987, in IAU Symp. 117 *Dark Matter in the Universe*, ed. J. Kormendy & G.R. Knapp (Dordrecht: Reidel) 283
Mulchaey J.S., David D., Mushotzky R.F. & Burstein D.: 1993, ApJ 404, L9
Ostriker J.P. & Hausman, M.: 1977, ApJ 217, L125
Ostriker J.P., Spitzer L. & Chevalier R.A.: 1972, ApJ 176, L51
Ponman T.J. & Bertram D.: 1993, Nature 363, 51
Postman M. & Geller M.J.: 1984, ApJ 281, 95
Prugniel Ph. & Combes, F.: 1992, A&A 259, 25
Ramella M., Geller M.J. & Huchra J.P.: 1989, ApJ 344, 57
Richstone D.O.: 1975, ApJ 200, 535
Richstone D.: 1990, in *Clusters of Galaxies*, ed. W.R. Oegerle, M.J. Fitchett & L. Danly (Cambridge: Cambridge University Press) 231
Richstone D., Loeb A.. & Turner E.L.: 1992, ApJ 393, 477
Roos N. & Norman C.A.: 1979, A&A 95, 349
Rubin V.C., Hunter D.A. & Ford W.K.: 1991, ApJS 76, 153
Salvador-Solé E., Sanromà M. & González-Casado G.: 1993, ApJ 402, 398
Salvador-Solé E., González-Casado G. & Solanes J.M.: 1993, ApJ 410, 1
Saslaw W.C.: 1985, *Gravitational Physics of Stellar and Galactic Systems* (Cambridge: Cambridge Univ. Press)
Schweizer L.: 1987, ApJS 64, 427
Spitzer L.: 1958, ApJ 127, 17
Tully R.B.: 1987, ApJ 321, 280
Turner E.L.: 1976a, ApJ 208, 20

Turner E.L.: 1976b, ApJ 208, 304
Villumsen J.V.: 1993, preprint
West M.J., Oemler G. & Dekel A..: 1988, ApJ 327, 1
White S.D.M.: 1983, in *Morphology and Dynamics of Galaxies*, ed. L. Martinet & M. Mayor (Sauverny: Obs. de Genève) 289
White S.D.M., Briel U.G. & Henry J.P.: 1993, MNRAS 261, L8
White S.D.M., Davis M., Efstathiou G. & Frenk C.S.: 1987, Nature 330, 451
White S.D.M., Huchra J.P., Latham D. & Davis M.: 1983, MNRAS 203, 701
Whitmore B.C. & Gilmore D.: 1991, ApJ 367, 64

E.2 The baryonic fraction in groups of galaxies from X-ray measurements

Henriksen & Mamon, 1994, *ApJ 421, L63–L66*

Les figures de cet article ont été permutées par mégarde par les éditeurs (mais les captions de figures sont placées correctement) :

Figure 1 $\longrightarrow$ $3^{\text{ème}}$ diagramme

Figure 2 $\longrightarrow$ 1^{er} diagramme

Figure 3 $\longrightarrow$ 2^{nd} diagramme

THE ASTROPHYSICAL JOURNAL, 421:L63–L66, 1994 February 1

THE BARYONIC FRACTION IN GROUPS OF GALAXIES FROM X-RAY MEASUREMENTS

MARK J. HENRIKSEN[1] AND GARY A. MAMON[2]
Received 1993 September 14; accepted 1993 November 12

ABSTRACT

The recent *ROSAT* X-ray detections of hot intergalactic gas in three groups of galaxies are reviewed, and the resulting baryonic fraction in these groups is reevaluated. We show that the baryonic fraction obtained, assuming hydrostatic equilibrium, should depend, perhaps sensitively, on the radius out to which the X-rays are detected, and the temperature profile of the gas. We find that the NGC 2300 group has a baryonic fraction out to 25′ of at least 20%, thus over 5 times higher than in the original analysis of Mulchaey et al. and also much higher than one would obtain from big bang nucleosynthesis, but similar to the other two groups as well as rich clusters. With this baryonic fraction, groups would be fair tracers of the distribution of baryons in the universe if $\Omega h_{50}^2 = 0.3$. A baryonic fraction that increases with radius is consistent with the X-ray data from all three groups. However, a detailed analysis of the NGC 2300 group shows that the dependence of baryonic fraction on radius is not well constrained by the data, in part because of uncertainties in the estimated background.

Subject headings: cosmology: observations — dark matter — galaxies: intergalactic medium

1. INTRODUCTION

While clusters of galaxies commonly emit diffuse X-rays associated with a hot intergalactic medium, as evidenced by numerous X-ray observations with the *Einstein Observatory* (e.g., Forman & Jones 1982), the presence of detectable diffuse hot X-ray–emitting gas in small groups of galaxies does not seem as common. *Einstein* observations have revealed diffuse hot gas in four compact groups (Biermann, Kronberg, & Madore 1982; Biermann & Kronberg 1983; Bahcall, Harris, & Rood 1984), but failed to detect X-rays in two other compact groups, while a third compact group emitted X-rays that were probably associated with the individual galaxies (Bahcall et al.). Recent higher-sensitivity *ROSAT* observations with the Position Sensitive Proportional Counter (PSPC) have confirmed that some groups of galaxies emit X-rays originating from a hot diffuse intergalactic medium. Indeed, short ($\simeq 10$ minutes) snapshots from the *ROSAT* survey mode have produced 12 X-ray detections among Hickson's (1982) 100 compact groups, and these detected X-rays are probably of intergalactic origin in roughly nine of these 12 compact groups (H. Ebeling, 1993 private communication). Deeper *ROSAT* PSPC images were recently obtained in four groups: the loose groups NGC 2300 (Mulchaey et al. 1993, hereafter MDMB), NGC 5044 (David, Forman, & Jones 1993), and the Hickson compact groups HCG 12 (H. Ebbeling, 1993 private communication) and HCG 62 (Ponman & Bertram 1993). In only one group (HCG 12) was there no intergalactic X-ray emission. The analysis of the X-ray properties of the NGC 2300 group has revealed a relatively low fraction of mass in gas and stars (hereafter, *baryonic fraction*). The Mulchaey et al. analysis produced a baryonic fraction of 4%, and their upper limit was 15%. On the other hand, Ponman & Bertram's (1993) baryonic fraction was greater than 13%, while David et al. (1993) get 10%, both within 250 kpc (throughout this *Letter* we assume $H_0 = 50\ \mathrm{km\ s^{-1}\ Mpc^{-1}}$).

The baryonic fraction in clusters has been used as a constraint on the cosmological density parameter Ω: if clusters are representative of the whole universe, one has $\Omega = \Omega_b/f_b$ (White 1992). Standard big bang nucleosynthesis produces a baryonic fraction on the scale of the whole universe of $0.04 < \Omega_b h_{50}^2 < 0.08$ (Steigman 1989), where $h_{50} = H_0/(50\ \mathrm{km\ s^{-1}\ Mpc^{-1}})$. The baryonic fraction in clusters of galaxies is typically around 25% (e.g., White 1992, and references therein). One thus obtains $\Omega \simeq 4\Omega_b \simeq 0.24\, h_{50}^{-2}$. As noted by MDMB, the implications of a baryonic fraction as small as Ω_b is that if the universe has a density near closure ($\Omega_0 \simeq 1$), groups of galaxies would be fair tracers of the baryonic content of the universe.

Another way to set constraints on Ω is to assume that groups are fair tracers of the ratio of mass to blue light in the universe. The luminosity density of the universe is such (Loveday et al. 1992) that the closure mass-to-light ratio is $M/L = 780\ h_{50}$, and in general one can write $\Omega = M/L/(780\ h_{50})$. The typical M/L of groups (e.g., Gourgoulhon, Chamaraux, & Fouqué 1992), computed with the assumption that groups are in virial equilibrium, yields $\Omega = 0.07$, while a value of $\Omega = 0.3$ is obtained with the correction for the nonvirialized cosmo-dynamical state of these systems (Mamon 1993).

In this *Letter* we consider how the baryonic fraction in groups (and clusters) of galaxies should vary with radius, assuming simple models for the properties of the hot X-ray–emitting diffuse gas. We analyze the published data for NGC 2300 using a similar model to that applied to rich clusters to reevaluate its baryonic fraction at the present limiting detection radius, and we indicate which future X-ray observations could place sufficient constraints on this parameter.

2. BARYONIC FRACTION VERSUS RADIUS

The X-ray surface brightness profile of groups and clusters are usually well fitted by a law of the form

$$S(R) = S_0[1 + (R^2/R_c^2)]^{1/2 - 3\beta} \quad (1)$$

unless these systems possess a central cooling flow, which produces a central peak in the surface brightness profile. Here β is an empirical rather than a physical parameter.

[1] Department of Physics and Astronomy, University of Alabama, Tuscaloosa, AL 35487.
[2] DAEC Observatoire de Paris-Meudon, F-92195 Meudon, France. Also CNRS URA 173 and associated with Université Denis Diderot (Paris 7).

Inverting the Abel equation relating X-ray surface brightness to the three-dimensional emissivity in the spectral passband of the instrument, noting that the emissivity of a hot plasma varies as $n^2\Lambda(T)$, where Λ is the cooling function, calling $\eta = d\ln\Lambda/d\ln T$, and assuming an equation of state $T \sim n^{\gamma-1}$ (i.e., isothermal for $\gamma = 1$ and polytropic otherwise), one obtains (see Cowie, Henriksen, & Mushotzky 1987)

$$n(r) = n_0[1 + (r^2/R_c^2)]^{-\delta}, \quad (2a)$$

$$T(r) = T_0[1 + (r^2/R_c^2)]^{-\delta(\gamma-1)}, \quad (2b)$$

$$\delta = \frac{3\beta/2}{1 + \eta(\gamma - 1)/2}. \quad (2c)$$

From equation (2a), the total mass in gas can be written

$$M_{\rm gas}(r) = 4\pi n_0 R_c^3 \mu m_p \tilde{M}(x), \quad (3a)$$

$$x = r/R_c, \quad (3b)$$

$$\tilde{M}(x) = \int_0^x \frac{y^2\,dy}{(1 + y^2)^\delta}, \quad (3c)$$

where μ is the mean particle weight in units of the proton mass m_p:

$$\tilde{M}(x) = \frac{x}{2}(x^2 + 1)^{1/2} - \frac{1}{2}\sinh^{-1} x \quad \text{for } \delta = \frac{1}{2}, \quad (4a)$$

$$\tilde{M}(x) = x - \tan^{-1} x \quad \text{for } \delta = 1, \quad (4b)$$

$$\tilde{M}(x) = \sinh^{-1} x - \frac{x}{(x^2 + 1)^{1/2}} \quad \text{for } \delta = \frac{3}{2}. \quad (4c)$$

Writing the equation of hydrostatic equilibruim, the total mass (that binds the gas) is (Cowie et al. 1987)

$$M_{\rm tot} = -\frac{kTr}{G\mu m_p}\left(\frac{d\ln n}{d\ln r} + \frac{d\ln T}{d\ln r}\right) = 2\gamma\delta\frac{kT_0 R_c}{G\mu m_p}\frac{x^3}{(1 + x^2)^{1+\delta(\gamma-1)}}. \quad (5)$$

Using equations (3) and (5), the gas fraction can be written

$$f_g = \frac{2\pi G\mu^2 m_p^2 n_0 R_c^2}{\gamma\delta kT_0}(1 + x^2)^{1+\delta(\gamma-1)}\frac{\tilde{M}(x)}{x^3}. \quad (6)$$

Figure 1 shows the gas fraction versus radius for isothermal models with different δ, scaled to $T = 1$ keV, $R_c = 100$ kpc, and $n_0 = 10^{-3}$ cm^{-3}. In general, the gas fraction should be multiplied by

$$(n_0/10^{-3}\ \text{cm}^{-3})(R_c/100\ \text{kpc})^2(T_0/1\ \text{keV})^{-1}. \quad (7)$$

From Figure 1, one sees that for $\delta = 1/2$, the gas fraction increases sharply with radius, while for $\delta = 3/2$, the reverse is true, and finally for $\delta = 1$ the gas fraction is asymptotically constant and equal to 2.3 times its core radius value. From equation (6) the gas fraction varies asymptotically as

$$f_g \sim (r/R_c)^{2-\delta[2-(\gamma-1)]}, \quad (8)$$

so that a constant asymptotic gas fraction implies $\delta = 1$ for isothermal models and $\delta = 3/2$ for $\gamma = 5/3$ polytropes. Figure 2 shows the same as Figure 1, but for polytropic models (all with $\delta = 1$). Again the gas fraction should in general be multiplied as in equation (7). For nonisothermal gas distributions, the gas fraction increases with radius outside of the central region.

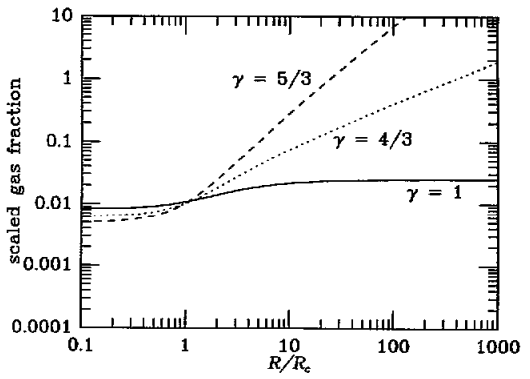

FIG. 1.—Scaled (see eq. [7]) gas fraction (eq. [6]) vs. radius for isothermal model

Note that certain parameters ($\delta = 1/2$ with $\gamma = 1$ or $\delta = 1$ with $\gamma = 5/3$) yield unphysical gas fractions over unity at large radii ($R \gtrsim 100R_c$).

3. COMPARISON WITH OBSERVATIONS

The *ROSAT* X-ray observations are not strongly constraining for NGC 2300. For example, in Figure 3, we plot the intergalactic X-ray surface brightness profile of the NGC 2300 group. The points are from MDMB (where we omit the three points at 18′, 21′, and 24′ for which there is obstruction from the window support structure) and uncorrected for the background while the curves are fits to these points using the model in equation (1), with a constant background $S_{\rm bg}$ added everywhere. Of course, MDMB have determined the background independently of their NGC 2300 observations, but their adopted value of $S_{\rm bg} = 7.0 \times 10^{-4}$ arcmin^{-2} s^{-1} (Burstein, 1993 private communication) could be uncertain by 10% or more, and this is why we allow it to be a free parameter. Figure 3 clearly shows that very different good fits (without the point at 39′, which is well above the surrounding points and may be contaminated by a point souce) provide very different δ and core radii.

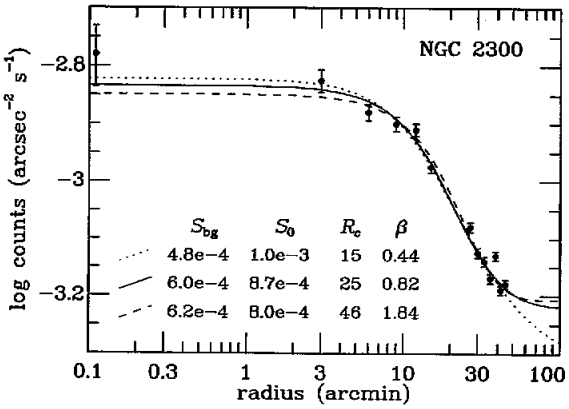

FIG. 2.—Scaled (see eq. [7]) gas fraction (eq. [6]) vs. radius for $\delta = 1$ polytropic models.

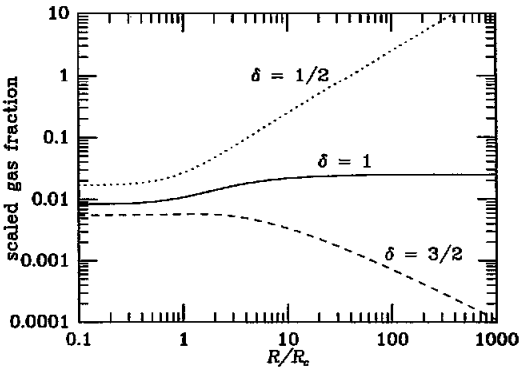

FIG. 3.—Surface brightness profile of the NGC 2300 group intergalactic X-ray emission. Data (uncorrected for background) from Mulchaey et al. (1993) are shown as points, while the best fits to isothermal-β models (eq. [1] plus a constant background) shown in the top three rows of Table 1 are respectively shown as dotted, solid, and dashed curves. Points at 18′, 21′, and 24′ are omitted as they suffer from obstruction from the window support structure of the PSPC.

Using the results from § 2, the top three rows in Table 1 illustrate how these three fits return different total mass ($M_{\rm tot}$, eq. [5]), gas mass ($M_{\rm gas}$, eqs. [3] and [4]), gas fraction (f_g, eqs. [4] and [6]), and baryonic fraction (f_b) within 25′ of the center of the diffuse gas in the NGC 2300 group. The fourth row in Table 1 lists what would be obtained if we adopted the MDMB parameters of $S_{\rm bg} = 7.0 \times 10^{-4}$, $\beta = 0.85$ (J. Mulchaey 1993, private communication), and in subsequent rows, we investigate alternative fits imposing either R_c or β in addition to $S_{\rm bg}$. As MDMB, we assume isothermality, and we convert gas fractions to baryonic fractions using $M_{\rm gal}(25') = 6 \times 10^{11}\, h_{50}^{-1}\, M_\odot$. The gas number density necessary to normalize the gas fractions (eq. [3a]) is obtained by writing the bolometric luminosity as

$$L_{\rm bol} = \int n^2 \Lambda(T) dV = 4\pi n_0^2 R_c^3 \Lambda(T_0) \int_0^{R_{\rm max}/R_c} x^2/(1+x^2)^{2\delta}\, dx\,,$$

where A is the Raymond & Smith (1977) cooling function. The density calculation uses the cooling function evaluated for the emission weighted temperature (0.86 keV) and is 8.6×10^{-24} ergs cm^3 s^{-1} (using a heavy element abundance of 6%, the best-fit value of MDMB), and $R_{\rm max} = 25'$ is the extent of the X-ray–emitting hot gas.

TABLE 1

REANALYSIS OF THE NGC 2300 GROUP FOR $R < 25'$

$S_{\rm bg}$ (1)	S_0 (2)	R_c (3)	β (4)	χ^2 (5)	$L_{\rm bol}$ (6)	n_0 (7)	$M_{\rm gas}$ (8)	$M_{\rm tot}$ (9)	f_g (10)	f_b (11)
4.8	10.3	15.0	0.44	19.9	49.0	1.97	2.49	10.2	0.24	0.30
6.0	8.7	25.0	0.82	18.8	38.7	1.66	2.21	13.0	0.17	0.22
6.2	8.0	46.0	1.84	16.8	38.0	1.48	2.21	13.3	0.17	0.21
7.0	10.5	15.0	0.85	148.3	23.8	2.14	1.61	19.9	0.08	0.11
7.0	8.9	18.0	0.85	121.2	26.4	1.84	1.76	17.7	0.10	0.13
7.0	9.7	15.0	0.76	138.1	25.3	2.04	1.70	17.9	0.09	0.13
6.5	9.8	15.0	0.65	66.6	30.9	1.99	1.92	15.1	0.13	0.17
6.5	8.7	25.0	0.99	35.8	33.0	1.68	2.01	15.7	0.13	0.17

NOTES.—(1) Background in 10^{-4} arcmin^{-2} s^{-1}. (2) Central surface brightness in 10^{-4} arcmin^{-2} s^{-1}. (3) Core radius in arcminutes. (4) Surface brightness shape (eq. [1]). (5) Goodness of fit. (6) Bolometric luminosity in 10^{42} ergs s^{-1}. (7) Central gas density in 10^{-3} cm^{-3}. (8) Gas mass within 25′ in $10^{12}\, M_\odot$. (9) Total mass within 25′ in $10^{12}\, M_\odot$. (10) Gas fraction within 25′. (11) Baryonic fraction within 25′.

Table 1 shows that the best fits (rows 1–3) conspire to a surprisingly robust gas mass within 25′. Moreover, the fit with the MDMB parameters is significantly worse than the three fits shown in Figure 3, because their adopted background is too high. The best-fit baryonic fractions are $\gtrsim$20%, over 5 times larger than the value quoted by MDMB (4%). In fact, our analysis shows that even the MDMB parameters should return a baryonic fraction as high as 11%. The discrepancy with MDMB's low result is due in part to MDMB probably computing the baryonic fraction within 15′ (as stated in the main body of their paper), while in their note added in proof they mention a total mass one-third lower within a region extending two-thirds further (25′). For comparison, NGC 5044 has a baryonic fraction of $\simeq$10% within 250 kpc (David et al. 1993) and HGC 62 > 13% within a similar region. Also, David et al. detect diffuse X-ray emission out to 400 kpc. Since NGC 2300 fills the PSPC field of view, the extent of its gas is greater than 0.5 Mpc.

The first two groups have low values of δ: Ponman's & Bertram's analysis of HGC 62 yields $\delta = 0.54$, while David et al. find $\delta = 0.79$ for NGC 5044. Also, the temperature profiles for NGC 5044 and HCG 62 are slightly nonisothermal outside of the cooling radius with effective γ of 1.1 and 1.15 respectively. These values of δ and γ imply that the gas fraction in HCG 62 and NGC 5044 is increasing with radius near the limit of the *ROSAT* detections. On the other hand, the NGC 2300 data are not constraining enough to evaluate δ (from eq. [2c], $\delta = 3\beta/2$ for the assumed isothermal model). Indeed, decent fits yield $\delta = 0.65$ to $\delta > 2.5$. The high background used by MDMB forces a high asymptotic slope for the surface brightness profile, yielding values of δ much higher than that found for the other groups and for clusters.

4. DISCUSSION

Groups are probably more representative of the universe than are clusters, as they include altogether perhaps 5 times as many galaxies as do clusters. With a baryonic fraction over 20%, the inner 25′ (330 h_{50}^{-1} kpc) of the NGC 2300 group would be a fair tracer of the baryonic fraction in the universe if $\Omega \simeq 5\Omega_b \simeq 0.3\ h_{50}^{-2}$. These numbers are similar to the constrants from group M/L, with (if $H_0 = 50$) and without corrections for nonvirialized states, respectively (see § 1).

From equation (8), a constant baryonic fraction can be reached with $\delta = 1$ isothermal gas or with $\delta = 3/2$ polytropic gas with index $\gamma = 5/3$. Figure 1 shows that for isothermal $\delta = 1$ gas, the asymptotic gas fraction is roughly 2–2.5 times larger than at 25′. Therefore, an extrapolation of the gas fraction to large scales will yield a baryonic fraction $f_b \geq 40\%$ and will thus be consistent with baryonic nucleosynthesis if $\Omega \leq 0.15\ h_{50}^{-2}$. Taken at face value, the observations of the three groups discussed here suggest $\delta < 1$ and $\gamma > 1$, both of which imply baryonic fractions that *increase* with radius, which extrapolates at large scales to even lower values of Ω. However, as noted in § 3, high values of δ can produce equally good fits to the NGC 2300 data, and thus produce constant or decreasing baryonic fractions. Note that a similar trend of increasing gas fraction is found in clusters (e.g., Durret et al. 1993).

To reconcile the data for groups with $\Omega = 1$, as favored by inflation, one requires a baryonic fraction that *decreases* at large radii to an asymptotic value near $\Omega_b \simeq 0.06\ h_{50}^{-2}$, hence implying $\delta > 1$ (isothermal gas) or $\delta > 3/2$ ($\gamma = 5/3$ polytropic gas). Although these values of δ seem inconsistent with the X-ray observational data of the three groups studied here, there are two possibilities to remain consistent with inflation: (1) While the gas fraction is nearly constant within the group, it could fall to zero outside of the group, so that groups of galaxies would be sites of higher baryonic fraction in the universe, that is, *biased* tracers of the distribution of the baryonic fraction in the universe; (2) the cosmological constant Λ (not to confuse with the cooling function used above with the same symbol) is nonzero, that is $\Omega = 0.2$ and $\Lambda = 0.8$, which is consistent with the distribution of cluster temperatures deduced from X-ray observations (Bartlett & Silk 1993).

The model surface brightness profiles of the NGC 2300 group have a similar shape in the inner region, and are thus indistinguishable, although uncertainties in the PSPC background subtraction allow these profiles to diverge significantly beyond $R > 45'$, as seen in Figure 3. This uncertain behavior at large radii for NGC 2300 and the increasing baryonic fraction in HCG 62 and NGC 5044 make clear that it is of fundamental importance to observe X-ray emission at relatively large distances from the centers of groups to determine the extent of the gas.

As a final note, if the three groups studied here are still in the stages of cosmological collapse (as is argued for *all* noncompact groups by Diaferio et al. 1993 and Mamon 1993), then the equation of hydrostatic equilibrium used here (eq. [5]) may not apply, for two reasons: (1) The gas may not have time to react to the rapid changes of the global potential of the group and (2) even if the gas follows the potential of the whole group, one needs to add a term $\partial(\rho\bar{v}_r)/\partial t$ in equation (5). Ponman & Bertram (1993) conclude that the compact group HCG 62 is past full collapse and currently in the process of slowly shrinking by orbital energy dissipation via dynamical friction. In general, it is reasonable to assume that during the collapse of a group, the denser inner parts will collapse earlier and be close to equilibrium today, the question then being how far out is the gas in equilibrium. It may well be that if hot intergalactic gas found in a group presents unusual properties, this could reflect a departure from hydrostatic equilibrium possibly caused by the group's cosmological collapse.

We thank Dave Burstein, Harald Ebeling, John Mulchaey, Jack Sulentic, and Joe Silk for useful discussions, as well as Renato Dupke, Jack Sulentic, and an anonymous referee for detailed and useful comments on the manuscript. This research was partly sponsored through NSF EPSCoR grant 8DP-UA2-92 and a travel grant from CNFA.

REFERENCES

Bahcall, N. A., Harris, D. E., & Rood, H. J. 1984, ApJ, 289, L29
Bartlett, J. G., & Silk, J. 1993, ApJ, 407, L45
Biermann, P., & Kronberg, P. P. 1983, ApJ, 268, 69
Biermann, P., Kronberg, P. P., & Madore, B. F. 1982, ApJ, 256, 37
Cowie, L. L., Henriksen, M., & Mushotzky, R. 1987, ApJ, 317, 593
David, L. P., Forman, W., & Jones, C. 1993, preprint
Diaferio, A., Ramella, M., Geller, M. J., & Ferrari, A. 1993, AJ, 105, 2035
Durret, F., Gerbal, D., Lachièze-Rey, M., Lima-Neto, G., & Sadat, R. 1993, A&A, submitted
Forman, W., & Jones, C. 1982, ARA&A, 20, 547
Gourgoulhon, E., Chamaraux, P., & Fouqué, P. 1992, A&A, 255, 69
Hickson, P. 1982, ApJ, 255, 382
Loveday, J., Peterson, B. A., Efstathiou, G., & Maddox, S. J. 1992, ApJ, 390, 338
Mamon, G. A. 1993, in Gravitational Dynamics and the N-Body Problem, ed. F. Combes & E. Athanassoula (Meudon: Obs. de Paris), 188
Mulchaey, J. S., Davis, D. S., Mushotzky, R. F., & Burstein, D. 1993, ApJ, 404, L9 (MDMB)
Ponman, T., & Bertram, D. 1993, Nature, 363, 51
Raymond, J. C., & Smith, B. W. 1977, ApJS, 35, 419
Steigman, G. 1989, in Cosmic Abundances of Matter, ed. C. Jake Waddington (Minneapolis: AIP), 310
White, S. D. M. 1992, in Clusters and Superclusters of Galaxies, ed. A. C. Fabian (Dordrecht: Kluwer), 17

E.3 Tangential large scale structure as a standard ruler: curvature parameters from quasars

Roukema & Mamon, 2000, *A&A sous presse, astro-ph/9911413*

A&A manuscript no.
(will be inserted by hand later)

Your thesaurus codes are:
2 (12.03.3; 12.03.4; 11.17.3; 12.04.3; 12.12.1; 05.18.1)

ASTRONOMY AND ASTROPHYSICS
May 16, 2000

Tangential Large Scale Structure as a Standard Ruler: Curvature Parameters from Quasars

B. F. Roukema[1] **and G. A. Mamon**[2,3]

[1] Inter-University Centre for Astronomy and Astrophysics, Post Bag 4, Ganeshkhind, Pune, 411 007, India *(boud@iucaa.ernet.in)*
[2] Institut d'Astrophysique de Paris (CNRS UPR 341), 98bis Bd Arago, F-75014 Paris, France *(gam@iap.fr)*
[3] DAEC (CNRS UMR 8631), Observatoire de Paris-Meudon, 5 place Jules Janssen, F-92195 Meudon Cedex, France

Le 16 mai 2000

Abstract. Several observational analyses suggest that matter is spatially structured at a scale of $L_{\rm LSS} \approx 130\,h^{-1}$ Mpc at low redshifts. This peak in the power spectrum provides *a standard ruler in comoving space* which can be used to compare the local geometry at high and low redshifts, thereby constraining the curvature parameters.

It is shown here that this power spectrum peak is present in the observed quasar distribution at $z \sim 2$: qualitatively, via wedge diagrams which clearly show a void-like structure, and quantitatively, via one-dimensional Fourier analysis of the quasars' tangential distribution. The sample studied here contains 812 quasars.

The method produces strong constraints (68% confidence limits) on the density parameter Ω_0 and weaker constraints on the cosmological constant λ_0, which can be expressed by the relation $\Omega_0 = (0.24 \pm 0.15) + (0.10 \pm 0.08)\,\lambda_0$. Independently of λ_0 (in the range $\lambda_0 \in [0,1]$), the constraint is $0.1 < \Omega_0 < 0.45$. Constraints if the cosmological constant is zero or if $\lambda_0 \equiv 1 - \Omega_0$ are $\Omega_0 = 0.24^{+0.05}_{-0.15}$ and $\Omega_0 = 0.30 \pm 0.15$ respectively.

The power spectrum peak method is independent from the supernovae Type Ia method by choice of astrophysical object, by redshift range, and by use of a standard ruler instead of a standard candle. Combination of the two results yields $\Omega_0 = (0.30 \pm 0.11) + (0.57 \pm 0.11)(\lambda_0 - 0.7)$, $0.55 < \lambda_0 < 0.95$, (68% confidence limits) *without assuming that* $\lambda_0 \equiv 1 - \Omega_0$. This strongly supports the possibility that the observable universe satisfies a nearly flat, perturbed Friedmann-Lemaître-Robertson-Walker model, *independently of any cosmic microwave background observations.*

Key words: cosmology: observations — cosmology: theory — distance scale — quasars: general — large-scale structure of Universe — reference systems

Send offprint requests to: B. F. Roukema

1. Introduction

It has been known for more than a decade (e.g. de Lapparent et al. 1986; Geller & Huchra 1989) that the spatial distribution of extragalactic objects is structured at length scales about an order of magnitude greater than the $r_0 \approx 5\,h^{-1}$ Mpc scale which characterises galaxy clustering via the two-point auto-correlation function. Observational analyses from several different data sets suggest that this is due to a characteristic length scale at $L_{\rm LSS} \approx 130\,h^{-1}$ Mpc, or in other words, that there is a maximum in the power spectrum at $k = 2\pi/L_{\rm LSS} \approx 0.05\,h\,{\rm Mpc}^{-1}$ (e.g. Broadhurst et al. 1990; Broadhurst 1999; Broadhurst & Jaffe 1999; da Costa 1992; da Costa et al. 1993; Baugh & Efstathiou 1993, 1994; Gaztañaga & Baugh 1998; Einasto et al. 1994, 1997a,b; Deng, Deng & Xia 1996 or Guzzo 1999 for a recent review).

It has already been suggested that this scale could be used as a standard ruler which could be compared at low and high redshifts in order to constrain the curvature parameters, Ω_0 (the density parameter) and λ_0 (the dimensionless cosmological constant). In the redshift direction, at least two analyses have been carried out based on this idea: one analysis of a quasar catalogue and one analysis of Lyman break galaxies.

Deng, Xiaoyang & Fang (1994) implicitly used the large scale structure scale as a curvature constraint in quasar data, under the assumption that $\lambda_0 \equiv 0$, and found that $\Omega_0 \approx 0.4$. Broadhurst & Jaffe used the radial (redshift) distribution of Lyman break galaxies at $z \sim 3$ (table 1, Giavalisco et al. 1998; fig. 2, Adelberger et al. 1998). They found a correlation scale of $\Delta z \approx 0.22 \pm 0.02$, and inferred a relation $3.2\,\Omega_0 - \lambda_0 \approx 0.7$.

The purpose of this paper is to (i) emphasise that the principle can be applied to a class of bright objects easily found at super-unity redshifts: quasars; (ii) show that redshift selection effects can be minimised by using the tangential distribution instead of the radial distribution; and (iii) show pictorially (i.e. qualitatively) that quasars do indeed trace large scale structure at $z \sim 2$.

(i) Because quasars are much brighter than Lyman break galaxies, they offer a potentially much more rapid method of obtaining high precision estimates of the curvature parameters than the latter. Both classes of objects have the advantage relative to supernovae type Ia (Perlmutter et al. 1999; Riess et al. 1998) of being at superunity redshifts, so that the dependence on the curvature parameters is strong.

(ii) In order to avoid the well-known selection effects in the redshift distribution of quasars (which could also in principle affect the redshift distribution of Lyman break galaxies), the *tangential* distance distribution of quasars is investigated.

(iii) However, two-dimensional wedge diagrams are also plotted to show clear qualitative evidence of the tracing of large scale structure by the quasar distribution.

Details of the method and selection of homogeneous quasar samples are described in Sect. 2. Results are presented in Sect. 3, and discussion and conclusions are presented in Sect. 4.

A perturbed Friedmann-Lemaître-Robertson-Walker cosmological model is assumed here. The context in which quasars could reasonably be expected to form a tracer population of large scale structure may be any model in which quasars form in galaxy centres or in which galaxies form around quasars. The expected short life times of quasars should not prevent them from forming a tracer population, though they might form a biased population which could either weaken or strengthen the amplitude of the signal.

The Hubble constant is parametrised here as $h \equiv H_0/100\,\mathrm{km\ s^{-1}\ Mpc^{-1}}$. Comoving coordinates are used throughout [i.e. 'proper distances', eq. (14.2.21), Weinberg (1972), equivalent to 'conformal time' if $c = 1$]. Values of the density parameter, Ω_0, and the dimensionless cosmological constant, λ_0, are indicated where used.

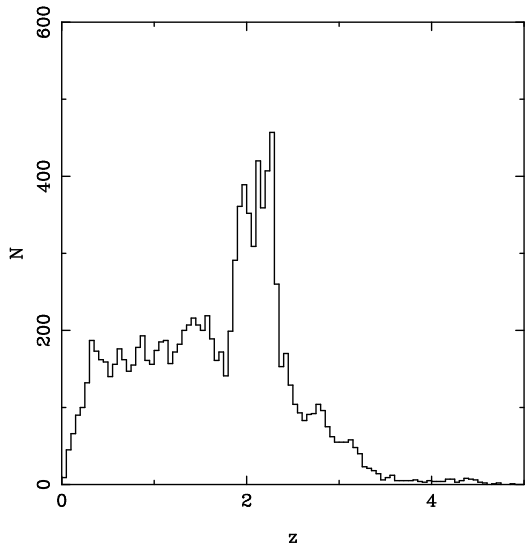

Fig. 1. Redshift distribution of quasars in the compilation of Véron-Cetty & Véron (1998).

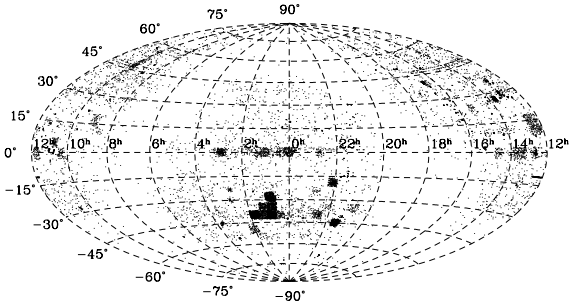

Fig. 2. Sky distribution of quasars in the compilation of Véron-Cetty & Véron (1998).

2. Method

2.1. Choice of catalogue and sky regions

There are now around 10^4 quasars which have publicly available redshifts and celestial positions (Véron-Cetty & Véron 1998). What is the optimal way to search for the power spectrum peak among these data?

Figs 1 and 2 show the redshift and sky distributions of these quasars. Depending on the redshift range of any quasar sample, a few hundred h^{-1} Mpc typically correspond to $\Delta z \sim 10^{-1}$ in redshift to within an order of magnitude, and at $z \sim 2$, where the peak in the redshift distribution lies, to $\Delta\theta \sim 1°$.

There is clearly structure in the combined redshift histogram for the full sky at around this scale. As discussed in detail by Scott (1991), the ratios in wavelength of important emission lines which contribute to the chance of detecting a quasar (Lyα, C IV, C III, Mg II) correspond to intervals $\Delta \ln\lambda \approx 0.2$ and clearly contribute to the obvious peaks in the distribution.

The alternative to searching for structure in the redshift direction is to search in the tangential direction. Most of the deep surveys visible in Fig. 2 are based on photometric selection from photographic plates of size roughly $6° \times 6°$, in particular from objective prism surveys. This is moderately larger than the scale of interest.

In order to minimise possible systematic effects due to obscuration by dust and modification of the sky back-

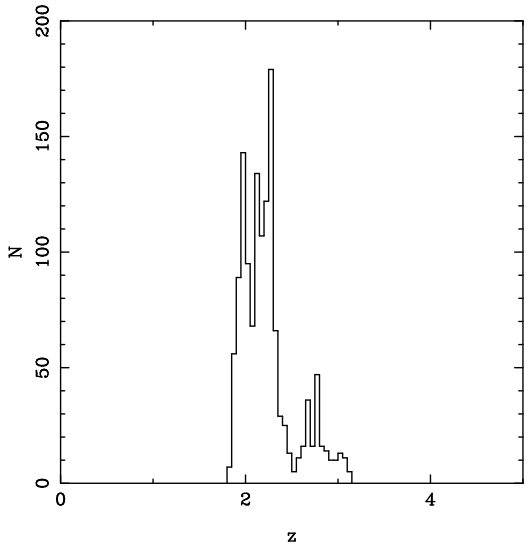

Fig. 3. Redshift distribution of quasars with redshifts from Iovino et al. (1996).

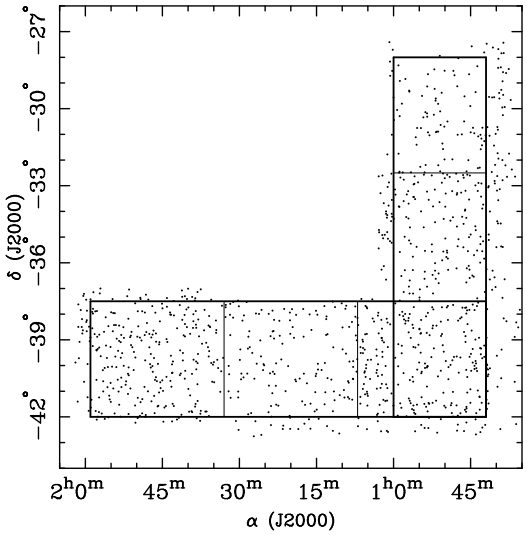

Fig. 4. Sky distribution of quasars with redshifts from Iovino et al. (1996), which lie in the redshift range $1.8 \leq z < 2.4$. Thick lines show the outlines of the right ascension and declination samples chosen for one-dimensional Fourier analysis. Thin vertical and horizontal lines show divisions in right ascension and declination in the right ascension and declination subsamples respectively, which simulated distributions are Poisson distributed. See Table 1 for numerical values of these limits.

Table 1. Definition of the two tangentially long, densely observed, homogeneous, subsamples of the Iovino et al. (1996) quasar survey listed in the Véron-Cetty & Véron (1998) catalogue, near the south galactic pole (SGP). The right ascension (first row) and declination (second row) subsamples are defined by J2000 limits ($\alpha_1 \leq \alpha \leq \alpha_2$, $\delta_1 \leq \delta \leq \delta_2$). For the purpose of Poisson simulations, these are subdivided in right ascension at (α', α'') and in declination at (δ', δ''), in order to allow for the possibility of different magnitude zero points or different magnitude cutoffs in the different plates. The number of objects N in each subsample is indicated. The total number of physically distinct quasars in the two subsamples is $N_{\rm tot} = 812$.

α_1	α_2	δ_1	δ_2	α'	α''	δ'	δ''	N
'Right ascension (α) subsample'								
0^h42^m	1^h59^m	−42.0	−37.5	1^h07^m	1^h33^m			604
'Declination (δ) subsample'								
0^h42^m	1^h00^m	−42.0	−28.0			−37.5	−32.5	373

ground by bright stars, surveys near the South or North galactic poles would be best.

Near the South galactic pole (SGP), several regions have been observed contiguously, with (at least to the eye) a reasonable homogeneity across the different plates in the region.

More objectively, the largest single homogeneous subset of the Véron-Cetty & Véron (1998) catalogue in the SGP region is that of Iovino, Clowes & Shaver (1996), who used an 'automatic quasar detection' method, i.e. applied a computer algorithm to the digitised images of objective prism plates taken on the UK Schmidt Telescope at Siding Spring, Australia.

This is the catalogue chosen for analysis here. The overall redshift distribution of this catalogue is shown in Fig. 3, and the sky distribution of the $1.8 \leq z < 2.4$ component is shown in Fig. 4.

Wedge diagrams of the catalogue, within the limits of Table 1 (see Sect. 2.2) are shown in Fig. 5. Note that the right ascension and declination subsamples are not entirely independent sets of quasars (see Fig. 4), though since only one angular coordinate is used in each analysis, they are very close to being effectively independent. Although quantitative analysis in these planes would be difficult to carry out due to the obvious redshift selection effects, it is qualitatively clear that a void-like structure is present, at a scale near $L_{\rm LSS} \sim 130\,h^{-1}$ Mpc for $(\Omega_0 = 0.3, \lambda_0 = 0.7)$. In order to avoid the redshift selection effects (see also Hartwick & Schade 1990; Scott 1991), the analysis here is restricted to Fourier space.

2.2. One-dimensional Fourier Analysis

The study of structure at $L_{\rm LSS}$ is made by one-dimensional Fourier analysis of two subsamples of the

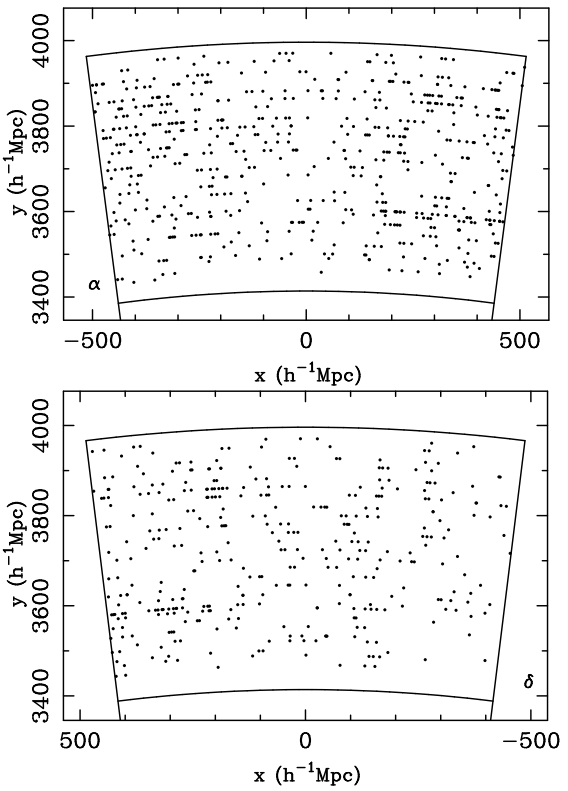

Fig. 5. Wedge diagrams for the for the right ascension (upper panel) and declination (lower panel) subsamples, for $(\Omega_0 = 0.3, \lambda_0 = 0.7)$. Since curvature is zero, rectlinear coordinates are defined: $x = d_{\rm pm}\cos(\theta^* - \theta)$, $y = d_{\rm pm}\sin(\theta^* - \theta)$, where $\theta^* \equiv (\theta_1 + \theta_2)/2 + \pi/2$ and $\theta, \theta_1, \theta_2$ and $d_{\rm pm}$ are defined in Sect. 2.2. Voids consistent with $L_{\rm LSS} = 130 \pm 10\,h^{-1}$ Mpc and not due to selection effects are clearly visible.

Iovino et al. (1996) sample [i.e. of the subset of the Véron-Cetty & Véron catalogue for which redshifts are obtained from Iovino et al. (1996)] which have maximum tangential survey length. That is, one subsample combining three plates in the right ascension direction and one subsample combining three plates in the declination direction are chosen.

The right ascension and declination boundaries are chosen conservatively, i.e. to within at most 2.5 great circle degrees from the plate centres, and are shifted even closer in where it looks like there may be incompleteness close to the boundary. Although what appears to be a lack of quasars near a few plate boundaries might in fact be due to real voids, it is preferable to risk losing some real signal rather than risk including some noise.

The angular limits chosen are indicated in Table 1. The redshift range used is $z_1 = 1.8 \leq z < z_2 = 2.4$, which includes most of the catalogue, and is small enough to superimpose only a few 'units' of large scale structure, i.e. the signal should not be significantly reduced by the superimposition of structures which are out of phase.

In each of the two subsamples, the angular positions in the long direction (right ascension and declination respectively) are converted to comoving tangential lengths $d_\perp$ by

$$\begin{aligned} d_\perp(z,\theta) &\equiv (\theta - \theta_1)\, d_{\rm pm}(z) \\ &= (\theta - \theta_1) \begin{cases} R_C \sinh[d(z)/R_C], & \kappa_0 < 0 \\ d(z), & \kappa_0 = 0 \\ R_C \sin[d(z)/R_C], & \kappa_0 > 0. \end{cases} , \end{aligned} \quad (1)$$

where the angular position $\theta = \alpha\cos\delta$ or $\theta = \delta$ and the survey limit is $\theta_1 = \alpha_1\cos\delta_1$ or $\theta_1 = \delta_1$ respectively (in radians), $d_{\rm pm}(z)$ is the proper motion distance,

$$d(z) = \frac{c}{H_0}\int_{1/(1+z)}^{1} \frac{{\rm d}a}{a\sqrt{\Omega_0/a - \kappa_0 + \lambda_0 a^2}}, \quad (2)$$

is the proper distance [eq. (14.2.21), Weinberg (1972)],

$$\kappa_0 \equiv \Omega_0 + \lambda_0 - 1 \quad (3)$$

is the (dimensionless) curvature of the observational Universe and

$$R_C \equiv \frac{c}{H_0}\frac{1}{\sqrt{|\kappa_0|}} \quad (4)$$

is its curvature radius.

The maximum tangential length considered is $d_\perp(z_1, \theta_2)$, where $z_1 = 1.8$ is the low redshift limit of the sample. This is the minimum tangential length corresponding to $\theta_2 - \theta_1$ over the range in z and the (Ω_0, λ_0) domain considered in this paper. For negative or zero curvature, $d_\perp$ is always an increasing function of z. For positive curvature and $\Omega_0 < 1.1, \lambda_0 < 1$, the $d/R_C = \pi/2$ point (halfway to the antipode) occurs at $z \gtrsim 8$, so the domain of decreasing $d_\perp$ is not reached here. Thus, $d_\perp$ is a strictly increasing function of z in the domain of interest of this paper and $d_\perp(z_1)$ provides the minimum tangential length.

Note that the choice of this cutoff throws away a small amount of data (e.g. for which $z \approx z_2, \theta \approx \theta_2$), but ensures that the one-dimensional number density distribution ${\rm d}N/{\rm d}d_\perp$ is a uniform projection of a (large) subset of the two-dimensional distribution ${\rm d}^2N/{\rm d}d_\perp{\rm d}d_{\rm pm}$. Inclusion of the small amount of lost data would create a nonuniform number density projection and would introduce non-physical power to the Fourier transform, so is not attempted here.

For values of (Ω_0, λ_0) in the range $0.0 \leq \Omega_0 \leq 1.1, -0.1 \leq \lambda_0 \leq 1.0$, the list of positions $0 \leq d_\perp \leq d_\perp(z_1, \theta_2)$ is binned into 1024 bins and fast Fourier transformed to a function $f(\nu|\Omega_0, \lambda_0)$. The results below are

found to change slightly but insignificantly if fewer bins, e.g. 128 bins, are used. The contours in the (Ω_0, λ_0) plane are more noisy with fewer bins.

Two null hypotheses are considered here for the Fourier spectrum for each pair (Ω_0, λ_0): the possibility that large scale structure is undetectable in the two quasar subsamples, and the possibility that the best estimate of the scale of large scale structure is $L_{\rm LSS} \pm \Delta L_{\rm LSS}$.

2.3. Null Hypothesis $\mathcal{H}_1$: No LSS peak is detectable

Informally, $\mathcal{H}_1(\Omega_0, \lambda_0)$ is the hypothesis that there is no peak in the tangential distributions of the quasars due to large scale structure.

More precisely, $\mathcal{H}_1(\Omega_0, \lambda_0)$ is the hypothesis that:

(i) the pair (Ω_0, λ_0) is correct;
(ii) the value of the Fourier transform f at the large scale structure frequency $\nu_0 \equiv 1/L_{\rm LSS}$, i.e. $f(\nu_0|\Omega_0, \lambda_0)$, is not significantly higher than that expected from the distribution of the same statistic evaluated for Poisson distributions in θ, for fixed values of $\nu_0, \Omega_0, \lambda_0$, for both subsamples; and
(iii) $\nu_{\rm max}$, defined as the local maximum in $f(\nu|\Omega_0, \lambda_0)$ at the greatest value of ν satisfying $\nu < 0.01\,h\,{\rm Mpc}^{-1}$, is not significantly higher than that expected from the distribution of the same statistic evaluated for Poisson distributions in θ, for fixed values of Ω_0, λ_0, for both subsamples.

The Poisson distributions are pseudo-random samplings of uniform distributions in θ within each of the three subdivisions of the sample as defined as in Table 1. The number of simulations calculated is 30. A Gaussian smoothing of standard deviation two bin widths is applied to the Fourier transform $f(\nu|\Omega_0, \lambda_0)$ before searching for the local maximum.

The purpose of criterion (ii) is that if a peak is present at the scale expected, then this may contribute to rejecting $\mathcal{H}_1$ by the presence of a strong peak. However, because the overdensity may not be very high, this may not be sufficient in itself to reject $\mathcal{H}_1$.

An independent and possibly more sensitive test is (iii): is the best estimate of the frequency of a peak significantly different from that for Poisson distributions, independently of any criterion on the absolute height of the peak? Likely values of $\langle \nu_{\rm max} \rangle$ for Poisson simulations are around $0.005\,h\,{\rm Mpc}^{-1}$, though this depends on the smoothness or roughness of f for the Poisson simulations. Since $1/L_{\rm LSS} \approx 0.0077\,h\,{\rm Mpc}^{-1}$, then, as long as the scatter in $\nu_{\rm max}$ for the simulations is small enough, criterion (iii) may enable rejection of $\mathcal{H}_1$ for pairs (Ω_0, λ_0) which correctly describe the observational Universe, because in that case (under the principle assumed for this paper), the peak is expected to occur at a special frequency rather than at an arbitrary frequency.

2.4. Null Hypothesis $\mathcal{H}_2$: The best estimate of the frequency of an LSS peak is at $1/L_{\rm LSS}$

The more interesting hypothesis is $\mathcal{H}_2(\Omega_0, \lambda_0)$, the hypothesis that the best estimate of a peak in the tangential distributions of the quasars due to large scale structure is at $L_{\rm LSS} \pm \Delta L_{\rm LSS}$, independently of whether the peak is significant or not.

$\mathcal{H}_2(\Omega_0, \lambda_0)$ is quantified as follows:

(i) the pair (Ω_0, λ_0) is correct;
(ii) $\nu_{\rm max}$ (defined as for $\mathcal{H}_1$) is consistent with $\nu_{\rm max} = 1/L_{\rm LSS}$ where the $1\,\sigma$ uncertainty in the external estimate of $L_{\rm LSS}$ is $\Delta L_{\rm LSS}$, and $\Delta\nu_{\rm max}$, the $1\,\sigma$ uncertainty in estimating $\nu_{\rm max}$ from the present data is obtained robustly by bootstraps (e.g. Barrow, Sonoda & Bhavsar 1984).

The estimate $\Delta L_{\rm LSS} = 10\,h^{-1}$ Mpc is adopted here.

The bootstrap method (e.g. Barrow et al. 1984) for a catalogue of N objects, is for N objects to be randomly drawn from the same sample, *allowing multiple sampling* of single objects. The statistical uncertainties in the properties of interest are then estimated by running several such bootstrap simulations, which are considered as independent experiments. This provides an upper estimate to the uncertainty. The number of bootstraps used here is 30.

The bootstrap $1\,\sigma$ uncertainty and $\Delta L_{\rm LSS}$ are assumed to be independent and to arise from Gaussian distributions, so are combined in quadrature.

Although $\mathcal{H}_2$ could in principle be consistent with the data for (Ω_0, λ_0) pairs which are also consistent with $\mathcal{H}_1$, the (Ω_0, λ_0) pairs for which $\mathcal{H}_1$ is rejected and $\mathcal{H}_2$ is not rejected are obviously of most interest.

3. Results

3.1. $\mathcal{H}_1$: Can the absence of a peak be rejected?

Confidence levels $1 - P_\alpha[f(\nu_0)]$, $1 - P_\alpha(\nu_{\rm max})$, $1 - P_\delta[f(\nu_0)]$ and $1 - P_\delta(\nu_{\rm max})$, for rejecting $\mathcal{H}_1$ are shown in Figs 6 and 7 for the right ascension and declination subsamples respectively.

These are defined by the probability of the observational results given the hypothesis:

$$P(t) \equiv P_{\rm gauss}(t, \overline{t}, \Delta t) \equiv \int_{|t-\overline{t}|/\Delta t}^{\infty} \frac{1}{\sqrt{2\pi}} e^{-u^2/2}\, du, = \frac{1}{2}{\rm erfc}\left(\frac{1}{\sqrt{2}}\frac{|t-\overline{t}|}{\Delta t}\right) \quad (5)$$

where t is the parameter studied (either $f(\nu_0)$ or $\nu_{\rm max}$), and $\overline{t}$ and Δt are the mean value of t and the standard deviation of t obtained from the Poisson simulations.

Since the question of interest is to find (Ω_0, λ_0) pairs for which there is, ideally, an excess of power at $L_{\rm LSS}$ and a frequency higher than that for Poisson distributions

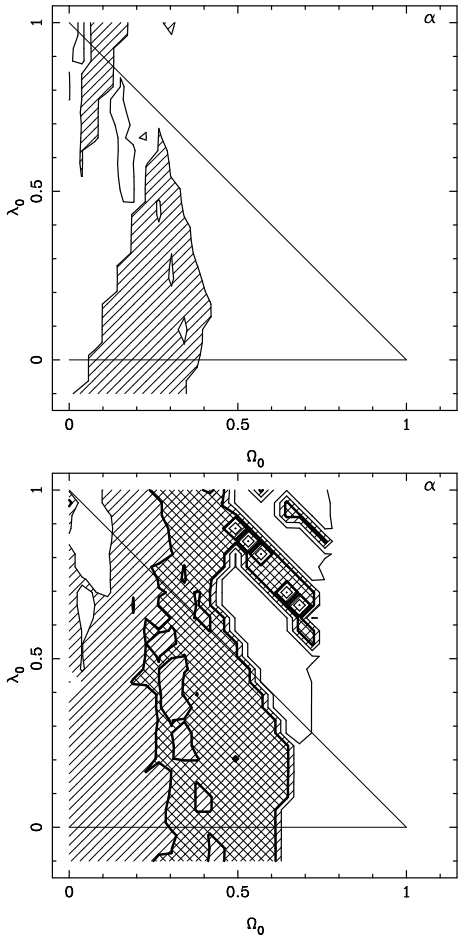

Fig. 6. Confidence levels for the different criteria for trying to reject $\mathcal{H}_1$, for the right ascension subsample. The upper panel is for $f(\nu_0)$, the lower panel for $\nu_{\max}$. Rejection of the null hypothesis $\mathcal{H}_1$ at $> 0\,\sigma$, $> 1\,\sigma$, $> 2\,\sigma$ and $> 3\,\sigma$ confidence levels, i.e. $1 - P > 50\%$, $1 - P > 84\%$, $1 - P > 98\%$ and $1 - P > 99.9\%$, is shown by contoured regions with light shading, light cross-hatched, medium cross-hatched and heavy cross-hatched shading, respectively. (In a few of this set of figures, a few contours at $< 0\,\sigma$ and $< -1\,\sigma$ are also shown. These are not useful for null hypothesis rejection.) Lines indicating $\lambda_0 = 0$ and $\lambda_0 = 1 - \Omega_0$ are shown for $\Omega_0 \leq 1$ as a guide to the eye.

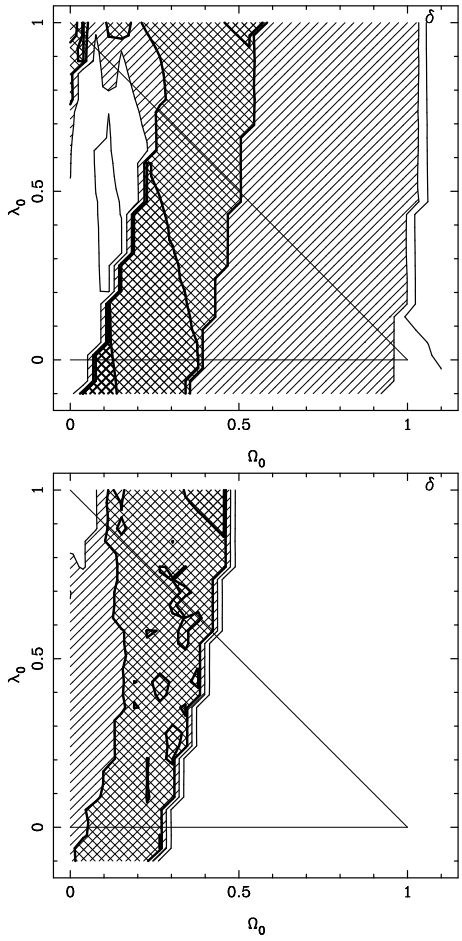

Fig. 7. Confidence levels for rejecting $\mathcal{H}_1$, for the declination subsample. The upper panel is for $f(\nu_0)$, the lower panel for $\nu_{\max}$. Shading is as for Fig. 6.

(given the limits for searching for a local maximum defined in Sect. 2.3), the probability above is defined to be one-sided.

The upper panel of Fig 6 shows that if there is a peak at $L_{\rm LSS}$ in the right ascension subsample, then it is not strong enough to significantly reject the null hypothesis $\mathcal{H}_1(\Omega_0, \lambda_0)$ of the non-existence of a peak for any pair (Ω_0, λ_0). Note, of course, that non-rejection of $\mathcal{H}_1$ does not imply that $\mathcal{H}_1$ is correct. It just implies (states) that $\mathcal{H}_1$ is not rejected.

However, the lower panel of Fig 6 shows that the best estimate of the frequency of a peak, independently of its significance, *is* rejected at the $1 - P > 84\%$ level for a large (though noisy) band in the (Ω_0, λ_0) plane, for $\Omega_0 \sim 0.4 \pm 0.1$.

Both the $f(\nu_0)$ amplitude test and the $\nu_{\max}$ test for the declination subsample (Fig 7) independently confirm, to $\sim \pm 0.2$ precision in Ω_0 and λ_0, the region of the (Ω_0, λ_0) plane which enables $1\,\sigma$ rejection of $\mathcal{H}_1(\Omega_0, \lambda_0)$. A small band within the latter, for the $\nu_{\max}$ test, enables rejection to $2\,\sigma$, i.e. $1 - P > 98\%$.

As noted above, the fact that the $f(\nu_0)$ test for the right ascension sample does not reject $\mathcal{H}_1$ is not a problem

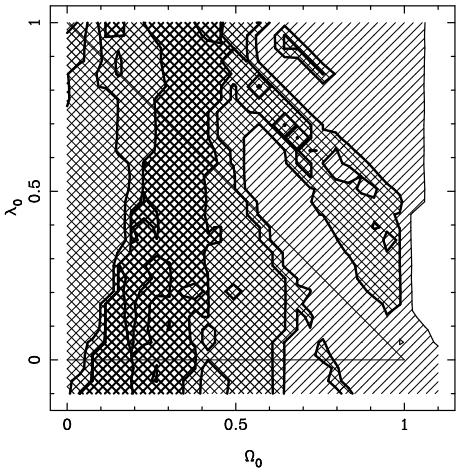

Fig. 8. Combined confidence levels for rejecting $\mathcal{H}_1$, using Eq. (6) to combine the results shown in Fig. 6 and Fig. 7. Shading is as for Fig. 6.

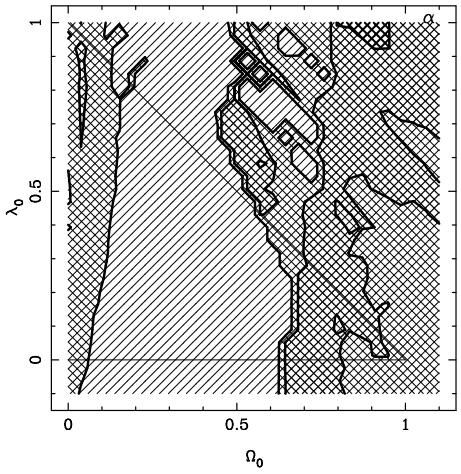

Fig. 9. Confidence intervals for rejecting $\mathcal{H}_2$, the hypothesis that the large scale structure peak occurs at $1/L_{\rm LSS}$, for the right ascension subsample. Shading styles are as for the previous figures, except that the confidence levels are two-sided, i.e. the four successively darker shadings are for $1-P>0\%$, $1-P>68\%$, $1-P>95\%$ and $1-P>99.7\%$ respectively.

for alternative hypotheses to $\mathcal{H}_1$ (in particular for $\mathcal{H}_2$). The failure of one test to reject a model does not imply that it is correct, and in the presence of independent tests which *do* reject the model, the overall result should be to reject the model. This is expressed mathematically as follows.

The results for the two tests, for the two subsamples, imply a confidence level

$$1-P = 1- \ P_\alpha[f(\nu_0)] \ \ P_\alpha[\nu_{\rm max}] \ \ P_\delta[f(\nu_0)] \ \ P_\delta[\nu_{\rm max}] \quad (6)$$

for rejecting $\mathcal{H}_1$. Note that although the $f(\nu_0)$ and $\nu_{\rm max}$ tests seem to be independent (e.g. Figs 6, 7), this has not been strictly proven, so the combined confidence levels for rejecting $\mathcal{H}_1$ may be slightly overestimated.

The final contours in confidence levels for rejecting $\mathcal{H}_1(\Omega_0,\lambda_0)$ are shown in Fig. 8.

These show that the null hypothesis of the absence of the large scale structure peak is rejected at at least the $1-P>84\%$ level for nearly all pairs (Ω_0,λ_0) with $0\lesssim\Omega_0\lesssim0.6$ and at the $1-P>98\%$ level for $0.1\lesssim\Omega_0\lesssim0.5$. Moreover, for a band running from $(\Omega_0\approx 0.15,\lambda_0=-0.1)$ to $(\Omega_0\approx0.4,\lambda_0=1)$, $\mathcal{H}_1(\Omega_0,\lambda_0)$ is rejected at the $1-P>99.9\%$ level.

In other words, if the matter density of the Universe is low, then the possibility that there is no large scale structure peak at $L_{\rm LSS}=130\,h^{-1}$ Mpc in the quasar sample is rejected, and it is rejected to high significance for the most favoured values of the (Ω_0,λ_0) pair: a low density hyperbolic model with $(\Omega_0\approx0.2,\lambda_0=0)$, or a low density flat model with $(\Omega_0\approx0.3,\lambda_0=1-\Omega_0)$.

For a flat, critical density model, $(\Omega_0=1,\lambda_0=0)$, $\mathcal{H}_1$ is not rejected. Could it be argued that if $(\Omega_0=1,\lambda_0=0)$ is correct, then the rejection of $\mathcal{H}_1$ for low values of Ω_0 is simply an artefact due to making a wrong assumption?

A simple, quantified counterargument to this is the following. If a peak really is present in the data, even though its amplitude may be low, then even for incorrect values of (Ω_0,λ_0) it is likely that non-random frequencies can be detected. Since the search for the frequency starts just a little above $1/L_{\rm LSS}$, then if a low value of Ω_0 is correct, the case of $(\Omega_0=1,\lambda_0=0)$ may lead to the detection of a low frequency harmonic. This is indeed the case. By substituting the word 'lower' for 'higher' in (iii) of the definition of $\mathcal{H}_1$ (Sect. 2.3), and recalculating the equivalent of Fig. 8, the confidence level for rejecting $\mathcal{H}_1(\Omega_0=1,\lambda_0=0)$ is found to be at the $1-P>98\%$ level.

3.2. $\mathcal{H}_2$: What pairs (Ω_0,λ_0) are consistent with the frequency of the peak being at $1/L_{\rm LSS}$?

Given that $\mathcal{H}_1$ is strongly rejected for interesting pairs of (Ω_0,λ_0) values, what are the pairs (Ω_0,λ_0) which are consistent with $L_{\rm LSS}=130\pm10\,h^{-1}$ Mpc?

For consistency, this question is formally answered by trying to reject the null hypothesis $\mathcal{H}_2(\Omega_0,\lambda_0)$, according to which the frequency of the peak is assumed to be at $L_{\rm LSS}=130\pm10\,h^{-1}$ Mpc. Two-sided confidence intervals are used [a factor of two is inserted in front of the integral in Eq. (5)], since the question of interest is now how close the best estimate of the frequency is to the hypothesised frequency, and both low and high frequencies would reject the hypothesis.

The region in the (Ω_0,λ_0) plane for which $\mathcal{H}_2$ cannot be significantly rejected provides an estimate of the values

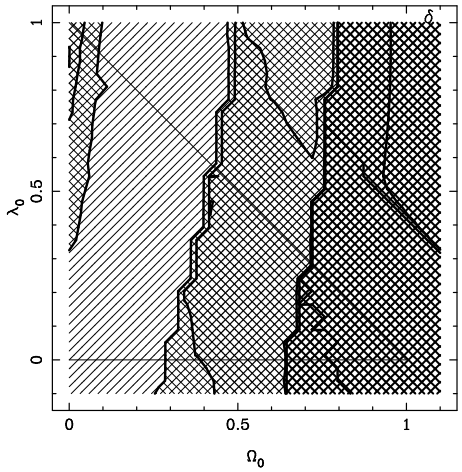

Fig. 10. Confidence intervals for $\mathcal{H}_2$, for the declination subsample, shading as for Fig. 9.

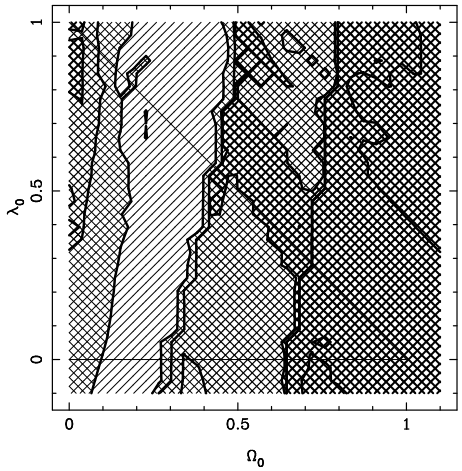

Fig. 11. Confidence intervals for $\mathcal{H}_2$, combining the information from the two subsamples. Shading is as for Fig. 9.

of Ω_0 and λ_0. In the present case, as for most other methods which provide significant constraints on the curvature parameters, there is a degeneracy between the latter, so that an estimate can only be provided for the relation between them, rather than for both parameters independently. A linear fit is used to describe this relation.

Figs 9 and 10 show the confidence levels for rejecting $\mathcal{H}_2(\Omega_0, \lambda_0)$ for the right ascension and declination subsamples respectively. Neither subsample is sufficient on its own to provide a precise estimate of an (Ω_0, λ_0) relation, although both reject $\Omega_0 \gtrsim 0.5$ to $\gtrsim 70\%$ significance.

However, the fact that they are independent subsamples implies that they can be combined via

$$1 - P = 1 - \; P_\alpha[\nu_{\max}] \;\; P_\delta[\nu_{\max}] \qquad (7)$$

to give Fig. 11, which shows that most values of (Ω_0, λ_0) can be rejected to $> 68\%$ confidence if $|\Omega_0 - 0.25| \gtrsim 0.15$.

More precisely, a linear relation between the two curvature parameters can be fitted to the points in Fig. 11 for which the probability P of obtaining the observations is highest, using the 68% confidence limits as uncertainties, by linear regression of Ω_0 as a function of λ_0.

This relation is

$$\Omega_0 = (0.24 \pm 0.04) + (0.10 \pm 0.08)\,\lambda_0. \qquad (8)$$

The uncertainties here relate to the fitting procedure. Since the $1\,\sigma$ (68% confidence) uncertainties on Ω_0 for each value of λ_0 are not mutually independent, the uncertainties in Eq. 8 do not represent measurement uncertainties.

Since the measurement uncertainty (including $\Delta L_{\rm LSS}$) is already expressed in the contours in Fig. 11, this is restored to the zero-point of the relation, giving

$$\Omega_0 = (0.24 \pm 0.15) + (0.10 \pm 0.08)\,\lambda_0, \qquad (9)$$

where the zero-point uncertainty includes known measurement uncertainties and the slope uncertainty relates to the fitting procedure.

Note that, as revealed by this relation, the point least rejected by the data for $\lambda_0 \equiv 0$ is much closer to the large Ω_0 68% confidence limit than to the low Ω_0 68% confidence limit, so the representation by Gaussian uncertainties is not an optimal approximation. However, if one deduces $\Omega_0 = 0.24 \pm 0.15$ for the case $\lambda_0 \equiv 0$ and assumes that this is a Gaussian $1\,\sigma$ uncertainty, then this will be sufficient for most applications, where one prefers overestimates of uncertainties to underestimates.

Alternatively, the $\lambda_0 \equiv 0$ result can be written as $\Omega_0 = 0.24^{+0.05}_{-0.15}$.

For a flat universe, i.e. $\lambda_0 \equiv 1 - \Omega_0$, use of the uncertainties in Eq. (9) as Gaussian uncertainties and combination in quadrature yields $\Omega_0 = 0.30 \pm 0.15$, which is consistent with Fig. 11.

A large part of the uncertainty here is due to the bootstraps. For example, if the intrinsic measurement uncertainty due to the bootstraps is removed, and only the uncertainty $\Delta L_{\rm LSS} = 10\,h^{-1}$ Mpc is used for the equivalent of Fig. 11, then the regions not rejected by the confidence level contours shrink considerably, and $\lambda_0 < 0.4$ is rejected at the $1 - P > 95\%$ level.

However, although bootstrap estimates of uncertainties provide an upper estimate to uncertainties, i.e. the true uncertainties may be smaller, it is prudent to retain the bootstrap estimate.

3.3. Amplitude of large scale structure peak

Since the main aim of the present study is to use the $L_{\rm LSS}$ scale as a ruler for measuring the curvature parameters, a statistically robust estimate of the *amplitude* of the power spectrum peak used as a standard ruler is beyond the scope of this paper.

Indeed, as can be seen in Fig. 6 (upper plot), the amplitude of the peak in the right ascension sub-sample is insufficient (on its own) to significantly rule out the hypothesis of no peak at all, with respect to the Poisson simulations. Of course, the search for a local maximum *does* find that this is closer to ν_0 than expected randomly, for a certain band in the (Ω_0, λ_0) plane.

However, as a guide to what might be expected in future less sparse surveys, the amplitude in the declination subsample, which has a stronger signal than that of the right ascension subsample, may be useful to quantify, though caution is recommended in the interpretation of this estimate.

For the pair $(\Omega_0 = 0.3, \lambda_0 = 0.7)$ (see Sect. 4), a crude estimate of the amplitude expressed as a signal-to-noise ratio,

$$A \equiv \frac{f(\nu_0|\mathrm{obsvn}) - \langle f(\nu_0|\mathrm{Poisson})\rangle}{\langle f(\nu_0|\mathrm{Poisson})\rangle} \pm \frac{\sigma[f(\nu_0|\mathrm{Poisson})]}{\langle f(\nu_0|\mathrm{Poisson})\rangle} \quad (10)$$

is $A \approx 1.7 \pm 0.5$.

This value is lower than the corresponding value in Broadhurst et al.'s (1990) one-dimensional survey, for which $A \approx 7$ at the L_{LSS} scale (from fig. 2b of that paper), but is similar in order of magnitude to the density contrast values of $\delta\rho/\rho \gtrsim 2.5$ found in the Las Campanas Redshift Survey (Tucker, Lin & Shectman 1998).

This is not surprising. Even for $(\Omega_0 = 0.3, \lambda_0 = 0.7)$, a somewhat lower amplitude of density contrast can be expected at $z \sim 2$ relative to $z \sim 0$, though this could be compensated for (or under- or over-compensated for) by positive biasing of the quasar distribution relative to that of galaxies, if quasars turn on at the densest points where galaxies are most likely to interact and/or merge.

A full analysis of the amplitude of the signal in analyses following the present one should potentially provide a useful constraint on models of quasar onset and lifetimes.

3.4. Selection Effects

The results above are strikingly consistent with the most recent expectations from independent observations regarding large scale structure and the curvature parameters: the power spectrum peak is present at $L_{\mathrm{LSS}} = 130 \pm 10\,h^{-1}$ Mpc for the popular curvature pair $(\Omega_0 = 0.3 \pm 0.15, \lambda_0 = 1 - \Omega_0)$.

Could this just be a coincidence due to selection effects? In the redshift direction, selection effects have long led to surprising results, though not to expected results, from quasar catalogues (see Scott 1991 and references therein).

The angular scale corresponding to $z \sim 2$ and $(\Omega_0 \sim 0.3, \lambda_0 = 1 - \Omega_0)$ is $\sim 2°$. This is half an order of magnitude smaller than the size of a UK Schmidt plate ($\approx 6°$). This is sufficiently small that the large scale structure scale is clearly smaller than the size of the plates, but not so much smaller that more subtle effects related to the plate size can be trivially excluded from contributing to the result found above.

Possible angular selection effects, instrumental and/or astrophysical, in objective prism quasar surveys include

(i) effects due to human subjectivity of selecting 'quasar-like' objects from the photographic plates
(ii) not finding quasars in regions where the sky background is noisy or there is no signal at all due to step wedges, large, bright galaxies or to bright stars and their ghosts (due to reflection from the secondary mirror support structure)
(iii) not finding quasars close to other quasars/stars due to overlapping spectra
(iv) differential apparent magnitude limits due to the vignetting function of the telescope plus instrument geometry
(v) differences in apparent magnitude limits between plates
(vi) differential apparent magnitude limits due to intervening dust
(vii) mistaking quasars for stars in low projected number density open (star) clusters which happen to lie in the survey region, thereby missing quasars in those regions
(viii) mistaking stars for quasars, which possibly explains the excess numbers of objects at some specific redshifts in Fig. 5.

Problem (i) is avoided by application of a computer algorithm to digital scans of the Schmidt plates. The validity of the precise quantification and relative weighting of the various 'quasar-like' criteria chosen by Iovino et al. (1996) to detect quasars could be debated, but since they are calculated automatically over the entire scanned regions, this aspect of human subjectivity is applied in a consistent, objective fashion across the plates.

Problems (ii), (iii) to some extent (quasar-star overlaps), (vi), (vii) and (viii) are likely to be minimised by the choice of a very high galactic latitude region, i.e. the SGP.

Problem (v) is corrected for in the control simulations by Poisson distributing points independently within the boundaries of individual plates in each of the two subsamples (see Sect. 2.2).

The largest obvious contaminants listed in item (ii) which ocur in the fields studied here are a moderately bright star near $\alpha \sim 1^h, \delta \sim -30°$ (field 411, see table 1 of Iovino et al. 1996) and a bright galaxy near $\alpha \sim 0^h 50^m, \delta \sim 39°$ (field 295), which occupy less than about 0.1 sq. deg. and 0.2 sq. deg. respectively. Neither corresponds to what visually appears to be a void in Fig. 4.

Counting the right ascension and declination analyses separately, the fraction of the solid angle biased by these two objects is $\lesssim [(0.2) + (0.2 + 0.1)]$ sq. deg./116.4 sq. deg. = 0.4% of the total solid angle included in the borders (as defined in Table 1). This

Table 2. Angular separation of plate centres (table 1, Iovino et al. 1996) from the four borders [$\alpha(1)$,(2), $\delta(1)$,(2) in table, from the borders in strictly increasing numerical α or δ values] and maximum centre-corner angle (3) of the fields for the right ascension (α) and declination (δ) subsamples, defined here in Table 1, in great circle degrees. Field numbers (#) are ESO/SERC field numbers.

	α			δ		
# :	295	296	297	295	351	411
$\alpha(1)$	2.37	2.55	2.53	2.37	1.73	1.40
$\alpha(2)$	2.43	2.45	2.47	1.09	1.97	2.51
$\delta(1)$	2.27	2.26	2.25	2.27	2.77	2.77
$\delta(2)$	2.23	2.24	2.25	2.23	2.23	1.73
(3)	3.33	3.41	3.38	3.29	3.40	3.74

is unlikely to be sufficient to mimic a large scale structure signal at $\sim 2°$ in the full data set.

Problem (iii) for quasar-quasar overlap could in principle cause a weakening of the real signal and not a false signal, although the low number density of the quasars implies this effect should probably be small. This is because overlaps are expected to occur at around $70''$ in the dispersion direction and $3''$ in the orthogonal direction. If close quasar pairs are missed due to this effect, then the angular distribution measured will be *smoother* than the intrinsic angular distribution, i.e. filamentary type structure would be less easy to detect than it should be.

Quasar-star overlap, and problems (vi), (vii) and (viii) should be uncorrelated with the intrinsic quasar distribution and are more likely to weaken any genuine signal rather than mimic an expected signal.

3.4.1. Differential magnitude limits?

Problem (iv) could, in principle, provide the largest systematic error. Fig. 3 of Dawe (1984) shows that from $\approx 2°$ to $\approx 4°$ from the centre of the UK Schmidt Telescope field, the apparent magnitude limit can become less faint from ~ 0.02 mag to ~ 0.2 mag respectively. That is, less quasars would be detectable by a fixed search algorithm towards the edges and corners of the plate than in the middle.

Table 2 lists the angular distances, in great circle degrees, from the boundaries and the corners of the plate images, assuming that the plate centres listed in table 1 of Iovino et al. (1996) are the correct (B1950) centres of the actual fields observed by those authors.

The borders of the fields, as analysed here (Table 1), are mostly about $2 - 2.5°$ from the centres, so the magnitude limits should vary much less than 0.1 mag over most of the plates. The furthest corners from the centres are mostly at about $3.3 - 3.4°$ from the centres, so the magnitude limit should be about 0.06 mag brighter at these corners.

Are differences in the (solid angular) quasar number densities due to these magnitude limit variations visible in Fig. 4? Possible voids in three of the $-42°$ corners of fields in this figure, and in the $(\alpha = 0^h 42^m, \delta = -37.5°)$ corner of field #351 (the middle declination field) could conceivably be related to the variation in magnitude limit.

However, since the majority of Iovino et al.'s quasars (see fig. 2 of Iovino et al. 1996) are roughly uniformly distributed over an interval of about one magnitude in apparent magnitude, a change in the magnitude limit of 0.06 mag could at most change the quasar number density by $\sim 6\%$.

Moreover, a small fraction of the quasars in the Iovino et al. sample have $z > 2.4$ and are not studied here. These are likely to have the faintest apparent magnitudes, so $\sim 6\%$ is an *upper* estimate to the expected reduction in number density at the furthest corners.

The apparent voids visible to the eye are presumably seen as voids because the number density is at least an order of magnitude lower than average. This is not explicable by a magnitude limit varying by 0.06 mag.

In addition, in at least some of the fields, the number density of quasars appears to be lower in 'voids' near the *centres* of the plates, where the exposure ought to be deepest.

Figure 4 suggests that the $\delta \sim -30°$ field might appear to have a circularly symmetric central concentration of quasars, apart from a cluster/filament near $(\alpha \sim 0^h 42^m, \delta \sim -31°)$. This is partly because the right ascension centres of the declination fields are offset from one another, which is why narrow limits in right ascension were chosen. This could affect an analysis using the boundaries adopted here if that analysis were carried out in right ascension in the 'declination' subsample. But that is not the case here: only the distribution in declination of the declination sample was studied, so the right ascension offsets cannot affect the results.

Another reason why problem (iv) is unlikely to be significant in the present study is that, as Dawe (1984) points out, departures from circular symmetry of the magnitude limit are below the measurement limits (0.01 mag) of his empirical estimates, and are not expected theoretically.

The variations in quasar density *around* the field centres appear about as strong as the variations leading to voids towards field edges or corners. For example, the void centred around $(\alpha = 0^h 50^m, \delta = -37°)$ in field #351 (the middle declination field) is adjacent to a quite dense region around $(\alpha = 0^h 55^m, \delta = -37°)$, which is about equidistant from the field centre. This strong variation cannot be caused by the circularly symmetric vignetting of the UK Schmidt Telescope.

Finally, shifting several of the borders defined in Table 1 by $0.5°$ typically modifies the slope and zeropoint of the (Ω_0, λ_0) relation of Eq. (9) by only about ± 0.01. Since magnitude limits should, statistically, have *some* effect at the corners, even if small, this shows that uncertainty due

the increased uncertainty per subsample, or some of the subsamples have to be (*a posteriori*) dropped.

Since the number of objects per subsample decreases by roughly a factor of four, a doubling of $\Delta L_{\rm LSS}$ to $\Delta L_{\rm LSS} = 20\,h^{-1}$ Mpc should be sufficient to allow for consistency with the analysis for the full redshift range. This results in a small region which provides a $1-P > 95\%$ solution in a small patch close to the $(\Omega_0 = 0.3, \lambda_0 = 0.7)$ point, but suggesting a hyperbolic universe model (Fig. 12).

Alternatively, retaining $\Delta L_{\rm LSS} = 10\,h^{-1}$ Mpc and just considering the four redshift intervals of the declination subsample leads to Fig. 13. This shows a band in the (Ω_0, λ_0) plane within the $1-P > 68\%$ contour, which is clearly consistent with (though narrower than) the corresponding contour for the declination sample considered as a single sample (Fig. 10).

It is therefore clear that the signal is present in most redshift interval subsets of the full data set, but that because of the increased noise, in order to combine those signals into a consistent solution, a more sophisticated technique than that presented here would be necessary.

4. Discussion and conclusions

It has been shown in this paper that the use of the power spectrum peak corresponding to large scale structure as a standard ruler in the tangential distribution of a homogeneous quasar survey at $z \sim 2$ provides a new and independent method of constraining the curvature parameters.

More precisely, what appears to be the optimal choice of homogeneous tangential quasar surveys publicly available was chosen and analysed. The quasar data analysed were the right ascension and declination subsamples (Table 1) of the Iovino et al. (1996) survey as provided in the Véron-Cetty & Véron (1998) quasar catalogue.

The null hypothesis $\mathcal{H}_1(\Omega_0, \lambda_0)$ according to which no peak can be detected at $L_{\rm LSS} = 130\,h^{-1}$ Mpc in the one-dimensional Fourier transform of the tangential proper motion distance distributions, and according to which the best estimate of the frequency of any such peak is random, is rejected to high significance for most 'interesting' pairs of (Ω_0, λ_0) in the range $(0.0 \leq \Omega_0 \leq 1.1, -0.1 \leq \lambda_0 \leq 1.0)$. The highest rejection (at a confidence level $1-P > 99.9\%$) is for a band in the (Ω_0, λ_0) plane running from $\sim (0.15, -0.1)$ to $\sim (0.4, 1.0)$.

Inversion of the frequency condition (iii) of $\mathcal{H}_1(\Omega_0, \lambda_0)$, by replacing 'higher' by 'lower', and recalculating confidence levels results in a rejection of $\mathcal{H}_1(\Omega_0 = 1, \lambda_0 = 0)$ at $1 - P > 98\%$.

Since $\mathcal{H}_1$ is rejected, this implies that a power spectrum peak is present in the data.

Can the power spectrum peak be seen as a 'periodicity' in the data? Fig. 14 allows the reader to judge this subjectively for the pair $(\Omega_0 = 0.3, \lambda_0 = 0.7)$.

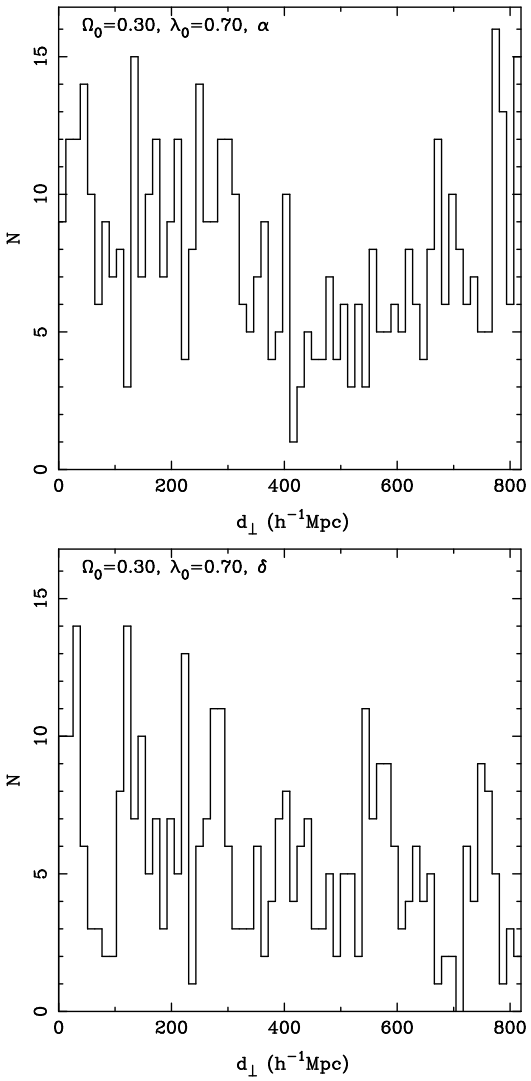

Fig. 14. Tangential length distribution for $(\Omega_0 = 0.3, \lambda_0 = 0.7)$, for the right ascension (upper panel) and declination (lower panel) subsamples (in bins of $12.8\,h^{-1}$ Mpc). The null hypotheses test relate to a power spectrum peak at $L_{\rm LSS} = 130 \pm 10\,h^{-1}$ Mpc. Differences in number density between the plate boundaries are not corrected for, these are corrected for in the simulations.

Consistently with the points at $(\Omega_0 = 0.3, \lambda_0 = 0.7)$ in the upper panels of Figs 6 and 7, a periodicity of significant amplitude should be hard to detect in the right ascension sample, but discernable in the declination sample. This is the case in Fig. 14.

Moreover, although the redshift direction is potentially plagued by selection effects, the wedge diagrams in Fig. 5

show clearly that large scale structure can be seen in the $z-\theta$ plane, where $\theta = \alpha\cos\delta$ or $\theta = \delta$ as above. Voids at a scale of around $L_{\rm LSS} \sim 130\,h^{-1}$ Mpc and difficult to explain by selection effects are visible in this figure.

A best estimate for the values of (Ω_0, λ_0) *consistent* with the occurrence of a large scale structure peak in the tangential quasar distribution is found by trying to reject the null hypothesis $\mathcal{H}_2(\Omega_0, \lambda_0)$ according to which the best estimate of the frequency of a peak below $1/d_\perp = 0.01\,h\,{\rm Mpc}^{-1}$ in the Fourier transforms occurs at $1/(L_{\rm LSS} \pm \Delta L_{\rm LSS})$. Bootstraps from the observational data set are used to robustly provide an upper estimate to the observational uncertainty.

Based on a linear fit to the resulting estimates in the (Ω_0, λ_0) plane, the relation $\Omega_0 = (0.24 \pm 0.15) + (0.10 \pm 0.08)\,\lambda_0$ is considered to best summarise the constraints on the two curvature parameters. For zero cosmological constant or flat models, the curvature parameter estimates are $(\Omega_0 = 0.24^{+0.05}_{-0.15}, \lambda_0 \equiv 0)$ and $(\Omega_0 = 0.30 \pm 0.15, \lambda_0 \equiv 1 - \Omega_0)$ respectively.

These estimates of the density parameter are in remarkable agreement with analogous estimates obtained from the kinematics of galaxy clusters (e.g. Carlberg, Yee & Ellingson 1997), collapsing galaxy groups (Mamon 1993), as well as from the baryonic fraction in clusters (White et al. 1993; Mohr, Mathiesen & Evrard 1999) and groups (Henriksen & Mamon 1994).

The estimate of the cosmological constant under the assumption of a flat model is also remarkably close to those which now tend towards a flat, cosmological constant dominated universe from faint galaxy number counts, the galaxy depletion curve behind clusters, the supernovae type Ia method (Fukugita et al. 1990; Fort et al. 1997; Chiba & Yoshii 1997; Perlmutter et al. 1999; Riess et al. 1998) and cosmic microwave background methods. Results from the latter are being updated rapidly at the moment, and are dependent on numerous assumptions which do not enter either the present method or the supernovae type Ia method, so are not discussed here.

The present method is very independent of the supernovae type Ia method: in choice of astrophysical object, in the redshift range and in the difference between using standard candles versus standard rulers. What is the result of combining the two?

The combination of the present result with the relation $0.8\,\Omega_0 + 0.6\,\lambda_0 = -0.2 \pm 0.1$ from Perlmutter et al. (1999), where the error is modelled as Gaussian, results in Fig. 15.

Although the two relations are not quite orthogonal, they have different enough slopes that the uncertainty in both is considerably reduced, such that a nearly flat model is implied *without using any cosmic microwave background* information.

A linear fit to the 68% confidence contour in Fig. 15, for Ω_0 as a function of $(\lambda_0 - 0.7)$, results in:

$$\Omega_0 = (0.30 \pm 0.02) + (0.57 \pm 0.11)(\lambda_0 - 0.7),$$

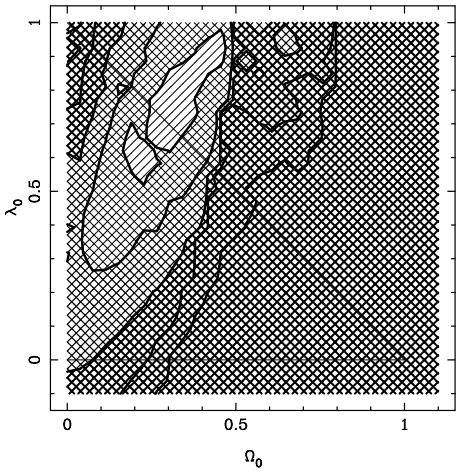

Fig. 15. Confidence intervals from combining Fig. 11 with the relation $0.8\Omega_0 - 0.6\lambda_0 = -0.2 \pm 0.1$ from Perlmutter et al. (1999). Shading is as for Fig. 9.

$$0.55 < \lambda_0 < 0.95, \qquad (11)$$

where as before, the uncertainties from linear regression relate to the fitting procedure and underestimate the true uncertainties shown in the figure.

In this case, the maximum uncertainty in Ω_0 for a given value of λ_0 in the range above is $\sigma(\Omega_0) = 0.11$. Restoring this to the relation as before yields:

$$\Omega_0 = (0.30 \pm 0.11) + (0.57 \pm 0.11)(\lambda_0 - 0.7), \quad 0.55 < \lambda_0 < 0.95. \qquad (12)$$

This combined result strongly supports the possibility that the observable universe satisifies a nearly flat, perturbed Friedmann-Lemaître-Robertson-Walker model, where 'nearly' is quantified as ± 0.1 in the two dimensionless curvature parameters. It does not require prior assumptions on the cosmological constant, nor does it use cosmic microwave background (CMB) data.

An independent confirmation that no systematic errors are present in the data studied here (or else an independent estimate of the systematic errors) would obviously be very desirable.

If further observations confirm that large scale structure can be used as a standard ruler, then surveys such as the 2dF (2 degree field) and SDSS (Sloan Digitial Sky Survey) quasar surveys should provide confirmation of the present results within the next few years.

The former risks systematic error from the fact that the angular scale corresponding to $L_{\rm LSS} = 130 \pm 10\,h^{-1}$ Mpc at $z \sim 2$ is 2°: this is the field size of the 2dF survey. Careful correction for this, use of lower redshift quasars, and a much higher signal-to-noise ratio would help in obtaining convincing results from the former. How-

ever, since the SDSS is digital, it should presumably avoid this problem.

The present method would be ideally suited to a deep right ascension survey (i.e. for a narrow band in declination but a long, e.g. 60°, band in right ascension), which avoids any risk of dependence of any angular scale near a few degrees but includes a fair sample of quasars at $z \sim 2$, sampling a few hundred quasars per great circle degree. A blind, deep, slit spectroscopic, right ascension survey, 'blind' in the sense of taking spectra of *all* objects in a very narrow declination interval, would provide possibly one of the fastest ways of obtaining constraints in the (Ω_0, λ_0) plane which should suffer little from possible selection effects. This offers a valuable cosmological project for the planned liquid mercury LZT (Large Zenith Telescope).

Another survey to which the present method could be usefully applied will be the combined VIRMOS (Visual and Infrared MultiObject Spectroscopy, on the VLT) and XMM (X-ray Multiple Mission, X-ray satellite) survey, which should trace out the filaments and/or walls of several units of large scale structure at super-unity redshifts via several different astrophysical tracers: galaxies, quasars and hot gas.

Over the next few years, if the precision in the present application of this method were increased by an order of magnitude in the new quasar surveys, then, together with more confidence in understanding systematic errors in the supernovae type Ia method and reduction in random errors by more detections at high redshifts, that would imply estimates on Ω_0 and on λ_0 to a precision of ± 0.01 — again without use of CMB data.

Interest may then shift to the other geometrical parameters: those required to determine the size of the Universe. As pointed out by Schwarzschild (1900, 1998), both the curvature and the topology of space need to be known in order to know the size of the Universe. For background and recent reviews on progress in observational methods for measuring the topological parameters, see Lachièze-Rey & Luminet (1995), Starkman (1998; and following papers in that volume), Luminet (1999) and Luminet & Roukema (1999). Moreover, a side effect of a significant measurement of the global geometry of the Universe would be a confirmation or refinement of the estimates of the local geometrical parameters (Roukema & Luminet 1999).

Acknowledgments

We thank Stéphane Colombi, Emmanuel Bertin, Guy Mathez, Bernard Fort, Enrique Gaztañaga, Jasjeet Bagla, Shiv Sethi, Daniel Kunth and Steve Hatton and an anonymous referee for useful comments. Use of the resources at the Centre de Données astronomiques de Strasbourg (*http://csdweb.u-strasbg.fr*), the support of the Institut d'astrophysique de Paris, CNRS, for a visit during which part of this work was carried out, and the support of la Société de Secours des Amis des Sciences are gratefully acknowledged.

References

Adelberger K. L., Steidel C. C., Giavalisco M., Dickinson M., Pettini M., Kellogg M., 1998, ApJ 508, 18
Barrow J. D., Sonoda D. H., Bhavsar S. P., 1984, MNRAS 210, 19P
Baugh C.M., Efstathiou G., 1993, MNRAS 265, 145
Baugh C.M., Efstathiou G., 1994, MNRAS 267, 323
Broadhurst T., 1999, in 'Clustering at High Redshift', ed. V. Le Brun, A. Mazure, O. Le Fèvre, in press
Broadhurst T. J., Ellis R. S., Koo D. C., Szalay A. S., 1990, Nature 343, 726
Broadhurst T., Jaffe A. H., 1999, submitted (arXiv:astro-ph/9904348)
Carlberg R. G., Yee H. K. C., Ellingson E., 1997, ApJ 478, 462
Chiba M., Yoshii Y., 1997, ApJ 489, 485
da Costa L. N., 1992, in The Distribution of Matter in the Universe, ed. G. A. Mamon, D. Gerbal (Meudon: Obs. de Paris), p163, ftp://ftp.iap.fr/pub/from_users/gam/PAPERS/DAECMTG/dacosta.dvi.Z
da Costa L. N. et al., 1993, in Cosmic Velocity Fields, ed. Bouchet, F., Lachièze-Rey, M., (Gif-sur-Yvette, France: Editions Frontières), p475
Dawe J. A., in IAU Coll. 78, Astronomy with Schmidt-type Telescopes, ed. Capaccioli M., Dordrecht: D. Reidel, p193
de Lapparent V., Geller M. J., Huchra J. P., 1986, ApJ 302, L1
Deng Z., Xiaoyang X., Fang L.-Zh., 1994, ApJ 431, 506
Deng X.-F., Deng Z.-G., Xia X.-Y., 1996, Chin.Astron.Astroph. 20, 383
Einasto M., Einasto J., Tago E., Dalton G. B., Andernach H., 1994, MNRAS 269, 301
Einasto, J., et al., 1997, MNRAS 289, 801
Einasto, J., et al., 1997, Nature 385, 139
Fort B., Mellier Y., Dantel-Fort M., 1997, A&A 321, 353
Fukugita M., Yamashita K., Takahara F., Yoshii Y., 1990, ApJ 361, L1
Gaztañaga E., Baugh C.M., 1998, MNRAS 294, 229
Geller M. J., Huchra J. P., 1989, Science 246, 897
Giavalisco M., Steidel C. C., Adelberger K. L., Dickinson M. E., Pettini M., Kellogg M., 1998, ApJ 503, 543 (arXiv:astro-ph/9802318)
Guzzo L., 1999, in proceedings of XIX Texas Symp. Rel. Astr. (arXiv:astro-ph/9911115)
Iovino A., Clowes R., Shaver P., 1996, A&AS 119, 265
Hartwick F. D. A., Schade D., 1990, ARA&A 28, 437
Henriksen M. J., Mamon G. A., 1994, ApJ 421, L63
Lachièze-Rey M., Luminet J.-P., 1995, PhysRep 254, 136 (arXiv:gr-qc/9605010)
Luminet J.-P., 1999, in Concepts de l'Espace en Physique, Les Houches, 29 sep - 3 oct 1997, Acta Cosmologica, 24,

(arXiv:gr-qc/9804006)
Luminet J.-P. & Roukema B. F., 1999, in Theoretical and Observational Cosmology, NATO Advanced Study Institute, Cargèse 1998, ed. Lachièze-Rey, M., Netherlands: Kluwer, p117 (arXiv:astro-ph/9901364)
Mamon G. A., 1993, in The N-Body problem & Gravitational Dynamics, ed. F. Combes & E. Athanassoula (Meudon: Obs. Paris), p188, (arXiv:astro-ph/9308032)
Mohr J. J., Mathiesen B., Evrard A. E., 1999, ApJ 517, 627
Perlmutter S. et al., 1999, ApJ 517, 565 (arXiv:astro-ph/9812133)
Riess A. G. et al., 1998, AJ 116, 1009
Roukema B. F., Luminet J.-P., 1999, A&A 348, 8 (arXiv:astro-ph/9903453)
Schwarzschild K., 1900, Vier.d.Astr.Gess. 35, 337
Schwarzschild K., 1998, ClassQuantGra 15, 2539 [English translation of Schwarzschild (1900)]
Scott D., 1991, A&A 242, 1
Shaver P. A., Wall J. V., Kellermann K. I., Jackson C. A., Hawkins M. R. S., 1996, Nature 384, 439
Starkman G. D., 1998, ClassQuantGra 15, 2529
Tucker D. L., Lin H., Shectman S., in Wide Field Surveys in Cosmology, ed. S. Colombi, Y. Mellier, B. Raban
Véron-Cetty M. P., Véron P., 1998, ESO Scientific Report 18, http://cdsweb.u-strasbg.fr/viz-bin/VizieR?-source=VII/207/
Weinberg S., 1972, Gravitation and Cosmology, New York, U.S.A.: Wiley
White S. D. M., Navarro J. S., Evrard A. E., Frenk C. S., 1993, Nature 366, 429

F Curriculum Vitae

Gary Allan MAMON

DOMICILE :
1, avenue de la Jonchère
92420 Vaucresson
Tél.: (1) 01 47 95 36 17
Né le 7 Février 1958 à New York (Etats-Unis)
Nationalités Française et Américaine
Marié, 3 enfants
No. SS : 1–58–02–99–404–151–44

TRAVAIL :
Institut d'Astrophysique
98 bis, blvd Arago
75014 Paris
Tél.: 01 44 32 81 15
FAX: 01 44 32 80 01
Email: `gam@iap.fr`
WWW: `http://www.iap.fr/users/gam`

EMPLOIS

1993– **Institut d'Astrophysique (IAP)**, Paris.
Astronome Adjoint 1ère Classe, associé au Département d'Astrophysique Extragalactique et de Cosmologie (DAEC) de l'Observatoire de Meudon (2ème Classe jusqu'en 1994).
Recherche en cosmologie. Responsable scientifique de l'extraction des galaxies pour le programme DENIS. Co-PI et responsable français du projet 6dF.

1990– **Observatoire de Paris-Meudon**, Meudon.
1993 *Astronome Adjoint 2ème Classe* au Département d'Astrophysique Extragalactique et de Cosmologie (DAEC).
Recherche en cosmologie.

1989– **ANSTEL, SA**, Paris.
1990 *Ingénieur Informaticien.*
Conception et développement de logiciels de gestion de base de données et gestion du parc informatique (stations UNIX) pour une P.M.E. de services télématiques.

1988– **Université de Paris VII**, Paris.
1989 *Maître de Conférences Associé 1ère classe*, attaché au Département d'Astrophysique Extragalactique et de Cosmologie (DAEC) à l'Observatoire de Paris-Meudon.
Recherche en cosmologie au DAEC. Enseignement de travaux dirigés et travaux pratiques de physique et supervision de projets de recherche à des étudiants de 1ère année de DEUG.

Eté 1987 **Université de Paris VII**, Paris.
Juin 1988 *Maître de Conférences Invité 1ère classe* (1987) et *Assistant de l'Université* (1988), attaché au Département d'Astrophysique Extragalactique et de Cosmologie (DAEC) à l'Observatoire de Paris-Meudon.
Recherche en cosmologie au DAEC (2 mois en 1987 et 1 mois en 1988).

1985– **New York University**, New York, Etat de New York, USA.
1988 *Assistant Research Scientist (chercheur postdoctoral)* au Département de Physique.
Adjunct Faculty (membre du corps enseignant) à partir de Janvier 1987.
Recherche en cosmologie et milieux circumstellaires.

1980– **Princeton University**, Princeton, Etat de New Jersey, USA.
1985 *Graduate Research Assistant* et *Teaching Assistant* (Février à Juin 1983) au Département de Sciences Astrophysiques. Recherche en cosmologie.

1979– **Institute for Advanced Study**, Princeton, Etat de New Jersey, USA.
1980 *Graduate Research Assistant*. Recherche en structure galactique.

SUJETS DE RECHERCHE

Dynamique des groupes et amas de galaxies. Nature des groupes compacts de galaxies. Origine de la ségrégation morphologique des galaxies dans les groupes et amas. Formation des galaxies et des structures de galaxies. Mesures des paramètres fondamentaux de l'Univers. Relevés de galaxies. Galaxies en infra-rouge proche. Cinématique interne des systèmes sphéroïdaux. Chimie circumstellaire.

ETUDES

1979– 1985 **Princeton University**, Princeton, Etat de New Jersey, USA.
Ph. D. (doctorat) en Sciences Astrophysiques, Juin 1985. Thèse : Compact Configurations within Small Evolving Groups of Galaxies.

1977– 1979 **Massachusetts Institute of Technology**, Cambridge, Etat du Massachusetts, USA.
S.B. (licence) en Physique, Juin 1979. Thèse : A Study of the Solar Variability.

1975– 1977 **Lycée Janson de Sailly**, Paris.
Mathématiques Supérieures et Spéciales P'.
Reçu 12ème au concours d'entrée à *l'Ecole Normale Supérieure de l'Enseignement Technique* (aujourd'hui *ENS Cachan*), ainsi qu'aux écoles d'ingénieur *Ponts & Chaussées, Télécoms, ENSTA, SupAéro, etc.* (Juillet 1977).

DISTINCTIONS

Baccalauréat C avec Mention Bien (Juillet 1975). Elu à la société honorifique pour scientifiques américains *Sigma Xi* (1979). Bourse *Thaw Fellow* (1979-1980). Membre de l'*American Astronomical Society* (depuis 1985) et de la *Société Française des Spécialistes d'Astronomie* (depuis 1993). Notes biographiques publiées dans le *Marquis Who's Who in Science & Engineering* (depuis 1994) et le *Marquis Who's Who in the World* (depuis 1999). Article (Henriksen & Mamon 1994) mentionné dans les journaux de vulgarisation *New Scientist* (18 Déc 1993) et *Sky & Telescope* (Mars 1994). Deuxième astronome Français le plus remercié en 1995 dans les revues internationales en Astronomie (A&A, A&AS, ApJ, ApJL, ApJS, AJ, MNRAS) (d'après la compilation faite aux Etats-Unis sur le site Web `http://www.pa.uky.edu/~verner/aai.html`). *Prime d'encadrement doctoral et de recherche* (1999–2003).

PUBLICATIONS (Voir bibliographie ci-jointe)

23 articles publiés dans des revues à referee (dont 7 en premier auteur et 9 en second auteur) : *Astronomy & Astrophysics* (6 articles), *Astronomy & Astrophysics Supplements* (2 article), *Astrophysical Journal* (7 articles), *Astrophysical Journal (Letters)* (5 articles), et *Monthly Notices of the Royal Astronomical Society* (2 articles). 58 contributions à des conférences internationales, dont un sommaire de conférence, 17 revues et longs exposés invités (dont 14 en premier auteur), 5 à jugement de rapporteur, et 3 autres contributions invitées. Ces articles et proceedings ont fait l'objet de 781 citations, dont 364 en 1er auteur et 296 en 2nd auteur (d'après ADS : `http://cdsads.u-strasbg.fr/abstract_service.html`). 1 autre article sous presse et 2 soumis. Editeur principal du *Second DAEC meeting :* Distribution of Matter in the Universe (1992) et du *XVIIth Moriond Astrophysics Meeting :* Extragalactic Astronomy in the Infrared (1997). Co-éditeur du *XVth IAP Meeting :* Dynamics of Galaxies: from the Early Universe to the Present (2000).

TRAVAUX DE REFEREE

Rapporteur sur 29 articles soumis aux revues : *Astronomy & Astrophysics* (17 articles), *Monthly Notices of the Royal Astronomical Society* (5 articles), *Astrophysical Journal* (3 articles), *Astrophysical Journal (Letters)* (3 articles), et *Europhysics Letters* (1 article).

SEMINAIRES (Voir bibliographie ci-jointe)

COMITÉS DE THESE

Octobre 1993 — Gastão BIERENBACH LIMA-NETO (Université de Paris 7)
Formation des galaxies elliptiques et structure des amas de galaxies

Juin 1994 — Guillermo GONZÁLEZ-CASADO (Universitat de Barcelona, ESPAGNE)
Small-scale substructure in galaxy clusters

Juillet 1996 — Christophe BALLAND (Université d'Aix-Marseille 2)
Physique des amas de galaxies et contraintes cosmologiques

Septembre 1996 — Philippe HÉRAUDEAU (Université de Paris 6)
Photométrie de surface des galaxies spirales en optique et infrarouge proche

Décembre 1997 — Jean-François BECQUAERT (Université de Paris 7)
La géométrie 3D des halos de matière noire par les disques d'hydrogène atomique HI

Décembre 1997 — Philippe BRIEU (Université de Paris 7)
Simulations cosmologiques sur superordinateurs : la saga P3M

Septembre 1999 — Sergio DOS SANTOS (Université de Paris 7)
Le plasma chaud dans les amas et les groupes de galaxies : étude théorique et observationnelle

LETTRES DE RECOMMENDATION

Lettres de recommendation écrites pour 20 doctorants ou chercheurs postulant pour des postes à l'étranger ou en France.

OPERATIONS GdR et PROGRAMMES NATIONAUX

1992–1995 — Responsable des opérations financées par le *GdR Cosmologie* :
Survey européen à 2 microns (1992), Galaxies & cosmologie en IR proche (1993,1994), et Groupes et mergings de galaxies (1994,1995).

1999–2000 — Responsable d'une opération financée et renouvelée par le *GdR Galaxies* :
Galaxies DENIS et effets d'environnement

2000 — Responsable de l'opération financée par le *PNC* :
Achèvement du relevé du ciel en IR proche DENIS

ENSEIGNEMENT (voir aussi ENACDREMENT D'ETUDIANTS, page suivante)

Fév. 1983 – Juin 1983 **Princeton University**
Correction d'examens pour un cours d'astronomie générale (licence).

Printemps 1986 **New York University**
Cours d'astrophysique (un mois intensif) à des étudiants de maîtrise de journalisme scientifique.

Printemps 1986 **New York University**
Cours d'électromagnétisme (un semestre) à des étudiants de 3$^{\text{ème}}$ année de licence de physique.

1987– 1988 **New York University**
Travaux Pratiques d'astronomie observationnelle (deux semestres) à des étudiants de licence (tous domaines confondus).

1988– 1989 **Université de Paris 7 (Denis Diderot)**
Travaux Dirigés, Travaux Pratiques & Supervision de Projets en mécanique et optique (un service à temps plein) à des etudiants de 1$^{\text{ère}}$ année de DEUG.

Février 1993 **DAEC, Observatoire de Paris-Meudon**
Cours sur le système UNIX (2h30) avec polycopié tiré à 40 exemplaires.

Septembre 1993 **Ecole de Cosmologie, Luminy**
Cours : Comment Extraire un Catalogue Homogène de Galaxies des Images DENIS? (1h).

Septembre 1994 **Ecole de Cosmologie, Luminy**
Cours : L'Univers en infra-rouge proche et le survey DENIS (2h).

Avril 1995 **Institut d'Astrophysique**
Cours sur le système UNIX (3h30) avec polycopié tiré à 50 exemplaires.

Novembre 1995 **Journées GdR Cosmologie, Garchy**
2 Cours : 1) L'Univers en infra-rouge proche et le survey DENIS (1h), 2) Groupes compacts et cosmologie (1h).

Automne 1997 **PCEM Lariboisière, Université de Paris 7, Paris**
Enseignement Dirigé de Physique (39 heures) à des étudiants de 1$^{\text{ère}}$ année de médécine.

Septembre 1998 **Ecole de Cosmologie, Luminy**
Cours : La dynamique de groupes et amas de galaxies (4h30)

Automne 1998 **PCEM Lariboisière, Université de Paris 7, Paris**
Enseignement Dirigé de Physique (66 heures) à des étudiants de 1$^{\text{ère}}$ année de médécine.

Automne 1999 **PCEM Lariboisière, Université de Paris 7, Paris**
Enseignement Dirigé de Physique (66 heures) à des étudiants de 1$^{\text{ère}}$ année de médécine.

Hiver 2000 **DEA Astronomie Fondamentale, Mécanique Céleste & Géodésie, Obs. Paris**
Cours de Dynamique gravitationnelle des systèmes sphériques en astrophysique (18 heures). Polycopiés sur le Web (`http://www.iap.fr/users/gam/DEA`).

2001– 2004 **Ecole Doctorale Ile de France**
Cours transversal de DEA : Dynamique gravitationnelle à N corps (15 heures).

ENCADREMENT D'ETUDIANTS

Encadrement principal de 3 doctorants, 7 stagiaires DEA et 11 autres stagiaires. Encadrement secondaire d'un doctorant, un stagiaire DEA et un autre stagiaire. Encadrement administratif d'un doctorat. *Prime d'encadrement doctoral et de recherche* (1999–2003).

Automne 1987 — **Thomas BUCKLEY**
Stage de *licence* (4ème année d'université) de Physique à New York University, sur les masses des groupes compacts.

1988 — **Darryl WALKE**
Doctorat de Physique (projet hors-thèse) à New York University, sur le calcul analytique des fréquences d'alignments fortuits dans les groupes de galaxies.

Printemps 1992 — **Sandra CODIS et Faïza BOUFRARA**
1ère année de *DEUG* de Physique à l'Université de Paris 7, sur les expériences numériques sur la dynamique à 3 corps.

Printemps 1992 — **Philippe BRIEU**
DEA d'Astrophysique à l'Université de Paris 7, sur les galaxies binaires dans les groupes de galaxies.

Printemps 1992 — **Francis LENNE**
DEA d'Astrophysique à l'Université de Paris 6, sur la séparation étoiles/galaxies aux basses latitudes galactiques pour le programme DENIS.

1992–1997 — **Philippe BRIEU**
Doctorat d'Astrophysique à l'Université de Paris 7, soutenu le 19 Décembre 1997. Simulations cosmologiques sur superordinateurs : la saga P3M (responsable administratif, dirigé par J. Ostriker à Princeton University [USA], puis par A. Evrard à University of Michigan [USA]).

Printemps 1993 — **Sophie GOSSET**
Stage de fin d'études à l'Ecole Polytechnique Féminine (co-directeur avec J. Léorat), sur les algorithmes pour l'astrométrie pour le projet LITE.

Eté 1993 — **Matthieu CONTENSOU**
Magistère de Physique à l'Université de Paris 11, sur la détection des galaxies pour le programme DENIS.

1994–1997 — **Vincent BANCHET**
Doctorat d'Astrophysique (boursier CIFRE) à l'Université de Paris 6, sur l'extraction des objets étendus pour le programme DENIS (abandonné 3 mois avant la fin).

Printemps 1994 — **Sergio DOS SANTOS**
DEA d'Astrophysique à l'Université de Paris 7, sur l'évolution morphologique des galaxies dans un Univers hierarchique.

1994–1995 — **Marisa MONTOYA**
Boursière pré-doctorale ERASMUS à l'Université de Paris 6, sur l'analyse statistique de la structure interne des groupes compacts de galaxies.

ENCADREMENT D'ETUDIANTS (suite)

Hiver 1995	**Cyrille MACH** *Stage de début de thèse* (non-officialisé) sur la séparation étoiles/galaxies dans le sondage DENIS.
Printemps 1995	**Frédéric ENGELMANN** *DEA* d'Astronomie à l'Université de Strasbourg et stage de fin d'études à l'ENSPS sur l'optimisation et la validation de l'extraction des galaxies du sondage DENIS.
Printemps 1995	**Laurent GANIER** *DEA* d'Astronomie à l'Université de Paris 6, sur les propriétés des groupes compacts de galaxies.
Oct. 1995– Septembre 1999	**Sergio DOS SANTOS** *Doctorat* d'Astrophysique à l'Université de Paris 7, soutenue le 6 Septembre 1999. Le plasma chaud dans les amas et les groupes de galaxies : étude théorique et observationnelle.
Printemps 1996	**David KATZ** *DEA* d'Astrophysique à l'Université de Paris 7, sur l'optimisation de l'extraction des galaxies du sondage DENIS.
Printemps 1996	**Matthieu TRICOTTET** *Stage de fin d'études* à l'ENSPS sur comptages de galaxies et diagrammes couleur-couleur des galaxies du sondage DENIS.
Printemps 1997	**William BONIN** Stage de *licence* de Physique à l'Université de Paris 11 sur l'analyse des images DENIS.
Juillet 1997– Automne 2000	**Barbara LANZONI** *Doctorat* d'Astrophysique à l'Université de Paris 7 (sur bourse européenne TMR) sur l'évolution morphologique des galaxies dans un univers hiérarchique et l'origine de la séquence de Hubble (co-dirigée par B. Guiderdoni).
Eté 1998	**Fabien WERNLI** *Maîtrise* de Physique à l'Université de Paris 7 sur le traitement de clichés IR dans le Plan Galactique.
Hiver-Printemps 1999	**Frédéric GIRAUD** *Magistère* de Physique à l'Ecole Normale Supérieure de Paris sur la distribution des galaxies tirées du sondage IR DENIS.
Printemps 1999	**Claudia QUERCELLINI** *Stage de l'Ecole Polytechnique* sur la généralisation du code Merging Cell Model aux cosmologies avec constante cosmologique non-nulle.
Printemps 2000	**Effrosyni RASSIA** *DEA* d'Astronomie à l'Université de Paris 6, sur le spectre de fluctuations primordiales de densité depuis les corrélations angulaires des galaxies DENIS.

TACHES DE SERVICE (voir aussi plus bas ORGANISATION DE CONGRES)

1990–1993 **Service Informatique de l'Observatoire de Meudon**
Administration de la station de travail SUN mesuna du SIO (administrateur principal de novembre 1990 à janvier 1992.

1992–1993 **DAEC, Observatoire de Meudon**
Administration des stations SUN maitai, kir & gin du DAEC (administrateur principal de juin 1992 à mars 1993).

1991– **Programme DENIS**
Conception et développement d'algorithmes pour la détection des objets, la séparation étoiles/galaxies, et la photométrie des galaxies pour ce programme européen de cartographie complète du ciel austral en IR proche (quart-temps depuis mars 1991). Mise en place d'un serveur Web des observations DENIS (automatiquement mis-à-jour quotidiennement) en particulier le ciel couvert par DENIS (publiquement accessible sur `http://www.iap.fr/users/gam/DENIS/slots.html`) et les variations temporelles des calibrations photométriques (accès restreint). Mise en place en avril 2000 de la version 1.0 de la chaîne d'extraction des galaxies.

1993–1994 **Institut d'Astrophysique**
Animateur du journal club *Groupes et Amas de Galaxies*.

1994–1997 **Institut d'Astrophysique**
Co-responsable des séminaires de l'IAP (avec F. Durret puis S. Charlot, puis B. Guiderdoni). Responsable principal au printemps 1997 (avec en moyenne deux séminaires par semaine).

1994–1995 **ASTRE**
Membre du Bureau du groupement *ASTronomes a la Rencontre de l'Entreprise*, pour favoriser les liens entre doctorants et postdocs d'une part et industriels de l'autre (Président : Laurent Petitbon).

1996–1999 **Conseil National des Universités**
Conception et maintenance du serveur Web (`http://www-cnu.iap.fr`) de la section 34 (Astronomie & Astrophysique).

1996– **getastroph, getads, getadscits**
Scripts `csh` disponibles sur le Web (`http://www.iap.fr/users/gam/software.html`) d'extraction automatique de préprints astro-ph, d'articles de l'ADS, et des citations d'articles pour un auteur donné (les deux premiers scripts sont installés pour tous sur les stations de travail de l'IAP). Nombreuses mises-à-jour.

Février 1998 **CSENV**
Mise sur le Web (`http://www.iap.fr/users/gam/software.html`) de mon code de chimie et transfert de rayonnement dans les enveloppes circumstellaires.

COMMISSIONS

1986–1988 **Département de Physique, New York University**
Commission des résaux informatiques.

1988–1991 **Projets POST, TESC**
Equipe scientifique sur des projets de télescope français dédiés à la cosmologie (P.I. : Jacques Léorat et Paul Felenbok).

1992–1993 **Projet LITE**
Equipe de réduction des données sur ce projet de télescope de 2.5m avec imagerie optique et infra-rouge proche de très haute-résolution (P.I. : Laurent Vigroux).

1991–1992 **Rapport de conjoncture CNRS 1992**
Comité de rédaction pour le thème Univers, Noyaux et Particules.

1991– **Programme DENIS**
Equipe scientifique sur ce programme de cartographie du ciel austral en infrarouge-proche (P.I. : Nicolas Epchtein). *Co-investigator* et *responsable de l'équipe extragalactique/cosmologie* (depuis 1992).

1991–1997 **GdR Cosmologie**
Conseil scientifique (Président : René Pellat jusqu'en 1993, puis Jean-Loup Puget). *Comité permanent* en 1991.

1995– **Projet 6dF**
Co-reponsable du *Scientific Advisory Group* pour le projet de cartographie 3D et 4D de l'Univers local sur le télescope UKST en Australie. Reçu promesse du directeur de l'AAO d'environ 480 nuits de télescope sur 2 ans (2001–2002) pour mener à bout la cartographie 3D (120 000 décalages spectraux de galaxies). Voir description du projet dans `http://www.iap.fr/users/gam/6DF/6df.html`

1996–1999 **Conseil National des Universités**
Membre (nommé) de la section 34 du CNU (astronomie-astrophysique, Président : Lucette Bottinelli). *Assesseur* (membre du bureau).

1996–1998 **CSES, Université Claude Bernard – Lyon 1**
Membre suppléant de la 34ème Commission de Spécialistes de l'Enseignement Supérieur (astronomie-astrophysique, Président : Jacques BERGEAT).

1998– **DENIS-HI**
Co-investigateur sur ce programme de suivi radio à Nançay de 6000 galaxies DENIS.

2000– **Equipe Cosmologie Structures et Galaxies à l'IAP**
Responsable d'une équipe de 15 chercheurs, 8 doctorants et 7 postdocs.

Printemps 2000 **Centre National de la Recherche Scientifique**
Membre élu de la Section 14 (système solaire et Univers lointain, Président : Michel Blanc) du Comité National de la Recherche Scientifique.

ORGANISATIONS DE CONGRES

Mars 1991 — **2nd DAEC Meeting**
Editeur principal des proceedings pour un congrès international à Meudon : Distribution of Matter in the Universe (premiers proceedings dans l'astronomie française utilisant un format uniforme : 3 mois de travail à temps plein pour la mise en page et les négociations avec les imprimeurs).

Janvier 1994 — **4th DAEC Meeting**
Comité local d'organisation pour le congrès international Unveiling Large-Scale Structures behind the Milky Way à Meudon.

Avril 1995 — **Atelier COBE**
Comité scientifique d'organisation pour le congrès international Unveiling the Cosmic Infrared Background à College Park (Maryland, USA).

Mars 1997 — **XVIIèmes Rencontres Astrophysiques de Moriond**
Co-responsable (avec Trinh Thuan) du comité scientifique, responsable du comité local d'organisation et éditeur principal pour le congrès international Extragalactic Astronomy in the Infrared aux Arcs. 3 mois de travail à temps plein. Mise en place du serveur Web (`http://www.iap.fr/coll/moriond97`).

Juin 1997 — **3rd DENIS Euroconference**
Comité scientifique d'organisation pour le congrès international The impact of near-infrared surveys on galactic and extragalactic astronomy à Meudon.

Décembre 1998 — **Cosmological Topology in Paris**
Comité local d'organisation pour un atelier international à Paris.

Juillet 1999 — **XVème Colloque IAP**
Co-responsable (avec Françoise Combes) du comité scientifique et responsable du comité local d'organisation ainsi que co-éditeur du congrès international Galaxy Dynamics: from the early Universe to the Present à Paris. Mise en place du serveur Web (`http://www.iap.fr/iapmtg99`). 2 mois de travail à temps plein.

Février 2000 — **Mapping the Hidden Universe**
Comité scientifique d'organisation pour ce congrès international (voir `http://cuevano.astro.ugto.mx/~kraan/zoahi/`) à Guanajato (MEXIQUE).

OBSERVATIONS

1994–2000 Programme DENIS (Programme-Clé ESO)
Co.I. (P.I. : Nicolas Epchtein). Télescope de 1m de l'ESO. Imagerie en bandes IJK de l'hémisphère austral.

1993 Imagerie IR proche de galaxies proches
Co.I. (P.I. : François Simien). 4 nuits sur le télescope de 2.2m de l'ESO.

1994 Imagerie IR proche du Plan Galactique
P.I. Une nuit sur le 2.2m de l'ESO.

1996 Imagerie IR proche du Centre Galactique
P.I. 3 nuits (juin 1996) sur le 2.2m de l'ESO.

1998 Spectroscopie multi-fibres de galaxies DENIS
P.I. 4 nuits sur le Schmidt (UKST) de l'AAO.

2001–2002 Sondage de décalages spectraux 6dF
Obtention de 480 nuits de télescope sur 2 ans pour entreprendre un sondage de 120 000 décalages spectraux sur le télescope de Schmidt UKST à Siding Spring (Australie).

VULGARISATION

1994–1995 **Expo Cosmologie**
Co-responsable d'une équipe visant à créer une exposition de vulgarisation de la cosmologie, itinérante à travers la France (Direction : Daniel Gerbal).

Fév. 1995 **La Cosmologie de Maïmonide**
Cours de vulgarisation (2h) donné a l'IAP (ouvert au public).

Automne 1996 **Controverses sur les groupes compacts de galaxies**
Revue *Quintessiences*, CNRS, Région Ile de France

Sept. 1996 **Les formes des galaxies et leurs origines**
Cours de vulgarisation (2h) donné a l'IAP (ouvert au public).

Oct. 1996 **Questions-réponses sur l'Univers**
Exposé (1h30) donné à l'IAP devant des élèves de CE2 durant la *Science en Fête*.

Automne 1998 **Ecole maternelle des Grandes Fermes**, Vaucresson
Questions-réponses (2 fois 1h) sur la Terre, le Système Solaire et l'Univers.

Printemps 2000 **ARTE**
Intervention avec B. Roukema, sur notre détermination du paramètre de densité de l'Univers par une nouvelle méthode de mètre cosmique, pour une émission de télévision consacrée aux échelles.

G Bibliographie complète

Gary A. MAMON

Bibliographie

dernière mise-à-jour : le 22 Juin 2000
(une version actualisée des mes publications est disponible sur
`http://www.iap.fr/users/gam/papers.html`)

I. Articles publiés dans des revues internationales à jugement de rapporteur

(1) **Gary A. MAMON** & Raymond N. SONEIRA : Stellar Luminosity Functions in the R, I, J, and K Bands, Obtained by Transformation from the Visual Band, 1982, *Astrophysical Journal*, **255**, 181–190.

(2) James BINNEY & **Gary A. MAMON** : M/L and Velocity Anisotropy of Spherical Galaxies, or Must M87 have a Massive Black Hole?, 1982, *Monthly Notices of the Royal Astronomical Society*, **200**, 361–375.

(3) **Gary A. MAMON** : Are Compact Groups of Galaxies Physically Dense?, 1986, *Astrophysical Journal*, **307**, 426–430.

(4) A. E. GLASSGOLD, **G. A. MAMON**, A. OMONT & R. LUCAS : Photochemistry and Molecular Ions in Carbon-Rich Circumstellar Envelopes, 1987, *Astronomy and Astrophysics*, **180**, 183–190.

(5) **Gary A. MAMON** : The Dynamics of Small Groups of Galaxies: I. Virialized Groups, 1987, *Astrophysical Journal*, **321**, 622–644.

(6) **G. A. MAMON**, A. E. GLASSGOLD & A. OMONT : Photochemistry and Molecular Ions in Oxygen-Rich Circumstellar Envelopes, 1987, *Astrophysical Journal*, **323**, 306–315.

(7) **G. A. MAMON**, A. E. GLASSGOLD, & P. J. HUGGINS : The Photodissociation of CO in Circumstellar Envelopes, 1988, *Astrophysical Journal*, **328**, 797–808.

(8) A. E. GLASSGOLD, **G. A. MAMON**, & P. J. HUGGINS : Molecule Formation in Fast Winds from Protostars, 1989, *Astrophysical Journal Letters*, **336**, L29–L32.

(9) **G. A. MAMON** : A Compact Group in Virgo, 1989, *Astronomy and Astrophysics*, **219**, 98–100.

(10) D. G. WALKE & **G. A. MAMON** : The Frequency of Chance Alignments of Galaxies in Loose Groups, 1989, *Astronomy and Astrophysics*, **225**, 291–302.

(11) A. E. GLASSGOLD, **G. A. MAMON**, & P. J. HUGGINS : The Formation of Molecules in Protostellar Winds, 1991, *Astrophysical Journal*, **373**, 254–265.

(12) A. BLANCHARD, D. VALLS-GABAUD, & **G. A. MAMON** : The Origin of the Galaxy Luminosity Function and the Thermal Evolution of the Intergalactic Medium, 1992, *Astronomy and Astrophysics*, **264**, 365–378.

(13) **Gary A. MAMON** : Are Cluster Ellipticals the Products of Mergers?, 1992, *Astrophysical Journal (Letters)*, **401**, L3–L6.

(14) Isabelle CHERCHNEFF, Alfred E. GLASSGOLD, & **Gary A. MAMON** : The Formation of Cyanopolyyne Molecules in IRC +10216, 1993, *Astrophysical Journal*, **410**, 188–201.

(15) Mark J. HENRIKSEN & **Gary A. MAMON**: The Baryonic Fraction in Groups of Galaxies from X-Ray Measurements, 1994, *Astrophysical Journal (Letters)*, **421**, L63–L66.

(16) Guillermo GONZÁLEZ-CASADO, **Gary A. MAMON**, & Eduard SALVADOR-SOLÉ: The Dynamical Survival Time of Small-Scale Substructure in Relaxed Galaxy Clusters, 1994, *Astrophysical Journal (Letters)*, **433**, L61–L64.

(17) Philippe HÉRAUDEAU, François SIMIEN, & **Gary A. MAMON**: Near-Infrared Surface Photometry of Spiral Galaxies: I. The Data, 1996, *Astronomy & Astrophysics Supplements*, **117**, 417–444.

(18) Maria-Luisa MONTOYA, Rosa DOMÍNGUEZ-TENREIRO, Guillermo GONZÁLEZ-CASADO, **Gary A. MAMON** & Eduard SALVADOR-SOLÉ: The Surface Density Profiles and Lensing Characteristics of Hickson's Compact Groups of Galaxies, 1996, *Astrophysical Journal (Letters)*, **473**, L83–L86.

(19) N. EPCHTEIN, E. DEUL, S. DERRIERE, J. BORSENBERGER, D. EGRET, G. SIMON, C. ALARD, L. G. BALÁZS, B. DE BATZ, M.-R. CIONI, E. COPET, M. DENNEFELD, T. FORVEILLE, P. FOUQUÉ, F. GARZÓN, H. J. HABING, A. HOLL, J. HRON, S. KIMESWENGER, F. LACOMBE, T. LE BERTRE, C. LOUP, **G. A. MAMON**, A. OMONT, G. PATUREL, P. PERSI, A. C. ROBIN, D. ROUAN, D. TIPHÈNE, I. VAUGLIN, S. J. WAGNER: A Preliminary Database of DENIS Point Sources, 1999, *Astronomy & Astrophysics*, **349**, 236–242.

(20) Sergio DOS SANTOS & **Gary A. MAMON**: Clumpy Diffuse X-Ray Emission from the Spiral-Rich Compact Galaxy Group HCG 16, 1999, *Astronomy & Astrophysics*, **352**, 1–18.

(21) P. FOUQUÉ;, L. CHEVALLIER, M. COHEN, E. GALLIANO, C. LOUP, C. ALARD, B. DE BATZ, E. BERTIN, J. BORSENBERGER, M. R. CIONI, E. COPET, M. DENNEFELD, S. DERRIERE, E. DEUL, P.-A. DUC, D. EGRET, N. EPCHTEIN, T. FORVEILLE, F. GARZÓN, H. J. HABING, J. HRON, S. KIMESWENGER, F. LACOMBE, T. LE BERTRE, **G. A. MAMON**, A. OMONT, G. PATUREL, S. PAU, P. PERSI, A. C. ROBIN, D. ROUAN, M. SCHULTHEIS, G. SIMON, D. TIPHÈNE, I. VAUGLIN & S. J. WAGNER: An Absolute Calibration of DENIS (Deep Near Infrared Southern Sky Survey), 2000, *Astronomy & Astrophysics Supplements*, **141**, 313–317

(22) B. LANZONI, **G. A. MAMON** & B. GUIDERDONI: Tests of the Rodrigues & Thomas Halo Merging Tree in the SCDM Cosmology, 2000 *Monthly Notices of the Royal Astronomical Society*, **312**, 781–793

(23) M.-R. CIONI, C. LOUP, H. J. HABING, P. FOUQUÉ, E. BERTIN, E. DEUL, D. EGRET, C. ALARD, B. DE BATZ, J. BORSENBERGER, M. DENNEFELD, N. EPCHTEIN, T. FORVEILLE, F. GARZÓN, J. HRON, S. KIMESWENGER, F. LACOMBE, T. LE BERTRE, **G. A. MAMON**, A. OMONT, G. PATUREL, P. PERSI, A. C. ROBIN, D. ROUAN, G. SIMON, D. TIPHÈNE, I. VAUGLIN & S. J. WAGNER The DENIS point source catalogue towards the Magellanic Clouds, *Astronomy & Astrophysics Supplement Series*, **144**, 235–245

(24) Boudewijn F. ROUKEMA & **Gary A. MAMON**: Tangential Large Scale Structure as a Standard Ruler: Curvature Parameters from Quasars, *Astronomy & Astrophysics*, sous presse.

(25) B. F. ROUKEMA, S. NININ, J. DEVRIENDT, F. BOUCHET, B. GUIDERDONI & **G. A. MAMON** : Star formation losses due to tidal debris in 'hierarchical' galaxy formation, *Astronomy & Astrophysics*, soumis.

(26) Ewa L. ŁOKAS & **Gary A. MAMON** : Properties of spherical galaxies and clusters with an NFW density profile, *Monthly Notices of the Royal Astronomical Society*, soumis

(27) F. MAGNARD, **G. A. MAMON**, F. DURRET & D. GERBAL : Biases in spectral fits of unresolved non-isothermal X-ray clusters and groups of galaxies, *Astronomy & Astrophysics*, écrit à 90%, à soumettre.

(28) **Gary A. MAMON** : The minimum velocity dispersion of virialized galaxy systems, *Astronomy & Astrophysics*, écrit à 90%, à soumettre.

(29) **Gary A. MAMON** & Sergio DOS SANTOS : Cosmological and dynamical constraints on the nature of the low velocity dispersion compact group HCG 16, *Astronomy & Astrophysics*, écrit à 95%, à soumettre

(30) **Gary A. MAMON**, Frédéric GIRAUD, Emmanuel BERTIN, Jean BORSENBERGER, Nicolas EPCHTEIN, Pascal FOUQUÉ & Matthieu TRICOTTET : Galaxies from the DENIS Near-Infrared survey. I. First star/galaxy separation, galaxy counts and comparison with optical surveys, *Astronomy & Astrophysics*, écrit à 85%, à soumettre

II. Articles publiés dans des revues internationales sans jugement de rapporteur

(1) N. EPCHTEIN *et al.* (48 auteurs) : The Deep Near-Infrared Southern Sky Survey (DENIS), 1997, *ESO Messenger*, **87**, 27–34

III. Conférences internationales : Avec jugement de rapporteur

(1) V. BANCHET, **G.A. MAMON** & M. CONTENSOU : The Detection of DENIS Galaxies, 1995, dans *"The World of Galaxies: II"*, ed. G. Paturel & C. Petit, *Astrophys. Lett. & Comm.*, **31**, 37–40

(2) Quentin A. PARKER, Matthew M. COLLESS & **G. A. MAMON** : The FLAIR-DENIS Redshift Survey, 1996, dans *HI in the Local Universe*, ed. L. Stavely-Smith, *Publ. Astr. Soc. Australia*, **14**, 125–126

(3) A. SCHRÖDER, R.C. KRAAN-KORTEWEG & **G. A. MAMON** : DENIS Observations of Multibeam Galaxies in the Zone of Avoidance, 1999, dans *Pub. Astron. Soc. Australia*, **16**, 42–47

(4) **G.A. MAMON** : The Nature of Compact Groups of Galaxies as Constrained by Cosmology and by X-Ray Observations, 1999, dans *"Interacting Galaxies: in Pairs, Groups and Clusters"*, ed. G.G.C. Palumbo & G. Longo, *Astrophys. Lett. & Comm.*, sous presse

(5) B.F. Roukema & **G.A. MAMON** : Large Scale Structure Among $z \sim 2$ Quasars as a Cosmological Standard Ruler, 2000, dans *IAU Symp. 199 "The Universe at Low Radio Frequencies"*, ed. A. P. Rao et al., ASP, sous presse

IV. Conférences internationales : Revues, longs exposés, et sommaires invitées

(1) **Gary A. MAMON** : Dynamical Theory of Dense Groups of Galaxies, 1990, dans *IAU Colloquium No. 124, "Paired and Interacting Galaxies"*, ed. J. W. Sulentic, W. C. Keel, & C. M. Telesco (Washington : NASA), 609–618.

(2) A. E. GLASSGOLD & **G. A. MAMON**: Circumstellar Chemistry, 1992, dans *"Chemistry and Spectroscopy of Interstellar Molecules"*, ed. D.K. Bohme, E. Herbst, N. Kaifu & S. Saito (Tokyo: Univ. of Tokyo Press), p. 261–266.

(3) **Gary A. MAMON**: Compact Group Modelling, 1992, dans *2nd DAEC Meeting, "The Distribution of Matter in the Universe"*, ed. G. A. Mamon & D. Gerbal (Meudon: Obs. de Paris), 51–66.

(4) Nicolas EPCHTEIN & **Gary A. MAMON**: The New Proposed Two Micron Survey and its Impact on Extragalactic Research, 1992, dans *2nd DAEC Meeting, "The Distribution of Matter in the Universe"*, ed. G. A. Mamon & D. Gerbal (Meudon: Obs. de Paris), 382–387.

(5) **Gary A. MAMON**: Dynamical Theory of Groups and Clusters of Galaxies, 1993, dans *"The N-Body Problem and Gravitational Dynamics"*, ed. F. Combes & E. Athanassoula (Meudon: Obs. de Paris), p. 188–203.

(6) **Gary A. MAMON**: Bulge/Disk Segregation in the Universe, 1993, dans *"The N-Body Problem and Gravitational Dynamics"*, ed. F. Combes & E. Athanassoula (Meudon: Obs. de Paris), p. 226–239.

(7) N. EPCHTEIN, B. DE BATZ, E. COPET, P. FOUQUÉ, F. LACOMBE, T. LE BERTRE, **G. MAMON**, D. ROUAN, D. TIPHÈNE, W.B. BURTON, E. DEUL, H. HABING, J. BORSENBERGER, M. DENNEFELD, A. OMONT, J.C. RENAULT, B. ROCCA-VOLMERANGE, S. KIMESWENGER, I. APPENZELLER, R. BENDER, T. FORVEILLE, F. GARZON, J. HRON, P. PERSI, M. FERRARI-TONIOLO & I. VAUGLIN: DENIS: A Deep Near-Infrared Survey of the Southern Sky, 1994, dans *Astrophysics & Space Science* **217***: "Science with Astronomical Near-Infrared Surveys"*, ed. N. Epchtein, A. Omont, B. Burton & P. Persi (Dordrecht: Kluwer), p. 3–9.

(8) **Gary A. MAMON**: Groups and Clusters in the Near-Infrared, 1994, dans *Ap. Sp. Sci.* **217***: "Science with Astronomical Near-Infrared Surveys"*, ed. N. Epchtein, A. Omont, B. Burton & P. Persi (Dordrecht: Kluwer), p. 237–242.

(9) **Gary A. MAMON**: How Well Should the DENIS Survey Probe Galaxies Behind the Galactic Plane?, 1994, dans *"Unveiling Large-Scale Structures Behind the Milky Way"*, ed. C. Balkowski & R.C. Kraan-Korteweg (San Francisco: A.S.P. [vol. **67**]), p. 53–61.

(10) **Gary A. MAMON**: Compact Groups: Observations and Theories, 1995, dans *STScI Workshop, "Groups of Galaxies"*, ed. O. G. Richter & K. Borne (San Francisco: A.S.P. [vol. **70**]), p. 83–94.

(11) **Gary A. MAMON**: Workshop Summary, 1995, dans *STScI Workshop, "Groups of Galaxies"*, ed. O. G. Richter & K. Borne (San Francisco: A.S.P. [vol. **70**]), p. 173–181.

(12) **Gary A. MAMON**, Vincent BANCHET, Catherine BOISSON, Véronique CAYATTE & Frédéric ENGELMANN: A First Look at Galaxies with the DENIS Survey, 1995, dans *Euroconference on "Near-Infrared Sky Surveys"*, ed. P. Persi, W.B. Burton, N. Epchtein & A. Omont (*Mem. Soc. Astr. It.* **66**), p. 693–698.

(13) **Gary A. MAMON**: The Dynamics of Groups and Clusters of Galaxies and Links to Cosmology, 1996, dans *3rd Paris Cosmology Colloquium "Daniel Chalonge"*, ed. H. de Vega & N. Sánchez (Singapore: World Scientific), p. 95–119.

(14) **Gary A. MAMON**: The DENIS & 2MASS Near Infrared Surveys and their Applications in Cosmology, 1996, dans *XXXIst Moriond Meeting: "Dark Matter*

in Cosmology, Quantum Measurements, Experimental Gravitation", ed. R. Ansari, Y. Giraud-Héraud & J. Trân Thanh Vân (Gif-sur-Yvette: Frontières), p. 225–232

(15) **Gary A. MAMON**, Vincent BANCHET, Matthieu TRICOTTET & David KATZ : Preliminary Galaxy Extraction from DENIS Images, 1997, dans *Euroconference on "The Impact of Large-Scale Near-IR Sky Surveys"*, ed. F. Garzón, N. Epchtein, A. Omont, B. Burton & P. Persi (Dordrecht: Kluwer), p. 239–248

(16) **Gary A. MAMON**, Matthieu TRICOTTET, William BONIN & Vincent BANCHET : Galaxies and Cosmology with DENIS, 1997, dans *XVIIth Moriond Astrophysics Meeting, "Extragalactic Astronomy in the Infrared"*, ed. G. A. Mamon, T. X. Thuan & J. Tran Van Thanh (Paris : Frontières), p. 369–380

(17) **Gary A. MAMON**, Jean BORSENBERGER, Matthieu TRICOTTET & Vincent BANCHET : Galaxies with DENIS: Preliminary Star/Galaxy Separation and First Results, 1998, dans *3rd DENIS/2MASS Euroconference on "The Impact of Near-Infrared Surveys on Galactic and Extragalactic Astronomy"*, ed. N. Epchtein (Dordrecht: Kluwer), p. 177–192

(18) **Gary A. MAMON** : Theory of Galaxy Dynamics in Clusters and Groups, 2000, dans *XVth IAP Meeting on "Dynamics of Galaxies: from the Early Universe to the Present"*, ed. F. Combes, G.A. Mamon & V. Charmandaris (San Francisco: ASP [vol. **197**]), p. 377–387

V. Conférences internationales : Autres contributions invitées

(1) Paul HICKSON, Zoran NINKOV, John P. HUCHRA & **Gary A. MAMON** : The Structure of Compact Groups of Galaxies, 1984, dans *"Clusters and Groups of Galaxies"*, ed. F. Mardirossian, G. Giuricin, & M. Mezzetti (Dordrecht : Reidel), p. 367–373.

(2) **Gary A. MAMON** : Group Dynamics and Compact Groups, 1991, dans *IAU Symposium No. 146, "Dynamics of Galaxies and their Molecular Cloud Distributions"*, ed. F. Combes & F. Casoli, p. 394–396.

(3) **Gary A. MAMON** : The DENIS Survey and its Cosmological Applications, 1995, dans *35th Herstmonceaux Conference: "Wide-Field Spectroscopy and the Distant Universe"*, ed. S.J. Maddox & A. Aragón-Salamanca (Singapore : World Scientific), p. 73–80.

VI. Conférences internationales : Autres contributions orales

(1) **G. A. MAMON** : Compact Configurations within Small Evolving Groups of Galaxies, 1985, *Bulletin of the American Astronomical Society*, **17**, 601.

(2) A. E. GLASSGOLD & **G. MAMON** : Circumstellar Chemistry of Cool Evolved Stars, 1987, dans *IAU Symposium No. 122, "Circumstellar Matter"*, ed. I. Appenzeller & C. Jordan (Dordrecht : Reidel), p. 549–550.

(3) **Gary A. MAMON** : On the Applicability of the Tremaine-Richstone Statistics, 1987, *Bulletin of the American Astronomical Society*, **19**, 651.

(4) **Gary A. MAMON** : Explaining Compact Groups as Chance Alignments, 1990, dans *IAU Colloquium No. 124, "Paired and Interacting Galaxies"*, ed. J. W. Sulentic, W. C. Keel, & C. M. Telesco (Washington : NASA), p. 619–628.

(5) Alain BLANCHARD, David VALLS-GABAUD & Gary MAMON : Cosmic Structures : from Mass to Light, 1990, dans *Xth Moriond Astrophysical Meeting: "Particle Astrophysics. The Early Universe and Cosmic Structures"*, ed. J.-M. Alimi, A. Blanchard, A. Bouquet, F. Martin de Volnay & J. Trân Thanh Vân (Gif-sur-Yvette : Editions Frontières), p. 403–410.

(6) **Gary A. MAMON** : Are Cluster Ellipticals Formed by Mergers?, 1992, dans *XIIth Moriond Astrophysics Meeting: "Physics of Nearby Galaxies: Nature or Nurture?"*, ed. T.X. Thuan, C. Balkowski, and J. Trân Thanh Vân (Gif-sur-Yvette : Editions Frontières), p. 329–336.

(7) **Gary A. MAMON** : Are Compact Groups Dense Quartets?, 1992, dans *XIIth Moriond Astrophysics Meeting: "Physics of Nearby Galaxies: Nature or Nurture?"*, ed. T.X. Thuan, C. Balkowski, and J. Trân Thanh Vân (Gif-sur-Yvette : Editions Frontières), p. 367–374.

(8) **Gary A. MAMON** : The Galaxy Group/Cosmology Connections, 1994, dans *XIVth Moriond Astrophysics Meeting: "Clusters of Galaxies"*, ed. F. Durret, A. Mazure, & J. Tran Thanh Van (Gif-sur-Yvette : Editions Frontières), p. 291–296.

(9) **G. MAMON** : Galaxies with the DENIS 2 Micron Survey: A Preliminary Report, 1996, dans *"Spiral Galaxies in the Near-IR"*, ed. D. Minniti & H.-W. Rix (Garching : ESO), p. 195–199

(10) P. HÉRAUDEAU, F. SIMIEN & **G. MAMON** : Mass Models from Near-Infrared Surface Photometry, 1996, dans *"Spiral Galaxies in the Near-IR"*, ed. D. Minniti & H.-W. Rix (Garching : ESO), p. 235–239

(11) M.-L. MONTOYA, R. DOMÍNGUEZ-TENREIRO, G. GONZÁLEZ-CASADO, **G.A. MAMON**, E. SALVADOR-SOLÉ : Statistical Determination of the Profiles of Hickson's Compact Groups, 1996, dans *Sesto workshop "Observational Cosmology: From Galaxies to Galaxy Systems"*, ed. G. Giuricin, M. Mezzetti & F. Mardirossian, sous presse

(12) Quentin A. PARKER, Matthew COLLESS & **G. MAMON** : The UKST FLAIR-DENIS Redshift Survey, 1996, dans *Wide Field Spectroscopy*, eds M. Kontizas & E. Kontizas, (Dordrecht: Kluwer), p. 303–304

(13) A. SCHRÖDER, R.C. KRAAN-KORTEWEG, **G. A. MAMON** & S. RUPHY : DENIS Galaxies in the Zone of Avoidance, 1997, dans *XVIIth Moriond Astrophysics Meeting "Extragalactic Astronomy in the Infrared"*, ed. G. A. Mamon, T. X. Thuan & J. Tran Van Thanh (Paris : Frontières), p. 381–386

(14) R.C. KRAAN-KORTEWEG, A. SCHRÖDER, **G. A. MAMON** & S. RUPHY : Large-Scale Structures Behind the Milky Way from Near-IR Surveys, 1998, dans *3rd DENIS/2MASS Euroconference on "The Impact of Near-Infrared Surveys on Galactic and Extragalactic Astronomy"*, ed. N. Epchtein (Dordrecht: Kluwer), p. 209–220

(15) **Gary A. MAMON** : The Wide-Field DENIS Near-IR Imaging Survey and 6dF Redshift and Peculiar Velocity Surveys, 1998, dans *XIVth IAP Meeting: "Wide-Field Surveys in Cosmology"*, ed. S. Colombi, Y. Mellier & B. Raban (Paris : Frontières), p. 323–326

(16) A. SCHRÖDER, R.C. KRAAN-KORTEWEG & **G. A. MAMON** : Near-Infrared Determination of Large-Scale Structures in the Zone of Avoidance, 1998, dans ASP vol. 151 *Cosmic Microwave Background and Large Scale Structure of the Universe"*, ed. Y. I. Byun & K. W. Ng (San Francisco : A.S.P. [vol. **151**]), p. 99

(17) **G. A. MAMON**: Near-Infrared Galaxy Surveys in 2D, 3D & 4D, 2000, dans *"Cosmic Flows 1999: Towards an Understanding of Large-Scale Structure"*, ed. S. Courteau, M. Strauss & J. Willick (San Francisco: A.S.P. [vol. **201**]), p. 103–106

(18) **G. A. MAMON**: Understanding Low and High Velocity Dispersion Compact Groups, 2000, dans IAU colloq. 174 *"Small Galaxy Groups"*, ed. M. Valtonen & C. Flynn (San Francisco: A.S.P.), sous presse

(19) Anja SCHRÖDER, Renée C. KRAAN-KORTEWEG & **Gary A. MAMON**: Multi-wavelength observations of galaxies in the Zone of Avoidance, 2000, dans *"Mapping the Hidden Universe: The Universe behind the Milky Way — The Universe in HI"*, ed. R. C. Kraan-Korteweg, P. A. Henning & H. Andernach (San Francisco: A.S.P.), sous presse

VII. Conférences internationales : Posters

(1) **Gary A. MAMON**: Kinematic Modelling of NGC 3379, 1983, dans *IAU Symposium No. 100, "Internal Kinematics and Dynamics of Galaxies"* ed. E. Athanassoula (Dordrecht: Reidel), p. 295–296.

(2) Paul HICKSON, Zoran NINKOV & **Gary A. MAMON**: The Shapes of Compact Groups of Galaxies, 1983, *Bulletin of the American Astronomical Society*, **15**, p. 619.

(3) **Gary A. MAMON**: Biases in Mass Estimates of Groups of Galaxies, 1986, dans *IAU Symposium No. 117, "Dark Matter in the Universe"*, ed. J. Kormendy & G. R. Knapp (Dordrecht: Reidel), p. 114.

(4) **Gary A. MAMON**: Merger Rates in Simulated and Observed Groups of Galaxies, 1988, dans *IAU Symposium No. 130, "Large Scale Structure of the Universe"*, ed. J. Audouze, M.-C. Pelletan, & A. Szalay (Dordrecht: Kluwer), 545.

(5) A. E. GLASSGOLD, **G. A. MAMON**, & P. J. HUGGINS: The Photodissociation of CO in Circumstellar Envelopes, 1988, dans *"Interstellar Matter"*, ed. J. M. Moran & P. T. P. Ho (New York: Gordon and Breach), p. 219–220.

(6) A. E. GLASSGOLD & **G. A. MAMON**: The Distribution of Cyanoacetylene in IRC +10216, 1988, dans *"Interstellar Matter"*, ed. J. M. Moran & P. T. P. Ho (New York: Gordon and Breach), p. 221–222.

(7) **Gary A. MAMON** & Daniel GERBAL: Are Cluster Ellipticals Formed by Mergers?, 1991, dans *IAU Symposium No. 146, "Dynamics of Galaxies and their Molecular Cloud Distributions"*, ved. F. Combes & F. Casoli (Dordrecht: Kluwer), p. 376.

(8) Robin HARMON & Gary MAMON: The Detection of Galaxies in Infrared Surveys, 1993, dans *Sky Surveys: Protostars to Protogalaxies*, ed. B.T. Soifer (San Francisco: A.S.P. [vol.**43**]), p. 15–18.

(9) D. VALLS-GABAUD, A. BLANCHARD & **G.A. MAMON**: The Evolution of the Intergalactic Medium and the Origin of the Galaxy Luminosity Function, 1993, dans *The Evolution of Galaxies and their Environment*, ed. D. Hollenbach, J.M. Shull & H.A. Thronson (Washington: NASA), p. 113–114.

(10) Guillermo GONZÁLEZ-CASADO, **Gary A. MAMON**, & Eduard SALVADOR-SOLÉ: Dynamics of Substructures Immersed in Galaxy Clusters, 1994, dans *XIVth Moriond Astrophysics Meeting: "Clusters of Galaxies"*, ed. F. Durret, A. Mazure, & J. Tran Thanh Van (Gif-sur-Yvette: Editions Frontières), p. 395–396.

(11) P. HÉRAUDEAU, F. SIMIEN & **G.A. MAMON** : Multiband Analysis of Central-Region Features, 1996, dans *"Spiral Galaxies in the Near-IR"*, ed. D. Minniti & H.-W. Rix (Garching : ESO), p. 248–249.

(12) M.-L. MONTOYA, R. DOMÍNGUEZ-TENREIRO, G. GONZÁLEZ-CASADO, **G.A. MAMON**, E. SALVADOR-SOLÉ : The Structure of Compact Groups of Galaxies, 1996, dans *"Clustering in the Universe"*, ed. A. Blanchard, S. Maurogordato & J. Tran Thanh Van (Gif-sur-Yvette : Editions Frontières), sous presse.

(13) B. LANZONI, **G.A. MAMON** & B. GUIDERDONI : Dark Matter Halos Merging Trees: the Merging Cell Model in a CDM Cosmology, 2000, dans *XVth IAP Meeting on "Dynamics of Galaxies: from the Early Universe to the Present"*, ed. F. Combes, G.A. Mamon & V. Charmandaris (San Francisco: ASP [vol. **197**]), p. 137–138

VIII. Articles de vulgarisation

(1) **Gary MAMON** : Controverses sur les groupes compacts de galaxies, 1996, *Quintessences*, **8**, 5–6

IX. Conférences de vulgarisation

(1) The distant Universe, Princeton, Octobre 1979.

(2) La cosmologie de Maïmonide, Octobre 1995, Institut d'Astrophysique.

(3) Les formes des galaxies et leurs origines, Septembre 1996, Institut d'Astrophysique.

(4) L'Univers en questions, Octobre 1996, Institut d'Astrophysique (dans le cadre de la Science en Fête).

X. Cours donnés

(1) Tout ce que vous avec toujours voulu savoir sur UNIX sans jamais oser le demander, Février 1993 (2h30), DAEC, Observatoire de Meudon.

(2) Comment Extraire un Catalogue Homogène de Galaxies des Images DENIS?, Septembre 1993 (1h), Ecole de Cosmologie, Centre de Physique Théorique, Luminy.

(3) L'Univers en infra-rouge proche et le survey DENIS, Septembre 1994 (2h), Ecole de Cosmologie, Centre de Physique Théorique, Luminy.

(4) Tout ce que vous avec toujours voulu savoir sur UNIX sans jamais oser le demander, Avril 1995 (3h30), Institut d'Astrophysique.

(5) L'Univers en infra-rouge proche et le survey DENIS, Novembre 1995 (1h), Ecole de Cosmologie, Garchy

(6) Groupes compacts et cosmologie, Novembre 1995 (1h), Ecole de Cosmologie, Garchy

(7) La dynamique de groupes et amas de galaxies, Septembre 1998 (4h30), Ecole de Cosmologie, Centre de Physique Théorique, Luminy

(8) Dynamique gravitationnelle des systèmes sphériques en astrophysique : amas globulaires, galaxies elliptiques et amas de galaxies, Janvier–Mars 2000 (18h), DEA Astronomie Fondamentale, Mécanique Céleste et Géodésie, Paris

XI. Thèses

(1) A Study of the Solar Variability, thèse de S.B. (licence), Département de Physique, *Massachusetts Institute of Technology*, Juin 1979.

(2) Compact Configurations within Small Evolving Groups of Galaxies, thèse de Ph.D. (doctorat), Département de Sciences Astrophysiques, *Princeton University*, Avril 1985.

XII. Séminaires

(1) The shapes of compact groups of galaxies, Avril 1983, Princeton University (Etats-Unis)

(2) Compact groups of galaxies, Mai 1985, New York University (Etats-Unis)

(3) Are compact groups physically dense?, Août 1985, Dominion Astrophysical Observatory (Canada)

(4) Les groupes compacts sont-ils physiquement denses?, Octobre 1985, Institut d'Astrophysique de Paris

(5) La dynamique des groupes de galaxies, Octobre 1985, DAEC, Observatoire de Meudon

(6) Are compact groups physically dense?, Octobre 1985, Kapteyn Institut (Groningen, Pays-Bas)

(7) Les groupes compacts de galaxies, Octobre 1985, Observatoire de Lyon

(8) Les groupes compacts de galaxies, Octobre 1985, Observatoire de Grenoble

(9) Les groupes compacts de galaxies, Avril 1986, Observatoire de Toulouse

(10) The chemistry of circumstellar envelopes, Février 1987, Harvard-Smithsonian Center for Astrophysics (Etats-Unis)

(11) La chimie des enveloppes circumstellaires, Juin 1987 DASGAL, Observatoire de Meudon

(12) Are compact groups of galaxies physically dense?, Septembre 1987, Columbia University (New York, Etats-Unis)

(13) POST: a polar specialized telescope, Février 1989, New York University (Etats-Unis)

(14) Are cluster ellipticals formed by mergers?, Mai 1991, University of California at Berkeley (Etats-Unis)

(15) Les elliptiques d'amas sont-elles produits de fusions?, Juillet 1991, DARC, Observatoire de Meudon

(16) Compact groups of galaxies, Décembre 1991, Universitat de Barcelona (Espagne)

(17) The DENIS 2 micron survey, Décembre 1991, Universitat de Barcelona (Espagne)

(18) Les elliptiques d'amas sont-elles produits de fusions?, Février 1992, Institut d'Astrophysique de Paris

(19) Cosmic mass and luminosity functions and the thermal history of the IGM, Avril 1992, Universita di Roma 2 (Italie)

(20) Les elliptiques d'amas sont-elles produits de fusions?, Mai 1992, Observatoire de Lyon

(21) The DENIS 2 micron survey, Juin 1992, New York University (Etats-Unis)

(22) Are cluster ellipticals the products of mergers?, Décembre 1992, Princeton University (Etats-Unis)

(23) Les premières contributions de Hubble, Février 1993, Observatoire de Meudon (séminaire Histoire de la Cosmologie)

(24) Cosmological infall, tidal shocks, galaxy mergers, and the formation of ellipticals in clusters of galaxies, Février 1993, Universitat de Barcelona (Espagne)

(25) The dynamics of groups and clusters of galaxies, Avril 1993, Sterrwacht Leiden (Pays-Bas)

(26) Dynamique des groupes et amas et évolution morphologique des galaxies, Mai 1993, Observatoire de Meudon (séminaire de l'observatoire)

(27) Le projet DENIS et ses applications extra-galactiques, Juin 1993, Observatoire Midi-Pyrénées (Toulouse)

(28) La cosmologie de Maïmonide, Octobre 1993, Observatoire de Meudon (séminaire Histoire de la Cosmologie)

(29) The nature and masses of groups of galaxies, Novembre 1993, Landeswarte Heidelberg (Allemagne)

(30) How to determine the cosmological state and mass of a given group of galaxies, Janvier 1994, Max Planck Institut für Astrophysik, Garching (Allemagne)

(31) How to determine the cosmological state and mass of a given group of galaxies, Février 1994, New York University, New York (Etats-Unis)

(32) How to determine the cosmological state and mass of a given group of galaxies, Février 1994, Harvard-Smithsonian Center for Astrophysics, Cambridge (Etats-Unis)

(33) How to determine the cosmological state and mass of a given group of galaxies, Février 1994, University of Alabama, Tuscaloosa (Etats-Unis)

(34) Groupes de galaxies et cosmologie, Mai 1994, Ecole Normale Supérieure de Lyon

(35) The DENIS 2 micron survey, Janvier 1995, Osservatorio di Roma, Monteporzio (Italie)

(36) The DENIS 2 micron survey and its extragalactic applications, Avril 1995, Center for Particle Astrophysics, University of California, Berkeley (Etats-Unis)

(37) The DENIS 2 micron survey, Avril 1995, Lawrence Berkeley Laboratories (Etats-Unis)

(38) Groups of galaxies and cosmology, Avril 1995, Lawrence Berkeley Laboratories (Etats-Unis)

(39) A unified theory of groups of galaxies, Avril 1995, University of Michigan (Etats-Unis)

(40) La nature des groupes compacts de galaxies contrainte par la cosmologie et les observations en rayons X, Février 1996, Laboratoire Astronomique Spatiale (Marseille)

(41) The FLAIR-DENIS Survey, Décembre 1996, Anglo-Australian Observatory à Coonabarabran (Australie)

(42) The 6DF: Large spectroscopic survey of DENIS NIR-selected galaxies with a new robotic multi-fibre instrument on the UK Schmidt Telescope, Septembre 1997, Institute of Astronomy, Université de Cambridge (Royaume-Uni)

(43) Counting galaxies with the DENIS NIR survey, Mars 1998, Observatoire du Mont-Stromlo (Australie)

(44) Galaxies et cosmologie avec le sondage DENIS et les suivis spectroscopiques à Nançay et avec le 6dF en Australie, Mai 1998, DAEC, Observatoire de Meudon

(45) Contraintes X et cosmologiques sur la nature des groupes compacts de galaxies, Mars 2000, Observatoire de la Côte d'Azur